

**NASA TECHNICAL
MEMORANDUM**

NASA TM X- 64652

**HIGH ENERGY ASTRONOMY OBSERVATORY
MISSION C
PHASE A FINAL REPORT**

Volume III - Appendices

(NASA-TM-X-64652-Vol-3) HIGH ENERGY
ASTRONOMY OBSERVATORY, MISSION C, PHASE A.
VOLUME 3: APPENDICES Final Report (NASA)
Jan. 1972 698 p CACL 14B

N72-21284

Unclas
23555
G3/11

By Program Development

January 1972

NASA



*George C. Marshall Space Flight Center
Marshall Space Flight Center, Alabama*

TABLE OF CONTENTS

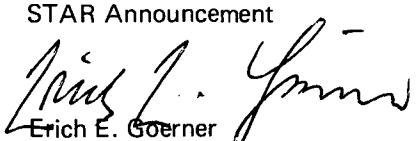
VOLUME I — EXECUTIVE SUMMARY

VOLUME II — PRELIMINARY ANALYSES AND CONCEPTUAL DESIGN

- Chapter I — Introduction
- Chapter II — Baseline Experiments for HEAO-C Phase A Study
- Chapter III — Mission Analysis
- Chapter IV — Observatory Baseline Design
- Chapter V — Structural Analysis
- Chapter VI — Thermal Control System
- Chapter VII — Attitude Sensing and Control System
- Chapter VIII — Electrical System
- Chapter IX — Communication and Data Handling System
- Chapter X — Space Shuttle Launch and Retrieval of HEAO-C

VOLUME III — APPENDICES

- Appendix A — Alternate Experiments for HEAO-C
- Appendix B — Mission Analysis and Launch Vehicle
- Appendix C — Alternate Observatory Configurations
- Appendix D — Thermal Control Trade Studies and Supporting Analyses
- Appendix E — Attitude Sensing and Control Analyses
- Appendix F — Electrical Systems
- Appendix G — Reliability Analysis

1. REPORT NO. TM X-64652		2. GOVERNMENT ACCESSION NO.		3. RECIPIENT'S CATALOG NO.	
4. TITLE AND SUBTITLE High Energy Astronomy Observatory, Mission C, Phase A Final Report Volume III - Appendices				5. REPORT DATE January 1972	
				6. PERFORMING ORGANIZATION CODE	
7. AUTHOR(S) Program Development				8. PERFORMING ORGANIZATION REPORT #	
9. PERFORMING ORGANIZATION NAME AND ADDRESS George C. Marshall Space Flight Center Marshall Space Flight Center, Alabama 35812				10. WORK UNIT NO.	
				11. CONTRACT OR GRANT NO.	
12. SPONSORING AGENCY NAME AND ADDRESS National Aeronautics and Space Administration Washington, D.C. 20546				13. TYPE OF REPORT & PERIOD COVERED Technical Memorandum	
				14. SPONSORING AGENCY CODE	
15. SUPPLEMENTARY NOTES Prepared by Preliminary Design Office, Program Development. This document is one of three volumes.					
16. ABSTRACT <p>In response to a request from the Office of Space Science, a Phase A study of the High Energy Astronomy Observatory Mission-C (HEAO-C) was undertaken by the George C. Marshall Space Flight Center. Results of this study are reported in three volumes, Volume I containing an executive summary, Volume II containing the preliminary analyses and conceptual design of a baseline mission and spacecraft, and Volume III containing supporting technical data and experiment and spacecraft alternatives.</p> <p>The HEAO-C is the third of four planned missions in the High Energy Astronomy Program. The primary objective of the first two missions, HEAO-A and -B, is a scanning survey of the celestial sphere to study X rays, gamma rays, and cosmic rays, and to map locations of high energy sources; the primary objective of HEAO-C is a detailed study of the more interesting high energy sources, using grazing-incidence X-ray telescopes and a spacecraft pointing accuracy of ± 1 arc minute.</p> <p>A principal design goal for the HEAO-C spacecraft was to maximize commonality with the spacecraft designed for Missions A and B; technical transfusion between the designs required the Phase A study to be accomplished in parallel with the Phase B definition of the precursor spacecraft. Plans call for a HEAO-C launch between 1 and 1½ years after the launch of HEAO-B.</p> <p>The HEAO-C will be launched from ETR on the Titan IIID and placed into a 270 nautical mile circular orbit with a 28.5 degree inclination; the Phase A baseline concept weighs under 16 000 pounds, provides the required ± 1 arc minute pointing accuracy, carries three grazing-incidence X-ray telescopes with multiple focal plane experiments plus several supporting experiments, and is designed for a two year operational life. The HEAO-C is a candidate for early satellite retrieval with the Space Shuttle.</p>					
17. KEY WORDS High Energy Astronomy Observatory Scientific Satellite High Energy Space Physics Conceptual Satellite Design Unmanned Spacecraft			18. DISTRIBUTION STATEMENT STAR Announcement  Erich E. Goerner Director, Preliminary Design Office		
19. SECURITY CLASSIF. (of this report) Unclassified		20. SECURITY CLASSIF. (of this page) Unclassified		21. NO. OF PAGES 682	22. PRICE \$9.00

ACKNOWLEDGMENTS

Phase A program management was assigned to the Space Physics Group in the Mission and Payload Planning Office of Marshall Space Flight Center's Program Development Organization. Program Development's Preliminary Design Office was assigned responsibility for the Phase A technical analyses and engineering design; the Program Planning Office assisted with cost analyses and trades; and Program Development's HEAO Task Team (now Program Management's HEAO Office) provided the required liaison with the Phase B contractors for HEAO missions A and B.

Science and Engineering's Laboratories gave valued consultation and support in many technical areas; of special note was the assistance of the Space Sciences Laboratory in the area of experiment requirements and the Astronautics Laboratory and Product Engineering and Process Technology Laboratory in the area of materials selection.

Grateful acknowledgment is made of the excellent efforts of MSFC's support contractor team. Teledyne Brown Engineering, under Contract NAS8-20073, made substantial contributions throughout the study and much of their design and analysis effort is incorporated in this final report.

The Physics and Astronomy Division of OSS worked closely with MSFC in establishing appropriate mission objectives and requirements and assigned the experiment complements to be investigated — both for the baseline concept and the candidate alternatives.

The following MSFC personnel were principal contributors to the study in the areas noted:

Overall Study Management	Mr. John M. Butler, Jr.	PD-DO-SI
	Mr. Carroll C. Dailey	PM-HE-X
	Mr. James W. Heyer	PD-DO-DIR
HEAO-C Experiments (Chapter II and Appendix A)	Mr. Carroll C. Dailey	PM-HE-X
	Mr. Stephen O. Larson	PD-MP-S
	Mr. Harold S. Manning	PD-DO-MT
	Mr. Richard A. Potter	PD-MP-S

Mission Analysis (Chapter III and Appendix B)	Mr. Rodney Bradford	PD-DO-PM
	Mr. Von L. Burton	PD-DO-PA
	Mr. Thomas C. French	PD-DO-PM
	Mr. John L. Fults	PD-DO-PA
	Mr. Richard I. Gold	PD-DO-PM
	Mr. Elbert L. Sullivan	PD-DO-PA
	Mr. Tommy J. Wheeler	PD-DO-PM
	Mr. Archie C. Young	PD-DO-PM
Observatory Design (Chapter IV and Appendix C)	Mr. D. Henry Black	PD-DO-SL
	Mr. Josef F. Blumrich	PD-DO-SL
	Mr. John M. Butler, Jr.	PD-DO-SI
	Mr. Carl E. Colley	PD-DO-SA
	Mr. Jerry A. Peoples	PD-DO-SI
	Mr. Jay D. Willard	PD-DO-SL
Structures (Chapter V)	Mr. Carl E. Colley	PD-DO-SA
Thermal Control (Chapter VI and Appendix D)	Mr. Carl G. Fritz	PD-DO-MT
	Mr. Gustav W. Mordan	PD-DO-MT
Attitude Sensing and Control (Chapter VII and Appendix E)	Mr. Billy G. Davis	PD-DO-ES
	Mr. Onis C. Green	PD-DO-ES
	Mr. William B. Price	PD-DO-MP
	Mr. David M. Schultz	PD-DO-ES
Electrical Power (Chapter VIII and Appendix F)	Mr. Richard J. Boehme	PD-DO-EP
	Mr. Robert W. Rood	PD-DO-EP
Communications and Data Handling (Chapter IX)	Mr. Edward C. Hamilton	PD-DO-EC
Reliability (Appendix G)	Dr. James W. Steincamp	PD-DO-ES

Space Shuttle Launch and Retrieval
(Chapter X)

Mr. D. Henry Black	PD-DO-SL
Mr. Josef F. Blumrich	PD-DO-SL
Mr. John M. Butler, Jr.	PD-DO-SI

Technical Editor

Mrs. Frances M. Andrews PD-DO-DIR

LIST OF ACRONYMS

ABR	analog bay rack
ACN	Ascension Island
AD	aspect detector
A/D	analog-to-digital
AGC	automatic gain control
AGE	automatic ground equipment
ASCS	attitude sensing and control system
AS&C	attitude sensing and control (system)
AS&E	American Science and Engineering
ATA	automatic threshold adjust (cell)
ATM	Apollo Telescope Mount
BCD	binary code digital
bdc	brushless dc
BDX	Bendix Aerospace Corporation
BECO	Teledyne Brown Engineering
B/Ep	boron/epoxy
BER	bit error rate
BOL	beginning-of-life
B/S/L	ball joints, shock mounts, and linkages (baseline bench mounting concept)

LIST OF ACRONYMS (Continued)

CCS	curved crystal spectrometer
C&DH	communication and data handling (system)
CFD	coarse flare detector
CG	center of gravity
CINDA	Chryster Improved Numerical Differencing Analyzer (computer program)
CIU	cable interface unit
CMD	command
CMG	control moment gyro
COMM	communication (system)
COTA	circle of total access
CP	central processor
CRA	celestial reference assembly
CRO	Carnarvon
CSM	command and service module
CYI	Canary Island
D/A	digital-to-analog
DBR	digital bay rack
DCU	digital computer unit
DHS	data handling system

LIST OF ACRONYMS (Continued)

DOD	depth-of-discharge
DSS	digital sun sensor
ECA	electrical control assembly
EDCS	electrical distribution and control subsystem
EIA	electrical integration assembly
EMI	electromagnetic interference
EOM	end-of-mission
EPS	electrical power system
ERTS	Earth Resources Technology Satellite
ESE	electrical support equipment
ESM	estimated secular momentum
ETR	Eastern Test Range
EVA	extravehicular activity
FCS	flat crystal spectrometer
FFD	fine flare detector
FHST	fixed-head star tracker
FOV	field of view
FST	fixed star tracker
FW	full width

LIST OF ACRONYMS (Continued)

FWHM	full width half maximum
FWHR	filter wheel high resolution (telescope)
FWLA	filter wheel large area (telescope)
FWLE	filter wheel low energy (telescope)
GAC	Grumman Aerospace Corporation
GEP	Goddard Experiment Package
g.g.	gravity gradient
Gr/Ep	graphite/epoxy
GSE	ground support equipment
GSFC	Goddard Space Flight Center
GST	gimbal star tracker
GWM	Guam
HAW	Hawaii
HEAO	High Energy Astronomy Observatory
HR	high resolution (telescope)
HRID	HR Imaging detector
I/O	input/output
IRIG	inertial rate-integrating gyro
ITL	integrate-transfer-launch

LIST OF ACRONYMS (Continued)

ITT	International Telephone and Telegraph
JPL	Jet Propulsion Laboratory
KSC	Kennedy Space Center
LA	large area (telescope)
LAIID	large area image detector
LBD	low background detector
LE	low energy (telescope)
LHCP	left-hand circular polarization
LMSC	Lockheed Missiles and Space Company
LON	lines of nodes
LOS	line of sight
LSI	large scale integration
MC	maximum contribution (CMG steering law)
MIB	minimum impulse bit
MIT	Massachusetts Institute of Technology
MOCC	missions operation control center
MPC	monitor proportional counter
MSFC	Marshall Space Flight Center
MSFN	Manned Space Flight Network

LIST OF ACRONYMS (Continued)

MTBF	mean time before failure
MUX	multiplexer
NAD	Naval Ammunition Depot (Crane, Ind.)
NEA	noise equivalent angle
NRZ	non-return-to-zero (pulse recording)
OAM	orbit adjust module
OAS	orbit adjust stage
ODC	optical data corrector
OG	objective grating
OU	optical unit
PCM	(1) pulse code modulator (encoder) (2) phase change materials
PEP	perpendicular to the ecliptic plane
PI	principal investigator
PLF	payload fairing
POP	perpendicular to the orbital plane
PRN	pseudo random noise
PSD	position sensitive detector
PSI	Pressure Systems Incorporated
PSK	phase shift keyed (demodulator)

LIST OF ACRONYMS (Continued)

RCM	reaction control module
RCS	reaction control system
REA	reaction engine assembly
REM	reaction engine module
RF	radio frequency
RFI	radio frequency interference
RGA	reference gyro assembly
RHCP	right-hand circular polarization
ROM	read-only memory
rss	root-sum-square
RTG	radioisotope thermoelectric generator
RZ	return-to-zero (pulse recording)
SΦM	split phase mark
SAN	Santiago
S/C	spacecraft
SCS	Satellite Control Section
SEC	secondary electron conduction (vidicon)
S/L	shock/link (concept)
SMAB	Solid Motor Assembly Building

LIST OF ACRONYMS (Concluded)

SPG	single-point ground
SRM	solid rocket motor
SSD	solid state detector
STADAN	Space Tracking and Data Acquisition Network
STPAN	Stiffened Panels (computer program)
STRESS	Structural Engineering Systems Solves (computer program)
SUVT	small ultraviolet telescope
TA	transfer assembly
TACS	thruster attitude control simulation
TCA	(1) thrust chamber assembly (2) tank control assembly (electrical system)
TCV	thrust chamber valve
TEX	Texas
TRW	TRW Systems, Inc.
UV	ultraviolet
VFC	voltage to frequency converter
VGP	vehicle ground point
WASS	wide angle sun sensor

TABLE OF CONTENTS

	Page
Experiments	A-1
1. List of Alternate Experiments	A-1
2. Experiment Parameters	A-1
3. Description of Experiments and Scientific Objectives	A-5
a. Goddard Experiment Package (GEP)	A-5
b. Fine Guidance System	A-6
c. Small Ultraviolet Telescope (SUVT)	A-7
General Experiment Information	A-7
1. South Atlantic Anomaly Effects	A-7
2. Gas Purges and Quenching Gas Quantities Required	A-7
3. Calibration	A-7
4. Launch Environment	A-7
5. Spacecraft Degraded Modes Operation	A-7

LIST OF TABLES

Table	Title	Page
A-1.	Alternate Experiments and Abbreviations	A-1
A-2.	Experiment Field of View, Size, Weight, and Power	A-2
A-3.	Requirements and Specifications of the Alternate Experiments	A-3
A-4.	Wavelength Sensitivities of Detectors	A-6

APPENDIX A. ALTERNATE EXPERIMENTS FOR HEAO-C

Experiments

1. List of Alternate Experiments. The feasibility of orbiting the following alternate experiments on HEAO-C was examined during this study. The experiments are listed in Table A-1 with the abbreviations used for them in the study and the type of measurement of which the experiment is capable. The specific combinations of the alternate experiments investigated in this study are defined in Appendix C with the results of the assessments.

TABLE A-1. ALTERNATE EXPERIMENTS AND ABBREVIATIONS

Experiment Hardware	Abbreviation	Type Of Measurement
Large Ultraviolet (UV) Telescope (38 in.) (Goddard Experiment Package)	GEP	Grating Spectrometry
Optical Unit	OU	
Analog Bay Rack	ABR	
Digital Bay Rack	DBR	
Small Ultraviolet (UV) Telescope (18 in.)	SUVT	

2. Experiment Parameters. Table A-2 lists the field of view, size, weight, and power of the alternate experiments. Table A-3 lists the requirements which the telescope packages place on the spacecraft. Since the SUVT is not well defined, many of the parameters and requirements listed under it are simply repetitions of the same parameters and requirements as for the GEP. This is because the GEP is an existing piece of hardware and its parameters and requirements are well known.

TABLE A-2. EXPERIMENT FIELD OF VIEW, SIZE, WEIGHT, AND POWER

Experiment Components	Field of View (Total Angle) (deg)	Size H × W × L (in.)	Total Weight (lb)	Average Power (W)	
				Inside Tube	Outside Tube
Large UV Telescope (GEP) (38 in.)				38 ^a	
Optical Unit	0.1	40 diam × 113 long	881		
Analog Bay Rack		6 × 18 × 18	43		
Digital Bay Rack		6 × 18 × 18	59		
Small UV Telescope (18 in.)	0.33	20 diam × 52 long	214	6 (camera)	

a. 60 W peak for 10 min per orbit (both these figures are for the entire GEP).

TABLE A-3. REQUIREMENTS AND SPECIFICATIONS OF THE ALTERNATE EXPERIMENTS

Principal Investigator	Principal Institution	Other Institutions	Experiment	Wavelength Range (Å)	Energy Range (keV)	Resolution	Typical Observing Program (Note: Normal daytime viewing band is ±15 deg, with capability of ±30 deg once per day for one orbit; ±15 deg max roll about optical axis.)	Expected Max Duration Of Pointing Per Target	Alignment	2 Axis Pointing Accuracy	Pointing Accuracy About Optical Axis	2 Axis Pointing Stability	Pointing Stability About Optical Axis	Max Allowable 2 Axis Pointing Jitter Rate	Max Allowable Rotation Rate About Optical Axis While Pointing	3 Axis Pointing Aspect Accuracy (for ground use) Note: Giacomini provides ±1 arc sec	Precision Slew Or Scan Maneuvers	Clock Resolution	Clock Accuracy	Clock Stability	Long-Term Drift Rate	Short-Term Drift Rate	Temperature Limits	Deflection Limits Lateral	Deflection Limits Longitudinal	Radiation Limits	Launch Environments	Command Requirements	Command Execution Time	Command Format	RFI Requirements	Meteoroid Protection Required	Magnetic Field Limits ^m	Size (in.)	Weight (lb)	Focal Length (in.)	Power Required (W) (Standby)	Power Required (W) (Average)	Power Required (W) (Peak)	Data Rate Required (kbs)	Voltage (Vdc)	Field of View (deg)		
R. Giacomini	AS&EA	Columbia University GSFC MITd	X-Ray Telescopes: High Resolution Telescope (HR) Large Area Telescope (LA)	3.1 - 62 (focal plane expts.)	4.0 - 0.2	≈1 arc sec max Variable, a few arc sec to 1 deg	≈1 source/orbit 1 source/orbit (nighttime hemisphere preferred)	≈ one-half orbit continuous typical; 1 week max integral viewing time ^e	(f)	(f)	No spec. f	No spec. f	1 to 5 arc sec per one-half orbit ^h	1 to 5 arc sec per one-half orbit ^h	1 arc sec per sec	1.5 arc min per sec ⁱ	Commensurate with pointing accuracy	Commensurate with pointing accuracy	Not required	1 msec	0.1 msec	±5 × 10 ⁻⁹ per day (-40°C to +70°C) +2 × 10 ⁻¹⁰ per sec (at constant ambient)	No spec.	No spec.	Bench temperature limits to be determined during study by deflection limits. Lens transverse limits ±5° F. Lens axial limits ±2.5° F.	±0.04 in. across each tube (allow only 0.005 of this for thermal)	±0.04 in. along HR tube; ±0.04 in. along LA tube	No spec.	No spec.	Titan OK (shock mounts may be required)	300	1 sec in 24 hr	24 text bits, 6 access code bits	No spec.	No spec.	No spec.	HR 315×45 diam (+ exp. box corner) LA 343×45 diam (+ exp. box corner)	5456 (excl. structure)	240 (HR) 312 (LA)	130 (including 81 W computer) 128 (including 81 W computer)	140 (including 81 W computer)	20	28 ±2	≈ 1 (lens) ⁿ
J. Underwood	GSFC ^b	MSFC University College London Cambridge University	X-Ray Telescopes: Large UV Telescope (LE) GEP	20 - 400	0.62 - 0.124	Variable, a few arc sec to 1 deg	1 source/orbit (nighttime hemisphere preferred)	≈ one-half orbit continuous (nighttime pointing only preferred)	(f)	(f)	No spec. f	No spec. f	1 to 5 arc sec per one-half orbit ^h	1 to 5 arc sec per one-half orbit ^h	0.1 msec	No spec.	15°C ±5°C external	Unknown	No spec.	1 msec	0.1 msec	1 msec per orbit	No spec.	No spec.	15°C ±5°C external	≈ 1 - 5 arc min	Unknown	No spec.	Titan OK	64	Unknown	24 text bits, 6 access code bits	Assumes ATMk specs.	Not required	1 Cursted	120 long × 24 diam	840 (incl. structure)	70	130 (including 81 W computer) None scientifically; possibly needed thermally	128 (including 81 W computer)	50	< 1	28 ±2	1.5 (lens) ⁿ
A. Bogress	GSFC ^b	None	Small UV Telescope	1150 - 3200	0.0107 - 0.0039	0.1 Å; 6 Å	≈ 1 source/orbit	≈ 0.5 hr typical, 6 hr max	(f)	(f)	No spec. f	No spec. f	±3 arc sec ^h	±1 arc min ^h	12.5 msec	No spec.	70° F ±10° F	No spec.	0.01 msec	0.02 msec	10% in 1 min	No spec.	No spec.	Spectrograph and primary mirror; 0°C ±10°C	No spec.	Unknown	Not required	Not required	135	15 sec in 24 hr	24 text bits, 6 access code bits	OAO specs.	No spec.	12 G	113 long × 40 diam	983 (incl. structure)	60	6 (camera-detector)	60 (for 10 min per orbit)	≈ 2	28 ±2	0.1 (lens) ⁿ		

A-3

a. American Science and Engineering.
b. Goddard Space Flight Center.
c. Marshall Space Flight Center.
d. Massachusetts Institute of Technology.
e. Interruptions of up to 2 min per orbit are permissible.
f. Maintain alignment of telescopes and miscellaneous experiments within ±1 arc min of each other; point spacecraft reference axis with 2 axis pointing accuracy of ±1 arc min.
g. Present attitude sensing and control system pointing accuracy about spacecraft reference axis is ±5 arc min.
h. Use Giacomini requirements for purposes of this study.
i. Present attitude sensing and control system constraints are ±5 arc min pointing stability about optical axis and ±5 arc sec per sec rotation rate about optical axis while pointing.
j. These represent maximum allowable relative shift between detector and focal point, (absolute expansion of either is not limited); allow only one-half of this for thermal.
k. Apollo Telescope Mount.
l. Orbital Astronomy Observatory.
m. The telescopes and miscellaneous experiments should be compatible with typical field profiles inside the spacecraft.
n. See Table A-2 for detector fields of view.

FOLDOUT FRAME 3

FOLDOUT FRAME 2

FOLDOUT FRAME 1

3. Description of Experiments and Scientific Objectives

a. Goddard Experiment Package (GEP). The major scientific portion of the GEP is the UV telescope and its spectrometer. The purpose of the spectrometer experiment is to obtain ultraviolet spectra (at 2 Å resolution where possible) of selected stars and nebulae in the spectral range of from 1100 Å to 4267 Å. This wavelength range is particularly interesting for studies of stellar atmospheres and of galactic structure; it may also provide information which will add to existing knowledge of interstellar extinction and reddening.

The telescope is a 38 inch diameter, f/5 Cassegrainian, Ritchey-Chretien type. The primary mirror is of S200B beryllium, which is overcoated with 0.006 ±0.001 inch of Kanigen before polishing. The secondary mirror is of clear fused quartz. It may be moved axially in orbit to make required focus corrections.

The spectrometer optics consist of a reflection grating and a concave mirror. Only the first-order spectrum is used. The dispersed light coming from the grating is then re-reflected by the spectrometer mirror and brought to a focus at the plane of the exit slits. The spectrometer mirror and grating are also made of S200B beryllium overcoated with 0.006 ±0.001 inch of Kanigen. The telescope-spectrometer optics are shown in Figure 2-2 of the GEP handbook.¹

The spectral resolution is controlled by the size of the exit slit. Three slit sizes are available: 2 Å, 8 Å and 64 Å. The full spectral range is covered by moving the grating so that the first-order spectrum is scanned across the six detectors. Five different scan modes can be used, offering three different resolutions, with the possibility of repeated observations at the same grating position, after beginning a scan with the grating at any specified position.

The size of the spectrometer entrance aperture can be chosen to control background noise if necessary. An opaque shutter blocks incoming light to the spectrometer if it exceeds safe intensities. The spectrometer is automatically shuttered if either the earth or moon is in the telescope's field of view.

1. Handbook for the Goddard Experiment Package. Prepared by Telescope Systems Section, Astrophysics Branch, Laboratory for Space Science of the NASA Goddard Space Flight Center, Greenbelt, Md., Sept. 1, 1967.

The spectrometer has six ultraviolet detectors, with wavelength sensitivities arranged so that almost the entire wavelength range is covered by more than one detector, as shown in Table A-4.

TABLE A-4. WAVELENGTH SENSITIVITIES OF DETECTORS

Detector Number	Wavelength Range
1	684 to 1702 Å
2	1193 to 2211 Å
3	1693 to 2708 Å
4	2289 to 3298 Å
5	2781 to 3783 Å
6	3274 to 4267 Å

The useful range of the entire detector array is assumed to be from 1100 to 4267 Å. Five of the six ultraviolet detectors use photomultiplier tubes; the sixth uses a photon scintillator. A seventh detector channel acquires data in the visible range from 3963 to 4454 Å. These intensities are used to correlate the ultraviolet intensities with stellar magnitudes.

b. Fine Guidance System. A fine guidance system is provided for star tracking. It produces error signals for tracking stars of +10 to +1 visual magnitude outside the earth's atmosphere. A star image in the entrance slot of the GEP optical system is relayed to a pair of vibrating reeds, which act as a light modulator. The optical system is shown in Figure 2-3 of the GEP handbook.²

The fine guidance system is intended to generate error signals in the pitch and yaw control axes. These error signals are transmitted to the spacecraft stabilization and control system and are used to control the fine attitude pointing of the spacecraft. A star presence signal is also generated to indicate that the system has acquired the star and is ready to transmit error signals. If the optical line-of-sight of the experiment is within the desired accuracy limits, an accuracy signal is generated which indicates that star data taking is permissible. This system was designed to be used on the Orbital Astronomy Observatory (OAO). Changes might be necessary to make it compatible with the HEAO-C star tracker system. A discussion of the potential utilization of this system with the HEAO-C attitude sensing and control system is provided in Appendix E.

2. Ibid.

c. Small Ultraviolet Telescope (SUVT). In this study, the primary interest was to determine whether the SUVT would fit into the spacecraft and what impact it might have. The outer telescope diameter was assumed to be about 20 inches and the weight about 200 pounds.

General Experiment Information

1. South Atlantic Anomaly Effects. This topic was discussed in Chapter II. In addition, it may be noted that there has been excessive noise in the OAO photomultiplier tubes in the South Atlantic Anomaly region. The noise presumably is caused by high-energy electrons. The long-term effects of radiation on the optical surfaces are unknown at this time. Dr. Boggess has indicated (April 30, 1971) that the GEP would probably remain turned on and possibly could collect data during the passage. Effects on the SUVT were not investigated.

2. Gas Purges and Quenching Gas Quantities Required. None is required because the detectors are photomultiplier tubes.

3. Calibration. After initial checkout it is expected that the GEP will be calibrated on the order of once per month on an external known source. No internal calibration is planned at the present time. The SUVT is expected to be similar in this respect, although it could have an internal calibration source or check.

4. Launch Environment. This area was discussed in Chapter II. Dr. Boggess has indicated that the GEP was designed to withstand launch on an Atlas Centaur. The SUVT could very likely be designed to withstand a normal Titan launch.

5. Spacecraft Degraded Modes Operation. This area was also discussed in Chapter II. Dr. Boggess has indicated that the most significant concern in this area is pointing stability amplitude (the size of the circle that the optical axis wanders in during one observation). Pointing stability for him does not equate with pointing accuracy or jitter rate. The SUVT has not been studied from this standpoint because of its lack of definition.

TABLE OF CONTENTS

	Page
Lifetime Analysis	B- 1
Orbit Adjust Stage (OAS) Separation	B-39
Launch Vehicle Description	B-51
1. Titan	B-51
2. Shroud	B-53
a. General	B-53
b. Nose Cone	B-53
c. Cylindrical Section	B-55
d. Separation System	B-56
3. OAS	B-58
a. General	B-58
b. OAS Description	B-62
c. Propulsion	B-62
d. OAM Life Characteristics	B-67
e. OAS Attached to Spacecraft in Inactive Mode	B-68
f. Main Power Characteristics	B-68
g. Pyrotechnic Power Requirements	B-69
4. Adapters	B-69
5. Facilities and Operations	B-70
a. Facilities	B-70
b. Ground Environment Control	B-70
c. OAS Servicing	B-73
d. Flight Operation	B-73
6. Loads and Environments	B-73
a. Contamination From Titan IIID SRM Jettison and Titan IIID/OAS Separation	B-73
b. Dynamic Environments	B-74
References	B-81
Bibliography	B-81

LIST OF ILLUSTRATIONS

Figure	Title	Page
B- 1.	HEAO-C Configuration I	B- 2
B- 2.	HEAO-C Configuration II	B- 3
B- 3.	Octacircular HEAO-C	B- 4
B- 4.	Sun-orbital plane geometry for minimum average drag . .	B- 6
B- 5.	Sun-orbital plane geometry for maximum average drag	B- 6
B- 6.	Sun-star-orbital plane geometry for minimum average drag	B- 7
B- 7.	Sun-star-orbital plane geometry for maximum average drag	B- 7
B- 8.	Variation in drag coefficient with angle-of-attack for Configuration I	B- 8
B- 9.	Variation in drag coefficient with angle-of-attack for Configuration II	B- 9
B-10.	Variation in drag coefficient with altitude	B-10
B-11.	Drag coefficient for octacircular HEAO-C in the fixed pointing mode of operation	B-11
B-12.	Current forecast of solar activity	B-12
B-13.	Variation in orbit lifetime with vehicle mass for Con- figuration I — scanning mode	B-14
B-14.	Variation in orbit lifetime with vehicle mass for Con- figuration II — scanning mode	B-15
B-15.	Variation in orbit lifetime with vehicle mass for Con- figuration I — pointing mode	B-16

LIST OF ILLUSTRATIONS (Continued)

Figure	Title	Page
B-16.	Variation in orbit lifetime with vehicle mass for Configuration II — pointing mode	B-17
B-17.	Variation in orbit lifetime with vehicle mass for Configuration I — scanning mode	B-18
B-18.	Variation in orbit lifetime with vehicle mass for Configuration II — scanning	B-19
B-19.	Variation in orbit lifetime with vehicle mass	B-20
B-20.	Variation in orbit lifetime with vehicle mass for Configuration II with and without OAS.	B-21
B-21.	Variation in orbit lifetime with vehicle mass	B-22
B-22.	Variation in orbit lifetime with vehicle mass for Configuration II with and without OAS.	B-23
B-23.	Variation in orbit lifetime with vehicle mass	B-24
B-24.	Variation in orbit lifetime with vehicle mass for Configuration II with and without OAS.	B-25
B-25.	Variation in orbit lifetime with vehicle mass	B-26
B-26.	Variation in orbit lifetime with vehicle mass	B-27
B-27.	Variation in orbit lifetime with vehicle mass for octa-circular HEAO-C without subsystem module	B-28
B-28.	Variation in orbit lifetime with vehicle mass for octa-circular HEAO-C with subsystem module	B-29
B-29.	Variation in orbit lifetime with vehicle mass for octa-circular HEAO-C with subsystem module	B-30
B-30.	Variation in orbit lifetime with vehicle mass for octa-circular HEAO-C with subsystem module	B-31

LIST OF ILLUSTRATIONS (Continued)

Figure	Title	Page
B-31.	Variation in orbit lifetime with vehicle mass for octa-circular HEAO-C with subsystem module	B-32
B-32.	Variation in orbit lifetime with vehicle mass for HEAO-C Configuration II in a 250 nautical mile altitude circular orbit	B-33
B-33.	Variation in orbit lifetime with vehicle mass for Configuration II	B-34
B-34.	Variation in orbit lifetime with vehicle mass for Configuration II	B-35
B-35.	Variation in orbit lifetime with vehicle mass for HEAO-C Configuration II in a 250 nautical mile altitude circular orbit	B-36
B-36.	Variation in orbit lifetime with vehicle mass for HEAO-C Configuration II in a 250 nautical mile altitude circular orbit	B-37
B-37.	Variation in altitude with time for a 260 nautical mile altitude initial orbit	B-38
B-38.	HEAO S/C, OAS separation by compression springs	B-40
B-39.	Relative vertical distance (ΔH) versus time	B-41
B-40.	Relative horizontal distance (ΔL) versus time	B-43
B-41.	Separation distance (D) versus time	B-44
B-42.	Angular displacement versus time	B-45
B-43.	Separation distance (D) versus time	B-46
B-44.	Separation distance (D) versus time	B-47

LIST OF ILLUSTRATIONS (Concluded)

Figure	Title	Page
B-45.	Separation distance (D) versus time	B-48
B-46.	Realignment period versus separation velocity	B-49
B-47.	Spring energy requirement	B-50
B-48.	Titan IID/OAS launch vehicle	B-52
B-49.	HEAO and shroud	B-54
B-50.	Super Zip separation system	B-57
B-51.	HEAO shroud separation reliability logic	B-59
B-52.	Longitudinal and circumferential separation joint redundancy scheme	B-60
B-53.	Stripped LMSC OAS for HEAO	B-61
B-54.	Module OAM assembly	B-64
B-55.	HEAO/OAS interface	B-71
B-56.	External acoustic excitation	B-75
B-57.	External shroud acoustic excitation	B-76
B-58.	Spacecraft/adaptor interface pyrotechnic shock environment from fairing separation	B-77
B-59.	Shock attenuation versus distance from interface	B-79
B-60.	Pyrotechnic shock environment	B-80

LIST OF TABLES

Table	Title	Page
B-1.	OAS Propellant Tank Characteristics	B-63
B-2.	Voltage Levels For Various OAS Load Conditions	B-69
B-3.	Ground Environmental Control Characteristics	B-72
B-4.	Ground Environmental Control Design Conditions	B-72

APPENDIX B. MISSION ANALYSIS AND LAUNCH VEHICLE

Lifetime Analysis

Two primary modes of spacecraft operation for the first three HEAO missions have been identified:

1. Normal Scanning Mode — The spacecraft rotates about its spin axis which nominally points toward the sun (HEAO-A and -B).
2. Fixed pointing Mode — The spacecraft remains fixed inertially for detailed investigation of selected sources. (Although HEAO-C has been designated as a "pointing" mission, orbit selection data for the "scanning" mode was computed for comparison.)

The candidate spacecraft configurations investigated in these parametric analyses were HEAO-C configurations I and II [with and without Orbital Adjust Stage (OAS) attached] and alternate HEAO-C configurations (with and without subsystem module). These spacecraft configurations are shown in Figures B-1 through B-3. Although the HEAO-C baseline that finally evolved during the Phase A study differed from these earlier candidates, the parametric trends are applicable.

Parametric data were computed to show the effect on lifetime of varying the spacecraft weights. The weight variations resulted in changes in spacecraft ballistic coefficients and, thus, changes in lifetimes. The effect on lifetime of changes in orbital drag resulting from changes in the spacecraft orientation for the scanning and pointing modes was determined. Orbital decay traces were computed to investigate the separation of the OAS from the spacecraft.

Since the data transmission from the spacecraft will be received at various ground tracking stations, minimum contact time restrictions must be established. These restrictions are based on the tracking stations' data acquisition equipment startup time, bit rates, etc. Ground contact time is a function of orbital altitude for a given inclination, thus a minimum contact time restriction would dictate a minimum altitude.

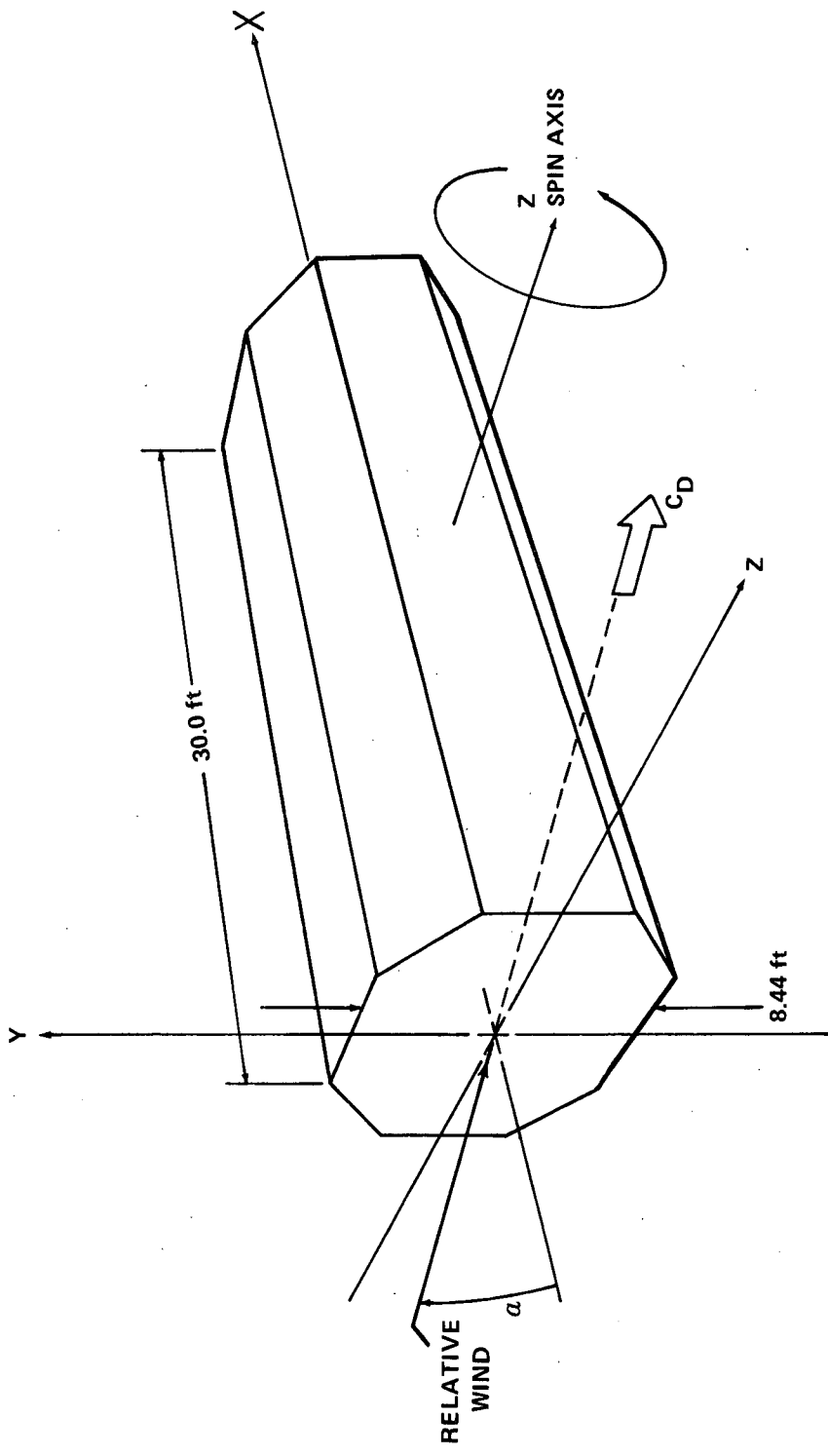


Figure B-1. HEAO-C Configuration I.

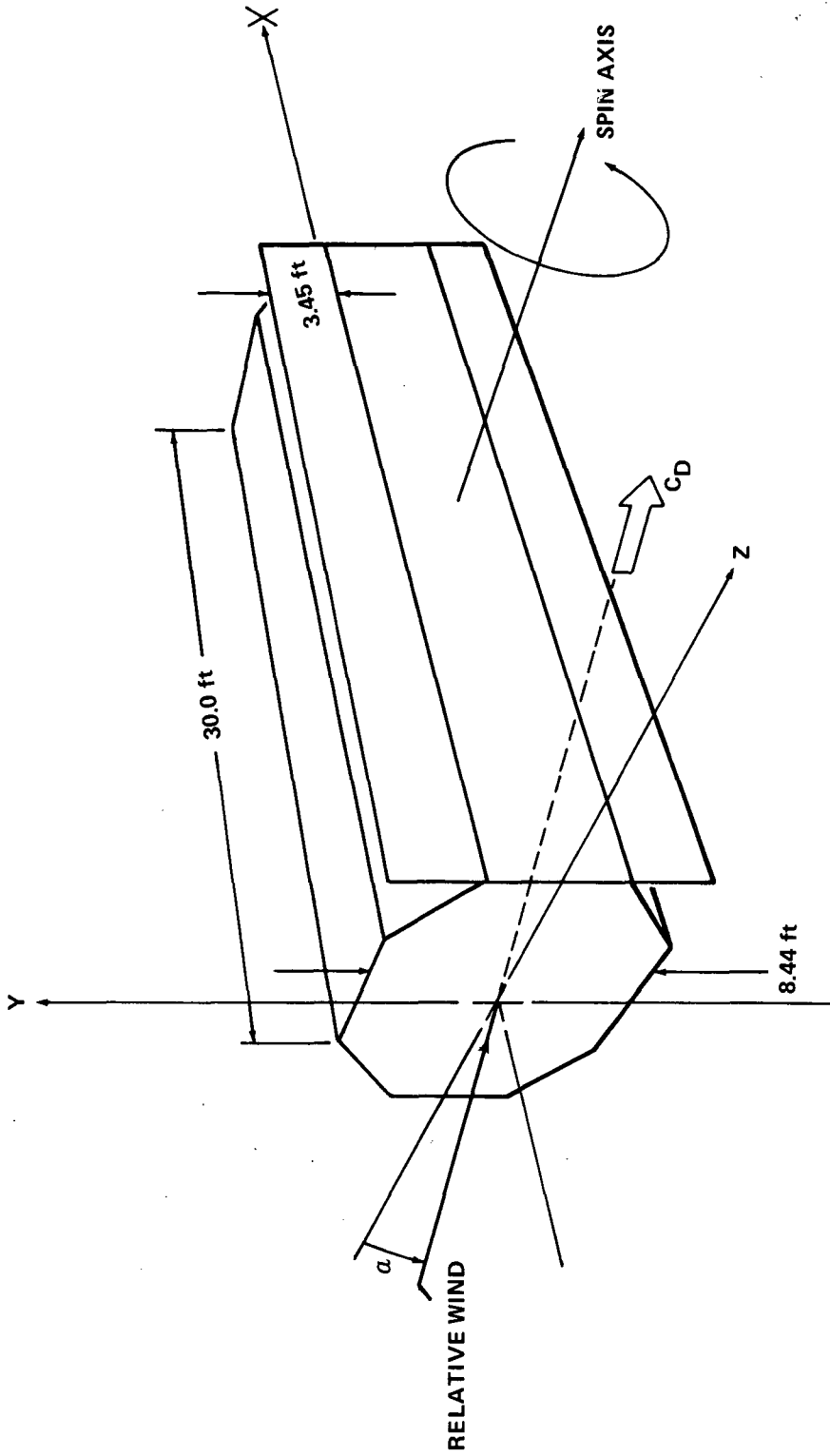


Figure B-2. HEAO-C Configuration II.

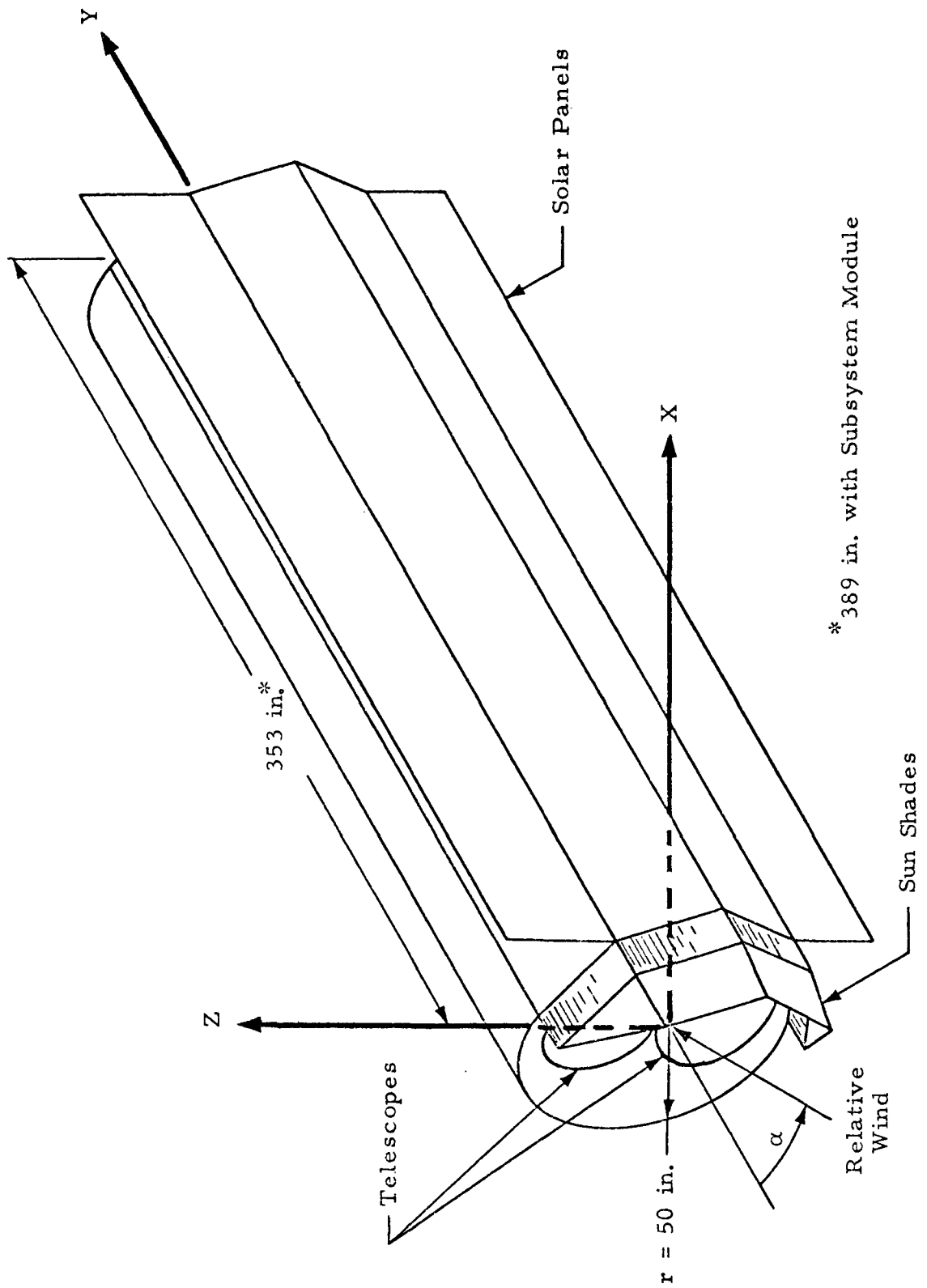


Figure B-3. Octacircular HEAO-C.

The orbital drag characteristics of the spacecraft configurations were computed for both the scanning and pointing modes. In Figures B-4 and B-5, the scanning mode sun-orbital plane geometries for minimum and maximum average drag are shown. ('Average drag' as used here implies an average over one orbital revolution.) In the scanning mode the spacecraft rotates up to 0.1 revolution per minute about its spin axis which points continuously toward the sun. The average drag values in this mode were obtained by computing an integrated average drag force at each spacecraft angle-of-attack for one rotation of the spacecraft about its spin axis.

In Figures B-6 and B-7 the pointing mode sun-star-orbital plane geometries are shown for minimum and maximum average drag. In this mode the spacecraft orientation remains fixed inertially with the longitudinal axis of the spacecraft aimed at the particular star of interest. Minimum average drag in this mode would occur when the star lies in the orbital plane and maximum average drag would occur when the earth-star line is perpendicular to the orbital plane.

The orbital drag data for HEAO-C Configurations I and II in the scanning and fixed pointing modes are shown in Figures B-8 and B-9. Drag coefficient, C_D , is shown as a function of angle-of-attack¹ for nominal altitudes from 200 to 250 nautical miles. These drag data are applicable for lifetime calculations over a wide range of altitudes. This fact is illustrated by Figure B-10 which shows orbital drag data for a configuration at 200 nautical miles and 300 nautical miles.

The dip in the fixed pointing mode drag curve on Figure B-8 at $\alpha = 90$ degrees is caused by the high ratio of end surface area to longitudinal surface area for Configuration I. The curve in Figure B-9 is inverted from that in Figure B-8 because of the different angle-of-attack reference for Configuration II. The maximum drag coefficients were essentially the same for both the scanning mode and the fixed pointing mode but the minimum value for the latter mode was much smaller.

The orbital drag data for the octacircular HEAO-C configuration with and without the subsystem module attached are shown in Figure B-11. In this figure the drag coefficient is plotted versus angle-of-attack. The range of attack was extended to 360 degrees for this configuration also, because of non-symmetry.

1. See Figures B-1 and B-2 for angle-of-attack definition.

- SCANNING MODE OF OPERATION
- EARTH-SUN LINE IS NORMAL TO ORBIT PLANE

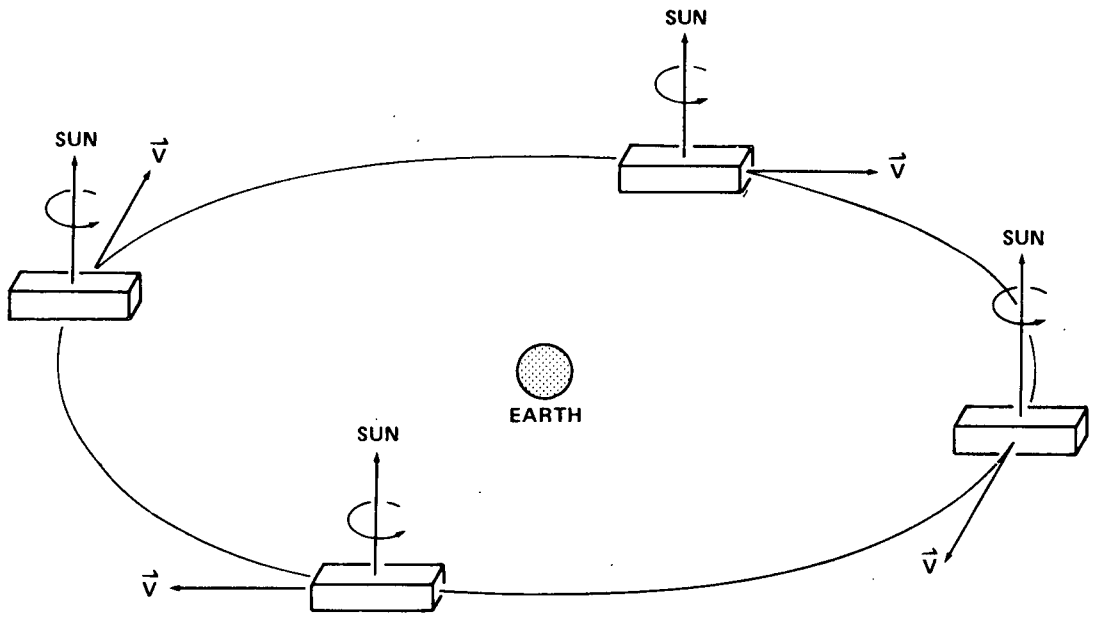


Figure B-4. Sun-orbital plane geometry for minimum average drag.

- SCANNING MODE OF OPERATION
- EARTH-SUN LINE LIES IN ORBIT PLANE

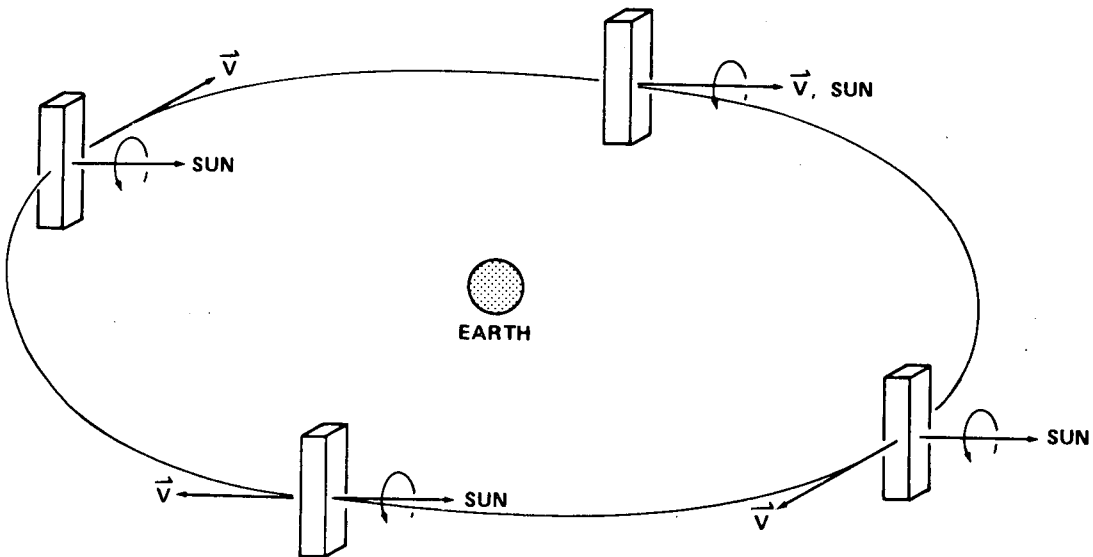


Figure B-5. Sun-orbital plane geometry for maximum average drag.

- FIXED-POINTING MODE OF OPERATION
- SUN AND STAR ARE IN THE ORBITAL PLANE

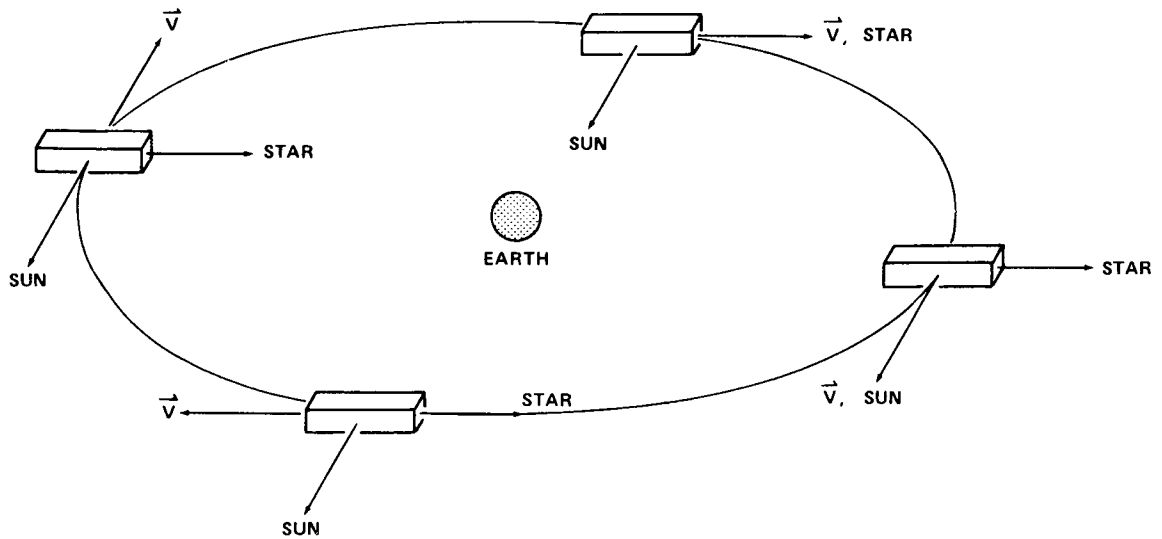


Figure B-6. Sun-star-orbital plane geometry for minimum average drag.

- FIXED-POINTING MODE OF OPERATION
- SUN IS IN THE ORBITAL PLANE AND THE EARTH-STAR LINE IS NORMAL TO THE ORBITAL PLANE

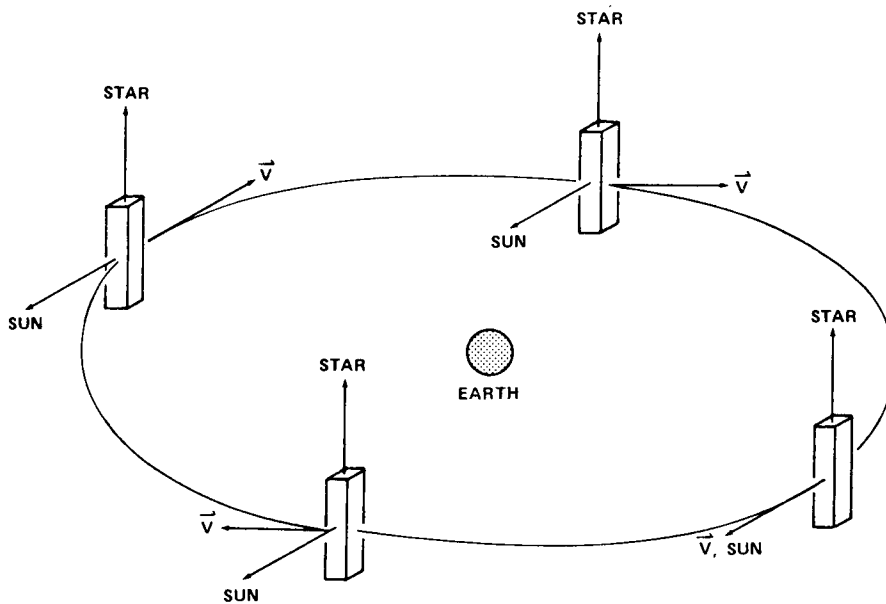


Figure B-7. Sun-star-orbital plane geometry for maximum average drag.

The lifetime of a spacecraft in orbit is a function of its launch date, orbital altitude and inclination, mass, and aerodynamic drag. The effect of orbital inclination on lifetime has been found to be small relative to the other variables. Lifetime is dependent upon launch date because of the variation of atmospheric density over time induced by variations in solar activity. Shown in Figure B-12 is a current forecast of solar activity for the 1970 through 1984 time period. As is shown by the figure, higher solar activity is incurred for launch dates in the 1976 to 1978 time period than in the 1974 to 1976 period; thus, higher altitudes are required for a given lifetime. The atmosphere model used in the lifetime calculations was the MSFC Modified 1967 JACCHIA with a $+2\sigma$ level of solar activity.

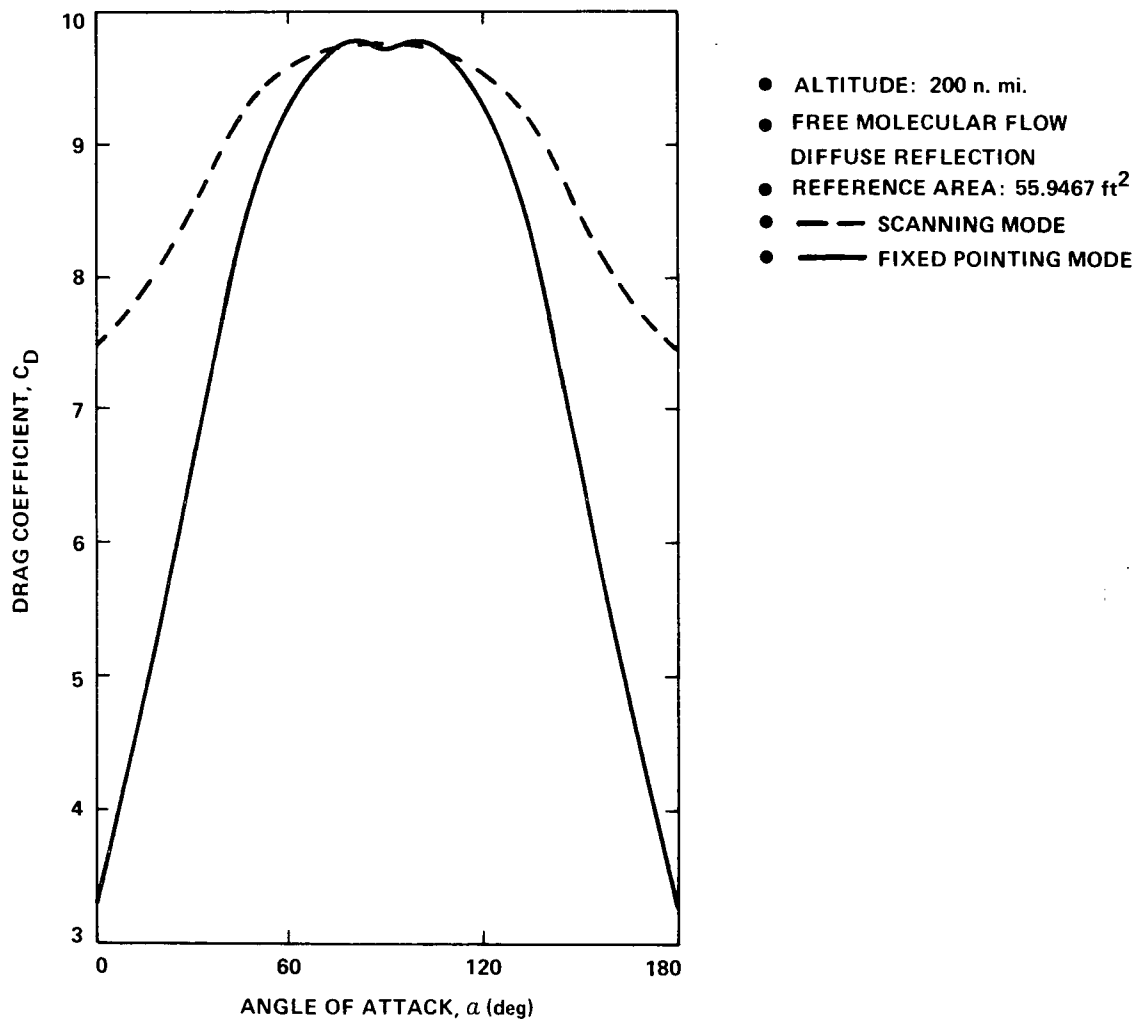


Figure B-8. Variation in drag coefficient with angle-of-attack for Configuration I.

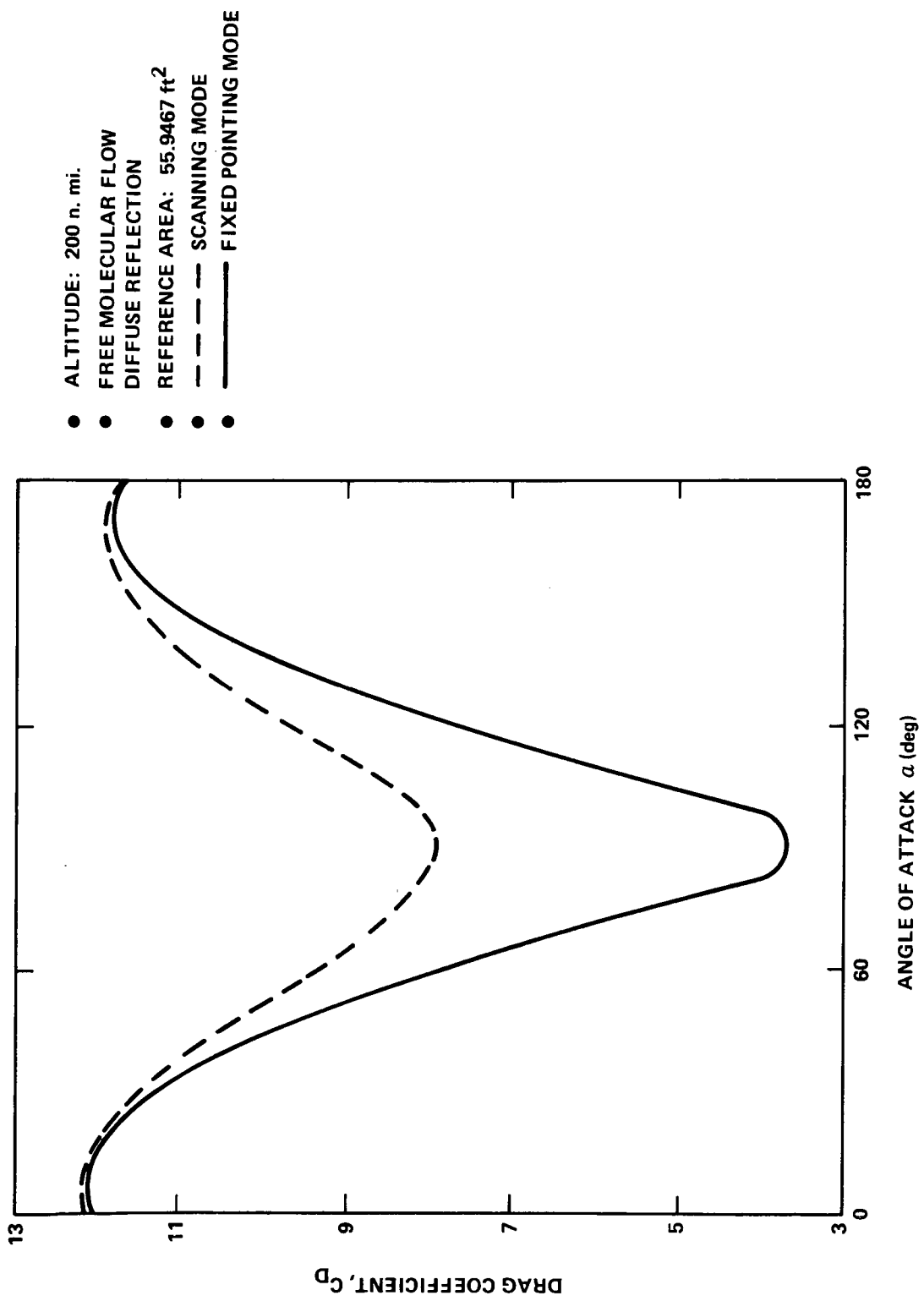


Figure B-9. Variation in drag coefficient with angle-of-attack for Configuration II.

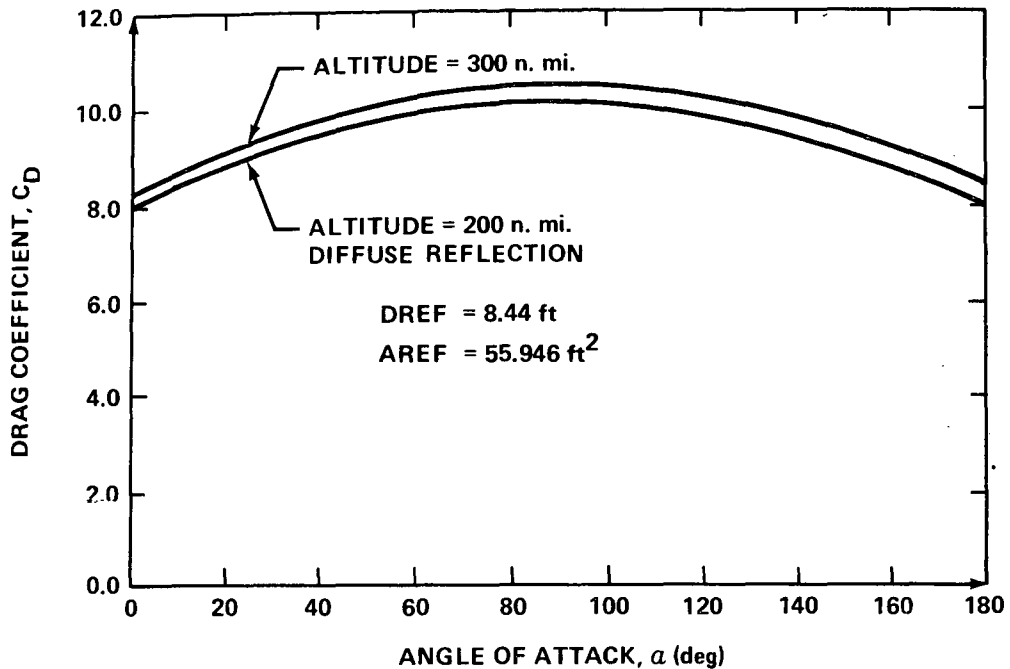


Figure B-10. Variation in drag coefficient with altitude.

The variations in orbital lifetime with vehicle mass for Configurations I and II in the scanning mode for maximum and minimum drag orientation are shown in Figures B-13 through B-18 for a range of launch dates from September 1, 1976, to September 1, 1978. Initial injection altitudes of 200 to 270 nautical miles are shown. The maximum and minimum drag curves for a given initial injection altitude define a band in which lifetimes for all spacecraft pointing orientations would be confined. The effect of launch date can be discerned from these figures by noting the downward shift of the lifetime bands with the later launch dates. However, the bands shift upward again for the late 1978 launch date. The reason for this is that the solar activity decreases during the latter part of the two year lifetime.

The variations in orbital lifetime for Configurations I, II, and II/OAS in the fixed pointing mode are shown in Figures B-19 through B-29. In these figures initial injection altitudes of 250 and 260 nautical miles are shown. These particular altitudes were used because the corresponding lifetime bands indicate a two year lifetime for a 17 200 pound spacecraft (this was taken as a nominal spacecraft weight).

● ALTITUDE: 250 n. mi.

● FREE MOLECULAR FLOW: DIFFUSE REFLECTION

● REFERENCE AREA: 55.9467 ft²

● CODE :

— WITH SUBSYSTEM MODULE

- - - WITHOUT SUBSYSTEM MODULE

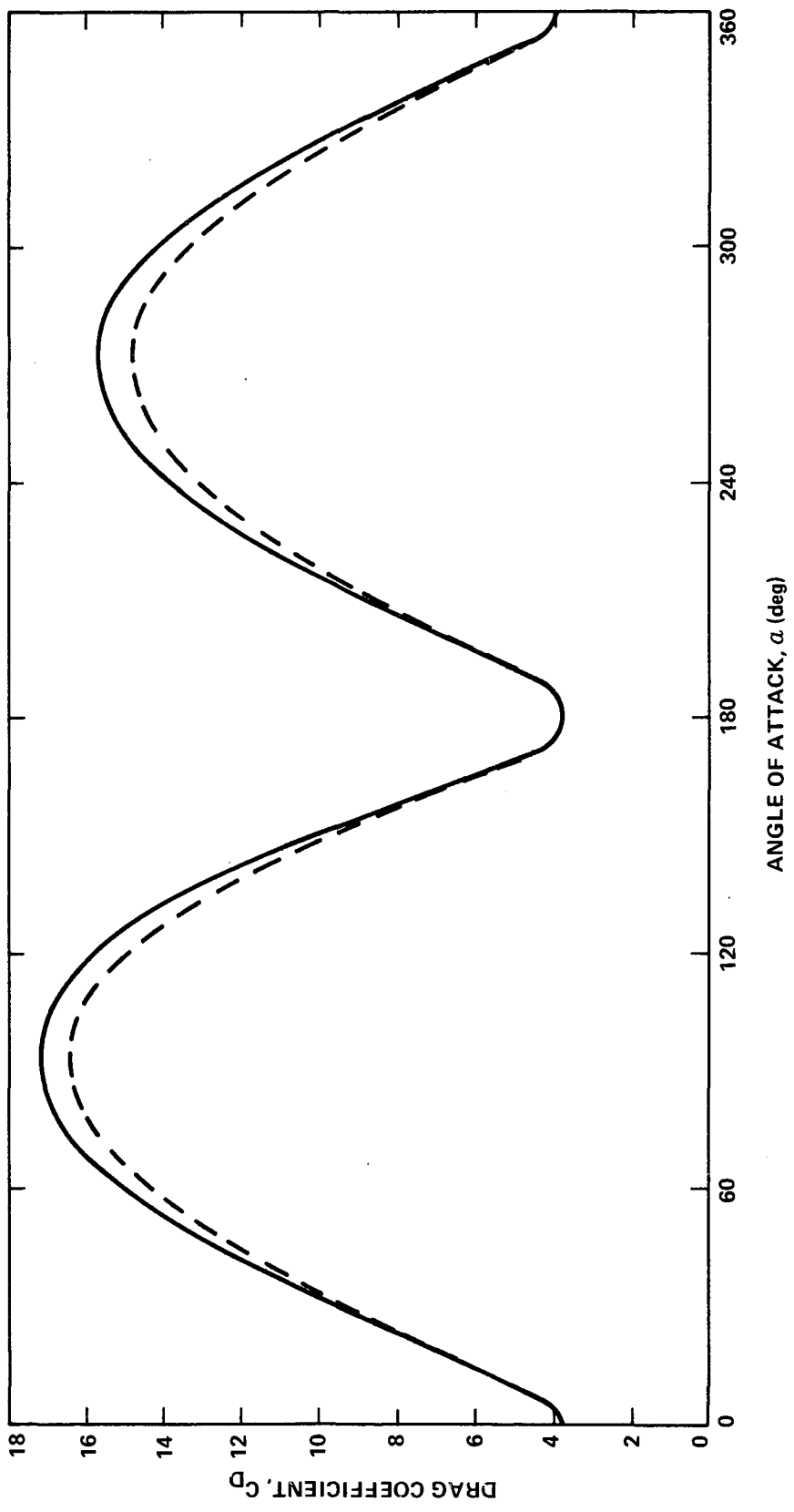


Figure B-11. Drag coefficient for octacircular HEAO-C in the fixed pointing mode of operation.

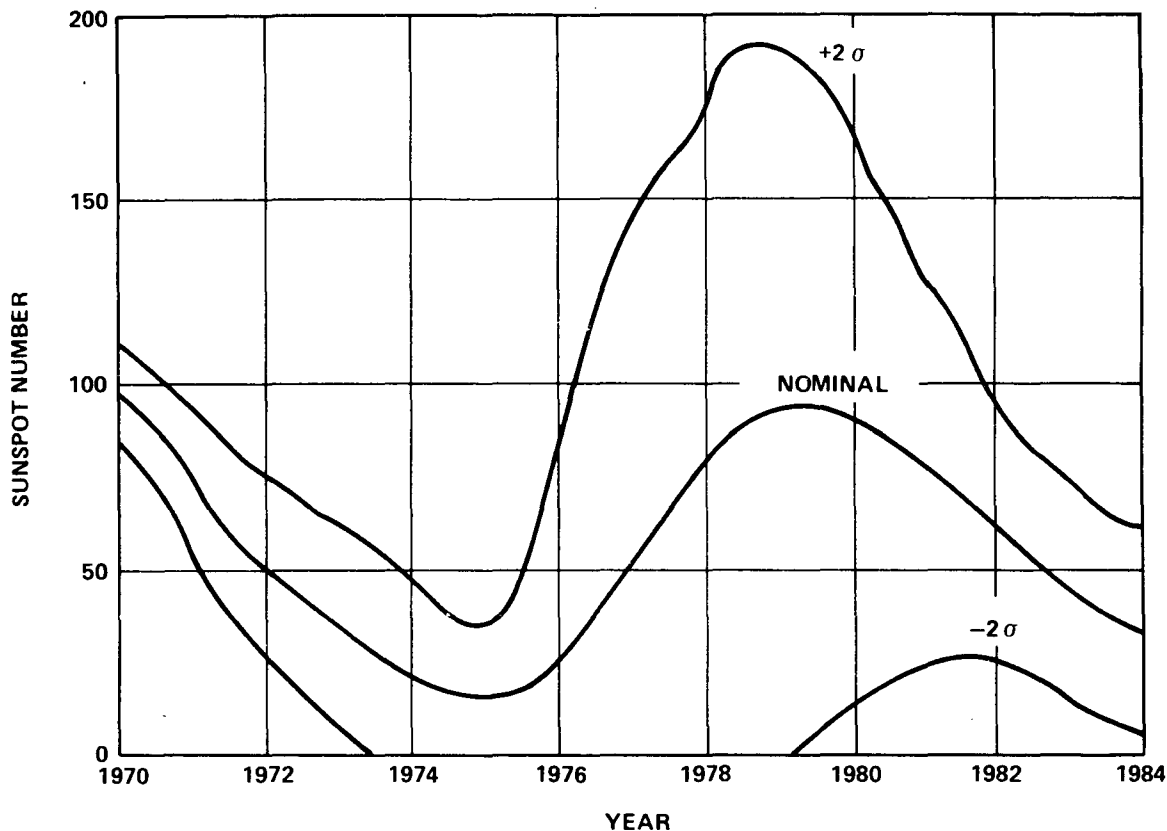


Figure B-12. Current forecast of solar activity.

In Figures B-19, B-21, B-23, and B-25, maximum and minimum lifetime bands for Configurations I and II are shown. In Figures B-20, B-22, and B-24, maximum and minimum lifetime bands for Configurations II and II/OAS are shown. From examination of these figures it can be seen that for the late 1977 and late 1978 launch dates a 250 nautical mile initial altitude will not guarantee a two year lifetime for Configuration II even in a constant minimum drag orientation. For Configuration II/OAS the 250 nautical mile initial altitude was inadequate over all the launch dates considered.

Figure B-26 shows the variation in orbital lifetime with vehicle mass for Configuration II in the fixed pointing mode for a March 21, 1977, launch date. As shown, a 250 nautical mile initial altitude will not guarantee a two year lifetime for a 17 200 pound spacecraft in the maximum drag orientation. However, a 260 nautical mile initial altitude is slightly more than adequate.

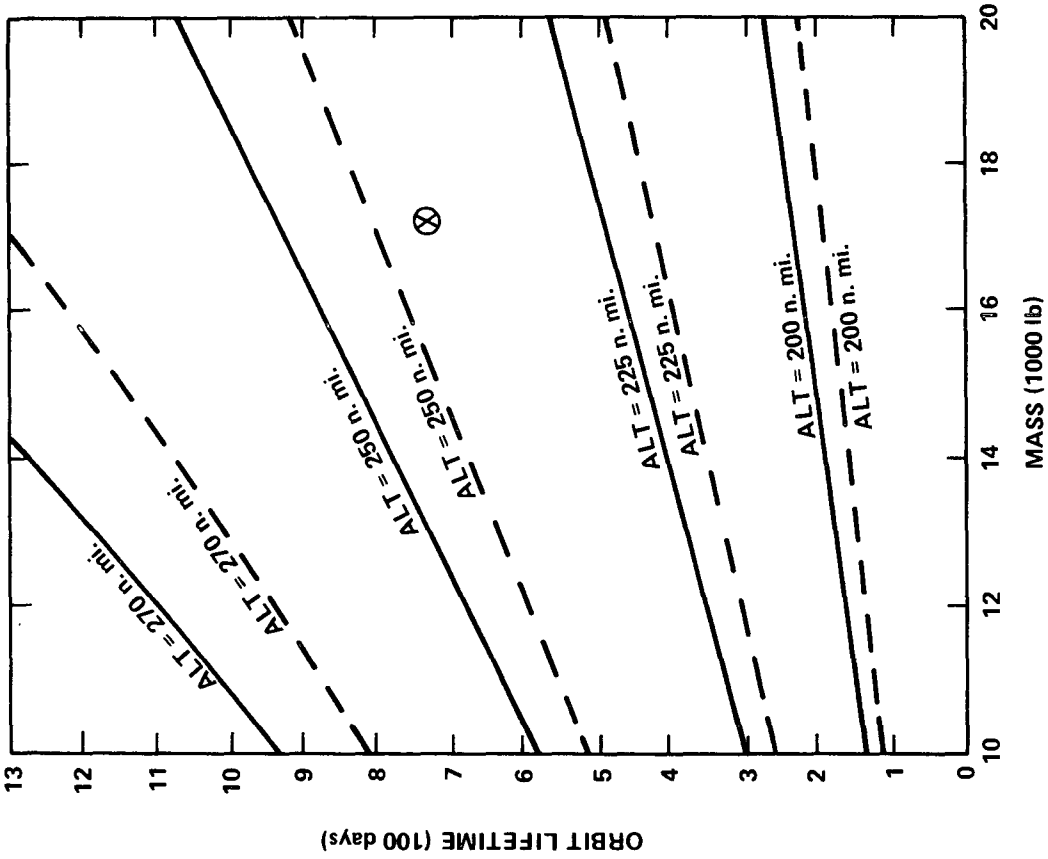
The variations in orbital lifetime with vehicle mass for the octacircular HEAO-C configuration are shown in Figures B-27 through B-31. In Figures B-27 and B-28 lifetime data are presented for this configuration both with and without the subsystem module attached for a launch date of March 21, 1977. These figures indicate that the attachment of the subsystem module increases the initial altitude required for a two year lifetime for spacecraft weights in the vicinity of 15 000 to 17 000 pounds by approximately 5 nautical miles. Lifetime data for launch dates ranging from late 1976 to late 1978 for the module-attached configuration are included in Figures B-29 through B-31.

The lifetime data presented above were computed assuming a 2σ high level of solar activity. Figures B-32 through B-36 show orbital lifetime as a function of vehicle mass for launch dates from late 1976 to late 1978 for both nominal (actual predicted solar activity) and 2σ high levels for Configuration II in a 250 nautical mile circular orbit. These figures demonstrate the conservatism of assuming a 2σ high level of solar activity.

The restrictions on the tracking stations data acquisition equipment startup times, bit rates, etc., dictate minimum contact times for equipment startup. Ground contact time is a function of orbital altitude for a given inclination and, thus, during the latter part of the HEAO-C spacecraft lifetime data acquisition could, possibly, be a problem because of low altitudes.

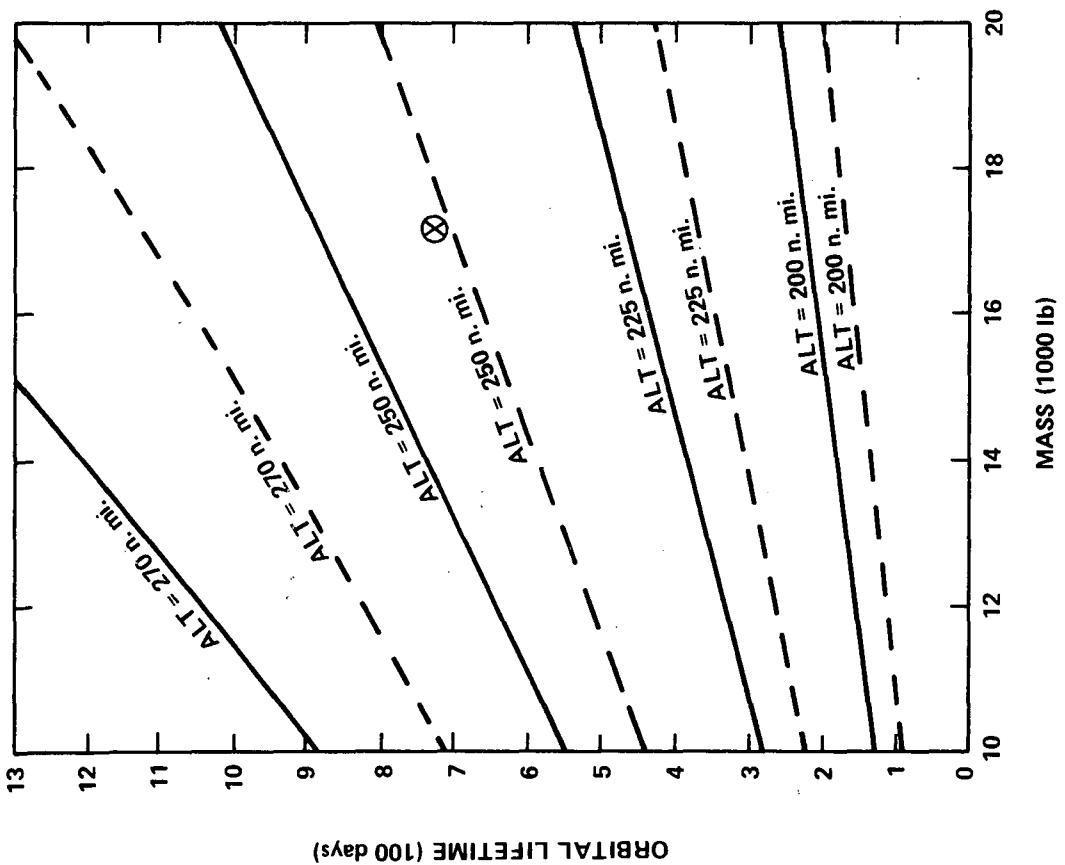
Shown in Figure B-37 is a typical decay trace for Configuration II and the OAS in the 260 nautical mile circular initial orbit. Configuration II was considered to be in a maximum drag orientation with a weight of 17 2000 pounds, the OAS in a random tumbling mode with a weight of 1223 pounds. As indicated, Configuration II fell below the 150 nautical mile altitude only during the last 25 days of its 770 day lifetime. Therefore, for the range of initial injection altitudes required to give the HEAO-C spacecraft a two year lifetime, minimum decay altitude constraints of 150 nautical miles or less are satisfied.

For some of the early candidate spacecraft, the OAS was separated following deployment into circular orbit. After separation it must not come near the spacecraft again. As illustrated by Figure B-37, after separation, the OAS orbit rapidly divaricates from the spacecraft.



- LAUNCH DATE: 9/1/76
- ATMOSPHERE MODEL: MODIFIED 1967 JACCHIA, +2 σ DENSITY
- ORBITAL INCLINATION: 28.5 deg
- SCANNING MODE OF OPERATION
- CODE: ——— MIN DRAG
- - - - - MAX DRAG

Figure B-13. Variation in orbit lifetime with vehicle mass for Configuration I — scanning mode.



- LAUNCH DATE: 9/1/76
- ATMOSPHERE MODEL: MODIFIED 1967 JACCHIA, +2σ DENSITY
- ORBITAL INCLINATION: 28.5 deg
- SCANNING MODE OF OPERATION
- CODE: ——— MIN DRAG
 - - - - - MAX DRAG

Figure B-14. Variation in orbit lifetime with vehicle mass for Configuration II — scanning mode.

- LAUNCH DATE: 9/1/77
- ATMOSPHERE MODEL: MODIFIED 1967 JACCHIA,
+2 σ DENSITY
- ORBITAL INCLINATION: 28.5 deg
- SCANNING MODE OF OPERATION
- CODE: ——— MIN DRAG
- - - - - MAX DRAG

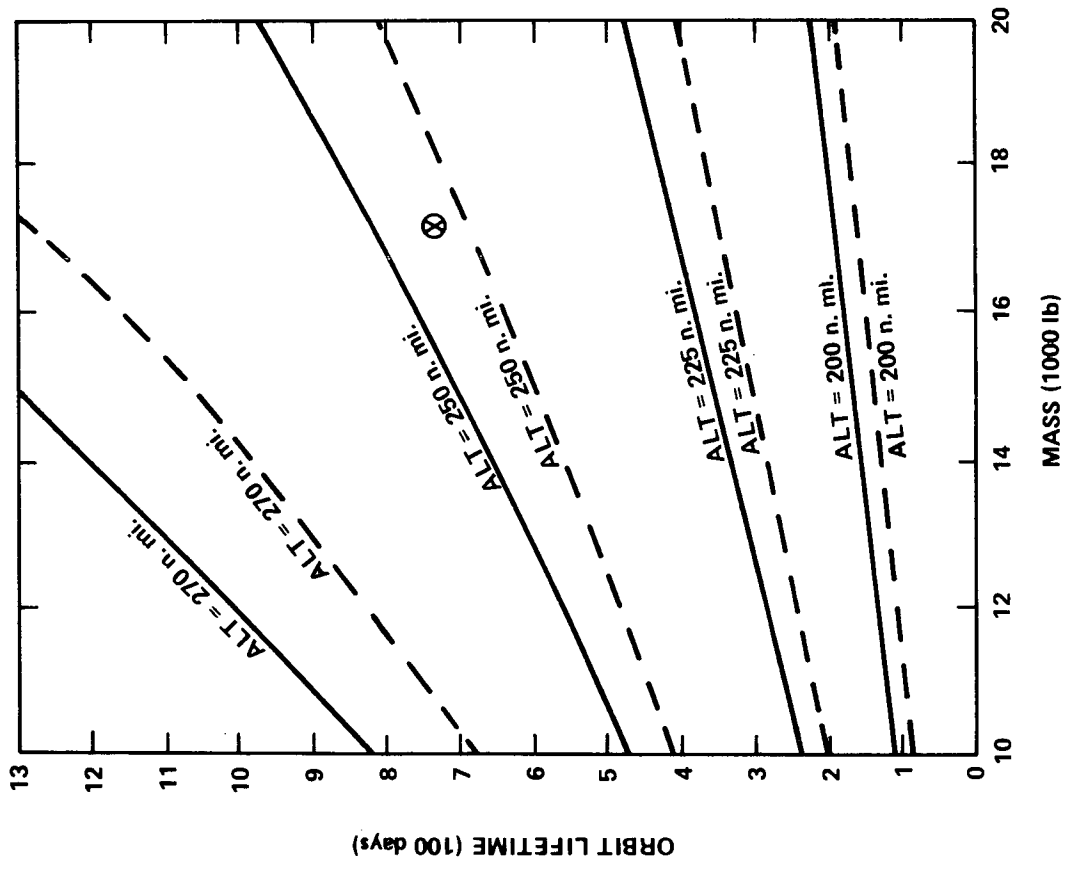


Figure B-15. Variation in orbit lifetime with vehicle mass for Configuration I — pointing mode.

- LAUNCH DATE: 9/1/77
- ATMOSPHERE MODEL:
MODIFIED 1967 JACCHIA,
+2 σ DENSITY
- ORBITAL INCLINATION :
28.5 deg
- SCANNING MODE OF
OPERATION
- CODE : — MIN DRAG
 -- -- MAX DRAG

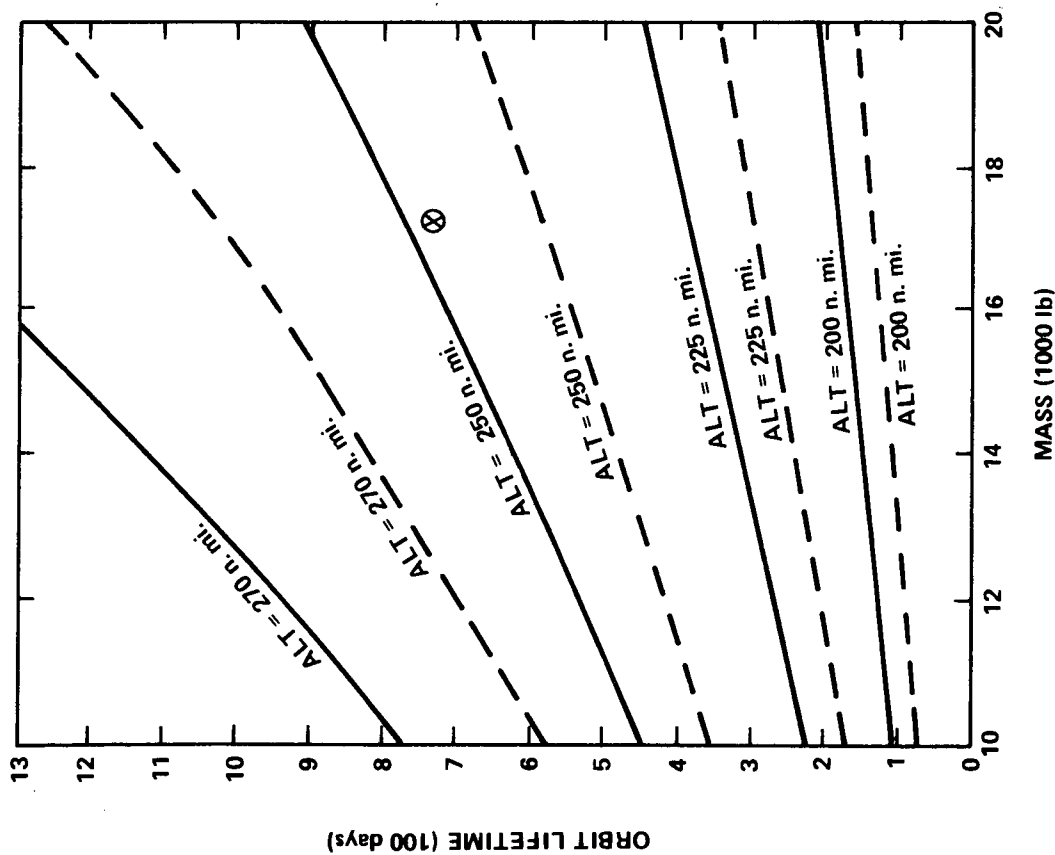


Figure B-16. Variation in orbit lifetime with vehicle mass for Configuration II — pointing mode.

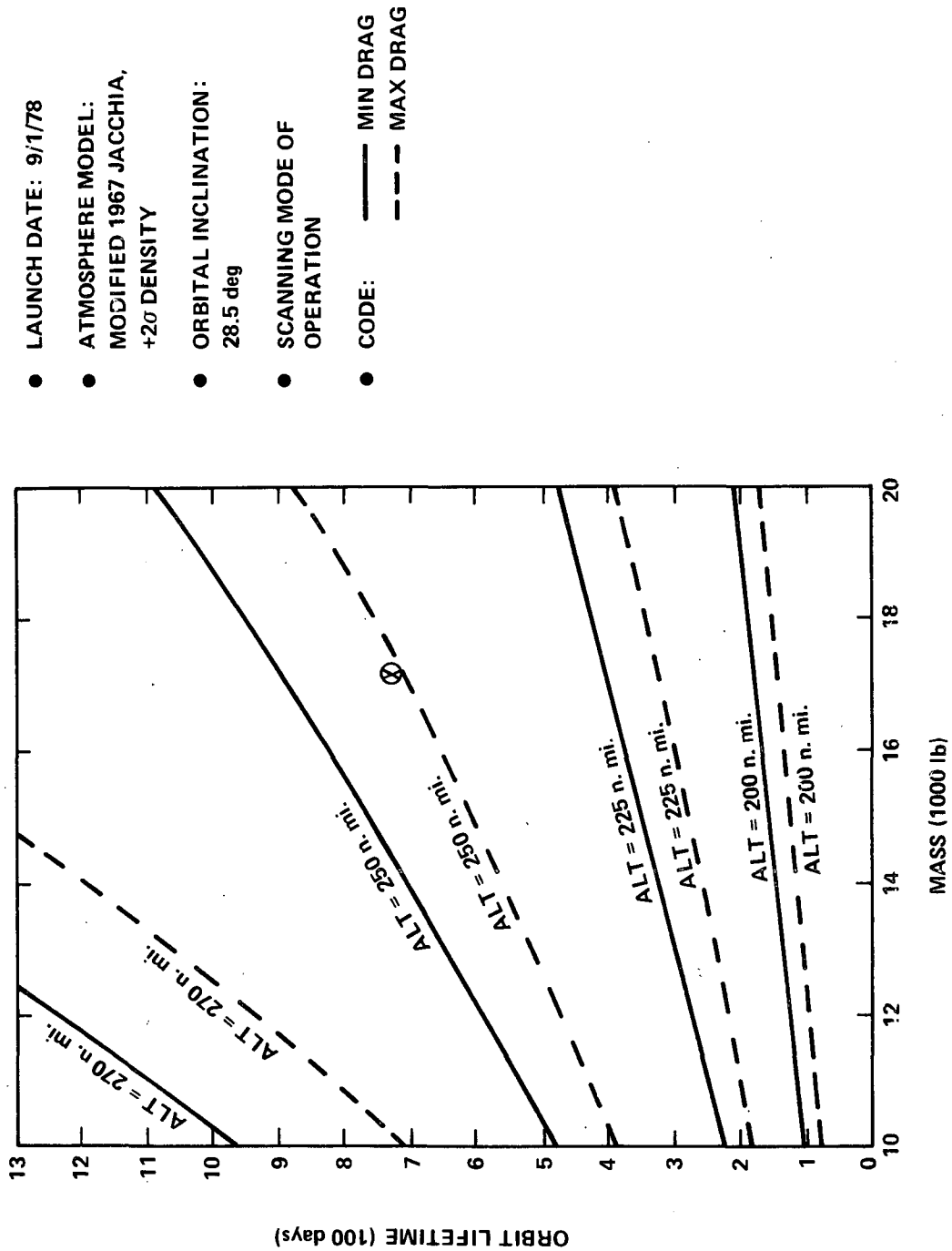
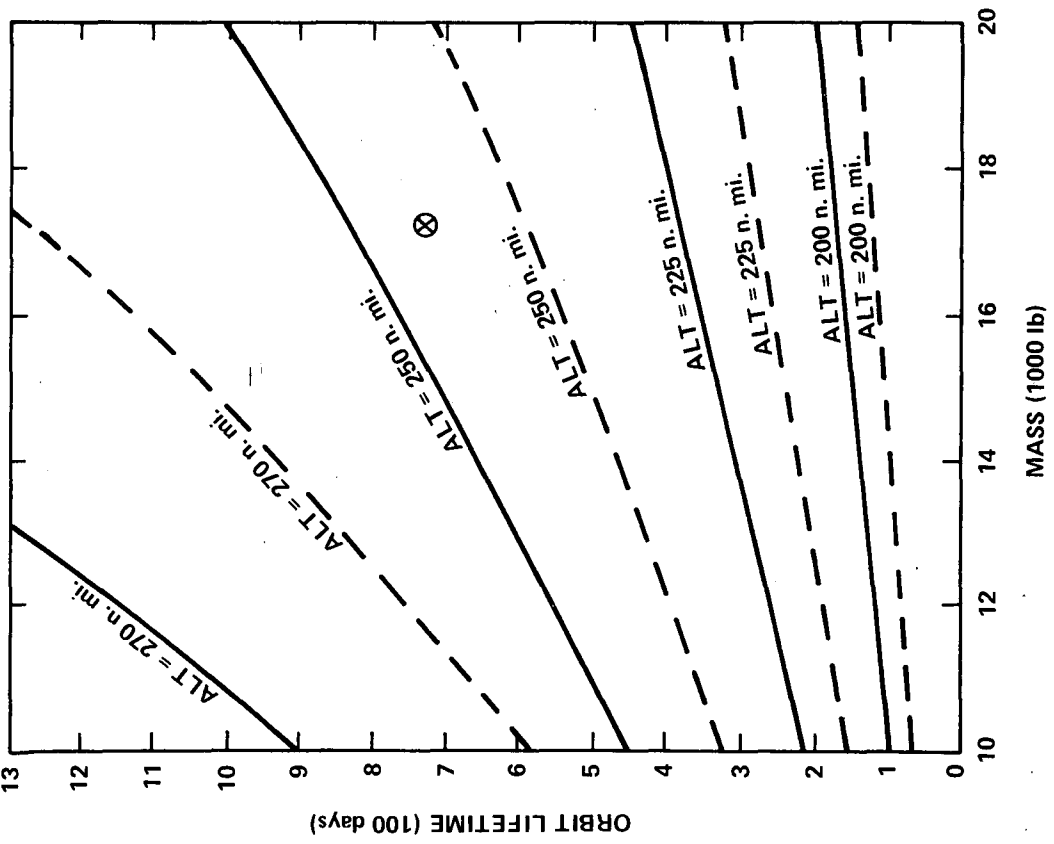


Figure B-17. Variation in orbit lifetime with vehicle mass for Configuration I — scanning mode.



- LAUNCH DATE: 9/1/78
- ATMOSPHERE MODEL: MODIFIED 1967 JACCCHIA +2σ DENSITY
- ORBITAL INCLINATION: 28.5 deg
- SCANNING MODE OF OPERATION
- CODE: ——— MIN DRAG
- - - MAX DRAG

Figure B-18. Variation in orbit lifetime with vehicle mass for Configuration II — scanning mode.

● LAUNCH DATE: 9/1/76

● ATMOSPHERE MODEL: MSFC MODIFIED 1967 JACCHIA
+2 σ DENSITY

● FIXED POINTING MODE OF OPERATION

● ORBIT: 28.5 deg INCLINATION
250 n. mi. CIRCULAR

● CODE: _____ CONFIGURATION I
 _____ CONFIGURATION II

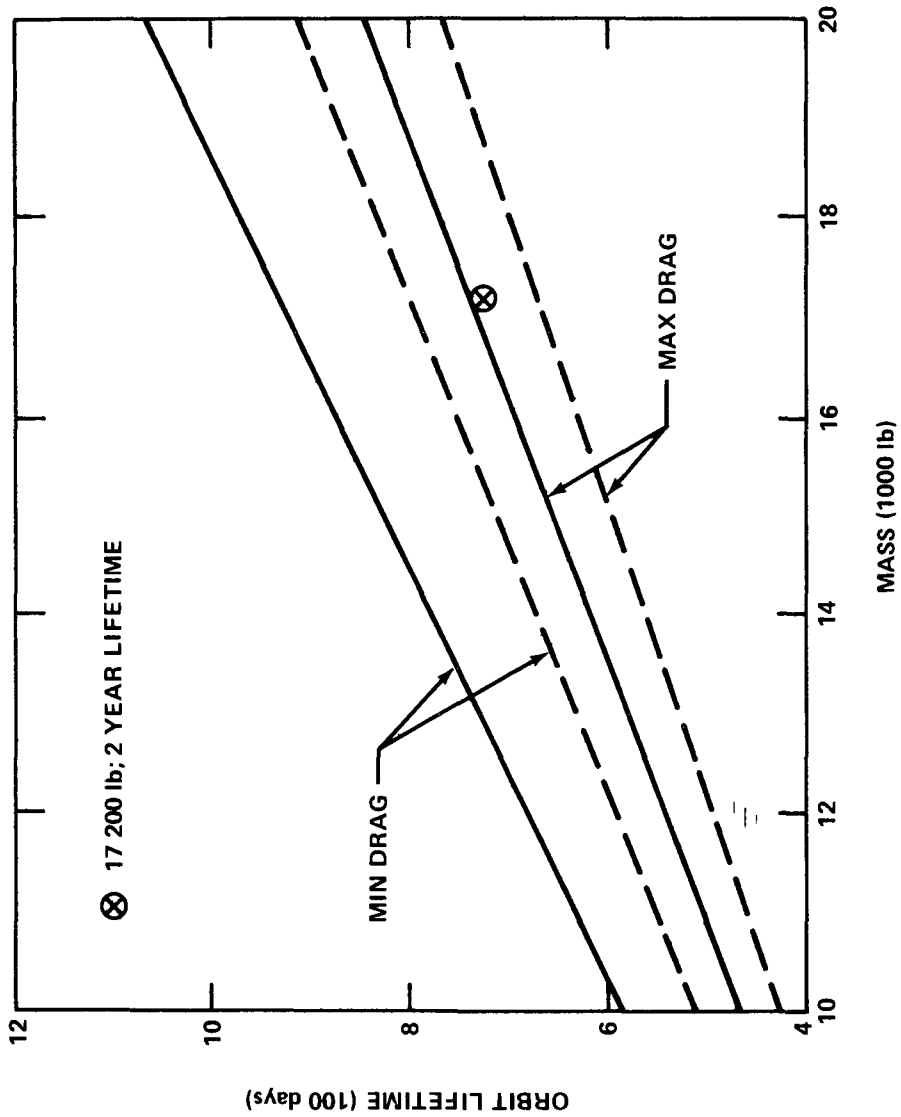


Figure B-19. Variation in orbit lifetime with vehicle mass.

● LAUNCH DATE: 9/1/76 ● ATMOSPHERE MODEL: MSFC MODIFIED 1967 JACCHIA +2σ DENSITY

● FIXED POINTING MODE OF OPERATION
 ● CIRCULAR ORBIT/28.5 deg INCLINATION

● CODE:

— 250 n. mi. MIN DRAG — 270 n. mi. MIN DRAG
 - - - 250 n. mi. MAX DRAG - - - 270 n. mi. MAX DRAG

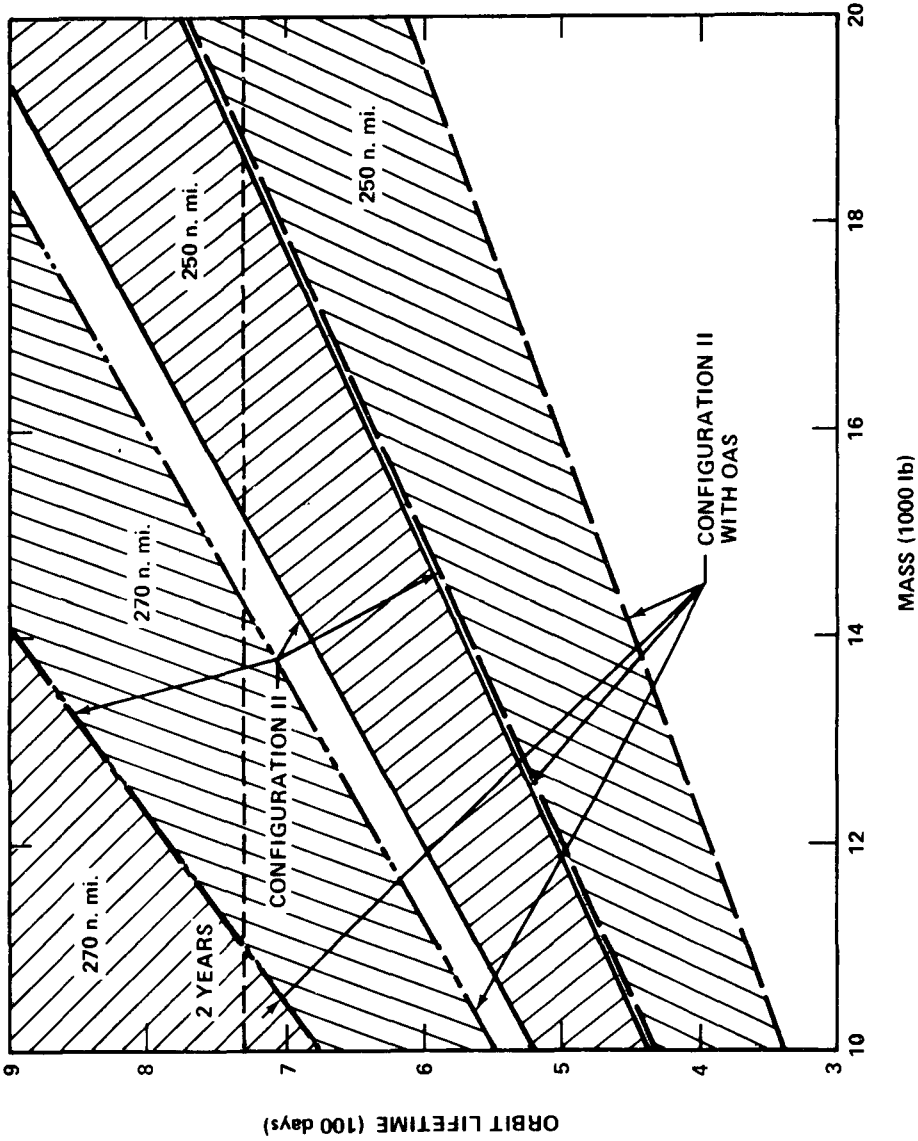


Figure B-20. Variation in orbit lifetime with vehicle mass for Configuration II with and without OAS.

- LAUNCH DATE: 3/21/77
- 28.5 deg INCLINATION ORBIT
- ATMOSPHERE MODEL: MSFC MODIFIED 1967 JACCHIA +2 σ DENSITY
- CODE:
- FIXED POINTING MODE OF OPERATION
- CONFIGURATION I, 250 n. mi.
- - - CONFIGURATION II, 250 n. mi.

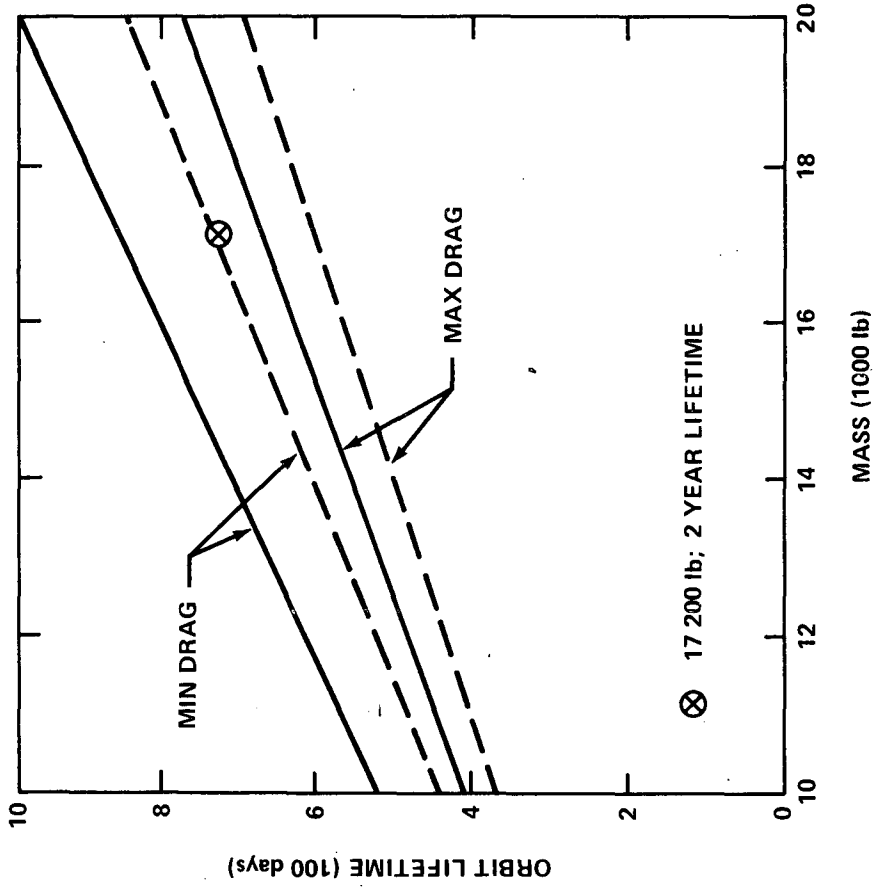


Figure B-21. Variation in orbit lifetime with vehicle mass.

● LAUNCH DATE: 9/1/77 ● ATMOSPHERE MODEL: MSFC MODIFIED 1967 JACCHIA +2 σ DENSITY

● FIXED POINTING MODE OF OPERATION

● CIRCULAR ORBIT/28.5 deg INCLINATION

● CODE:

—— 250 n. mi. MIN DRAG
 - - - 250 n. mi. MAX DRAG

—— 270 n. mi. MIN DRAG
 - - - 270 n. mi. MAX DRAG

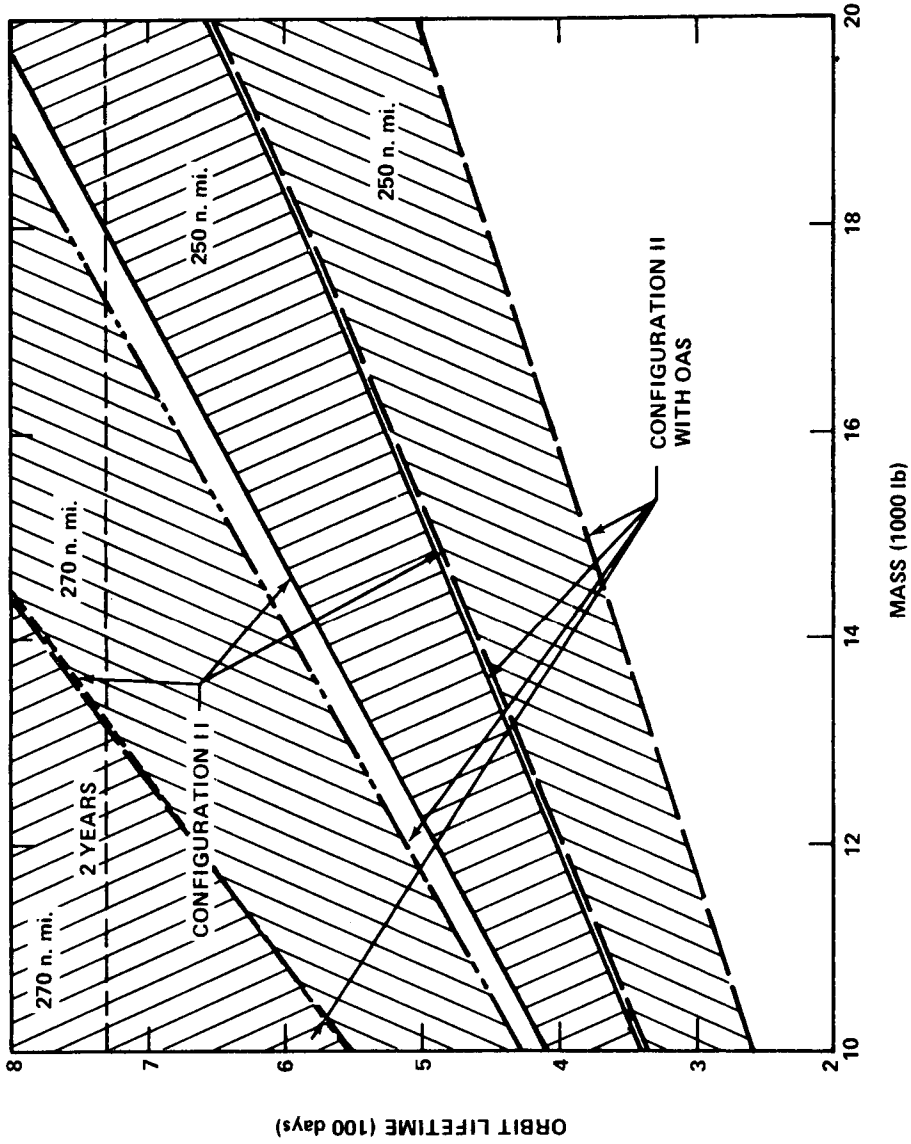


Figure B-22. Variation in orbit lifetime with vehicle mass for Configuration II with and without OAS.

- LAUNCH DATE: 9/1/77
- ATMOSPHERE MODEL: MSFC MODIFIED 1967 JACCHIA
+2 σ DENSITY
- FIXED POINTING MODE OF OPERATION

- ORBIT: 28.5 deg INCLINATION
250 n. mi. CIRCULAR

- CODE: ——— CONFIGURATION I
 - - - CONFIGURATION II

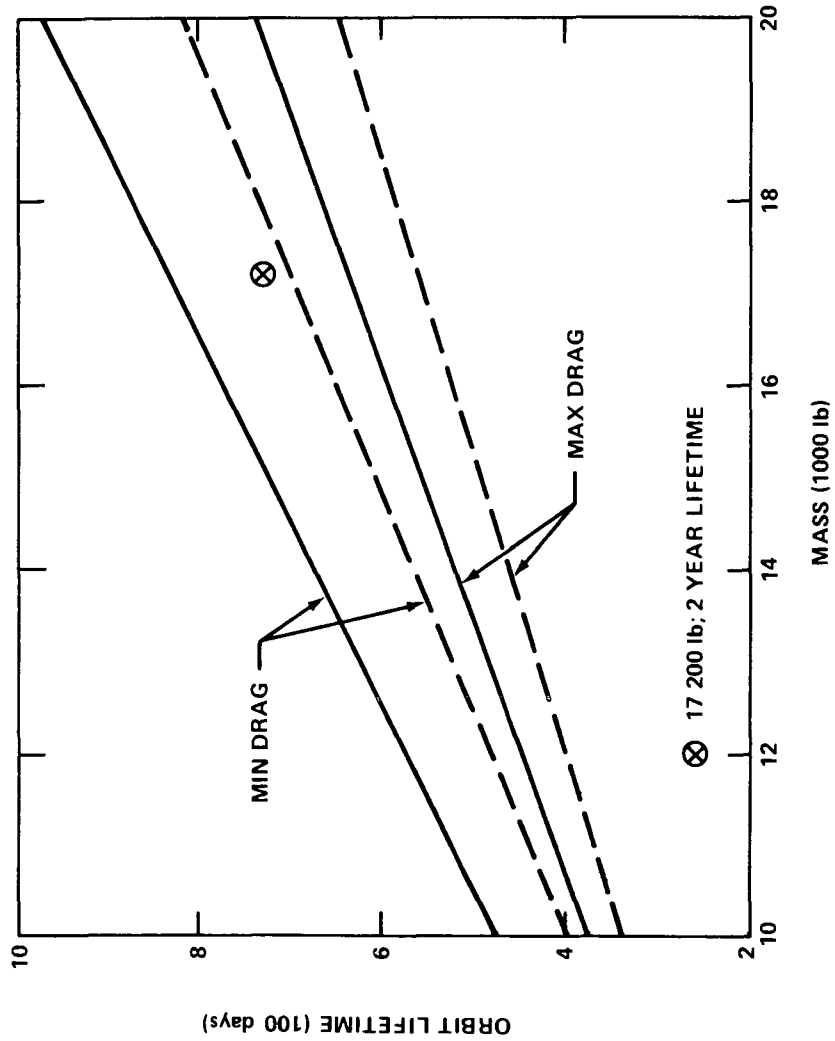


Figure B-23. Variation in orbit lifetime with vehicle mass.

- LAUNCH DATE: 9/1/78
- FIXED POINTING MODE OF OPERATION
- CIRCULAR ORBIT/28.5 deg INCLINATION
- CODE:
 - 250 n. mi. MIN DRAG
 - 250 n. mi. MAX DRAG
 - 270 n. mi. MIN DRAG
 - 270 n. mi. MAX DRAG
- ATMOSPHERE MODEL : MSFC MODIFIED 1967 JACCCHIA +2 σ DENSITY

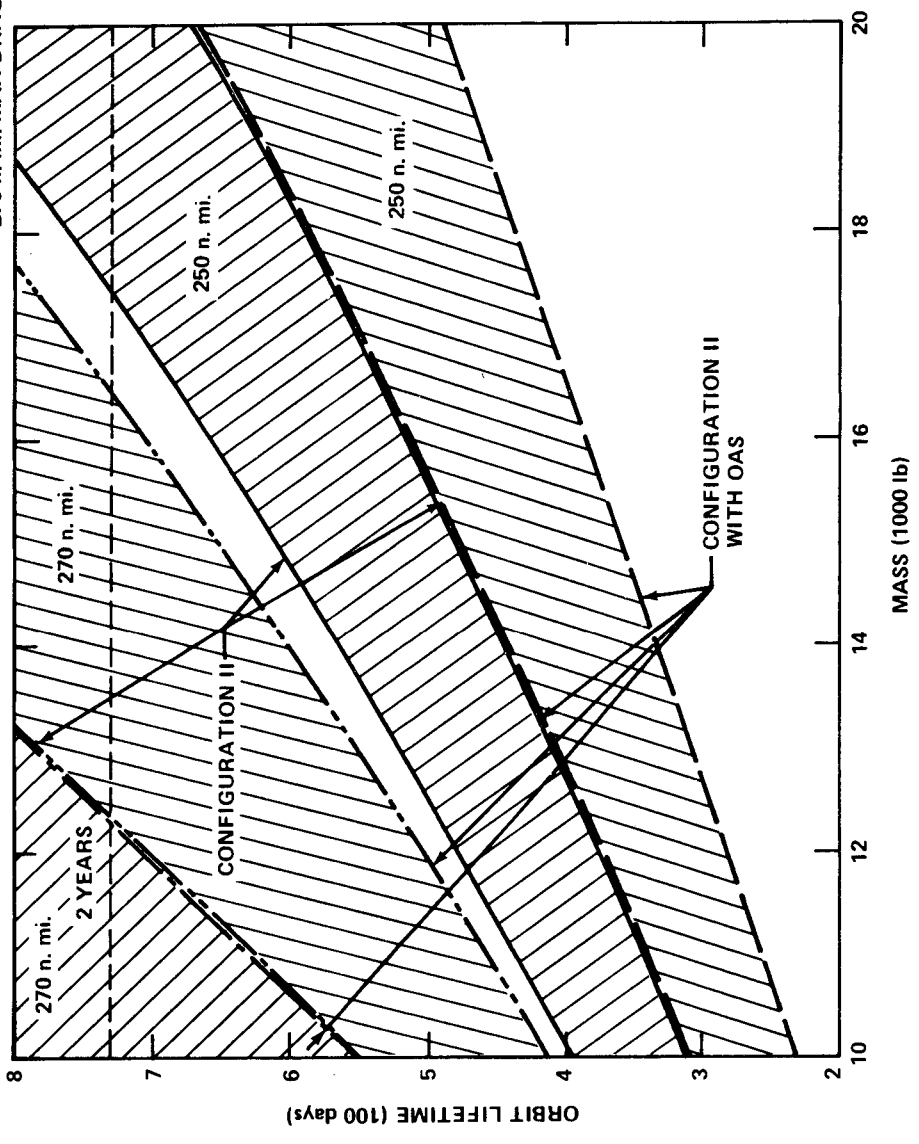


Figure B-24. Variation in orbit lifetime with vehicle mass for Configuration II with and without OAS.

- LAUNCH DATE: 9/1/78
- ATMOSPHERE: MSFC MODIFIED 1967
JACCHIA +2 σ DENSITY
- FIXED POINTING MODE OF OPERATION
- ORBIT: 28.5 deg INCLINATION
250 n. mi. CIRCULAR
- CODE: ——— CONFIGURATION I
——— CONFIGURATION II

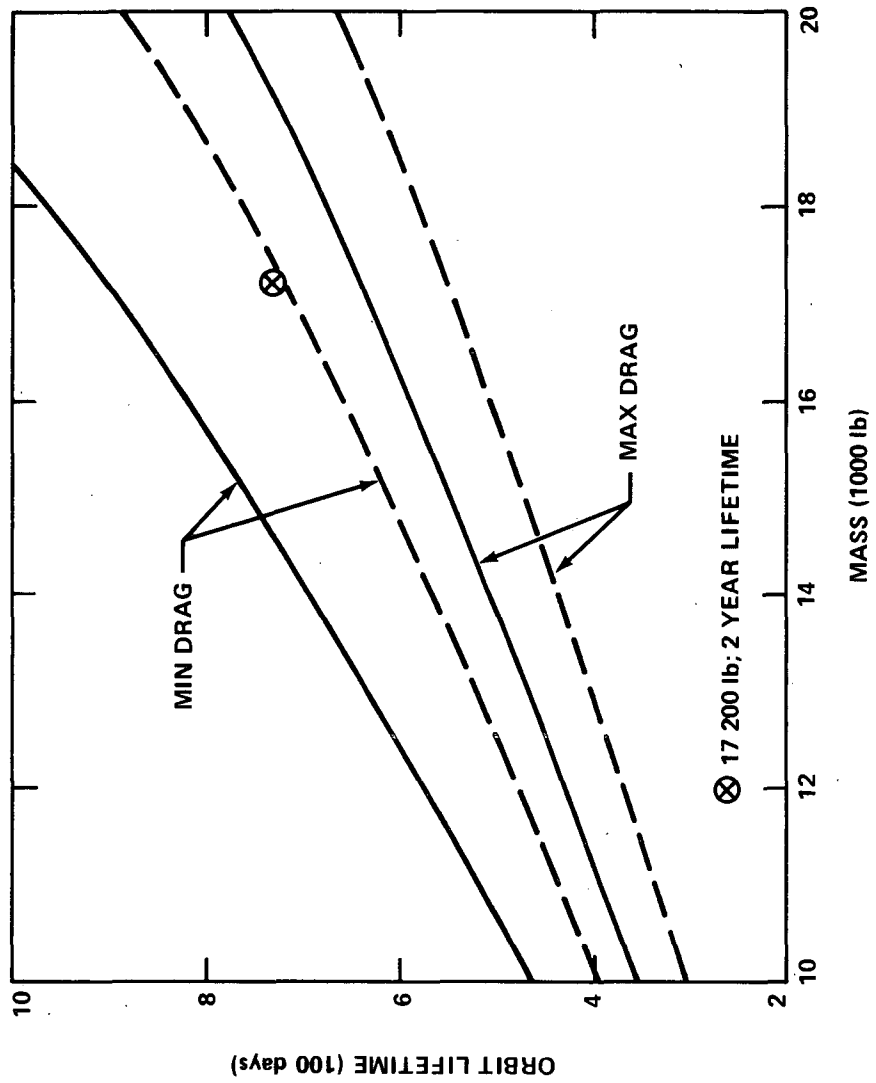


Figure B-25. Variation in orbit lifetime with vehicle mass.

- LAUNCH DATE: 3/21/77
- ORBIT: 28.5 deg INCLINATION
- ATMOSPHERE MODEL: MSFC MODIFIED
- 250 n. mi. CIRCULAR
- 1967 JACCHIA +2 σ DENSITY
- CODE: _____
- CONFIGURATION I
- FIXED POINTING MODE OF OPERATION
- _____
- CONFIGURATION II

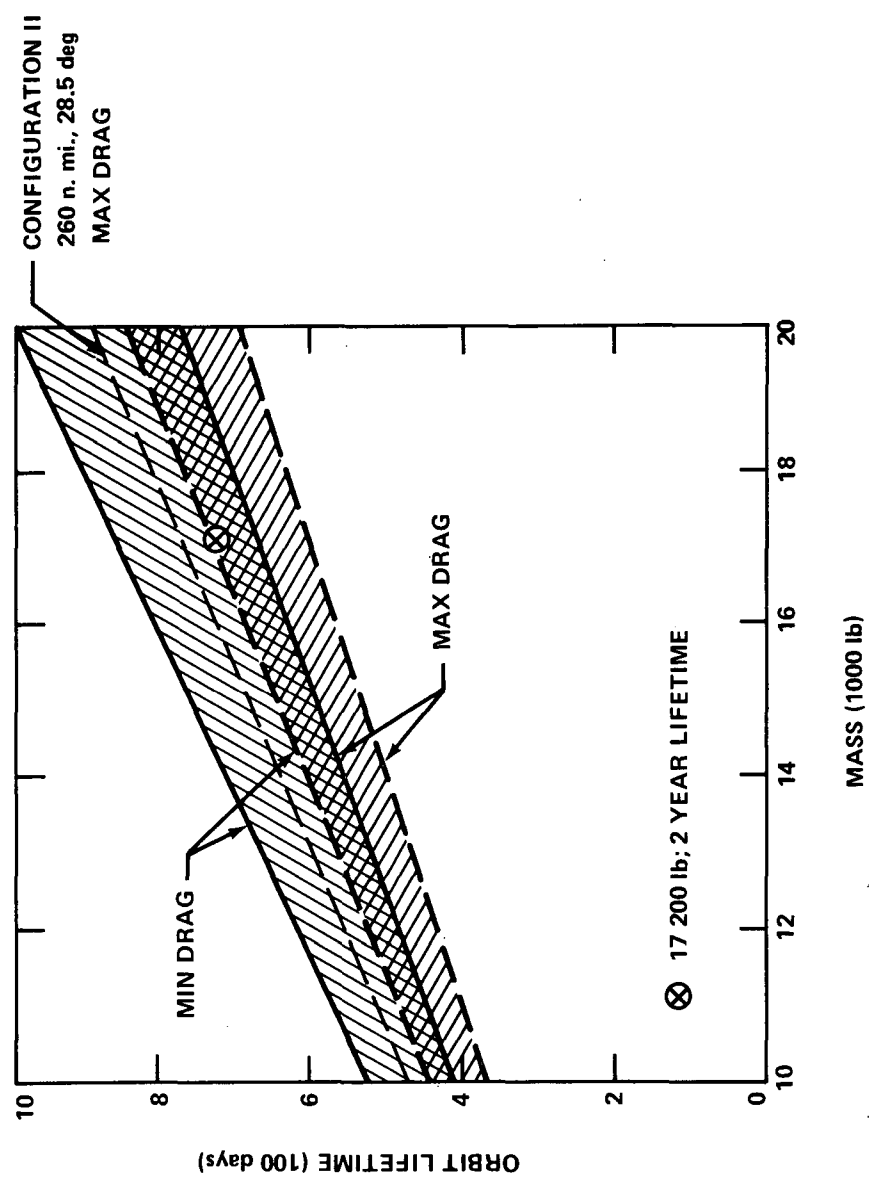


Figure B-26. Variation in orbit lifetime with vehicle mass.

- LAUNCH DATE: 3/21/77
- ATMOSPHERE MODEL: 1967 MSFC MODIFIED
JACCHIA + 2 σ DENSITY
- FIXED POINTING MODE OF OPERATION
- 28.5 deg INCLINATION CIRCULAR ORBIT
- CODE: ——— 260 n.mi., MIN DRAG
- - - 260 n.mi., MAX DRAG
- · - 270 n.mi., MAX DRAG

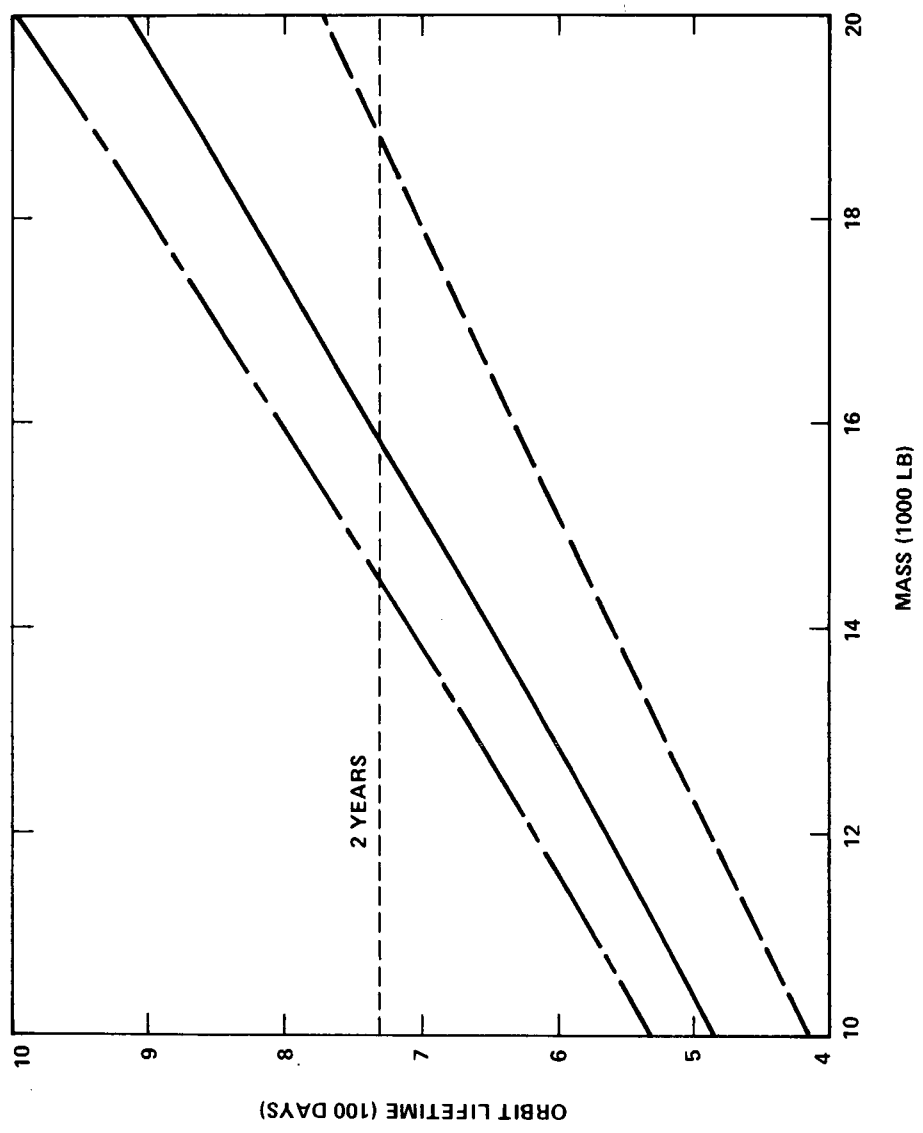


Figure B-27. Variation in orbit lifetime with vehicle mass for octacircular HEAO-C without subsystem module.

- LAUNCH DATE: 3/21/77
- ATMOSPHERE MODEL: 1967 MSFC MODIFIED
- FIXED POINTING MODE OF OPERATION
- 28.5 deg INCLINATION CIRCULAR ORBIT
- CODE: ——— 260 n. mi., MIN DRAG
- - - 260 n. mi., MAX DRAG
- - - 270 n. mi., MAX DRAG

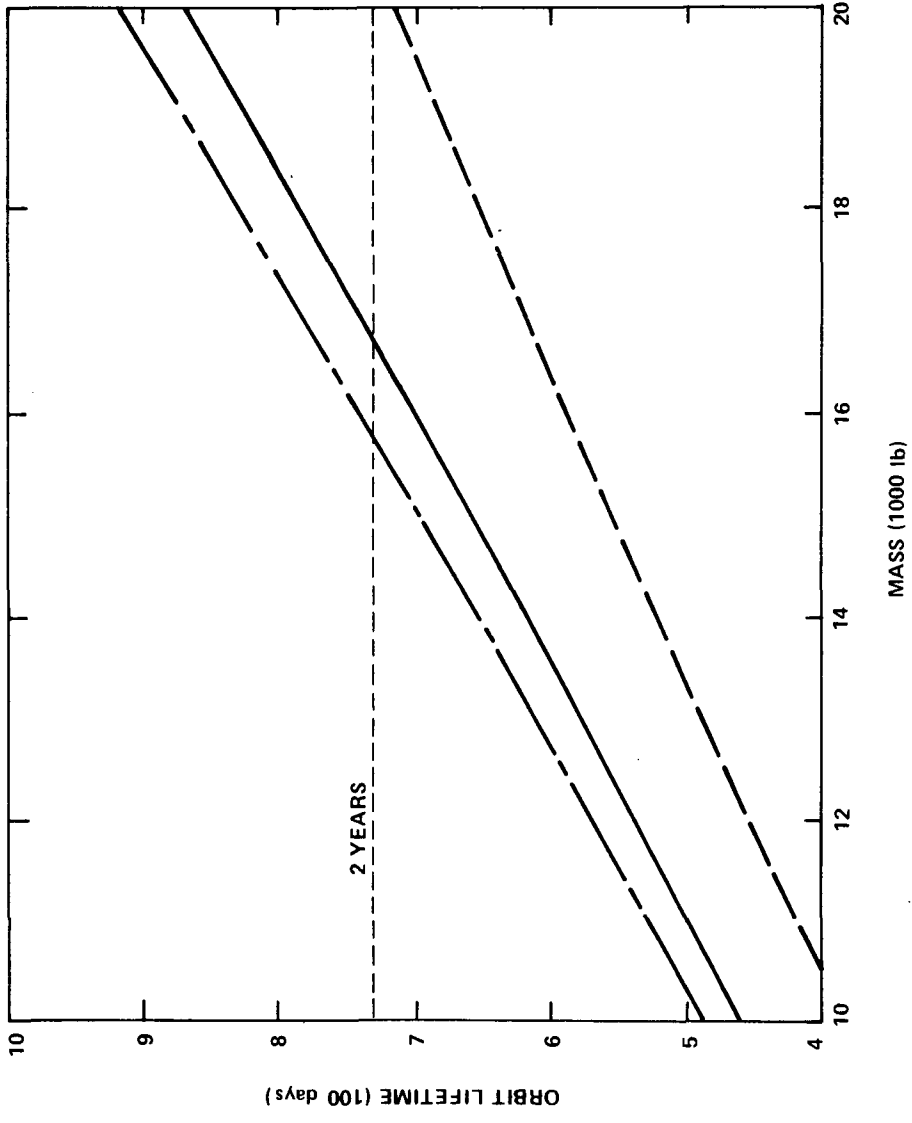


Figure B-28. Variation in orbit lifetime with vehicle mass for octacircular HEAO-C with subsystem module.

20

- LAUNCH DATE: 9/1/76
- 28.5 deg INCLINATION CIRCULAR ORBIT
- ATMOSPHERE MODEL: 1967 MSFC MODIFIED
- CODE: ——— 260 n. mi., MIN DRAG
- JACCHIA + 2 σ DENSITY
- ——— 260 n. mi., MAX DRAG
- FIXED POINTING MODE OF OPERATION
- ——— 270 n. mi., MAX DRAG

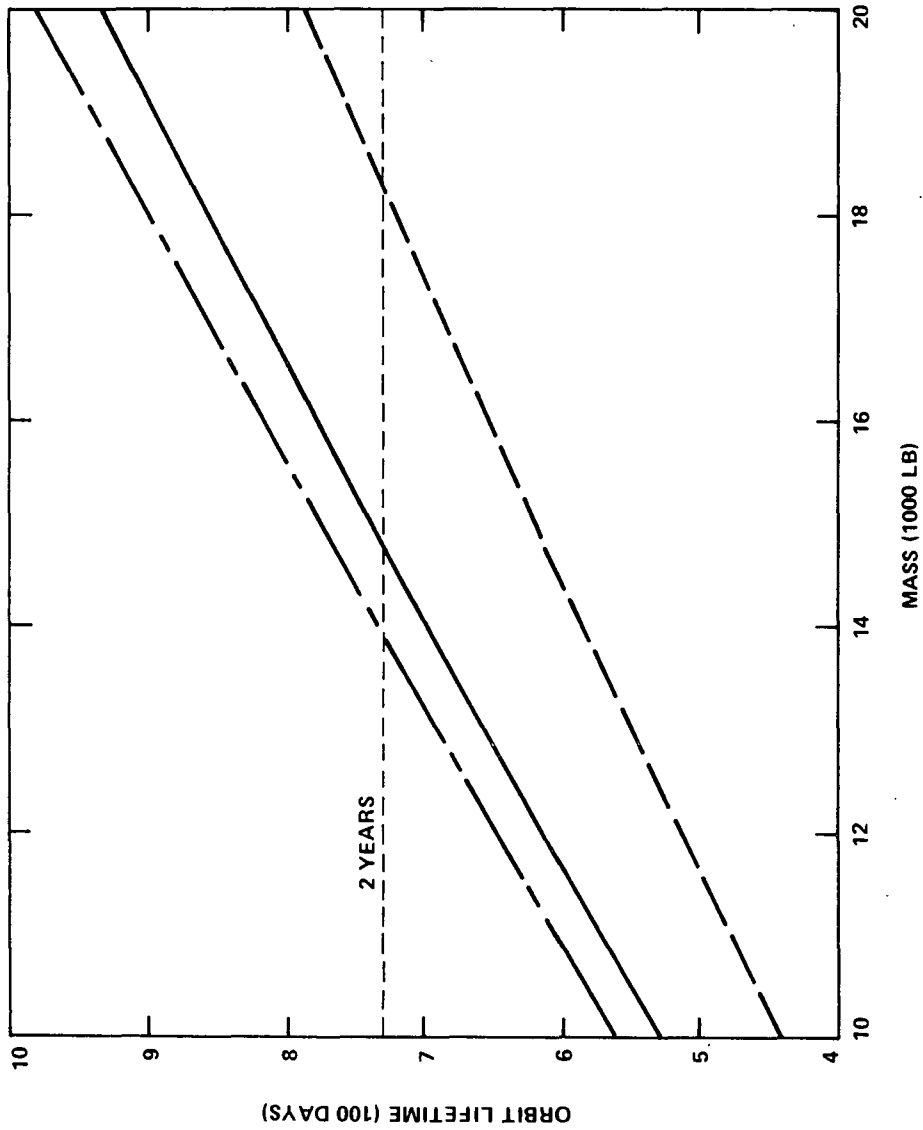


Figure B-29. Variation in orbit lifetime with vehicle mass for octacircular HEAO-C with subsystem module.

- LAUNCH DATE : 9/1/77
- ATMOSPHERE MODEL: 1967 MSFC MODIFIED
JACCHIA + 2 σ DENSITY
- FIXED POINTING MODE OF OPERATION
- 28.5 deg INCLINATION CIRCULAR ORBIT
- CODE: ——— 260 n. mi., MIN DRAG
——— 260 n. mi., MAX DRAG
——— 270 n. mi., MAX DRAG

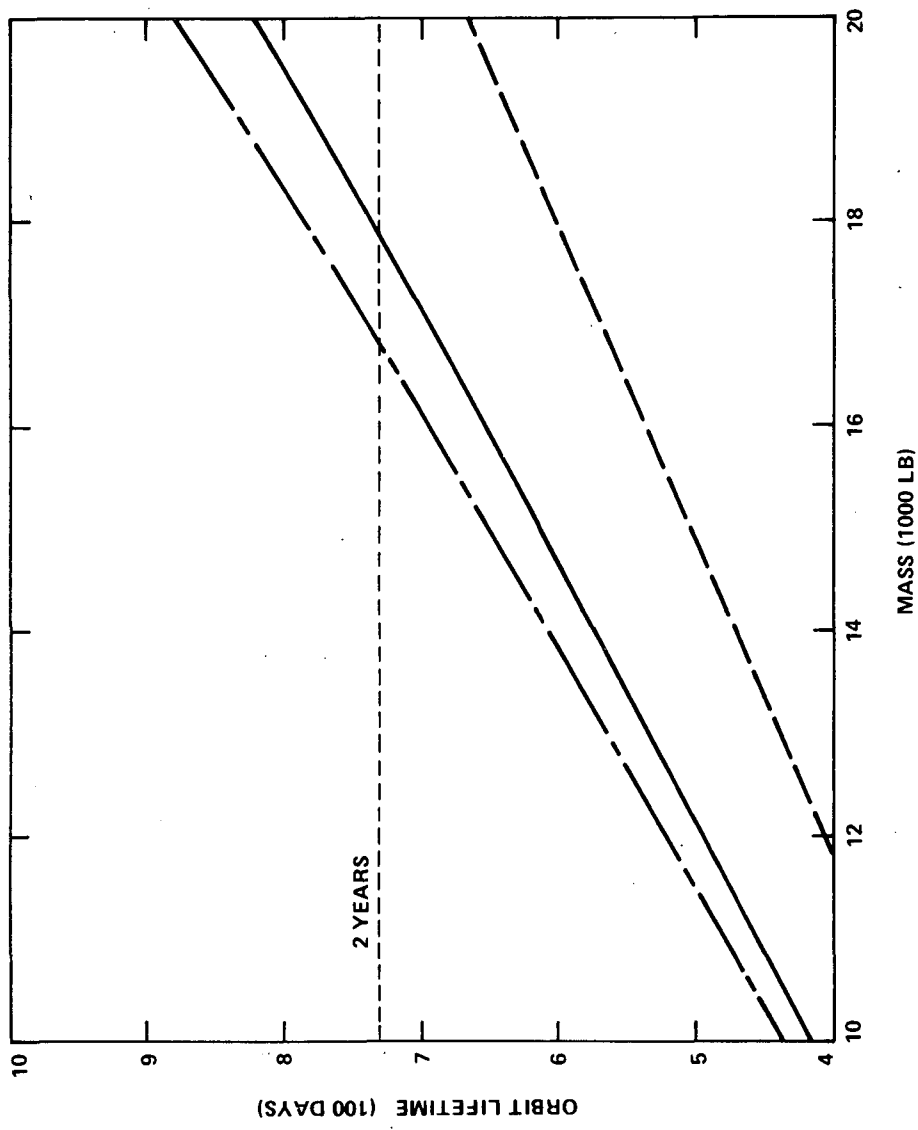


Figure B-30. Variation in orbit lifetime with vehicle mass for octacircular HEAO-C with subsystem module.

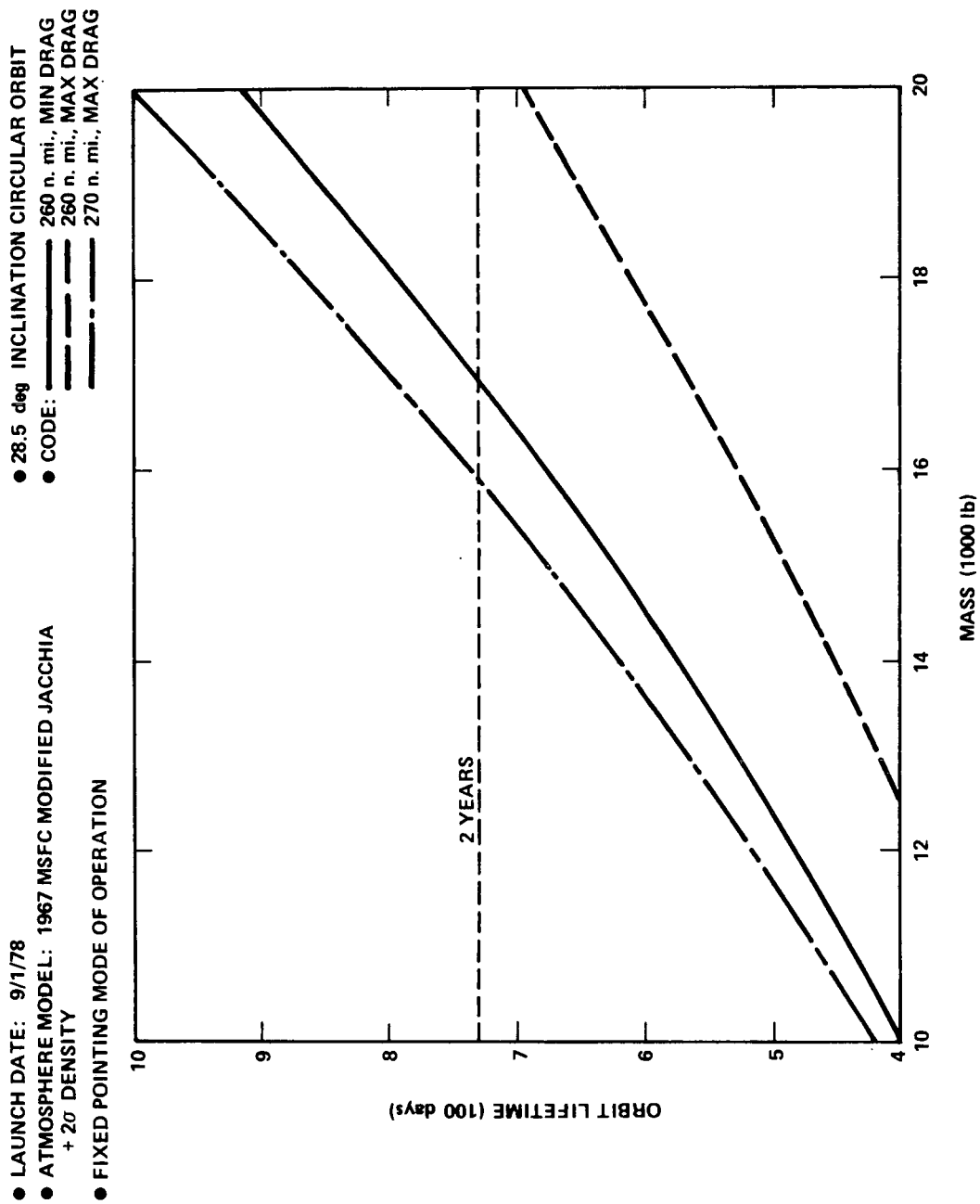


Figure B-31. Variation in orbit lifetime with vehicle mass for octacircular HEAO-C with subsystem module.

- LAUNCH DATE: 9/1/76
- ATMOSPHERE MODEL: MSFC MODIFIED 1967 JACCHIA
- FIXED POINTING MODE OF OPERATION
- 28.5 deg INCLINATION ORBIT
- CODE: ——— MIN DRAG
- ——— MAX DRAG

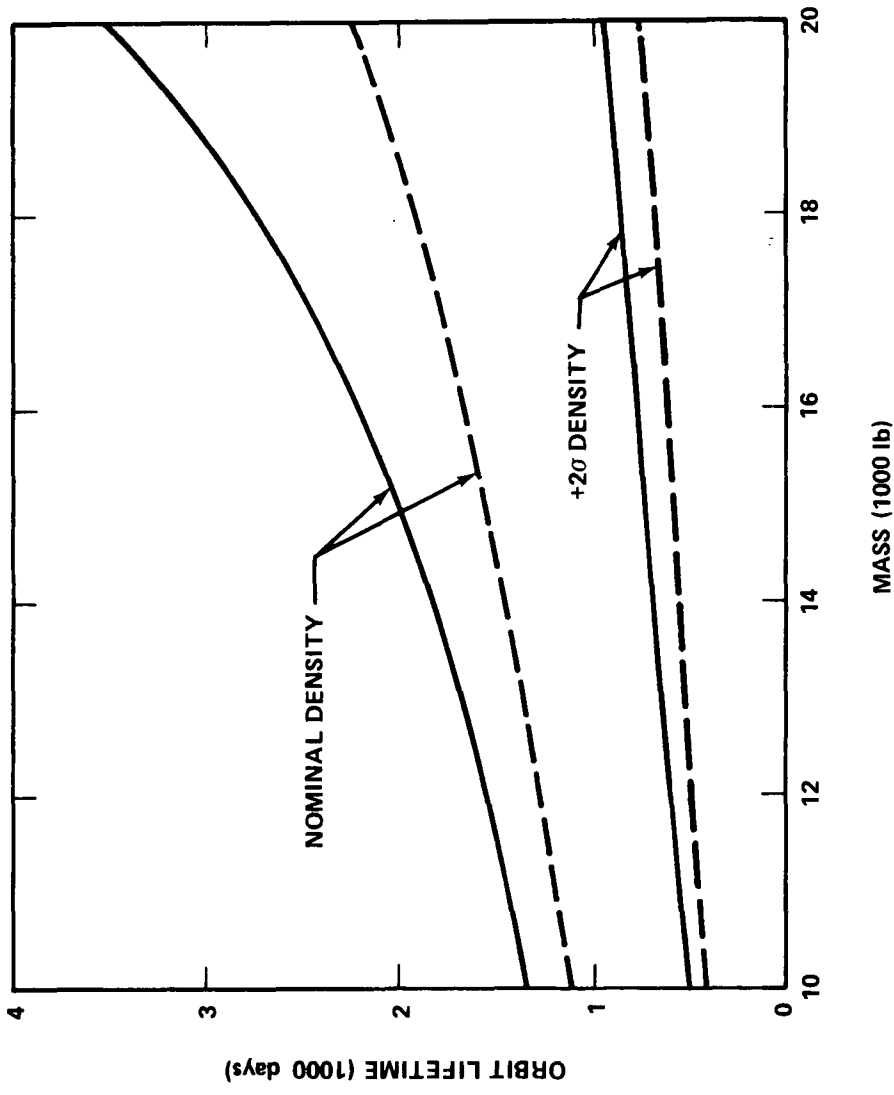


Figure B-32. Variation in orbit lifetime with vehicle mass for HEAO-C Configuration II in a 250 nautical mile altitude circular orbit.

- LAUNCH DATE: 3/21/77
- ORBIT INCLINATION: 28.5 deg
- ATMOSPHERE MODEL: MSFC MODIFIED 1967 JACCHIA
- MIN DRAG, 250 n. mi.
- FIXED POINT MODE OF OPERATION
- MAX DRAG, 250 n. mi.
- MAX DRAG, 260 n. mi.

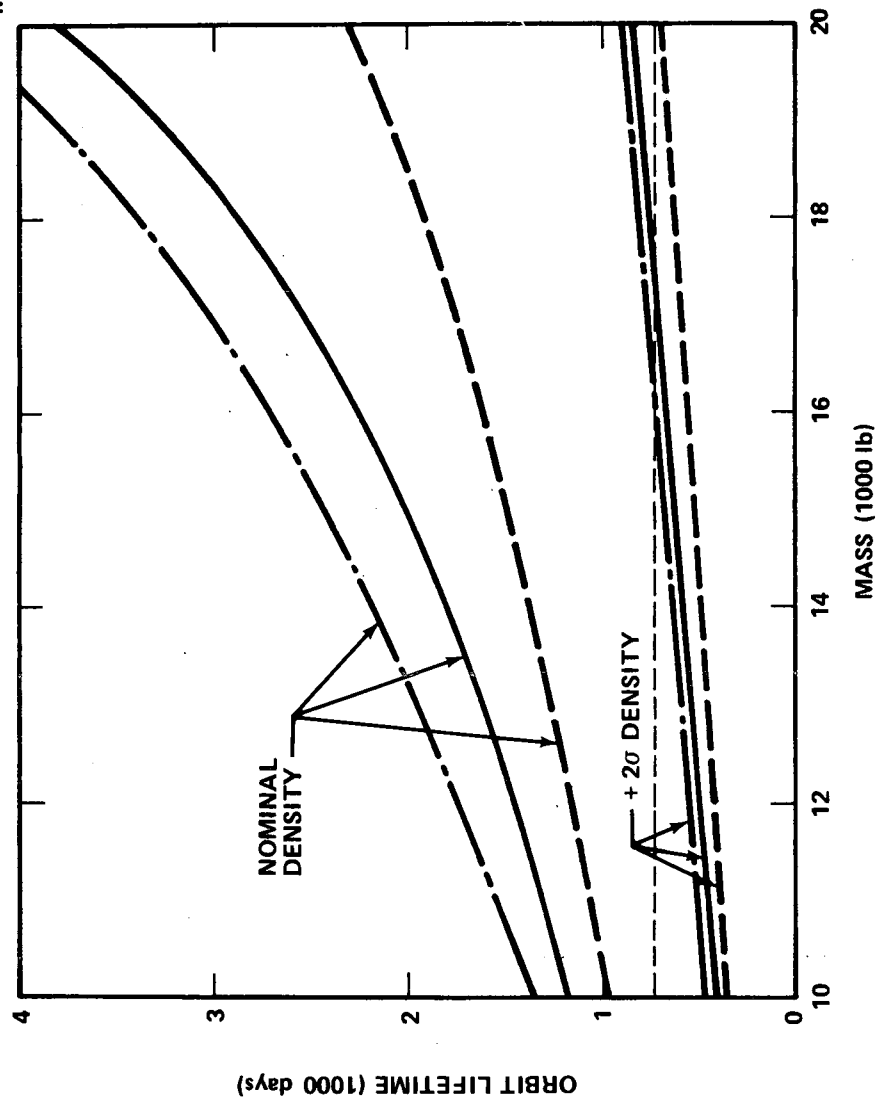


Figure B-33. Variation in orbit lifetime with vehicle mass for Configuration II.

- LAUNCH DATE: 3/21/77
- ATMOSPHERE MODEL: MSFC MODIFIED 1967 JACCHIA
- FIXED POINTING MODE OF OPERATION
- 28.5 deg INCLINATION ORBIT
- CODE:
 - MIN DRAG, 250 n. mi., ALTITUDE
 - MAX DRAG, 250 n. mi., ALTITUDE
 - MAX DRAG, 260 n. mi., ALTITUDE

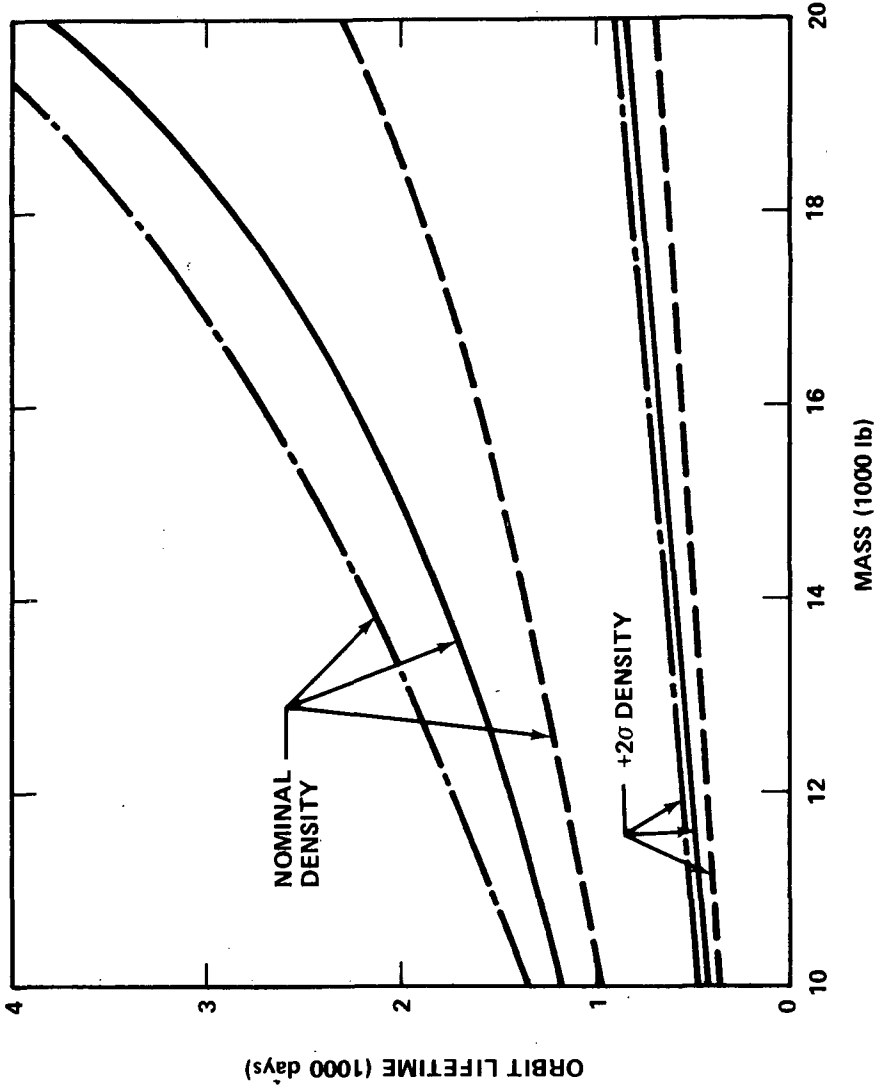


Figure B-34. Variation in orbit lifetime with vehicle mass for Configuration II.

- LAUNCH DATE: 9/1/77
- ATMOSPHERE MODEL: MSFC MODIFIED 1967 JACCHIA
- FIXED POINTING MODE OF OPERATION
- 28.5 deg INCLINATION ORBIT
- CODE: _____
- MIN DRAG _____
- MAX DRAG _____

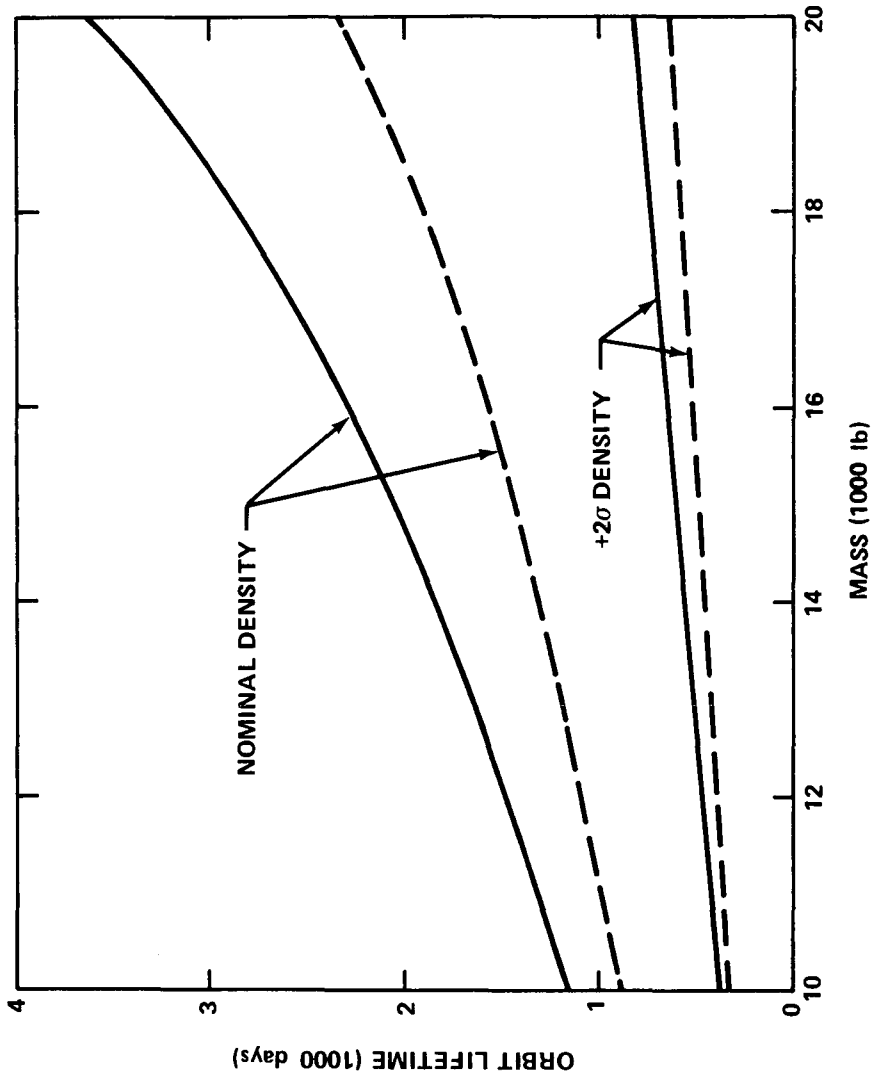


Figure B-35. Variation in orbit lifetime with vehicle mass for HEAO-C Configuration II in a 250 nautical mile altitude circular orbit.

- LAUNCH DATE: 9/1/78
- ATMOSPHERE MODEL: MSFC MODIFIED 1967 JACCHIA
- FIXED POINTING MODE OF OPERATION
- 28.5 deg INCLINATION ORBIT
- CODE: ——— MIN DRAG
- ——— MAX DRAG

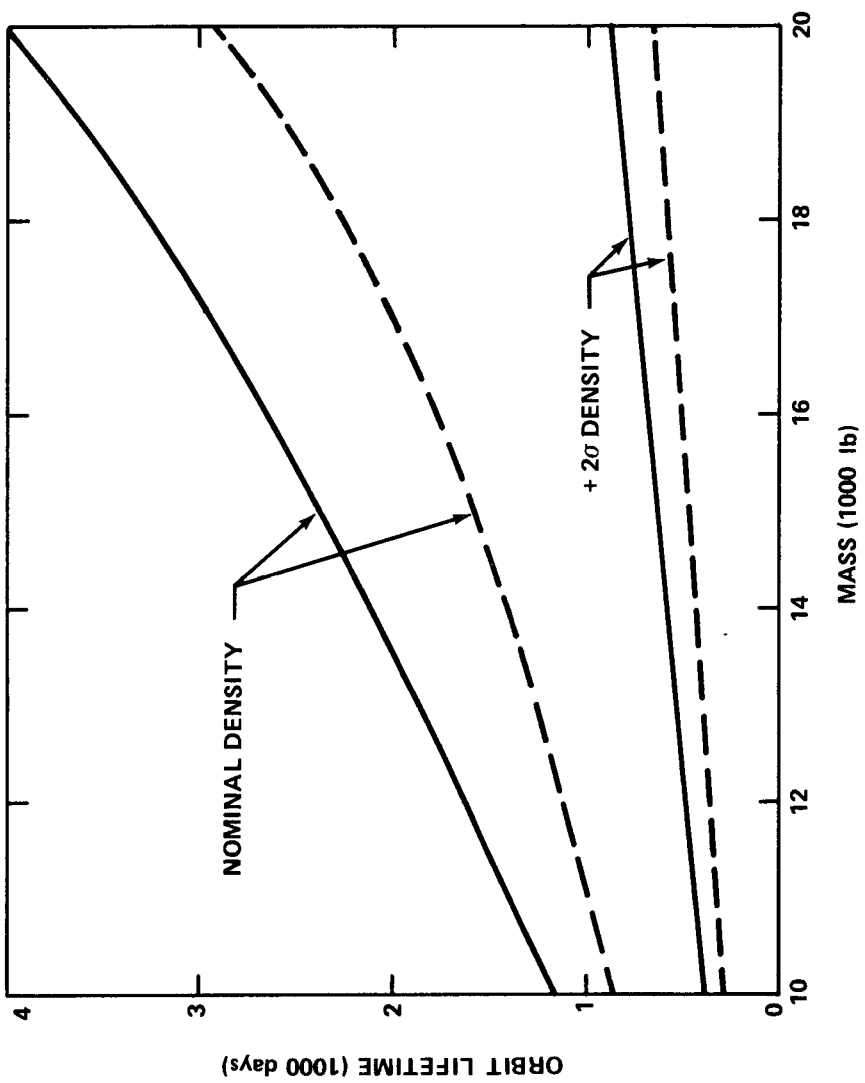


Figure B-36. Variation in orbit lifetime with vehicle mass for HEAO-C Configuration II in a 250 nautical mile altitude circular orbit.

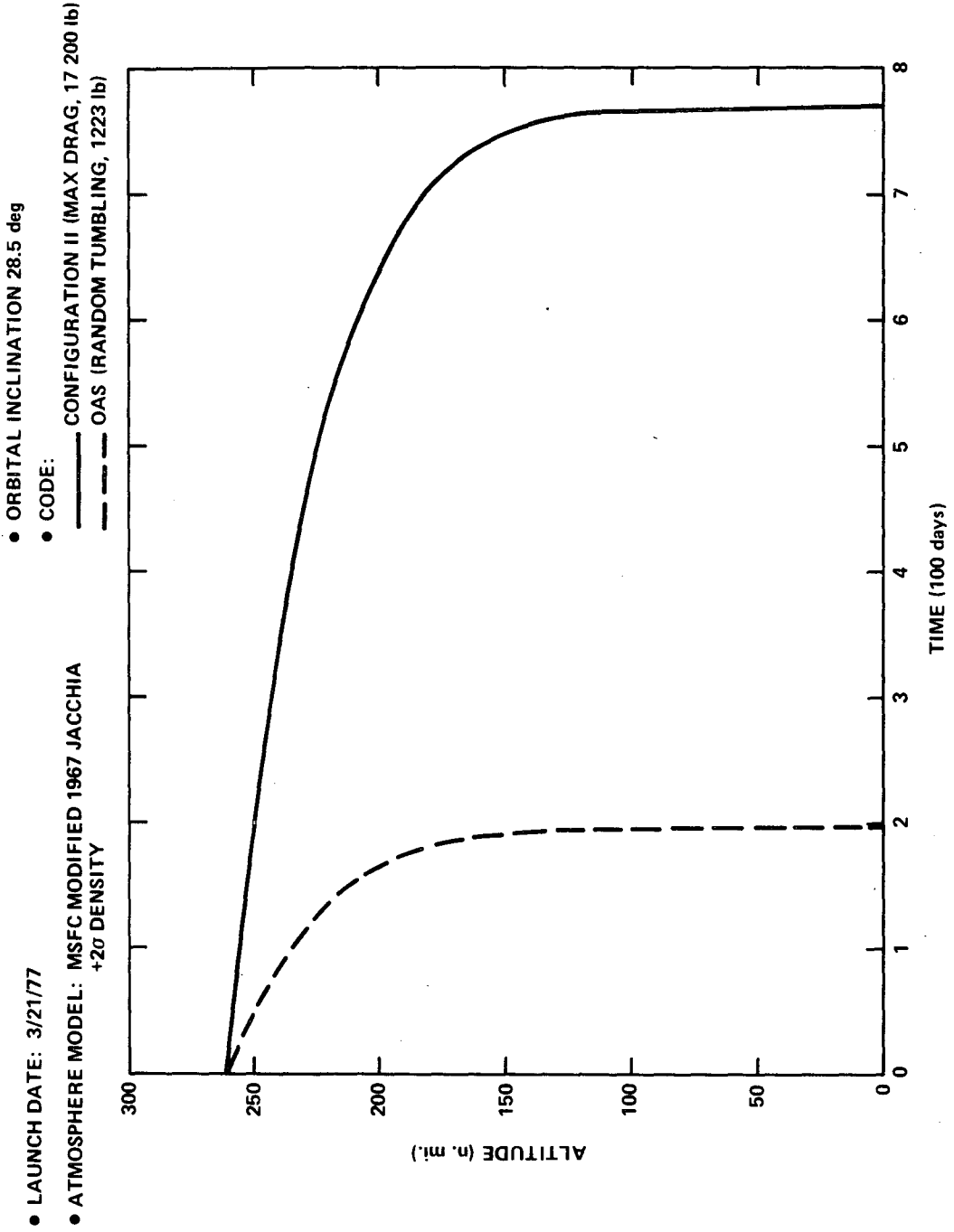


Figure B-37. Variation in altitude with time for a 260 nautical mile altitude initial orbit.

Orbital Adjust Stage (OAS) Separation

Separation of the HEAO-C spacecraft (S/C) from the OAS would be initiated by a spring system after the S/C and OAS have been inserted into the desired orbit. The relative motion and displacement between the HEAO S/C and OAS after separation have been investigated to determine OAS interference on HEAO operation.

The HEAO S/C weight was assumed to be 17 000 pounds and the OAS weight 1223 pounds at the separation point. The target orbit's altitude was considered to be 270 by 270 nautical miles with an inclination of 28.5 degrees. Atmospheric drag effect was not considered in the relative motion and displacement investigation.

Geometric relationships between the HEAO S/C and OAS are given in Figure B-38. The spring separation system will impart a retro ΔV_K on the OAS causing its orbit to have a perigee altitude slightly lower than the initial separation point altitude. A small forward ΔV_H will be imparted to the HEAO S/C causing its orbit to have an apogee altitude slightly higher than the initial separation point altitude. Theta (θ) represents the lead angle of the OAS relative to the HEAO S/C; ΔH represents the vertical separation distance and is shown, Figure B-39, versus time for the first two orbits after separation. The maximum vertical separation distance for the first two orbits occurs 180 degrees from the separation point and is equal to the difference between the perigee altitude of the OAS and the apogee altitude of the HEAO S/C. A separation, ΔV , of 1 foot per second will result in a vertical separation distance between perigee and apogee altitudes of 3600 feet.

Immediately after separation, the OAS will trail the HEAO S/C and the maximum trail distance will be 432 feet for every 1 foot per second ΔV ; this maximum distance will occur 11 minutes after separation is initiated.

- θ = SEPARATION ANGLE
- D = SEPARATION DISTANCE
- ΔH = DIFFERENCE IN ALTITUDE
- ΔL = HORIZONTAL SEPARATION
- ΔV_H = VELOCITY IMPARTED TO HEAO S/C
- ΔV_K = VELOCITY IMPARTED TO OAS
- ΔV = TOTAL SEPARATION VELOCITY

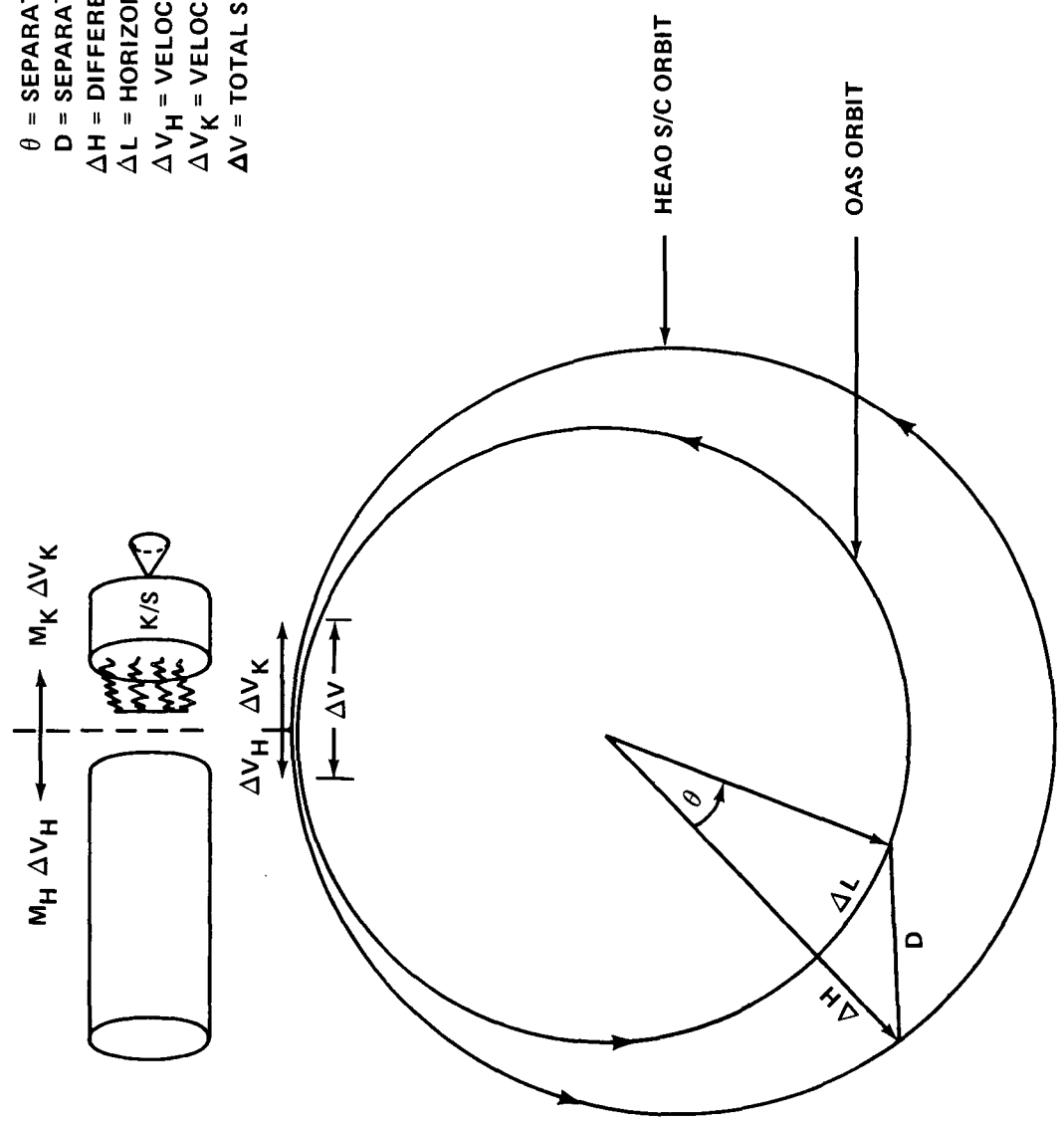


Figure B-38. HEAO S/C , OAS separation by compression springs.

- 270 n. mi. INITIAL ALTITUDE
- HEAO S/C WEIGHT = 17 000 lb
- OAS WEIGHT = 1223 lb

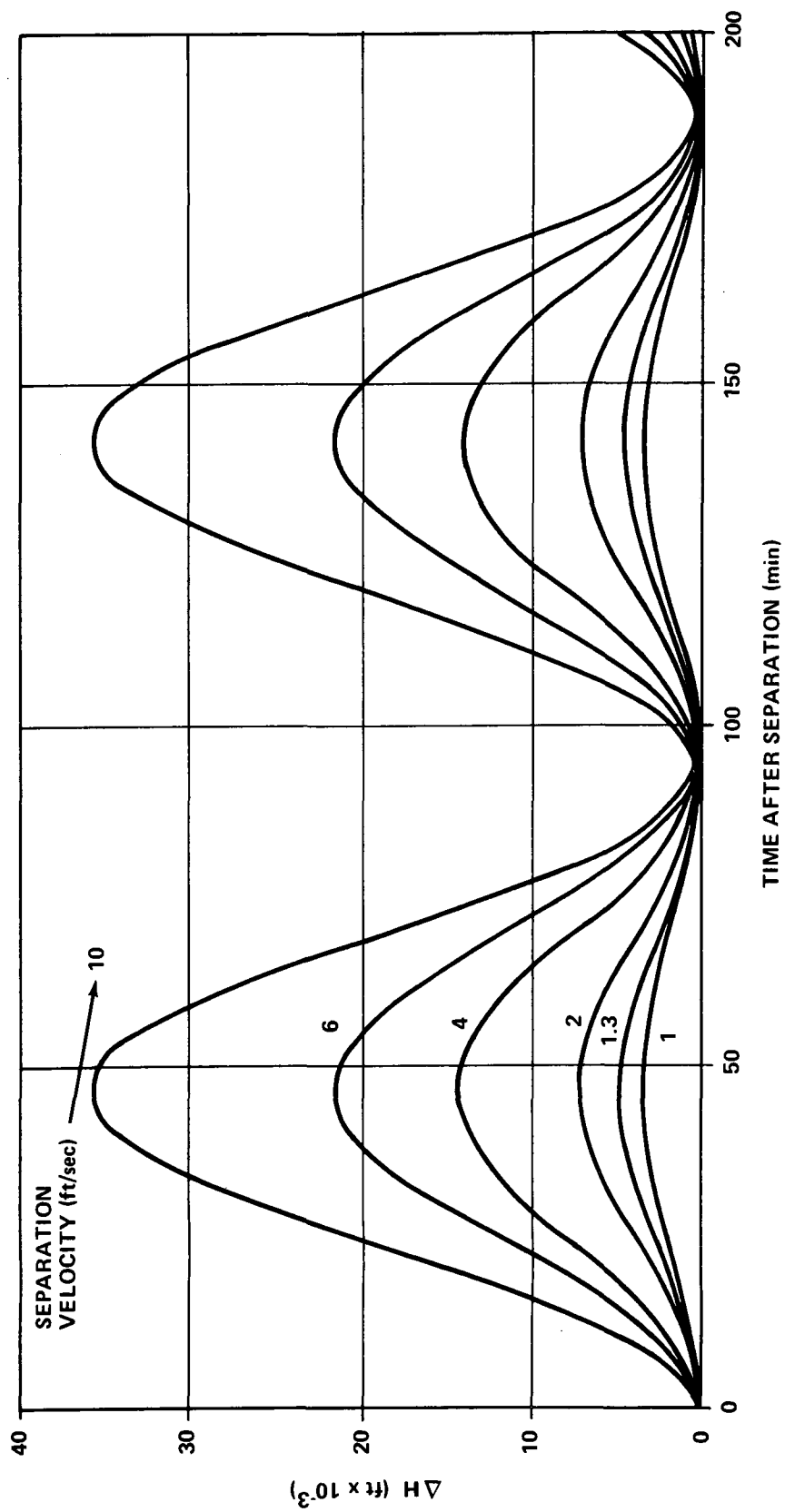


Figure B-39. Relative vertical distance (ΔH) versus time.

From this point the OAS will begin to catch up with the S/C and 19 minutes after separation will be vertically aligned with the S/C but at a lower altitude. The vertical distance between the S/C and OAS, after 19 minutes, will be 1300 feet for every 1 foot per second ΔV . The above separation conditions are shown in Figures B-40 and B-41.

Figure B-42 shows the angular displacement (θ) by which the OAS will lead the HEAO S/C. An angular displacement of less than 30.5 degrees could cause viewing interference at some point in the orbit if the HEAO S/C were gathering data from a source which has a line-of-sight in the orbit plane. The interference time would be around 3 minutes per orbit. This chance of interference time would occur in the first 23 days of the mission and again during 252 to 298 days in the mission for a separation ΔV of 2 feet per second.

The total separation distance between the OAS and S/C is given for the first two orbits (Fig. B-43), for the first day (Fig. B-44), and up to 50 days in the mission (Fig. B-45). In Figure B-43, a local maximum point on the curves occurring near 90 and 180 minutes after separation is due, essentially, to horizontal displacement at these points.

The angular realignment period versus separation ΔV is shown in Figure B-46. A separation velocity of 2 feet per second would result in a realignment 275 days after separation.

The spring energy required to provide various separation velocities is given in Figure B-47. A separation velocity of 2 feet per second would require a total spring energy of 71 foot-pound. Assuming an eight-spring system and the spring compressed 2 inches, a spring constant of 639 pounds/foot would be required for each spring.

This separation analysis was conducted to determine the relative motion between the HEAO S/C and OAS immediately after separation and up to 50 days after separation. The data generated indicated that there should be no problem of collision between the S/C and OAS after a clean separation has been obtained. The analysis did not consider atmospheric drag; however, the effect of drag being included would cause the separation distance and angle to be greater than those determined in Figures B-38 through B-46 because the OAS has a faster decay rate than the HEAO S/C. A separation velocity between 1 and 4 feet per second would be a range of minimum and maximum magnitude, the minimum value being set by minimum spring force to effect separation and the maximum value being determined by the impingement force which would impact the S/C and OAS.

- 270 n. mi. INITIAL ALTITUDE
- HEAO S/C WEIGHT = 17 000 lb
- OAS WEIGHT = 1223 lb

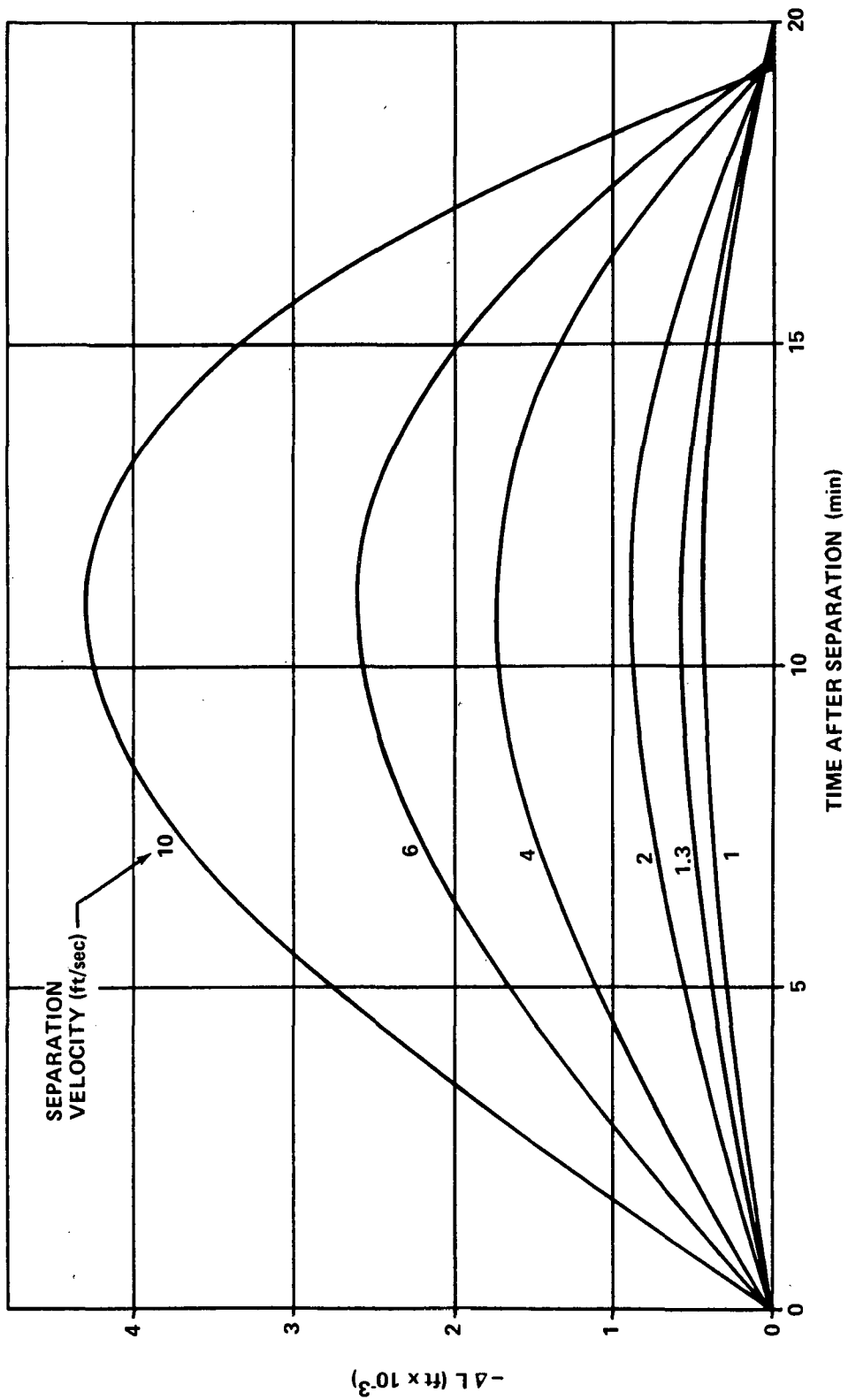


Figure B-40. Relative horizontal distance (ΔL) versus time.

- 270 n. mi. INITIAL ALTITUDE
- HEAO S/C WEIGHT = 17 000 lb
- OAS WEIGHT = 1223 lb

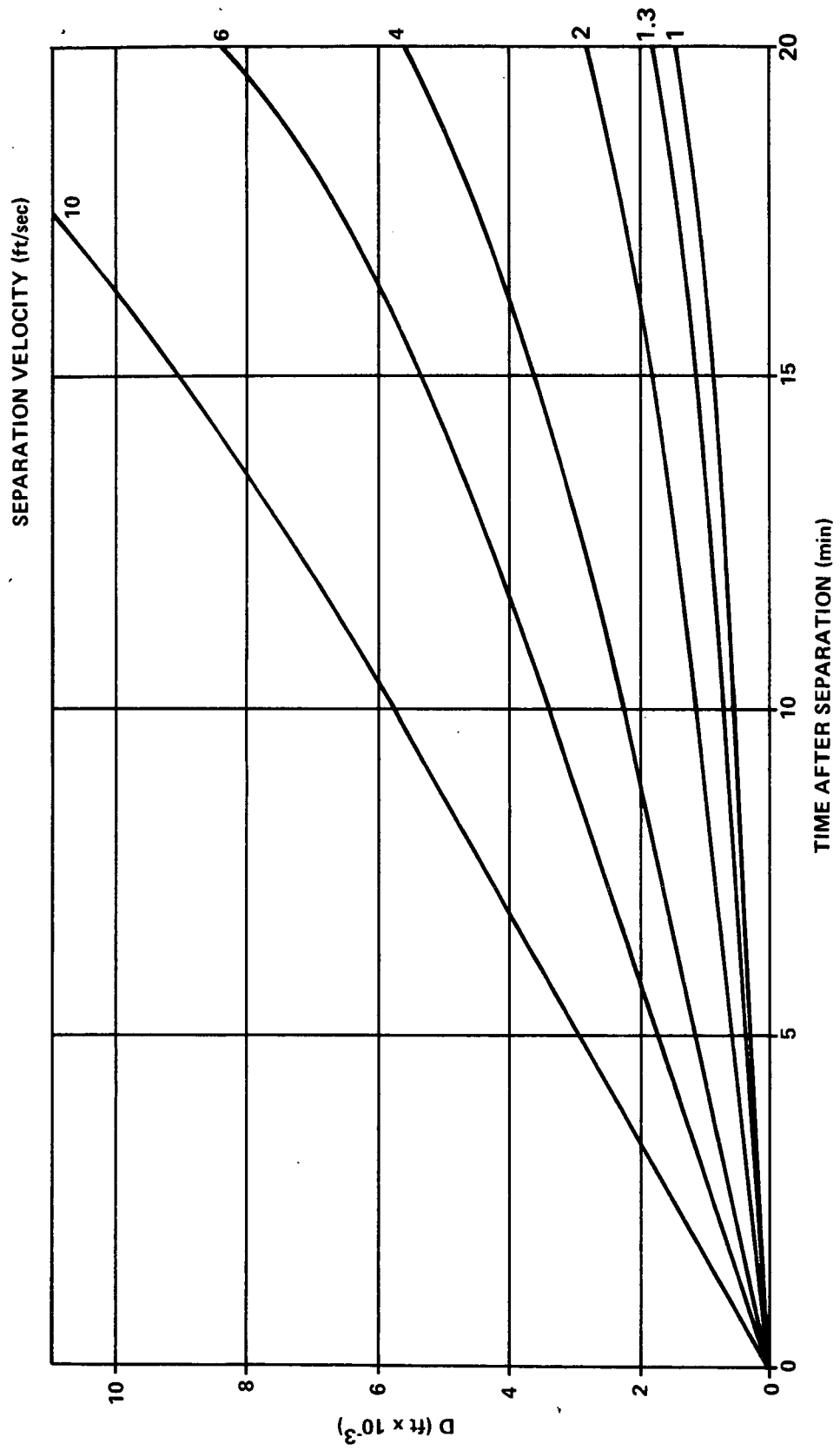


Figure B-41. Separation distance (D) versus time.

- 270 n. mi. INITIAL ALTITUDE
- HEAO S/C WEIGHT = 17 000 lb
- OAS WEIGHT = 1223 lb

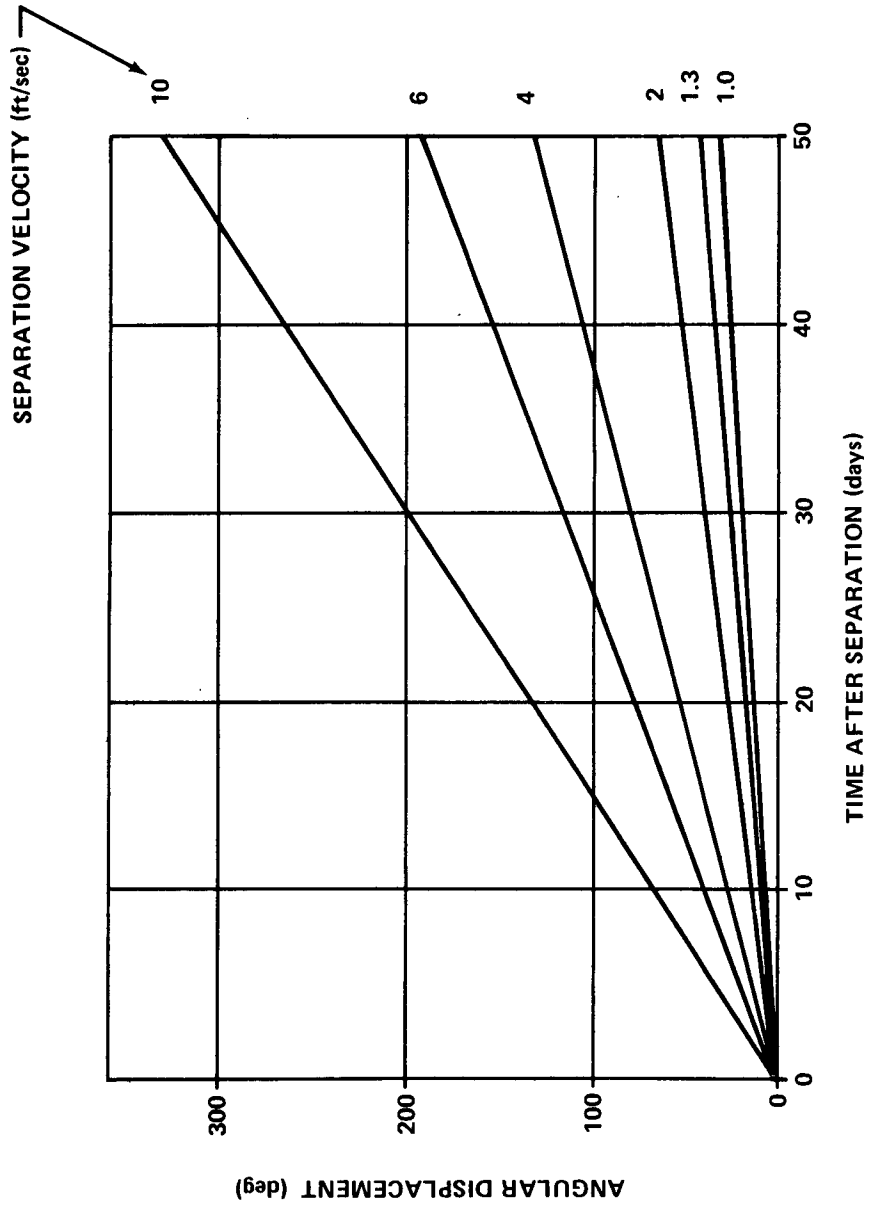


Figure B-42. Angular displacement versus time.

- 270 n. mi. INITIAL ALTITUDE
- HEAO S/C WEIGHT = 17 000 lb
- OAS WEIGHT = 1223 lb

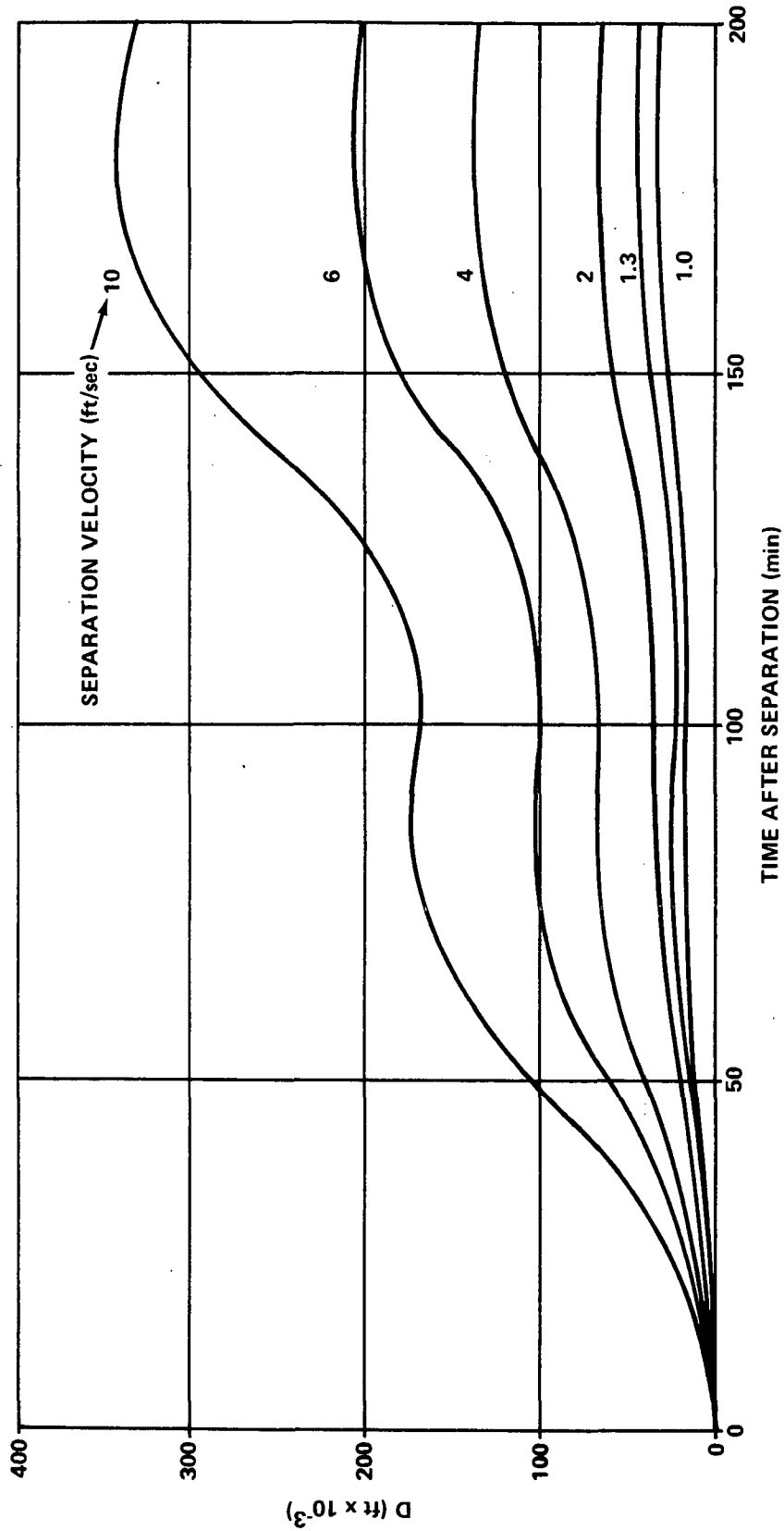


Figure B-43. Separation distance (D) versus time.

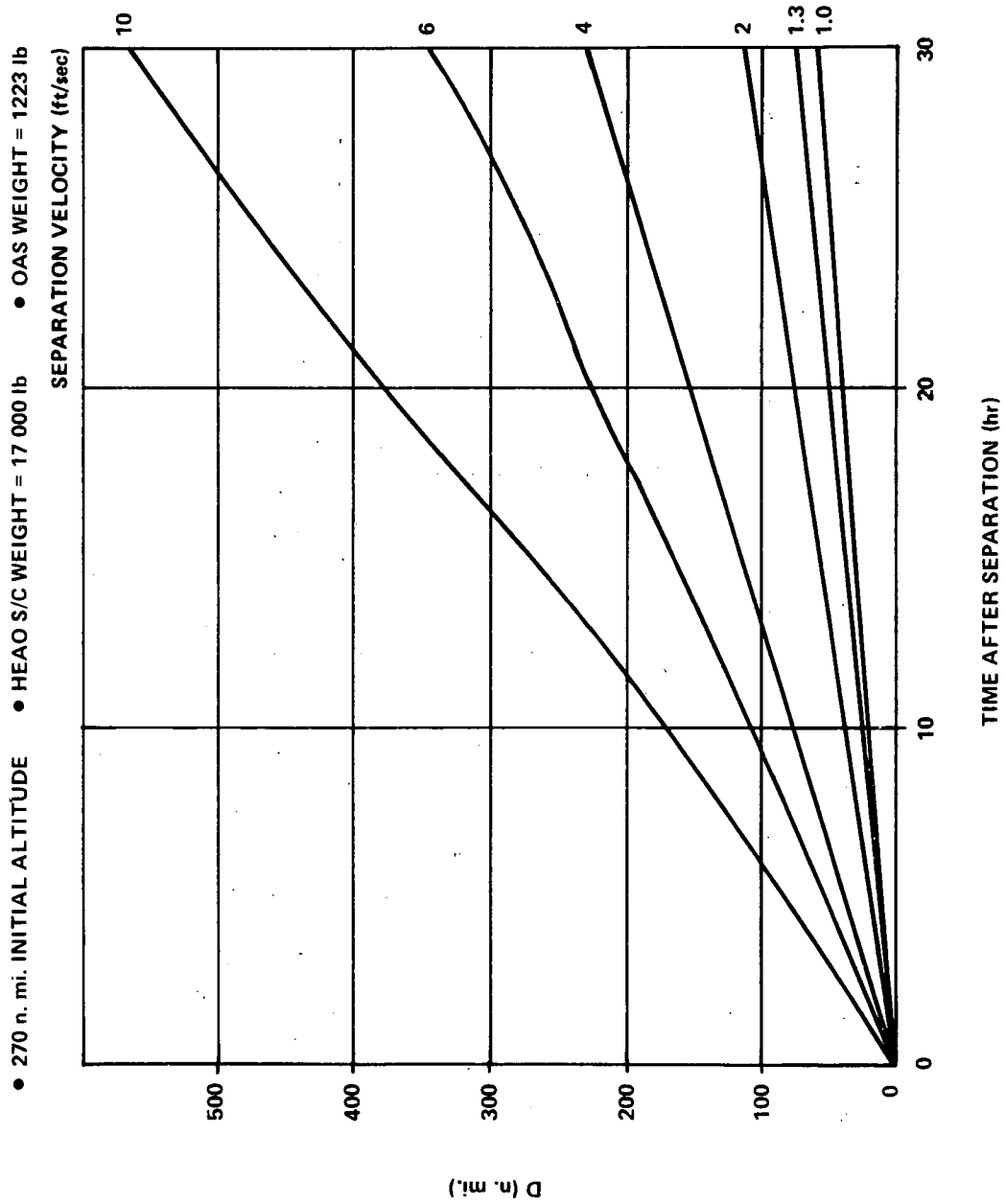


Figure B-44. Separation distance (D) versus time.

• 270 n. mi. INITIAL ALTITUDE • HEAO S/C WEIGHT = 17 000 lb • OAS WEIGHT = 1223 lb

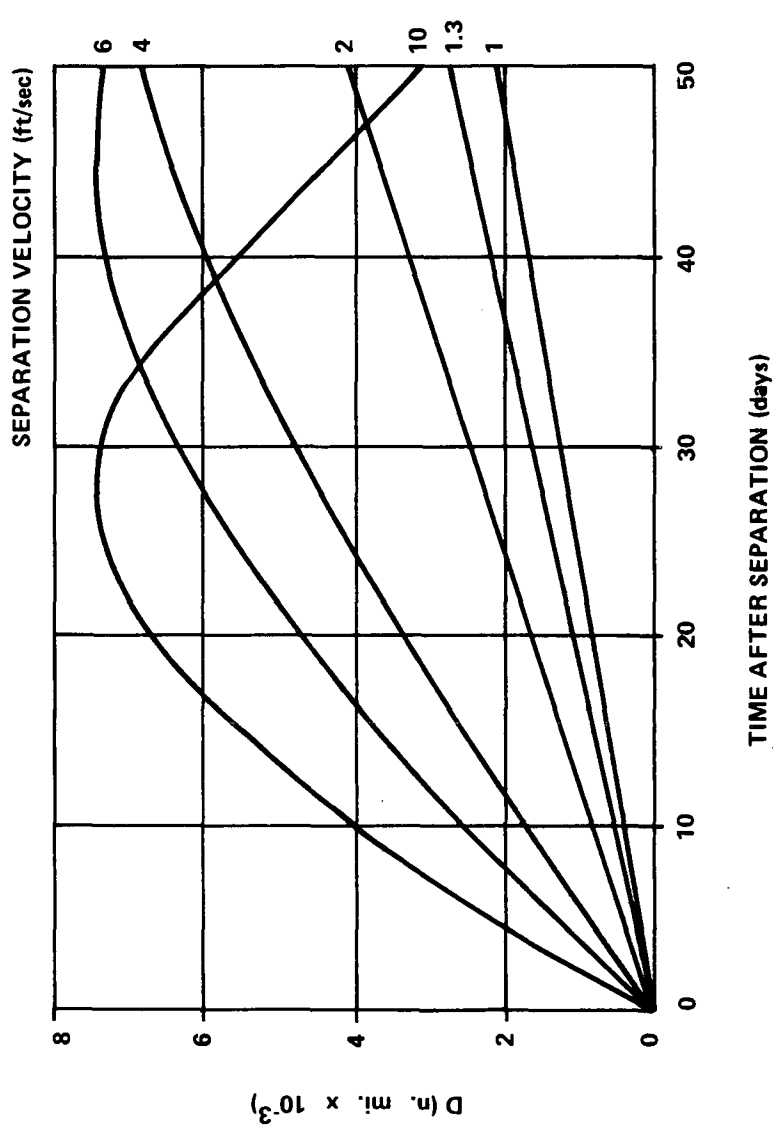


Figure B-45. Separation distance (D) versus time.

• OAS WEIGHT = 1223 lb • HEAO S/C WEIGHT = 17 000 lb • 270 n.mi. INITIAL ALTITUDE

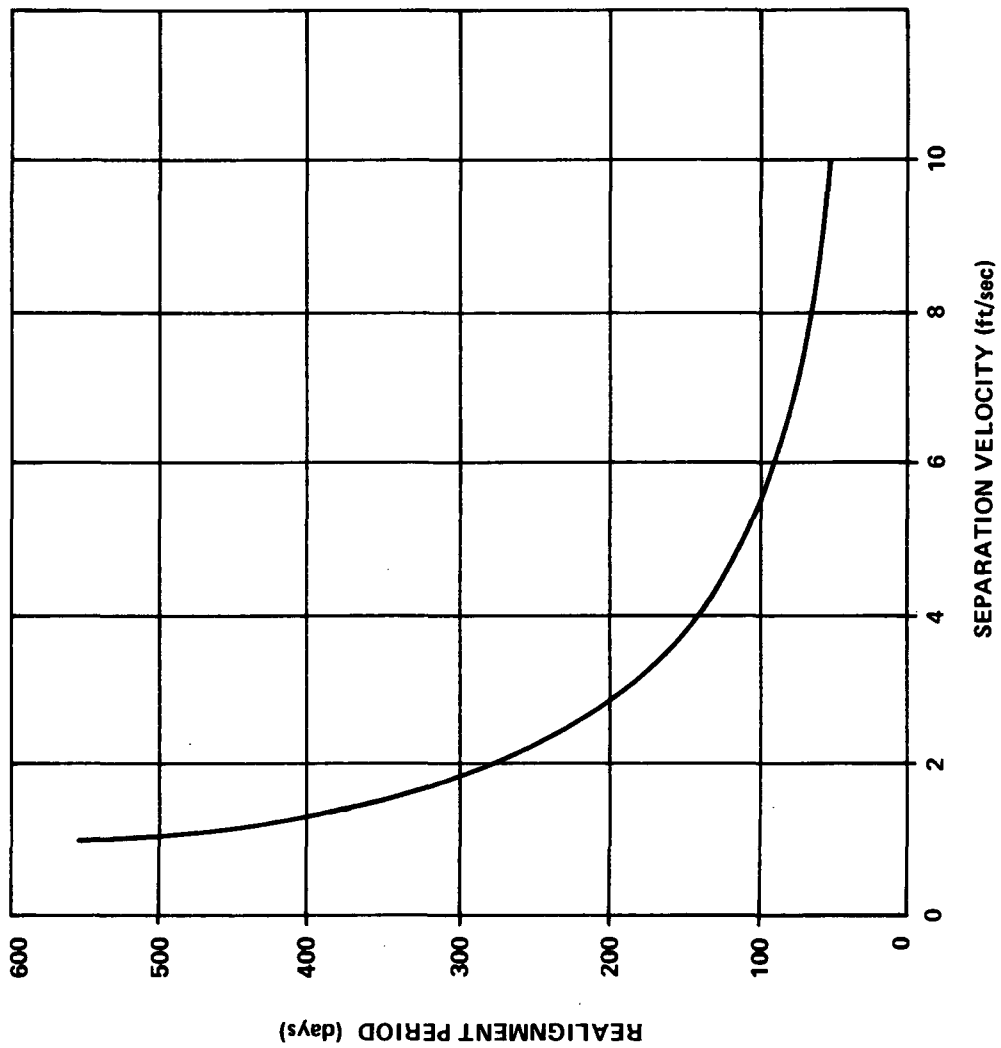


Figure B-46. Realignment period versus separation velocity.

- HEAO S/C WEIGHT = 17 000 lb
- OAS WEIGHT = 1223 lb
- SPRING CONSTANT, $K = 9 \times \text{SPRING ENERGY (lb/ft)}$
FOR 2 in. COMPRESSION
FOR 8 SPRING SYSTEM

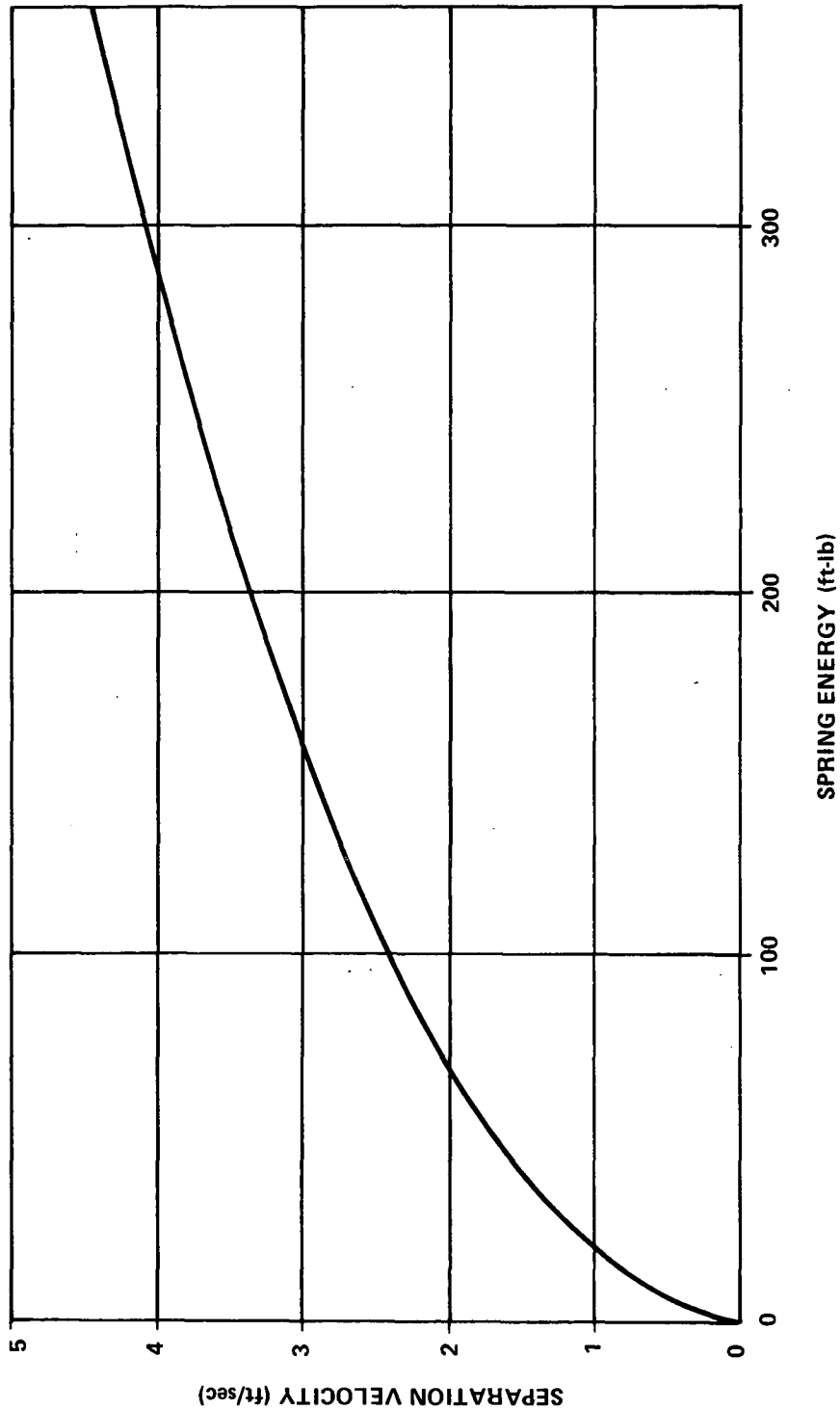


Figure B-47. Spring energy requirement.

Launch Vehicle Description

Most of the data provided herein were compiled from References B-1 through B-4. For the purpose of the study, it is assumed that the same launch vehicle which was used for HEAO-A and -B would be used for Mission C, i. e., the Titan IIID/OAS (Fig. B-48) with a 1 percent programmer. A brief description of the launch vehicle is provided below for reference.

1. Titan. The basic Titan IIID consists of two 5-segment, strap-on, 120 inch solid motors (Stage 0), a liquid fueled core stage (Stage 1) which is ignited before jettison of the solid motors, and another liquid fueled core stage (Stage 2) which is ignited in-the-hole to fly away from the spent Stage 1. Retro-rockets are used to assist the separation of the payload. The guidance equipment to be used for the HEAO launches is a programmed (open-loop) guidance system with 1 percent accuracy; this necessitates hand selection of guidance components since the off-the-shelf version is a 2 percent programmer which causes a higher probability of unacceptable trajectory dispersions. Total lift-off weight of the three stages (without shroud) is 1 365 900 pounds and total thrust is 2 307 000 pounds.

The Titan instrumentation system is a remote-multiplexed PCM-NRZ system with a programmable memory. The system operates at 384 kilobits per second with 20 major frames per second. The present Titan telemetry requirements are approximately 1596 eight-bit words, with the probability of an increase of another 200 for mission-peculiar measurements. The present system capability is 2106 words, and, therefore, preliminary indications are that a maximum of approximately 300 words is available for HEAO and other uses. There are many possible combinations of sampling rates which could be used for these 300 words. An example of one possible combination is given below:

<u>Number of Measurements</u>	<u>Samples per Second</u>	<u>Words</u>
8	400	160
10	200	100
20	40	<u>40</u>
		300

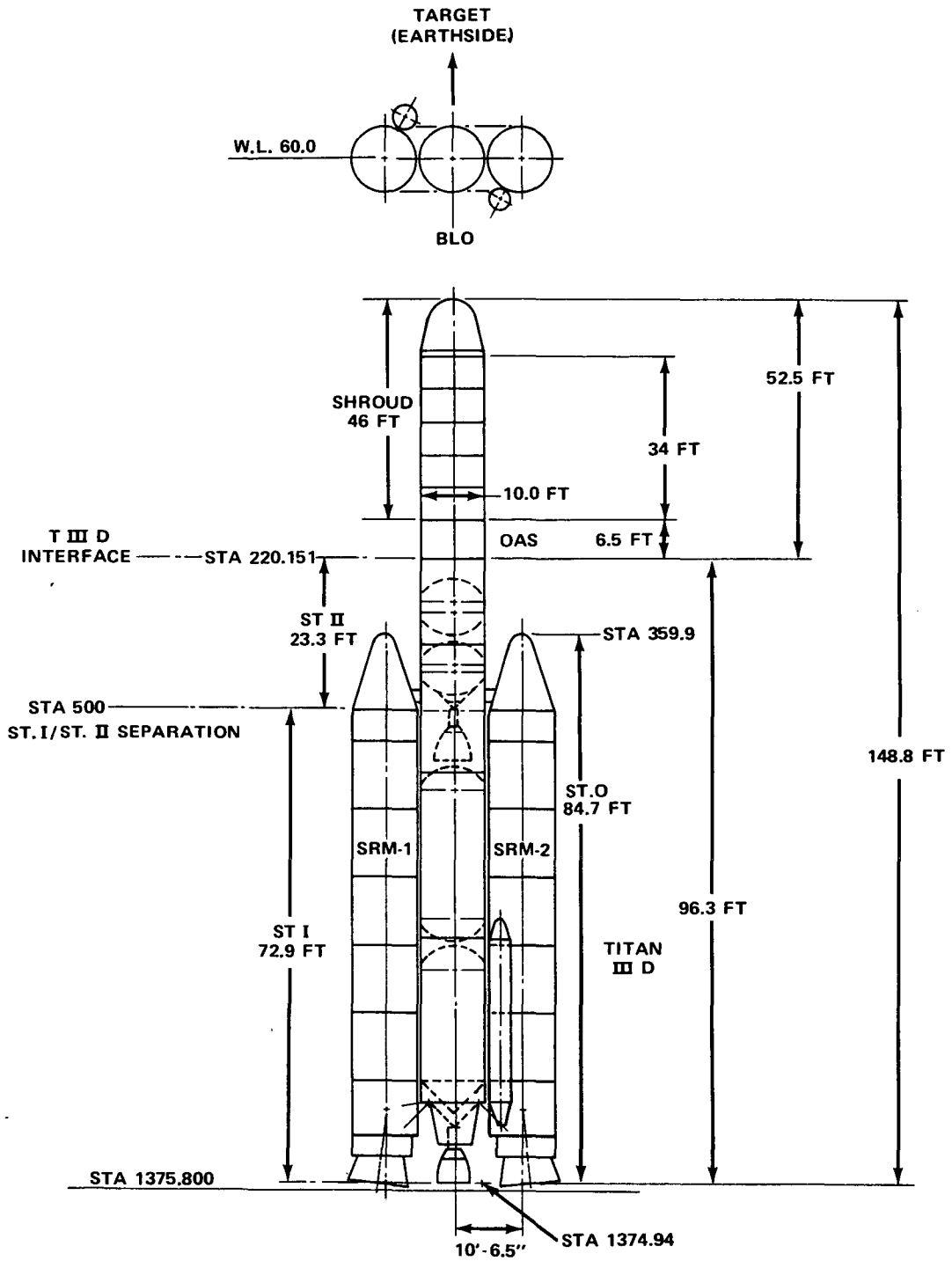


Figure B-48. Titan IIID/OAS launch vehicle.

2. Shroud

a. General. The HEAO shroud (a modified LMSC P-123) is an aerodynamic payload fairing (PLF) which provides protection for the HEAO payload during all phases of the normal prelaunch and launch operations and at a prescribed altitude while the vehicle is under powered flight ejects itself from the vehicle. It has a cylindrical metal body with a double conic nose; it is 10 feet in diameter and 46 feet long and is attached structurally to the OAS. The shroud is shown in Figure B-49.

b. Nose Cone. The nose cone is a double conic configuration 131 inches long, with the aft 55.7 inches, a 10 degree cone, and the forward 75.3 inches, a 25 degree cone tangent to a 24 inch radius dome. The construction is a stiffened skin configuration with the forward cone consisting of three intermediate rings machined from magnesium-thorium and riveted to 0.156 inch thick magnesium-thorium skins that have been welded and rolled to form the conic geometry. The aft cone is of similar construction with the two intermediate rings riveted to 0.135 inch skins.

The nose dome, a spherical/cone section 15.0 inches high with an outside radius of 24.0 inches, is tangent to the 25 degree half-cone angle established by the forward cone. The dome, constructed by shear forming of 17-7 stainless steel sheet, will have a finished thickness of 0.070 inch.

To have a uniform 0.1 emittance on the inside surface and to help control temperature in the higher temperature areas, thermal control liners are attached to the rings with titanium clips. These liners are made from alclad sheet.

The entire cone is constructed in two halves to accommodate the Super Zip pyrotechnic separation joint. Separating the joint will produce symmetrical halves except for the nose dome and conical thermal shield, which will remain intact to separate with the +Z half. The domed half will contain the Super Zip crossover tube and the expanded tube in the separation joint. The joint is attached to an aluminum longeron along each edge of each shell half to give rigidity after separation. There is an RF window in the conical section of the off-the-shelf P-123 shroud. Its location has been optimized for a classified payload. Similar windows can be placed in the conical or cylindrical portions to meet HEAO requirements.

c. Cylindrical Section. The fairing section from the end of the cone assembly to the OAS interface is 421.6 inches long and is a cylinder 120 inches in diameter to the inside of the skin. The construction is a corrugated skin stiffener structure consisting of 7075 T6 alclad corrugations running lengthwise, attached to 7075 alclad skins. Inside, 2021 extruded aluminum rings spaced approximately 15 inches apart are riveted to the skin and corrugation. Thicknesses of the skin and corrugation are stepped in the length direction to provide the best compromise between structural capability, weight, material size, fabrication complexity, and cost. Where lengthwise splices of the corrugation are required, a splice hat section is used at each corrugation. The entire cylinder is constructed in two halves attached by the pyrotechnic separation joint. An aluminum extruded longeron is attached along each edge of each half to obtain structural rigidity after separation.

Field joints, to allow for restricted hook heights at the launch pad, are provided at the forward end of the cylinder and 201.1 inches from the forward end of the cylinder.

The aft end on the cylinder contains the circumferential Super Zip pyrotechnic separation joint, separation spring thrusters, hinges to control the shroud half trajectory, and an interface ring containing a mastered pattern of 204 holes for a 5/16 inch diameter fastener. This ring is made from a 7079 aluminum rolled ring forging.

Access through the cylinder will be provided, as required, by access doors for service to the payload and to components of the shroud itself. Shroud service access consists of doors for access to electrical disconnects and for installation of automatic ground equipment (AGE) spring cocking devices. All doors have load-carrying capability and are constructed of aluminum; a skin/stiffener type configuration is used in lieu of corrugation. All payload access doors will have weather seals of silicone rubber and use standard hex screws and capped nutplates.

An air-conditioning inlet door and coupling receptacle will be provided in the cylinder. The door is hinged at the forward end and is held open by the inserted ground half coupling. At lift-off, on release of the ground half coupling, gravity and a torsion spring slam the door shut and it is latched and sealed in the closed position. This door, the same that has been used on previous programs, is a tested and flight-proven door.

The cylinder section is composed of modules identified as C, D, E, F, G. Access doors and other provisions peculiar to HEAO will be installed. The forward end of Module C is configured for an outside bolting flange for the field joint, so this area will be revised to accommodate the nose cone shear-type field joint by increasing the length of the corrugation panels to line up with the edge of the skin.

d. Separation System. The pyrotechnic system splits the fairing assembly into two halves, after which a mechanical system ejects the two halves in a trajectory that prevents collision with the vehicle. This mechanical system consists of two sets of spring thruster devices and two hinge brackets on each shell half. Mating hinge brackets are installed on the interface ring just aft of the circumferential pyrotechnic joint. This hinge half must react loads applied from the upper half and, to react the loads, must have a load path into the equipment module. The hinge brackets establish a hinge line parallel to the fairing base and parallel to the plane established by the two edges of the open end of the shell half. The springs are positioned in the bottom of each shell half and exert a force adjacent and parallel to the edge of the open shell half and perpendicular to the fairing base. This force is reacted by the hinges and produces a rotary motion about the hinge line. The hinge brackets are configured to allow a hinge point for rotation and incorporate a slot which reacts the forward spring force during spring action and also prevents vehicle motions from disengaging the hinges until the proper release angle is obtained.

The separation springs will be tailored to supply the separation energy required under maximum g acceleration and with a stroke that is active until the center of gravity (CG) of each shell is over the hinge point. These are recommended guidelines for each application. Since the stroke required to place the CG over the hinge is dependent on the CG position, this stroke will become longer for shorter fairings. Likewise, the energy required is peculiar to the CG position, weight, and g level acceleration at the time of separation. The fairing contains pyrotechnic-initiated joints to segment the assembly into two shell halves that can then be ejected mechanically (Fig. B-50). These separation joints contain a separation system called Super Zip, which uses a jacketed powder train of temperature-resistant HMX mild detonating fuse cord encased in a flattened steel tube to contain the products of combustion. The explosive cord is initiated by side priming using an electric detonator from a programmed source. The explosive force causes adjacent notched structural doublers to fracture and the tube to go around. Dual runs of the

INSERT

- SILICONE RUBBER EXTRUSION WITH MDF CORDS INSERTED (9GR/FT HMX)

FLATTENED TUBE

- 5/8 DIA. X 0.030 WALL
- 347 STAINLESS STEEL
- FULL ANNEALED

FRANGIBLE DOUBLER

- HM 31A MAGNESIUM EXTRUSION - LONGITUDINAL JOINT
- 7075 ALUMINUM ALLOY - CIRCUMFERENTIAL JOINT

DETONATOR BLOCK AND DETONATORS WIRE HARNESSSES

A. COMPONENTS

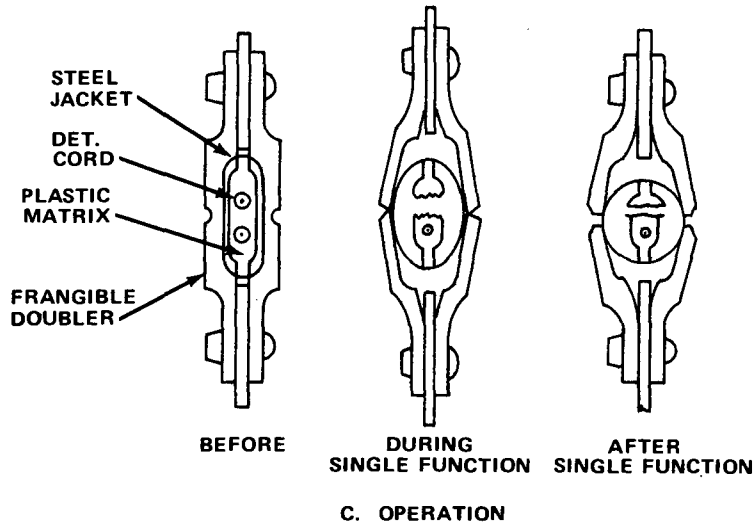
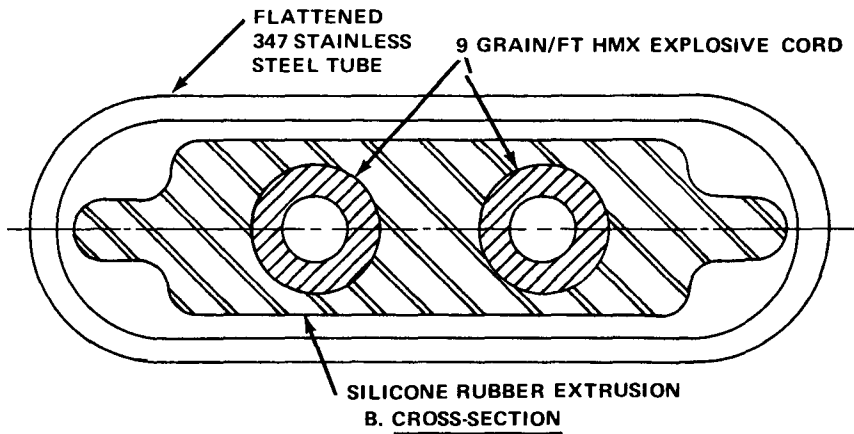
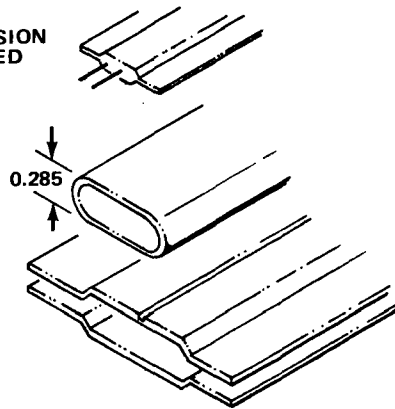


Figure B-50. Super Zip separation system.

explosive cord are used to provide redundancy, one designated a primary system, and the other a backup (Figs. B-51 and B-52). Each system is fired by detonators on each end of each cord. The primary system is fired first, and the signal to the second system is delayed so that in the event of a normal separation from the primary system, the signal to the backup systems will be stopped at the separated electrical disconnect. The electrical disconnect will interface with the payload adapter so that it will not become a clearance problem at shroud separation.

Figures B-51 and B-52 show the separate and redundant signal paths and components, and, as is shown, the primary pyro firing circuit is protected against short circuit by an isolation diode and by a fuse on the input to the secondary 400 millisecond time delay circuit. The primary and secondary pyro firing circuit have identical protection against short circuit. Premature separation is prevented by the sequential receipt of the arming commands to the arming relays and the booster firing commands to the respective pyro firing circuits. The isolation diodes also prevent the 400 millisecond delayed pyro firing commands from feeding back across the booster interface.

As can be seen, a minimum of dual redundancy is provided in paths and components. Considering that each of the booster primary and secondary firing commands splits into a primary and secondary firing command through the cross-strapped, 400 millisecond time delay feature, quadruple redundancy assures that a firing command will arrive at the separation joints. In case a short exists in either cross-strapped time delays, the same fuses mentioned above prevent simultaneous firing of both the primary and secondary pyro separation joints. Each of the primary and secondary pyro separation systems contains a pyro cord, and each cord end is provided with a detonator that can fire the cord; thus, each cord is provided with dual redundant detonators. The present design gives a high confidence that no single-point failure mode exists that could cause premature shroud separation, or could prevent shroud separation upon receipt of the separation command(s) at the booster interface.

3. OAS

a. General. The OAS functions as a portion of the launch vehicle, although it is retained in orbit with the remainder of the spacecraft and is considered an element of the spacecraft. The baseline HEAO-C OAS is a modified version of the LMSC SCS¹ which is presently operational with a classified military payload. A "stripped" OAS (see Figure B-53 for major elements) consisting of at least a multiple-restart main propulsion system, separation logic and pyrotechnics, thruster modules, some attitude control

1. Lockheed Missiles and Space Company Satellite Control Section.

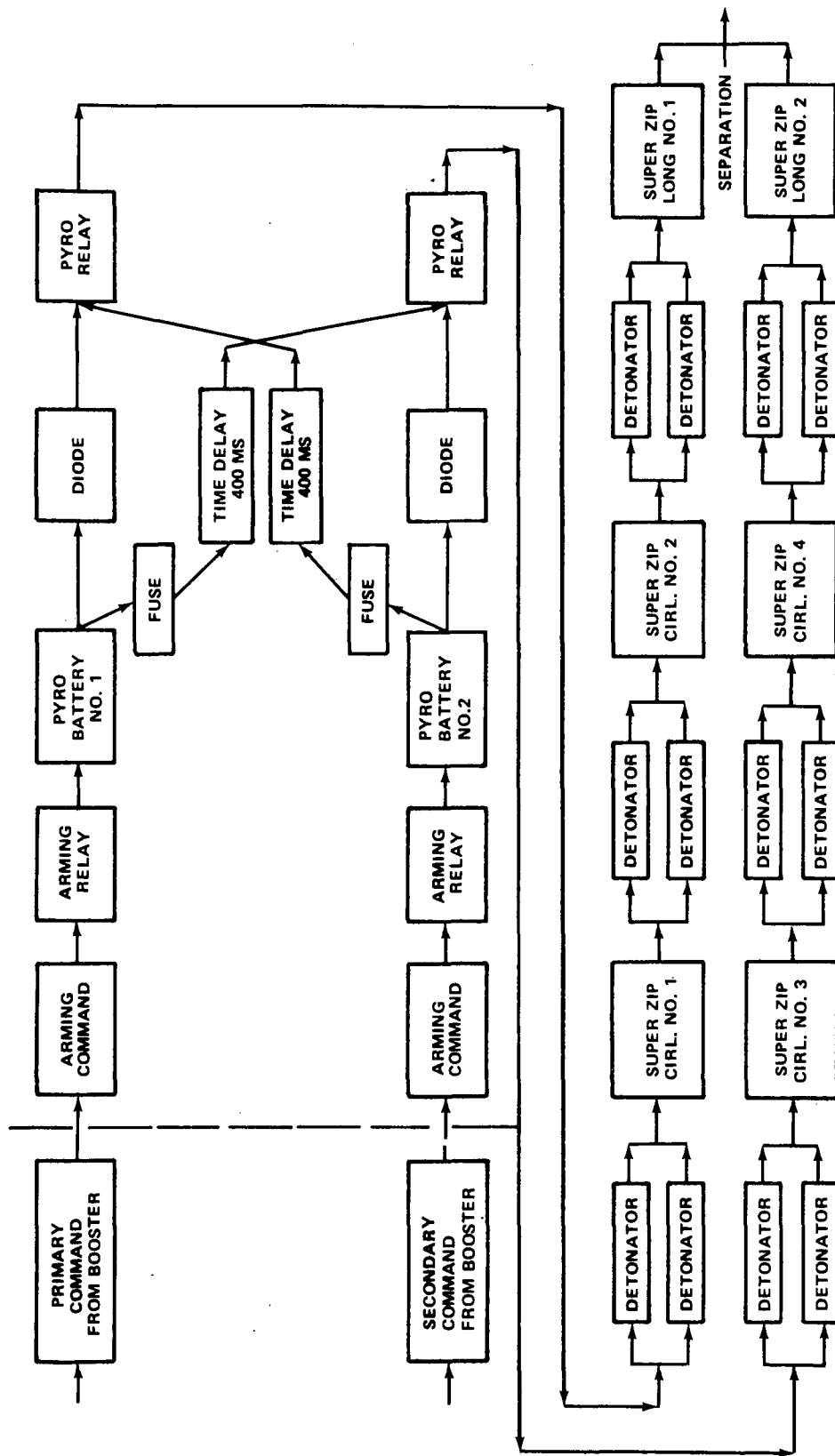


Figure B-51. HEAO shroud separation reliability logic.

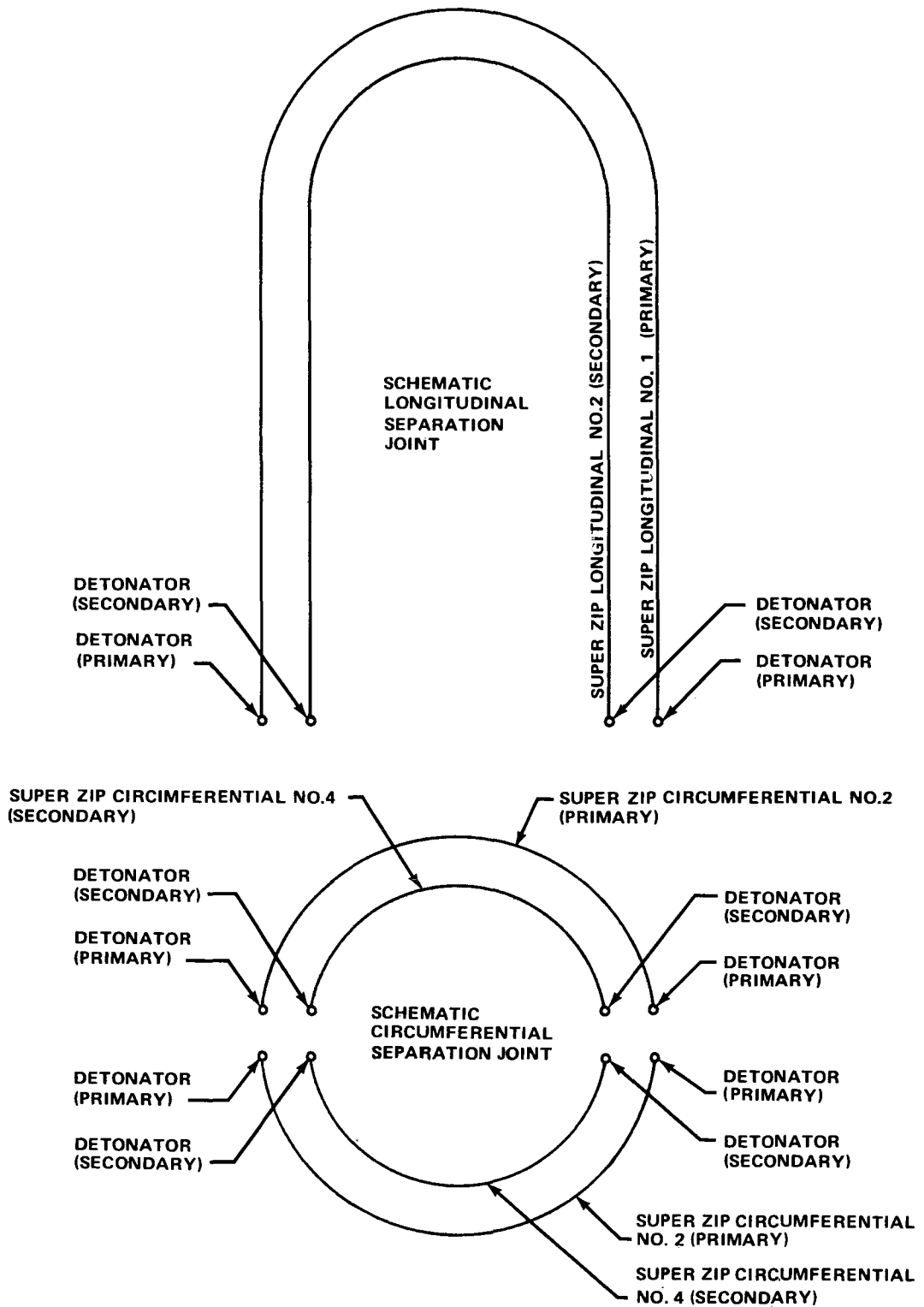


Figure B-52. Longitudinal and circumferential separation joint redundancy scheme.

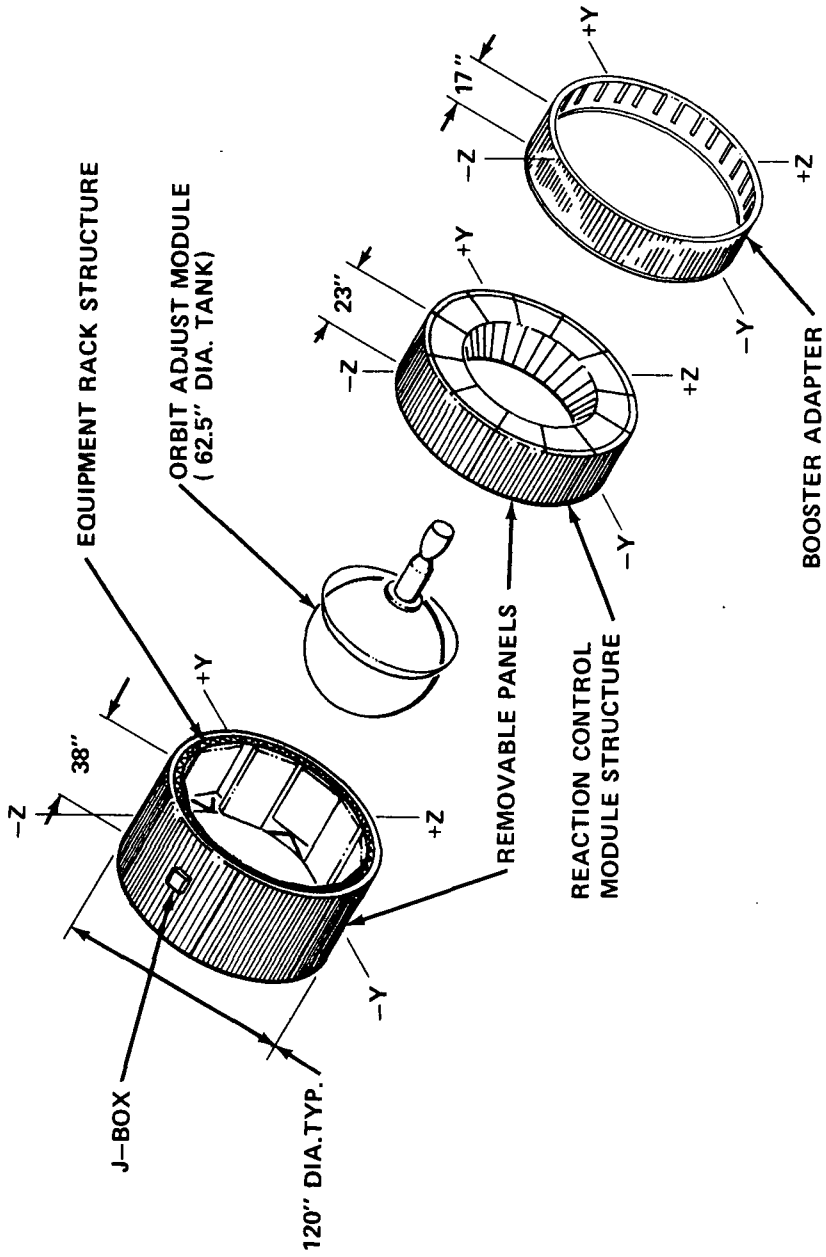


Figure B-53. Stripped LMSC OAS for HEAO.

bottles, heaters, and measurement circuitry will be purchased as off-the-shelf hardware; additional attitude control bottles and HEAO-C lines and valves must be added. The spacecraft attitude control system utilizes the same propellant (monopropellant hydrazine) as the main propulsion system. The remainder of this section describes the stripped OAS and its functions as part of the launch vehicle.

b. OAS Description. The OAS provides the system to separate the HEAO payload from the Titan and provides the engine, propellant tankage, and necessary engine controls to adjust the spacecraft orbit after injection. Structural, electrical, and environmental interfaces are also provided. Physically, the Titan adapter interfaces with the T-IIID and is joined through the Titan/OAS pyrotechnic separation joint to the reaction control module (RCM) of the OAS. The OAS equipment module is bolted to the RCM. The spacecraft adapter and the fairing interface with the OAS at a flange at the top of the equipment module. The orbit adjust module (OAM) includes the engine or thrust chamber assembly (TCA) and the propellant tank. It is attached internally and concentrically to the RCM and protrudes into the equipment module and spacecraft adapter. The electrical umbilical and the fill and drain valves are mounted on the RCM. Two J-boxes are required: The OAM/RCM J-box, containing engine circuitry, is mounted in Bay 2 of the RCM; the Pyro J-box is mounted in bay 4 of the equipment module.

c. Propulsion. The OAS is a hydrazine monopropellant propulsion system consisting of a single 250 to 130 pound thruster, spherical aluminum propellant tank with an internal diameter of 62.2 inches, a cavitating venturi, four propellant control valves in a series/parallel redundancy arrangement, adjustable links and a flexible mounting coupling for preflight thrust chamber alignment, a combined propellant/pressurant fill valve, a drain valve, instrumentation, and electrical control wiring. Propellant feed pressure is provided by pressurizing the propellant tank ullage volume. As propellant is used, the pressure and thrust are reduced in a blowdown mode of operation. Thrust is generated by the acceleration of exhaust gases resulting from exothermic catalytic decomposition of hydrazine (N_2H_4) in the thrust chamber.

A simple blowdown type pressurization system provides high reliability and low cost, yet retains relatively high performance ($I_{sp} > 230$ lb-sec/lb). The components are assembled into a module for ease of checkout. All propellant plumbing connections except for the engine/tank feed-tube connection are made by induction brazing to provide a leak-tight system. The engine feed-tube connection design has redundant O-ring seals. The OAS has been qualified to operate over a propellant temperature range of 70 to 100° F.

The propellant tank, shown in Figure B-54, has a capacity for 2911 pounds of hydrazine and enough nitrogen pressurant to provide total expulsion of the hydrazine within the specified pressure and thrust limits. Table B-1 lists the tank design characteristics. The tank has stress safety factor of 2 to 1 to permit personnel access for leak testing and for propellant loading. This permits the use of more reliable manual fill and drain valves with redundant seal caps rather than a quick-disconnect fill device. The propellant tank serves as the mounting base for the thrust engine assembly, the chamber alignment links, and the thermal shield. The tank cone supports the OAM.

TABLE B-1. OAS PROPELLANT TANK CHARACTERISTICS

Internal Diameter (in.)	62.2
Internal Volume (ft ³)	72.2
Burst Pressure (psia, min)	600
Working Pressure (psia, max at 100° F)	310
Working Pressure (psia, min at 70° F)	100
Material	2021 Aluminum Alloy
Ullage Volume (percent)	35 ^a
Propellant Load (lb, max)	2911 ^a

- a. Minimum ullage and maximum propellant load result in a blowdown pressure ratio of 2.86 at 70° F and 3.1 over the temperature range of 70 to 100° F.

The propellant is hydrazine as specified in MIL-P-26536. The gas used in servicing, checkout, and cleaning of the OAS is nitrogen as specified in MIL-P-27401 or helium as specified in MIL-P-27407. The pressurant is nitrogen as specified above.

The OAS tank is equipped with on-orbit active and passive thermal management devices. The design criterion is for the thermal devices to

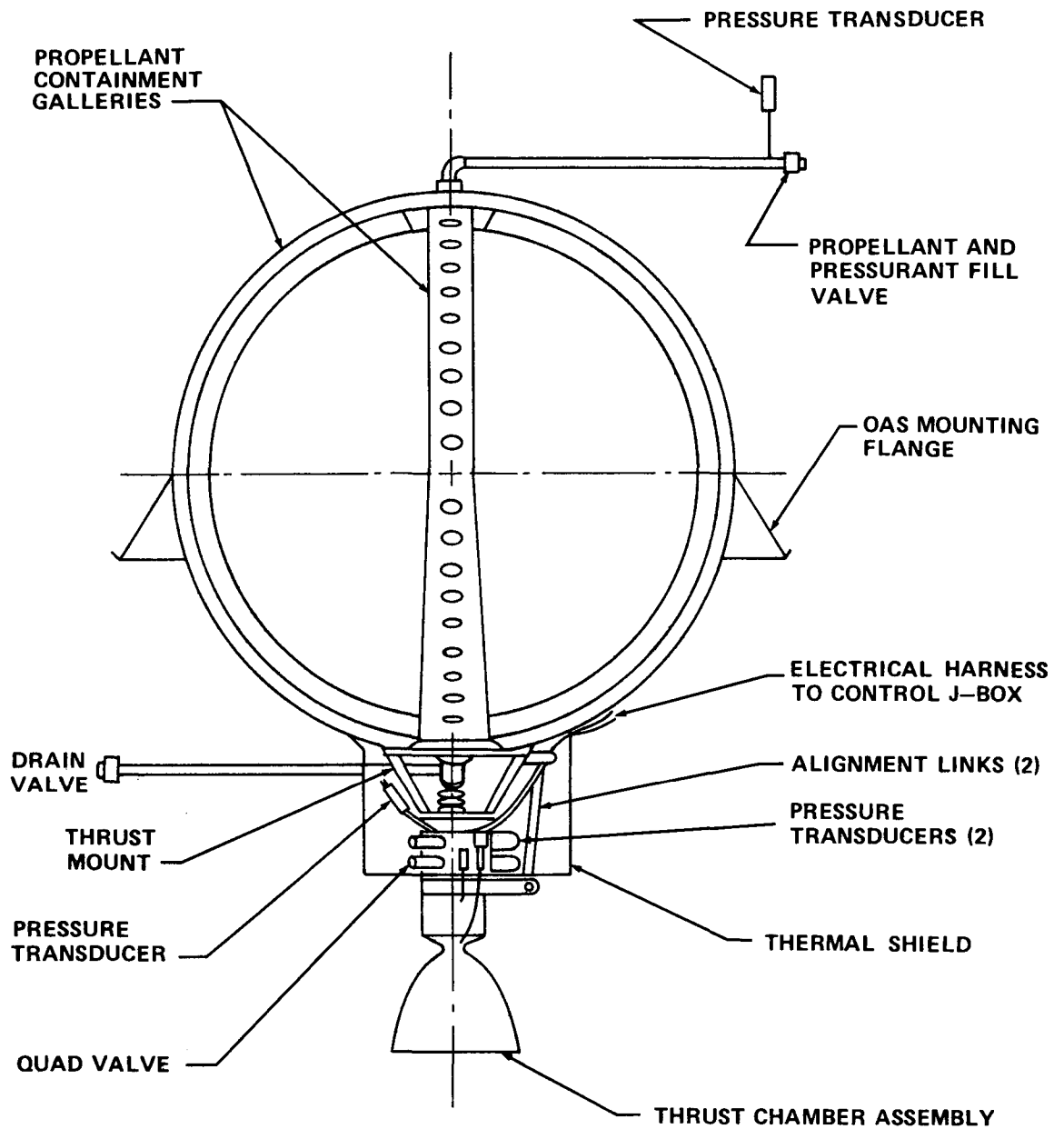


Figure B-54. OAM assembly.

maintain the in-orbit propellant tank temperature above 70° F in the worst case orbital thermal environment. The tank insulation limits the radiation and convection heat losses, and the OAS tank heaters compensate for the in-orbit tank heat losses due to radiation, convection, and conduction. Two sets of heaters are provided and each can be independently turned on or off by ground commands. Each set requires 42 watts maximum at 33 volts dc.

Gas-free propellant feed under orbital conditions is assured at the tank outlet at all times, up to propellant exhaustion, by a system of collection and feed galleries leading to the lower receiver and tank outlet. Propellant is collected, held, and transported through these galleries to the tank outlet by surface tension forces in the propellant. The lower receiver also provides for 50 micron filtration of the propellant. The propellant containment system is fully operative following booster shutdown and during pre- and post-separation time spans under the following maximum accelerations:

Lateral accelerations immediately following booster shutdown not exceeding 3.8×10^{-2} g.

Shock impulse. The vehicle separation shock impulse not exceeding 2.5×10^{-2} g seconds.

The propellant containment system is capable of supplying to the main engine 1.13 pounds per second while subjected to the following Orbit Acceleration:

Translational, Rearward, Aero drag nose forward

$$\text{Steady Loading} = 4.4 \times 10^{-5} \text{ g}$$

$$\text{Nonsteady Loading} = 5 \times 10^{-3} \text{ g}$$

Translational, Nonaxial Aero drag nose 45 degrees down, 0 degrees yaw

$$\text{Steady Loading} = 1.25 \times 10^{-4} \text{ g}$$

$$\text{Nonsteady Loading} = 5 \times 10^{-3} \text{ g}$$

Translational, Forward, Engine Thrust + Aero drag + pitch - yaw

$$\text{Rate Induced} = 2.02 \times 10^{-2} \text{ g}$$

$$\text{Centripetal, Normal x-x tumble} = 2.8 \times 10^{-3} \text{ g}$$

$$\text{Centripetal, Normal y-y or z-z tumble} = 5 \times 10^{-4} \text{ g}$$

The expulsion efficiency is judged to be 99.5 percent and the system pressure loss is less than 0.9 psia at maximum flow rate condition.

(1) Thrust Chamber Assembly (TCA). The thrust chamber assembly includes a flexible mount and feed coupling, a cavitating venturi, a series/parallel quad valve cluster, a propellant injector, a catalyst bed, an expansion nozzle, propellant valve, and manifold heaters. The maximum thrust level, including thrust overshoot at the 310 psia tank pressure, is 280 pounds and 130 pounds minimum at 100 psia tank pressure.

The flexible mount and feed coupling and the chamber alignment links allow adjustment of ± 3 degrees in a square pattern. Sufficient space is allowed to permit replacement of the adjustable links with gimbal actuators, which would permit inflight thrust vector control. The propellant control valve, the only moving part of the OAS, is provided with redundancy to protect against single malfunction and to enhance reliability. Parallel flow paths are provided to assure high reliability in opening. Each flow path has two valves in series to assure high reliability in closing. Total valve power consumption is 300 watts maximum.

The thrust chamber incorporates a Shell 405 catalyst bed in which hydrazine is decomposed in an exothermic reaction into nitrogen, hydrogen, and ammonia at a maximum temperature of approximately 1800° F. The exhaust products expand through the nozzle and produce thrust.

The quad valve has two identical heaters (one primary and one standby redundant). Design criteria for the valve heater are to maintain the quad

valve housing and propellant passages at or above 40° F in the worst case orbital environment. In addition to the valve heaters, the quad valve assembly is protected by a heat shield to limit radiation heat losses. One of the quad valve heaters is energized prior to launch and remains on continuously during entire orbit life. The power requirement is 4 watts maximum at 33 volts dc.

The design criterion for the manifold heaters is that each heater is capable of raising the temperature of the catalyst bed from 0° F to 70° F within 2 1/2 hours. One or both heaters are energized a minimum of 2 1/2 hours prior to a scheduled OAS burn. Power requirements for two heaters is 132 watts maximum with 33 volts dc.

(2) Fill and Drain Valve. The propellant and pressurant are loaded and unloaded through manually operated fill valve and drain valve located near the external skin of the OAS module. The stem and fill ports of the valves are equipped with redundant sealing caps.

(3) Junction Box. An electrical junction box provided as a part of the OAS module contains thruster control relays and instrumentation signal circuitry. Electromagnetic interference suppression circuits are provided at the thruster valve solenoids. The operating voltage range is 24.5 to 33 volts dc at the electrical interface connectors.

(4) Commands and Instrumentation. Forty-eight discrete measurements, 21 analog measurements, and 32 commands are required for flight operations and diagnostic analysis (see Chapter IV). Flight instrumentation power requirement is 18 watts (peak) at 33 volts vdc.

d. OAM Life Characteristics. The OAM has the following items currently under limited calendar life control. Current procurement and assembly documents require that these items have a minimum assembly life of 36 months.

- Thrust Chamber Assembly
- Fill and Drain Valves
- OAS Tank
- Pressure Transducer

The above have in their design EPR, BUNA-N, or butyl type O-rings.

The thrust chamber uses EPR O-rings as backup to the all-welded valve bellows assemblies to preclude external leakage. The OAM fill and drain valves used a BUNA-N O-ring as the primary seat seal and EPR static O-rings for redundant sealing. The tank has series redundant static butyl type O-ring seals. The thrust chamber tank assembly has a series redundant butyl type-O-ring coupling design. Two ethylene-propylene O-rings are used to protect the pressure transducer electronic components from humidity and dirt contamination.

Design conservatism has caused the rated life capability of these type O-rings to be limited to 36 months. The actual performance capability of the O-ring materials, in all probability, is well beyond this time limit.

The OAM is delivered in a clean and dried condition. It will be pressurized with nitrogen and maintained at a pressure within the limits of 5 to 10 psig, and must be maintained at a temperature of $+80 \pm 40^\circ \text{F}$ during the entire storage period.

e. OAS Attached to Spacecraft in Inactive Mode. The Phase B study results on HEAO-A and -B indicated that no problem is anticipated by leaving the OAS attached to the spacecraft with residual propellants in an inactive pressurized system and that materials compatibility is satisfactory for 2 years in orbit. The system contains at least double seals in all locations where active components are used and the plumbing system is assembled by brazed joints. The Phase B study results also indicated that no contamination is anticipated due to leakage or materials incompatibility. Micro-meteoroid protection to the pressurized system is provided by aluminum metal at least 0.020 inch thick on pressurized surfaces.

f. Main Power Characteristics. Main power supplied for the OAS at the SC/OAS electrical interface shall be continuous, unregulated dc and shall possess the following characteristics under no load conditions of the OAS:

Maximum Open Circuit Voltage	33.0 Vdc
Nominal Voltage	28.0 Vdc
Ripple	0.250 V zero/peak ac from dc to 20 kHz (about the dc level)
Transients	± 12.5 V maximum

The voltage levels to be maintained under various OAS load conditions shall be as presented in Table B-2.

TABLE B-2. VOLTAGE LEVELS FOR VARIOUS OAS LOAD CONDITIONS

OAS Utilization Mode	Max Power (W)	Max Current at Min Volts (A)	Min Voltage Max Current (Vdc)	Average Current (A)
OAS Burn	300	6.75	24.5	7.75
TCA Propellant Valve Heater	4	0.09	24.5	0.11
TCA Injector Manifold Heater 1	66	1.50	24.5	1.70
TCA Injector Manifold Heater 2	66	1.50	24.5	1.70
OAS Tank Primary Heaters	42	0.95	24.5	1.08
OAS Tank Redundant Heaters	42	0.95	24.5	1.08
OAS Instrumentation	18	0.41	24.5	0.46

g. **Pyrotechnic Power Requirements.** Each of the two independent pyrotechnic activation links shall be served by a power source that is capable of serving 40 ampere for 1 second duration repetitively (3 times minimum) during any (TBS) second interval at a minimum bus (in Pyro J-Box) voltage of 20.0 volts dc. If a single source is to serve both pyrotechnic activation links, it shall be capable of serving 80 ampere for 1 second duration repetitively (3 times minimum) during (TBS) second interval at a minimum bus voltage of 20.0 volts dc. Electrical power (main power and pyrotechnic power) shall be supplied and distributed to the OAS by the SC.

4. **Adapters.** There are two adapters, one of which is off-the-shelf (Titan-to-OAS) and one of which is a new-build (OAS-to-HEAO). The former

one (see Figure B-55) remains with the Titan after separation and the latter one (described in Chapter V) remains with the HEAO.

5. Facilities and Operations. Although little effort was expended in this area during the study, a few important considerations are listed for reference.

a. Facilities. The Eastern Test Range (ETR) facilities were designed to provide an integrate-transfer-launch (ITL) capability. In addition to the solid rocket motor (SRM) segment receiving and processing facilities, the ITL capability consists of the Vertical Integration Building where the core is placed on the transporter and checked out; the Solid Motor Assembly Building (SMAB) where solid stages are installed; and the two launch pads (40 and 41). This mobile mode of operation can provide quick turnaround capability.

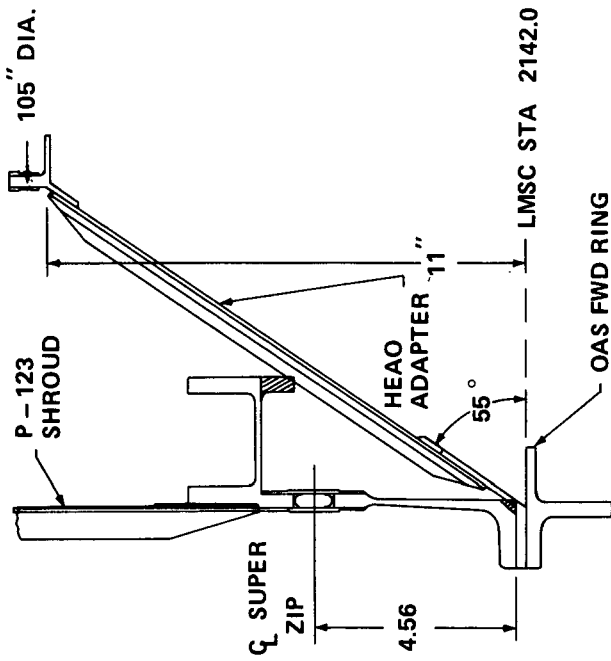
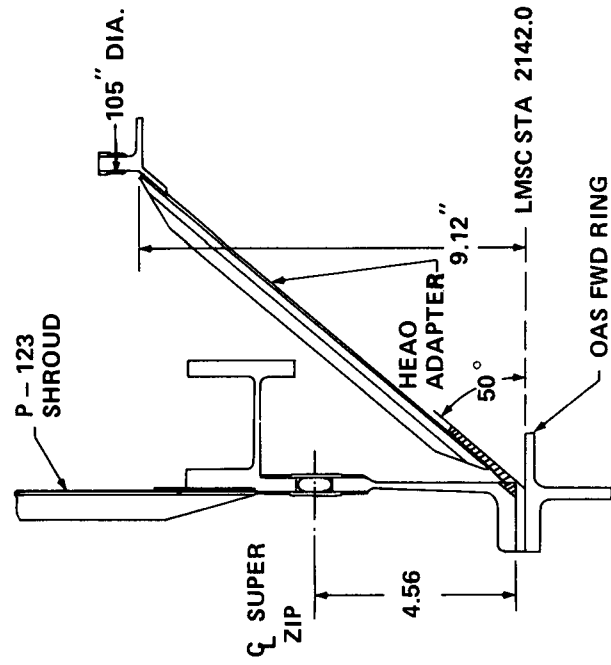
b. Ground Environment Control. Spacecraft environmental requirements will be met on the ground by flowing conditioned air into the cavity between the shroud and the external spacecraft envelope. Air conditioning will moderate the environmental extremes at the launch site as well as conditioning or precooling the spacecraft for the ascent phase of flight. Conditioned air flow must maintain OAS hydrazine above 70° F and below 100° F.

The environmental heat load on the conditioning air will be minimized by finishing a majority of the shroud external surfaces so that they have a low solar absorptance, α_s , and high infrared emittance, ϵ . Heat transfer from the environment is further reduced by leaving the shroud interior surfaces unfinished. These procedures increase the effectiveness of the conditioned air to control the spacecraft environment. Ground environmental control is characterized by the features listed in Table B-3.

The environment imparted to the spacecraft during ground air conditioning will be based on the assumed design conditions presented in Table B-4.

Final air conditioning analysis should include a complete internal/external heat balance and be based upon specified launch site environmental extremes and spacecraft heat loads.

Depending on air velocity and pressure requirements, an internal air duct/diffuser can be employed inside the shroud to direct the inlet air upward at an initial velocity within the required spacecraft limits. This duct is not part of the baseline shroud thermal design, and it will affect the clearance envelope.




 MODIFICATION

Figure B-55. HEAO/OAS interface.

TABLE B-3. GROUND ENVIRONMENTAL CONTROL CHARACTERISTICS

Parameter	Requirement	Method of Implementing
Exterior Finish Conic/Nose Cap Barrel Sections	Uncontrolled $\alpha_s < 0.35, \epsilon > 0.7$	Dow 17 Clear Anodized Alclad
Interior Finish Nose Cap Conic/Barrel Sections	Uncontrolled $\epsilon < 0.15$	Unfinished Alclad and Magnesium
Conditioning Air	Flow Rate 150 lb per minute, 60 to 80° F Inlet Temp- erature, Minimum Humidity consistent with spacecraft re- quirements and condensation on interior shroud surfaces	AGE

TABLE B-4. GROUND ENVIRONMENTAL CONTROL DESIGN CONDITIONS

Condition	Design Case	
	Hot	Cold
Inlet Air Temperature	60° F	80° F
External Ambient	100° F	30° F
Solar Heat Load	Noon with clear skies	0
Wind Velocity	0	30 knots
Spacecraft Heat Rejection	0	0

c. OAS Servicing. Preflight servicing consists of loading hydrazine propellant and nitrogen pressurant. The AGE is attached to the OAS manual fill and drain valves. After venting of the low gas pressure maintained during test operations, a predetermined amount of propellant preheated to 90° F to 105° F is loaded, followed by pressurization. Tank temperature and pressure of the OAS are continuously monitored to ensure the proper loadings. The fill valve poppet is manually closed, the AGE disconnected, and the valve stem and port sealing caps installed. By controlling the pad hold time and thermal environmental condition, the OAS propellant temperature is maintained above 70° F at launch. To assure a 2 to 1 factor of safety the maximum pressure of 314 psia and tank temperature of 120° F maximum are observed.

d. Flight Operation. Operation of the OAS requires only electrical actuation of the redundant propellant valves and turning on the manifold heaters prior to firing. The valve heaters are turned on with power to vehicle. The required thrusting initiation time and duration are predetermined for each firing and entered into the command programmer. Impulse prediction is based on readout of OAS performance parameters. The required thrust duration for a given impulse is calculated, based on telemetered tank pressure and temperature, updated vehicle weight, and system calibration data.

Two relays are used to operate the four propellant valves. Each relay operates a pair of series valves so that a single relay failure will not prevent OAS operation. Thruster operation with either of the parallel flow paths inactive results in a slightly degraded thrust due to the higher valve assembly pressure drop.

6. Loads and Environments

a. Contamination from Titan IIID SRM Jettison and Titan IIID/OAS Separation. Potential contamination sources are primarily rocket motor exhausts associated with the SRM jettison event and the second stage retro-motor firings. The venting system of the shroud cavity must be designed to prevent ingestion of undesirable particulate and gaseous exhaust products during SRM jettison when the shroud is in place. An ingestion of 0.05 pound of Al_2O_3 contaminant could take place through the booster adapter vent ports and possibly find its way into the spacecraft adapter cavity. The design requirements for the spacecraft/OAS adapter vents must preclude this possibility.

The primary contaminant associated with the second stage retromotor is the alumina (Al_2O_3) particulate in the exhaust. For the HEAO vehicle configuration with the retros canted outboard by 30 degrees, the maximum integrated alumina flux in the vicinity of the payload is expected to be less

than 4×10^{-5} gm/cm². The degradation potential of this contaminant level on solar cell glass transmittance, assuming the deposition was equal to integrated flux, even though the particulate flow is nearly parallel to the spacecraft center line, would be less than 4 percent (assuming an unlikely asymmetrical separation top off of 6 degrees).

b. Dynamic Environments

(1) Acoustic Environment — External to Shroud. Acoustic excitation of the shroud at lift-off results from radiated and reflected noise generated by turbulent mixing of the engine exhaust streams. The definition of this environment, based upon surface pressure measurements obtained during launch of the Titan IIID Booster System, is shown in Figures B-56 and B-57. This environment retains a significant level between maximum and 6 decibels below maximum level for a period of 10 seconds.

During ascent, the outer shroud is subjected to noise environment generated in turbulent boundary layers which extend aft of regions of separated flow. Also, due to interaction of oscillating shocks and turbulent boundary layers, intense localized noise environments are created in the vicinity of shroud profile discontinuities.

In establishing the ascent noise environments, it was assumed that the following dynamic pressures would be encountered:

$$\begin{aligned} \text{Dynamic pressure at } M_{0.9} &= 600 \text{ psf} \\ \text{Maximum dynamic pressure} &= 900 \text{ psf} \end{aligned}$$

These environments retain significant levels (between maximum and 6 decibels below maximum level) for a period of approximately 50 seconds.

(2) Imparted Environment. Pyrotechnic shock results during shroud separation; this is initiated by detonation of the Super Zip separation joint. Firing of one of two 9 grains/foot MDF cords encased in a flattened metallic tube causes fracturing of the joint frangible doubler strips. The metal tube then expands into a circular configuration containing all the products of combustion.

The fracturing of the frangible doubler strips together with the explosive shock results in the creation of a high amplitude, high frequency impulse at the separation joint. This pyrotechnic shock is transmitted

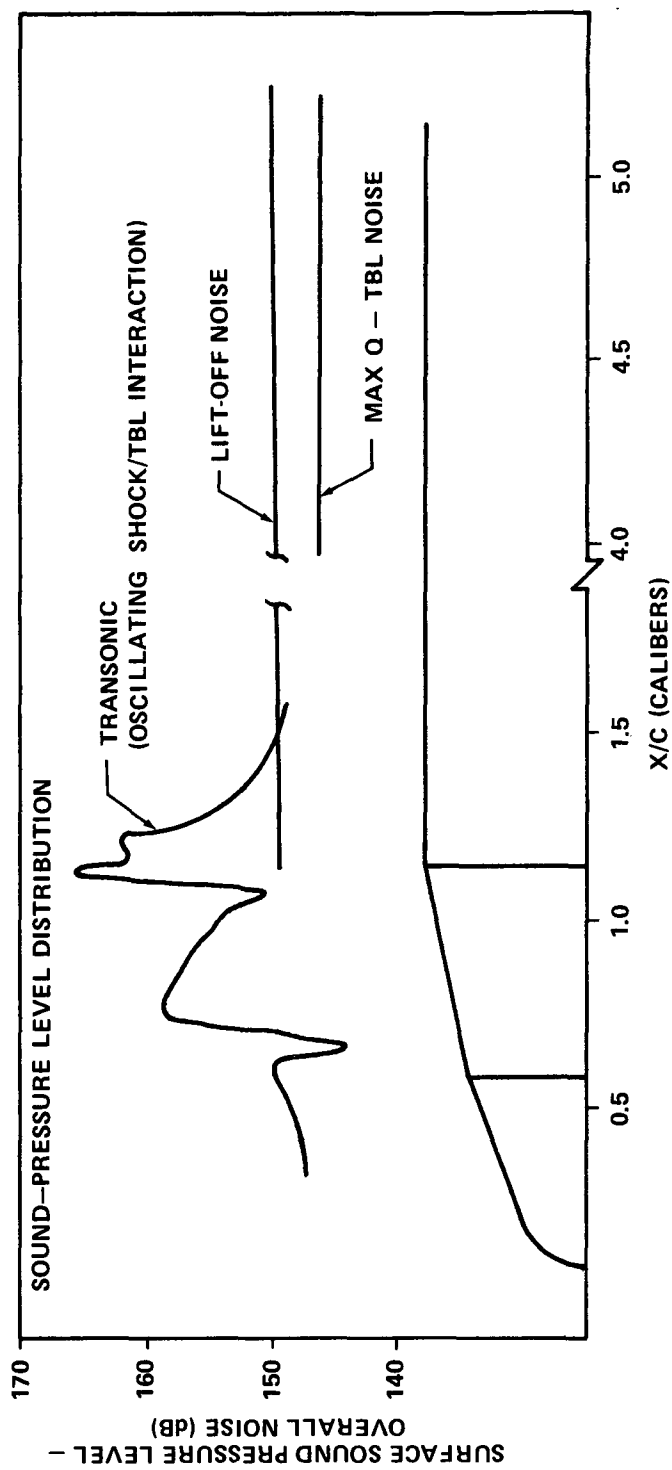


Figure B-56. External acoustic excitation.

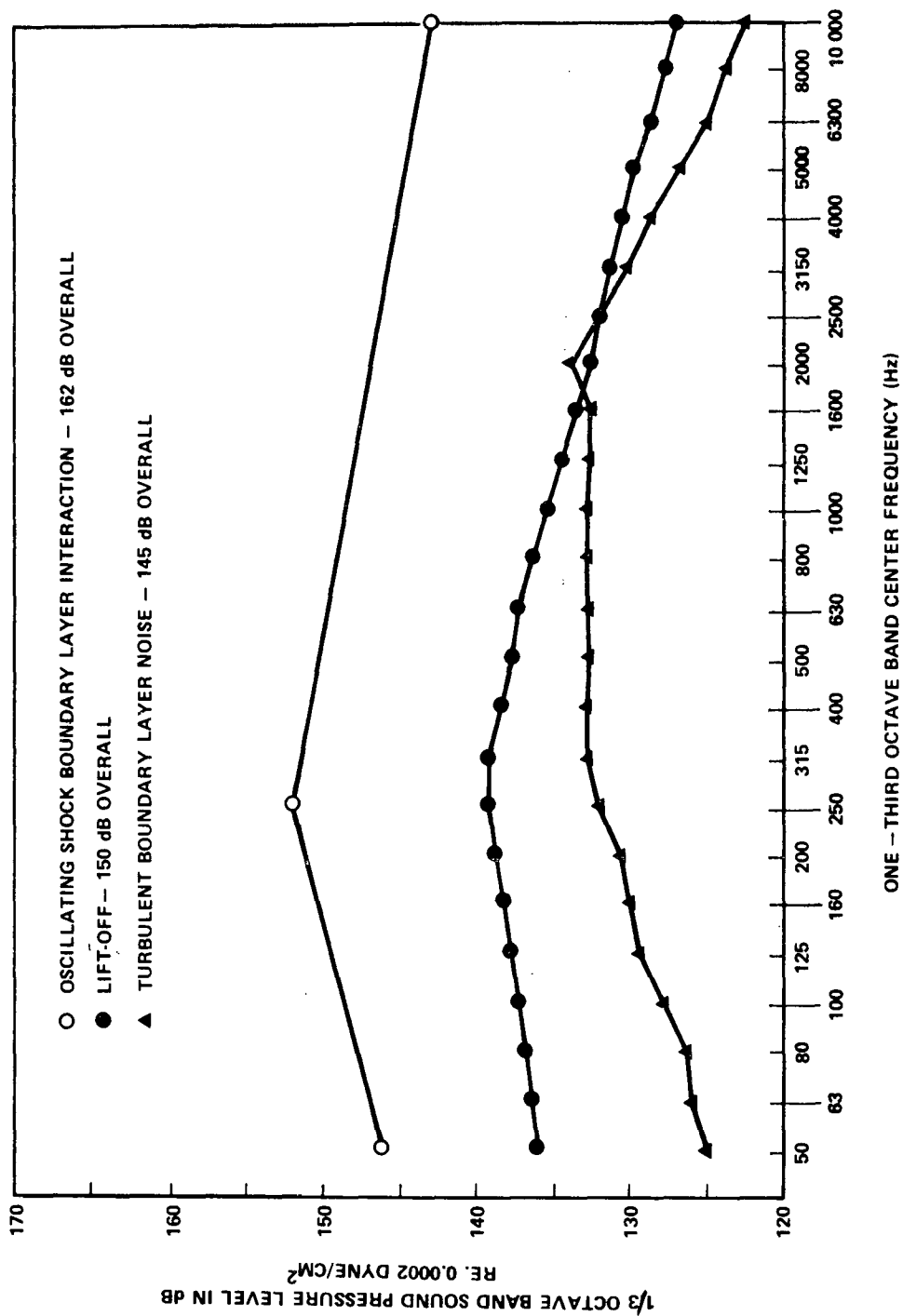


Figure B-57. External shroud acoustic excitation.

through the structure, causing transient oscillations that are substantially attenuated from the initial shock pulse as distance from the source increases. Figure B-58 presents the shock spectrum of this pyrotechnic shock environment ($Q = 25$) at the HEAO spacecraft/spacecraft adapter interface plane. Figure B-59 presents an attenuation curve that may be used to estimate the shock magnitude at other locations (in relation to the interface plane) on the

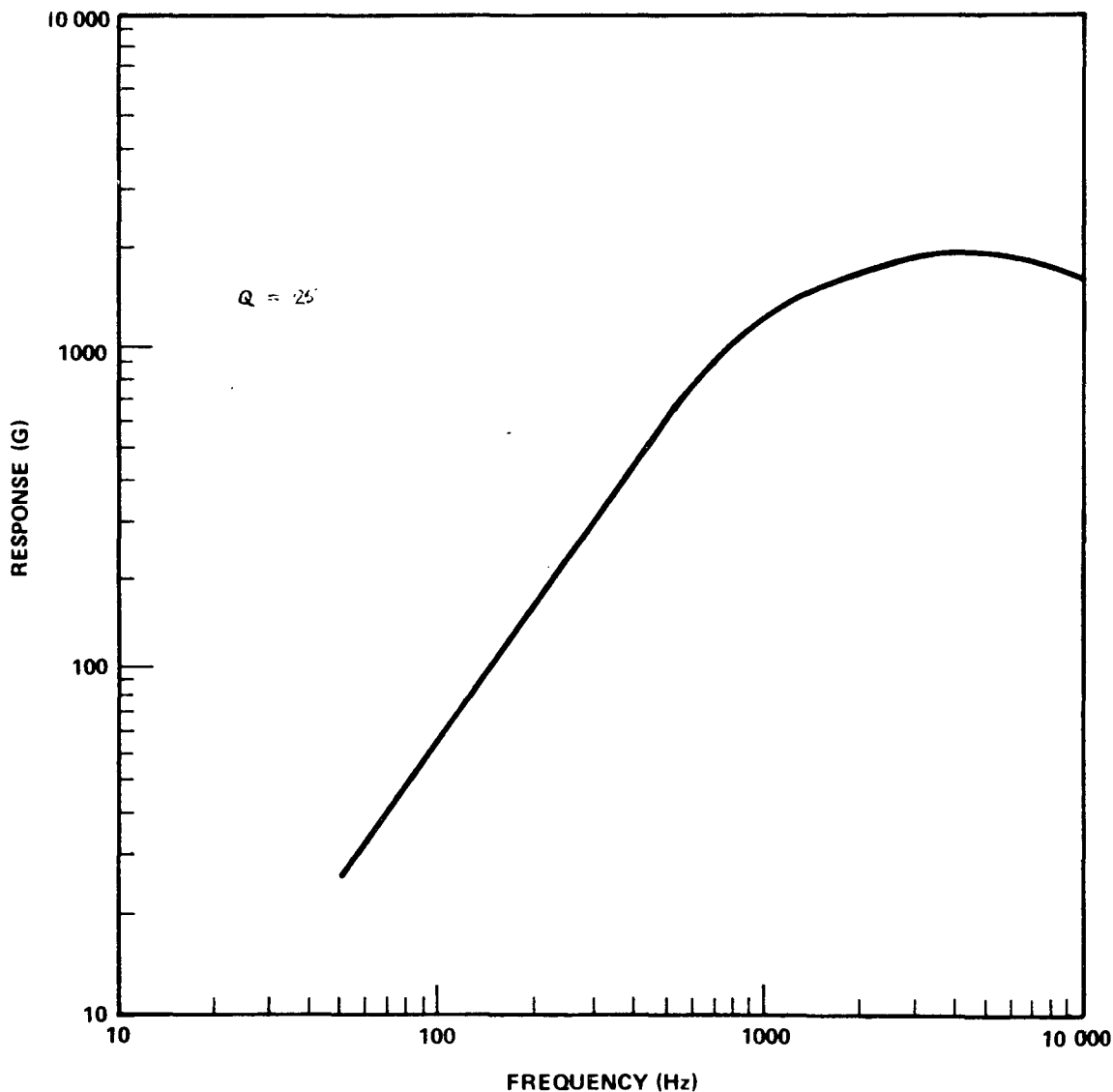


Figure B-58. Spacecraft/adapter interface pyrotechnic shock environment from fairing separation.

spacecraft structure. Figure B-60 shows the estimated shock spectrum (determined using Figures B-59 and B-60, at a point on the HEAO spacecraft approximately 90 inches from the interface plane and compares the estimated spectrum to measurements made on typical spacecraft structure during a shroud separation test.

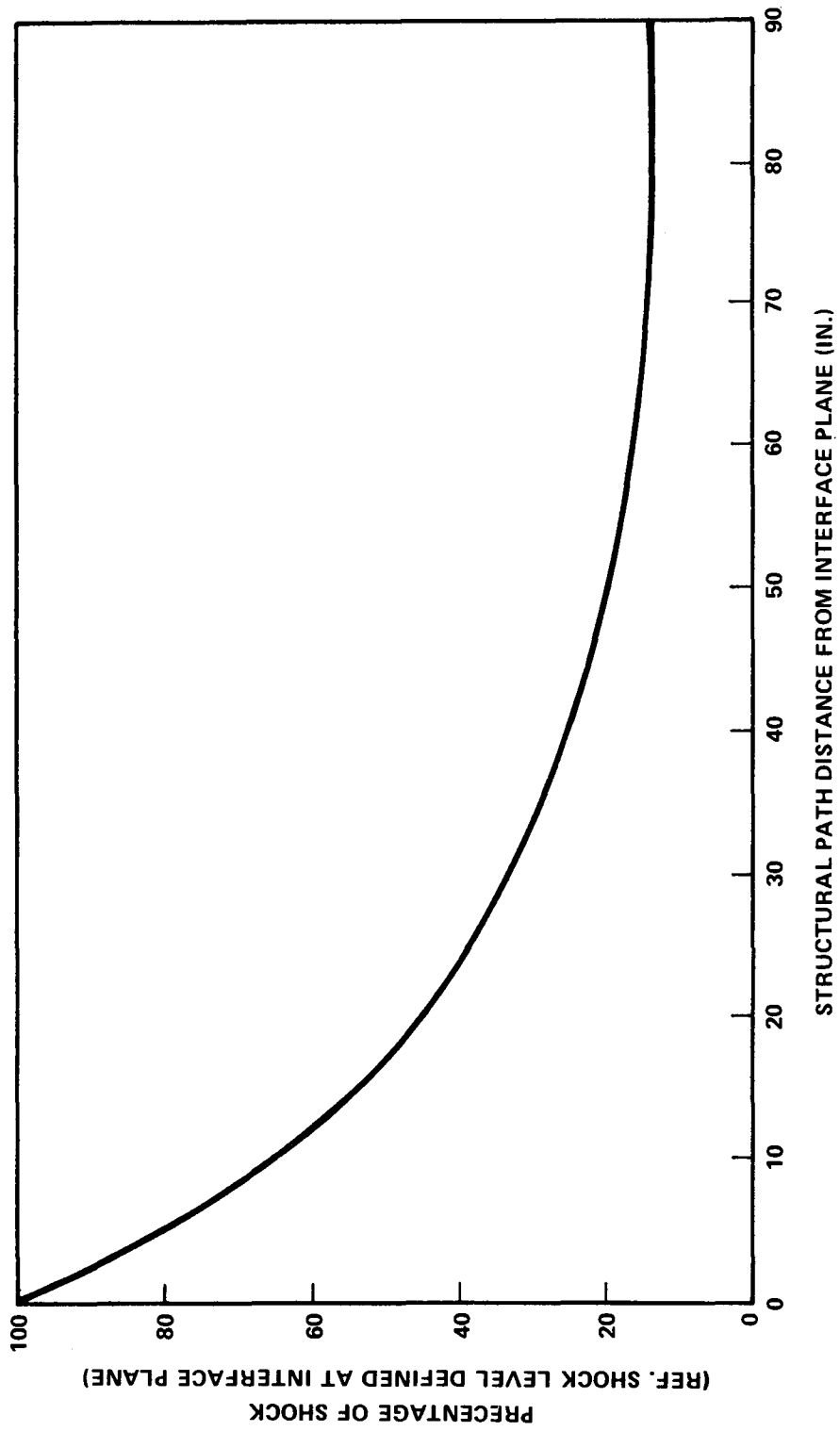


Figure B-59. Shock attenuation versus distance from interface.

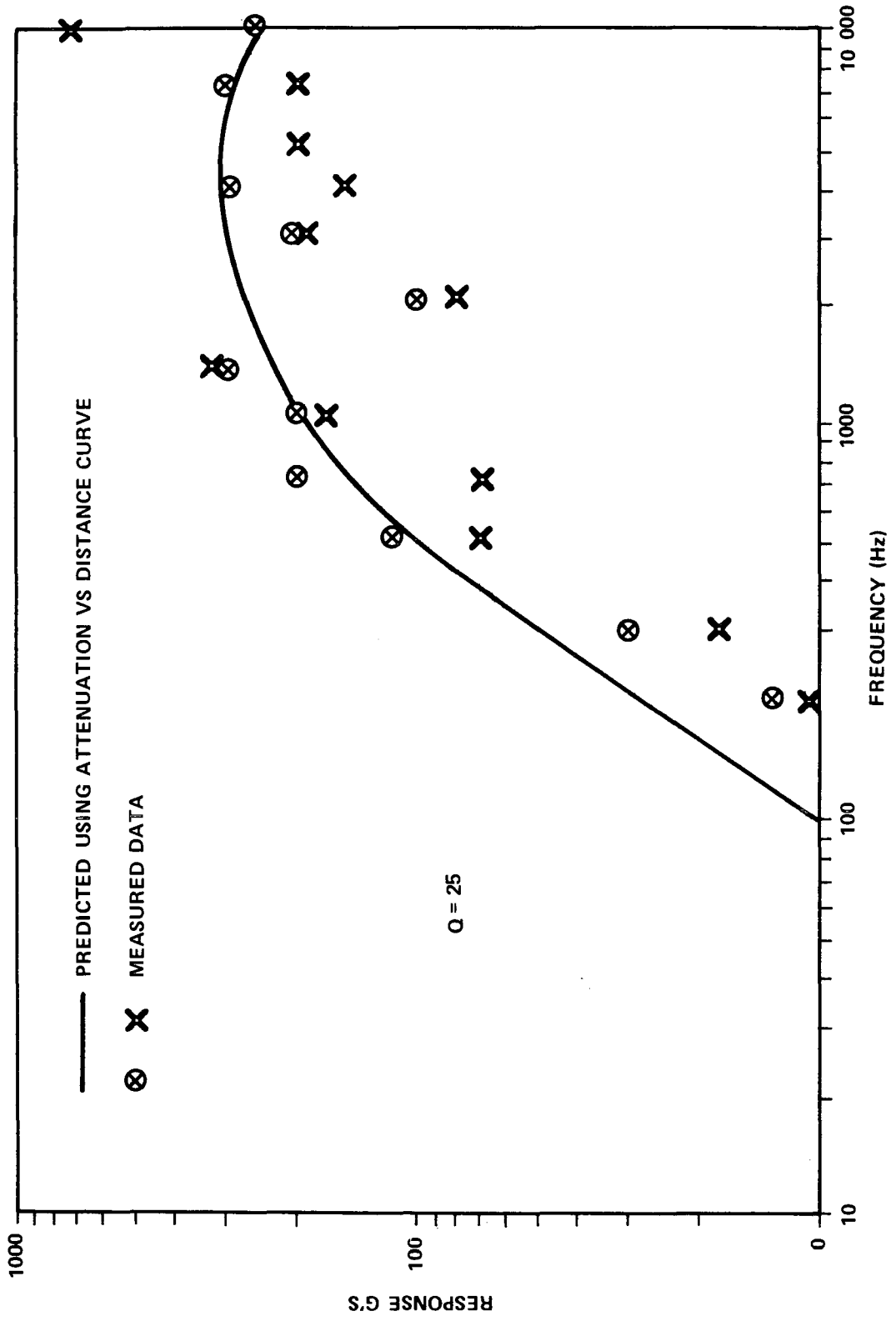


Figure B-60. Pyrotechnic shock environment.

REFERENCES

- B-1. Martin Marietta Corporation: TIIID Launch Vehicle at ETR for High Energy Astronomy Observatory. Rev. 1, Denver Div., Sept. 1969.
- B-2. Lockheed Missiles and Space Company: LMSC Satellite Control Section for NASA HEAO. LMSC-A972292, Rev. B, Space Systems Div., Sunnyvale, Calif., Oct. 12, 1970.
- B-3. Martin Marietta Corporation: Titan IIID Launch Vehicles. LV-105-71, S-71-41545-1, Denver Div.
- B-4. Program Development: HEAO Phase C/D Statement of Work for Missions A&B, Appendix 7 — Orbit Adjust Stage Data. RFP No. DCN-1-1-21-00109, George C. Marshall Space Flight Center, July 1971.

BIBLIOGRAPHY

Program Development: Conceptual Design of a High Energy Astronomy Observatory, Volume 1 — Preliminary Analysis, Volume II-Appendices. NASA TM X-53976, George C. Marshall Space Flight Center, Feb. 16, 1970.

Weidner, Don K.: Space Environment Criteria Guidelines for Use in Space Vehicle Development (1969 Revision). NASA TM X-53957, Oct. 17, 1969.

Weidner, Don K.; West, G.S.; and Swenson, G.R.: Variations in Orbital Altitude Atmospheric Density for MSFC 1971-1976 Space Station Programs. NASA TM X-53815, Aero-Astroynamics Laboratory, George C. Marshall Space Flight Center, Feb. 13, 1969.

Whitt, Ellis E.: Orbit Lifetime Analysis for the High Energy Astronomy Observatory (HEAO), Mission C. LMSC-HREC Technical Note D 162777, Feb. 1971.

Whitt, Ellis E.: Parametric Orbit Lifetime, Orbital Decay and Trapped Radiation Studies Related to the High Energy Astronomy Observatory (HEAO), Mission C. LMSC-HREC Technical Note D 162955, Mar. 1971.

Whitt, Ellis E.: Aerodynamic Drag and Orbit Lifetime Analysis for Octacircular HEAO-C. LMSC-HREC Technical Note D 225000, Apr. 1971.

TABLE OF CONTENTS

	Page
General Configuration Considerations	C- 1
Experiment Complement Options.	C-15
Mass Characteristics	C-23
Alternate Bench Mounting Concepts	C-27
1. Shock/Link (S/L) Concept.	C-27
2. Hard Mount Scheme	C-31
Transport Mechanism Growth.	C-37
Focal Point Determination	C-42
1. Physical Requirements	C-42
2. Performance Requirements	C-42
3. Position Sensor Concepts Considered.	C-42
4. Conclusions and Recommendations	C-48
References	C-52

LIST OF ILLUSTRATIONS

Figure	Title	Page
C-1.	Tapered configuration with reduced diameter	C- 4
C-2.	Truss bench	C- 5
C-3.	Small gamma-ray and X-ray telescope payload	C- 7
C-4.	Single-tube concept	C- 8
C-5.	Configuration with square outer structure	C- 9
C-6.	Subsystem module configuration	C-10
C-7.	Subsystem module roll-out	C-11
C-8.	Sunshade	C-12
C-9.	Concept without subsystem module	C-13
C-10.	32 foot concept	C-14
C-11.	HEAO-C sunshade	C-15
C-12.	Option 2 experiment complement	C-18
C-13.	Option 3 experiment complement	C-19
C-14.	Option 4 experiment complement	C-20
C-15.	Deployable flat crystal spectrometer (transverse stowage)	C-21
C-16.	Deployable flat crystal spectrometer (longitudinal stowage)	C-22
C-17.	Tandem telescopes	C-24
C-18.	Upside-down launch configuration	C-25

LIST OF ILLUSTRATIONS (Concluded)

Figure	Title	Page
C-19.	Normal launch configuration	C-25
C-20.	Outer structure deflection (360 inch length)	C-26
C-21.	Bench mounting configurations	C-29
C-22.	Shock mounts and linkages mounting scheme (linkages retained in orbit)	C-30
C-23.	HEAO-C joint shift analysis configurations	C-32
C-24.	Joint shift analysis	C-33
C-25.	Experiment misalignments after joint shifts (rss analysis) for hard-mount and ball-link configurations	C-36
C-26.	Experiments misalignments after joint shifts (worst - case analysis) for hard-mount and ball-link configurations	C-36
C-27.	HR telescope transport mechanism growth envelope . . .	C-38
C-28.	LA telescope transport mechanism growth envelope . . .	C-39
C-29.	HR telescope transport mechanism envelope for addition of two experiments	C-40
C-30.	LA telescope transport mechanism envelope for addition of one experiment	C-41
C-31.	Defocused conditions for one fiducial light	C-44
C-32.	Centroid displacements caused by defocusing	C-46
C-33.	Change in centroid separation as a function of focal point displacement	C-46
C-34.	Defocusing concept	C-49

LIST OF TABLES

Table	Title	Page
C-1.	Major Features of Baseline and Alternate Configurations	C- 3
C-2.	Experiment Complement Options.	C-16
C-3.	Upside-Down and Normal Launch Configuration Mass Data	C-25
C-4.	Truss Bench and Tube Bench Configurations Mass Data	C-27
C-5.	Weights Table for HEAO Variations.	C-27
C-6.	Mass Data for Equipment Module and OAS Variations	C-28
C-7.	Comparison of Candidate Measurable Quantities	C-47
C-8.	Performance Summary of Position Sensor Concepts	C-50

APPENDIX C. ALTERNATE OBSERVATORY CONFIGURATIONS

General Configuration Considerations

Several alternate configurations were studied at various points in the HEAO-C study. Some of the drawings depicting these configurations show slightly different Observatory diameters since the deflection of the upper end of the Observatory during launch was not accurately known early in the study and the mass distributions were different in the different configurations. Some of the configurations have tapered outer structures (because of the deflection problem) and some have tapered optical bench members. Some of the configurations have outer structures with octagonal cross sections, some have modified-octagonal cross sections, and some have square cross sections. Some have separate equipment modules for subsystems and some have the subsystems distributed inside the spacecraft. Some have the Orbit Adjust Stage (OAS) attached and some have it detached. Different complements of experiments are included in some of the configurations, but it is believed they are similar enough in nature to the baseline experiments to allow the conclusions drawn from the study of the configurations to be relevant. A common feature of all the concepts is the dual-structure concept (an outer main Observatory structure and an inner optical bench structure). Table C-1 provides a summary of the major features appearing in these concepts and gives the advantages and disadvantages of each.

Drawings are provided to show various combinations of the features mentioned above. The drawings are not all complete, as each was taken only far enough to verify certain aspects of the configurations. Each drawing is discussed below.

Figure C-1 shows a configuration with tapered outer structure (107 inches maximum outside diameter to 96 inches minimum outside diameter) with tapered tubes inside (to allow more packaging space). This configuration would be launched with the mirrors down, hence the mirror end is the largest. The ball-shock-linkage bench mounting concept is similar to that in the baseline; the linkages are retained in orbit. Spacecraft subsystems are not shown in this drawing.

Figure C-2 shows the truss bench concept. The subsystems and low energy (LE) telescope are not shown in this configuration, and it would be very difficult, or impossible, to package them in addition to this bench. Here, as

in the previously mentioned concept, the mirrors are down at launch. The outer structure sides are not tapered, but the truss bench is tapered. Linkages from the bench to the outer structure at the upper end help limit deflections of the outer structure during launch (this bench is heavier and stiffer than the outer structure). The links are dropped after launch so that thermal deflection of the outer structure would not induce a stress into the bench. Strut-type shock absorbers are provided at the mirror end to damp out launch vibrations at the experiments. The tubular members of the truss bench would be either Invar or graphite/epoxy.

Figure C-3 shows a configuration with two short telescopes — a gamma ray telescope and a soft X-ray telescope. Although subsystems are not shown, it is obvious that there is a considerable amount of unused space, and this concept is not considered desirable due to the volumetric and payload inefficiency.

Figure C-4 depicts a configuration which provides great structural efficiency; one large telescope tube supports the other large telescope lens and detector equipment, without the second tube having to be a continuous structure. More volume for packaging subsystems is allowed by this telescope configuration than by any other telescope arrangement. It is probably not possible to thermally control the lens and detector equipment within the required limits, however, as membranes or insulation could not be installed on the aft end of the lens and the forward end of the detector assemblies without reducing the sensitivity of the telescope. Therefore, thermal radiation into and out of these areas would be difficult to control. It was concluded that this concept is not feasible.

Figure C-5 shows the results of an attempt to package the HEAO-C experiments in a square outer structure (the square structure was one of the competing concepts in the Phase B studies of HEAO-A and -B). The outer structure and the tubes are tapered because of deflection. The mirrors would be down at launch, hence that end is larger. It can be seen that the packaging in the viewing (mirror) end is too tight, and the instruments would not fit at all inside the square enclosure at the other end. Insufficient internal volume severely limits this configuration.

Figure C-6 shows the effects of incorporating a subsystems module at the aft end of the telescopes. (Figure C-7 shows a rollout drawing of the subsystems module.) This module increases the length of the entire spacecraft 3 feet, increasing weight and lateral launch deflections, and requires an increase in shroud length. The packaging flexibility is actually decreased and the subsystems would probably run hotter since all of them cannot be radiatively-coupled to the antisolar side as efficiently as in the cases where the subsystems

TABLE C-1. MAJOR FEATURES OF BASELINE AND ALTERNATE CONFIGURATIONS

Considerations and Their Assessments		Feature		Cross-sectional Shape of Outer Structure		Location of Viewing ^b End of Spacecraft at Launch		Solar Array Configuration Mounting		OAS Disposition		Location of Subsystems		Type of Optical Bench							
Foldout Frame 1	Modified Octagonal	+ Slightly more internal volume than octagonal configuration	+ Slightly better torsional and bending stiffness than octagonal	- No commonality with present HEAO-A and -B concepts	- Weak torsional and bending stiffness	Mirrors-Up Launch ^a	+ Experiment view not blocked if OAS fails to separate	+ Higher center of gravity allows structure to be lighter	+ Could have slightly larger mirrors if tapered outer structure is utilized	- Sunshade must be deployable	- A possibility of experiment contamination from OAS separation	+ Lower vibration levels on miscellaneous experiments	- Higher vibration levels at focal plane	- Possibility of contamination from shroud separation	Octagonal ^a	+ Commonality with HEAO-A and -B	+ Good internal volume	+ Good torsional and bending stiffness			
	Square	- Insufficient internal volume	- No commonality with present HEAO-A and -B concepts	- Weak torsional and bending stiffness			Mirrors-Down Launch	- Experiment view blocked if OAS fails to separate	+ Lower center of gravity allows structure to be lighter	+ Could have slightly larger mirrors if tapered outer structure is utilized	- Sunshade must be deployable	- A possibility of experiment contamination from OAS separation	+ Lower vibration levels on miscellaneous experiments	- Higher vibration levels at focal plane		- Possibility of contamination from shroud separation		+ Slightly more internal volume than octagonal configuration	+ Slightly better torsional and bending stiffness than octagonal	- No commonality with present HEAO-A and -B concepts	- Weak torsional and bending stiffness
Foldout Frame 2	Jettisoned	+ Greater orbital drag, but more than offset by better ballistic coefficient due to increased weight	+ Eliminates separation hardware and potential failure modes	+ Eliminates separation contamination possibility	- Thrusters can be mounted on rear of OAS, but net lever arm is worsened, since center of gravity shifts	+ Can fill RCS main propulsion tank and eliminate some bottles	+ Thrusters do not have to be relocated to spacecraft	- Can buy them in present locations as part of stripped OAS for periodic orbit adjust or deorbit	+ Can use OAS for mounting some subsystems, if desired	+ Opens possibility of using some of the AF version OAS systems in addition to stripped OAS hardware - possibly can eliminate some new design	+ Greater orbital drag, but more than offset by better ballistic coefficient due to increased weight	+ Eliminates separation hardware and potential failure modes	+ Eliminates separation contamination possibility	- Thrusters can be mounted on rear of OAS, but net lever arm is worsened, since center of gravity shifts	+ Can fill RCS main propulsion tank and eliminate some bottles	+ Thrusters do not have to be relocated to spacecraft	- Can buy them in present locations as part of stripped OAS for periodic orbit adjust or deorbit	+ Can use OAS for mounting some subsystems, if desired	+ Opens possibility of using some of the AF version OAS systems in addition to stripped OAS hardware - possibly can eliminate some new design		
		Retained ^a	+ Eliminates separation hardware and potential failure modes	+ Eliminates separation contamination possibility	- Thrusters can be mounted on rear of OAS, but net lever arm is worsened, since center of gravity shifts	+ Can fill RCS main propulsion tank and eliminate some bottles	+ Thrusters do not have to be relocated to spacecraft	- Can buy them in present locations as part of stripped OAS for periodic orbit adjust or deorbit	+ Can use OAS for mounting some subsystems, if desired	+ Opens possibility of using some of the AF version OAS systems in addition to stripped OAS hardware - possibly can eliminate some new design											
Foldout Frame 3	Equipment Module	- Poor packaging flexibility	- Thermal control flexibility not as good	- Some subsystems must be mounted on solar side	- Fighter packaging, runs hotter	- Requires longer spacecraft, hence another shroud section, greater structure weight to limit deflections, and greater drag area	+ Center of gravity is lowered, allowing structure to be lighter	- Center of gravity is closer to thrusters, decreasing lever arm													
		Distributed ^a	+ Better packaging flexibility	+ Good thermal control flexibility	+ Most subsystems can be mounted on antisolar side and run cooler	+ Better packaging flexibility	+ Good thermal control flexibility	+ Not as good	+ Some subsystems must be mounted on solar side	+ Fighter packaging, runs hotter	+ Requires longer spacecraft, hence another shroud section, greater structure weight to limit deflections, and greater drag area	+ Center of gravity is lowered, allowing structure to be lighter	- Center of gravity is closer to thrusters, decreasing lever arm								

C-3

a. Baseline
 b. This consideration and the assessments were applicable prior to the decision to retain the OAS attached to the space-craft and would be applicable again if a decision is made to change launch vehicles.

FOLDOUT FRAME

FOLDOUT FRAME 2

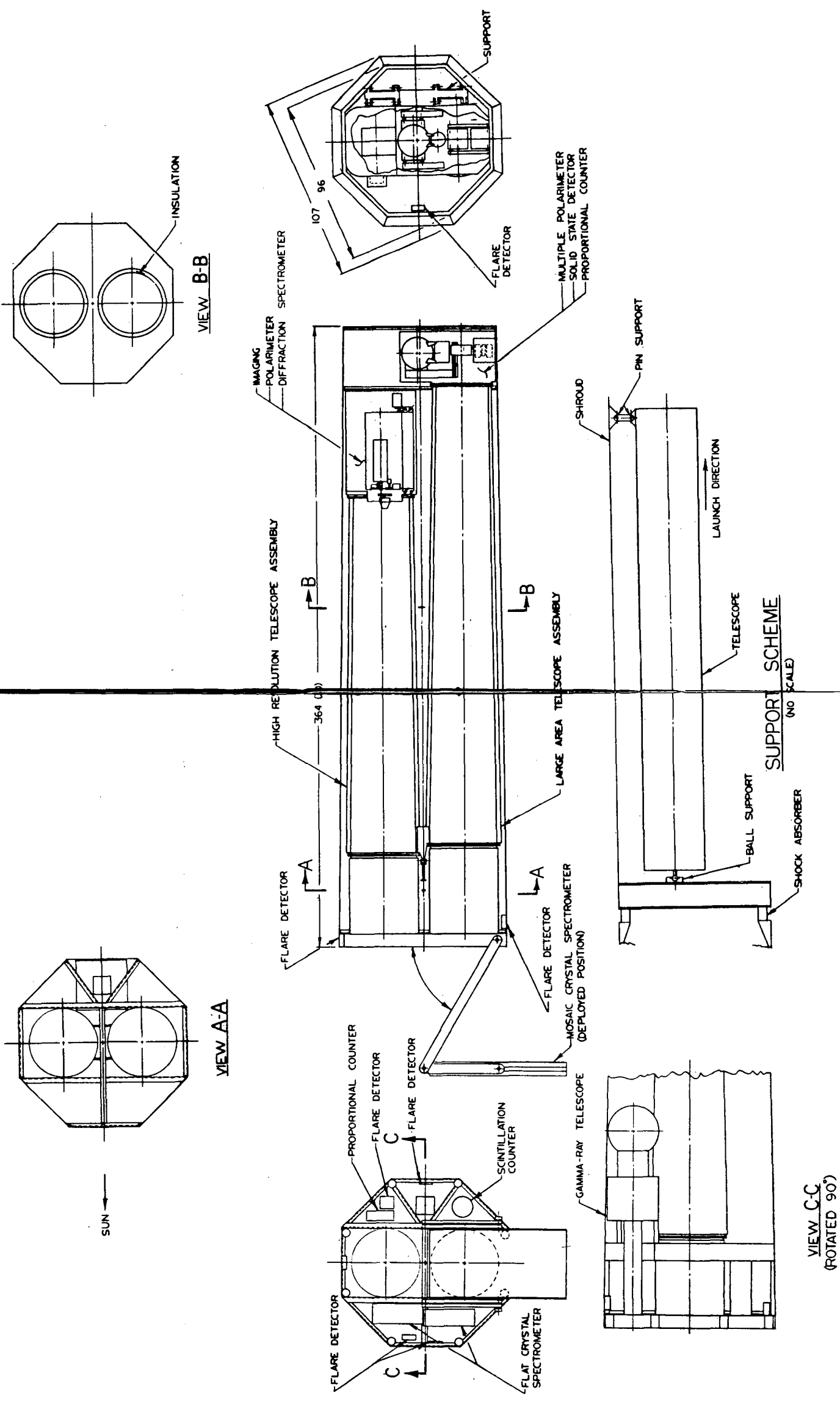


Figure C-1. Tapered configuration with reduced diameter.

are distributed along the antisolar side. Packaging volume between the telescopes and the outer structure is largely wasted. The concept of a subsystems module would be more desirable if it were a standard building block which could be used with many types of payloads on many missions. The outer structure cross-sectional shape was made circular on the antisolar half, providing a little more room for the cosmic X-ray (low energy) telescope. The mirror end of the spacecraft would be the upper end at launch, since the large mass of the subsystems module would cause greater deflections if it were on the upper end. Consequently, there is no reason to taper the outer structure and, hence, not as much reason to taper the tubes. Also, the ball-shock-linkage concept for bench mounting is used here. A fixed sunshade is shown on the mirror end of the spacecraft. Figure C-8 shows a more detailed representation of this sunshade, which was designed for a simultaneous 30 degree tilt of the X-axis toward the sun and a 30 degree roll about the X-axis. The dotted line shows the shadowed area at such a tilt and roll. It can be seen that both large telescopes are shaded. The other experiments are recessed well below the ends of the large telescope mirrors and, hence, are not illuminated by the sun's rays at such a tilt. There could possibly be some reflection on these experiments from the sun's rays striking the inside of the back spacecraft surface, but that surface could be coated with a nonreflective substance or truncated, if desired.

The concept in Figure C-9 is the same as that in Figure C-6 except that the subsystems are distributed throughout the spacecraft instead of being in the subsystems module.

Figure C-10 depicts the utilization of a 32 foot long outer structure (for greater structural commonality with HEAO-A and -B). It was undesirable to mount the lenses of the large telescopes flush with the end of the outer structure, because this raises the center of gravity in the launch configuration (mirrors up) and increases deflections. As shown, however, the sun would impinge on the inside back surface of the spacecraft at tilt angles greater than 30 degrees, due to the extra length of the spacecraft beyond the mirrors (see Figure C-11). This problem was solved on the baseline configuration by eliminating the extra 2 foot section beyond the mirrors. If the slightly greater structural commonality with HEAO-A and -B of retaining the 2 foot section is a more cost-effective manufacturing approach, the back surface of the spacecraft could still be truncated after manufacturing to accomplish the same thing.

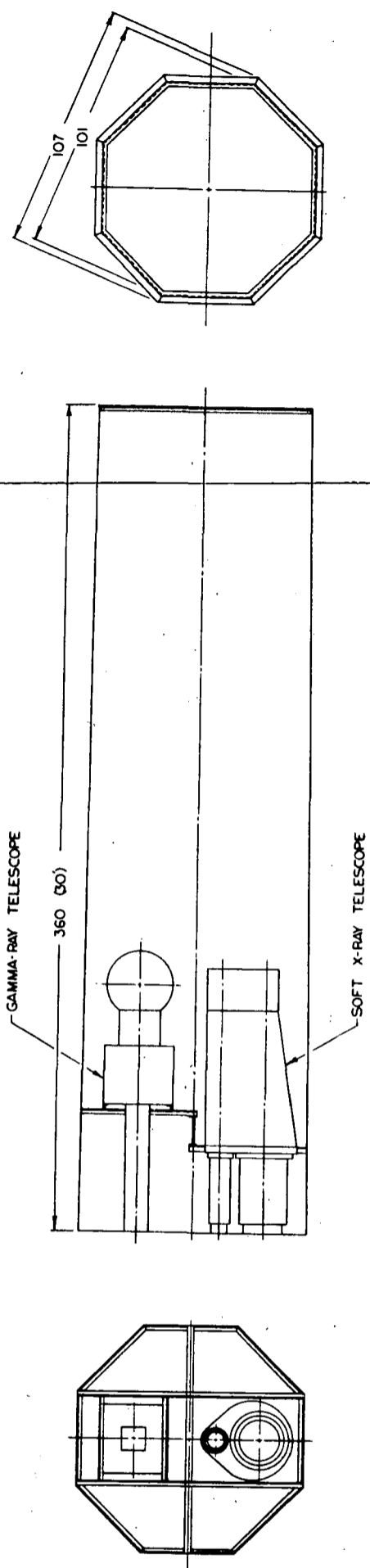


Figure C-3. Small gamma-ray and X-ray telescope payload.

FOLDOUT FRAME 1

FOLDOUT FRAME 2

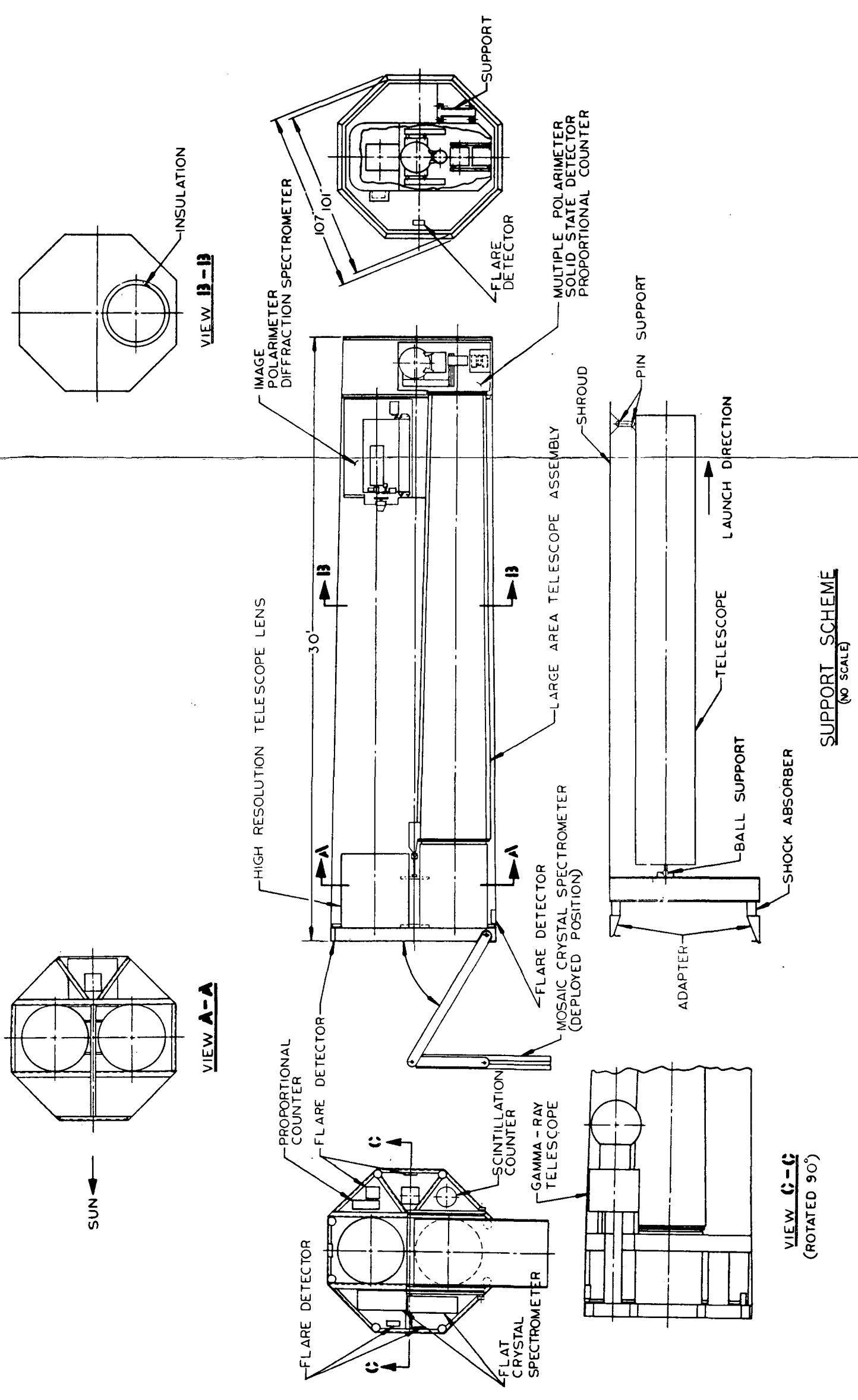


Figure C-4. Single-tube concept.

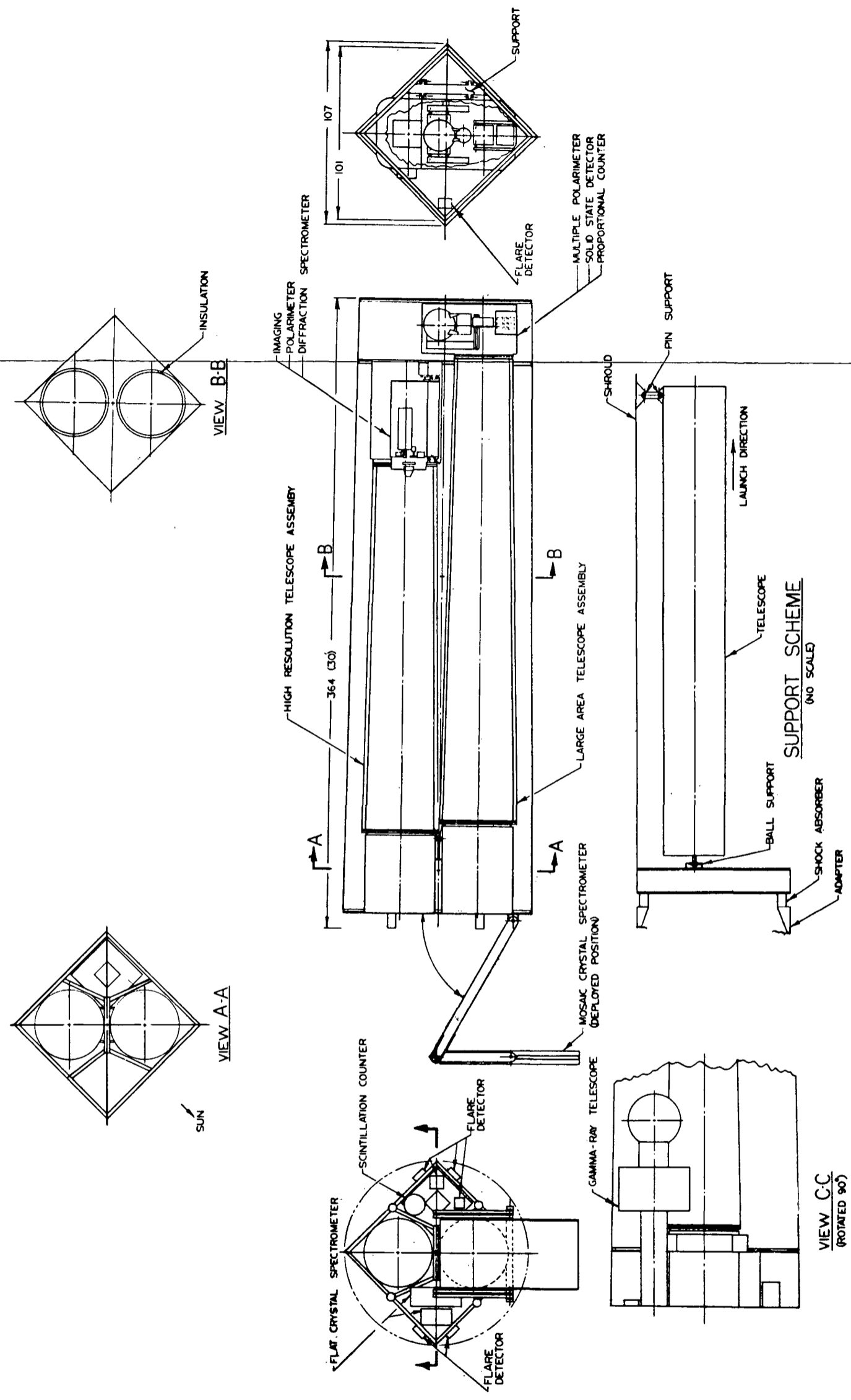


Figure C-5. Configuration with square outer structure.

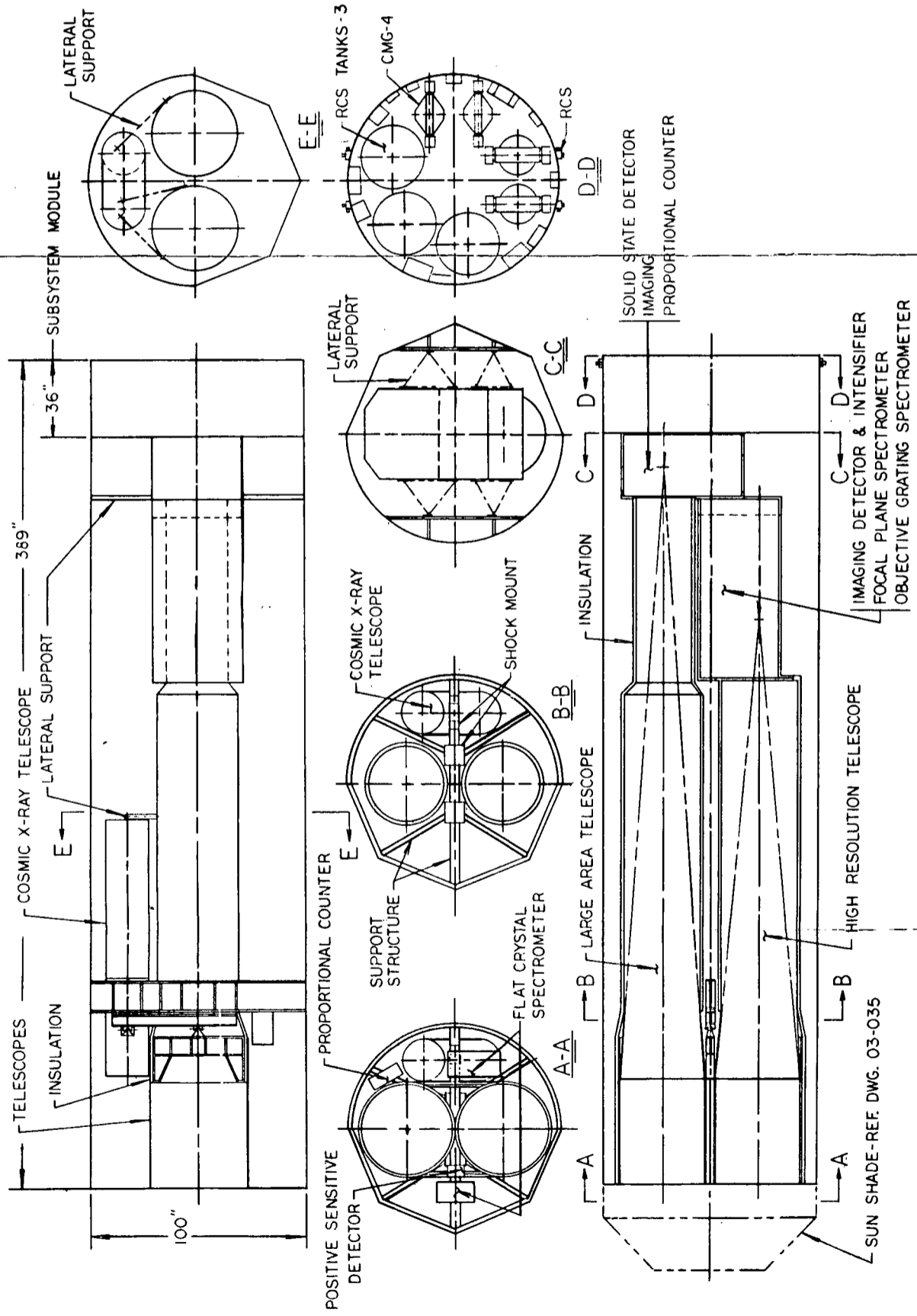


Figure C-6. Subsystem module configuration.

- 1 - SOLAR POWER DISTRIBUTOR
- 2 - POWER CONTROL ASSY
- 3 - BATTERY ASSY
- 4 - REGULATOR ASSY
- 5 - BATTERY CHARGER ASSY
- 6 -
- 7 -
- 8 - CMG ELECTRONICS
- 9 - COMPUTER
- 10 - GYRO PKG
- 11 - MEMORY
- 12 - PCM ENCODER, FORMAT GEN.
- 13 - COMMAND PROCESSOR, CLOCK
- 14 - FREQ MUX
- 15 - PSK DEMODULATION
- 16 - TRANSPONDER
- 17 - DATA STORAGE CONTROL
- 18 - TAPE RECORDER

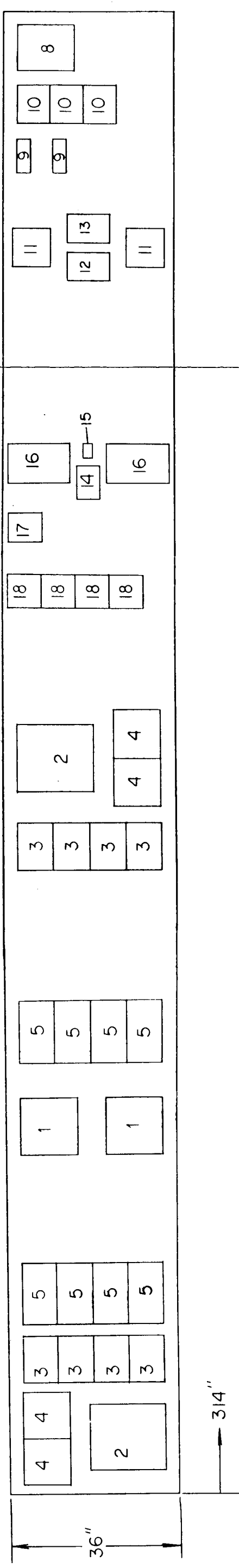


Figure C-7. Subsystem module roll-out.

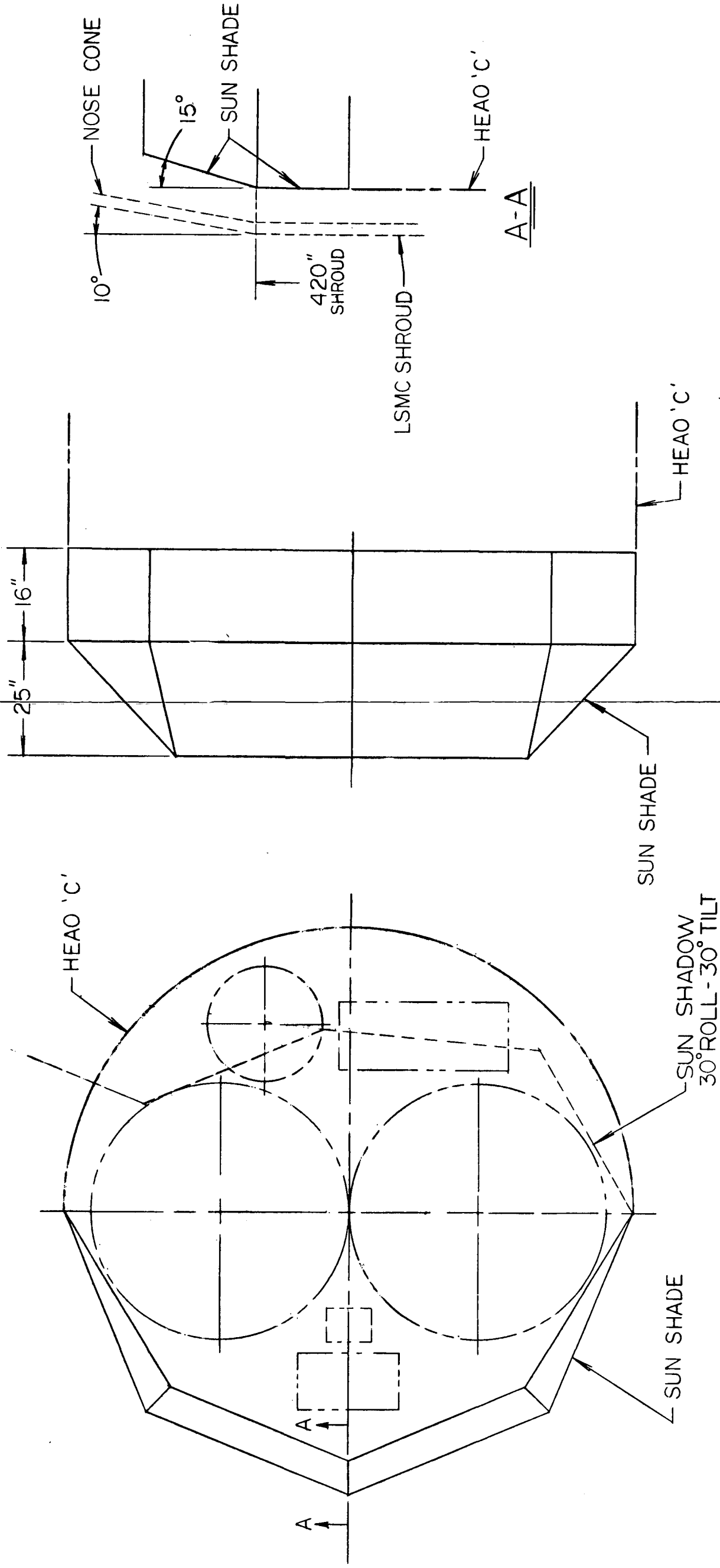


Figure C-8. Sunshade.

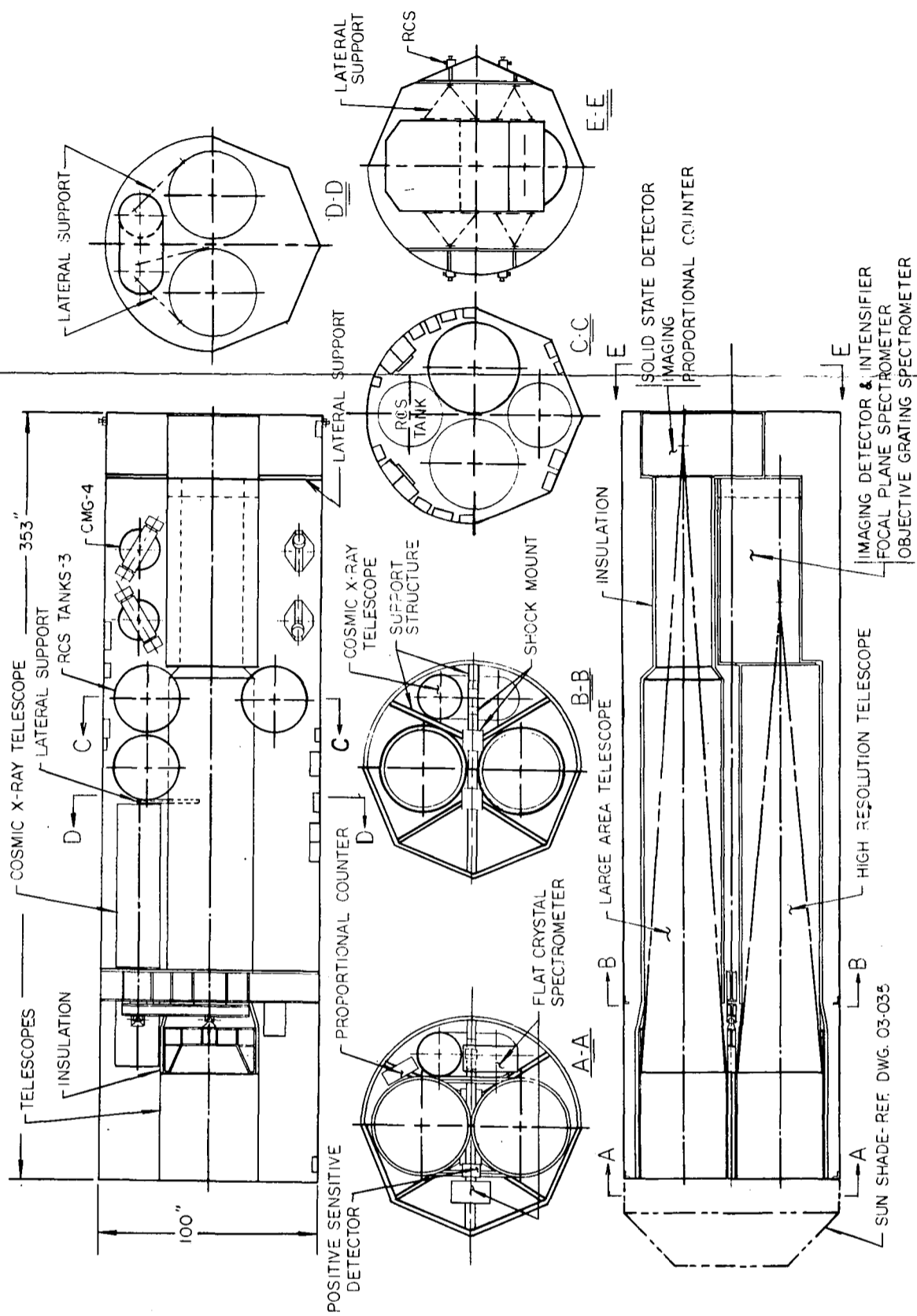
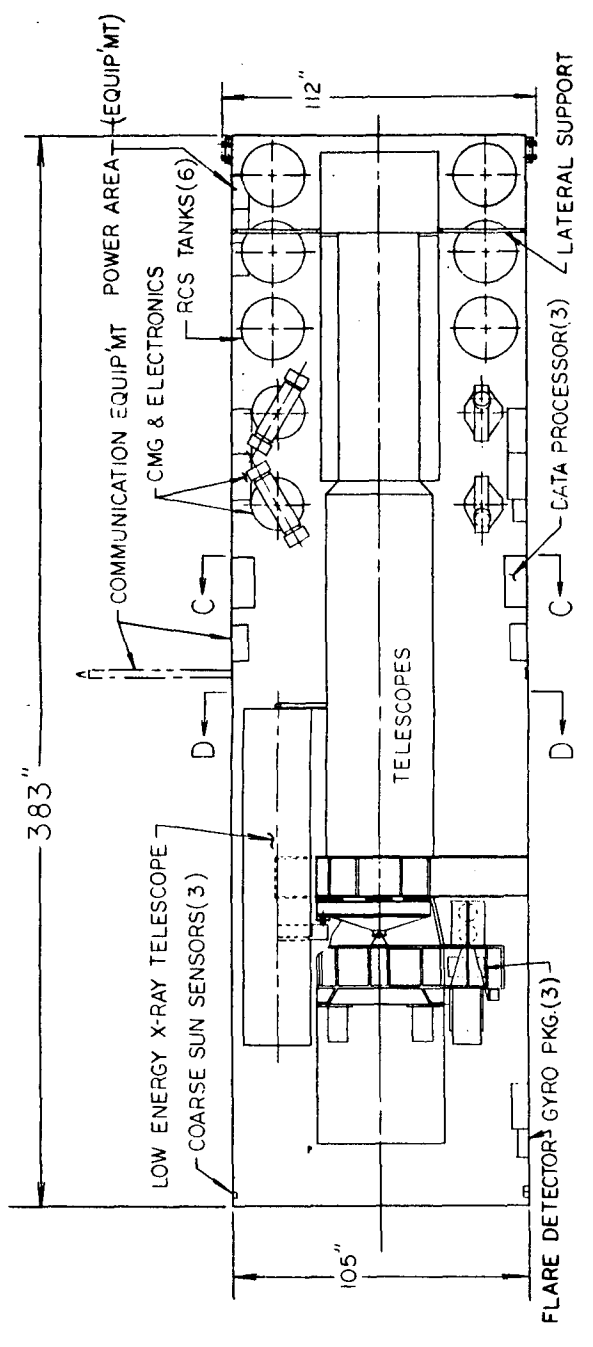


Figure C-9. Concept without subsystem module.

FOLDOUT FRAME 1



FOLDOUT FRAME 2

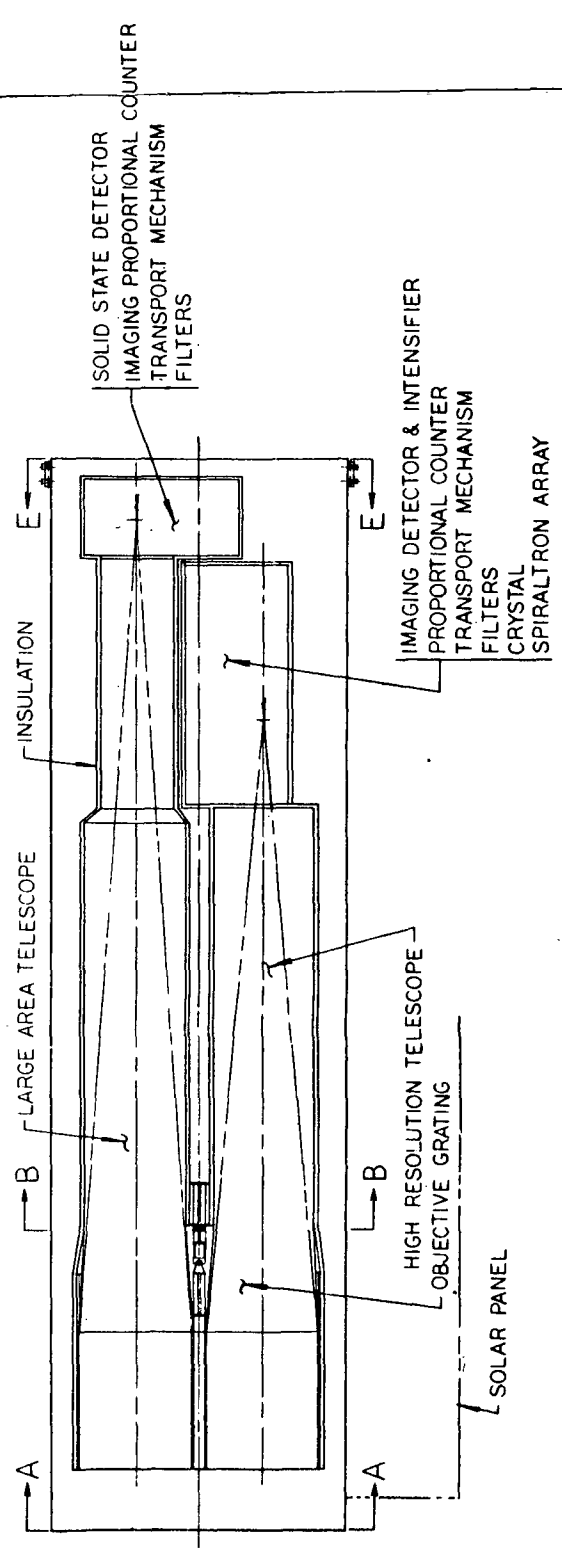
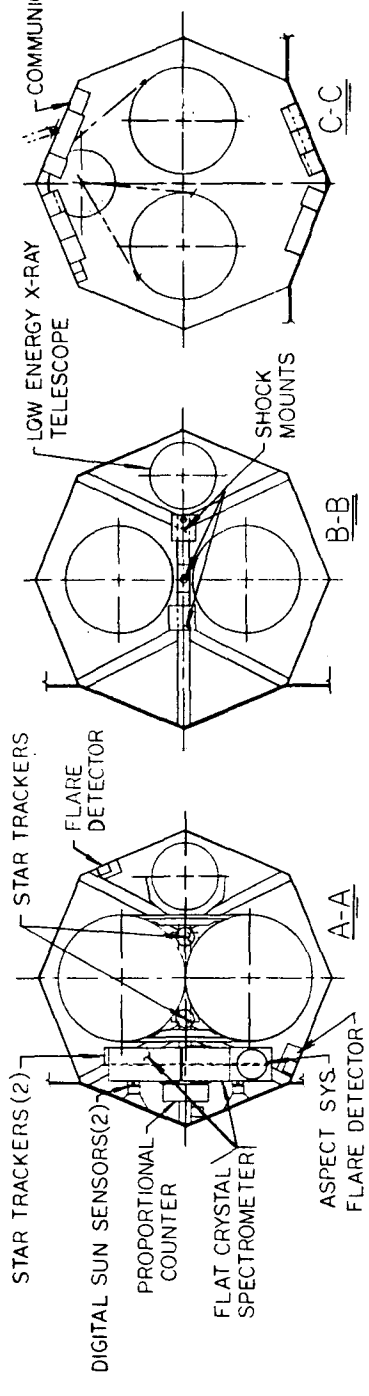
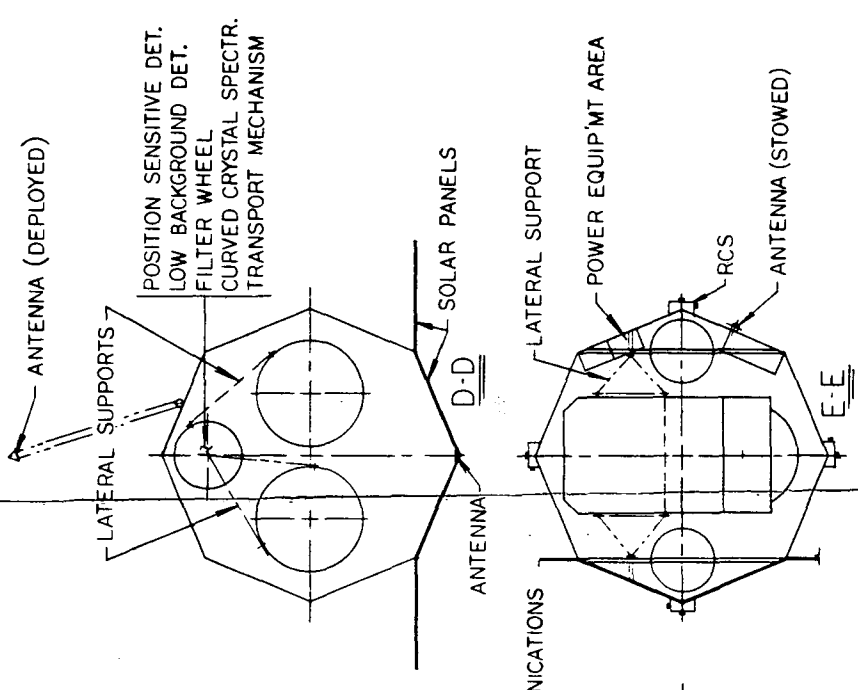


Figure C-10. 32 foot concept.

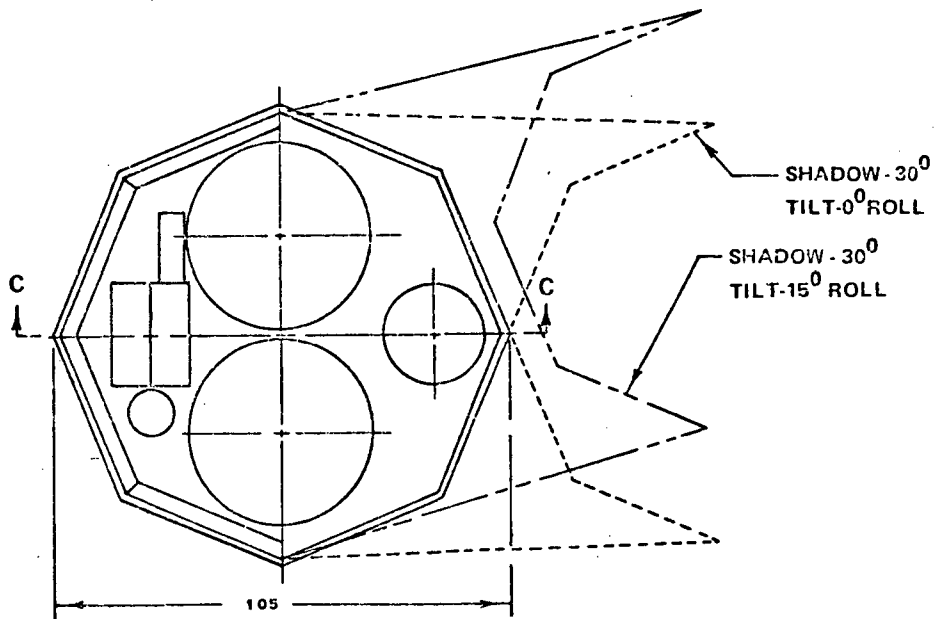
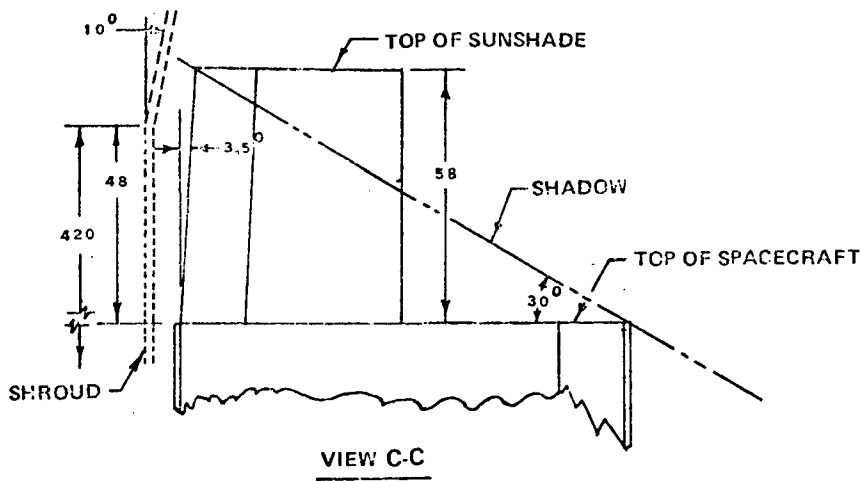
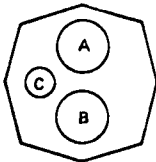
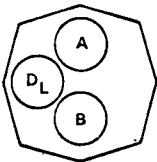
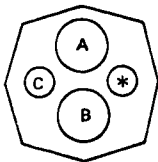
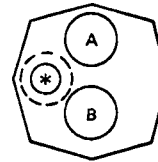


Figure C-11. HEAO-C sunshade.

Experiment Complement Options

When the complement of experiments shown on the baseline spacecraft was selected, three other options of experiment complements were selected for assessment. These are defined in Table C-2 and the individual experiments are described in Appendix B.

TABLE C-2. EXPERIMENT COMPLEMENT OPTIONS

<p>OPTION 1 BASELINE</p> 	<p>OPTION 2</p> 	<p>OPTION 3</p>  <p>*D_S</p>	<p>OPTION 4</p>  <p>*C POINTS WITH A & B D_L POINTS OPPOSITE C</p>
<p>A. IIR Telescope</p> <p>Image Intensifier, Objective Grating, Filter Spectrometer, Curved Crystal Spectrometer</p> <p>B. LA Telescope</p> <p>Solid State Detector, Filter Spectrometer, Position Sensitive Detector</p> <p>C. LE Telescope</p> <p>Filter Spectrometer, Position Sensitive Detector</p> <p>D. UV Telescope (none)</p> <p>E. Miscellaneous (not shown)</p> <ol style="list-style-type: none"> 1. All-Sky Flare Detector 2. Fine Flare Detector 3. Monitor Propor- tional Counter 4. Flat Crystal Spectrometer 	<p>A. Same as 1</p> <p>B. Same as 1 except for C. below</p> <p>C. None (moved to LA telescope)</p> <p>D. Large UV Telescope (GEP)^a 10 ft long 40 in. dia 982.2 lb</p> <p>E. Same as 1</p>	<p>A. Same as 1</p> <p>B. Same as 1</p> <p>C. Same as 1</p> <p>D. Small UV Telescope (smaller and lighter than large UV)</p> <p>E. Same as 1</p>	<p>A. Same as 1</p> <p>B. Same as 1</p> <p>C. Same as 1</p> <p>D. Same as 2</p> <p>E. Same as 1</p>

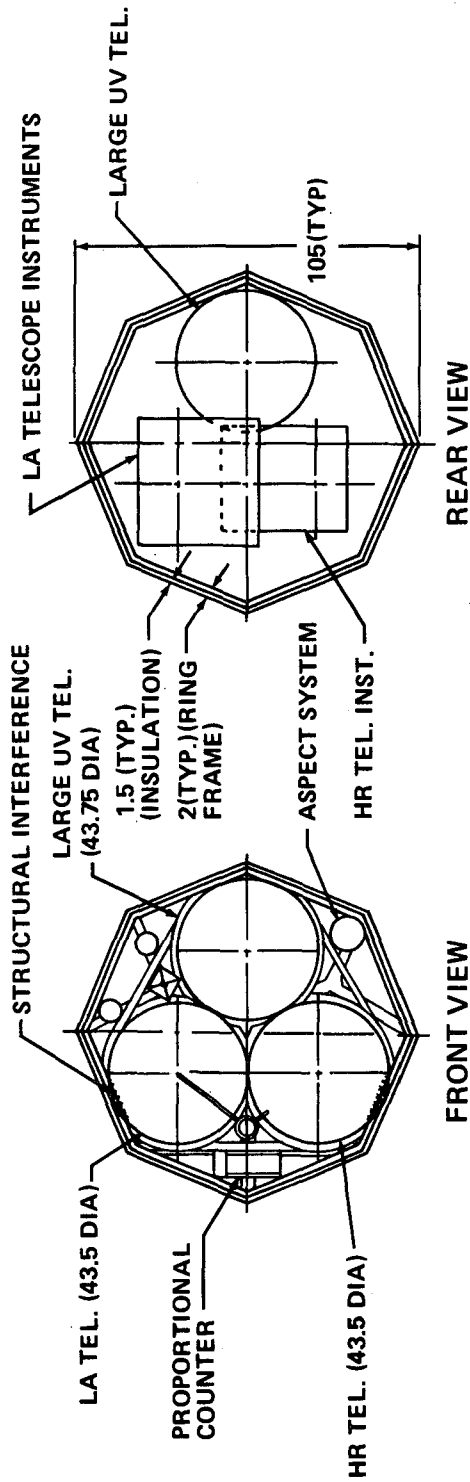
a. Goddard Experiment Package

The baseline configuration (Option 1) is shown and discussed in Chapter IV. Option 2 is depicted in Figure C-12. As can be seen by the crosshatched areas, the three large telescopes violate structural members. Also, their fields of view are partially blocked by the sunshade (not shown) in the forward end. The envelopes of the focal plane mechanisms are limited in the directions in which they can expand, should additional experiments be added. This concept cannot be made to work unless the X-ray telescopes are reduced in size (the large UV telescope is already built and cannot be reduced). Also, the flat crystal spectrometer of the same size as that shown in Option 1 cannot be accommodated in the Option 2 configuration.

Figure C-13 shows the layout of Option 3 experiments. Here, a small UV telescope of the same size as the baseline low energy (LE) telescope is about the largest size that can be accommodated. Here, also, the baseline flat crystal spectrometer cannot be accommodated. Front and rear views are shown of this configuration with the centerlines of the large telescopes offset from the center of the spacecraft. Such an arrangement causes violation of the outer structure envelope at the front end, and the telescope fields of view would be partially blocked by the sunshade (not shown).

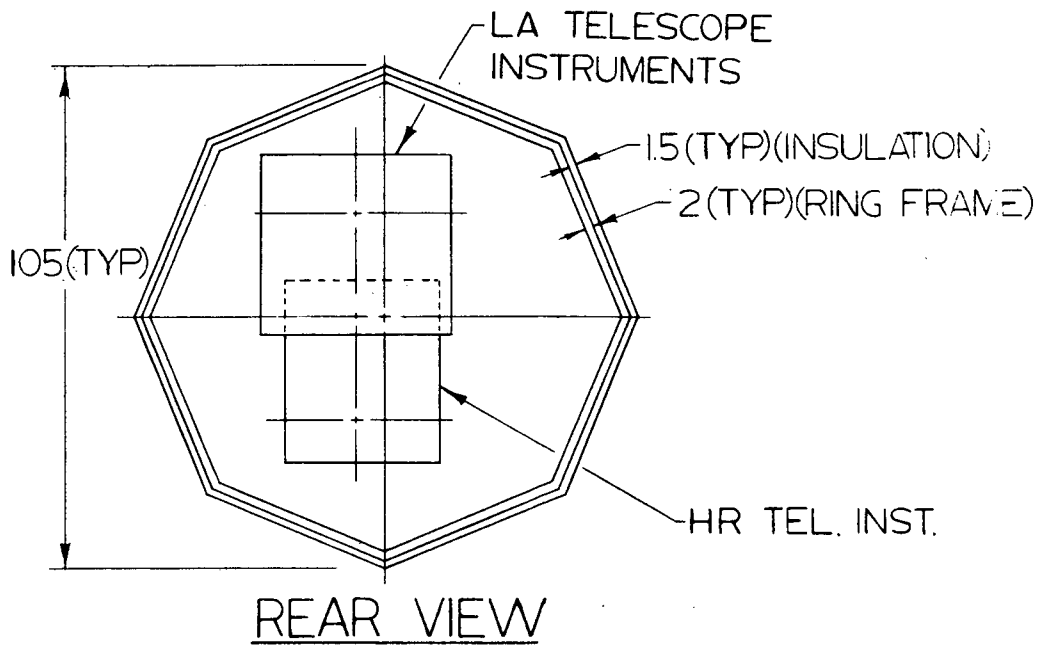
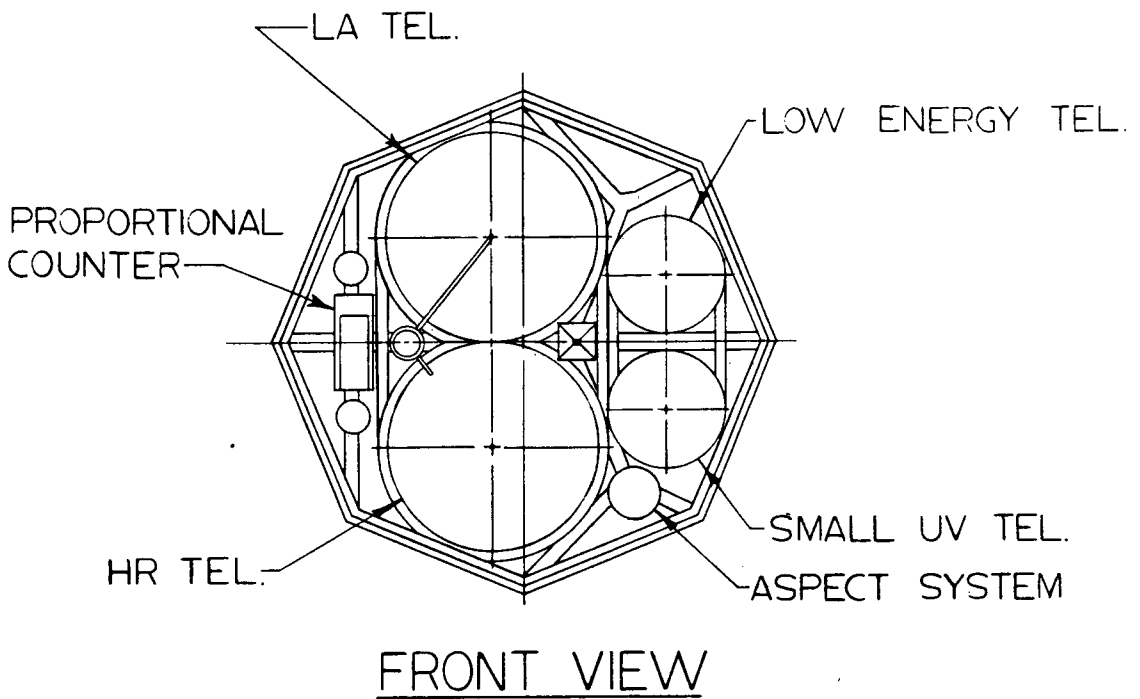
Option 4 was considered a possibility before the decision was made to retain the OAS in orbit. Because of that decision, it automatically became an impossible configuration. However, it is shown in Figure C-14 that Option 4 is not a feasible concept regardless of the OAS disposition because there is violation of the outer structure envelope no matter how the telescopes are positioned and blockage of fields of view by the sunshade (not shown). There would also be the possibility of contamination of the large UV telescope, which is rearward-looking in this configuration, due to OAS separation (if that were baselined) and/or thruster operation, since they are located on the aft end.

Two sketches were made of configurations with different types of deployable flat crystal spectrometers (Figs. C-15 and C-16). Alignment would be difficult to maintain with such a deployable concept, and the experiment would have less protection from the environment. The sunshade would have to be extended, as the present design would cause impingement on the spectrometers. Also, should deployment failure occur, the fields of view of the flat crystal spectrometer and both small telescopes would be blocked in the configuration shown in Figure C-15, and one small telescope would be blocked in Figure C-16. Consequently, this does not appear to be feasible.



NOTE:
FLAT CRYSTAL SPECTROMETER WILL
NOT FIT INTO THIS CONFIGURATION

Figure C-12. Option 2 experiment complement.



NOTE:

FLAT CRYSTAL SPECTROMETER WILL NOT FIT INTO THIS CONFIGURATION

Figure C-13. Option 3 experiment complement.

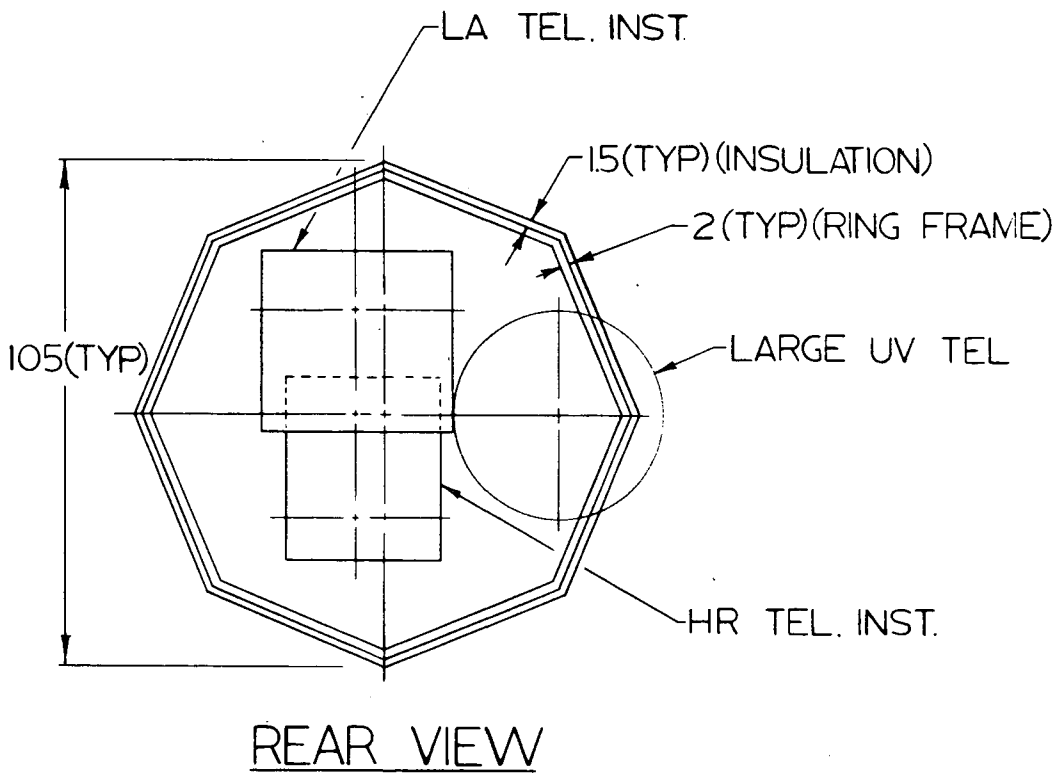
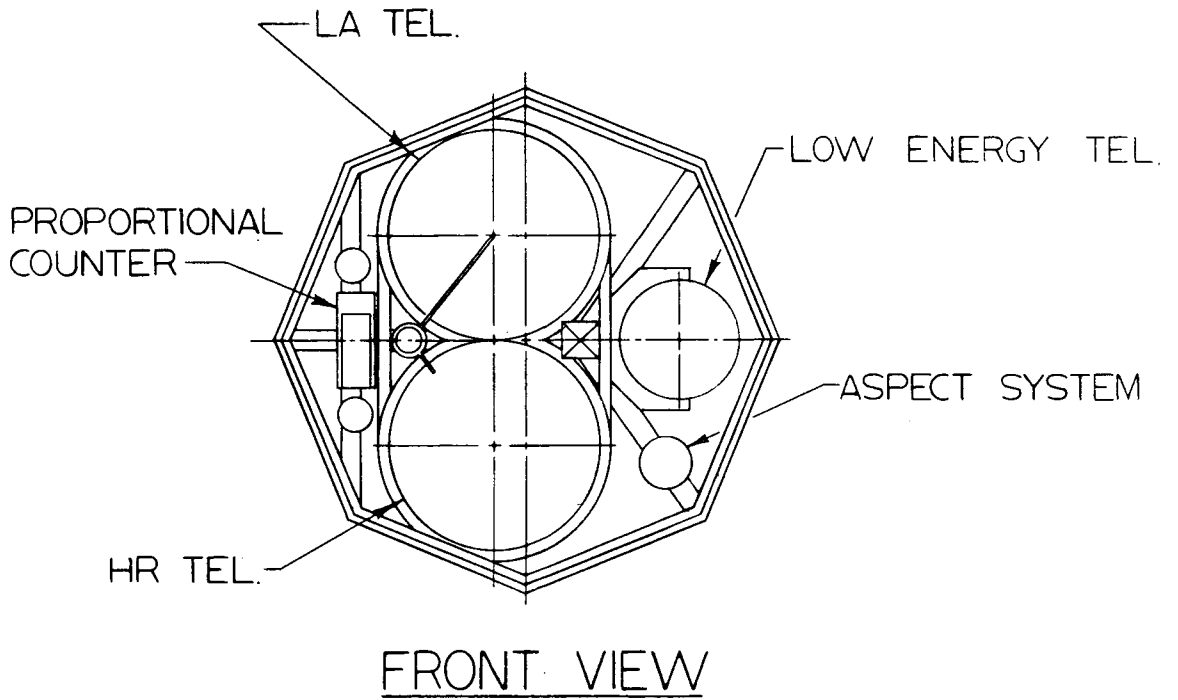


Figure C-14. Option 4 experiment complement.

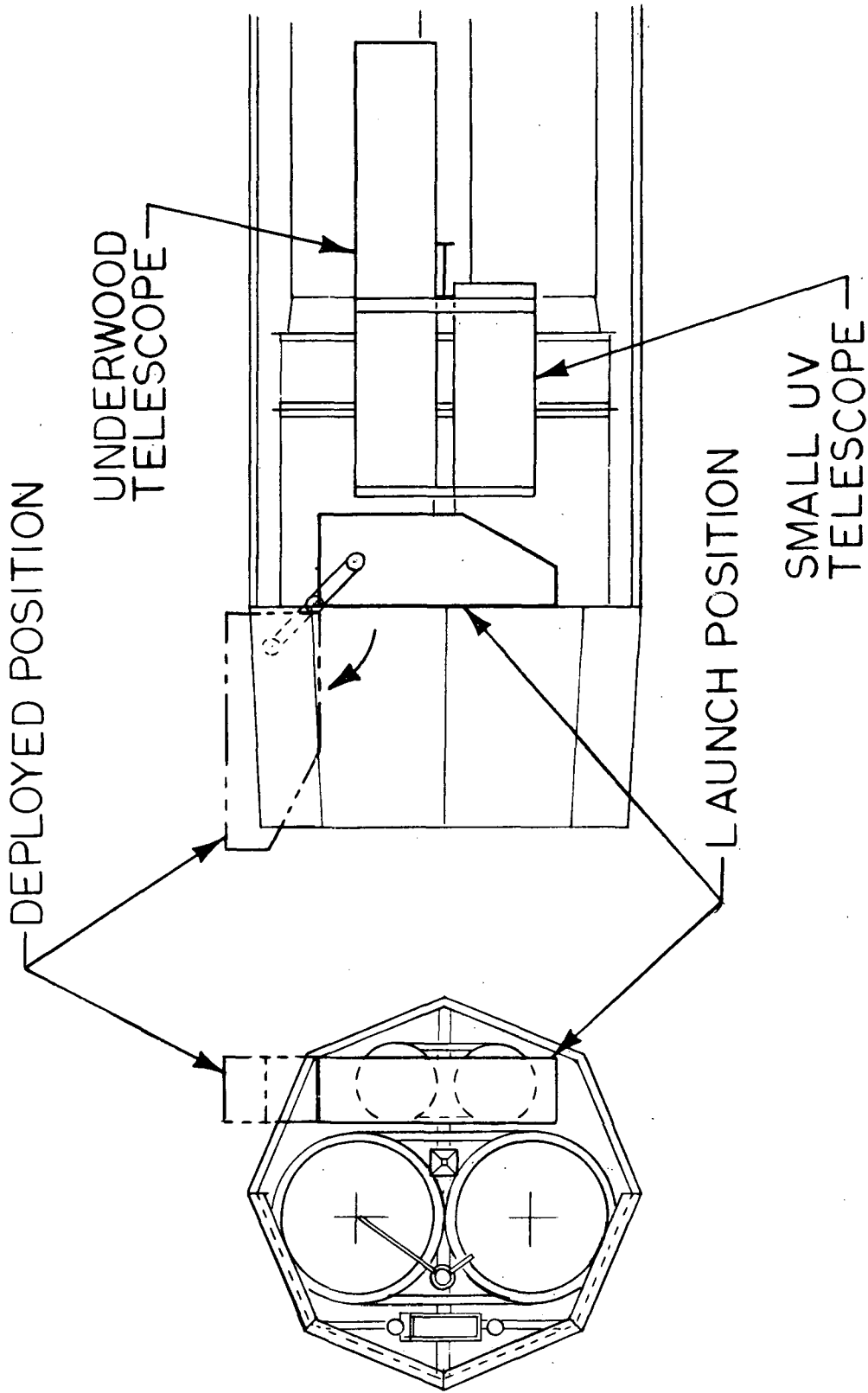


Figure C-15. Deployable flat crystal spectrometer (transverse stowage).

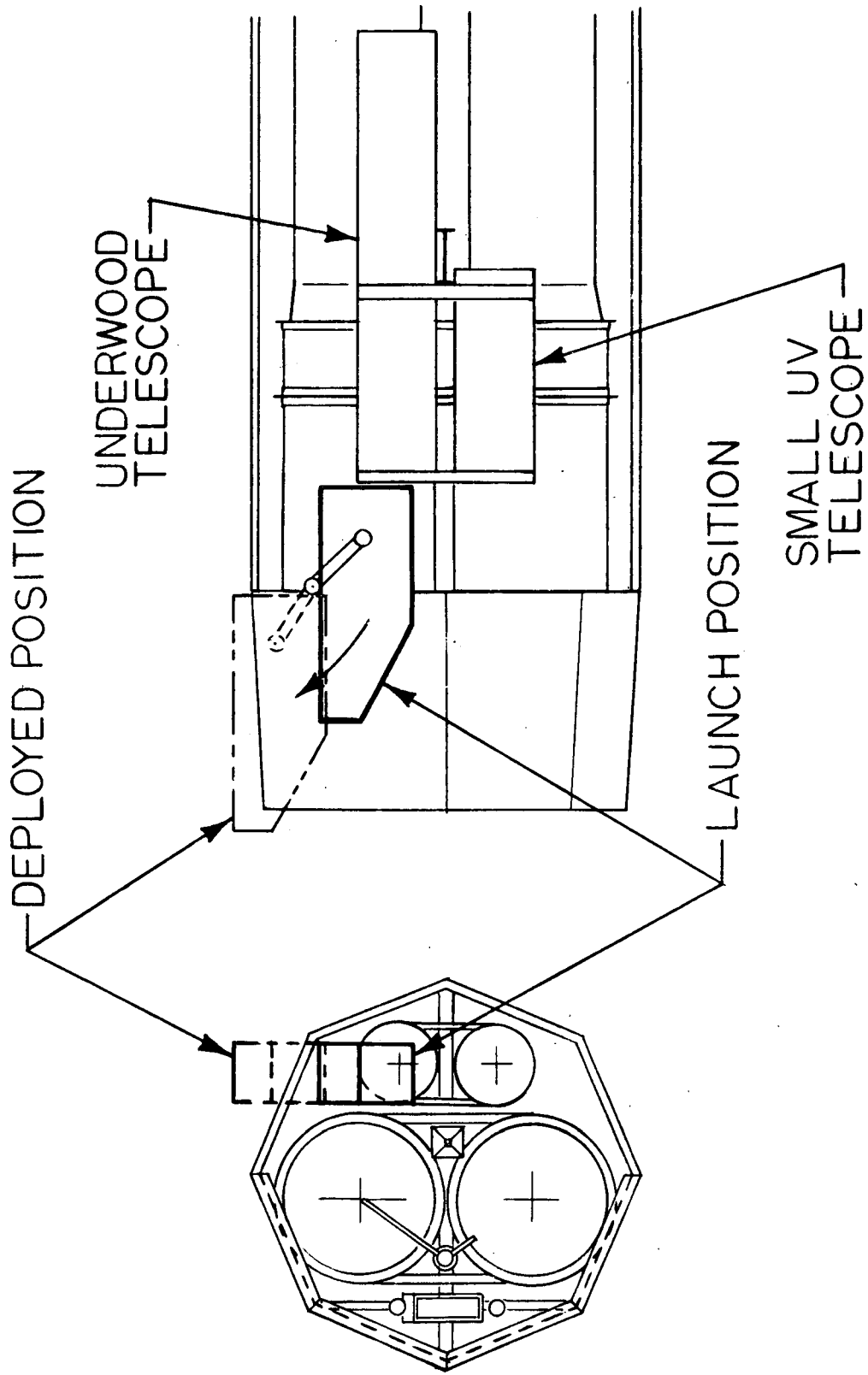


Figure C-16. Deployable flat crystal spectrometer (longitudinal stowage).

Figure C-17 shows "tandem" configuration in which the small UV telescope is mounted directly in front of the LE telescope, but the field of view of the LE telescope is not obscured because of the grazing incidence angles. This provides a very compact arrangement. However, the size of the small UV telescope is limited by the LE telescope's field of view, and mounting hardware for the small UV telescope may partially obscure the LE telescope field of view. The possibilities of secondary reflections would have to be investigated further for this configuration.

In summary, it appears that the basic trade in experiment complement options would have to be between carrying a flat crystal spectrometer or a small UV telescope; both can be accommodated only if their sizes are decreased by an unacceptable amount.

Mass Characteristics

Mass data for several of the alternate configurations were generated during the study. Although there are some variations in weights for any given system among the configurations, since they were assessed at different times during the study, the weights are similar enough that the assessments of the concepts are still relevant.

The possibility of a launch with the mirrors in a downward position (upside-down launch) was investigated. The primary advantage of the upside-down launch is that the spacecraft's center of gravity in the launch position can be lowered, easing the structural deflection problem. The upside-down launch exhibits much smaller inertia about the Y and Z axes. This fact results from the concentration of the large mass contributors (mirrors and OAS) on the same end of the spacecraft. This situation is illustrated in Figure C-18. Figure C-19 illustrates the normal launch configuration. At this point in the study, payload weights of 15 279 pounds had been identified. These weights resulted in the mass data summarized in Table C-3.

Figure C-20 represents the results of a simplified analysis to provide an indication of the dynamic deflection of the outer structure and its natural frequency for different relative values of structural weight. Curves are plotted for the cases with mirrors aft and with mirrors forward, and the latter case includes a 22 percent increase in structure weight for stiffness to decrease deflections. Even with this increase in weight, it can be seen that deflections are considerably larger with the mirrors forward. Structural weight increases help decrease the deflection and increase the natural frequency, for both cases,

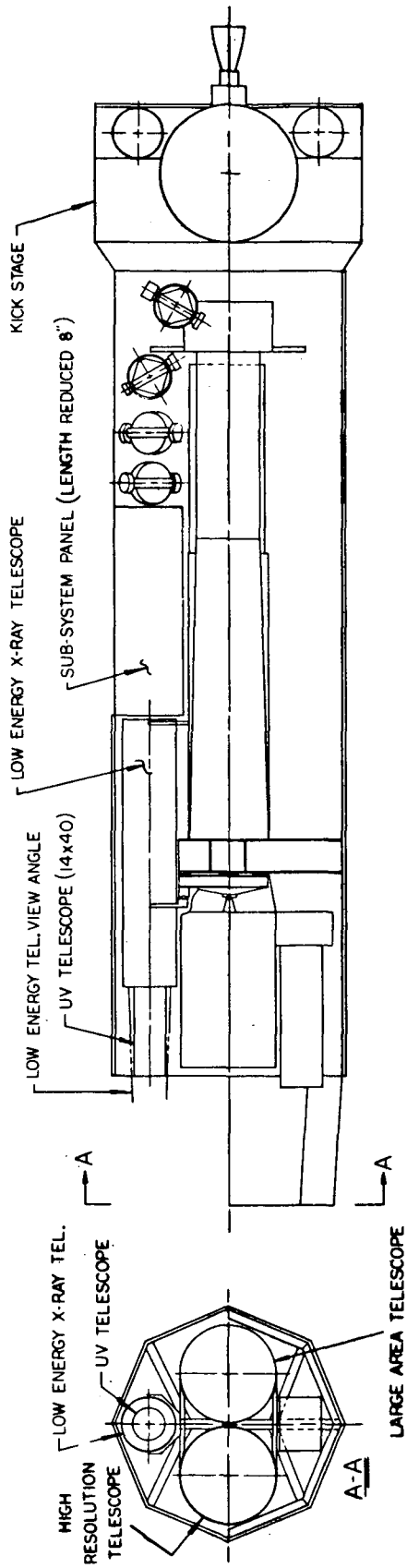


Figure C-17. Tandem telescopes.

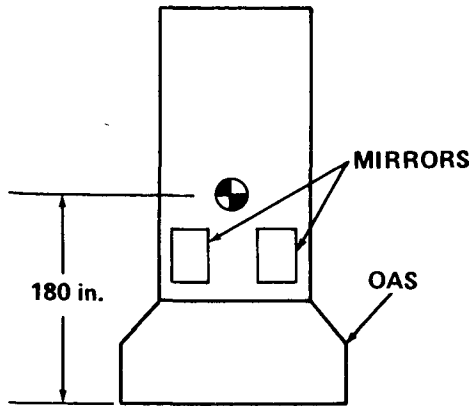


Figure C-18. Upside-down launch configuration.

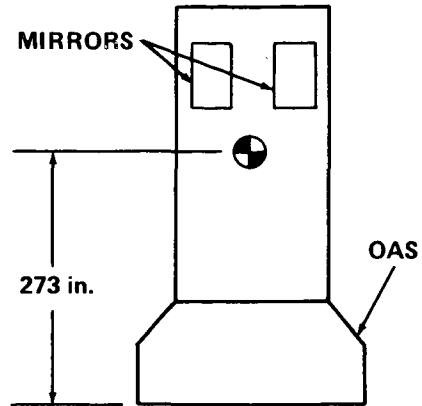


Figure C-19. Normal launch configuration.

TABLE C-3. UPSIDE-DOWN AND NORMAL LAUNCH CONFIGURATION MASS DATA

Configuration	Torque Arm (in.)	Centroidal Inertia (lb-in. ² × 10 ⁶)		
		I _x	I _y	I _z
Upside-Down	180	11.3	246.6	247.4
Normal	273	11.3	326.8	329.6

but not significantly unless very large weight increases are made. Mass data were generated for both the truss bench and tube bench concepts. Tube-mounted mirrors provide a lower-weight configuration. Originally, a weight of 3000 pounds was estimated for the truss bench but this was later reduced to 2000 pounds. Along with the weight of the bench, an additional 1200 pounds were required for mounting the bench, resulting in a total structural weight of 4200 pounds. The basic structure for the tube-mounted mirrors is about 1700 pounds, with the tubes and other supports weighing approximately 1600 pounds, resulting in a total structure weight of 3300 pounds. The resulting mass data are given in Table C-4. (The data in this table cannot be compared with that in Table C-3 because the configurations were different.) These data indicate that there is not a significant difference between the inertias or torque arms for the truss bench and those for the tube bench.

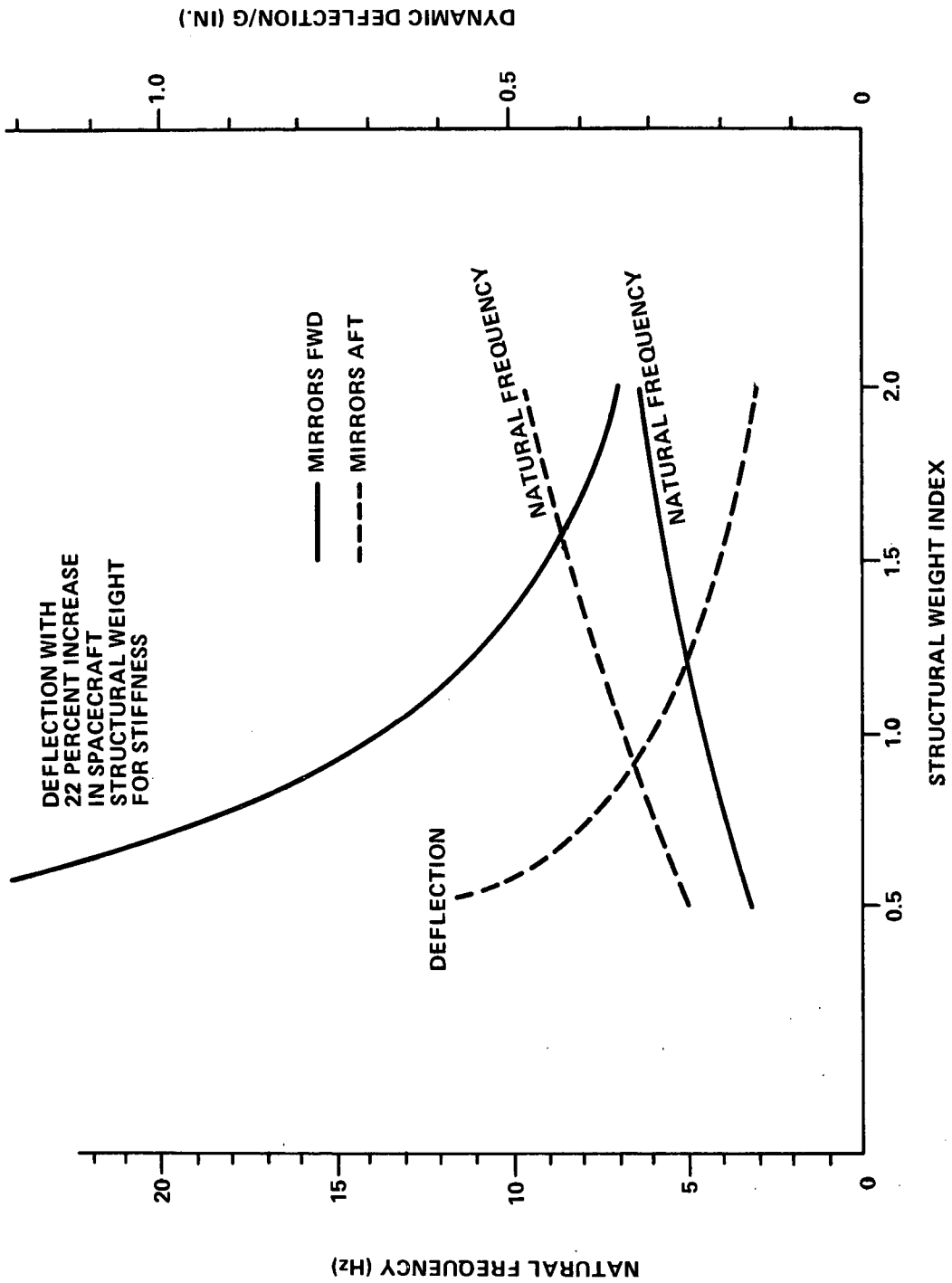


Figure C-20. Outer structure deflection (360 inch length).

TABLE C-4. TRUSS BENCH AND TUBE BENCH CONFIGURATIONS
MASS DATA

Configuration ^a	Torque Arm (in.)	Centroidal Inertia (lb-in. ² × 10 ⁶)		
		I _x	I _y	I _z
Tube Bench	229	11.1	179.8	180.4
Truss Bench	219	11.5	174.4	174.5

a. No OAS; RCS thruster on aft end of spacecraft.

Configurations with and without an equipment module and with and without an OAS were analyzed, making four possible combinations of these features. A weight tabulation is given in Table C-5 and the mass data are summarized in Table C-6. In general, HEAO-C has a very unbalanced inertia distribution, and this is aggravated by utilization of the subsystems module.

TABLE C-5. WEIGHTS TABLE
FOR HEAO VARIATIONS

Component	Weight (lb)
Subsystems	3764
Structure	
Spacecraft	2330
Equipment Module	250
Experiments	8153
OAS and Adapter	2647

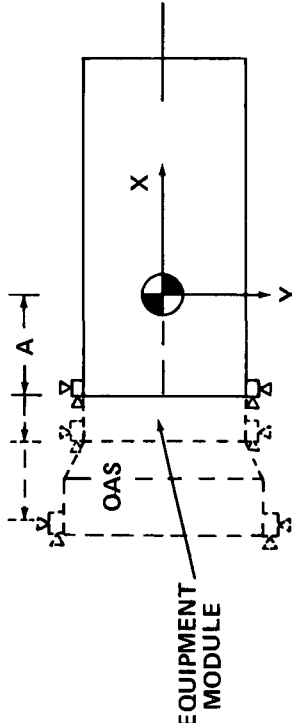
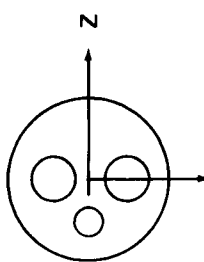
Alternate Bench Mounting Concepts

The baseline bench mounting concept, which utilizes ball joints, shock mounts, and linkages (B/S/L), is described in Chapter IV. Two alternate concepts (the shock/link concept and the hard mount concept) were investigated and compared with the baseline scheme. These concepts are depicted diagrammatically in Figure C-21. Discussion of the concepts and data from analyses are provided in succeeding paragraphs.

1. Shock/Link (S/L) Concept. In this scheme, the ball joints are eliminated. Two cases of this concept were analyzed: (1) linkages retained in orbit and (2) linkages disconnected in orbit. In the first case, the shock mounts serve as flexure joints about which the optical bench pivots, similar to

TABLE C-6. MASS DATA FOR EQUIPMENT MODULE AND OAS VARIATIONS

	Weight (lb)	Torque Arm (in.) ^a	Centroidal Inertia (lb-in. ² × 10 ⁶)		
			I _x	I _y	I _z
With Equipment Module	OAS Attached	174	11.2	429.5	432.3
	OAS Detached	206	9.2	319.4	322.2
Without Equipment Module	OAS Attached	175	11.22	276.6	279.4
	OAS Detached	209	9.2	164.5	167.3

The diagram on the left shows a rectangular 'EQUIPMENT MODULE' with a central circular feature. A coordinate system (X, Y) is centered on the module. The OAS (Orbit Attitude Sensor) is located at a distance 'A' from the center along the X-axis. Thrusters are shown at the corners of the module. The diagram on the right shows a circular cross-section with three smaller circles inside, representing the mass distribution for calculating centroidal inertia. A Z-axis is shown passing through the center of mass.

a. Center of gravity sometimes shifts further than the thruster location shifts.

● ANALYSIS OF MOUNTING CONFIGURATIONS:

- (1) BALL/SHOCK/LINK
- (2) SHOCK/LINK (WITH AND WITHOUT LINK IN ORBIT)
- (3) HARD MOUNT (SAME AS (2) EXCEPT WITHOUT SHOCKS) *

● CONFIGURATIONS:

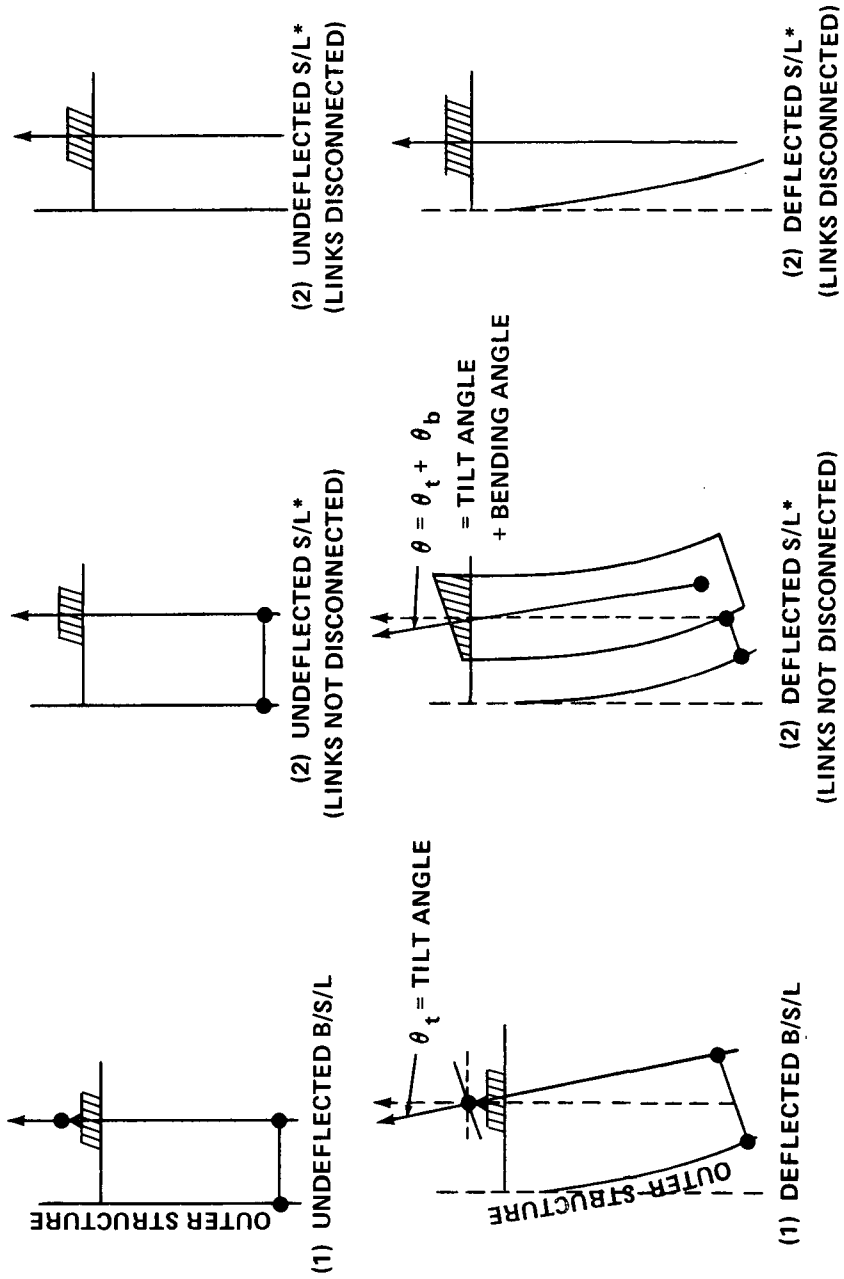


Figure C-21. Bench mounting configurations.

the ball joint concept. In the second case, the approach becomes more similar to the hard mount concept, except that the natural frequency of the bench in its mount is lower, due to the flexibility of the mount. Data derived from an analysis of this scheme presented in Chapter V are shown in Figure C-22. The following conclusions can be drawn from this figure:

a. For the shock material used, the ratio of tube bending angle to total angle (tube bending angle plus tube tilt angle) is fairly small (varies from approximately 6:1 to 12:1 depending on tube thickness). This implies that the concept is feasible, particularly with small ΔT across the outer structure, but it is still not as good as the B/S/L scheme which has zero tube bending, even if the thermal control system failed completely.

b. A reference line representing a 1 to 1 ratio of bending angle to total angle is shown in Figure C-22 to represent deflection angles of the hard mount scheme with linkages (assuming they failed to disconnect in orbit). Thus it can be seen that failure to disconnect linkages causes considerably more bending in the hard mount scheme than in the S/L scheme.

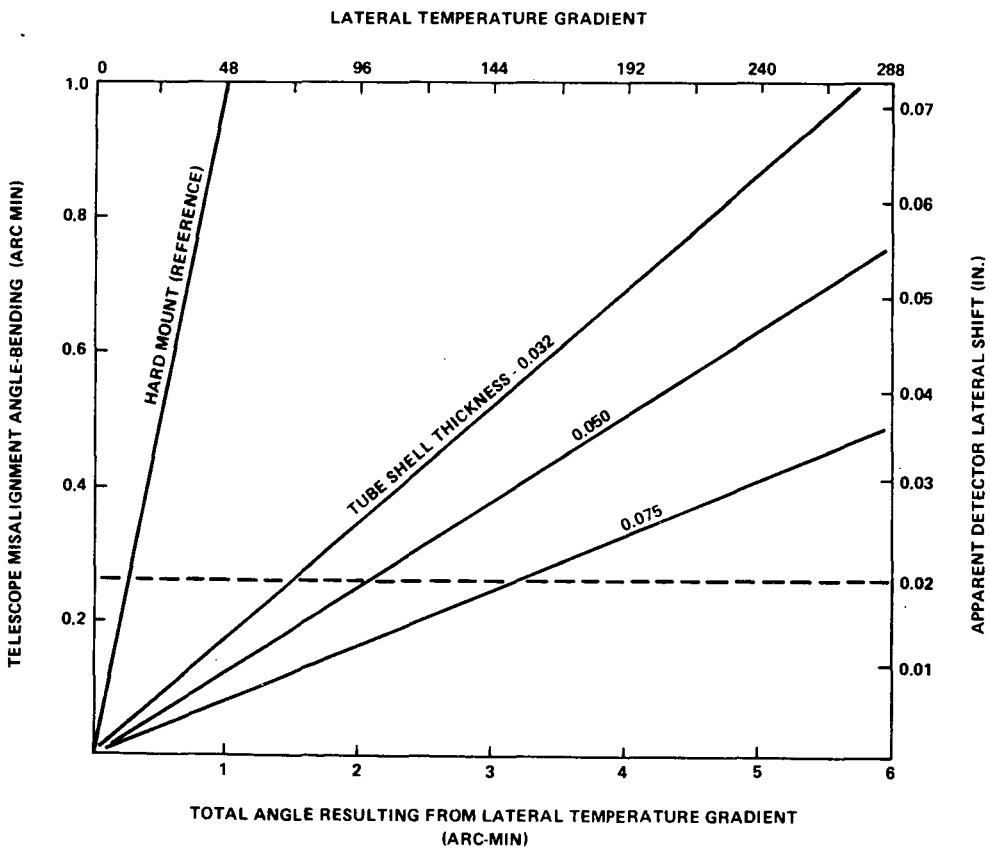


Figure C-22. Shock mounts and linkages mounting scheme (linkages retained in orbit).

c. It is feasible to increase the tube thickness to help relieve the bending problem.

d. If 0.02 inch lateral deflection is allowable due to thermal gradients, the temperature across the outer structure can be as high as approximately 100° F with a 0.050 inch thick tube; with a 0.075 inch thick tube, it can be approximately 156° F.

The natural frequency of a bench with shock mounts, with linkages to the outer structure disconnected in orbit, was not computed but will be lower than the hard-mount scheme (6.23 Hz). The natural frequency could be so low that coupling with the attitude control system would result.

From the thermal control standpoint, the shock mounts provide good thermal isolation of the bench from the crowfoot beam assembly, which is desirable. Retention of the linkages in orbit causes some heat leak, but this can be minimized by using attachment hardware with good thermal isolation properties. (Note: Since linkages are required for launch loads for all configurations, there is no way to eliminate attach points and whatever associated thermal radiation they cause, even though the conduction can be eliminated by disconnecting linkages.) From these considerations, it appears that the S/L scheme for the case with linkages retained in orbit is feasible, but not as desirable as the B/S/L scheme (see Chapter IV for B/S/L advantages); the S/L scheme with linkages dropped is probably not feasible.

2. Hard Mount Scheme. In this scheme, the telescopes and other experiments are hard-mounted to the supporting beam assembly with no shock mounts or ball joints utilized. The absence of shock mount material or other thermally-insulating material at the mounting interface would cause greater thermal coupling of the experiments to the spacecraft outer structure, which is undesirable. Aft linkages are required on the telescopes for launch, and must be disconnected in orbit to prevent bending of the tubes. The natural frequency of the hard-mount bench with linkages disconnected computed to be 6.23 Hz. The estimated bench response to input disturbances equivalent to the greatest expected attitude maneuver rates was low enough to prevent the aft ends of the telescopes from hitting the sides of the spacecraft with the linkages dropped.

A gross analysis of the effects of joint slippages (due to handling, shipping, launch environment, thermal distortions, etc.) on the hard mount and B/S/L schemes was made. A diagrammatic representation of the major joints considered in each mounting scheme is shown in Figure C-23. (The S/L configuration would tend to behave somewhat like either of the other two, depending

I. WORST-CASE ANALYSIS USING 0.0005 in. SHIFT PER JOINT

A. BALL JOINTS/LINKS CASE

ASSUME: MISC. DIA. = 10 in.
LA AND HR DIA. = 45 in.
LE DIA. = 24 in.
LA AND HR BALL-TO-LINK = 250 in.
LE BALL-TO-LINK = 75 in.

1. TILT OF TELESCOPES WITH RESPECT TO MISC. EXPERIMENTS, STAR TRACKERS, ETC.:

ASSUME MISC. TILTS TO LEFT BY

$$\Theta_M = \frac{0.001}{10} (57.3) 3600 = 20.6 \text{ arc sec}$$

ASSUME HR TILTS TO RIGHT DUE TO REAR END MOVEMENT TO LEFT AND FRONT END MOVEMENT TO RIGHT:

$$\begin{aligned}\Theta_{HR} &= 1R, 2R, 3R, 4L, 5L, 6L, 7L, 8R \\ &= \frac{8(0.0005)}{250} (57.3)(3600) = 2.05 \text{ arc sec}\end{aligned}$$

ASSUME LE TILTS TO RIGHT BY

$$\begin{aligned}\Theta_{LE} &= (9R, 10R, 11L, 12L) + \Theta_{HR} \\ &= \frac{4(0.0005)}{75} (57.3)(3600) + 2.05 = 5.5 + 2.05 = 7.55 \text{ arc sec}\end{aligned}$$

HENCE WORST-CASE MISALIGNMENT OF MISC.-TO-TELESCOPE IS

$$\Theta_M + \Theta_{LE} = 28.15 \text{ arc sec} = \Theta_{TM}$$

2. TILT OF TELESCOPES WITH RESPECT TO EACH OTHER:

$$\Theta_{LA} = 1L = \frac{0.005}{250} (57.3)(3600) = 0.26 \text{ arc sec TO LEFT}$$

$$\Theta_{HR} = 6L, 7L, 2R, 8R = \frac{4(0.0005)}{250} (57.3)(3600) = 1.04 \text{ arc sec TO RIGHT}$$

$$\Theta_{LE} = 11L, 12L, 10R, 9R + \Theta_{HR} = 5.5 + 1.04 = 6.54 \text{ arc sec TO RIGHT}$$

Figure C-24. Joint shift analysis.

HENCE WORST-CASE MISALIGNMENT TELESCOPE-TO-TELESCOPE IS

$$\Theta_{LA} + \Theta_{LE} = 6.80 \text{ arc sec} = \Theta_{TT}$$

3. TILT OF MISC. WITH RESPECT TO MISC.:

$$\Theta_{MM} = 2\Theta_M = 41.2 \text{ arc sec}$$

B. HARD-MOUNT CASE (LINK TO OUTER STRUCTURE DROPPED IN ORBIT)

1. TILT OF TELESCOPE WITH RESPECT TO MISC. EXPERIMENT, STAR TRACKERS, ETC.:

$$\Theta_{LE} = \frac{0.001}{24} (57.3)(3600) = 8.57 \text{ arc sec}$$

ASSUME MISC. TILTS TO LEFT, TELESCOPE TO RIGHT:

$$\Theta_{LE} + \Theta_M = 8.57 + 20.6 = 29.17 \text{ arc sec} = \Theta_{TM}$$

2. TILT OF TELESCOPES WITH RESPECT TO EACH OTHER:

$$\Theta_{HR} \text{ MAX TILT (SAME AS BALL JOINT/LINK CASE)} = 2.05 \text{ arc sec}$$

$$\Theta_{LE} + \Theta_{HR} = 8.57 + 2.05 = 10.62 \text{ arc sec} = \Theta_{TT}$$

3. TILT OF MISC. WITH RESPECT TO MISC.:

$$\Theta_{MM} = 2\Theta_M = 41.2 \text{ arc sec}$$

II. RSS ANALYSIS (0.0005 SHIFTS)

A. BALL JOINTS/LINKS

$$\begin{aligned} 1. \quad \Theta_{TM} &= \sqrt{(20.6)^2 + 8(0.26)^2 + 4(0.51)^2} = \sqrt{424.36 + 0.54 + 1.04} \\ &= \sqrt{425.94} = 20.7 \text{ arc sec} \end{aligned}$$

$$\begin{aligned} 2. \quad \Theta_{TT} &= \sqrt{(0.26)^2 + 4(0.26)^2 + 4(1.4)^2} = \sqrt{0.0676 + 0.27 + 7.84} \\ &= \sqrt{8.18} = 2.86 \text{ arc sec} \end{aligned}$$

Figure C-24. (Continued).

$$3. \quad \Theta_{MM} = \sqrt{(20.6)^2 + (20.6)^2} = \sqrt{424.36 + 424.36}$$

$$= \sqrt{848.72} = 29.1 \text{ arc sec}$$

B. HARD-MOUNT

$$1. \quad \Theta_{TM} = \sqrt{(20.6)^2 + (8.57)^2} = \sqrt{424.36 + 73.44}$$

$$= \sqrt{497.80} = 22.3 \text{ arc sec}$$

$$2. \quad \Theta_{TT} = \sqrt{(2.05)^2 + (8.57)^2} = \sqrt{4.20 + 73.44}$$

$$= \sqrt{77.6} = 8.8 \text{ arc sec}$$

$$3. \quad \Theta_{MM} = \sqrt{(20.6)^2 + (20.6)^2} = \sqrt{424.36 + 424.36}$$

$$= \sqrt{848.72} = 29.1 \text{ arc sec}$$

SHIFT PER JOINT	BALL AND LINK ^a						HARD-MOUNT ^a					
	WORST-CASE			RSS			WORST-CASE			RSS		
	Θ_{TM}	Θ_{TT}	Θ_{MM}	Θ_{TM}	Θ_{TT}	Θ_{MM}	Θ_{TM}	Θ_{TT}	Θ_{MM}	Θ_{TM}	Θ_{TT}	Θ_{MM}
0.0005 in.	28.15	6.80	41.2	20.7	2.86	29.1	29.17	10.62	41.2	22.3	8.8	29.1
0.001 in.	56.3	13.6	82.4	41.4	5.78	58.2	58.34	21.24	82.4	44.6	17.6	58.2

a. Θ is in arc sec.

Figure C-24. (Concluded).

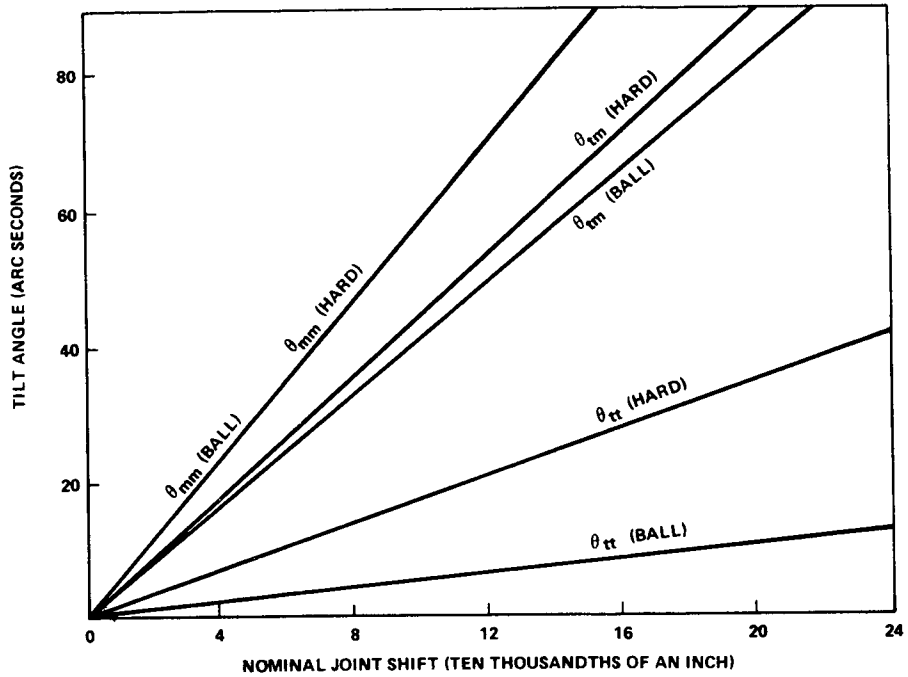


Figure C-25. Experiment misalignments after joint shifts (rss analysis) for hard-mount and ball-link configurations.

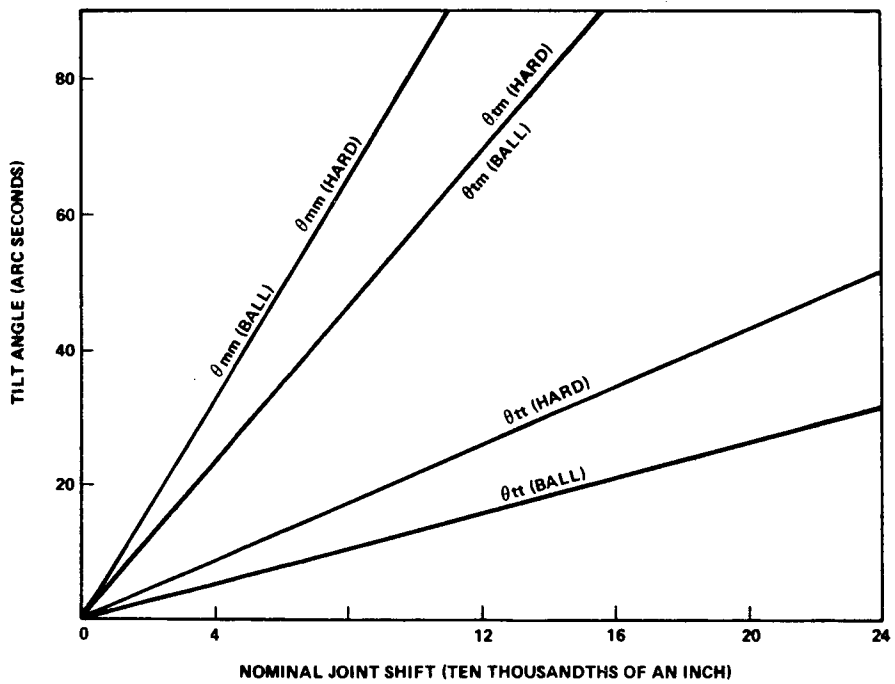


Figure C-26. Experiments misalignments after joint shifts (worst-case analysis) for hard-mount and ball-link configurations.

b. The coalignments between the telescopes and the miscellaneous equipment will be the next most difficult to maintain; the misalignments are fairly close for both mounting schemes.

c. The coalignments among telescopes will be the easiest to maintain; there is a clear superiority of the B/S/L configuration over the hard-mount configuration per this analysis.

Transport Mechanism Growth

The existing sizes and the maximum expansion limits of the transport mechanism envelopes for the HR and LA telescopes are shown in Figures C-27 and C-28. Figures C-29 and C-30 show how the envelopes would increase for "typical" addition of experiments in each telescope. The arrows indicate the directions in which the detectors would have to be moved to reach the focal point. These envelopes assume that a modification of the existing transport mechanism design would be made, with detector movement along the X, Y, and/or Z axes performed to achieve detector alignment.

Another approach would be the mounting of all the experiments on a turret arrangement which would then be mounted to a transport mechanism with traverse in the X and Z directions. This has the advantage of providing fine adjustment in the Y direction by using the turret.

A still different approach would be the use of small booms to swing the new experiments into the focal point after the present experiments have been moved. The booms could be attached to the present transport mechanism or to some other structure. Envelope sizes could possibly be improved by judiciously locating the booms.

In most of the foregoing approaches, the envelopes will not be symmetrical about the tube centerlines; by judiciously selecting the axes of movement of experiments and choosing the schemes which allow the transport mechanism envelopes of the two large tubes to best complement each other, any of these approaches could probably be made to work.

Further study of these approaches should be initiated when the quantity and sizes of experiments are better defined.

The main design drivers for determining the required traverse directions of the basic transport mechanisms are the capability to adjust out the worst-case expected tube deflections (normally in the Z direction, since worst-case gradients across the tube would normally be in that direction) and the

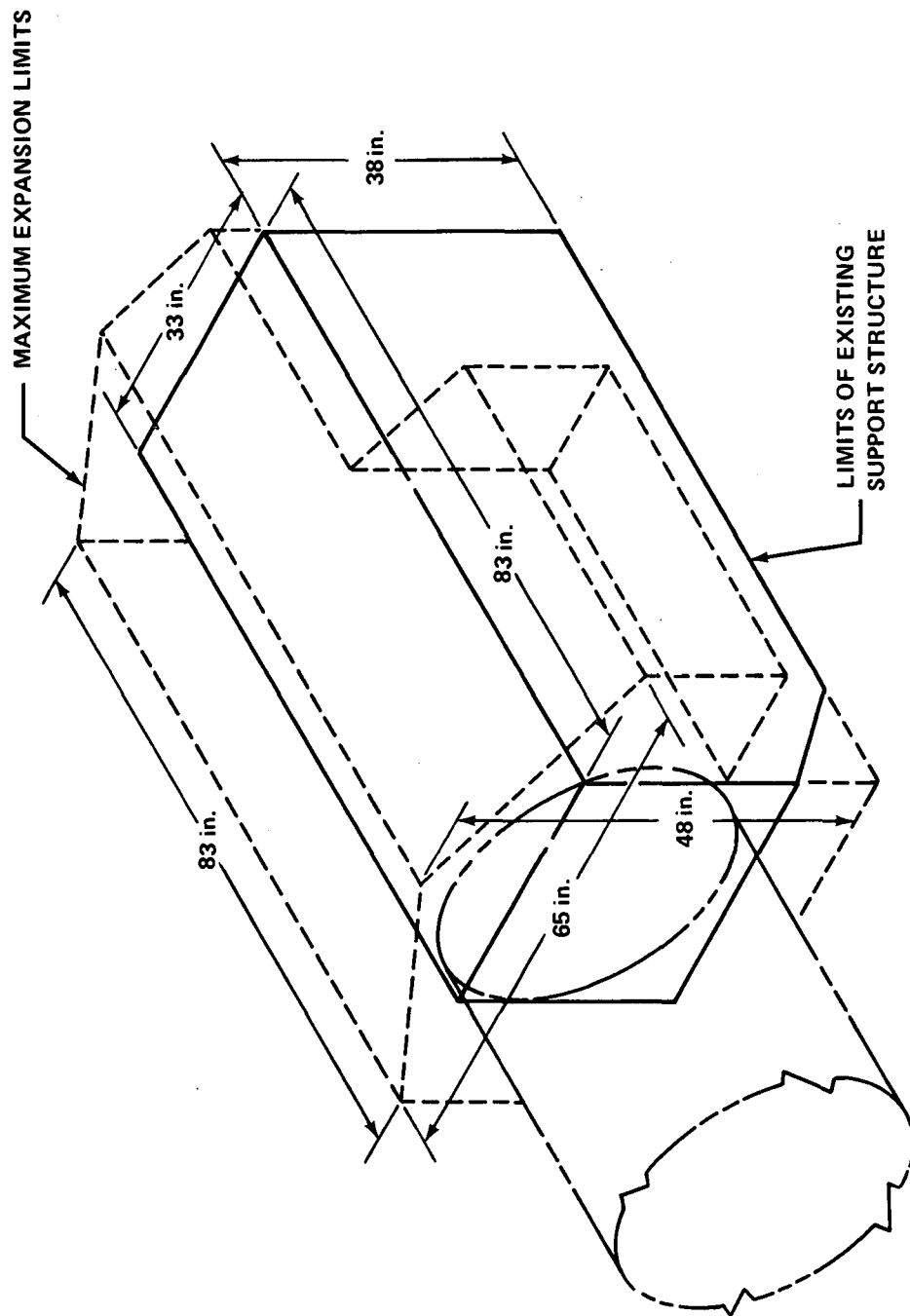


Figure C-27. HR telescope transport mechanism growth envelope.

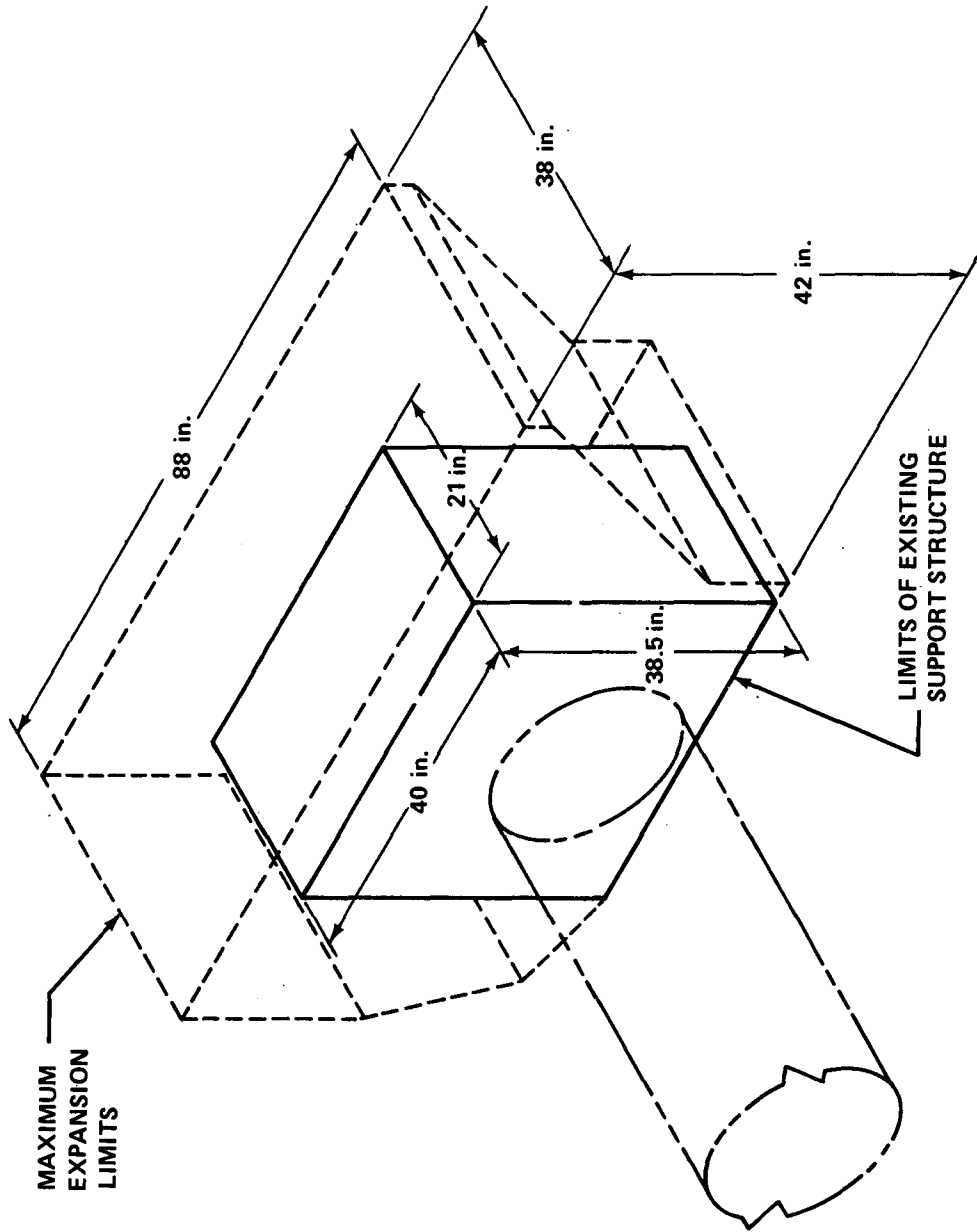


Figure C-28. LA telescope transport mechanism growth envelope.

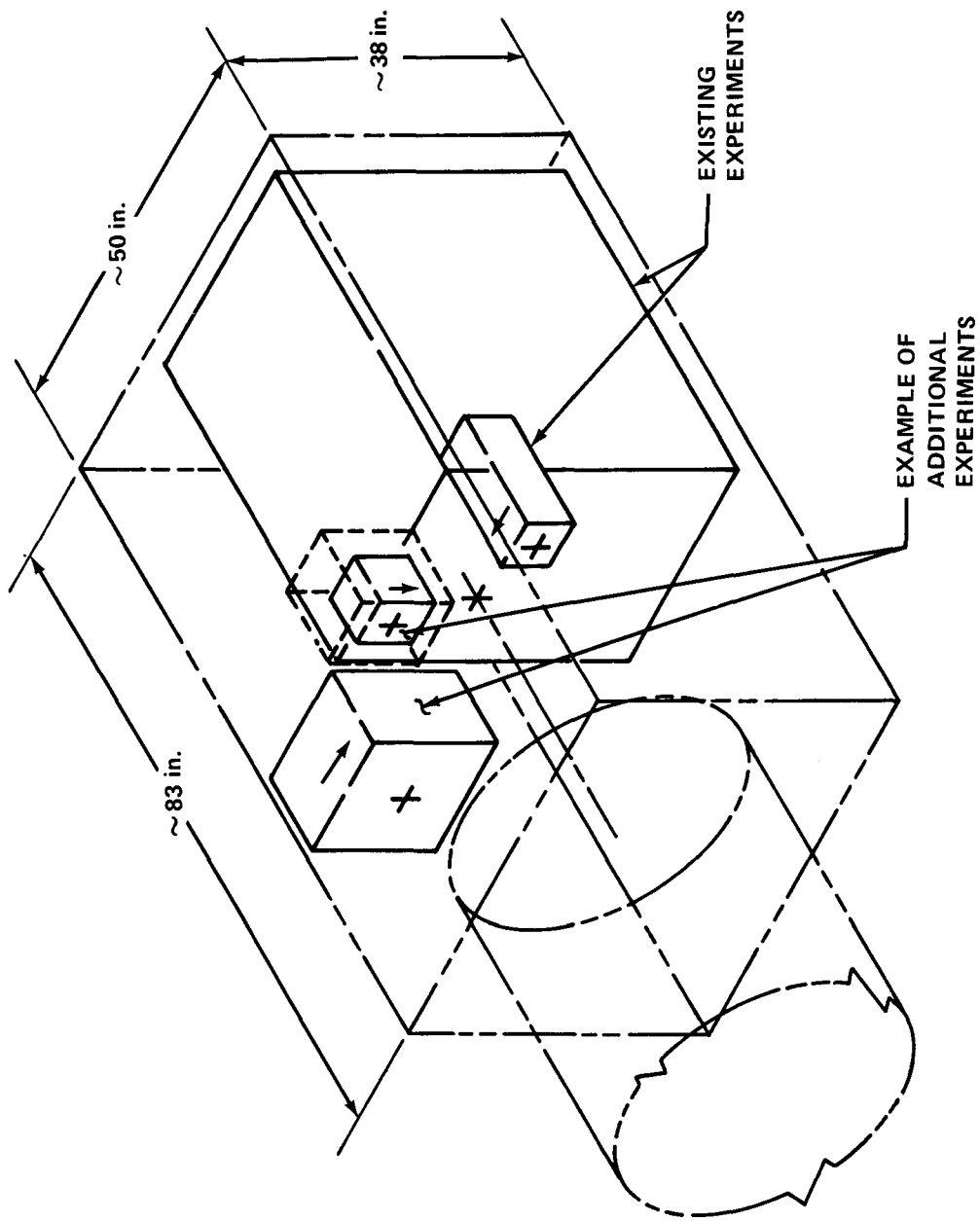


Figure C-29. HR telescope transport mechanism envelope for addition of two experiments.

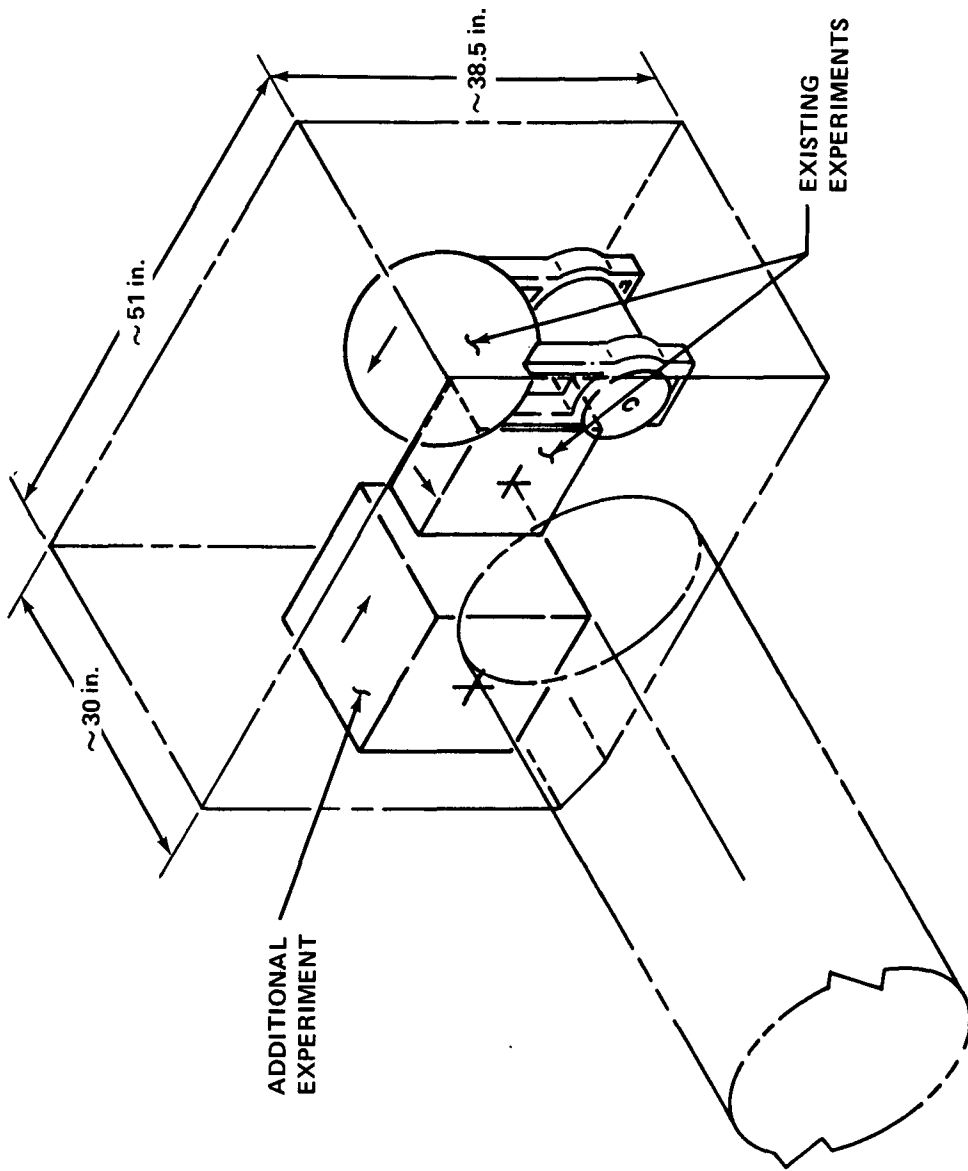


Figure C-30. LA telescope transport mechanism envelope for addition of one experiment.

capability to adjust out the tube and mirror expansion effects (shift of focal point in the X direction). If traverse capability is provided in two mutually-perpendicular transverse directions, then any transverse orientation of the mechanism is satisfactory.

To allow optimum packaging at the focal plane, one of the key design factors of the experiments is to make the sizes of the detectors as small as possible and to package them separately from any large complement of electronics, so that the detectors can be located as near each other as possible.

Focal Point Determination

If a suitable method of determining the detector position error could be found, preferably using equipment already provided in the Observatory design, the error signal could be used to "peak" the detectors at the focal plane, by ground command or automatically. Several concepts have been investigated for the HR telescope and a description of the one believed to be most promising is presented in this section. Brief comparisons of alternate measurement schemes which are believed to be less suitable are also given. More details are provided in Reference C-1.

1. Physical Requirements. Generally, the detector position sensor must fit in the high resolution telescope tube in such a way that it does not interfere optically, mechanically, or electronically with the operation of the telescope. In addition, it must be as compact as possible, use a minimum of power, be launch qualified, and have a two year lifetime under maximum-use conditions.

2. Performance Requirements. The depth of focus of the high resolution telescope is ± 0.004 inch and its focal length is 240 inches. Focal distance excursions are not expected to exceed 0.5 inch because of temperature variations and launch load distortions. The position sensor is required to measure the 240 inch focal distance to an accuracy of ± 0.002 inch (± 8 parts per million) over the 0.5 inch range, and it must provide an output error signal suitable for use in the closed loop focusing system. The error signal should preferably include any change in the focal length of the high resolution telescope mirrors, as well as length variations of the telescope tube.

3. Position Sensor Concepts Considered. The performance requirements are severe for both geometric and interferometric optical instruments. The resolution of ± 8 parts per million using geometrical optics is a difficult

goal. On the other hand, a range of 0.5 inch is a demanding task for an interferometer, representing over 25 000 wavelengths of visible light. Three of the four concepts investigated were applications of geometrical optics; the fourth concept was an application of interference techniques. For this reason, the most critical performance requirement was the resolution. In each case, the optics and the detecting system were defined and a parametric analysis was made to obtain an estimate of the resolution capability.

The aspect system concept was considered to be the most promising. This concept, which simply makes use of an already available error signal from the existing experiment aspect sensor, is described in considerably more detail than the others. The principal features of the aspect system concept are as follows:

- No modifications to the existing optics or additional optical components are required.
- Since the error signal is directly proportional to the change in the separation distance between the centroids of the fiducial light images, only minimal additional electronics are required.
- The error signal is linear over the entire range.
- The current aspect system accuracy is within an order of magnitude of satisfying the resolution requirement.
- Each fiducial light image pair will produce an error signal, making the system triply redundant.
- The error signal includes any change in the focal length of the telescope mirrors themselves.
- The error signal is independent of lateral errors in the positions of the detector packages.

Aspect System Concept. The experiment aspect sensing system, which is designed to provide pointing information on the X-ray telescopes, also can be used to measure the position of the focal point. The optical arrangement of the aspect system directs the light from three small fiducial lights (mounted on the experiment detector) in the detector plane out through the X-ray telescope mirrors and back into the aspect telescope, imaging them on the face of a SEC vidicon camera (Fig. C-31). Electronic processing results in an output of the precise location of the centroids of these three images, as described in Reference C-2.

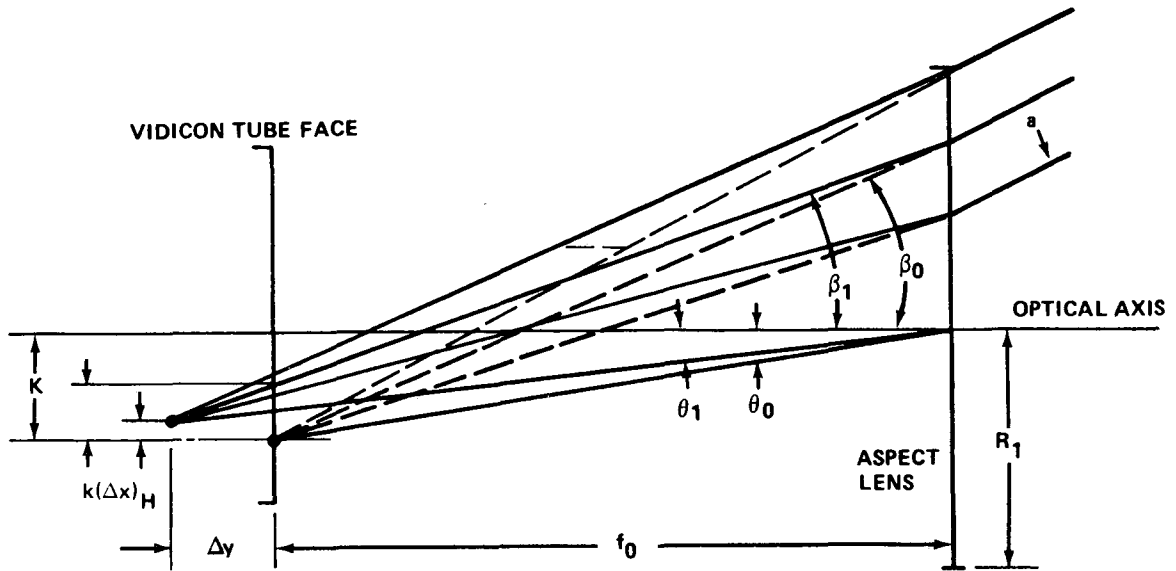


Figure C-31. Defocused conditions for one fiducial light.

If the fiducial light is displaced axially by a given amount, Δx , the change, Δy , in its image distance is given by

$$\Delta y = \left(\frac{f_0}{L} \right)^2 \Delta x$$

The centroid of the out-of-focus image on the vidicon tube will also undergo a lateral displacement, $k(\Delta x)$. Referring to Figure C-31, this is found to be

$$k(\Delta x) = \frac{f_0}{L} \left[\frac{\frac{f_0}{L} (\tan \beta_1 - \tan \theta_0) + \tan \theta_0 + \frac{f_0}{L} \tan \beta_1 \frac{\Delta x}{L}}{1 + \frac{\Delta x}{L}} \right] \Delta x$$

Likewise, similar equations apply to the second and third images, $k'(\Delta x)$ and $k''(\Delta x)$. All of the terms in these equations possess rotational symmetry around the optical axes, so these equations are correct for the second and third fiducial lights and their images that are not in the plane of the paper indicated in Figure C-31.

Since these expressions represent the displacements of the end-points of the separation lengths between the centroids' positions, the changes in the separation between each of the three possible pairs of images are given by

$$\Delta_1 = (k - k') a_1$$

$$\Delta_2 = (k - k'') a_2$$

$$\Delta_3 = (k' - k'') a_3$$

where, for the case in which the images define a centered equilateral triangle (Fig. C-32), the quantities a_1 , a_2 , and a_3 (the fiducial light parameters for each set of lights) are given as

$$a_1 = a_2 = a_3 = \frac{4}{\sqrt{3}}$$

Thus, for this example, Δ_1 is given by

$$\Delta_1 = \frac{4}{\sqrt{3}} \frac{f_0}{L} \left[\left(\frac{1 - \frac{f_0}{L}}{1 + \frac{\Delta x}{L}} \right) [\tan \theta_0 - \tan \theta_0'] - \frac{a}{2L} \left(\frac{\sec \theta_1 - \sec \theta_1'}{1 + \frac{f_0}{L} \cdot \frac{\Delta x}{L}} \right) \right]$$

This equation is plotted in Figure C-33. Assuming a fiducial light blur circle which subtends a 10 arc second angle when in focus, the blur circle radius r_0 is 0.97×10^{-3} inch. Expressing Δ_1 as a percentage of r_0 gives a value of 0.70 percent at $\Delta x = 0.002$ inch. For comparison, two other measurable quantities which vary with Δx (i. e., the relative change in the intensity ΔI of the enlarged defocused light spot and its diameter ρ relative to r_0) are given in Table C-7.

TABLE C-7. COMPARISON OF CANDIDATE MEASURABLE QUANTITIES

Axial Displacement (in.)	Relative Centroid Separation Change (%)	Relative Intensity Change (%)	Relative Diameter Change (%)
Δx	Δ_1 / r_0	$\frac{\Delta I}{I_0} \left[\left(1 + \frac{af_0}{2L^2} \cdot \frac{ \Delta x }{r_0} \right)^{-2} - 1 \right]$	$\frac{\Delta \rho}{r_0} = \frac{af_0}{2L^2} \cdot \frac{ \Delta x }{r_0}$
± 0.002	± 0.70	-0.07	+0.036
0.5	179.00	-15.9	+9.0

NOTES: a = 0.5 in.

$f_0 = 40$ in.

L = 240 in.

$R_1 = 3.57$ in.

$\theta_1 \approx \theta_0 = 0.75$ deg

The large relative change in $k(\Delta x)$ makes it the best parameter to be measured. Since it is the change in location of the centroid of the image spot, all of the electronics for detecting it are already a part of the system. Noting that the aspect system centroid locating circuit can determine the center of a blur circle to within one-tenth its diameter [C-2, p. 3-128], one can see that the existing aspect system already is supplying information on the axial displacements down to 0.057 inch. This is according to the value of 0.194×10^{-3} inch for Δ_1 , shown in Figure C-34, being equal to one-tenth of twice the radius r_0 .

If a timing clock is used which can provide an order of magnitude better counting resolution, this figure becomes 0.0057 inch, which is within the depth of focus (± 0.004 inch) of the X-ray telescope.

Improved accuracy can also be obtained by mounting the fiducial lights as far off-axis as possible, thereby increasing the value of θ_0 .

In conclusion, the aspect system provides a ready-built system which can provide an error signal output for axial displacements of 0.057 inch without modification or addition of any other components. The error signal includes any change in the focal length of the X-ray mirrors as well as any change in the focal distance of the system. Improved timing circuits, the feasibility of which are noted in Reference C-1, can increase the resolution to displacements of 0.0057 inch, as compared to the telescope depth of focus of ± 0.004 inch. However, to meet the resolution requirement of ± 0.002 inch would require a further improvement by about a factor of two. It is felt that this could be done by a more detailed study of the system parameters, since no fundamental objections to further optimization have been found in the scope of this work.

4. Conclusions and Recommendations. Of the four concepts defined, only one was found to have a serious fault which could not be at least conceptually eliminated. This concept, utilizing a translating mirror, was found to have a mirror tilt angle tolerance of about ± 0.013 arc seconds. Of the three remaining systems, the aspect system concept has several clear advantages over the defocusing concept and the grating interferometer concept. Table C-8 summarizes the characteristics and performance of the four systems.

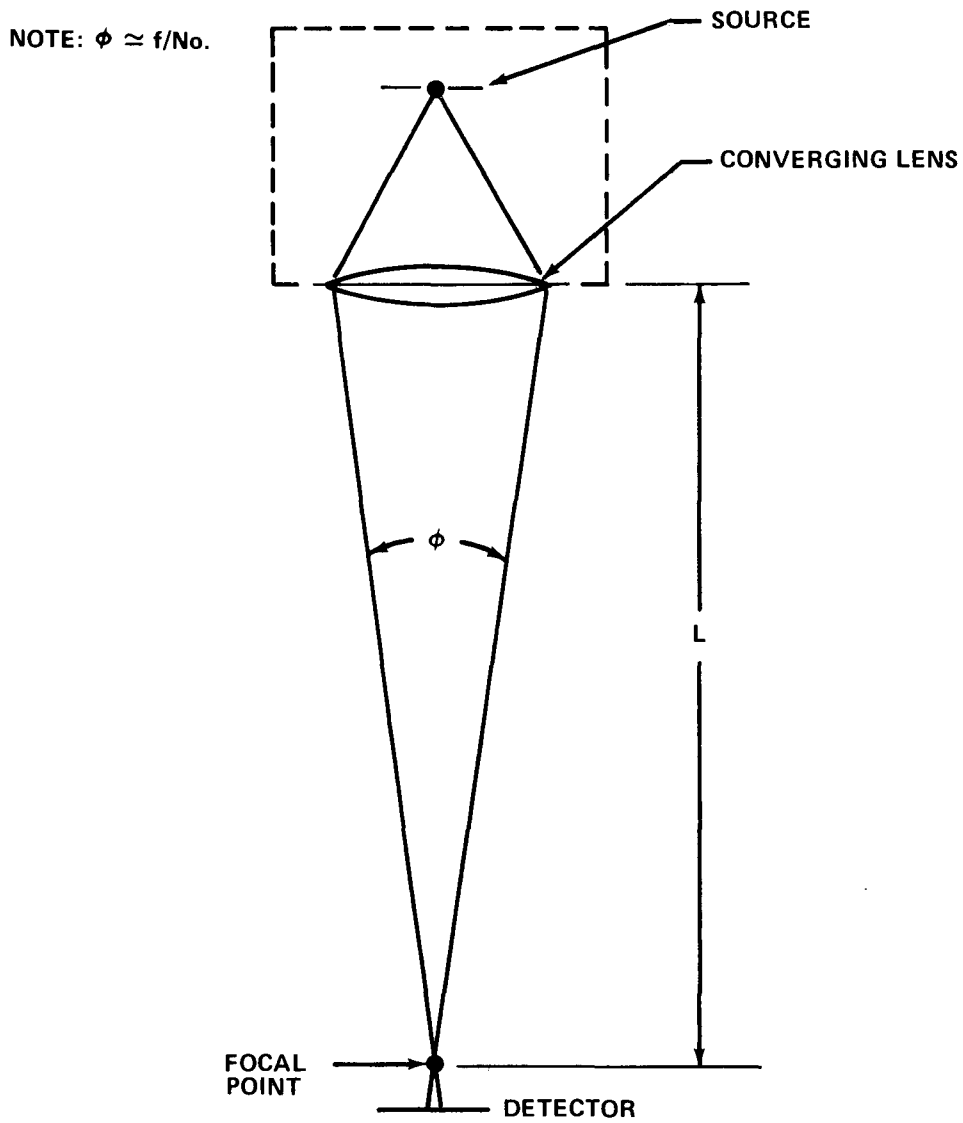


Figure C-34. Defocusing concept.

TABLE C-8. PERFORMANCE SUMMARY OF POSITION SENSOR CONCEPTS

	Aspect System	Defocusing System	Translating Mirror	Grating Interferometer
Quantity Detected	<ul style="list-style-type: none"> Centroid separation Δ_1 	<ul style="list-style-type: none"> Intensity, I Spot diameter, ρ 	<ul style="list-style-type: none"> Area of spot image on the detector 	<ul style="list-style-type: none"> Fringe spacing, s
Additional Components Required	<ul style="list-style-type: none"> Minor electronics to process existing error signal 	<ul style="list-style-type: none"> Point source Converging lens Vidicon camera Frame processing electronics similar to aspect system 	<ul style="list-style-type: none"> Collimated source Mirror Angled detector Signal processing electronics 	<ul style="list-style-type: none"> Monochromatic source Lens system Grating Vidicon camera Frame processing electronics Scan analysis electronics Signal processing electronics
Resolution of Quantity Detected	Δ_1/r_0 percent $(r_0 = 0.97 \times 10^{-3} \text{ inch})$	$\Delta I/I_0$ and $\Delta\rho/r_1$ percent $(r_1 = 2.88 \times 10^{-3} \text{ inch})$	$\Delta A/A_0$ percent $(A_0 = 0.12 \text{ inch}^2)$	$\Delta s/s_0$ percent $(s_0 = 3.07 \times 10^{-3} \text{ inch})$
Minimum $\Delta x = \pm 0.002$ inch	± 0.70 percent	-1.15 and 0.58 percent	± 0.2 percent	± 0.011 percent
Maximum $\Delta x = +0.5$ inch	+179 percent	-83.2 and +144 percent	+100 percent	-2.7 percent
Comments	<ul style="list-style-type: none"> All major components are currently incorporated in LOXT Conceptually feasible 	<ul style="list-style-type: none"> Intensity gives non-linear error signal Diameter gives linear error signal Conceptually feasible 	<ul style="list-style-type: none"> Severe mirror angle tolerance of ± 0.013 arc second Conceptually unfeasible 	<ul style="list-style-type: none"> Parametrically complex system Calculations unoptimized Feasibility not determined

It is recommended that the following effort be accomplished on the indicated concepts:

- Aspect System Concept
 - A parametric optimization should be performed to determine the best placement of the fiducial lights, the correct intensity, and effects due to changes in the focal length of the aspect system telescope.
 - The electronics necessary to process the centroid location information and generate an appropriate error signal should be defined.
 - The timing circuit modifications should be specified and their practicality determined.
- Defocusing System
 - A feasibility analysis should be made which includes intensity stability requirements, signal-to-noise ratio, aperture constraints, and centroid point location errors.
 - All electronics and logic requirements should be determined so that the required circuits and components can be specified.
- Translating Mirror Concept
 - Modifications to the concept which could produce tilt angle rotational invariance should be investigated.
 - Further work on the configuration of the detector or detector array, as well as the shape of the light spot, should be done to improve the signal-to-noise requirement.
- Grating Interferometer
 - Further work should be done to clarify the capabilities of this concept.

REFERENCES

- C-1. Teledyne Brown Engineering Company: HEAO-C Experiments and Transport Mechanisms Interim Report. SE-PD-1310, Huntsville, Alabama, March 1971.
- C-2. Giacconi, R., et al.: Large Orbiting X-Ray Telescope for the HEAO. 2410-I, American Science and Engineering, Cambridge, Massachusetts, May 27, 1970.

TABLE OF CONTENTS

	Page
Candidate Optical Bench (Tube) Material Comparison	D- 1
1. Thermal Expansion Comparison	D- 3
2. Weight Comparison	D- 5
3. Thermal Conductivity Comparison	D- 7
4. Cost Comparison	D- 7
5. Overall Comparison	D- 8
6. Conclusions	D-10
7. Discussion	D-12
Sunshade Feasibility Analysis	D-14
Alternate Solar Array Configurations	D-21
1. Proposed Thermal Control Schemes	D-22
2. Rotation of Center Solar Panel Off Solar Vector	D-22
3. Removal of Insulation Behind Solar Panels	D-26
4. Folding Out of Side Solar Panels	D-28
5. Reduced Solar Cell Packing Density on Center Panel	D-31
6. Reflective Strip on Center Solar Panel	D-35
7. Summary of Solar Panel Thermal Control Analyses	D-37
Employment of Louvers, Heat Pipes, and a Thermal Capacitor	D-41
1. Louvers	D-41
2. Incorporation of Circumferential Heat Pipes into Spacecraft Skin	D-45
3. Thermal Capacitor	D-51
Investigation of Operating Temperature Limits for HEAO-C Solar Panels.	D-54
Subsystem Module Thermal Control Feasibility Analysis	D-55

LIST OF ILLUSTRATIONS

Figure	Title	Page
D-1.	HEAO-C optical bench (truss)	D-2
D-2.	Allowable mean temperature change versus focal length for three candidate tube materials	D-13
D-3.	Thermal control scheme proposed for truss bench concept	D-15
D-4.	Effect of sunshade on longitudinal temperature distribution of truss optical bench	D-16
D-5.	Alternate (truss bench) thermal control concept	D-18
D-6.	Transient response of optical bench and telescope mirrors of off-perpendicular orientations	D-20
D-7.	Alternate observatory concept with body-mounted solar panels	D-23
D-8.	Solar panel and spacecraft temperatures for body- mounted configuration	D-24
D-9.	Body-mounted solar panel temperature histories with center panel oriented 22.5 degrees off sun line	D-25
D-10.	Body-mounted solar panel temperature history with insulation removed from backsides	D-27
D-11.	Alternate foldout solar panel concept	D-29
D-12.	Alternate foldout solar panel temperature history	D-30
D-13.	Solar panel temperature control by reducing solar cell packing density on center panel	D-32

LIST OF ILLUSTRATIONS (Concluded)

Figure	Title	Page
D-14.	Body-mounted solar panel temperature history with reduced solar cell packing density	D-34
D-15.	Solar panel temperature control by adding reflective strip	D-36
D-16.	Body-mounted solar panel temperature history with reflective strip on center panel	D-38
D-17.	Early Phase A thermal control concept	D-40
D-18.	Maximum body-mounted solar panel temperature as a function of solar cell packing density	D-42
D-19.	Schematic of louver thermal control concept	D-42
D-20.	Effect of variation in emissivity on center solar panel temperature	D-44
D-21.	Heat pipe scheme for solar panel thermal control	D-46
D-22.	Effect of heat pipe spacing on solar panel temperature	D-47
D-23.	Solar panel orbital average circumferential temperature distribution with heat pipe spacing as a parameter	D-49
D-24.	Solar panel maximum circumferential temperature distribution with heat pipe spacing as a parameter	D-50
D-25.	Solar panel temperature history with 90 pounds of a phase change material behind center solar panel	D-53
D-26.	Arrangement of subsystems within equipment module	D-56

LIST OF TABLES

Table	Title	Page
D-1.	Thermal Expansion Comparison	D-4
D-2.	Material Properties	D-5
D-3.	Weight Comparison	D-6
D-4.	Thermal Conductivity Comparison	D-7
D-5.	Cost Comparison	D-8
D-6.	Overall Comparison	D-9
D-7.	Final Performance Indices	D-11
D-8.	Summary of Solar Panel Thermal Control Scheme Evaluation	D-39
D-9.	Summary of Subsystems Equipment Module Thermal Analysis	D-59

APPENDIX D. THERMAL CONTROL TRADE STUDIES AND SUPPORTING ANALYSES

Candidate Optical Bench (Tube) Material Comparison

To maintain the focal length of the High Resolution (HR) telescope within acceptable bounds and to aid in the thermal control of the two X-Ray telescope systems, the HEAO-C telescopes are to be attached to an optical bench. The optical bench proposed by American Science and Engineering (AS&E) is represented in Figure D-1. Although this truss bench configuration was assumed for this analysis, the methods and results are seen as being applicable to the tubular bench concept also. The truss or tubular structure would, ideally, be fabricated from a material that is rigid, inexpensive, easily formed, and possesses high thermal conductivity and low thermal expansion characteristics. American Science and Engineering has proposed the use of Invar as an optical bench material, primarily because it has a low coefficient of linear thermal expansion. The thermal expansion characteristics of the material chosen for the optical bench are, undoubtedly, highly significant; however, other parameters should also be considered.

The purpose of this study was to determine the relative advantages of a number of materials for use in the optical bench. Beryllium, titanium, Invar, aluminum, boron/epoxy, and graphite/epoxy are compared considering weight (density and stiffness), thermal conductivity, thermal expansion, and cost (material cost and ease of fabrication). The results include a rating of the relative attractiveness of the six materials for use in the optical bench.

The following definitions apply to this section:

- Rating Parameter — A physical or mechanical property or characteristic of a material used as a basis for comparison. There are four rating parameters in this study.
- Rating Factor — A dimensionless number, less than or equal to 1.0, obtained from a ratio of rating parameter values. The rating factors indicate the relative attractiveness of the materials in a particular rating parameter category.
- Weight Operator — A dimensionless number, greater than or equal to 1.0, assigned to each rating parameter. This number indicates the relative importance of the rating parameters.

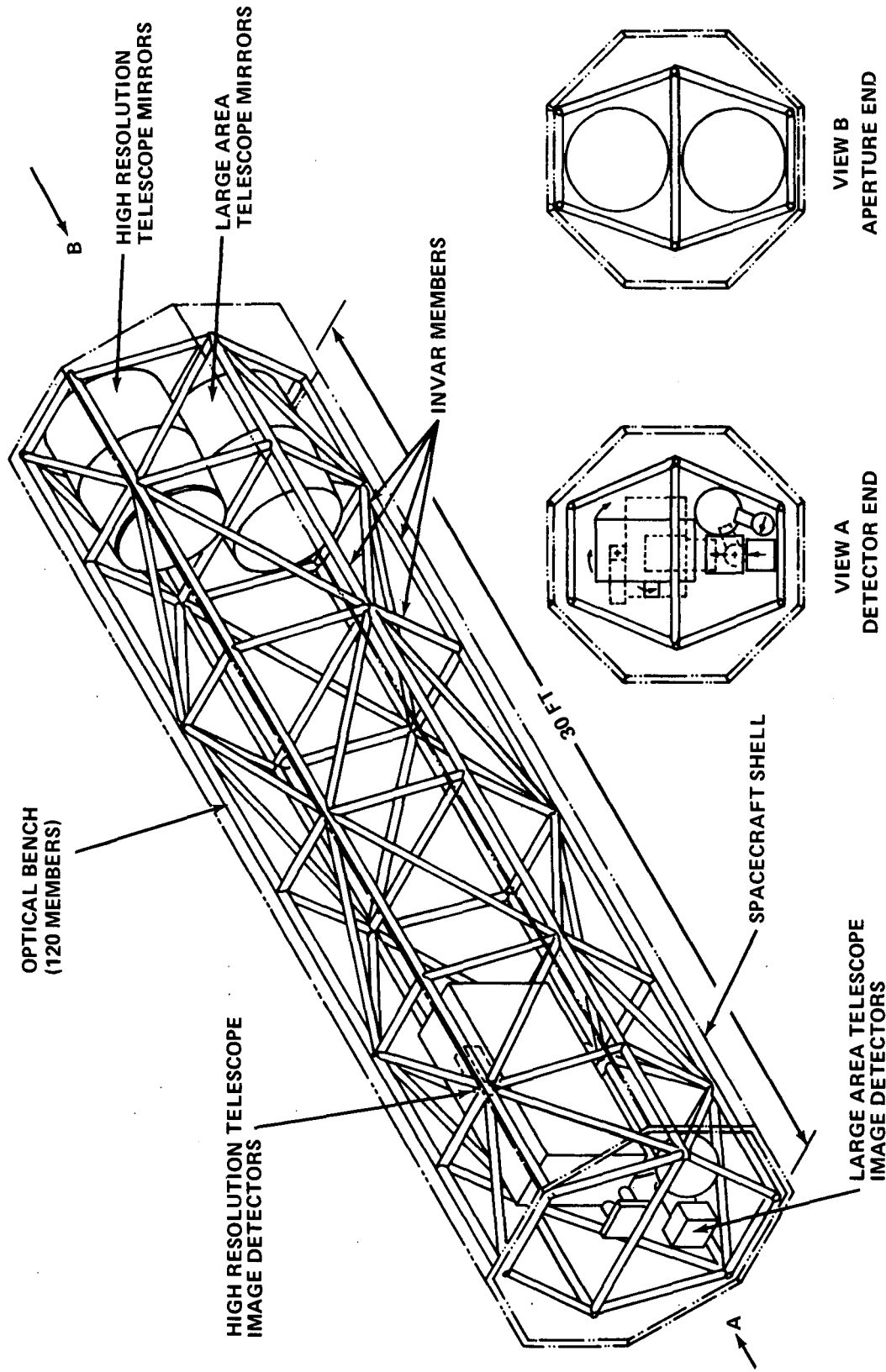


Figure D-1. HEAO-C optical bench (truss).

- Performance Index — A dimensionless number assigned to each material, based on the above three terms, which indicates the overall relative attractiveness of the materials.
- B/Ep — The abbreviation for the composite material boron/epoxy.
- Gr/Ep — The abbreviation for the composite material graphite/epoxy.

The general approach used in this analysis was that for the six candidate materials, in each of the four rating parameter categories, a rating factor was determined in such a way that for each rating parameter the least attractive material would possess the maximum rating factor of 1.0, the rating factors of the remaining five materials decreasing from 1.0 as the relative attractiveness of each material increased. By summing the four rating factors for each material, a list of performance indices resulted and the relative attractiveness of the six materials, based on the four rating parameters, was determined.

Optical bench weight, thermal expansion, thermal conductivity, and cost are all of major concern in the choice of a bench material. It is recognized, however, that one rating parameter may be considered as being more or less influential than another on the final choice of a material and that a determination of that relative importance (weight operators) of the rating parameters is largely subjective. The weight operators applied to the rating parameters are judiciously chosen, but nonetheless arbitrary.

1. Thermal Expansion Comparison. As an example of the method of analysis used in this study, consider Table D-1. The six materials are compared against one of the rating parameters, the coefficient of linear thermal expansion (α). The first column contains the α values of each material and in the second column the values are normalized yielding the rating factors such that the least attractive material (aluminum), from a thermal expansion viewpoint, possesses the maximum rating factor of 1.0.

Table D-1 reveals that, for this rating parameter, beryllium is twice as attractive as aluminum. The third column of figures maintains the relativity of the rating factors of the materials since all are multiplied by the same weight operator; however, with a weight operator of 2.0, thermal expansion is raised to an importance twice that of an unweighted rating parameter. Any one or more of the rating parameters may be weighted and the weight operators are chosen based on the requirements of the overall system (optical bench).

TABLE D-1. THERMAL EXPANSION COMPARISON

	$\alpha \left(\frac{\text{in.}}{\text{in. } ^\circ\text{F}} \right) \times 10^{-6}$	Rating Factor $\left(\alpha / \alpha_{\text{Al}} \right)$	Rating Factor $\times 2.0$ (Weight Operator)
Be	6.4	0.5	1.0
Ti	5.0	0.39	0.78
Invar	0.7	0.06	0.12
Al	12.7	1.0	2.0
B/Ep	2.0	0.16	0.32
Gr/Ep	0.02	0.0015	0.003

The rating factors of the six materials are determined in the following tables for the remaining three rating parameters (weight, thermal conductivity, and cost), thermal expansion having been considered as an example above. Finally, the overall material comparison is made by combining the results of the individual comparisons.

Table D-2 is a summary of the mechanical and physical properties necessary for the rating factor calculations.

TABLE D-2. MATERIAL PROPERTIES

	Density ρ (lb/ft ³)	Modulus $E \left(\frac{\text{lb}}{\text{in.}^2} \right) \times 10^6$	Thermal Expansion $\alpha \left(\frac{\text{in.}}{\text{in.} \cdot ^\circ \text{F}} \right) \times 10^{-6}$	Thermal Cond. $k \left(\frac{\text{Btu}}{\text{hr-ft } ^\circ \text{F}} \right)$
Be	115.8	42.5	6.4	104.0
Ti	276.5	16.0	5.0	4.0
Invar	504.6	21.0	0.7	73.0
Al	173.5	10.3	12.7	78.0
B/Ep	123.0	30.0	2.0	1.0
Gr/Ep	100.0	22.0	0.02	28.0

2. Weight Comparison. It is assumed that the optical bench thermal loads impose, primarily, compressive and tensile stresses in the bench members and that bending is secondary and is, therefore, neglected. As a result of this assumption, the analysis is conducted with solid bars (instead of tubes) as bench members without loss of accuracy. It is assumed that the bars have the same cross-sectional area as the tubes.

With these assumptions, it can be shown that if the weight of an optical bench fabricated from one material is known, the weight for another material may be calculated from

$$W_2 = W_1 \left(\frac{\rho_2}{\rho_1} \right) \left(\frac{E_1}{E_2} \right)^{1/3}$$

where W_1 is the known weight, (lb)¹; W_2 is the unknown weight; ρ is the density, (lb/ft³), and E is the modulus of elasticity.

Referring to Table D-3, it can be seen that Invar optical bench is least attractive from a weight viewpoint and that beryllium and the two composites can be used to fabricate optical benches which are approximately equal in weight.

TABLE D-3. WEIGHT COMPARISON

	Weight (lb)	Rating Factor ($W_t/W_{t_{Inv}}$)	Rating Factor $\times 1.0$ (Weight Operator)
Be	201	0.10	0.10
Ti	681	0.34	0.34
Invar	2000	1.0	1.0
Al	482	0.24	0.24
B/Ep	241	0.12	0.12
Gr/Ep	218	0.11	0.11

Since it is considered that "attractive" means "lightweight" and since it has been postulated that the least attractive material will possess the maximum rating factor of 1.0, the rating factor for each material, based on weight, is represented by the ratio of the optical bench weight for that material to the bench weight for Invar. The values listed in Table D-3, column 2, are comparable to those listed in Table D-1, column 2; both lists comprise the rating factors of the six materials for the rating parameters considered. Optical bench weight has subjectively been assigned a weight operator of 1.0, as shown in Table D-3, column 3. That is, for the purpose of this Phase A Study, weight is considered as one of the least important rating parameters.

1. $W_1 = 2000$ lb, the weight of an Invar optical bench.

3. Thermal Conductivity Comparison. The stringent limitations imposed on changes of the focal length of the telescope necessitate the use of a material for the optical bench which possesses at least a moderate, if not a high, coefficient of thermal conductivity. The procedure for determining the rating factors of the six materials based on thermal conductivity is similar to the procedure employed above in the rating factor calculations based on thermal expansion and weight. An additional step is involved here, however, since it is considered that "attractive" means the material has a high level of thermal conductivity. In the second column of Table D-4, the rating factor of each material is shown as being the multiplicative inverse of the thermal conductivity of each material. A normalizing ratio need not be determined since the conductivity of boron/epoxy is 1.0.

TABLE D-4. THERMAL CONDUCTIVITY COMPARISON

	Thermal Cond. $k \left(\frac{\text{Btu}}{\text{hr-ft } ^\circ\text{F}} \right)$	Rating Factor (1/k)	Rating Factor $\times 1.5$ (Weight Operator)
Be	104.0	0.0096	0.0144
Ti	4.0	0.25	0.375
Invar	73.0	0.0137	0.0206
Al	78.0	0.0128	0.0192
B/Ep	1.0	1.0	1.5
Gr/Ep	28.0	0.0357	0.0535

Thermal conductivity is assigned a weight operator of 1.5, and the final rating factors for the six materials, based on thermal conductivity, are shown in Table D-4, column 3.

4. Cost Comparison. From the point of view of overall optical bench development cost, the six candidate materials are compared considering two factors: (1) Material cost and (2) ease of fabrication, which includes cost of tooling, manpower, etc. In addition to the assignment of

weight operators to the four rating parameters, this cost comparison is largely subjective, due to the lack of firm data, but is based on a significant amount of manufacturing experience and on the most up-to-date cost information available.

The determination of the rating factors for the six materials based on cost is outlined in Table D-5 with the rating factors listed in column 5. The procedure is essentially identical to that employed above. Two points, however, bear elaboration: (1) The rating factor for each material based on cost is the sum of the rating factor for the material based on material cost and the rating factor based on ease of fabrication. Each rating factor sum is normalized by dividing by the rating factor of the least attractive material (beryllium in this case); (2) Fabrication considerations are deemed to be at least 10 times as influential on overall cost as on material cost. From column 6 of Table D-5 it is evident that aluminum is, by far, the most attractive material from a cost viewpoint. Data more recent than that reflected in Table D-5 indicate that the total cost of a graphite/epoxy telescope tube is approximately three times that of an aluminum tube.

TABLE D-5. COST COMPARISON

	Material Cost (\$)	Rating Factor (\$/\$ _{B/Ep})	Rating Factor Ease of Fabrication	Rating Factor Ease of Fabrication × 10	Sum (R)	R / R _{Be}
Be	21 000	0.14	1.0	10.0	10.14	1.0
Ti	16 000	0.1	0.5	5.0	5.1	0.51
Invar	30 000	0.2	0.4	4.0	4.2	0.42
Al	2 000	0.01	0.1	1.0	1.01	0.1
B/Ep	150 000	1.0	0.75	7.5	8.5	0.85
Gr/Ep	120 000	0.8	0.45	4.5	5.3	0.53

5. Overall Comparison. Table D-6 summarizes the overall comparisons presented above. Intermediate calculations are omitted. The last two columns of this table contain the final relative performance indices for the six materials based on the four rating parameters. The performance indices are shown for two sets of weight operators:

TABLE D-6. OVERALL COMPARISON

	Weight ^a Rating Factor	Thermal Expansion		Thermal Conductivity		Cost ^a		Performance Index	
		Rating Factor		Rating Factor		Rating Factor	Performance Index		
		Unweighted	Weighted	Unweighted	Weighted		Unweighted	Weighted	
Be	0.1	0.50	1.0	0.0096	0.0144	1.0	0.76	0.76	
Ti	0.34	0.39	0.78	0.25	0.375	0.51	0.70	0.72	
Invar	1.0	0.06	0.12	0.0137	0.0206	0.42	0.70	0.56	
Al	0.24	1.0	2.0	0.0128	0.0192	0.1	0.64	0.85	
B/Ep	0.12	0.16	0.32	1.0	1.5	0.85	1.0	1.0	
Gr/Ep	0.11	0.0015	0.003	0.0357	0.0535	0.53	0.32	0.25	

a. For the weight and cost rating parameters, the weighting factor is 1.0.

- All weight operators equal to 1.0; i.e., the four parameters are equally important.
- Weight operators for the cost and weight rating factors equal to 1.0, thermal conductivity weight operator equal to 1.5, and the thermal expansion weight operator equal to 2.0.

6. Conclusions. The calculations involved in this analysis have been based on the postulate that, for each rating parameter, the least attractive material would possess the maximum rating factor of 1.0, the rating factors of the other materials decreasing from 1.0 as the relative attractiveness of each material increases. In Table D-6, for example, the most attractive material (graphite/epoxy) has the lowest performance index. This approach was taken in the interest of simplicity of calculation since in three of the four rating parameter categories a material is most attractive when the rating parameter is the lowest. Since it is more common to relate good performance with a high grade or rating, it is advantageous in the statement and discussion of the conclusions of this analysis to invert the procedure and consider the most attractive material as possessing the maximum rating factor of 1.0, the rating factors of the remaining materials decreasing proportionately.

Table D-7 is a summary of the results of this analysis with the performance indices increasing proportionately to the maximum value of 1.0 as the material becomes more attractive.

TABLE D-7. FINAL PERFORMANCE INDICES

	Performance Index (Unweighted)	Performance Index (Weighted)
Gr/Ep	1.0	1.0
Invar	0.46	0.45
Be	0.42	0.33
Ti	0.46	0.34
Al	0.5	0.29
B/Ep	0.32	0.25

The following conclusions and comments are applicable:

- Primarily because of its low thermal expansion characteristic, the graphite/epoxy composite material is most attractive for application in the optical bench. There appears to be no advantage of the boron/epoxy composite over the graphite/epoxy.
- The disadvantages of graphite/epoxy are that the current material costs are high (but decreasing rapidly) and its thermal conductivity is only moderate but quite acceptable.
- Invar, although the heaviest material considered, is generally quite attractive.
- Although not considered in this analysis, it should be mentioned that Invar is a "hard" magnetic material and, consequently, causes the attitude control system of the HEAO-C to be more complex than if the optical bench material were magnetically "soft." This problem is not seen as being sufficiently severe to disqualify Invar as an optical bench material; however, further analysis of the problem is recommended.

- The undesirable thermal expansion properties of beryllium, titanium, and aluminum tend to disqualify these materials as candidates for use in the optical bench.
- The iron nickel alloy, Invar, and the composite graphite/epoxy appear to be the most attractive materials based on this analysis.

7. Discussion. During the course of the Phase A Study a number of different telescope support schemes and optical bench materials were considered. Originally, the hexagonal truss structure suggested by AS&E was baselined. After Invar was ruled out because of its undesirable magnetic properties (should a magnetic attitude control system be chosen), aluminum, titanium, beryllium, and graphite/epoxy were considered, with the latter emerging as the most attractive material for use in the truss bench. Packaging considerations and dynamic deflection during launch made it advisable to eliminate the truss bench concept. The tubular telescope structure and "crowfoot" support scheme was then developed. Graphite/epoxy was chosen for the tube material. Its attractiveness is highlighted in Figure D-2 where it is seen that to maintain the ± 0.002 inch axial deflection limit, a maximum allowable temperature variation of 139°F is acceptable.

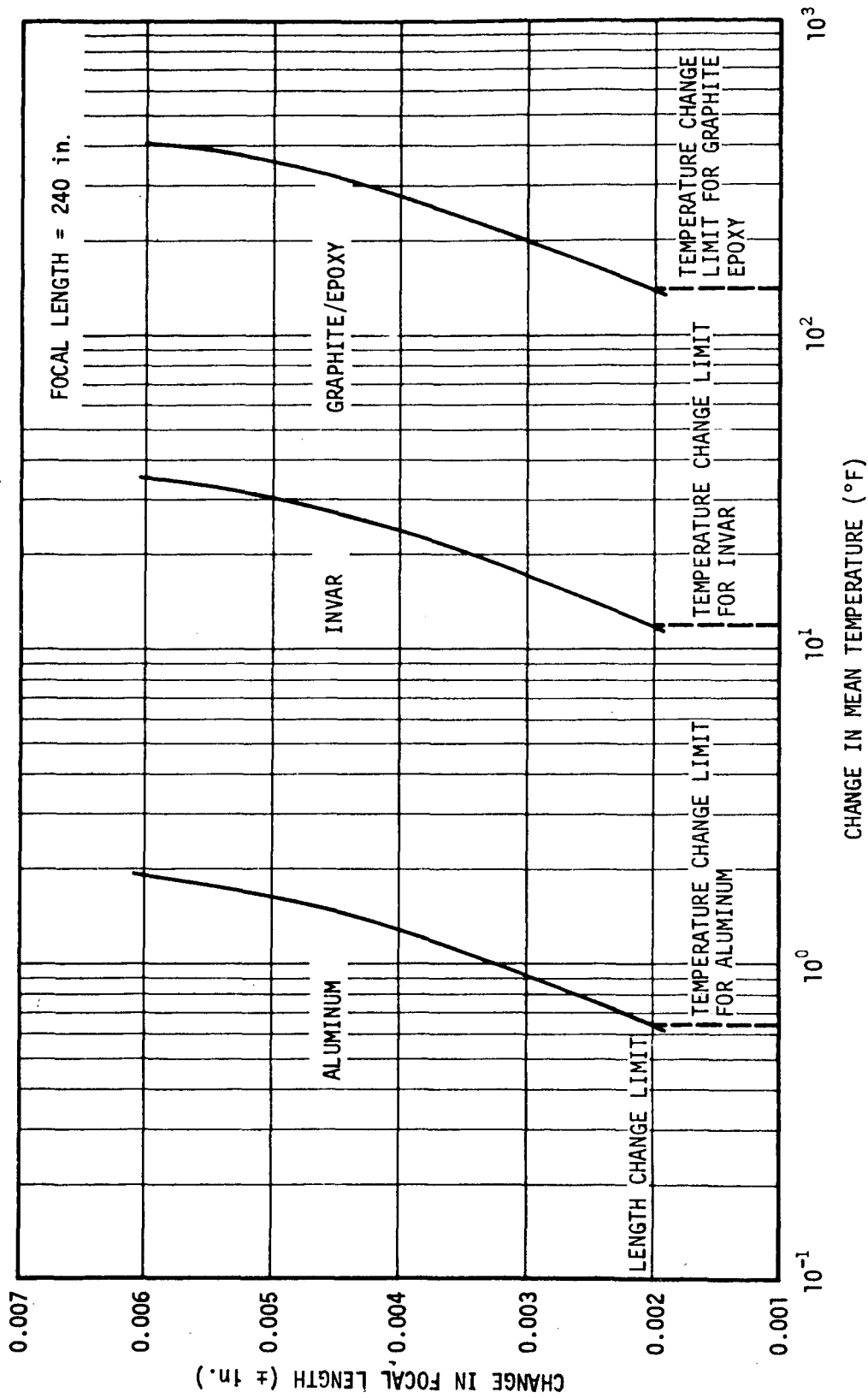


Figure D-2. Allowable mean temperature change versus focal length for three candidate tube materials.

Sunshade Feasibility Analysis²

Two mission requirements which have a significant impact on the HEAO-C thermal design are the required spacecraft pointing modes of ± 15 degrees and ± 30 degrees off the normal to the solar vector, especially with the viewing end inclined toward the sun. The prescribed ± 15 degree off-normal orientation provides the desired width of the celestial viewing band, and this orientation may last indefinitely. The ± 30 degree off-normal orientation provides a capability for temporary viewing of X-ray flares and is expected to last for only one orbit per day, typically.

The thermal control design baselined for the pre-Phase A Study was such that virtually all the heat that is generated within the optical bench is radiated and conducted to a thermal control filter which covers the viewing end of the bench (Fig. D-3). The filter ultimately reradiates this heat to space. To permit passage of the target X-rays through the filter to the mirrors, at least the fraction of the filter area which covers the apertures of the two telescopes must be constructed of a lightweight material, e.g., a thin skin of aluminized mylar.

The HEAO-C pre-Phase A Study revealed that an aluminized mylar filter performs adequately with the spacecraft oriented broadside to the sun so that no direct solar radiation falls on the filter. However, with the viewing end inclined toward the sun, solar radiation strikes the filter as a function of the cosine of the angle of solar incidence. The radiation absorbed increases the filter temperature and reverses the heat flow such that the direction is from outside to inside, and the temperature level of the entire optical bench becomes excessive. These facts are illustrated by the curve labeled "15° Tilt Without Sunshade" in Figure D-4 which presents the predicted temperature distribution along the bench without a sunshade after 16 hours of simulated orbit time. Examination of the temperature predictions revealed that the level of the predicted temperature profile was still rising after 61 hours of simulated time.

The use of a protective sunshade to permit the desired inclination of the spacecraft viewing end toward the sun for extended periods of time was evaluated. The sunshade length was sized to shield the entire viewing end

-
2. The analysis described in this section is based on the pre-Phase A HEAO-C conceptual design. Although the latest HEAO-C configuration is different from the configuration which was analyzed, the conclusions regarding the performance of the sunshade are still considered to be valid.

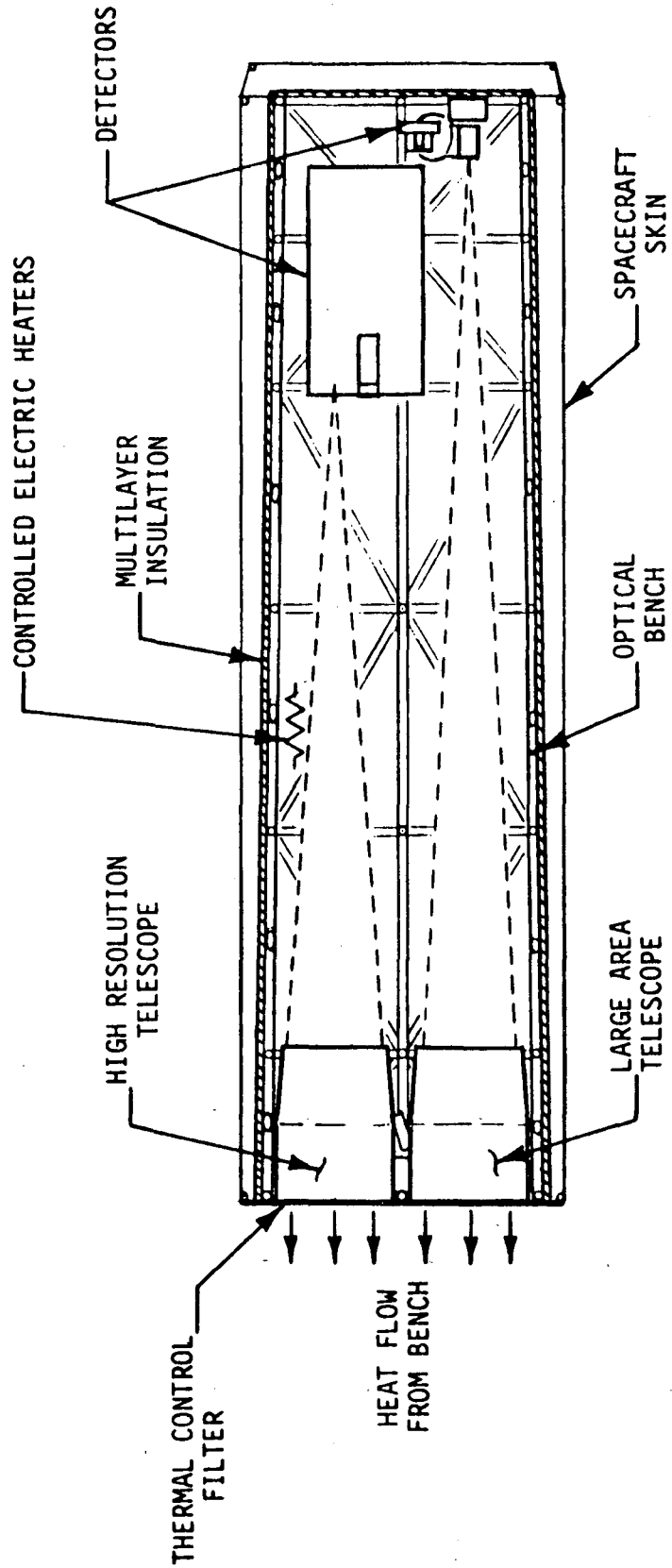


Figure D-3. Thermal control scheme proposed for truss bench concept.

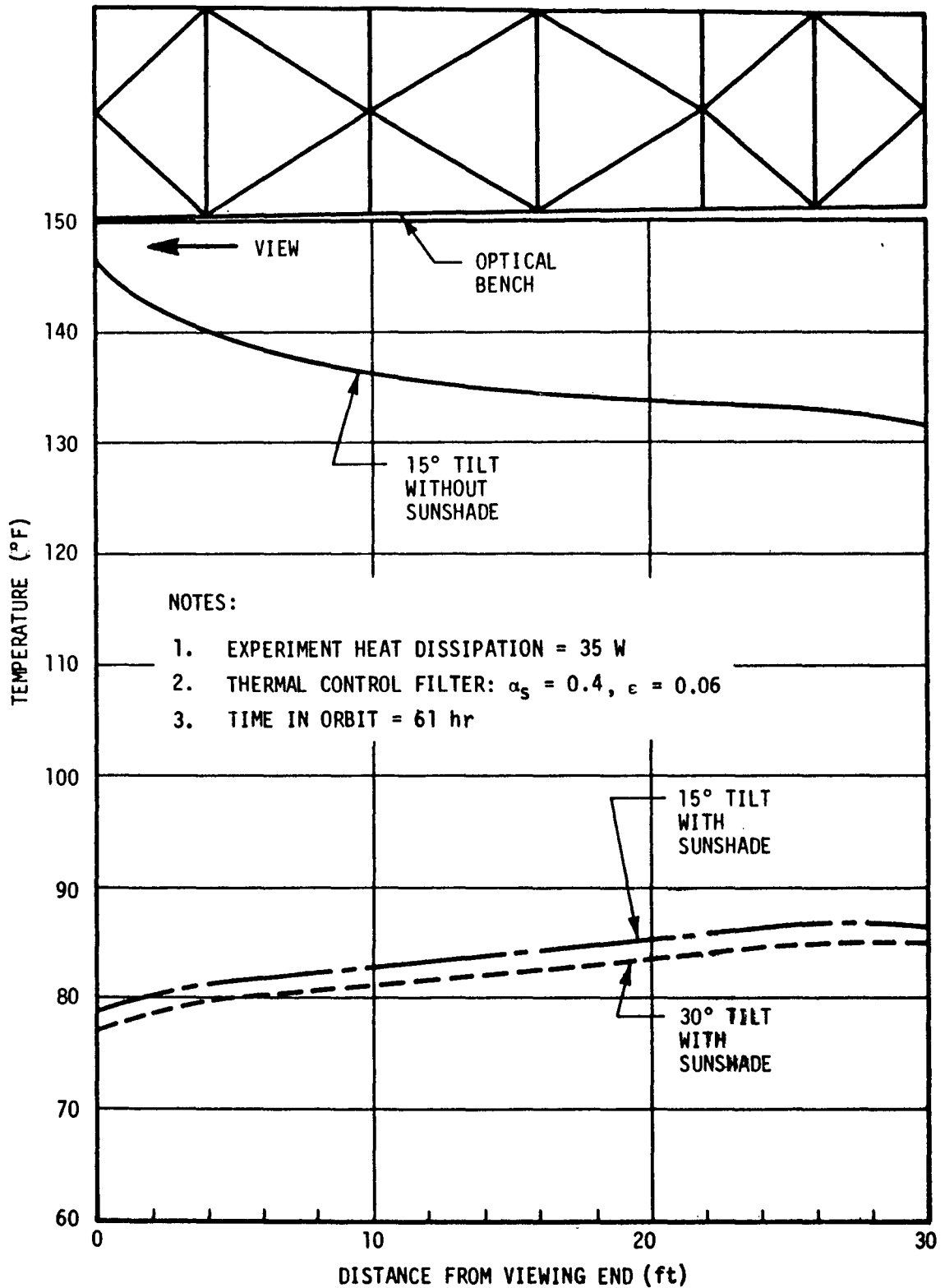


Figure D-4. Effect of sunshade on longitudinal temperature distribution of truss optical bench.

of the spacecraft when tilted toward the sun at an angle of 30 degrees from the normal to the solar vector. The sunshade model considered in the thermal analysis consisted of three aluminum panels extending 4.72 feet from the three solar panels as shown in Figure D-5.

The resulting optical bench temperatures after 61 hours of simulated orbit time with the sunshade installed and the spacecraft inclined 15 and 30 degrees toward the sun are illustrated in Figure D-4. A comparison of the predicted temperature profiles for the cases with and without the sunshade in this figure illustrates the effectiveness of the sunshade in maintaining an acceptable temperature level of the optical bench at off-normal pointing angles.

It is interesting to note from Figure D-4 that the level of the predicted optical bench temperature profile is greater for a 15 degree inclination than for a 30 degree inclination toward the sun. This phenomenon may be explained by consideration of the governing relationship for absorbed solar energy by an exposed surface:

$$Q_{\text{abs}} = \alpha_s (\cos \theta) G$$

where Q_{abs} is heat absorbed by sunshade (Btu/hr-ft²); α_s is absorptivity; G is the solar constant (Btu/hr-ft²); and θ is the angle between surface normal and solar vector (radians).

From this equation it may be seen that the sunshade's absorbed solar radiation flux is greater for a spacecraft inclination of 15 degrees toward the sun than for a value of 30 degrees, because the term $\cos \theta$ is greater. Likewise, the amount of the absorbed solar energy which is reradiated from the sunshade to the thermal control filter is greater for an inclination of 15 degrees than for 30 degrees because of the higher sunshade temperature. This increased amount of absorbed solar energy results in an increased level of temperature of the thermal control filter, which, in turn, maintains the temperature level of the optical bench at a higher level. This pattern of behavior prevails only for values of up to 30 degrees.

As θ is increased beyond 30 degrees, solar radiation impinges directly on a fraction of the thermal control filter, and the level of the optical bench temperature profile begins to increase, as expected. The variation in optical bench temperature profile with θ , at values between 0 and 30 degrees, may be reduced by providing a sunshade design which minimizes the transmission of heat from its outer surface to the inner surface which views the thermal control filter. (For the analysis described herein, the sunshade

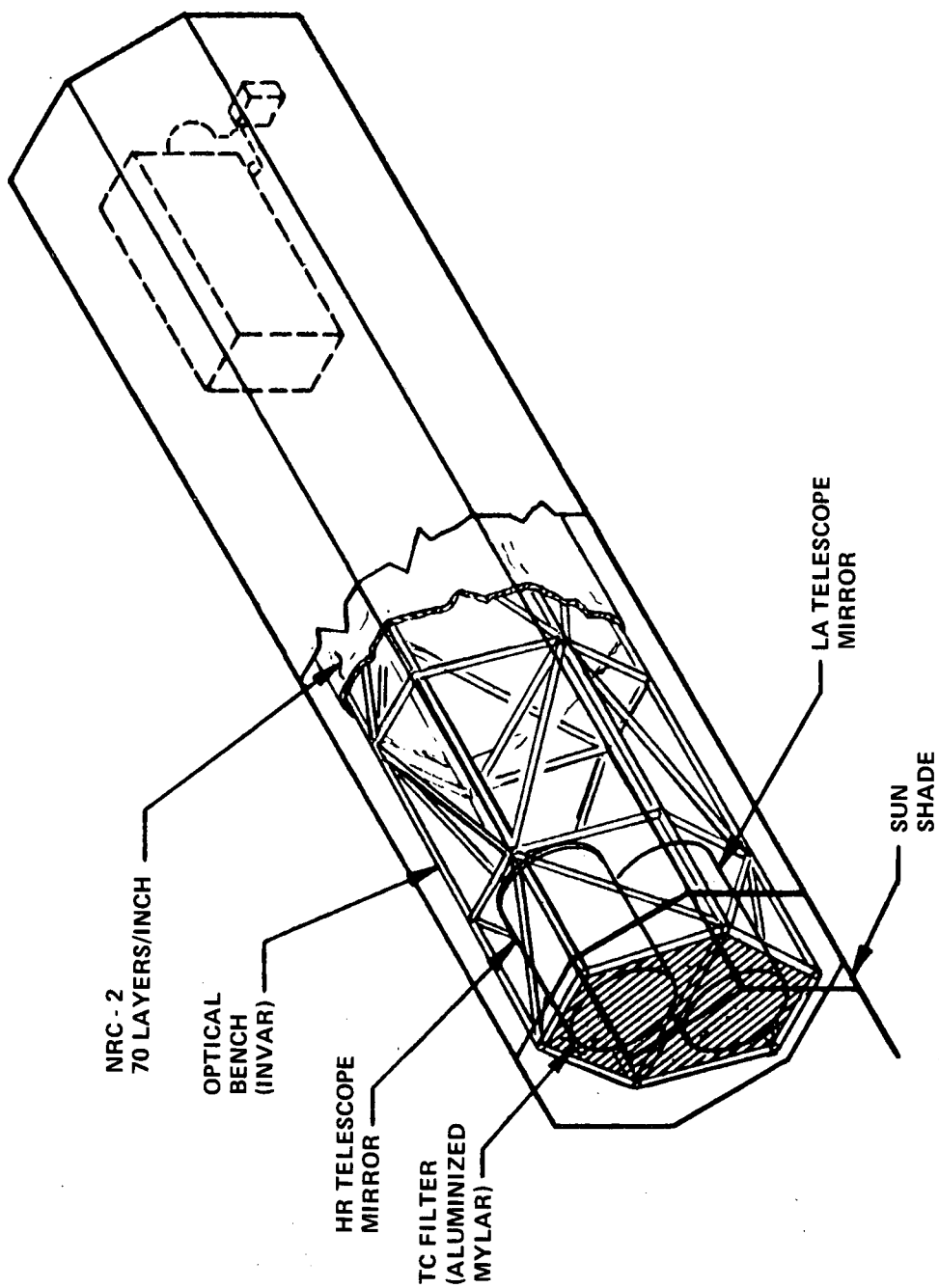


Figure D-5. Alternate (truss bench) thermal control concept.

was assumed to be thermally thin, i. e., to have no lateral temperature gradient.)

It is noteworthy that the optical bench temperature level will be slightly higher with the sunshade than without when the spacecraft is oriented perpendicular to the sun line. There are two reasons for this:

- Reradiation from the sunshade
- Decrease of the radiation shape factor from the filter to space due to the sunshade, which retards the ultimate rejection of heat generated inside the optical bench.

Additional cases were evaluated with the spacecraft viewing end inclined toward the sun at angles of 45 and 60 degrees to estimate the maximum periods of time for which these orientations could be maintained from a thermal standpoint. The results of these evaluations are presented in Figure D-6, where the predicted length-averaged temperatures of the optical bench and mirrors are plotted as a function of simulated orbit time. Figure D-6 could be used, with a knowledge of the operating temperature limits of the optical bench and telescope mirrors, to estimate the maximum permissible duration of off-normal pointing for the optical bench configuration shown in Figure D-5. Although the operating temperature limits of the Invar optical bench design considered herein have not been firmly established, preliminary calculations indicated that adherence to the following limits would provide satisfactory thermal control:

- Maintenance of the length-averaged temperature of the optical bench within $\pm 18^\circ\text{F}$ of the length-averaged value at the time of experiment calibration.
- Maintenance of the temperature at any given point on the telescope mirrors and adjacent optical bench structure within $\pm 10^\circ\text{F}$ of its value at the time of experiment calibration.³
- Maintenance of the difference between the average temperatures of opposite sides of the Invar optical bench below a maximum value of 21°F .

3. Information reviewed from AS&E subsequent to this analysis indicated that the mirror temperature requirement is as stated in Chapter VI.

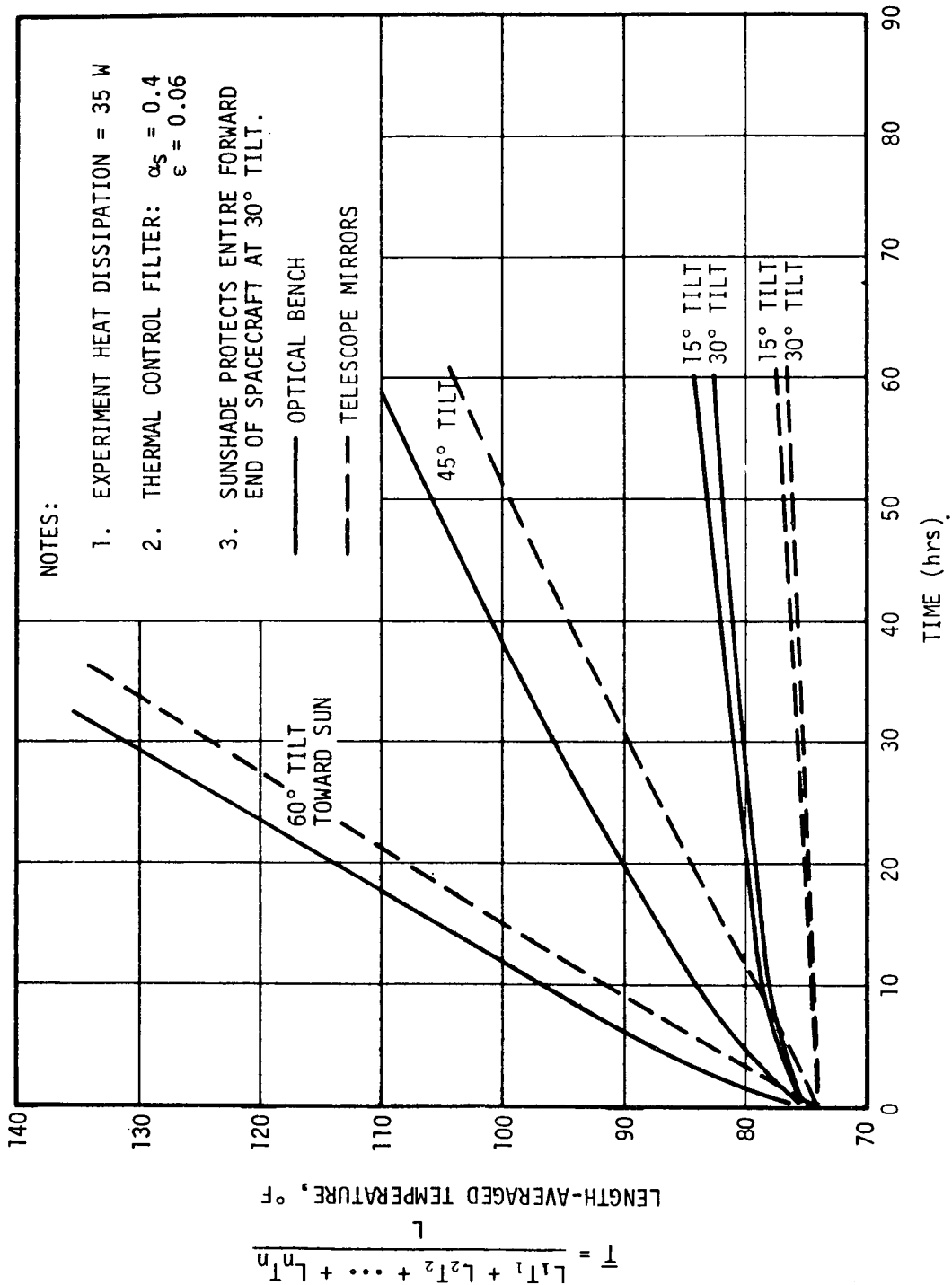


Figure D-6. Transient response of optical bench and telescope mirrors to off-perpendicular orientations.

The preferred HEAO-C experiment calibration temperature has not been established. To minimize thermally-induced structural elongations in orbit, it will be desirable to calibrate the experiment assembly at a temperature level which is approximately equivalent to the predicted level for orbital conditions. However, the selected calibration temperature must be within the practical limits dictated by laboratory environmental control capabilities. Examination of the predicted optical bench temperature profile presented in Figure D-4 reveals that an experiment calibration temperature of approximately 80° F would correspond approximately to the expected operating temperature level during orbit. Assuming a calibration temperature of 80° F and the temperature requirements listed above, the upper temperature limit of the optical bench would be 98° F (length-averaged), and the telescope mirror temperature would be limited to a maximum value of 90° F. For this hypothetical situation, Figure D-6 indicates that, with the spacecraft viewing end inclined 45 degrees toward the sun, the length-averaged optical bench temperature would reach its maximum value after approximately 35 hours. However, the telescope mirror temperature would reach its upper limit of 90° F (at any point on the mirror) much sooner, because the predicted length-averaged temperature of the mirror, which includes local temperatures greater than 90° F, reaches a value of 90° F after only 31 hours in orbit. For the case with the spacecraft viewing end inclined 60 degrees toward the sun, the predicted length-averaged optical bench temperature reaches its maximum value of 98° F after approximately 12 hours; whereas, the length-averaged telescope mirror temperature reaches a value of 90° F after approximately 8 hours. From these results it may be concluded that, although the temperature limits of the experiment assembly have not been firmly established, the use of a sunshade will permit off-normal pointing at angles greater than 60 degrees for at least a few hours.

It is obvious from the results described herein that the sunshade is essential if an aluminized mylar filter is used and the viewing end is to be tilted toward the sun for an indefinite period of time. The possibility exists that a different thermal control filter with different surface optical properties might control the temperature during off-normal orientations without a sunshade. Future analysis should include an investigation of additional thermal control filter designs.

Alternate Solar Array Configurations

The Observatory configuration which formed the basis for the pre-Phase A feasibility study of the HEAO-C was composed of an octagonal spacecraft, body-mounted solar arrays (with a flat side normal to the sun line), and the

hexagonal optical bench recommended by AS&E. During that study, excessive heating of the center solar array (Fig. D-7) was identified. This conclusion was based on the fact that the maximum predicted instantaneous temperature of the center solar panel was 220° F which exceeds the chosen maximum allowable value of 212° F (Fig. D-8).

It is important to note that, although the value of 212° F has been tentatively accepted as the design guideline for maximum allowable solar panel temperature, there is some question concerning its applicability to HEAO-C. Reduction of the maximum solar panel temperature is desirable, however, regardless of the established upper temperature limit because of the attendant gain in power conversion efficiency.

1. Proposed Thermal Control Schemes. As a result of the HEAO-C pre-Phase A thermal analysis, the following thermal control schemes for reducing the temperature of the center solar panel were recommended for investigation:

- Selection of a spacecraft orientation having no solar panel positioned exactly perpendicular to the solar vector. This would result in a reduction of the temperature of the center solar panel, hopefully without causing an excessive penalty in available power.
- Removal of the 0.5 inch thickness of multilayer insulation which was assumed to be directly in contact with the backsides of the solar panels. This would permit slightly increased heat transfer from the backsides of the solar panels, although radiation blockage by the insulated optical bench would limit the reduction in solar panel temperature.
- Folding out the two side solar panels to provide increased heat rejection by radiation from their backsides and improved heat conduction from the center solar panel.

2. Rotation of Center Solar Panel Off Solar Vector. To evaluate the merits of orienting the center solar panel other than perpendicular to the solar vector, a thermal analysis of the spacecraft was conducted with the spacecraft positioned such that the angle between the solar vector and the normal to the center solar panel was 22.5 degrees.

The predicted orbital temperature histories of the three solar panels with the 22.5 degree off-axis rotation are illustrated in Figure D-9.

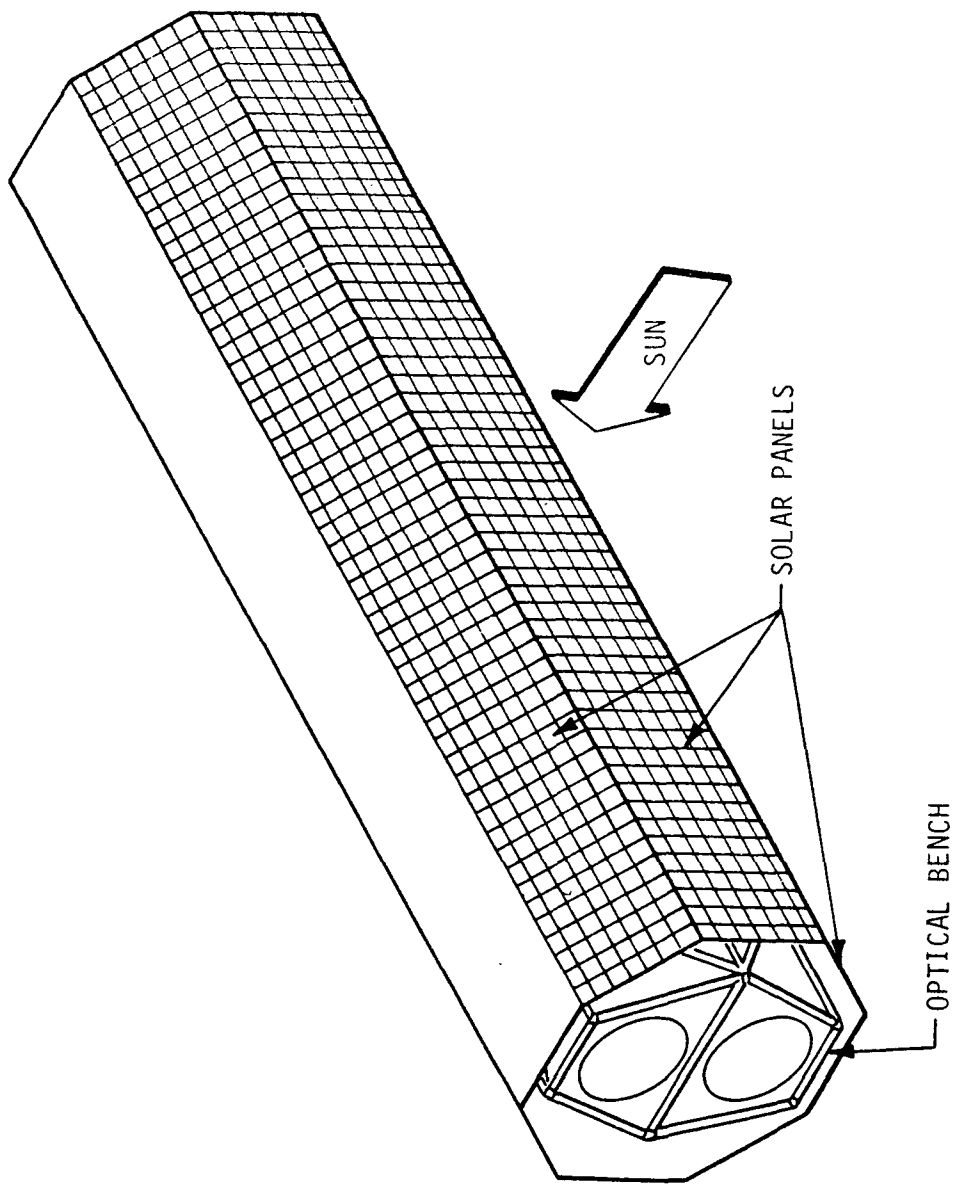


Figure D-7. Alternate Observatory concept with body-mounted solar panels.

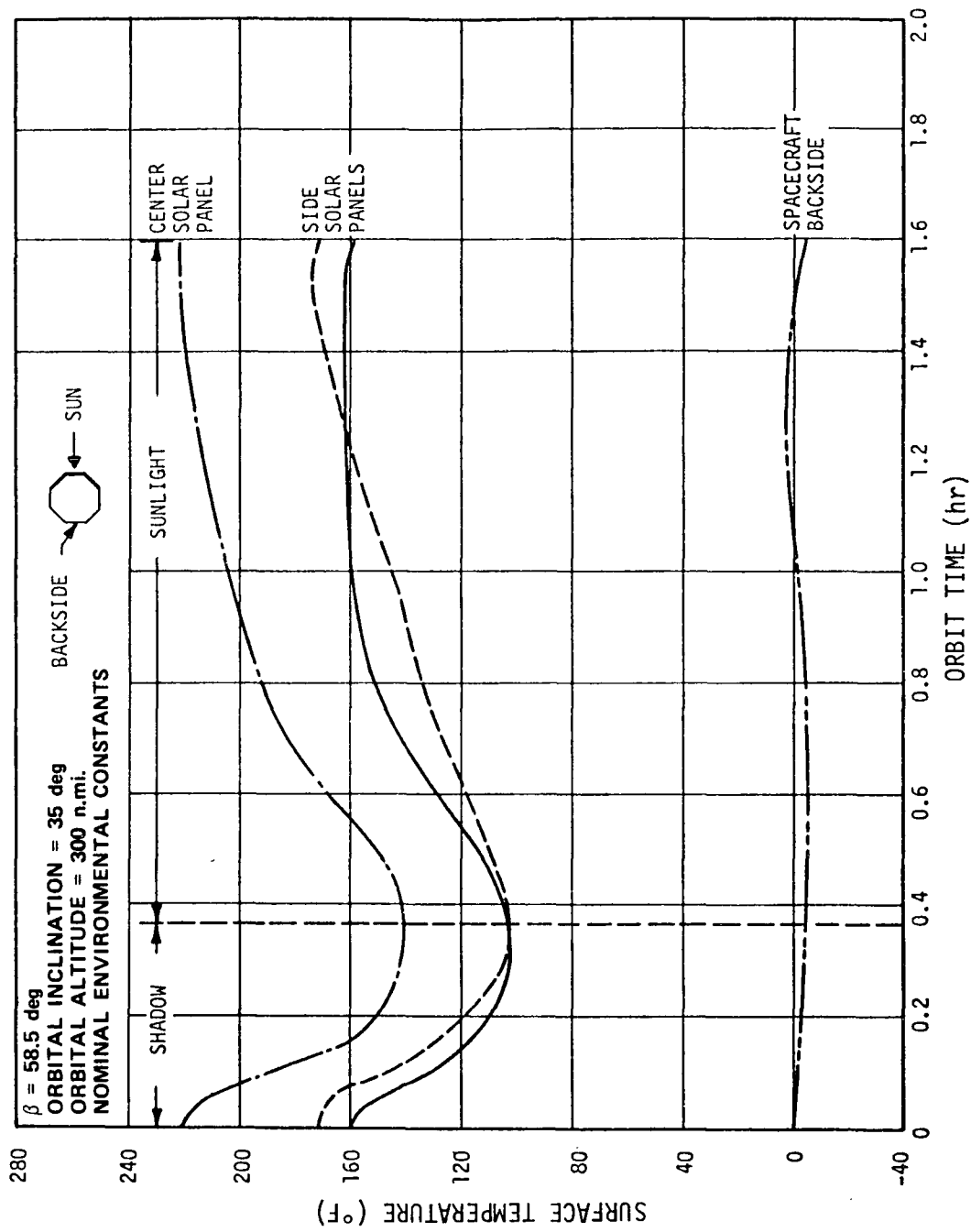


Figure D-8. Solar panel and spacecraft temperatures for body-mounted configuration.

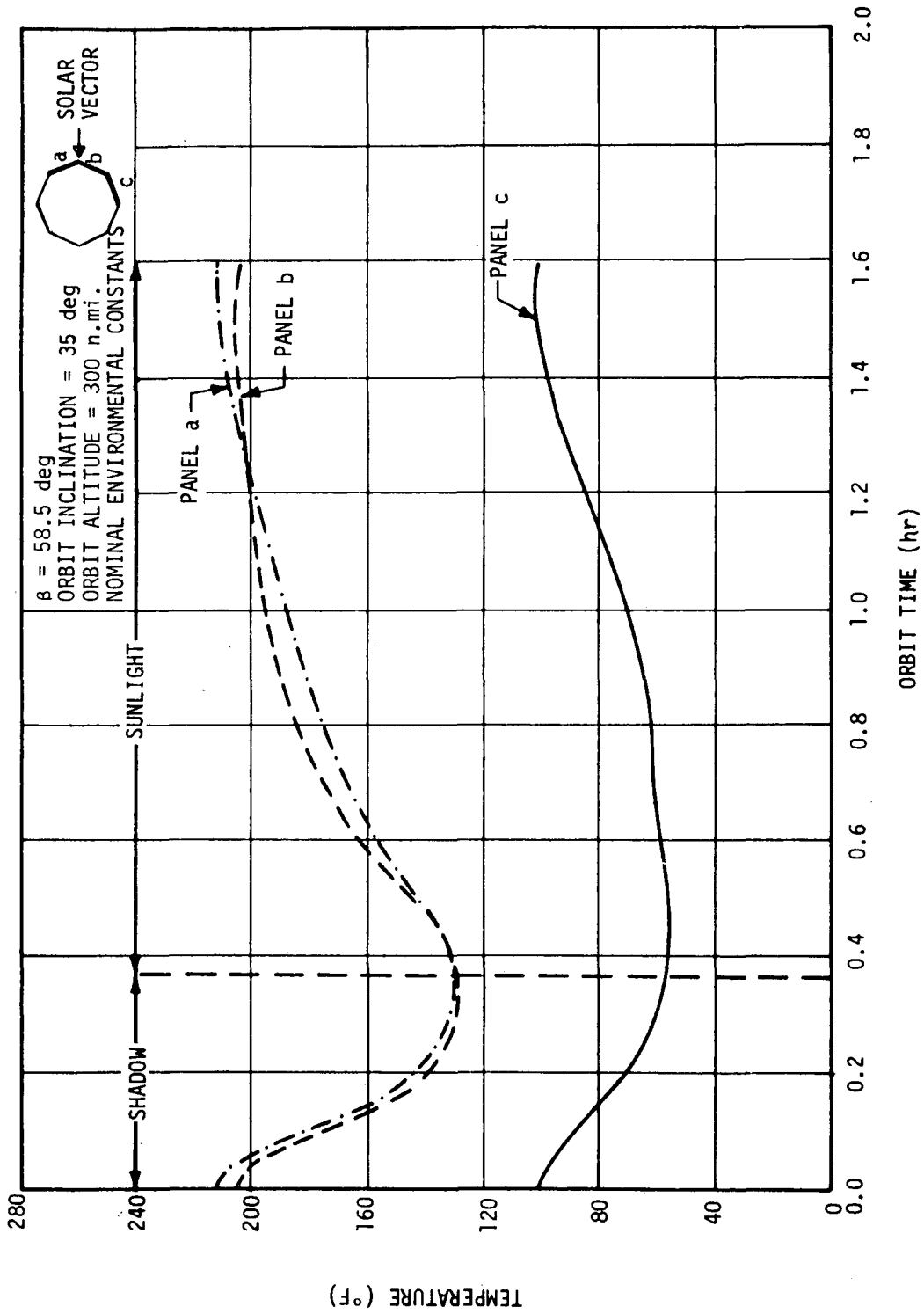


Figure D-9. Body-mounted solar panel temperature histories with center panel oriented 22.5 degrees off sun line.

Comparison of Figures D-9 and D-8 reveals that the 22.5 degree off-axis rotation yields a reduction in maximum solar panel temperature of only 8° F, from 220° F to 212° F. Since the temperature predictions presented in Figure D-9 are, again, based on nominal environmental heating constants and optical surface properties, consideration of worst case values of these pertinent parameters would result in a predicted maximum temperature which exceeds the prescribed 212° F upper limit. Therefore, it may be concluded from this analysis that the reduction in maximum solar panel temperature which results from orienting the center solar panel off-normal to the solar vector is insufficient to solve the problem of excessive solar panel heating.

3. Removal of Insulation Behind Solar Panels. Another thermal analysis was performed to evaluate the effect on solar panel temperature of removal of the specified 0.5 inch thickness of multilayer insulation located directly behind the solar panels.

The predicted solar panel temperature histories during orbit, with the 0.5 inch thickness of insulation at their backsides removed, are presented in Figure D-10. These calculations are based on nominal values of environmental constants (solar, albedo, earth infrared) and solar panel surface optical properties. Removal of the insulation reduces the maximum predicted solar panel temperature from 220° F to 198° F. Moreover, it is estimated that the maximum predicted temperature would increase only to approximately 209° F considering worst case environmental constants and optical properties. Therefore, it may be concluded that removal of the solar panel backside insulation would reduce the maximum expected operating temperature to slightly below the prescribed upper limit of 212° F. However, the removal of this insulation unfortunately results in overheating of some of the subsystem components located between the optical bench and the solar panels. For example, the predicted maximum temperature of the control moment gyros (CMGs) without the protective solar panel insulation was 166° F. The allowable upper temperature limit of the CMGs was initially reported to be 120° F. Additional vendor information indicates that the allowable temperature limits of the CMGs are -40° F to 180° F. Consideration of worst case environmental heating parameters could increase the maximum predicted CMG temperature to approximately 177° F, which is crowding the maximum allowable temperature. Also, the predicted maximum temperatures of the electronic packages associated with the high resolution image detector (173° F), fine flares detectors (162° F), and the aspect detector (161° F) exceed their maximum allowable value of 160° F. It may be concluded that reduction of the maximum solar panel temperature to an acceptable level through removal of the 0.5 inch thickness of insulation from behind the solar panels is a feasible approach only if a practical method may be conceived for thermal control of the adjacent subsystems.

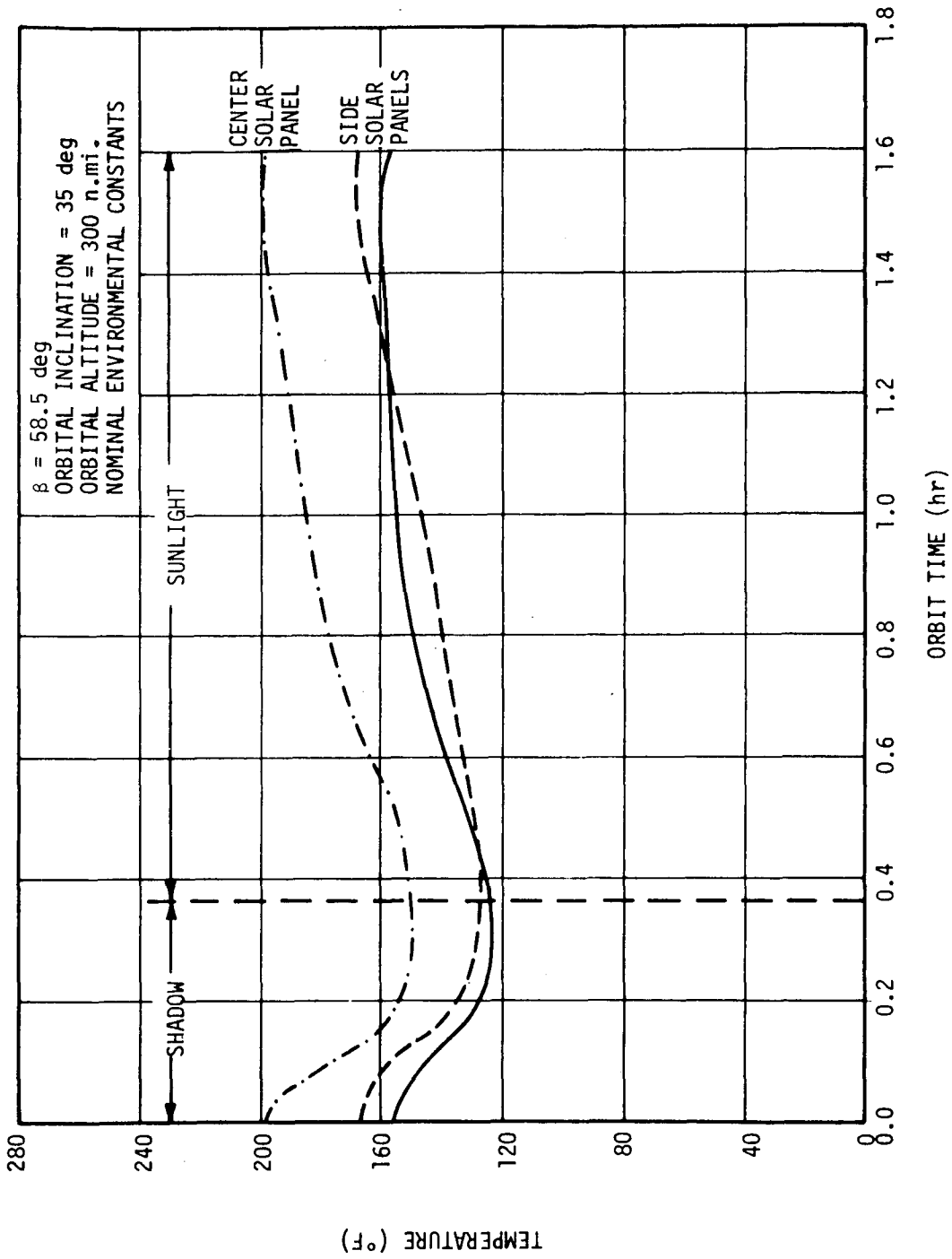


Figure D-10. Body-mounted solar panel temperature history with insulation removed from backsides.

4. Folding Out of Side Solar Panels. A thermal analysis was performed to predict the reduction in center solar panel temperature which would result from folding out of the two adjacent solar panels, as illustrated in Figure D-11.

As illustrated by Figure D-12, the predicted maximum temperature of the center solar panel with the adjacent solar panels folded out is 212° F, which represents a reduction of only 8° F below the predicted maximum of 220° F for the baseline body-mounted configuration. This reduction is not sufficient to solve the solar panel heating problem, because the consideration of worse-case environmental constants (solar, albedo, earth infrared) would result in a predicted maximum temperature well in excess of the allowable 212° F. (The temperature predictions illustrated in Figures D-8 and D-12 were based on nominal values of the environmental constants.) It is noted that the temperature predictions for the foldout configuration were based on values of orbital inclination and altitude of 28.5 degrees to the equator and 270 nautical miles, respectively; whereas the temperature predictions for the body-mounted arrays were based on corresponding values of 35 degrees and 300 nautical miles; however, the effect of these relatively small differences on the solar panel temperature predictions are considered to be negligible.

A comparison of Figures D-8 and D-12 reveals that there is virtually no difference between the predicted maximum temperature of the side solar panels in the deployed position and the body-mounted configuration. This fact results from two counteracting thermal effects which accompany the foldout configuration. The first of these effects is a tendency toward reduced temperature of the deployed solar panels which results from increased radiation from the backsides to space. However, this effect is counteracted by a tendency toward increased temperatures which results from increased solar radiation flux due to the normal orientation of the deployed panels relative to the solar vector.

It is noted that the thermal model which was used in evaluating the foldout concept included the 0.5 inch thickness of multilayer insulation directly behind the center solar panel and adjacent skin panels as specified during the pre-Phase A Study. Removal of this insulation would result in a further decrease in the predicted maximum temperature of the center solar panel to an estimated value of approximately 190° F based on nominal environmental constants. It is estimated that the predicted maximum temperature of the center solar panel without backup insulation would increase to an acceptable value of approximately 200° F, considering worst case environmental constraints and optical properties. Therefore, the

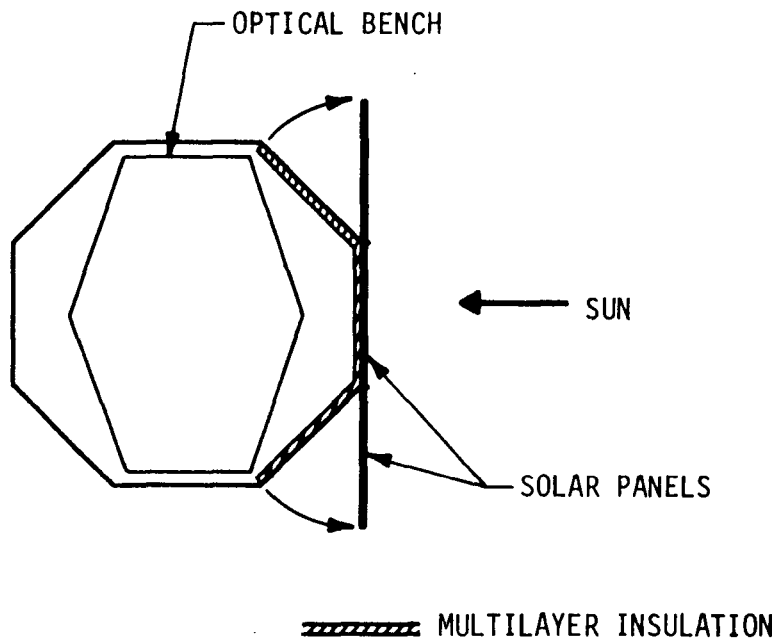


Figure D-11. Alternate foldout solar panel concept.

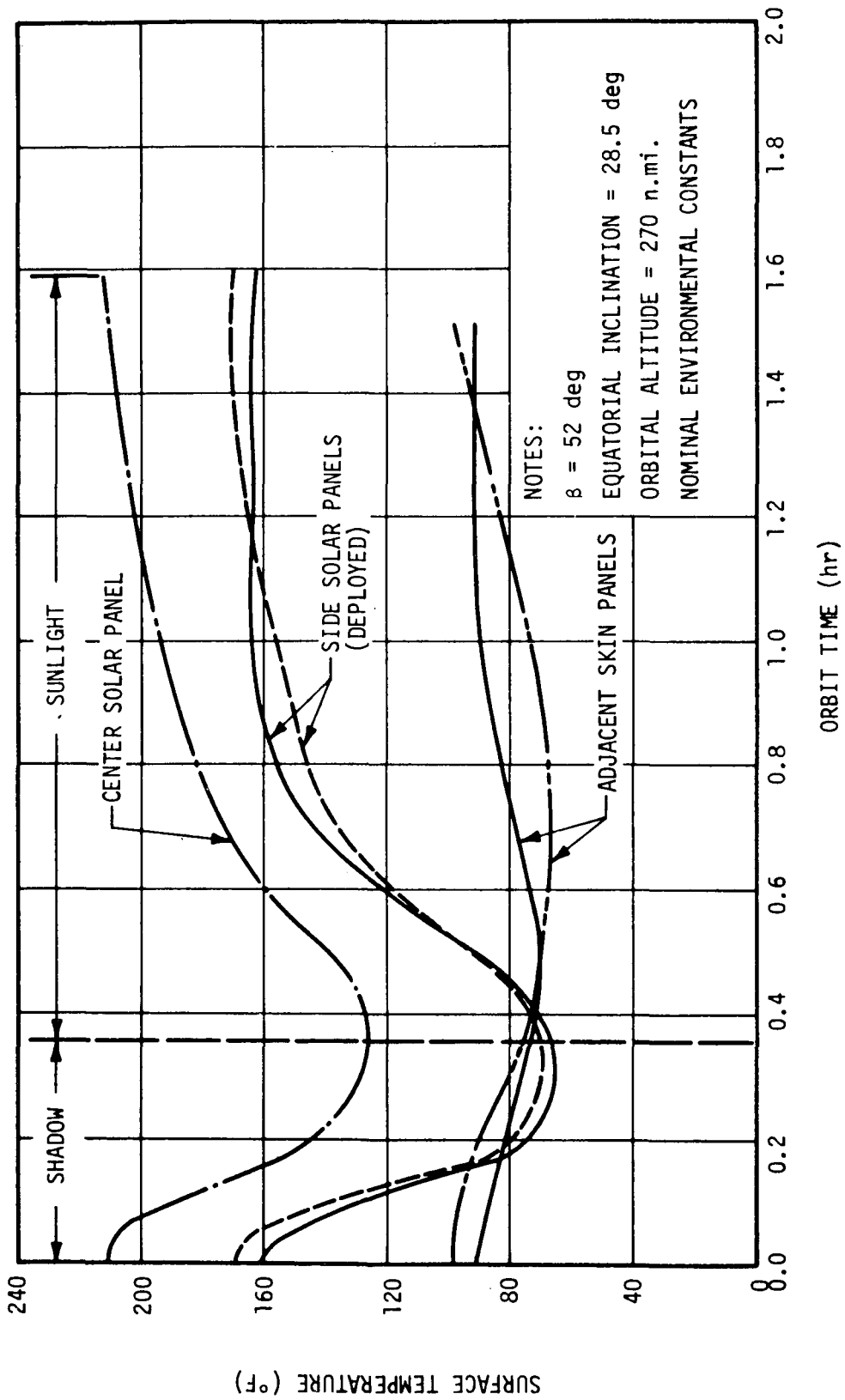


Figure D-12. Alternate foldout solar panel temperature history.

combination of folding out the side solar panels and deleting the 0.5 inch thickness of solar panel backup insulation appears to be a promising approach for controlling the center solar panel temperature provided the adjacent subsystems (CMGs, primarily) do not become excessively warm. Previous calculations indicate that, with the backup insulation removed, a center solar panel temperature is approximately 177° F. This temperature is crowding the allowable upper temperature limit (180° F) of the CMGs, however, and may be considered to be excessive. Additional thermal modeling computations are recommended to fully evaluate the combination of deployed side solar panels and removed solar panel backup insulation.

5. Reduced Solar Cell Packing Density on Center Panel. Preliminary analysis indicated that the maximum temperature of the HEAO-C center solar panel could be reduced to less than 212° F by spacing the highly absorptive solar cells farther apart than in the Apollo Telescope Mount (ATM) type modules and coating the inactive spaces between cells with a reflective material as illustrated in Figure D-13. Thus, the solar cell packing density and the average solar absorptivity of the center panel would be reduced, resulting in a reduced level of absorbed solar flux and a reduced average solar panel temperature. The adjacent side solar panels would be deployed as shown in Figure D-13 to compensate for the loss in available power which would accompany reduction of the solar cell packing density on the center panel.

The average solar absorptivity of the center panel is determined from the relation

$$\bar{\alpha}_s = (\alpha_s)_{sc} f + (\alpha_s)_{rc} (1-f) \quad ,$$

where $\bar{\alpha}_s$ is the average solar absorptivity of center panel; $(\alpha_s)_{sc}$ is the solar absorptivity of conventional solar cell modules; $(\alpha_s)_{rc}$ is the solar absorptivity of reflective coating between cells; and f is the fraction of total area of center panel covered by conventional solar cell modules⁴. Likewise, the average emissivity of the center panel is given by the relation

4. Each conventional (ATM-type) solar cell module has a packing density (fraction of module area occupied by solar cells) of approximately 0.83.

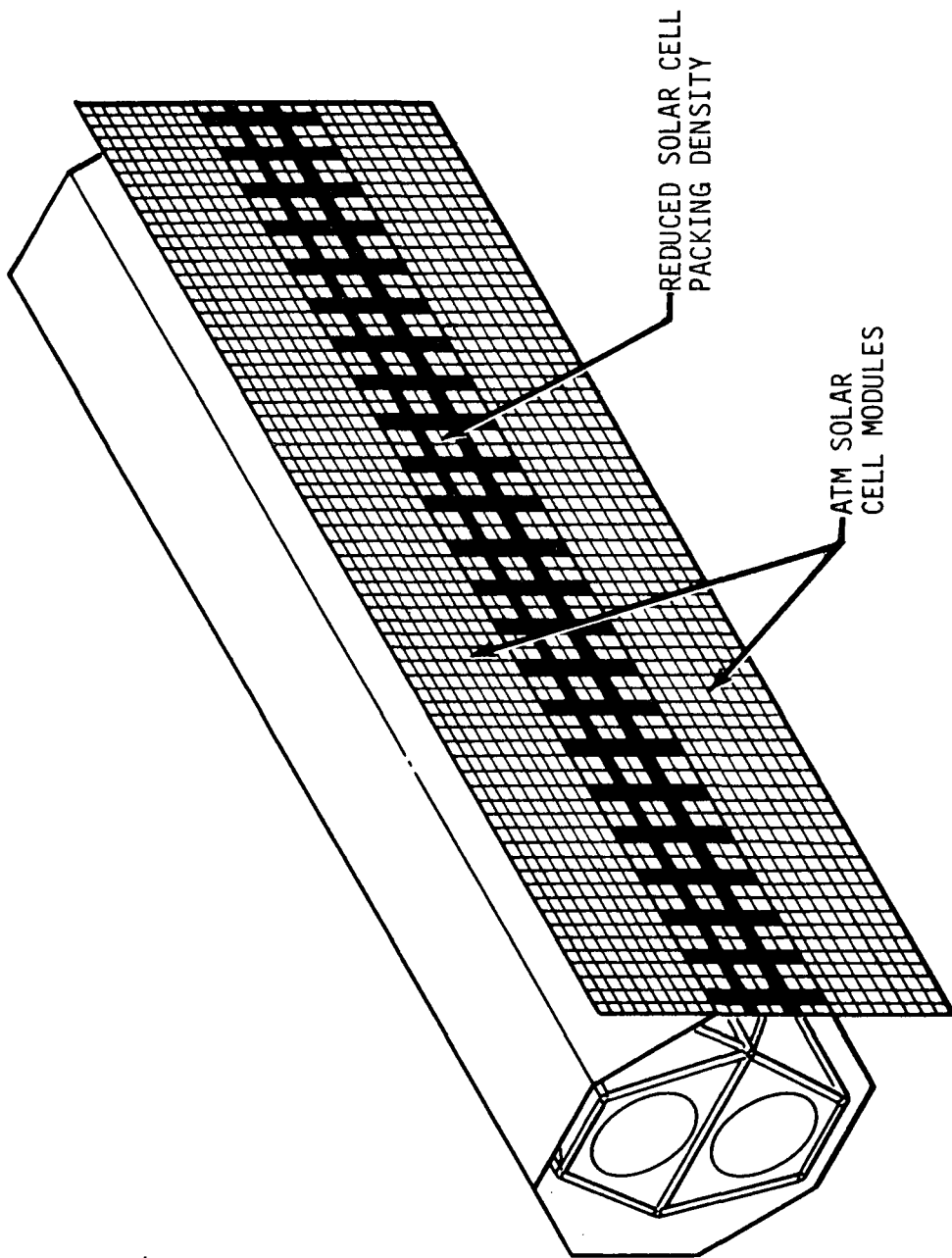


Figure D-13. Solar panel temperature control by reducing solar cell packing density on center panel.

$$\bar{\epsilon} = \epsilon_{sc} f + \epsilon_{rc} (1 - f) \quad ,$$

where $\bar{\epsilon}$ is the average emissivity of center panel; ϵ_{sc} is the emissivity of conventional solar cell modules; and ϵ_{rc} is the emissivity of reflective coating.

For this analysis, it was assumed that the reflective coating between solar cells is Z-93, a well-known zinc-oxide thermal control paint. Experimental data have shown that the solar absorptivity, α_s , and emissivity, ϵ_s , of Z-93 after degradation from the extended exposure to the solar/vacuum environment are approximately 0.35 and 0.85, respectively. These values of α_s and ϵ_s were assumed for the reflective coating in the analysis described herein. Likewise, the assumed values of solar absorptivity and emissivity for the conventional solar cell modules were 0.71 and 0.82, respectively.

The center solar cell packing density, f , was considered to be 0.67 in this analysis. This value of f resulted from calculations of required solar cell area to achieve a 10 percent increase in available load power above the level of approximately 824 watts. The 10 percent increase was considered desirable because the power contingency level provided by the pre-Phase A design was found to be marginal based on a two year mission.

The predicted orbital temperature histories of a center solar panel having a packing density, f , of 0.67 and of deployed side solar panels having an idealistic packing density, f , of 1.00 are presented in Figure D-14. (The physically unrealizable packing density of 1.0 was assumed for conservatism and analytical simplicity.) These temperatures represent maximum values, since maximum values were assumed for the heat source constants (solar, albedo, earth infrared) and for the orbital parameter β . The currently accepted maximum values of the environmental constants are as follows:

$$\text{Solar constant} = 448 \text{ Btu/hr-ft}^2$$

$$\text{Albedo} = 0.4$$

$$\text{Earth infrared} = 82.6 \text{ Btu/hr-ft}^2$$

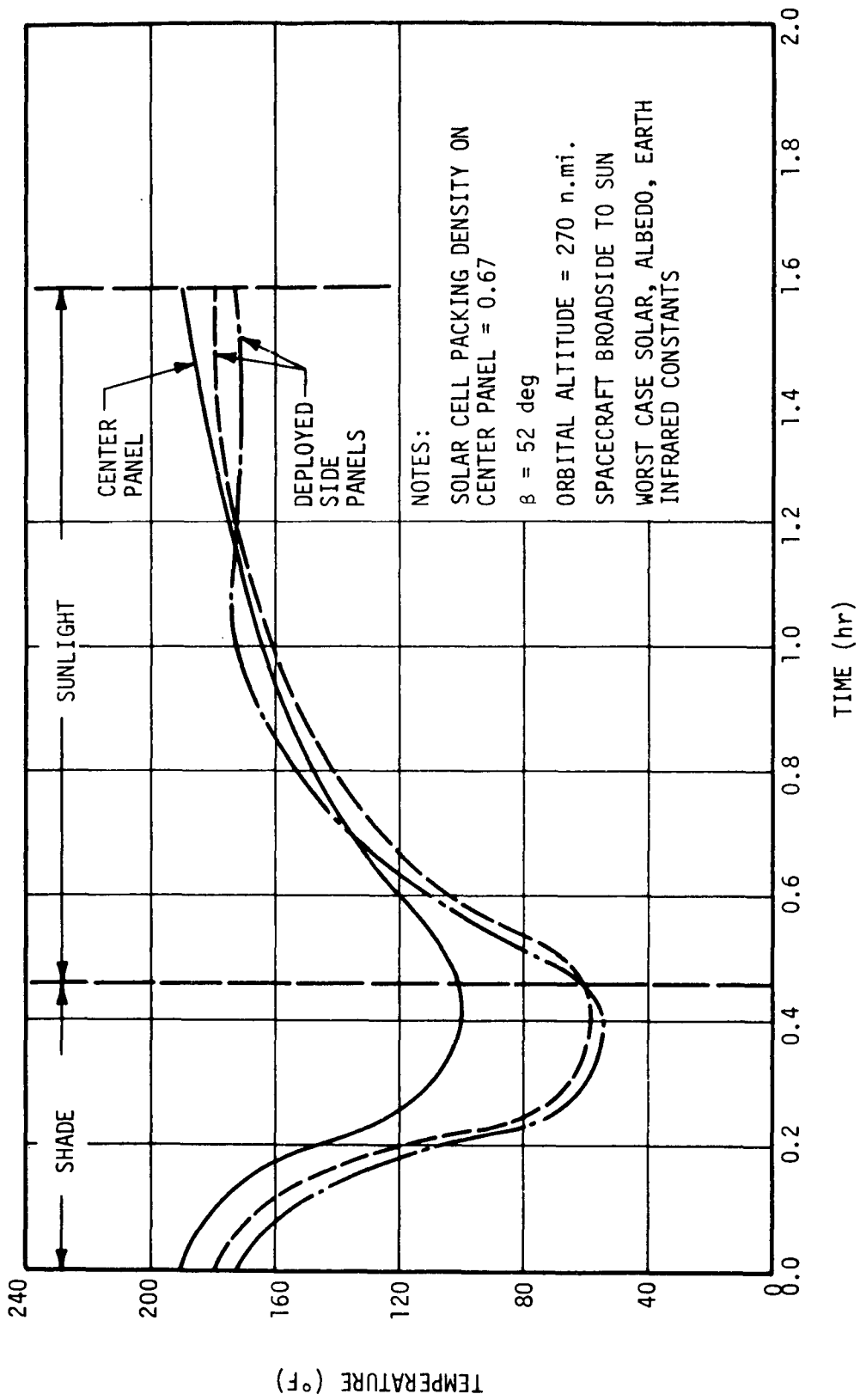


Figure D-14. Body-mounted solar panel temperature history with reduced solar cell packing density.

The angle β , the declination of the sun with respect to the orbit plane, was assumed to be equal to its maximum possible value of 52 degrees (based on the assumed angle of inclination of the orbit plane to the equator of 28.5 degrees). This value of β results in the maximum duration of exposure of the spacecraft to direct solar radiation.

As illustrated in Figure D-14, the use of a solar cell packing density of 0.67 on the center panel results in a predicted maximum center panel temperature of 190° F. This represents a reduction of 30° F below the corresponding value of 200° F which was predicted previously for the center panel of the pre-Phase A conceptual design with a packing density of 1.0. Moreover, the previously predicted value of 220° F was based on the assumptions of less severe, nominal environmental heat source constants. Therefore, it may be concluded that reduction of the solar cell packing density indeed provides an effective method for controlling the maximum temperature of the center solar panel without creating a power deficit. In fact, preliminary calculations indicate that the solar cell packing density of the center panel could be increased to approximately 0.8, providing an additional 5 percent increase in total available load power without resulting in an excessive solar panel temperature.

6. Reflective Strip on Center Solar Panel. An analysis was performed to determine the feasibility of reducing the maximum center solar panel temperature to less than 212° F by replacing a fraction of the warmest solar cell modules in the center of the panel with an equal rectangular area which is coated with a reflective material, as illustrated in Figure D-15. This concept provides an alternate method of reducing the solar cell packing density of the center panel. The adjacent side solar panels would be folded out, as shown in Figure D-15, to compensate for the loss in available power which would accompany reduction of the solar cell packing density on the center panel. The reflective center strip would have a low ratio of solar absorptivity, α_s , to emissivity, ϵ , and would operate at a significantly lower temperature than the conventional solar cell modules. Thus the reflective center strip would provide an additional heat sink to which heat could be conducted from the adjacent solar cell modules of the center panel.

The effectiveness of the reflective center strip in removing heat from the adjacent modules would depend primarily on its width and its surface optical properties. As the width of the reflective strip is reduced, its effect on the temperature response of the adjacent modules is diminished. As the α_s/ϵ ratio of the reflective strip is decreased, the reduction in temperature of the adjacent modules increases. Thus, it would be beneficial to use a reflective coating with the lowest possible α_s/ϵ ratio.

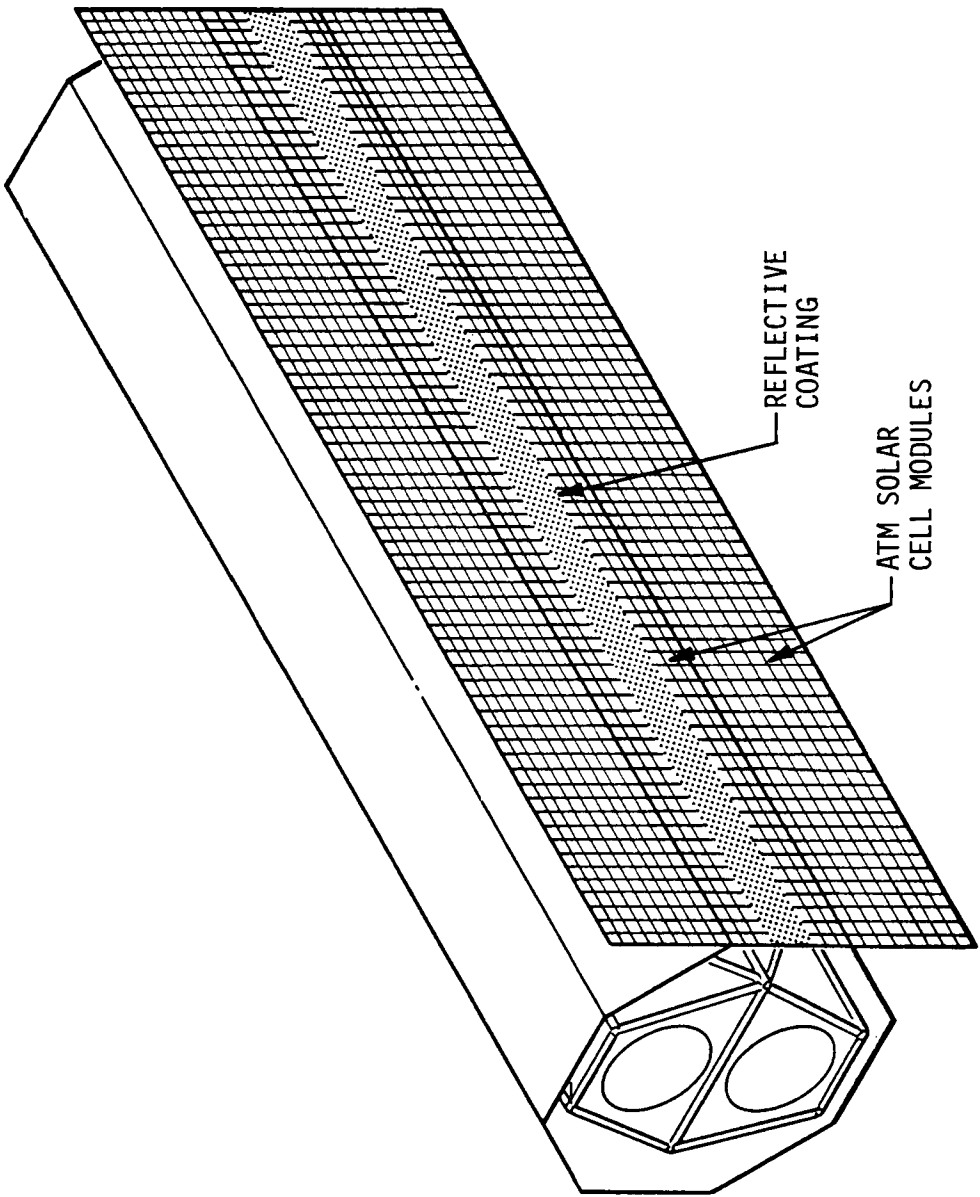


Figure D-15. Solar panel temperature control by adding reflective strip.

The predicted orbital temperature histories of the solar panels and the reflective strip are presented in Figure D-16. The results shown in this figure illustrate that the predicted maximum temperature of the solar cell modules which are adjacent to the reflective strip on the center panel is 202° F. Since this value is well below the prescribed upper limit of 212° F, the "reflective center strip" concept considered herein appears to be a feasible approach for thermal control of the center solar panel. Moreover, a further increase in available power could be achieved by reducing the width of the reflective strip to less than one-third of the total width of the center panel. However, the width of this reflective strip must be maintained sufficiently large to prevent the temperature of the adjacent solar cell modules from exceeding the prescribed upper limit of 212° F. It is estimated that the minimum width of the reflective strip which would be compatible with the upper temperature limit of 212° F would be 0.67 feet, or one-fifth of the center panel width. This would result in use of 80 percent of the area of the center panel for solar cell modules. The resulting total available power (average) would increase by approximately 5 percent through increasing the solar cell packing density of the center panel from 0.67 to 0.8. Thus, considering a representative available power level (average) of 800 to 900 watts, as determined from the conceptual design studies, the total available load power would increase by approximately 40 to 45 watts as a result of increasing the solar cell packing density of the center panel from 0.67 to 0.80.

Of course, the desired reduction in center solar panel temperature could also be achieved through the utilization of a uniformly reduced solar cell packing density over the center panel, as described previously, rather than with the reflective center strip concept considered here.

As shown in Figure D-16, the deployed side solar panels reached a maximum predicted temperature of 180° F when considering maximum environmental constants; whereas, their maximum predicted temperature when considering nominal values of these constants (solar constant = 429 Btu/hr-ft²; albedo = 0.3; earth infrared = 75 Btu/hr-ft²) was 170° F as described previously (Fig. D-12).

7. Summary of Solar Panel Thermal Control Analyses. The results of the evaluations of the candidate solar panel thermal control concepts are summarized in Table D-8 in the order in which they were discussed previously. The selected solar panel thermal control concept is illustrated in Figure D-17. A comparison of Figures D-17 and D-1 reveals the additional modifications in the HEAO-C spacecraft design which evolved. The truss-type

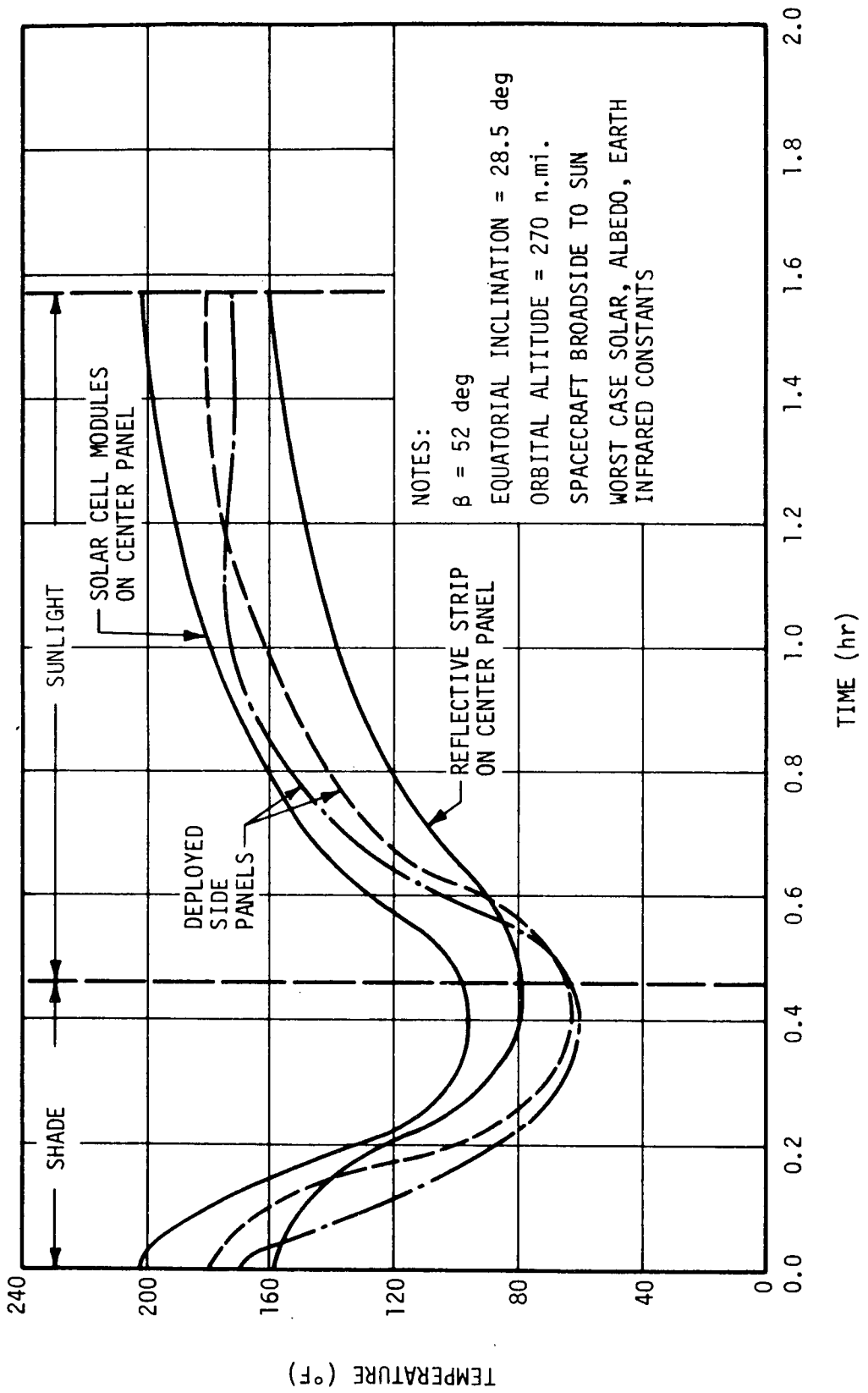


Figure D-16. Body-mounted solar panel temperature history with reflective strip on center panel.

TABLE D-8. SUMMARY OF SOLAR PANEL
THERMAL CONTROL SCHEME EVALUATION

Concept	Max Solar ^a Panel Temp. (° F)	Remarks
Rotation of Center Solar Panel Off Solar Vector	222	
Removal of Insulation Behind Solar Panels	209	Adjacent subsystem operating temper- atures marginal
Folding Out of Side Solar Panels Without Further Modifications	222	
Reduced Solar Cell Packing Density on Center Panel with Foldout Side Panels	190	Provides power growth potential; requires nonstandard solar cell module design
Reflective Strip on Center Solar Panel with Foldout Side Panels	202	Provides power growth potential; standard solar cell module designs may be employed
Baseline	187	Combines advantages of above 5 concepts

a. Worst case environmental constants

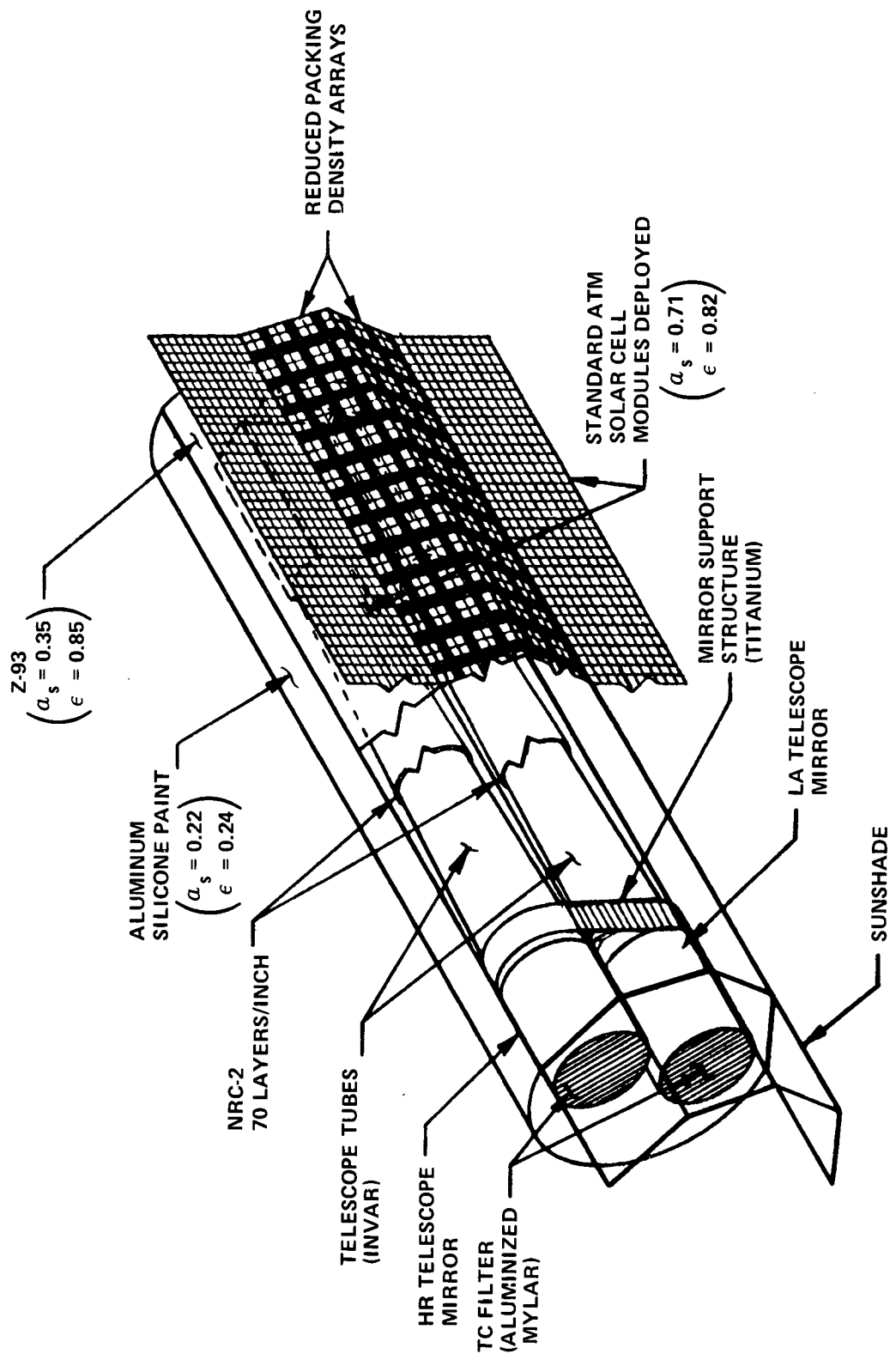


Figure D-17. Early Phase A thermal control concept.

optical bench was discarded in favor of the two-tube design and the octagonal spacecraft geometry was modified as illustrated. Both of these changes were necessitated by space requirements associated with the addition of a third X-ray telescope and the need to mount the telescope mirrors at the top of the spacecraft in the launch position.

The selected solar panel design uses two body-mounted panels with reduced solar cell packing density and two deployed panels with conventional packing density. The spacecraft is oriented corner-to-the-sun, which results in an angle between the solar vector and the normal to each body-mounted solar panel of 22.5 degrees. The selected concept combines the desirable thermal control features of the reduced packing density scheme, the off-normal pointing scheme and the foldout scheme, all of which were discussed previously. Moreover, additional solar panel area was provided through the addition of a fourth panel. This additional area greatly increases the margin of available power and, thereby, provides a power growth potential which could not be attained with three solar panels. This latter feature was probably the most important factor in the selection of the illustrated solar panel design.

It is important to note that, if the deployment of the two outer solar panels becomes objectionable because of aerodynamic drag or reliability considerations, this requirement could be eliminated through the application of the thermal capacitor or heat pipe concepts discussed below. Either of these concepts would permit the use of all body-mounted solar panels with conventional solar cell packing density. As illustrated in Figure D-18, the packing density of the body-mounted solar arrays can be as high as approximately 62 percent before the maximum possible array temperature exceeds the allowable 212° F.

Employment of Louvers; Heat Pipes; and a Thermal Capacitor

1. Louvers. The use of louvers was considered as a method to reduce the temperatures of the spacecraft outer skin panels and, consequently, the maximum temperature of the solar panels. Previous thermal analysis performed on the HEAO-C spacecraft can be used to estimate the effectiveness of louvers to provide increased heat conduction from the solar panels.

The proposed application of louvers is illustrated in Figure D-19. Since the optical bench blocks radiation from the backsides of the solar panels to space, even with the louvers open, the only apparent advantage of louvers

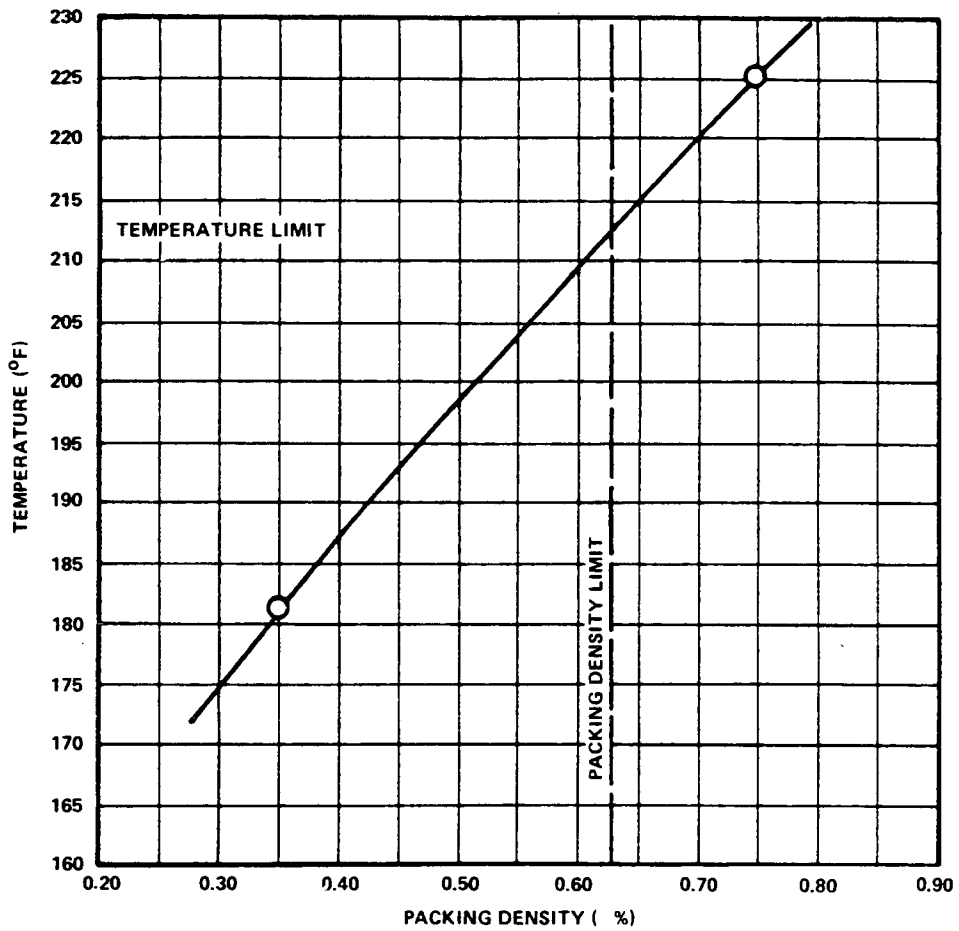


Figure D-18. Maximum body-mounted solar panel temperature as a function of solar cell packing density.

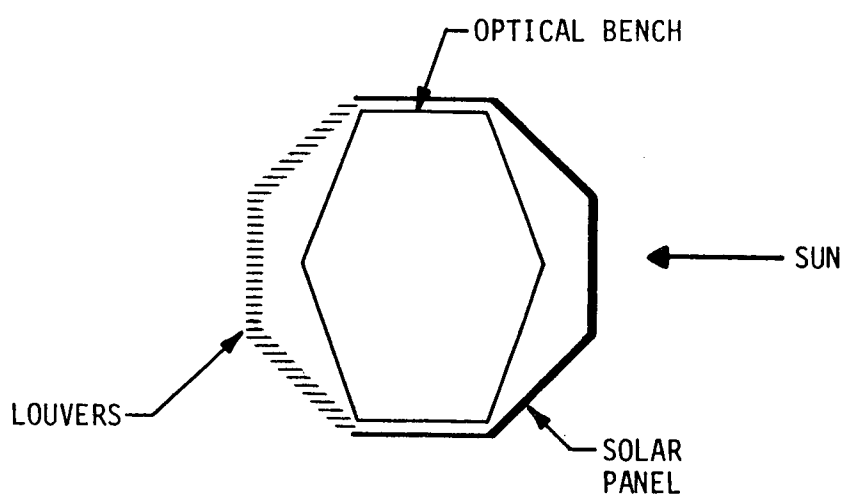


Figure D-19. Schematic of louver thermal control concept.

in the proposed application would be to increase the effective emissivities of the skin panels to which they are attached. Increased emissivity would indeed reduce the adjacent skin panel temperatures; however, high emissivities of these panels could be achieved simply through the application of appropriate thermal control paints to the panels.

Moreover, the reduction in solar panel temperature which could be achieved by decreasing the spacecraft skin panel temperatures through increased emissivity is insufficient to solve the solar panel heating problem. This fact may be illustrated by examination of previously predicted HEAO-C solar panel and spacecraft backside temperature histories based on two contrasting cases of high and low emissivities of the remaining five sides of the spacecraft. The predicted temperature histories based on a relatively high emissivity of 0.85 are approximately equivalent to those that would result from the proposed use of louvers.

Figure D-20 presents the predicted temperature histories of the center solar panel and of the spacecraft backside based on assumed emissivities of the remaining five skin panels of 0.24 and 0.85, respectively. These calculations correspond to the spacecraft/orbit orientation with the spacecraft broadside-to-the-sun and earth-sun vector lying in the orbit plane ($\beta = 0$ degrees). As illustrated in Figure D-20, increasing the emissivity of the five skin panels from 0.24 to 0.85 results in a large reduction of approximately 60°F to 70°F in the temperature of the spacecraft backside; whereas, the maximum predicted temperature of the center solar panel decreases by only 12°F , from 206° to 194°F .

The maximum predicted solar panel temperature of 220°F discussed previously was based on the spacecraft/orbit orientation with the spacecraft broadside-to-the-sun, $\beta = 58.5$ degrees. Unfortunately, predicted solar panel temperature histories have not been computed for this orientation with an assumed emissivity of 0.85 on the five remaining skin panels. However, it is reasonable to expect that the corresponding reduction in maximum solar panel temperature for the $\beta = 0$ degree orientation with increased emissivity on the five skin panels would be approximately equal to the reduction of 12°F which was predicted for the $\beta = 58.5$ degree orientation. Making this assumption, the reduction in maximum solar panel temperature which would result from the proposed use of louvers would be from 220°F to approximately 208°F for the $\beta = 58.5$ degree orientation. Since these temperature predictions are based on nominal values of environmental constants (solar, albedo, earth infrared) and solar panel surface optical properties, consideration of off-nominal variations in

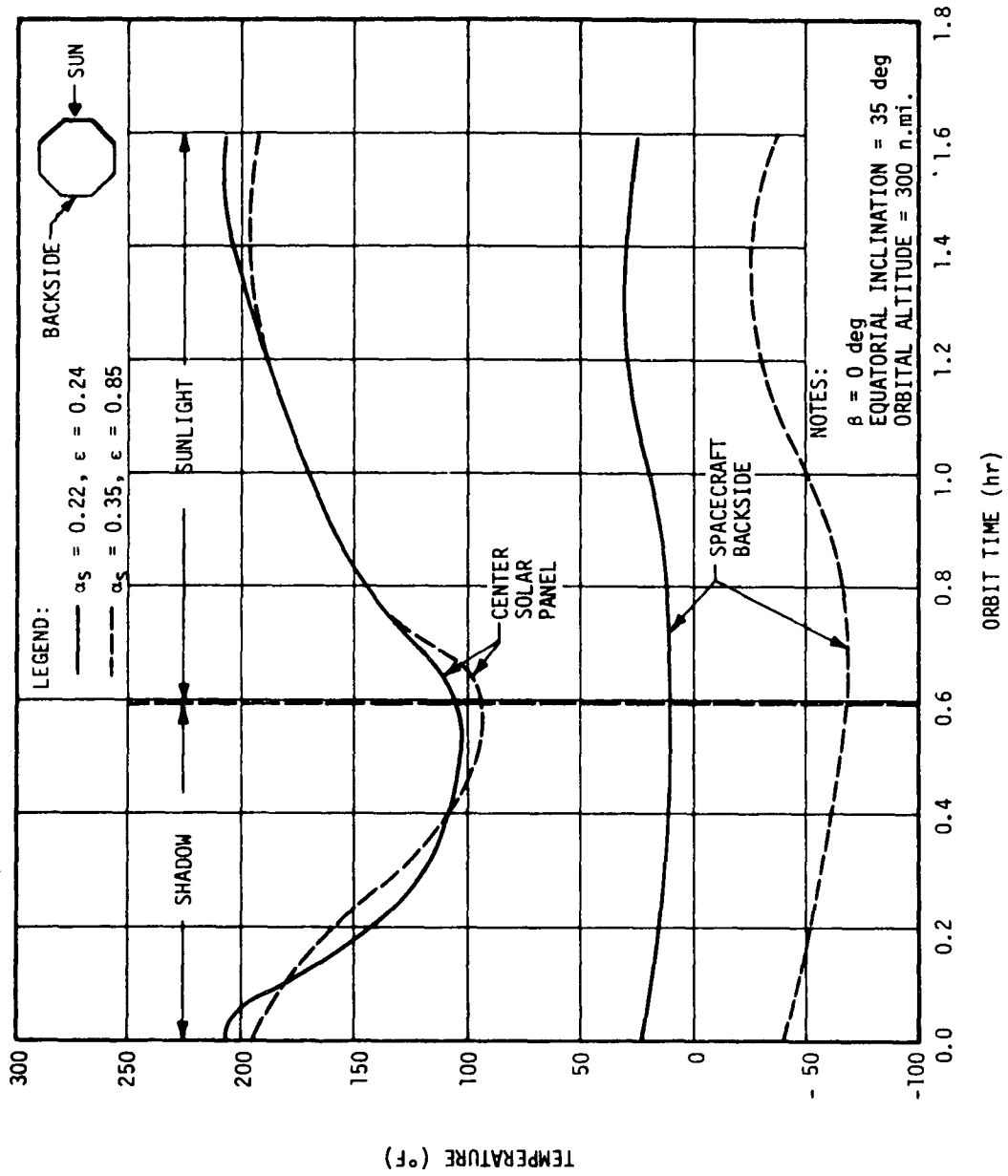


Figure D-20. Effect of variation in emissivity on center solar panel temperature.

these parameters would surely result in predicted solar panel temperatures exceeding the prescribed upper limit of 212° F. Therefore, it may be concluded that the proposed use of louvers would not reduce the maximum solar panel temperature sufficiently to solve the excessive heating problem.

2. Incorporation of Circumferential Heat Pipes into Spacecraft Skin.

An analysis was performed to evaluate the reduction in center solar panel temperature which could be achieved through the incorporation of circumferential heat pipes in the spacecraft skin, as illustrated in Figure D-21.

The highly efficient heat pipes would transfer heat almost isothermally from the warm side of the spacecraft to the cold side. The temperature distribution of the spacecraft skin structure would become progressively more uniform as the longitudinal heat pipe spacing is decreased; however, closer heat pipe spacing would also result in increased weight. Therefore, a tradeoff exists between the desired degree of temperature uniformity and the weight penalties which accompany close heat pipe spacing.

The potential benefits to be gained from employing circumferential heat pipes as described above are illustrated by the steady-state temperature predictions shown in Figure D-22. The predicted maximum solar panel temperature, which occurs midway between heat pipes on the surface of the center solar panel, versus heat pipe spacing is plotted in Figure D-22. The predicted heat pipe temperature, which is virtually invariant with circumferential position on the spacecraft, and the predicted surface temperature midway between heat pipes at the backside of the spacecraft are also plotted as a function of heat pipe spacing. It is noted that temperature predictions are presented in Figure D-22 for both the worst case instantaneous and the worst case orbital average environmental heat flux distributions.

The results presented in Figure D-22 indicate that the maximum solar panel temperature can be maintained below the allowable upper limit of 212° F with a heat pipe spacing of 4 feet or less. However, the environmental heat flux distributions used in these calculations were based on nominal values of environmental constants (solar, albedo, earth infrared), and the use of worst case values of these constants would result in calculated temperatures which would exceed those illustrated in Figure D-22 by approximately 11° F. Therefore, a maximum heat pipe spacing of 3 feet should be selected to provide assurance that the maximum solar panel temperature will not exceed 212° F during the mission. Moreover, the selected heat pipe spacing, ΔL , should result in an integral number of heat pipes in accordance

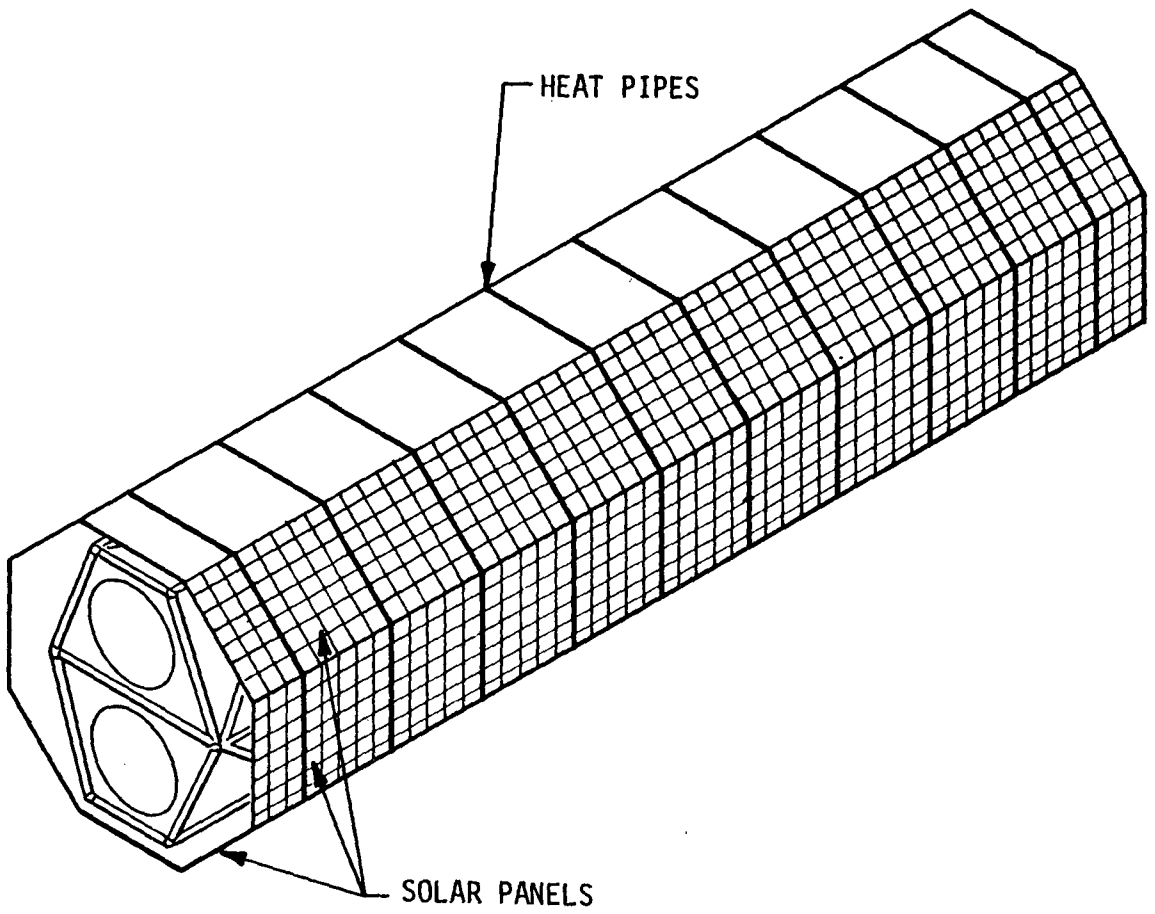


Figure D-21. Heat pipe scheme for solar panel thermal control.

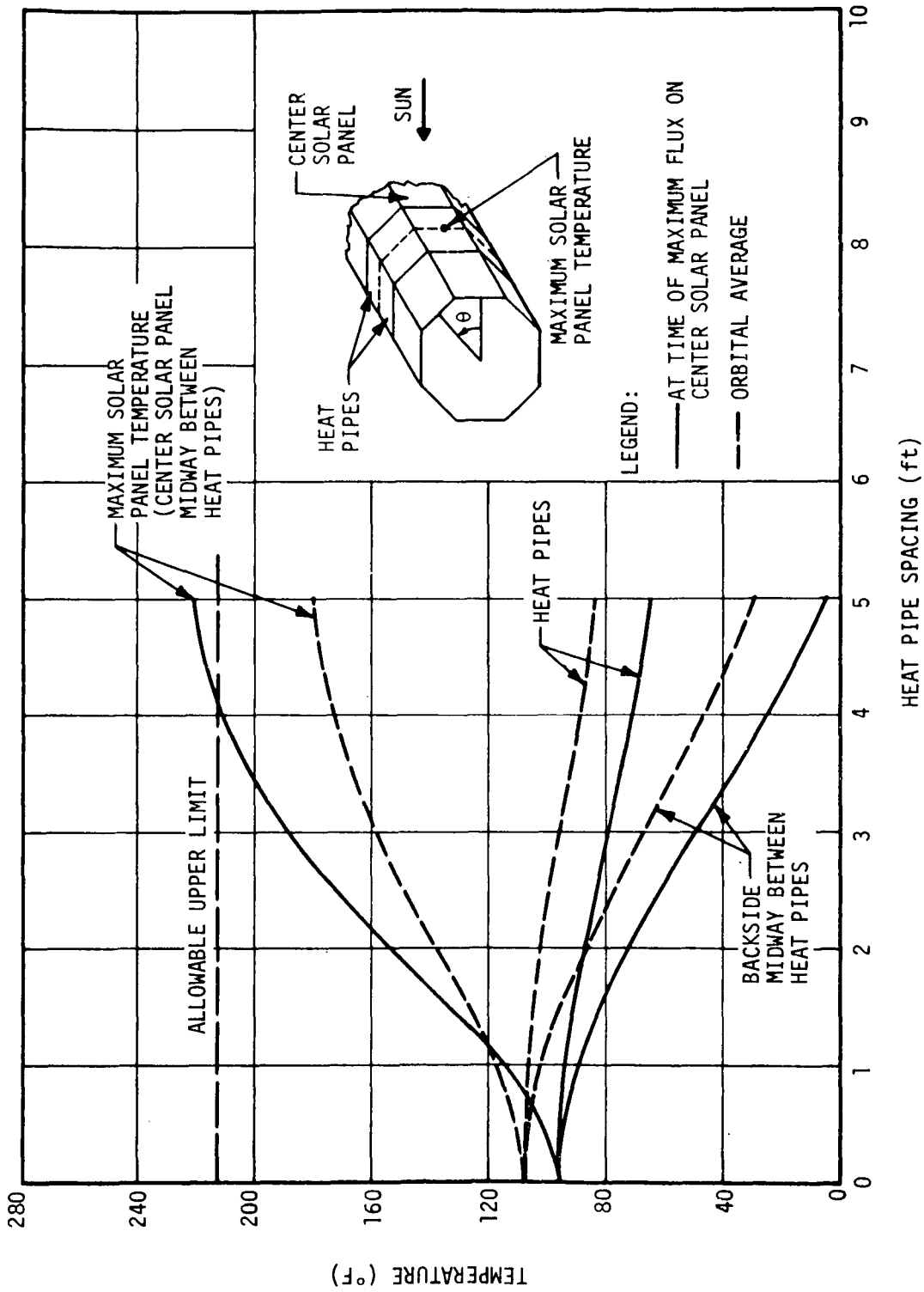


Figure D-22. Effect of heat pipe spacing on solar panel temperature.

with the relation

$$N = L/\Delta L,$$

where N is the number of heat pipes; L is the spacecraft length, ft; and ΔL is the heat pipe spacing, ft. The HEAO-C spacecraft length is approximately 30 feet. A heat pipe spacing of 3 feet would require 10 heat pipes and would result in a maximum solar panel temperature, based on nominal environmental constants, of approximately 188° F. When worst case environmental constants are considered, the predicted maximum solar panel temperature increases to an estimated value of 199° F. Utilization of a heat pipe spacing of 2 feet would require 15 heat pipes and would reduce the predicted maximum solar panel temperature, based on nominal environmental constants, to approximately 154° F. Consideration of worst case environmental constants would increase this temperature to an estimated value of 165° F.

The selection of the most advantageous heat pipe spacing should be based on a tradeoff study considering the following criteria:

- Increase in solar cell power conversion efficiency with temperature reductions caused by decreased heat pipe spacing.
- Increase in weight penalty with decrease in heat pipe spacing.
- Increase in temperature of the backside of the spacecraft and accompanying degradation (increase) of heat sink temperature for rejection of subsystem heat load.
- Decrease in thermal bending of spacecraft with decreased lateral temperature difference which accompanies decreased heat pipe spacing.

The predicted circumferential temperature distributions around the surface of the spacecraft midway between heat pipes are plotted in Figures D-23 and D-24 as a function of heat pipe spacing for the orbital average and worst case instantaneous environmental heat flux distribution, respectively. The asymmetrical shape of the surface temperature distribution shown in Figure D-24 reflects the nonuniform environmental heat flux distribution around the spacecraft at the selected worst-case position in orbit.

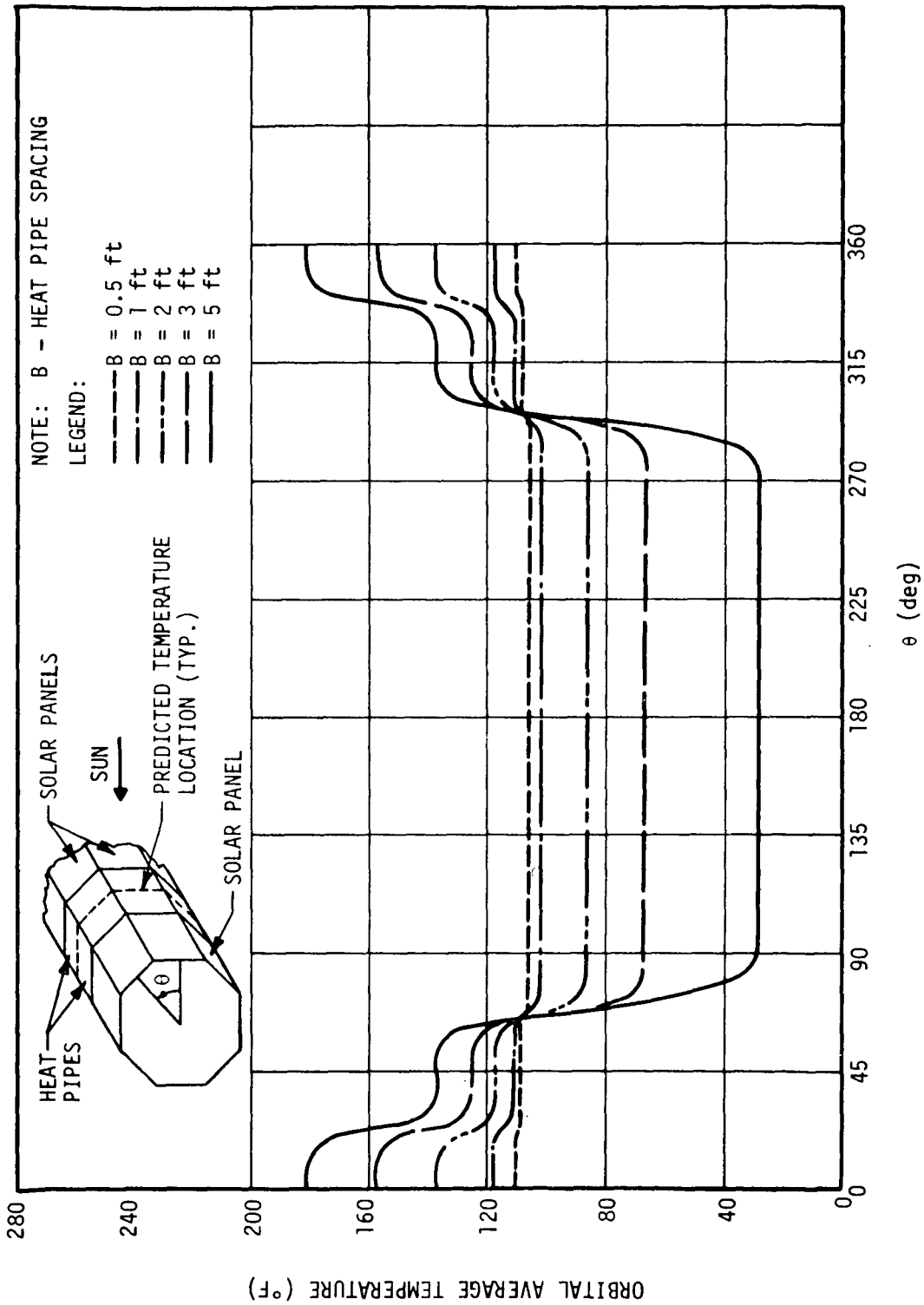


Figure D-23. Solar panel orbital average circumferential temperature distribution with heat pipe spacing as a parameter.

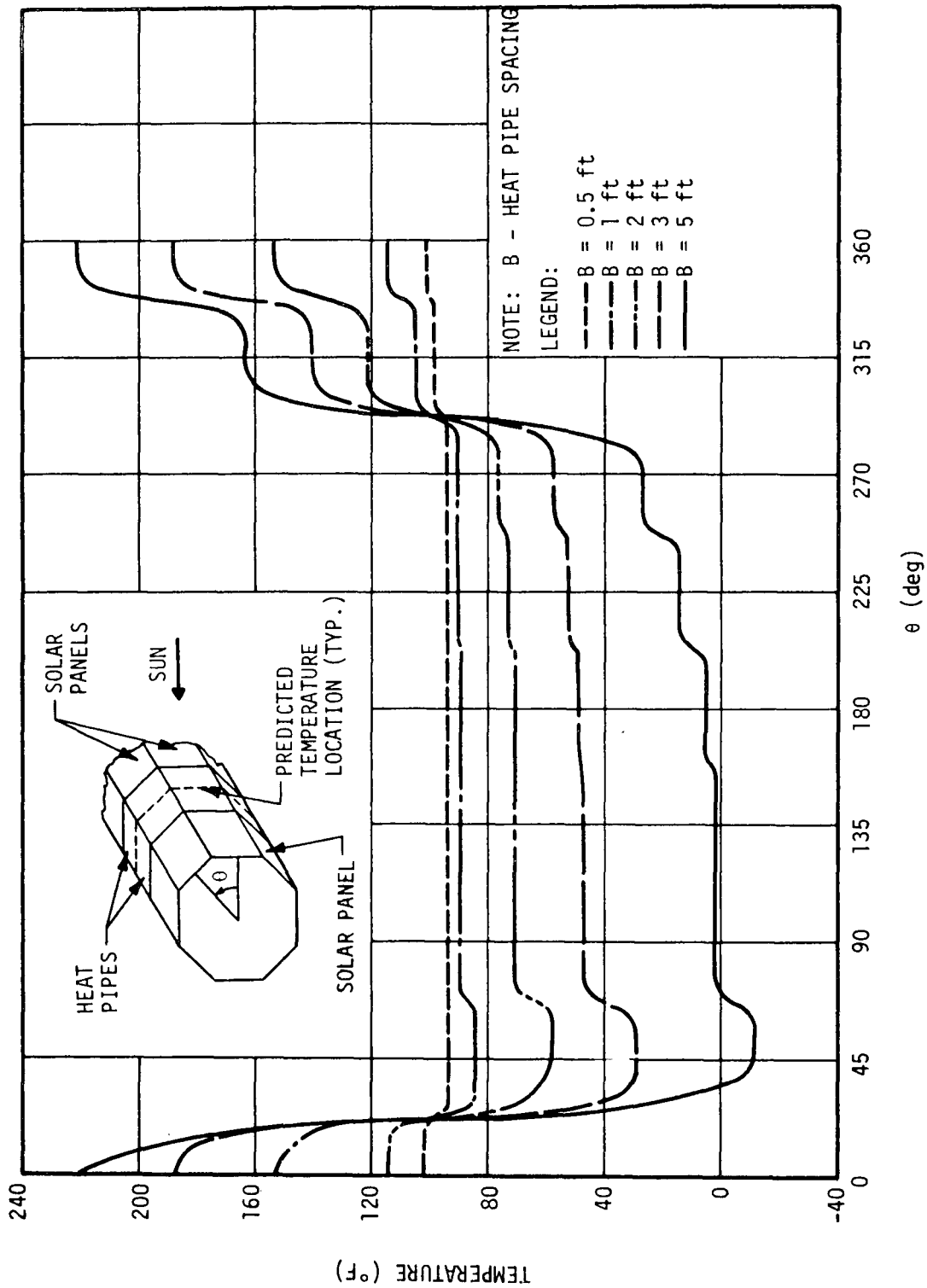


Figure D-24. Solar panel maximum circumferential temperature distribution with heat pipe spacing as a parameter.

As illustrated by Figures D-23 and D-24, a rather small heat pipe spacing of 1 foot or less would be required to provide an extremely uniform surface temperature distribution around the circumference of the spacecraft. However, even the rather wide heat pipe spacing of 3 feet, selected previously, would reduce the maximum temperature differential between the subsolar and antisolar sides of the spacecraft from approximately 220° F without heat pipes to approximately 156° F. This reduction would result in a decrease of approximately 29 percent in the lateral deflection or "hot dogging" of the spacecraft shell due to differential thermal expansion of the warm and cold sides.

Preliminary heat pipe sizing calculations indicated that the heat pipes for use in the application described herein should have an inside diameter of 1 to 2 inches, and that water or ammonia would be a suitable working fluid; however, compatibility between working fluids and container material should be carefully considered prior to selection of either. For example, water and aluminum would seem to represent the best working fluid/container material combination based on separate evaluations of their performance characteristics; however, in a water/aluminum heat pipe, hydrogen is generated so rapidly that the heat pipe ceases to operate efficiently within hours. Therefore, ammonia/aluminum may prove to be the most advantageous working fluid/container material combination. Calculations indicate that the required liquid capillary pumping requirements for continuous heat pipe operation could be provided by available heat pipe wick materials.

From this analysis, and from past experience (e.g., ATS-E satellite), it is apparent that the use of circumferential heat pipes provides an effective method for controlling the temperature of body-mounted solar panels. If employed on the HEAO-C spacecraft, the circumferential heat pipes would permit the use of a conventional solar cell packing density on the center panel, and the need for folding out the side solar panels would be eliminated (unless additional solar panel area is required for power purposes). Since the heat pipe contains no moving parts, the reliability of this system would be excellent. Moreover, the reduced aerodynamic drag which would result from using all body-mounted solar panels would permit achievement of a two year orbital lifetime from a lower initial orbital altitude.

3. Thermal Capacitor. The use of phase change materials (PCM) in passive thermal control systems is becoming quite attractive for long-life satellites and spacecraft. Basically, a system utilizing PCM consists of a core filled with a substance that is capable of undergoing a solid-to-liquid phase change at a desired operating temperature. This material is put close to the component that is to be controlled. Excessive temperature

variation of the critical component will be dampened as a result of heat absorption and rejection by the PCM at a nearly constant temperature.

This method of thermal control was applied to the middle solar panel in the HEAO-C spacecraft thermal model. The thermal and physical characteristics of acetamide (CH_3CONH_2), an organic compound, were used. It was assumed that the acetamide is encapsulated by the cells of the aluminum honeycomb which acts as a substrate for the solar cells. Ninety pounds of the compound were assumed to be added to the panel. This amount would fill the cells to a depth of 0.29 inch, allowing 0.085 inch for the column to expand.

The orbital temperature histories of the three solar panels, with the PCM contained in the honeycomb substrate of the center solar panel, were predicted using a modified version of the HEAO-C/CINDA⁵ thermal model.

Figure D-25 presents the predicted temperature response of the solar panels utilizing the acetamide behind the middle solar panel. These calculations are based on nominal values of environmental constants (solar, albedo, earth infrared) and a β angle of 58.5 degrees. The results show the temperature cycling to be reduced from 82° F (without PCM) to 19° F (with PCM), with a maximum temperature of 187° F.

Since temperature cycling and overheating are considered to be two of the major problems with the HEAO-C solar panels, it is concluded that this method of thermal control should be considered as a possible solution. Sufficient research has been done on PCM to indicate that some of these materials will perform satisfactorily in space application.

5. CINDA is the acronym for Chrysler Improved Numerical Differencing Analyzer.

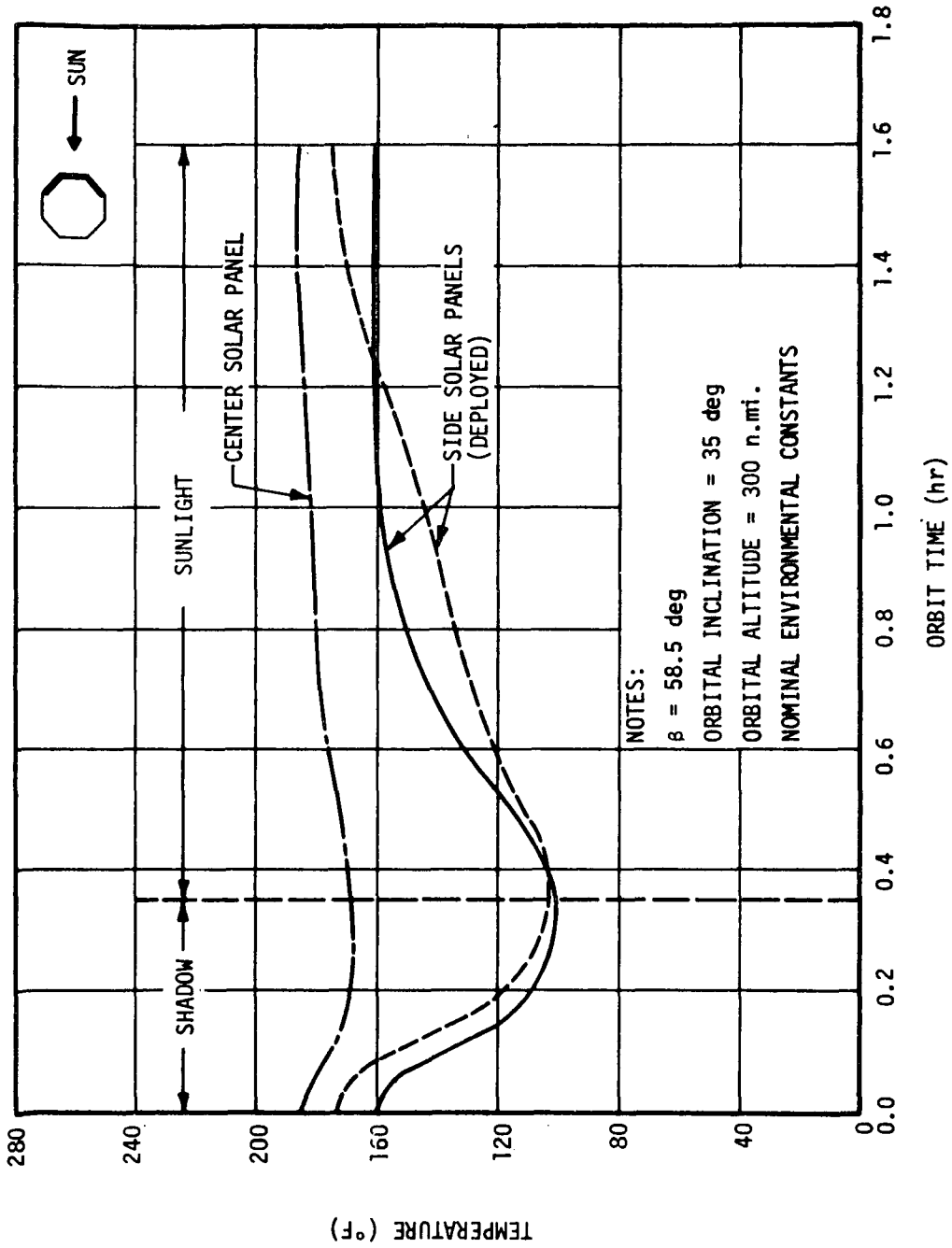


Figure D-25. Solar panel temperature history with 90 pounds of a phase change material behind center solar panel.

50

Investigation of Operating Temperature Limits for HEAO-C Solar Panels

The maximum allowable temperature limit of 212° F for the HEAO-C solar panels was assumed for the Phase A Study. This prescribed upper limit was based on previous test experience with ATM solar cell modules in which prolonged thermal cycling between the temperature limits of -31° F to 212° F resulted in cracks and plastic deformation of the cell interconnecting tabs and solder joints. Because of system redundancy, no electrical performance degradation occurred during any of the tests.

The primary cause of the failures was determined to be inadequate stress relief in the bus bar interconnections. The excessive stresses resulted from differences in thermal expansion rates between the aluminum, silicon, copper, and adhesive material used in module construction. No differentiation was made in this report between the contribution to the failures made by the maximum temperature and by the difference between maximum and minimum temperatures experienced in the cycling. It appears that the temperature change per cycle would have made as much or more contribution to the failures as would the maximum temperature value. However, a module design change was tested and approved; this eliminated the high failure mode which had been experienced with the original design. Unfortunately, tests were not conducted at temperatures above 212° F for the improved design; therefore, the actual maximum allowable temperature was not established.

It is also important to note that the predicted variation in solar panel temperature during orbit for the HEAO-C spacecraft is much smaller than the variation imposed during the ATM thermal cycling tests. The predicted variation in the HEAO-C center solar panel temperature, considering body-mounted solar panels, solar cell packing density of 0.89, and maximum values of the environmental heat source constants, ranged from 150° F to 230° F; whereas, the ATM solar cell modules were subjected to thermal cycling between the much wider temperature limits of -31° F to 212° F. Thus, the range of temperature variation imposed during the ATM thermal cycling tests (243° F) was three times greater than the predicted variation (80° F) in the HEAO-C solar panel temperature. Since the thermal stresses are proportional to the range of variation in temperature, rather than to the maximum temperature alone, it is obvious that the HEAO-C solar panels will be subjected to a less severe thermal stress environment than the previously tested ATM solar cell modules. Therefore, it becomes questionable as to whether the prescribed maximum allowable temperature of 212° F is really applicable to HEAO-C.

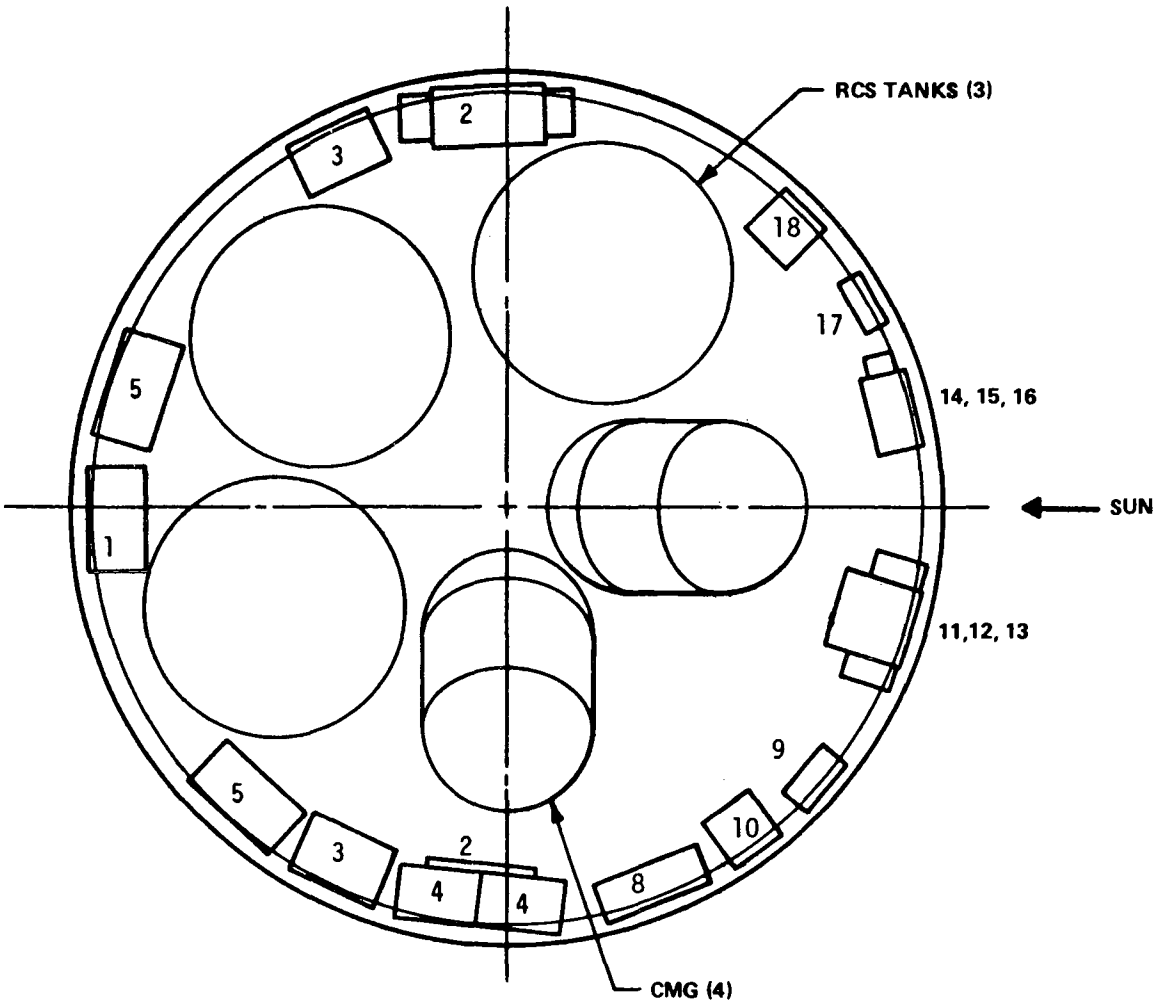
From the information presented herein, it may be concluded that further investigation is warranted to define more accurately the allowable solar panel temperature limits (upper and lower) for HEAO-C. Specification of an upper temperature limit of 212° F based on previous ATM test results may place an unnecessary restriction on the spacecraft design which could result in unwarranted and costly design modifications. It would appear that design improvements since the ATM problem, which occurred approximately two years ago, will permit solar panel operation above the recommended 212° F upper limit.

Subsystem Module Thermal Control Feasibility Analysis

An alternative method of accommodating the HEAO-C subsystems would consist of packaging them inside a cylindrical module which would be attached to the nonviewing end of the spacecraft. One possible arrangement of the subsystems inside the equipment module is illustrated in Figure D-26. A preliminary design of the equipment module indicated that its dimensions would be approximately 10 feet in diameter and 3 feet deep.

A preliminary thermal analysis was performed to estimate the temperature response of the subsystems within the module during orbit. Environmental heating rates for the module were determined using an orbital heat rate program for a 270 nautical mile circular orbit, inclined 28.5 degrees to the equator. The angle β between the orbit plane and the solar vector was assumed to be equal to its maximum value of 52 degrees, which allows maximum duration of exposure to direct solar radiation. Maximum values of the environmental heat source constants (solar, albedo, earth infrared) were used to ensure consideration of the maximum heating situation. The longitudinal axis of the equipment module was assumed to be oriented perpendicular to the solar vector.

The predicted environmental heating rates were input to a transient thermal model of the module which consisted of 44 nodes. The required thermal radiation interchange factors between nodes were evaluated using a separate digital computer program. The forward bulkhead of the module



- | | |
|--------------------------------|----------------------------------|
| 1 SOLAR POWER DISTRIBUTOR (2) | 10 GYRO PACKAGE (3) |
| 2 POWER CONTROL ASSEMBLY (2) | 11 MEMORY (2) |
| 3 BATTERY ASSEMBLY (8) | 12 PCM ENCODER, FORMAT GENERATOR |
| 4 REGULATOR ASSEMBLY (2) | 13 COMMAND PROCESSOR, CLOCK |
| 5 BATTERY CHARGER ASSEMBLY (8) | 14 FREQUENCY MUX |
| 6 * | 15 PSK DEMODULATION |
| 7 * | 16 TRANSPONDER (2) |
| 8 CMG ELECTRONICS | 17 DATA STORAGE CONTROL |
| 9 COMPUTER (2) | 18 TAPE RECORDER (4) |

*NOT SPECIFIED

Figure D-26. Arrangement of subsystems within equipment module.

was assumed to be adiabatic; i. e., heat exchange between the subsystems module and the spacecraft was considered to be negligible. All other outer surfaces of the module were considered to be exposed to the space environment. The module skin material was assumed to be 6064-T6 aluminum. Heat transfer to or from the RCS tanks and the CMGs was assumed to result solely from thermal radiation since their mounting structures were undefined. Surface optical properties assumed in the analysis were:

- External skin: $\alpha_s = 0.35$, $\epsilon = 0.85$
- RCS tanks: $\epsilon = 0.04$
- Remaining inside surfaces: $\epsilon = 0.9$.

Perfect thermal contact was assumed between the wall-mounted subsystem components and the adjacent wall structure. Neither the inside surface of the module wall nor the RCS tank walls was considered to be insulated.

The thermal model described above was input into the CINDA digital computer program for simulation of the heat transfer process during orbit. Subsystem temperatures were predicted as a function of time for a total simulated orbit time of 55 hours. The results of the thermal analysis of the subsystems equipment module are summarized in Table D-9, where the required heat dissipation, allowable temperature limits, and predicted temperature range during orbit for each subsystem component are presented.

Examination of Table D-9 reveals that all of the subsystems were predicted to remain within their allowable operating temperature limits with the exception of the two computers. The computers were predicted to experience an operating temperature range of 234° F to 241° F during orbit, which greatly exceeds their maximum allowable temperature limit of 120° F; however, the excessive predicted computer temperatures are readily explainable since each of these units generated a relatively large amount of excess heat (65 W/unit) within a small envelope (3 inches by 3 inches by 7 inches). Moreover, the computers were considered to be in perfect contact with the warm subsolar surface of the module and close to each other. Therefore, it appears likely that relocation of the computers to a cooler area of the module, e. g., the antisolar surface, and spacing them farther apart, would reduce their operating temperatures significantly. Whether additional thermal control measures would be required to reduce the computer temperatures to an acceptable level cannot be determined without further analysis.

The preliminary thermal analysis described herein indicates that the subsystems equipment module would be feasible from a thermal control standpoint; however, several simplifying assumptions were invoked to facilitate performance of the analysis within the allotted time frame, e.g., the assumption of perfect thermal contact between the subsystem components and the wall structure. Therefore, it is recommended that final conclusions regarding the thermal control feasibility of the subsystems equipment module be withheld until a more rigorous thermal analysis is performed.

TABLE D-9. SUMMARY OF SUBSYSTEMS EQUIPMENT
MODULE THERMAL ANALYSIS

Subsystem Component	Number of Units	Average Heat Dissipation Per Unit (W)	Allowable Temperature Limits (°F)	Temperature Range ^a (°F)
Solar Power Distributors	2	20	160 Max	-2 to 2
Power Control Assemblies	2	30	160 Max	26 to 35 ^b
Battery Assemblies	8	15	0 to 50	26 to 34 ^b
Regulator Assemblies	2	30	160 Max	48 to 50
Battery Charger Assemblies	8	3.8	160 Max	-15 to 6
CMG Electronics	1	9	160 Max	104 to 132
Computers	2	65	0 to 120	234 to 241
Gyro Packages	3	15	0 to 140	114 to 126
Memories	2	28	0 to 120	71 to 102 ^b
PCM Encoder, Format Generator	1	5.3	160 Max	52 to 73
Command Processor, Clock	1	12.7	160 Max	64 to 87
Frequency MUX	1	2	160 Max	28 to 64
PSK Demodulation	1	0.4	160 Max	38 to 65
Transponders	2	18.5	160 Max	44 to 64 ^b
Data Storage Control	1	1	160 Max	29 to 63
Tape Recorders	4	3.3	0 to 130	25 to 32
RCS Tanks	3		40 to 140	60 to 63 ^b
Control Moment Gyros	4	18	-40 to 120	38 to 42 ^b

NASA-MSFC

a. Range represents variation during orbit after 55 hours of flight.

b. Signifies that variations are primarily due to component locations, rather than to transient effects.

TABLE OF CONTENTS

	Page
Coordinate Systems	E- 1
1. Reference Coordinates	E- 1
2. Sun Sensor Outputs	E-16
3. Target Star Pointing	E-23
Euler Equations for the HEAO-C.	E-37
Disturbing Torques.	E-42
Star Tracker Selection Analysis	E-51
HEAO-C Star Search Program	E-58
Alternate Sensors.	E-62
1. Gimbal Star Tracker (GST)	E-62
2. Reference Gyro Assembly (RGA)	E-65
3. Magnetometer	E-66
Alternate Control Moment Gyro Configurations	E-67
1. Scissored Pair CMG Configuration	E-67
2. Skewed Configuration of Five or More Gyros.	E-69
Control Law Summary.	E-70
1. Attitude Control Using Reaction Control System (RCS)	E-70
2. Attitude Control Using CMGs	E-75
a. Four-Skewed CMG Configuration.	E-79
b. Skew Angle and Momentum Capacity	E-85
c. CMG Gimbal Control.	E-87
d. The Pseudo Inverse Steering Law	E-94
e. The MSFC Maximum Contribution Steering Law	E-98

TABLE OF CONTENTS (Continued)

	Page
Linear Analysis of HEAO-C Control Systems	E-103
1. Equations of Motion and System Linearization	E-103
2. Linear System Analysis	E-115
a. System I	E-115
b. System II	E-120
c. System III	E-124
d. System IV	E-131
3. Conclusions	E-135
Alternate System Description	E-138
1. Description	E-138
2. Magnetic Torquer	E-140
3. Magnetic Control Law	E-141
4. Electromagnet Sizing	E-143
5. Location of Electromagnets	E-147
6. Magnetic Field Distribution	E-148
7. Magnetic Shielding	E-153
8. Magnetic Field Effects on Components	E-155
9. CMG Steering Law	E-158
10. Magnetometer	E-159
CMG Momentum Envelope Program	E-160
Pointing Capability Study of the HEAO-C Attitude Controller	E-167
Attitude Sensing and Control System Performance Simulations	E-174
1. Reaction Control System Simulation	E-174
a. General Equations	E-174
b. Rotational Dynamics	E-176
c. Vehicle Dynamics	E-176

TABLE OF CONTENTS (Continued)

	Page
d. Translational Dynamics	E-176
e. Simulation Results	E-177
f. Baseline System.	E-177
g. Alternate RCS Configuration.	E-183
h. Conclusions.	E-187
2. Control Moment Gyro Performance Simulations.	E-188
Reaction Control System	E-199
1. Reaction Engine Assembly/Reaction Engine Module Design and Performance Aspects	E-199
a. Overall Configuration	E-199
b. REA/REM Performance and Requirements	E-206
c. Rocket Engine Assembly Design	E-206
d. Thrust Chamber Valve	E-209
e. Thrust Chamber Assembly.	E-209
f. Heat Shield Assembly	E-209
g. REM Thermal Design	E-212
h. REM Structural Design	E-215
i. REA Performance	E-217
j. Conclusions.	E-218
2. Alternate Reaction Control System Concepts for the Baseline HEAO-C Spacecraft	E-221
a. Baseline HEAO-C RCS Alternate REM Location.	E-221
b. RCS/OAS Main Tank Manifold.	E-224
c. A Cold Gas RCS/Magnetic Torquer Concept	E-228
3. Reaction Control System Concepts for Alternate HEAO-C Spacecraft.	E-232

TABLE OF CONTENTS (Concluded)

	Page
4. Other Reaction Control System Analyses	E-239
a. Other Thrusters.	E-241
b. Blowdown Versus Pressure Regulated Pressurization System	E-242
c. Catalyst Bed Lifetime	E-242
d. Contamination Due to Thruster Exhaust	E-244
References	E-245

LIST OF ILLUSTRATIONS

Figure	Title	Page
E-1.	HEAO-C body reference coordinates	E- 2
E-2.	Earth-sun inertially referenced to Aries	E- 3
E-3.	Earth-orbit-ecliptic geometry	E- 4
E-4.	Geocentric coordinate systems	E- 5
E-5.	Geomagnetic coordinates, \tilde{X}_m , relative to the Greenwich Meridian.	E- 9
E-6.	Sun sensor output angles relative to two-body fixed planes and the sunline vector	E-17
E-7.	Celestial reference for a star.	E-24
E-8.	Solar coordinates	E-25
E-9.	Target star pointing	E-30
E-10.	The (1, 3, 2) sequence for target pointing and guide star acquisition	E-35
E-11.	Required tracker field: fraction of hemisphere observed .	E-54
E-12.	Permissible fixed tracker designs.	E-55
E-13.	Tracker field of view versus star magnitude relations . . .	E-57
E-14.	Star search coordinate systems	E-59
E-15.	Star search flow diagram.	E-61
E-16.	Star-empty look directions (northern hemisphere).	E-63
E-17.	Star-empty look directions (southern hemisphere).	E-64

LIST OF ILLUSTRATIONS (Continued)

Figure	Title	Page
E-18.	4-FACS CMG configuration	E- 68
E-19.	The RCS control law used in the baseline studies	E- 71
E-20.	The first RCS control law used in the alternate HEAO-C	E- 73
E-21.	Final control law for the alternate RCS configuration	E- 74
E-22.	CMG coordinate system.	E- 76
E-23.	CMG null coordinate	E- 77
E-24.	Skewed CMG geometry and null coordinates	E- 80
E-25.	HEAO single axis linear models constant gain steering law	E-109
E-26.	HEAO single axis linear models transpose steering law	E-110
E-27.	Linear system configurations	E-114
E-28.	System I, position gain versus position error due to dis- turbance torques	E-118
E-29.	System I, design — analysis chart.	E-119
E-30.	System II, error due to cyclical torques	E-124
E-31.	System II, root locus analysis	E-126
E-32.	System II, root locus analysis	E-126
E-33.	System II, root locus analysis	E-127
E-34.	System III, root locus analysis	E-131
E-35.	System III, root locus analysis	E-132

LIST OF ILLUSTRATIONS (Continued)

Figure	Title	Page
E-36.	System III, root locus analysis	E-133
E-37.	System IV, design example	E-136
E-38.	Open loop gain plots for typical System I, II, and III designs.	E-139
E-39.	Layout of the electromagnets and the magnetic field profile inside the spacecraft for Case I	E-148
E-40.	Layout of the three electromagnets inside the OAS.	E-149
E-41.	Magnetic field at point P due to a dipole magnet.	E-151
E-42.	Magnetic field distribution inside the spacecraft for Case II.	E-152
E-43.	Location of boxes P and Q in the spacecraft	E-154
E-44.	CMG configuration	E-161
E-45.	Four-skewed CMGs maximum momentum envelope	E-163
E-46.	Four-skewed CMGs maximum momentum envelope	E-164
E-47.	Four-skewed CMGs maximum momentum envelope	E-165
E-48.	Four-skewed CMGs maximum momentum envelope	E-166
E-49.	Linear analysis diagram	E-169
E-50.	Simulation diagram.	E-170
E-51.	Star tracker deadspace = 0 arc sec	E-172
E-52.	Star tracker deadspace = 1 arc sec	E-173

LIST OF ILLUSTRATIONS (Continued)

Figure	Title	Page
E-53.	TACS flow diagram.	E-175
E-54.	HEAO-C thruster characteristics	E-178
E-55.	Baseline HEAO engine layout and logic.	E-179
E-56.	Alternate RCS configuration.	E-184
E-57.	Performance of pseudo inverse law magnetics.	E-189
E-58.	CMG gimbal angles with magnetic CMG dump	E-190
E-59.	Dipole moment components versus orbital time (10^3 sec) .	E-191
E-60.	Magnetic torque component to dump CMG momentum	E-192
E-61.	Pointing performance with the maximum contribution steering law	E-193
E-62.	CMG gimbal angles with maximum contribution steering law	E-195
E-63.	Solar pointing and jitter for maximum contribution steering law with magnetic dump.	E-196
E-64.	Momenta dumped by electromagnets	E-197
E-65.	Euler angles versus orbital time (10^3 sec)	E-198
E-66.	Solar offset angle and pointing error	E-200
E-67.	Stored CMG and secular gravity momenta.	E-201
E-68.	Dipole components versus orbital time (10^3 sec)	E-202
E-69.	Magnetic torque versus orbital time (10^3 sec).	E-203

LIST OF ILLUSTRATIONS (Continued)

Figure	Title	Page
E-70.	CMG gimbal angle versus orbital time (10^3 sec)	E-204
E-71.	Reaction engine module (REM)	E-205
E-72.	Reaction engine assembly, MR-50A	E-208
E-73.	MR-50A thrust as function of propellant feed pressure . . .	E-219
E-74.	MR-50A REA impulse bit as a function of pulse frequency.	E-220
E-75.	MR-50A REA vacuum specific impulse as a function of pulse frequency	E-220
E-76.	MR-50A REA impulse bit as a function of pulse width. . . .	E-221
E-77.	Layout of alternate baseline RCS major component locations	E-222
E-78.	RCS/OAS maintank manifold isometric layout	E-225
E-79.	System schematic of the RCS/OAS main tank manifold concept	E-226
E-80.	Cold gas RCS/magnetic torquer isometric layout	E-229
E-81.	System schematic of the cold gas RCS	E-230
E-82.	Alternate cold gas RCS concept	E-232
E-83.	HEAO-C spacecraft concept with subsystem module	E-233
E-84.	HEAO-C spacecraft concept without the subsystem module	E-235

LIST OF ILLUSTRATIONS (Concluded)

Figure	Title	Page
E-85.	System schematic of alternate HEAO-C spacecraft RCS with and without the subsystem module	E-236
E-86.	Alternate HEAO-C spacecraft concept	E-238
E-87.	System schematic of the alternate HEAO-C spacecraft RCS	E-240

LIST OF TABLES

Table	Title	Page
E-1.	Euler Angles for Target Star Pointing	E- 34
E-2.	Disturbance Torque Magnitudes	E- 51
E-3.	Typical Performance of Star Trackers Suitable for HEAO for HEAO-C	E- 52
E-4.	Maximum Momentum Capability for Four-Skewed CMGs	E- 88
E-5.	CMG Steering Law Comparison	E- 91
E-6.	System I Design Examples	E-120
E-7.	System II Design Examples	E-125
E-8.	System III Design Examples	E-130
E-9.	Comparison of Simple Formulas for Pointing Error, ϕ_e , and CMG Gimbal Angle, α_i , due to Cyclical Disturbance Torques	E-137
E-10.	Electromagnetic Torquer Design Data	E-146
E-11.	Magnetic Field Tolerances and Shielding Requirements for Spacecraft Components	E-156
E-12.	HEAO-C Fuel and Impulse Budget for the Baseline RCS Configuration.	E-180
E-13.	HEAO-C Fuel and Impulse Budget for the Alternate RCS Configuration.	E-186
E-14.	REA/REM Performance Capabilities	E-207
E-15.	TCV Performance/Design Characteristics	E-210

LIST OF TABLES (Concluded)

Table	Title	Page
E-16.	REA Design Summary	E-211
E-17.	REM-MONO Thermal Design/Management Summary	E-213
E-18.	REM-MONO Thermal Management Requirements (Passive Mode)	E-215
E-19.	REM-MONO Thermal Management (Active Model)	E-216
E-20.	RCS Power Requirements	E-216
E-21.	Engine Performance/Requirements	E-218
E-22.	REA Performance Summary Nominal Operating Conditions	E-219
E-23.	RCS/OAS Main Tank Manifold Concept Weight Summary . .	E-227
E-24.	Alternate RCS Propellant Tank Data	E-237
E-25.	Alternate RCS Weight Summary	E-237
E-26.	Alternate RCS Weight Summary	E-239
E-27.	Major Hydrazine Thrusters Considered for the HEAO-C Spacecraft	E-241

APPENDIX E. ATTITUDE SENSING AND CONTROL ANALYSES

Coordinate Systems

1. Reference Coordinates. The coordinate systems utilized for HEAO-C are basically the same as those used for HEAO-A. However, a different Euler sequence has been used in all HEAO-C simulations, and the transformation between the earth's magnetic field and the Observatory axes has been redefined to permit the use of a subroutine which calculates the geomagnetic field from spherical harmonic expansions. The basic Observatory axes are illustrated in Figure E-1; however, for analysis purposes the principal axes are redefined so that the solar reference coordinates coincide with the Observatory reference axes without perturbations. The redefined body axes are denoted by x_r , y_r , and z_r . The x_r -axis is normal to the solar panels; the y_r -axis is aligned with the axis of minimum inertia; and the z_r -axis completes a right-hand triad. For completeness, the coordinates defined in the Phase A document for HEAO-A (NASA TMX-53976) are repeated and additional coordinates are defined as required.

For practical design purposes it can be assumed that the earth's orbit about the sun is circular instead of elliptical, the earth-moon barycenter is identical with earth center, and the spacecraft orbit is circular. These assumptions result in considerable simplifications in geocentric earth-sun inertial reference coordinates and orbital dynamics. The earth moves about the sun at a constant angular rate (Fig. E-2) of approximately 1 degree per day, the earth's solstices and equinoxes occur at even 90 degree intervals measured from Aries (an inertial reference denoted by Υ): the moon's gravitational effects are ignored; and ephemeris tables or calculations are not necessary to specify the earth's seasonal position.

Three planes relative to the celestial sphere provide the basic references for development of the coordinate systems necessary to describe the HEAOs attitude reference at any time: the orbital plane, equatorial plane, and ecliptic plane. When defining axes relative to a plane, the following philosophy should be observed: The X-axis is utilized as a pointing axis in the plane (e. g., along the ascending line of nodes, the sunline vector, Aries inertial direction, etc.) directed from the geocenter or spacecraft to the object being located; the Z-axis is always perpendicular to the plane directed in a northern direction [e. g., perpendicular to the orbital plane (POP), the

- 4-250 ft-lb-s CMGS
- NULL POSITION SHOWN.
- CMGS CONFIGURED SYMMETRICALLY ABOUT THE SUNWARD AXIS.
- SKEWED 53.1 deg = β

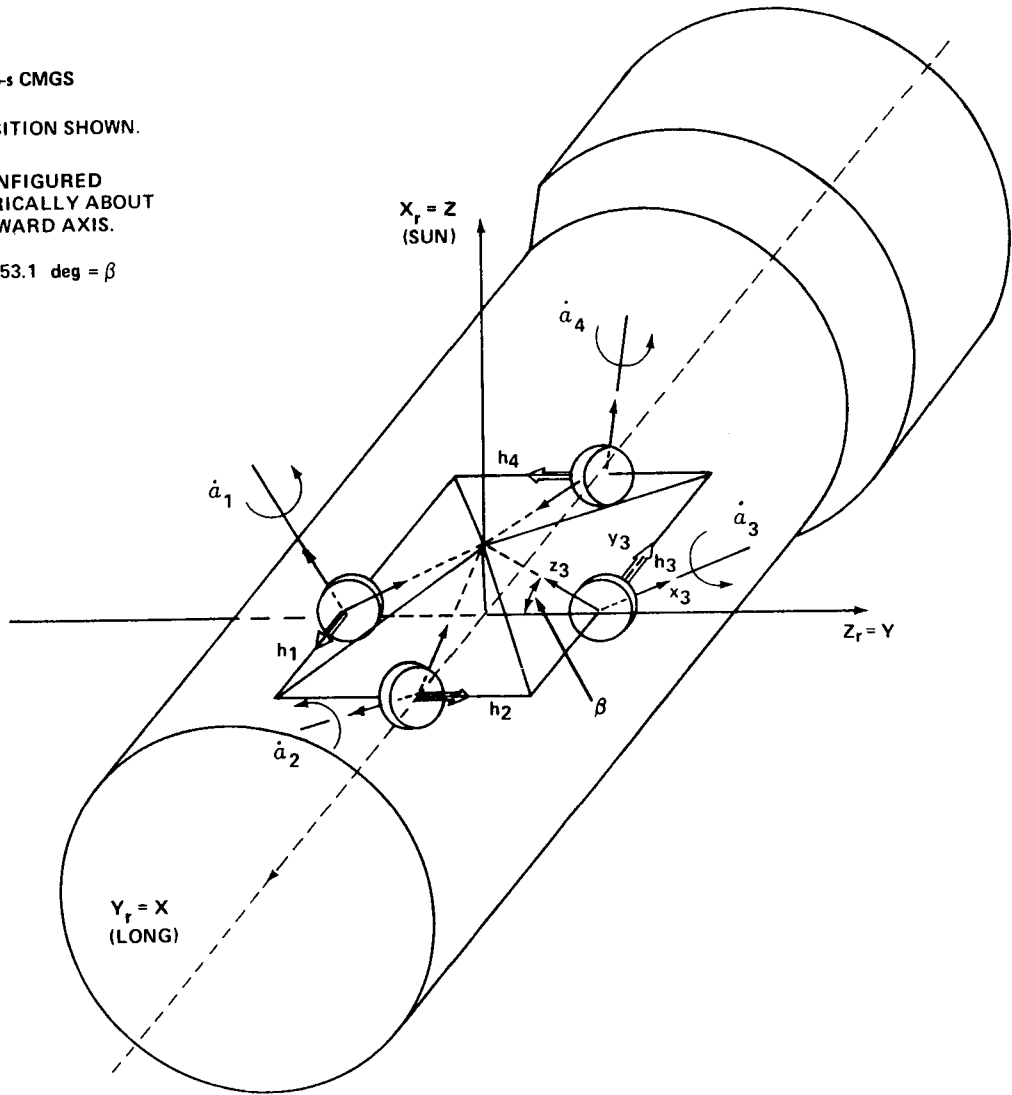


Figure E-1. HEAO-C body reference coordinates.

ecliptic plane (PEP), etc.]; and the Y-axis completes a right-hand triad in the plane. Angles are always defined in a positive sense by the right-hand rule being applied to the (X, Y, Z) triad. Unit vectors along the reference axis are denoted by the (i, j, k) triad. A subscript on the triads indicates a specific coordinate system. In addition, a standard Euler angle sequence is necessary to express attitude errors from the desired reference frame. Since HEAO must be oriented toward the sun to receive the proper amount of solar energy for power conversion, solar coordinates are selected as the body reference frame and the Euler angles (ϕ, θ, ψ) are used to express the vehicle's attitude relative to the solar reference frame.

Figure E-3 indicates the earth-orbit-ecliptic plane geometry and the angular relations necessary to relate the spacecraft's orbital position to either inertial or solar coordinates. The subscripts on angles indicate the sequence in which the rotations must occur. The count may be either forward or backward, but the arrows indicate a forward count rotation that brings the solar into the orbital coordinate system. The angles and coordinates between the three planes are shown in more detail in Figure E-4.

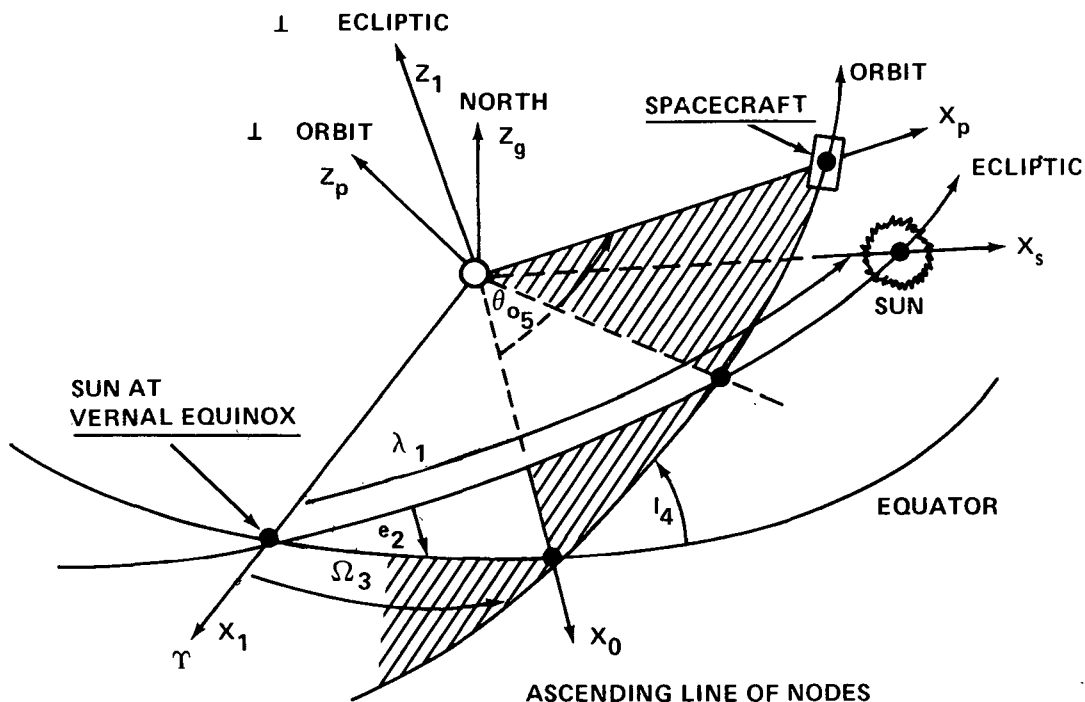


Figure E-3. Earth-orbit-ecliptic geometry.

In performing transformations between coordinates, vector matrix notation is used for simplification whenever practical. For example, \tilde{X}_s denotes the transpose of the triad (X_s, Y_s, Z_s) and the subscript s indicates solar coordinates. Capital letters are used to indicate matrices or transformations between coordinates, and a double subscript indicates the coordinates being related by the transformation. For example, A_{ab} denotes a matrix operation which carries the b into the a coordinate frame and is written algebraically as $\tilde{X}_a = A_{ab} \tilde{X}_b$. The elements of A_{ab} are identified by double numerical subscripts which indicate the row and column, respectively.

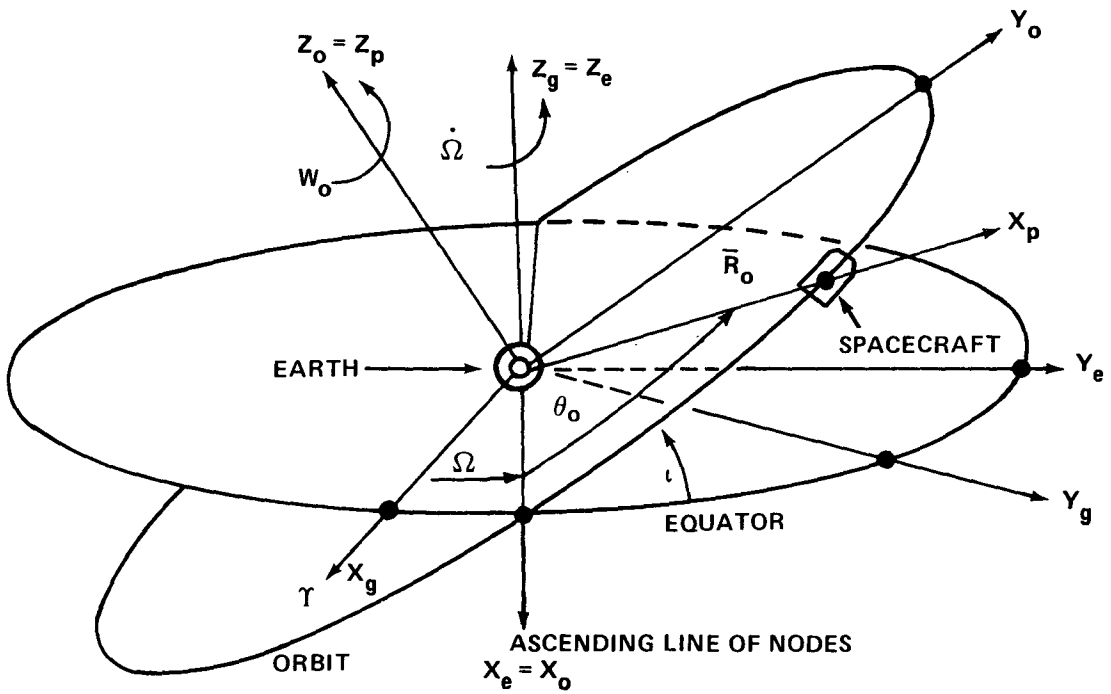
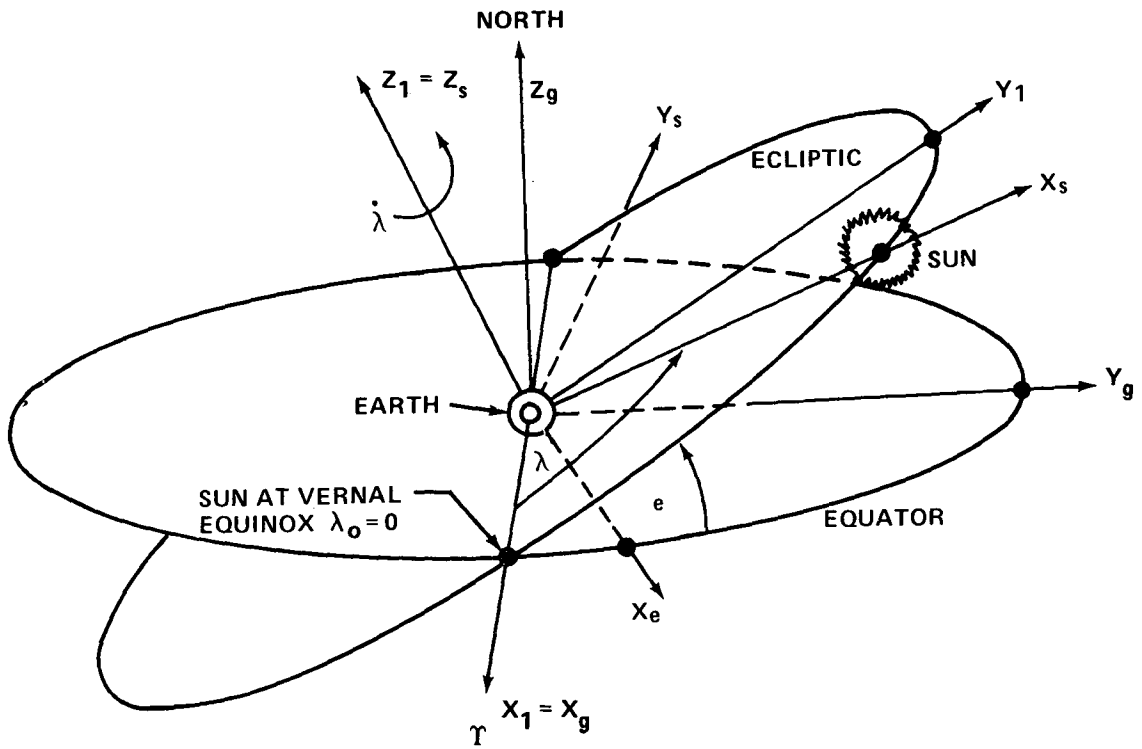


Figure E-4. Geocentric coordinate systems.

Since the matrices used in the transformations are orthogonal, the reciprocal (inverse) matrix is identical to the transposed matrix which is denoted by a superscript asterisk. Hence, $A_{ab} A_{ab}^* = I = A_{ab}^* A_{ab}$ where I is the identity matrix and A_{ab}^* is the inverse of A_{ab} . The specific reference frames are defined in the following paragraphs.

X_s, Y_s, Z_s are solar fixed coordinates (the HEAO body reference coordinates) with X_s directed from the earth to the sun in the ecliptic plane, Z_s PEP directed northward, and Y_s completing the right-hand triad.

X_1, Y_1, Z_1 are solar inertial coordinates referenced to the ecliptic plane with X_1 directed toward Aries, $Z_1 = Z_s$ PEP, and Y_1 completing the triad in the ecliptic plane. The inertial coordinates are transformed into solar coordinates by rotating about Z_1 by the angle λ ; $\tilde{X}_s = A_{s1} \tilde{X}_1$. The angle λ represents the apparent rotation of the earth about the sun as measured from the vernal equinox and indicates the seasonal time of the year.

X_g, Y_g, Z_g are geocentric inertial coordinates referenced to the equatorial plane with $X_g = X_1$ pointing toward Aries, Z_g perpendicular to the equatorial plane directed northward, and Y_g completing the triad. The geocentric is transformed into inertial by rotating about X_g by the angle $e = 23.45$ degrees, $\tilde{X}_1 = A_{1g} \tilde{X}_g$. The angle e , between the ecliptic and equatorial planes, is always constant and X_g is always on the ascending line of nodes between the two planes.

X_e, Y_e, Z_e is an earth-equatorial system referenced to the equatorial plane with X_e on the ascending line of nodes between the equatorial and orbit planes, $Z_e = Z_g$ perpendicular to the equatorial directed northward, and Y_e completing the triad. The geocentric is carried into the earth-equatorial by a rotation about Z_g by the angle Ω between the ecliptic-equatorial and equatorial-orbital lines of nodes (LON). The angle Ω is known as the orbital regression angle and its time derivative as the orbital regression rate. The rate is always negative for orbital inclinations less than 90 degrees. The initial angle value may be related to orbital injection conditions necessary to produce the LON. The transformation is $\tilde{X}_g = A_{ge} \tilde{X}_e$.

X_o, Y_o, Z_o is an orbit-fixed system referenced to the orbital plane with $X_o = X_e$ on the ascending LON, Z_o POP in a northern direction, and Y_o completing the triad. The earth-equatorial system is transformed into the orbital system by a rotation about X_e by the orbital inclination angle ι , and $\tilde{X}_e = A_{eo} \tilde{X}_o$. The angle of inclination is measured positively at the ascending LON when the spacecraft crosses the equator going from southern to northern hemisphere.

X_p, Y_p, Z_p is a local vertical (plumb line) system referenced to the orbital plane and the vehicle's position in orbit. The X_p -axis is directed from the earth's center to the spacecraft in orbit (opposite the local gravity vector); $Z_p = Z_o$ is POP; and Y_p completes the triad (aligned with the orbital velocity vector). The orbital plane is carried into local vertical coordinates by a positive rotation about Z_o by the orbital position angle θ_o , $\tilde{X}_o = A_{op} \tilde{X}_p$. The orbital angle is measured from the ascending LON, to the spacecraft in orbit, and is defined for circular orbits by $\theta_o = W_o t$, where W_o is the orbital rate and t is the orbital time from the LON.

The individual transformational matrices between local vertical and solar (reference) axes are combined to give $\tilde{X}_s = A_{sp} \tilde{X}_p$. The elements of A_{sp} are defined in Reference E-1 and are shown below:

$$\begin{aligned}
 A_{11} &= C\theta_o [C\lambda C\Omega + S\lambda S\Omega Ce] + S\theta_o [-C\lambda S\Omega C\iota + S\lambda C\Omega Ce C\iota + S\lambda Se S\iota] \\
 A_{12} &= -S\theta_o [C\lambda C\Omega + S\lambda S\Omega Ce] + C\theta_o [-C\lambda S\Omega C\iota + S\lambda C\Omega Ce C\iota + S\lambda Se S\iota] \\
 A_{13} &= S\iota [C\lambda S\Omega - S\lambda C\Omega Ce] + C\iota S\lambda Se \\
 A_{21} &= -C\theta_o [S\lambda C\Omega - C\lambda S\Omega Ce] + S\theta_o [S\lambda S\Omega C\iota + C\lambda C\Omega Ce C\iota + C\lambda Se S\iota] \\
 A_{22} &= S\theta_o [S\lambda C\Omega - C\lambda S\Omega Ce] + C\theta_o [S\lambda S\Omega C\iota + C\lambda C\Omega Ce C\iota + C\lambda Se S\iota] \\
 A_{23} &= -S\iota [S\lambda S\Omega + C\lambda C\Omega Ce] + C\iota C\lambda Se \\
 A_{31} &= -C\theta_o S\Omega Se - S\theta_o [C\Omega Se C\iota - Ce S\iota] \\
 A_{32} &= S\theta_o S\Omega Se - C\theta_o [C\Omega Se C\iota - Ce S\iota] \\
 A_{33} &= C\Omega Se S\iota + Ce C\iota
 \end{aligned}$$

where S is the symbol for sine and C is the symbol for cosine.

X_r, Y_r, Z_r are body fixed coordinates which are usually chosen so that the cross products of inertia are zero. The HEAO principal axes have been assumed to be identical to the body control axes. Since several configurations are being studied, confusion between relating structural axes to control axes and reference axes can be avoided by defining a consistent reference of body fixed coordinates for attitude control purposes. It is suggested that the following axis definitions be utilized for the HEAO: Let X_r be directed toward the sun and be the axis about which the vehicle normally rotates to point to an X-ray source; let Y_r be the Observatory pointing axis, as such the experiments must view in the general direction of Y_r ; and let Z_r complete the triad. In a solar-oriented mode the body axes are ideally aligned with the solar axis, $\tilde{X}_s = \tilde{X}_r$ without perturbations; however, if the spacecraft is perturbed from the desired reference or if a solar offset angle is commanded, as in the solar offset pointing mode, a three-angle modified Euler transformation is utilized to relate the two systems. The transformation from solar to body reference coordinates is denoted by $\tilde{X}_r = B_{rs} \tilde{X}_s$, where the elements of B_{rs} depend upon the specific Euler rotational sequence used.

X_m, Y_m, Z_m are geomagnetic coordinates which have been selected to correspond with outputs of the spherical harmonic expansion model representing the earth's magnetic field. The X_m -axis is directed from the earth's center to the spacecraft in orbit. Both Y_m and Z_m are tangent to the surface of a sphere with Y_m directed eastward and Z_m directed northward. Relative to the Greenwich Meridian the longitude and latitude of the spacecraft are α_m and β_m , respectively. The geometry between the geomagnetic and geocentric inertial is illustrated in Figure E-5.

X_G, Y_G, Z_G are Greenwich coordinates with X_G directed from the earth's center to the crossing of the Greenwich Meridian at the equator, Z_G directed northward perpendicular to the equatorial plane, and Y_G completing the right-hand triad in the equatorial plane.

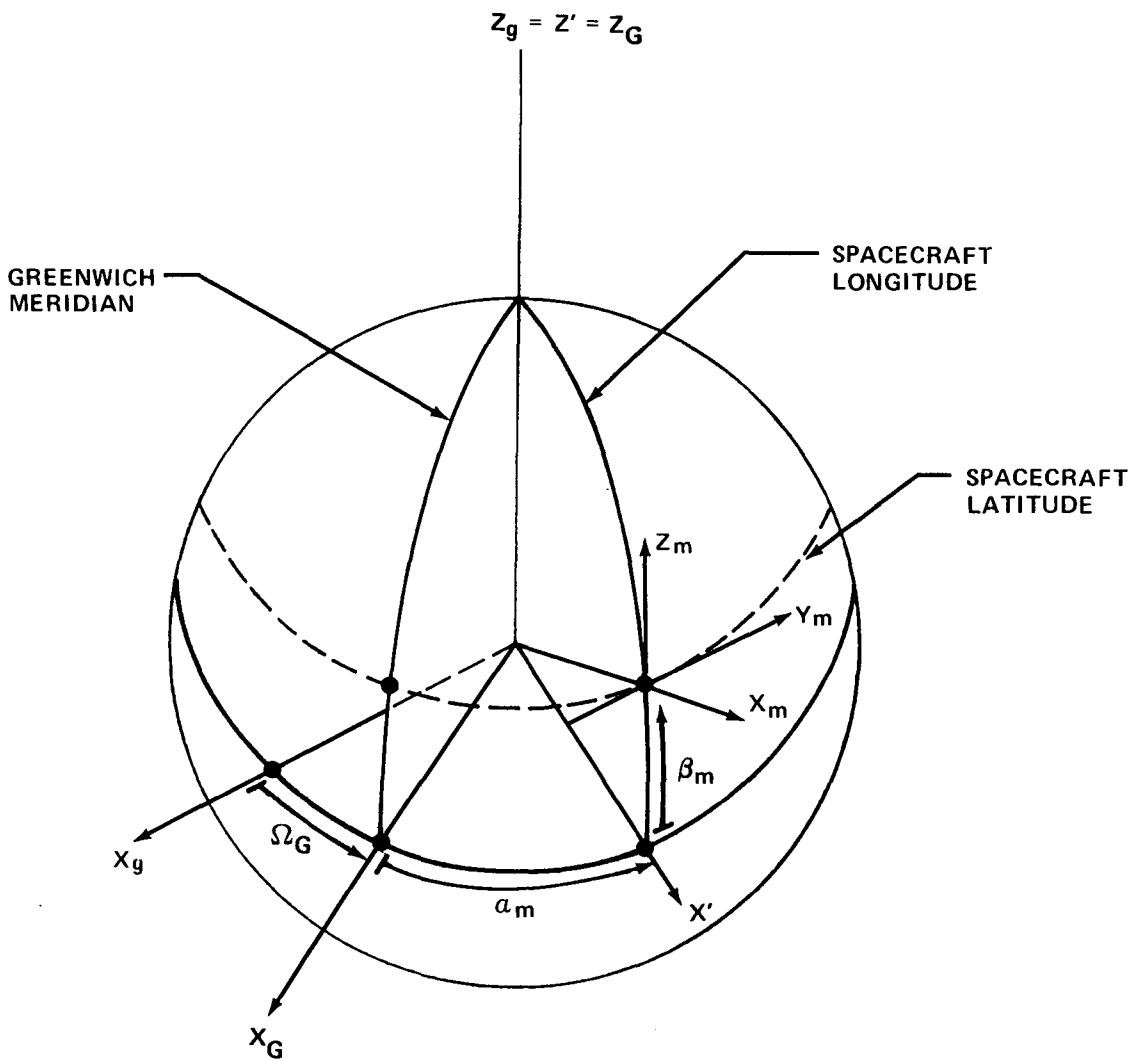


Figure E-5. Geomagnetic coordinates, \tilde{X}_m , relative to the Greenwich Meridian.

The geomagnetic coordinates, \tilde{X}_m , are related to the geocentric inertial coordinates, \tilde{X}_g , by first rotating about the Y_m -axis by β_m and then about the once transformed Z_m axis by the angle $\Omega_m = -(\Omega_G + \alpha_m)$. The results are summarized by $\tilde{X}_m = M_{mg} \tilde{X}_g$ with the matrical elements as follows:

$$\left[\begin{array}{lll} M_{11} = C\Omega_m C\beta_m & M_{12} = -S\Omega_m C\beta_m & M_{13} = S\beta_m \\ M_{21} = S\Omega_m & M_{22} = C\Omega_m & M_{23} = 0 \\ M_{31} = -C\Omega_m S\beta_m & M_{32} = S\Omega_m S\beta_m & M_{33} = C\beta_m \end{array} \right]$$

where

$$\Omega_m = -\Omega_G - \alpha_m \quad \text{with} \quad \Omega_G = \Omega_e + W_e t$$

and where Ω_e is the initial longitude of Greenwich Meridian relative to Aries; W_e is the earth's rotational rate; t is time; α_m is spacecraft longitude relative to Greenwich Meridian; and β_m is spacecraft latitude. The longitude and latitude are obtained as functions of the orbital position, orbital inclination, orbital regression, and the earth's position relative to the orbit by equating the vector components of a local vertical unit vector, \bar{R}_o . Relative to geomagnetic coordinates, $\bar{R}_o = i_m$ but can be expressed in the geocentric frame with the aid of M_{mg} :

$$\bar{R}_o = i_m = C\Omega_m C\beta_m i_g - S\Omega_m C\beta_m j_g + S\beta_m k_g. \quad (1)$$

However, relative to local vertical coordinates, $\bar{R}_o = i_p$, which may also be related to the geocentric frame by

$$\tilde{X}_p = E_{gp}^* \tilde{X}_g. \quad (2)$$

The elements of E_{gp} are as follows:

$$\begin{array}{ll} E_{11} = C\theta_o C\Omega - S\theta_o S\Omega C\iota & E_{23} = -C\Omega S\iota \\ E_{12} = -S\theta_o C\Omega - C\theta_o S\Omega C\iota & E_{31} = S\theta_o S\iota \\ E_{13} = S\Omega S\iota & E_{32} = C\theta_o S\iota \\ E_{21} = C\theta_o S\Omega + S\theta_o C\Omega C\iota & E_{33} = C\iota \\ E_{22} = -S\theta_o S\Omega + C\theta_o C\Omega C\iota & \end{array}$$

where $\theta_o = W_o t$; $\Omega = \Omega_o + \dot{\Omega}t$, θ_o is the spacecraft orbital position (measured from the ascending line of nodes); W_o is the orbital angular rate; Ω is the angle between Aries and the ascending line of nodes; $\dot{\Omega}$ is the orbital regression; Ω_o is the initial angle to ascending line of nodes; and t is the orbital time.

With the aid E_{gp} , a second expression for R_o is

$$\begin{aligned} \bar{R}_o = & (C\theta_o C\Omega - S\theta_o S\Omega C\iota) i_g + (C\theta_o S\Omega + S\theta_o C\Omega C\iota) j_g \\ & + S\theta_o S\iota k_g . \end{aligned} \quad (3)$$

The vector components in the two expressions for R_o are equated and the resulting equations solved for the spacecraft longitude and latitude relative to Greenwich Meridian. The equations are

$$\beta_m = \sin^{-1} (S\theta_o S\iota) \quad (4)$$

and

$$\alpha_m = \tan^{-1} \left[\frac{S\theta_o C\iota C\Omega^1 - C\theta_o S\Omega^1}{S\theta_o C\iota S\Omega^1 + C\theta_o C\Omega^1} \right] \quad (5)$$

where $\Omega^1 = \Omega_G - \Omega$ and $\Omega_G = \Omega_e + W_e t$.

The transformation from geocentric inertial to solar reference coordinates is given by

$$\tilde{X}_s = S_{sg} \tilde{X}_g . \quad (6)$$

The elements of the matrix S_{sg} are given as follows:

$$\begin{array}{lll}
S_{11} = C\lambda & S_{12} = S\lambda Ce & S_{13} = S\lambda Se \\
S_{21} = -S\lambda & S_{22} = C\lambda Ce & S_{23} = C\lambda Se \\
S_{31} = 0 & S_{32} = -Se & S_{33} = Ce
\end{array}$$

where $e = 23.45$ degrees; $\lambda = \lambda_0 + \dot{\lambda} t^1$; λ is the earth's seasonal position; λ_0 is the initial position of the earth; $\dot{\lambda} = 0.98565$ deg/day; and t^1 is the number of days from vernal equinox. Combining the elements of S_{sg} and E_{gp} produces the elements of A_{sp} , as previously listed.

The latitude and longitude are used as inputs to the subroutine which generates the earth's magnetic field components in the geomagnetic coordinate system. The field components must then be transformed into the solar reference and Observatory coordinate systems. The field components represent the earth's magnetic field as would be measured by magnetometers mounted along the spacecraft axes. If B_{rs} represents the Euler transformation from solar reference to body reference axes, the transformation from geomagnetic to body axes is obtained by combining the previously defined matrices:

$$\tilde{X}_r = (B_{rs} \ S_{sg} \ M_{mg}^*) \tilde{X}_m = (B_{rs} \ D_{sm}) \tilde{X}_m \quad (7)$$

In geomagnetic coordinates, the earth's magnetic field vector is

$$\bar{B} = B_v i_m + B_e j_m + B_n k_m \quad (8)$$

where B_v is the vertical component; B_e is the east components; and B_n is the north component as generated by the field subroutine.

Initially the solar and body axes are assumed to be misaligned and the solar axes are carried into the misaligned body axes by a three angle Euler sequence. For HEAO-C either the (1, 2, 3) or the (1, 3, 2) sequence is

recommended. Since the (1, 2, 3) is a standard sequence which is listed in most references on transformations, only the elements of the (1, 3, 2) sequence and kinematic relations are included herein. For the (1, 3, 2) sequence, the first rotation is about the sunline, X_s , by the angle ϕ , followed by a rotation about the once-transformed Z_s^1 -axis by the angle ψ , and the third rotation is about the twice-transformed Y_s'' -axis by the angle θ . During normal experiment operations, ϕ is measured from the ecliptic plane to the sunline-X-ray source plane, ψ is measured in the sun-X-ray source plane, and θ is measured about the experiment line of sight. Let the commanded values of the Euler angles be denoted by a subscript c. Assuming a small angle approximation, the solar offset angle, δ_s , is given by

$$\delta_s = (\theta^2 + \psi^2)^{\frac{1}{2}} \quad (9)$$

and the pointing error, δ_p , is given by

$$\delta_p = [(\phi - \phi_c)^2 + (\psi - \psi_c)^2]^{\frac{1}{2}} .$$

The elements of the (1, 3, 2) Euler sequence are as follows:

$$\begin{aligned} B_{11} &= C\theta C\psi & B_{12} &= C\theta S\psi C\phi + S\theta S\phi & B_{13} &= C\theta S\psi S\phi - S\theta C\phi \\ B_{21} &= -S\psi & B_{22} &= C\psi C\phi & B_{23} &= C\psi S\phi \\ B_{31} &= S\theta C\psi & B_{32} &= S\theta S\psi C\phi - C\theta S\phi & B_{33} &= S\theta S\psi S\phi + C\theta C\phi \end{aligned}$$

The approximate jitter rate, Δ , is given by either

$$\Delta = (W_{xr}^2 + W_{yr}^2 + W_{zr}^2)^{\frac{1}{2}}$$

or

$$\Delta = (\dot{\phi}^2 + \dot{\theta}^2 + \dot{\psi}^2)^{\frac{1}{2}} .$$

The kinematic relations are commonly derived by transforming each angular rate into body coordinates and then summing the components to produce the equivalent body rates, W_{xr} , W_{yr} , and W_{zr} . The kinematic relations for the (1, 3, 2) type transformation are as follows:

$$\left. \begin{aligned} W_{xr} &= \dot{\phi} C\theta C\psi - \dot{\psi} S\theta \\ W_{yr} &= \dot{\theta} - \dot{\phi} S\psi \\ W_{zr} &= \dot{\psi} C\theta + \dot{\phi} S\theta C\psi \end{aligned} \right\} . \quad (10)$$

The inverse relations are

$$\left. \begin{aligned} \dot{\phi} &= (C\theta W_{xr} + S\theta W_{zr}) / C\psi \\ \dot{\theta} &= W_{yr} + \dot{\phi} S\psi \\ \dot{\psi} &= C\theta W_{zr} - S\theta W_{xr} \end{aligned} \right\} . \quad (11)$$

For small angles in θ and ψ ,

$$\left. \begin{aligned} \dot{\phi} &= W_{xr} \\ \dot{\theta} &= W_{yr} \\ \dot{\psi} &= W_{zr} \end{aligned} \right\} . \quad (12)$$

The vectors normally required to evaluate the environmental forces are the local radius, velocity, and the earth's magnetic field. These vectors are obtained in the solar reference coordinate system by use of the previously defined transformations. Unity local vertical (for gravity gradient) is given by

$$\bar{R}_O = A_{11} i_s + A_{21} j_s + A_{31} k_s . \quad (13)$$

Unity velocity vector (for aerodynamic torque) is given by

$$\bar{V}_o = A_{12}i_s + A_{22}j_s + A_{32}k_s \quad (14)$$

Earth's magnetic field (for magnetic torque) is given by

$$\bar{B} = B_{xs}i_s + B_{ys}j_s + B_{zs}k_s \quad (15)$$

where

$$\begin{bmatrix} B_{xs} \\ B_{ys} \\ B_{zs} \end{bmatrix} = D_{sm} \begin{bmatrix} B_v \\ B_e \\ B_n \end{bmatrix}$$

The vector components in body reference coordinates are obtained with the aid of B_{rs} . For example, the unity local vertical vector is

$$\bar{R}_o = R_x i_r + R_y j_r + R_z k_r \quad (16)$$

where

$$\begin{bmatrix} R_x \\ R_y \\ R_z \end{bmatrix} = B_{rs} \begin{bmatrix} A_{11} \\ A_{21} \\ A_{31} \end{bmatrix}$$

Equivalently, in expanded form

$$\left. \begin{aligned} R_x &= B_{11} A_{11} + B_{12} A_{21} + B_{13} A_{31} \\ R_y &= B_{21} A_{11} + B_{22} A_{21} + B_{23} A_{31} \\ R_z &= B_{31} A_{11} + B_{32} A_{21} + B_{33} A_{31} \end{aligned} \right\} . \quad (17)$$

The body angular rates are obtained from the solution of the Euler rotational dynamics for HEAO-C, which will be derived later. Integration of the inverse kinematic relations provides the angles required to evaluate the direction cosine matrix B_{rs} and to obtain the attitude errors for HEAO-C.

2. Sun Sensor Outputs. Assume that the sun sensor's optical axis is aligned with the vehicle reference sun pointing axis, X_r , and that the sun sensor outputs are two angles whose rates are about the Y_r and Z_r axes. Let ϕ_y and ϕ_z be the sun sensor outputs which represent angular errors about the Y_r and Z_r axes, respectively. The angle ϕ_y is measured from the X_r axis to the vertical projection, e_{xz} , of the sunline onto the X-Z plane. The angle ϕ_z is measured from the X_r axis to the vertical projection, e_{xy} of the sunline onto the $X_r - Y_r$ plane. The sunline and optical axis geometries are illustrated in Figure E-6. The following parameters are defined to correspond with the notation shown in Figure E-6:

- \hat{S} a unit vector from the spacecraft center of mass toward the sun.
- \hat{e}_{xy} a unit vector along the perpendicular sunline projection onto the $X_r - Y_r$ plane.
- \hat{e}_{xz} a unit vector along the perpendicular sunline projection onto the $X_r - Z_r$ plane.
- ϕ_y the sun sensor Y_r axis output representing the angle subtended by X_r and \hat{e}_{xz} .

(i_r, j_r, k_r) . Projecting \hat{e}_{xy} and \hat{e}_{xz} onto the body reference axes produces the following equations:

$$\hat{e}_{xy} = C \phi_z i_r + S \phi_z j_r \quad , \quad (18)$$

$$\hat{e}_{xz} = C \phi_y i_r - S \phi_y k_r \quad . \quad (19)$$

Note that the sun sensor angular rates are assumed to be positively directed with the body angular rates ω_y and ω_z .

The unit sunline vector, \hat{S} , can be written as (assuming angle $\hat{S}, e_{xy} = \phi_y$)

$$\hat{S} = i_s = C \phi_y \hat{e}_{xy} - S \phi_y k_r \quad . \quad (20)$$

Substituting equation (18) into equation (20) produces the following results:

$$\hat{S} = C \phi_y C \phi_z i_r + C \phi_y S \phi_z j_r - S \phi_y k_r \quad . \quad (21)$$

But by definition of the HEAO Euler kinematic relations, the solar-to-body-axis transformation is

$$\tilde{X}_r = B_{rs} \tilde{X}_s \quad , \quad (22)$$

where

$$B_{rs} = \begin{bmatrix} B_{11} & B_{12} & B_{13} \\ B_{21} & B_{22} & B_{23} \\ B_{31} & B_{32} & B_{33} \end{bmatrix} .$$

Hence,

$$\hat{S} = B_{11} i_r + B_{21} j_r + B_{31} k_r . \quad (23)$$

Equating the components of equations (23) and (21) provides a method of relating the sun sensor outputs to the HEAO Euler angles (ψ , θ , ϕ) referenced to solar coordinates. The elements of B_{rs} for a (3, 2, 1) Euler sequence are obtained from Appendix J, Table J-4, of the HEAO Phase A report. Hence,

$$\left. \begin{aligned} B_{11} &= C\theta C\psi = C\phi_y C\phi_z \\ B_{21} &= S\phi S\theta C\psi - C\phi S\psi = C\phi_y S\phi_z \\ B_{31} &= C\phi S\theta C\psi + S\phi S\psi = -S\phi_y \end{aligned} \right\} . \quad (24)$$

The use of small angle approximations for all angles in equation (24), except the scan angle ϕ , produces

$$\left. \begin{aligned} 1 &= 1 \\ \phi_z &= \theta S\phi - \psi C\phi \\ \phi_y &= \theta C\phi - \psi S\phi \end{aligned} \right\} . \quad (25)$$

From a sun sensor point of view, this shows that the (3, 2, 1) Euler sequence is not a good choice to characterize the sun sensor outputs since all angles are required for the calculation. If the Euler angles are known for the (3, 2, 1) sequence, equations (25) can be used to calculate the sun sensor outputs.

Taking the time derivative of equations (25) produces

$$\left. \begin{aligned} \dot{\phi}_y &= -\dot{\theta} C\phi - \dot{\psi} S\phi + (\theta S\phi - \psi C\phi) \dot{\phi} \\ \dot{\phi}_z &= \dot{\theta} S\phi - \dot{\psi} C\phi + (\theta C\phi + \psi S\phi) \dot{\phi} \end{aligned} \right\} , \quad (26)$$

which can be rewritten as

$$\left. \begin{aligned} \dot{\phi}_y &= -\dot{\theta} C\phi - \dot{\psi} S\phi + \phi_z \dot{\phi} \\ \dot{\phi}_z &= \dot{\theta} S\phi - \dot{\psi} C\phi - \phi_y \dot{\phi} \end{aligned} \right\} . \quad (27)$$

The HEAO Euler kinematic relations for the (3, 2, 1) sequence are as follows:

$$\left. \begin{aligned} \omega_{xr} &= \dot{\phi} - \dot{\psi} S\theta \\ \omega_{yr} &= \dot{\theta} C\phi + \dot{\psi} S\phi C\theta \\ \omega_{zr} &= \dot{\psi} C\phi C\theta - \dot{\theta} S\phi \end{aligned} \right\} , \quad (28)$$

which for small angles in θ and ψ reduce to

$$\left. \begin{aligned} \omega_{xr} &= \dot{\phi} - \dot{\psi} \theta \\ \omega_{yr} &= \dot{\theta} C\phi + \dot{\psi} S\phi \\ \omega_{zr} &= \dot{\psi} C\phi - \dot{\theta} S\phi \end{aligned} \right\} . \quad (29)$$

The last two of equations (13) can be used to introduce body rates into equations (27) which, in turn, produces the sun sensor dynamic equations:

$$\left. \begin{aligned} \dot{\phi}_y &= -\omega_{yr} + \theta_z \dot{\phi} \\ \dot{\phi}_z &= -\omega_{zr} - \phi_y \dot{\phi} \end{aligned} \right\} \quad (30)$$

If it is assumed that the Observatory is maneuvering about the sunline at a relatively constant rate, $\dot{\phi} = \omega_s$, then

$$\left. \begin{aligned} \dot{\phi}_y - \omega_s \phi_z &= -\omega_{yr} \\ \dot{\phi}_z + \omega_s \phi_y &= -\omega_{zr} \end{aligned} \right\} \quad (31)$$

Equations (31) can be solved for the sun sensor outputs if the body rates relative to solar coordinates are known. If the vehicle is not maneuvering, then $\dot{\phi}$ should be small, in which case the nonlinear terms can be neglected so that the sun sensor output angles are approximately equal to the negative time integral of the rate gyro outputs:

$$\left. \begin{aligned} \phi_y &\approx - \int \omega_{yr} dt = -\theta \\ \phi_z &\approx - \int \omega_{zr} dt = -\psi \end{aligned} \right\} \quad (32)$$

As an alternate approach, consider the (1, 2, 3) Euler sequence where

$$\left. \begin{aligned} B_{11} &= C\theta C\psi \\ B_{21} &= -C\theta S\psi \\ B_{31} &= S\theta \end{aligned} \right\} \quad (33)$$

Equations (24) become

$$\left. \begin{aligned} C\theta C\psi &= C\phi_y C\phi_z \\ -C\theta S\psi &= C\phi_y S\phi_z \\ S\theta &= -S\phi_y \end{aligned} \right\} \cdot \quad (34)$$

Solving equations (34) for ϕ_y and ϕ_z yields the following equations:

$$\left. \begin{aligned} \phi_y &= -\theta \\ \phi_z &= -\psi \end{aligned} \right\} \cdot \quad (35)$$

It is noteworthy that no approximations or linearizations have been used to derive equations (35). Using a (1, 2, 3) Euler sequence, the sun sensor outputs are identical to the Euler angles but opposite in sign. If the spacecraft is maneuvering about the sun line, the rotation angle ϕ does not enter into the equations. The kinematic relations for the (1, 2, 3) Euler sequence are as follows:

$$\left. \begin{aligned} \dot{\phi} &= (\omega_{xr} C\psi - \omega_{yr} S\psi) / C\theta \\ \dot{\theta} &= \omega_{yr} C\psi + \omega_{xr} S\psi \\ \dot{\psi} &= \omega_{zr} - \dot{\phi} S\theta \end{aligned} \right\} \cdot \quad (36)$$

Using a small angle approximation for θ and ψ and assuming large values for ϕ , such as would be encountered if the spacecraft were rotating about the sunline, equations (36) reduce to the following:

$$\left. \begin{aligned} \dot{\phi} &= \omega_{xr} \\ \dot{\theta} &= \omega_{yr} \\ \dot{\psi} &= \omega_{zr} - \dot{\phi} \end{aligned} \right\} , \quad (37)$$

even though one of the Euler angles can be arbitrarily large.

Comparing the (3, 2, 1) and (1, 2, 3) Euler sequence with the corresponding sun sensor kinematics indicates that system analysis and simulations can be greatly simplified, especially for a maneuvering vehicle, by utilizing the (1, 2, 3) Euler sequence. Hence, it is recommended that the (1, 2, 3) Euler sequence be used in all HEAO simulations and analyses.

3. Target Star Pointing. Given the right ascension α and the declination β of an arbitrary star relative to the celestial sphere, a unit vector P directed from the earth's center to the target star is defined in geocentric coordinates by the following equation

$$\hat{P} = C\alpha C\beta \mathbf{i}_g + S\alpha C\beta \mathbf{j}_g + S\beta \mathbf{k}_g \quad (38)$$

The star's parameters and P are illustrated in Figure E-7. The geocentric coordinates are defined by the celestial sphere with X_g pointing toward Aries on the LON between the equatorial and ecliptic planes. The Z_g axis is perpendicular to the equatorial plane directed northerly and the Y_g axis completes a right-hand triad in the equatorial plane. The components of P in geocentric coordinates, equation (38), are obtained by the projection of P onto the (X_g, Y_g, Z_g) system.

As shown in Section 1 of this Appendix, the geocentric and solar coordinates are related by the transformation

$$\tilde{X}_s = (A_{s1} \ A_{1g}) \tilde{X}_g = S_{sg} \tilde{X}_g \quad (39)$$

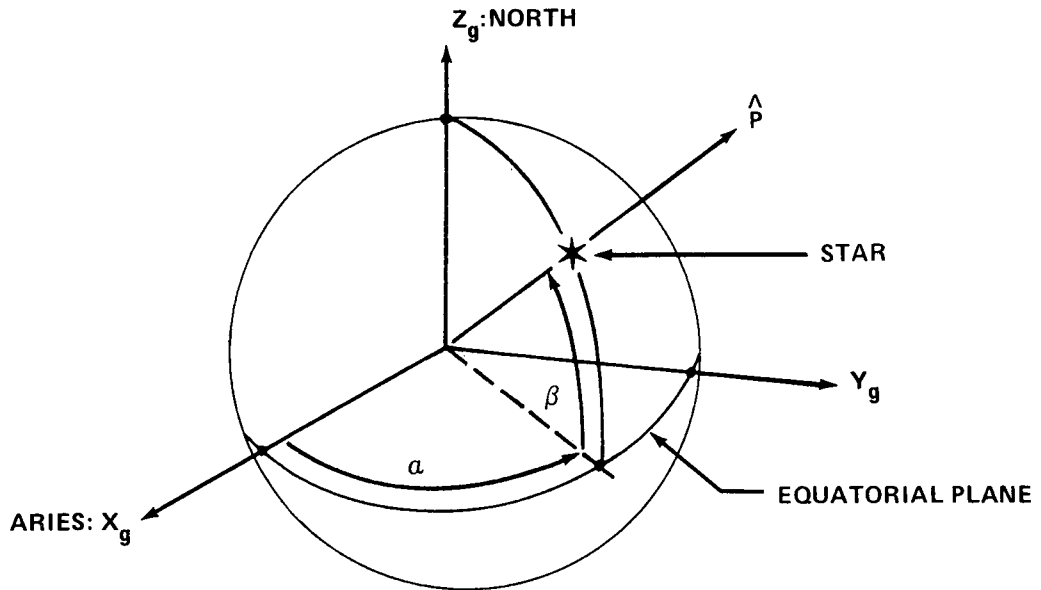


Figure E-7. Celestial reference for a star.

$$\tilde{X}_s = \begin{bmatrix} C\lambda & S\lambda & 0 \\ -S\lambda & C\lambda & 0 \\ 0 & 0 & 1 \end{bmatrix} \begin{bmatrix} 1 & 0 & 0 \\ 0 & C_e & S_e \\ 0 & -S_e & C_e \end{bmatrix} \tilde{X}_g .$$

$$\tilde{X}_s = \begin{bmatrix} C\lambda & S\lambda C_e & S\lambda S_e \\ -S\lambda & C\lambda C_e & C\lambda S_e \\ 0 & -S_e & C_e \end{bmatrix} \tilde{X}_g .$$

The relations between solar and geocentric coordinates are shown in Figure E-8. The angle between the equatorial and ecliptic plane, $e = 23.45$ degrees, is constant, and the sun's apparent rotation about the earth is given by the angle λ which has an angular rate of about 1 degree per day. At the vernal equinox $\lambda = 0$ and at the winter solstice $\lambda = 270$ degrees. The X_s axis points to the sun; the Z_s axis is perpendicular to the ecliptic plane (northward) and the Y_s axis completes a right-hand triad in the ecliptic plane.

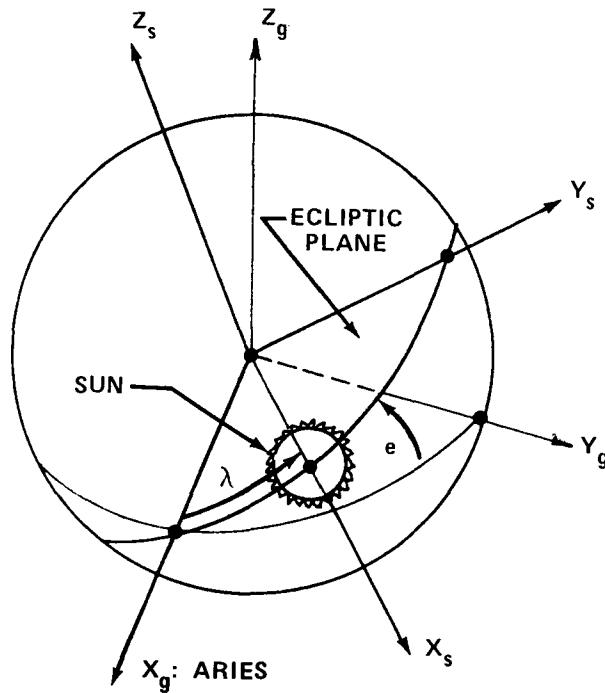


Figure E-8. Solar coordinates.

The vector components of $P(\alpha, \beta)$ are projected onto the solar frame by transformation (39):

$$\hat{P} = P_{xs} i_s + P_{ys} j_s + P_{zs} k_s \quad , \quad (40)$$

where

$$P_{xs} = C\lambda C\alpha C\beta + S\lambda Ce S\alpha C\beta + S\lambda Se S\beta \quad ,$$

$$P_{ys} = -S\lambda C\alpha C\beta + C\lambda Ce S\alpha C\beta + C\lambda Se S\beta \quad ,$$

and

$$P_{zs} = -Se S\alpha C\beta + Ce S\beta \quad .$$

Once the target star and time of year are specified, the components of P in solar coordinates become constants. The only time-varying parameter in the coefficients of equation (40) is the sun's position which is specified by the angle λ .

Relative to solar coordinates, the right ascension, α_s , and the declination, β_s , specify the target star's position. Analogous to the procedure used to obtain equation (38), the unit vector P is projected onto solar coordinates using the angles α_s and β_s to obtain

$$\hat{P} = C\alpha_s C\beta_s i_s + S\alpha_s C\beta_s j_s + S\beta_s k_s \quad , \quad (41)$$

where i_s , j_s , and k_s are unit vectors along the solar X_s , Y_s , and Z_s axes, respectively. Equating the coefficients of equation (41) to those of equation (40) provides the following two equations for α_s and β_s as functions of P_{xs} , P_{ys} , and P_{zs} :

$$\alpha_s = \tan^{-1} (P_{ys} / P_{xs}) \quad (42)$$

and

$$\beta_s = \sin^{-1} (P_{zs}) \quad . \quad (43)$$

Conversely, if α_s and β_s are given, the star's coordinates relative to the celestial sphere are obtained by first projecting $P(\alpha_s, \beta_s)$ into geocentric coordinates. Use of equation (39) yields

$$\hat{P} = P_{xg} i_g + P_{yg} j_g + P_{zg} k_g \quad , \quad (44)$$

where

$$P_{xg} = C\alpha_s C\beta_s C\lambda - S\alpha_s C\beta_s S\lambda \quad ,$$

$$P_{yg} = C\alpha_s C\beta_s C\lambda C\epsilon + S\alpha_s C\beta_s C\lambda C\epsilon - S\beta_s S\epsilon \quad ,$$

and

$$P_{zg} = C\alpha_s C\beta_s S\lambda S\epsilon + S\alpha_s C\beta_s C\lambda S\epsilon + S\beta_s C\epsilon \quad .$$

Secondly, the vector components are equated to those of $P(\alpha, \beta)$ in equation (38) to obtain

$$\alpha = \tan^{-1} (P_{yg}/P_{xg}) \quad (45)$$

and

$$\beta = \sin^{-1} (P_{zg}) \quad (46)$$

The HEAOs attitude relative to solar reference coordinate may be defined by an Euler angle sequence; either the (3, 2, 1) or the (1, 2, 3) sequence may be used. In either case the transformation from solar-to-body control axes is given in vector matrix form as

$$\tilde{X}_r = B_{rs} \tilde{X}_s \quad , \quad (47)$$

where B_{rs} is composed of direction cosines between axes. The Euler angles are denoted as ϕ , θ , and ψ , which for small angles represent rotations about the X, Y, and Z axes, respectively. The solar offset angle, δ , is defined as the angle subtended by the sunline, X_s , and the body solar pointing axis, X_r .

By basic definition, δ is defined by the direction cosine between the two vectors as follows:

$$\hat{X}_s \cdot \hat{X}_r = B_{11} = C\delta \quad . \quad (48)$$

For small angles, 45 degrees or less, δ is approximately

$$\delta = (\theta^2 + \psi^2)^{\frac{1}{2}} = (\phi_y^2 + \phi_z^2)^{\frac{1}{2}}, \quad (49)$$

where θ and ψ are Euler angles and ϕ_y and ϕ_z are sun sensor outputs. Either set of relations may be used to calculate δ unless extreme accuracy is required. Simulations have shown that for very small angles, 1 degree or less, the approximate equations are much more accurate for calculation purposes than are arc cosine subroutines.

In a solar pointing mode, δ is used to measure the spacecraft's pointing performance. However, in a solar offset pointing mode, the Euler angles are selected so that a particular vehicle axis, about which an experiment is aligned, points toward a target star. In this case, δ becomes a constant angle within the solar panel power constraint of 37 degrees. Hence, target star pointing for a particular body axis must be selected at specific times of year so that δ is less than 37 degrees. Without constraints, only two Euler angles are needed to point any spacecraft axis to a target star; however, the maximum value of δ could be exceeded in many cases, hence reducing the pointing opportunities. In general, star pointing opportunities are maximized by using all three Euler angles, and the sign ambiguities may be eliminated by using the solar offset constraint. For any given star, δ is minimized by requiring that the sun axis, X_r , lie in a plane defined by P and a vector along the sunline, S . The problem is to define Euler angles so that a particular vehicle axis points toward the selected target star while minimizing the solar offset angle.

For HEAO-C, the long vehicle axis, Y_r , must point to an X-ray source. For study purposes, it is assumed that the X-ray source is also a target star and a star tracker is hard-mounted to the vehicle with its optical axis aligned with the long body axis. Assuming that the long axis is pointing to the target, Y_r and P must be colinear, so without perturbations, the following equation is obtained:

$$\hat{Y}_r = j_r = \hat{P} \quad (50)$$

By utilizing transformation (47), Y_r is projected into solar coordinates by assuming that Euler angles exist such that equation (50) is satisfied. The solar projection produces the following equation:

$$\hat{Y}_r = B_{21} i_s + B_{22} j_s + B_{23} k_s \quad (51)$$

The vector components of $P(\alpha, \beta)$ in solar coordinates are given by equation (40), hence equating components yields

$$\left. \begin{aligned} B_{21} &= P_{xs} \\ B_{22} &= P_{ys} \\ B_{23} &= P_{zs} \end{aligned} \right\} \quad (52)$$

The elements B_{ij} depend, of course, upon the Euler sequence used. The algebraic complexity of obtaining the Euler angle solutions required for star pointing can be greatly reduced by selecting the proper rotational sequence. Use of the (1, 2, 3) sequence results in a simpler solution for long axis pointing than does use of the (3, 2, 1) sequence. Using the (1, 2, 3) sequence (whose elements are listed in the next section of this Appendix), yields

$$\left. \begin{aligned} B_{21} = P_{xs} &= -C\theta S\psi \\ B_{22} = P_{ys} &= C\phi C\psi - S\phi S\theta S\psi \\ B_{23} = P_{zs} &= S\phi C\psi + C\phi S\theta S\psi \end{aligned} \right\} \quad (53)$$

At this point several values of the Euler angles satisfy equations (53) without either solution set being unique. A single solution may be obtained by imposing the solar offset angle constraint.

In solar coordinates,

$$\hat{Z} = B_{31} \hat{i}_S + B_{32} \hat{j}_S + B_{33} \hat{k}_S \quad (57)$$

and

$$\hat{X}_S = \hat{S} = \hat{i}_S \quad (58)$$

The box product, equation (56), reduces to

$$B_{31} = 0 \quad (59)$$

Using the (1, 2, 3) sequence

$$B_{31} = S\theta \quad (60)$$

Imposing the coplaner condition, δ is minimized by setting

$$\theta = 0 \quad (61)$$

Reverting to equations (53) and setting $\theta = 0$ gives the following equations:

$$\left. \begin{aligned} S\psi &= -P_{xS} \\ C\phi C\psi &= P_{yS} \\ S\phi C\psi &= P_{zS} \end{aligned} \right\} \quad (62)$$

Then, from the last two of equations (62), the following formula is obtained:

$$P_{zs}/P_{ys} = \tan \phi \quad . \quad (63)$$

Summarizing equations (61), (62), and (63), the Euler angle solutions for target pointing of the long vehicle axes with a minimum solar offset angle are given for a (1, 2, 3) sequence by the following equations:

$$\left. \begin{aligned} \phi &= \tan^{-1} (P_{zs}/P_{ys}) \\ \theta &= 0 \\ \psi &= \sin^{-1} (-P_{xs}) \end{aligned} \right\} . \quad (64)$$

If the target star's right ascension and declination are given relative to the celestial sphere, use equations (40) for components of $P(\alpha, \beta)$; alternatively, use equations (41) for solar referenced $P(\alpha_s, \beta_s)$.

With $\theta = 0$, the solar offset angle is given by

$$C\delta = C\psi = (1 - P_{xs}^2)^{\frac{1}{2}} \quad (65)$$

for the (1, 2, 3) sequence Euler angle commands. Within the power constraint, ψ must be less than 37 degrees but ϕ can take on all values. To minimize the rotation required, ϕ should be commanded negatively for angles exceeding 180 degrees. To acquire the target with the long axis, the vehicle is rolled about the sunline by the angle ϕ until the Y_r axis intersects the $X_s - P$ plane. Then, the vehicle is rotated about the Z_r axis by the angle ψ until the target is acquired. Only two Euler angles have been utilized in the (1, 2, 3) commanded sequence. The third angle could be used to facilitate finding a guide star by a star tracker mounted on an axis transverse to the target pointing axis. In this case, a (1, 3, 2) Euler sequence would be more appropriate, with the third rotation being about the twice-transformed Y_s

axis, which is the line of sight of the target source, to acquire a second guide star by a sensor aligned with the spacecraft Z_r axis.

The foregoing equations were programmed in Fortran for the CDC 3200 computer. The inputs are time of year, longitude, and latitude of the target star (or X-ray source) relative to the celestial sphere. The program outputs are longitude and latitude of the target star relative to solar coordinates and the two Euler angles, for a (1, 2, 3) sequence, which are required to maneuver the vehicle such that the long axis points to the target. The solar offset angle, given by equation (65) is equal to the Euler angle ψ . Ten target sources can be loaded in simultaneously. Table E-1 represents a typical run from the program, where λ represents the time of year; α and β the longitude and latitude, respectively; S indicates solar reference; and ψ and ϕ indicate the Euler angles required for target pointing. In each case ψ is also the solar panel offset from the sunline. The third Euler angle, θ , is always zero as required to minimize the solar offset angle. For the cases shown, VEGA, at the winter solstice, produced the largest solar offset angle, -28.1 degrees. All angles are given in degrees.

The calculated Euler angles were used as commands for the HEAO simulations to obtain typical vehicle pointing performance data.

By utilizing the (1, 3, 2) Euler sequence, the third rotation about the twice-transformed Y-axis by the angle θ can be used to roll the vehicle about the target source to facilitate finding a guide star transverse to the experiment line of sight. The sequence of rotations is illustrated in Figure E-10, in which case the solar offset angle is due to only the second and third rotations. For the (1, 3, 2) sequence, the box product [equation (60)] to minimize the solar offset angle is

$$\hat{X}_r \cdot (\hat{P} \times \hat{X}_s) = B_{31} = S\theta C\psi \quad , \quad (66)$$

from which it is desirable to set θ as small as possible. However, rolling about the target source makes it impossible to set equation (66) to zero. Equations (52) for the (1, 3, 2) sequence are as follows:

$$\left. \begin{aligned} B_{21} &= P_{xs} = -S\psi \\ B_{22} &= P_{ys} = C\psi C\phi \\ B_{23} &= P_{zs} = C\psi S\phi \end{aligned} \right\} \quad . \quad (67)$$

TABLE E-1. EULER ANGLES FOR TARGET STAR POINTING

Case	Source	λ	α	β	α_s	β_s	ϕ	ψ
1	SCOX-2	0	258.8	-38.4	260.9	-15.3	-164.5	8.8
2	SCOX-3	0	260.7	-44.3	262.9	-21.1	-158.8	6.6
3	SCOX-4	0	264.3	-40.4	265.5	-17.0	-162.9	4.3
4	SCOX-2	180	258.8	-38.4	80.9	-15.3	-15.5	-8.8
5	SCOX-3	180	260.7	-44.3	82.9	-21.1	-21.2	-6.6
6	SCOX-4	180	264.3	-40.4	85.5	-17.0	-17.1	-4.3
7	CANOPUS	0	95.0	-52.7	102.5	-75.9	-76.3	3.0
8	CANOPUS	270	95.0	-52.7	195.5	-75.9	-95.1	13.7
9	VEGA	270	278.0	38.0	13.1	61.1	82.9	-28.1
10	VEGA	0	278.0	38.0	283.1	61.1	118.3	-6.3

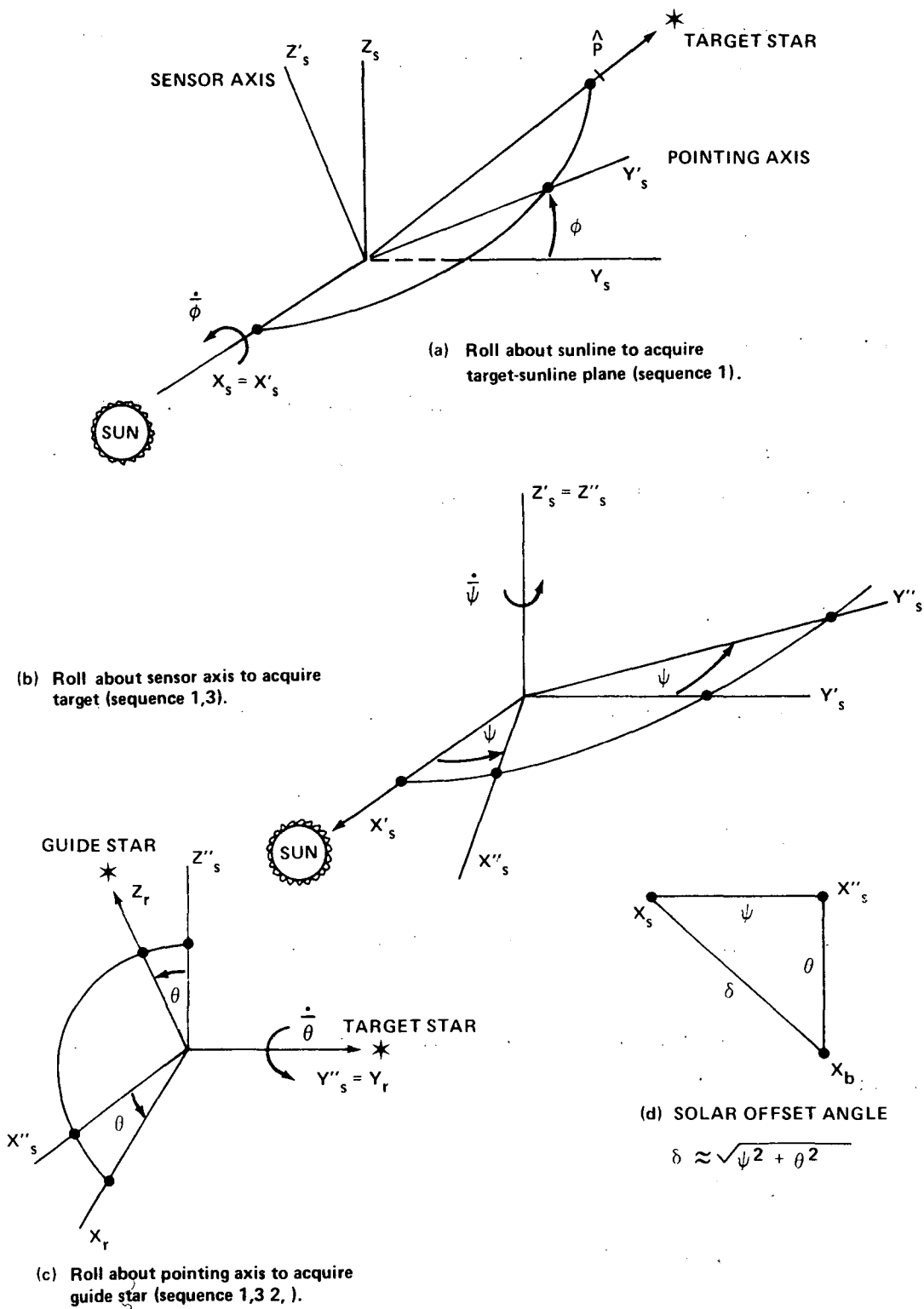


Figure E-10. The (1, 3, 2) sequence for target pointing and guide star acquisition.

The Euler angles required for target pointing are obtained from equations (67) without using the box product equation (66):

$$\left. \begin{aligned} \phi &= \tan^{-1} (P_{zs} / P_{ys}) \\ \psi &= \sin^{-1} (-P_{xs}) \end{aligned} \right\} , \quad (68)$$

which are identical to the (1, 2, 3) sequence solution.

Let α_g and β_g be the celestial coordinates of a guide star transverse to the target star. The sensor axis, Z_r , must be aligned with the guide star unit vector $P(\alpha_g, \beta_g)$, in which case

$$\hat{Z}_r = \hat{P}_g . \quad (69)$$

Utilizing the previously developed transformations, equation (69) in solar coordinates is

$$B_{31} i_s + B_{32} j_r + B_{33} k_s = P'_{xs} i_s + P'_{ys} j_s + P'_{zs} k_s \quad (70)$$

where the primed elements of P represent the guide star and not the target star.

Equating components and substituting for the elements of B_{ij} for the (1, 3, 2) sequence gives

$$\left. \begin{aligned} P'_{xs} &= B_{31} = S\theta C\psi \\ P'_{ys} &= B_{32} = S\theta S\psi C\phi - C\theta S\phi \\ P'_{zs} &= B_{33} = S\theta S\psi S\phi + C\theta C\phi \end{aligned} \right\} . \quad (71)$$

Since ψ and ϕ are specified by the target star, one needs to solve only the first of equations (71); thus

$$S\theta = P'_{XS} / C\psi \quad (72)$$

Since ψ will be less than 90 degrees, its cosine will be positive and may be replaced by its expression defined by equations (67) to give

$$\left. \begin{aligned} S\theta &= P'_{XS} / (1 - P_{XS}^2)^{\frac{1}{2}} \\ \theta &= \sin^{-1} [P'_{XS} / (1 - P_{XS}^2)^{\frac{1}{2}}] \end{aligned} \right\} \quad (73)$$

as the roll angle about the target source required to pick up a specified guide star.

The approximate expression for the solar offset angle is given by

$$\delta = (\psi^2 + \theta^2)^{\frac{1}{2}} = [P_{XS}^2 + (P'_{XS})^2 / (1 - P_{XS}^2)]^{\frac{1}{2}} \quad (74)$$

after the guide star has been acquired. If δ is greater than 37 degrees, either a new guide star, target star, or both must be selected to maintain proper solar power.

Euler Equations for the HEAO-C

The dynamic equations which govern the rotational motion of a rigid HEAO with four skewed single gimbal CMGs are obtained by equating the time derivative of the total system angular momentum to the sum of the applied torques; that is,

$$\dot{\bar{H}}_t = \Sigma \bar{T} \text{ applied} \quad (75)$$

Since all derivations will utilize the redefined or reference body axis system as defined in Section E-1, the subscript r will be dropped whenever convenient in all subsequent derivations. The total angular momentum, \bar{H}_t , is given by

$$\bar{H}_t = \bar{H}_v + \bar{H}_{cmg} \quad (76)$$

where

$$\bar{H}_v = \begin{bmatrix} I_x & \omega_x \\ I_y & \omega_y \\ I_z & \omega_z \end{bmatrix},$$

which is the vehicle angular momentum; the Observatory axes are assumed to be principal axes; and I_x , I_y , and I_z are the principal moments of inertia.

Similarly, the following equation is the CMG momentum for the four-skewed CMG configuration:

$$\bar{H}_{cmg} = \begin{bmatrix} H_x \\ H_y \\ H_z \end{bmatrix} \quad (77)$$

$$= \begin{bmatrix} h S\beta (S\alpha_1 + S\alpha_2 + S\alpha_3 + S\alpha_4) \\ h (C\alpha_1 - S\alpha_2 C\beta - C\alpha_3 + S\alpha_4 C\beta) \\ h (S\alpha_1 C\beta + C\alpha_2 - S\alpha_3 C\beta - C\alpha_4) \end{bmatrix}$$

where \bar{H} is the vector components of angular momentum in matrix form; h is the angular momentum magnitude of a single CMG; β is the CMG skew angle; and $\alpha_{1,2,3,4}$ is the CMG gimbal angle. The total time derivative of \bar{H}_t

relative to inertial space is

$$\dot{\bar{H}}_t = \dot{\bar{H}}_v + \dot{\bar{H}}_{\text{cmg}} \quad (78)$$

Relative to the HEAO reference coordinates,

$$\dot{\bar{H}}_v = (\dot{\bar{H}}_v)_r + \bar{\omega} \times \bar{H}_v \quad ; \quad (79)$$

$$\dot{\bar{H}}_v = \begin{bmatrix} I_x \dot{\omega}_x + (I_z - I_y) \omega_y \omega_z \\ I_y \dot{\omega}_y + (I_x - I_z) \omega_x \omega_z \\ I_z \dot{\omega}_z + (I_y - I_x) \omega_x \omega_y \end{bmatrix} \quad ; \quad (80)$$

$$\dot{\bar{H}}_{\text{cmg}} = (\dot{\bar{H}}_{\text{cmg}})_r + \bar{\omega} \times \bar{H}_{\text{cmg}} \quad ; \quad (81)$$

$$(\dot{\bar{H}}_{\text{cmg}})_r = \begin{bmatrix} h S\beta (\dot{\alpha}_1 C\alpha_1 + \dot{\alpha}_2 C\alpha_2 + \dot{\alpha}_3 C\alpha_3 + \dot{\alpha}_4 C\alpha_4) \\ h (-\dot{\alpha}_1 S\alpha_1 - \dot{\alpha}_2 C\beta C\alpha_2 + \dot{\alpha}_3 S\alpha_3 + \dot{\alpha}_4 C\alpha_4 C\beta) \\ h (\dot{\alpha}_1 C\alpha_1 C\beta - \dot{\alpha}_2 S\alpha_2 - \dot{\alpha}_3 C\alpha_3 C\beta + \dot{\alpha}_4 S\alpha_4) \end{bmatrix} \quad (82)$$

$$= \begin{bmatrix} \dot{H}_x \\ \dot{H}_y \\ \dot{H}_z \end{bmatrix} \quad ;$$

and

$$\bar{\omega} \times \bar{H}_{\text{cmg}} = \begin{bmatrix} H_z \omega_y - H_y \omega_z \\ H_x \omega_z - H_z \omega_x \\ H_y \omega_x - H_x \omega_y \end{bmatrix} . \quad (83)$$

The Euler equations for HEAO-C may be determined by substituting for $\dot{\bar{H}}_t$ in the original equations and using the following relationship:

$$\Sigma \bar{T} \text{ applied} = \bar{T} \text{ gravity} + \bar{T} \text{ magnetic} = \bar{T}_g + \bar{T}_m \quad (84)$$

where \bar{T}_g is the external disturbance torque due to gravity gradient and \bar{T}_m is the magnetic CMG desaturation torque, if used. The resulting Euler equations which describe the rotational motion of the HEAO-C spacecraft are as follows:

$$\left. \begin{aligned} I_x \dot{\omega}_x + (I_z - I_y) \omega_y \omega_z + \dot{H}_x + H_z \omega_y - H_y \omega_z &= T_{mx} + T_{gx} \\ I_y \dot{\omega}_y + (I_x - I_z) \omega_x \omega_z + \dot{H}_y + H_x \omega_z - H_z \omega_x &= T_{my} + T_{gy} \\ I_z \dot{\omega}_z + (I_y - I_x) \omega_x \omega_y + \dot{H}_z + H_y \omega_x - H_x \omega_y &= T_{mz} + T_{gz} \end{aligned} \right\} . \quad (85)$$

The body fixed angular rates ω_x , ω_y , and ω_z are related to the Euler angle rates $\dot{\phi}$, $\dot{\theta}$, and $\dot{\psi}$ by

$$\left. \begin{aligned} \dot{\phi} &= (\omega_x C\psi - \omega_y S\psi) / C\theta \\ \dot{\theta} &= \omega_y + C\psi + \omega_x S\psi \\ \dot{\psi} &= \omega_z - \dot{\phi} S\theta \end{aligned} \right\} , \quad (86)$$

where a (1, 2, 3) rotation order is assumed. Furthermore, the elements of the direction cosine matrix, B, transforming solar coordinates to body coordinates is given below.

$$\begin{aligned}
 B_{11} &= C\theta C\psi \\
 B_{12} &= C\phi S\psi + S\phi S\theta C\psi \\
 B_{13} &= S\phi S\psi - C\phi S\theta C\psi \\
 B_{21} &= -C\theta S\psi \\
 B_{22} &= C\phi C\psi - S\phi S\theta S\psi \\
 B_{23} &= S\phi C\psi + C\phi S\theta S\psi \\
 B_{31} &= S\theta \\
 B_{32} &= -S\phi C\theta \\
 B_{33} &= C\phi C\theta \quad .
 \end{aligned}$$

The solar offset angle is given by

$$\delta = \cos^{-1} (B_{11}) \approx \sqrt{\theta^2 + \psi^2} \quad (87)$$

and the target pointing error is given by

$$\delta_p = [(\phi - \phi_c)^2 - (\psi - \psi_c)^2]^{\frac{1}{2}} \quad , \quad (88)$$

where ϕ_c and ψ_c are the commanded Euler angles required for target pointing the long spacecraft axis to an experiment target source. The total spacecraft jitter rate is given by

$$\Delta = (\omega_x^2 + \omega_y^2 + \omega_z^2)^{\frac{1}{2}} \quad (89)$$

Disturbing Torques

Both external and internal disturbing torques will be acting on HEAO in orbit during normal operations. A basic prerequisite for the rational design of the attitude control system is a knowledge of disturbing torques and their effect on the spacecraft. The external torques are due to the external environmental conditions surrounding the spacecraft such as the gravitational field, air density, magnetic field, and solar radiation; whereas, the internal torques are due to physical spacecraft characteristics such as gas venting, mass movements, and actuation misalignments. All torques that tend to disturb the attitude of HEAO must be evaluated; however, an accurate evaluation depends upon a precise knowledge of the spacecraft physical properties, many of which are unknown during the preliminary design phase of HEAO-C. As examples, the spacecraft magnetic properties needed to evaluate magnetic torques are presently unknown. Also the amount of gas vented and the expulsion points are not defined. Moreover, the aerodynamic coefficients needed to evaluate aerodynamic torques are, at best, only estimates. The limiting factor in the assessment of gravitational disturbance torque is the difficulty of accurately determining the spacecraft inertial properties.

To facilitate the assessment of disturbing torques during the preliminary design phase of any spacecraft, the "NASA Space Vehicle Design Criteria" monographs in guidance and control provide a basis for calculating the disturbing torques. These monographs are based on previous experience and give guides for estimating torques even when the exact vehicle properties are unknown. In evaluating the disturbance torque magnitudes, worst case conditions and estimations will be assumed for those unknowns which are needed for an evaluation. These estimates will be combined with the known parameters to obtain conservative values for disturbing torques based upon simple calculations. If these calculations indicate that any torque is significant when compared to other disturbance torques, the more complex and accurate methods will be employed.

An initial 270 nautical mile circular orbit at an inclination of 28.5 degrees has been selected for HEAO-C. The launch date will be in the 1976 to 1978 time frame. During the mission, the altitude decays to 140 nautical miles at the end of two years. It seems rather unrealistic to use either the highest or lowest altitude to calculate environmental torques; hence, the altitude at

the end of one year, 240 nautical miles, will be used to establish environmental conditions at the year 1978. For disturbance torque calculation purposes the environmental conditions and their symbols are listed as follows:

$T = 1977$, year of launch;

$AL = 240$ n. mi., altitude above earth surface;

$i = 28.5$ degrees, orbital inclination;

$R_o = 0.3684 \times 10^4$ n. mi., orbit radius;

$M = 0.625525 \times 10^5$ n. mi.³/sec², gravitational constant;

$P_s = 0.965 \times 10^{-7}$ lb/ft², solar radiation pressure;

$P = 0.19403 \times 10^{-13}$ slug/ft³, air density;

$B = 0.3$ gauss, earth's magnetic field;

$W_o = 0.1036 \times 10^{-2}$ rad/sec, orbital angular rate;

and

$V = R_o W_o = 0.23214 \times 10^5$ ft/sec, spacecraft velocity.

The vehicle properties needed to calculate the disturbing torques are the inertial properties and the locations at which various forces act. For various HEAO-C configurations, the principal inertia values range from a low of 2878 slug-ft² on its minimum axis of inertia to a high of 98 000 slug-ft² on its maximum axis of inertia. Although the center of mass is defined for each configuration option, the centers of aerodynamic and solar radiation pressure must be estimated to obtain effective lever arms through which the environmental forces act. For disturbance torque calculation purposes, the following vehicle characteristics, along with appropriate symbols, are assumed:

$W = 16\ 000$ lb, vehicle weight;

$L = 21.5$ ft, RCS lever arm;

$I_{\min} = 3000$ (slug-ft²), minimum principal inertia;

$I_{\max} = 80\,000$ slug-ft², maximum principal inertia;

$L_t = 36$ ft, length of HEAO-C;

$d_o = 10$ ft, diameter of the OAS stage;

$d = 9$ ft, diameter of the HEAO stage;

$A = (10)(36) = 360$ ft², broad side surface area;

$L_a = L_t/3 = 12$ ft, aerodynamic lever arm;

$L_s = L_t/3 = 12$ ft, solar pressure lever arm;

and

$L_e = 2$ ft, estimated experiment disturbance lever arm.

In the following paragraphs, simplified equations are utilized to calculate each disturbing torque magnitude. For each calculation, a "NASA Space Vehicle Design Criteria" monograph will be referenced as a basis for making the required assumptions and for a derivation of the equations utilized.

The gravity gradient torque, T_g , results from the variation of the gravitational force over the distributed mass of the spacecraft. Vehicle orientations can be selected in which the torque is minimized; however, the maximum gravity torque [E-2] is given by

$$T_g (\text{max}) = 3M (I_{\max} - I_{\min})/2 [R_o (\text{min})]^3 . \quad (90)$$

Utilizing the appropriate parameters, the maximum gravity torque is

$$T_g (\text{max}) = \frac{(1.5) (0.625525 \times 10^5) (80\,000 - 3000)}{(0.368 \times 10^4)^3} ,$$

$$T_g (\text{max}) = 0.145 \text{ ft-lb} \quad (91)$$

In general, the gravity torque will dictate the energy requirements (CMG momentum or RCS fuel) and minimum actuator sizing for earth orbiting vehicles. The other environmental torques are expected to be much smaller.

The aerodynamic torque, T_a , results from the interaction between the spacecraft and the atmosphere and is determined to a large extent by atmospheric density. The aerodynamic force [E-3] is given by

$$F_a = (1/2) C_o P V^2 A \quad , \quad (92)$$

where a conservative estimate for the dimensionless drag coefficient is 2.6 and the estimated atmospheric density is 10^{-14} g/cm^3 which converts to $0.19403 \times 10^{-13} \text{ slug/ft}^3$. The aerodynamic force at 240 n. mi. is

$$F_a = (1/2) (2.6) (0.19403 \times 10^{-13}) (0.23214 \times 10^5)^2 (360) \quad ,$$

$$F_a = 0.4893 \times 10^{-2} \text{ lb} \quad . \quad (93)$$

When using approximations for torque calculations, the spacecraft is assumed to be broadside to the velocity vector and the moment arm, L_a , is taken to be one-third of the maximum spacecraft dimension.

The maximum aerodynamic torque is calculated in the following manner:

$$T_a (\text{max}) = F_a L_a \quad ,$$

$$T_a (\text{max}) = (0.4893 \times 10^{-2}) (12) \quad ,$$

$$T_a (\text{max}) = 0.0587 \text{ ft-lb} \quad . \quad (94)$$

The solar radiation torque, T_s , is caused primarily by solar photon radiation; other sources of radiation are usually at least an order of magnitude smaller and are negligible. Solar radiation varies as the inverse square of the distance between the spacecraft and the sun. Consequently, for earth orbiting vehicles, the radiation force is essentially independent of altitude and depends mainly upon the surface area exposed to the sun [E-4]. In the vicinity of the earth, the solar radiation pressure is considered constant, $P_s = 0.965 \times 10^{-7}$ lb/ft². To maximize the radiation torque, the broadside of the vehicle is normal to the sunline and the body is assumed to be completely reflective. Since the solar radiation lever arm is unknown, it is estimated to be one-third of the maximum vehicle dimension, $L_s = 12$ ft. Under the conditions assumed, the solar radiation torque is given by [E-5]:

$$T_s = 2 P_s L_s A (\cos E)^2 \quad , \quad (95)$$

where the angle of incidence, E , is zero. Substituting appropriate values gives

$$T_s = 2 (0.965 \times 10^{-7}) (12) (360) (1) \quad ,$$

$$T_s = 0.8338 \times 10^{-3} \text{ ft} - \text{lb} \quad . \quad (96)$$

Since the radiation sources such as earth reflection, earth emission, and spacecraft emission are expected to be much smaller than solar photon radiation, their torque magnitudes will not be evaluated.

The magnetic disturbance torque is caused by the interaction of the spacecraft's magnetic dipole moment with the earth's magnetic field. That is, the spacecraft tends to act like a compass and align itself with the earth's magnetic field. The following spacecraft sources cause magnetic torques [E-6a]:

Permanent magnetism in the spacecraft,

Spacecraft generated current loops,

Magnetism induced by external fields,

Currents induced by external fields, and

Rapidly spinning parts (CMGs) .

Since the parameters needed for an accurate evaluation are unknown, the HEAO-C will be classified as a Class II spacecraft. The design includes advisory specifications and guidelines for material and parts selection, avoidance of magnetic materials and current loops, and awareness of good design practices. The quality control includes inspection or test of parts. The vehicle or components are tested and depermed, with compensation as required. In a Class II nonspinning spacecraft [E-6a], the estimated dipole moment per unit mass is 3.5×10^{-3} A-m²/kg. The weight of HEAO-C is about 16 000 lb (7256 kg); therefore, the estimated dipole moment is

$$M = (3.5 \times 10^{-3}) (7256) \quad , \quad (97)$$
$$M = 25.396 \text{ (A-m}^2\text{)} = 0.1873 \times 10^{-2} \text{ ft-lb/gauss} \quad .$$

The maximum magnetic disturbance torque, T_m , calculation is as follows:

$$T_m = \sqrt{2} B M = \sqrt{2} (0.3) (0.1873 \times 10^{-2}) \quad , \quad (98)$$
$$T_m = 0.7945 \times 10^{-3} \text{ ft-lb} \quad ,$$

where B is the earth's magnetic field magnitude.

The venting torque due to RCS gas leakage or gas used in purging the HEAO experiments is expected to be small. About 10 lbm of gas is to be vented by the experiments during the two year mission; this is not necessarily continuous venting. There is no available estimate of ECS gas leakage. For worst case disturbance torque calculations, assume that 30 lbm of RCS hydrazine (about four percent of the total RCS fuel) is inadvertently leaked at a constant rate during the two year mission. To simplify the calculations, assume that the experiment gas is also hydrazine; therefore 18.14 kg (40 lbm) hydrazine is vented over the 0.63072×10^8 sec (2 yr) mission, resulting in the following equations:

$$dm/dt = 18.14/0.63072 \times 10^8 = 0.2877 \times 10^{-6} \text{ kg/sec} \quad (99)$$

which is the change in mass per unit time.

The venting force [E-6b] is given by

$$F_v = \frac{(dm)}{(dt)} V_e = \frac{(dm)}{(dt)} \sqrt{3kT/M} \quad , \quad (100)$$

where V_e (m/sec) is the velocity of the expelled gas relative to the vehicle, k (J/ $^{\circ}$ K) is the Boltzmann constant, T ($^{\circ}$ K) is the absolute temperature of the gas, and M (kg) is the mass of a single molecule. The molecular weight of hydrazine is 32.0453, which divided by Avogadro's number, 6.023×10^{23} mole $^{-1}$, gives 5.3205×10^{-26} kg. Assuming a gas temperature of 80° F gives $T = 300^{\circ}$ K. Boltzmann's constant is 1.381×10^{-23} J/ $^{\circ}$ K. Evaluating the venting force gives

$$F_v = (0.2877 \times 10^{-6}) [3 (1.381 \times 10^{-23}) (300)/5.3205 \times 10^{-26}]^{\frac{1}{2}} \quad , \quad (101)$$

$$F_v = 0.1391 \times 10^{-3} \text{ (N)} = 0.3126 \times 10^{-4} \text{ lbf} \quad .$$

To maximize the venting disturbance torque, the gas expulsion is assumed to occur at the RCS engine location; hence, the moment arm, L , is 21.5 ft. Based on the assumptions made, the maximum venting torque is

$$T_v = F_v L = (0.3126 \times 10^{-4}) (21.5) \quad , \quad (102)$$

$$T_v = 0.672 \times 10^{-3} \text{ ft-lb} \quad .$$

If the venting is at discrete intervals instead of continuous, the magnitude could increase by a factor of 10.

The disturbance torque due to internal moving parts on HEAO will be due to movement of experiment components near the focal plane of the telescope. The movements will be deliberately made slowly and will probably be performed

during the time experiment observations are not being made. Movement of experiments from one place to another is assumed to take about 5 minutes. During this time, momentum builds up during initial acceleration, but is taken out during the deceleration process, leaving no net momentum. The high resolution crystal spectrometer detector weighs about 389 lbm [E-7] and moves about 90 degrees in 5 minutes in an arc of 2 foot length [E-8] about an axis perpendicular to the longitudinal vehicle axis. The movement of 90 degrees in 5 minutes requires an average angular rate of 0.005233 rad/sec. The inertia associated with the moving mass is given by the following equation:

$$I_e = \frac{wt}{g} (L)^2 = 49.2 \text{ slug-ft}^2 \quad , \quad (103)$$

and the angular momentum is given by

$$h_e = I_e W_e = 0.257 \text{ ft-lb-sec} \quad . \quad (104)$$

If the assumption is made that electric motors produce the angular rate in one second, then the disturbance torque is

$$T_{e1} = dh_e/dt = 0.257 \text{ ft-lb} \quad (105)$$

due to rotation of the high resolution crystal spectrometer. A second disturbance source is from the movement of the total high resolution detector assembly 12 inches along the long vehicle axis as required to accommodate either the image detector or the crystal spectrometer. The assembly weight is about 517 lbm (16.06 slugs). Movement of 12 inches in 5 minutes requires an average velocity of 0.0033 ft/sec. Further, assuming that electric motors produce the average velocity in one second and that the mass is located two feet off the vehicle's centerline, the disturbance torque is given by

$$T_{e2} = m\dot{v}L = [16.06 (0.0033) (2)] = 0.106 \text{ ft-lb} \quad . \quad (106)$$

There are other internal movements such as the large area telescope, solid state detector, imaging proportional counter, and flat crystal

spectrometer; however, the associated mass moved is far less than that associated with the high resolution telescope and the expected disturbance torque is proportionally lower. As discussed previously, the disturbance torques due to internal movements exist only for very short intervals and the net momentum is zero. Since the CMGs can produce much higher torque levels than those due to internal movements, the design of the control system will not be impacted by movements associated with the experiments. Moreover, the movement of one experiment is not expected to affect the pointing stability of another experiment. The transport mechanisms are relatively undefined; hence the foregoing analysis is, at best, only an estimate.

The actuator misalignment torque is caused by the OAS engine misalignment relative to the longitudinal body axis. At most, the misalignment angle, E , is one-half of a degree. The lever arm, L_o , from the engine bell to the center of mass is about 23 ft and, while the OAS engine is burning its thrust, F_o , is about 275 lbf. The maximum disturbance torque is given by

$$T_o = L_o F_o \sin E = (23) (275) (0.00873) \quad ,$$

$$T_o = 55 \text{ (ft-lb)} \quad .$$
(107)

The torque due to OAS thruster misalignment far exceeds the other torque magnitudes, indicating that completely different thrust levels are needed to control attitude errors due to environmental torques than is needed for control during OAS burn.

The maximum magnitudes of the disturbing torques which are expected to act on HEAO-C are summarized in Table E-2. Of the environmental torques, only gravity gradient and aerodynamic are of sufficient magnitude to warrant further analysis. For comparative purposes, the torque magnitudes are also expressed as percentages of the gravity gradient. Since the disturbance torque during OAS burn is so large, further analysis is needed to establish the thrust level of the RCS needed for attitude control. Most of the torques, except gravity gradient, are expected to be cyclic in nature so that the long-term accumulated momentum is zero. However, for an inertially oriented spacecraft [E-1], gravity gradient torque always produces an accumulated momentum component which tends to establish the energy requirements for

attitude hold. Although the torque due to internal movements is relatively high, it is of very short duration and leaves the net system momentum unchanged. Internal movement torques are not considered as an important factor in the control system design.

TABLE E-2. DISTURBANCE TORQUE MAGNITUDES

Torque Source	Vehicle Axis	Max Magnitude (ft-lb)	Percent g. g. ^a
Gravity Gradient	Y	0.145	100
Aerodynamic	Y	0.587×10^{-1}	40
Solar Radiation	Y	0.834×10^{-3}	0.58
Magnetic	X, Y or Z	0.794×10^{-3}	0.55
Venting	Y or Z	0.672×10^{-3}	0.46
Internal Movement	Y or Z	0.257	177
OAS Misalignment	Y or Z	55.0	38 000

a. g. g. - gravity gradient.

Star Tracker Selection Analysis

The performance of the attitude sensing and control system (ASCS) can be expressed in terms of the following three quantities:

- Pointing — Error between actual and desired average pointing directions.
- Stability — Maximum amplitude of excursions about actual average pointing direction.
- Jitter — Maximum speed of excursions about actual average pointing direction.

Table E-3 gives the likely range of these quantities for HEAO-C type equipment, allowing for appropriate system gains and sensor dead zone.

TABLE E-3. TYPICAL PERFORMANCE OF STAR TRACKERS SUITABLE FOR HEAO-C

	Fixed Tracker (6 deg dia FOV) ^a		Gimballed Tracker	
	Nominal	Ultimate	Nominal	Ultimate
Pointing (arc sec)	30	20	5	2
Stability (arc sec)	2	0.4	1	0.2
Jitter (arc sec/sec)	0.2	0.05	0.4	0.03

a. FOV - field of view

The stability and jitter figures do not include any contributions for the effects of CMG nonlinearities. Use of a simplified CMG simulation indicates that CMG effects would be negligible insofar as HEAO-C jitter requirements are concerned. In practice, CMG behavior may prove to be the limiting factor when very low jitter and stability figures are sought. The stability and jitter estimates presented in Table E-3 are approximate and might be considerably revised after a more detailed simulation of the system dynamics.

In the fixed star tracker, nonlinearities in the electron optics result in a large pointing error for targets at the edge of the field of view that is proportional to the diameter of the field of view. This completely overshadows a small field-independent pointing error due to mechanical misalignment, thermal distortion, and imperfect knowledge of star position. Exceptionally precise manufacturing and calibration can reduce this minor error to as little as one or two arc seconds.

Jitter and stability errors in a fixed tracker are due to temperature changes, sensor noise, quantization in the electronics, and changing external magnetic fields. The best performance requires careful local temperature control, efficient signal processing, and extensive magnetic shielding or compensation.

The gimballed tracker can drastically reduce pointing error by using a much smaller optical field of view. However, its mechanical components introduce other errors which can be eliminated only by near perfect gimbal locking during star tracking.

A fixed tracker performs best if its field of view is no larger than required to provide star availability. At present only very limited data are available on the relation between tracker field, tracker limiting magnitude, and probability of star availability for random pointing direction. Figure E-11 shows empirical data (points up to magnitude +4.7) for guaranteed star availability, together with an extrapolation to fainter magnitudes based on the total number of stars at each magnitude. This extrapolation is somewhat subjective and should be replaced by empirical data generated by computer searches of star catalogs.

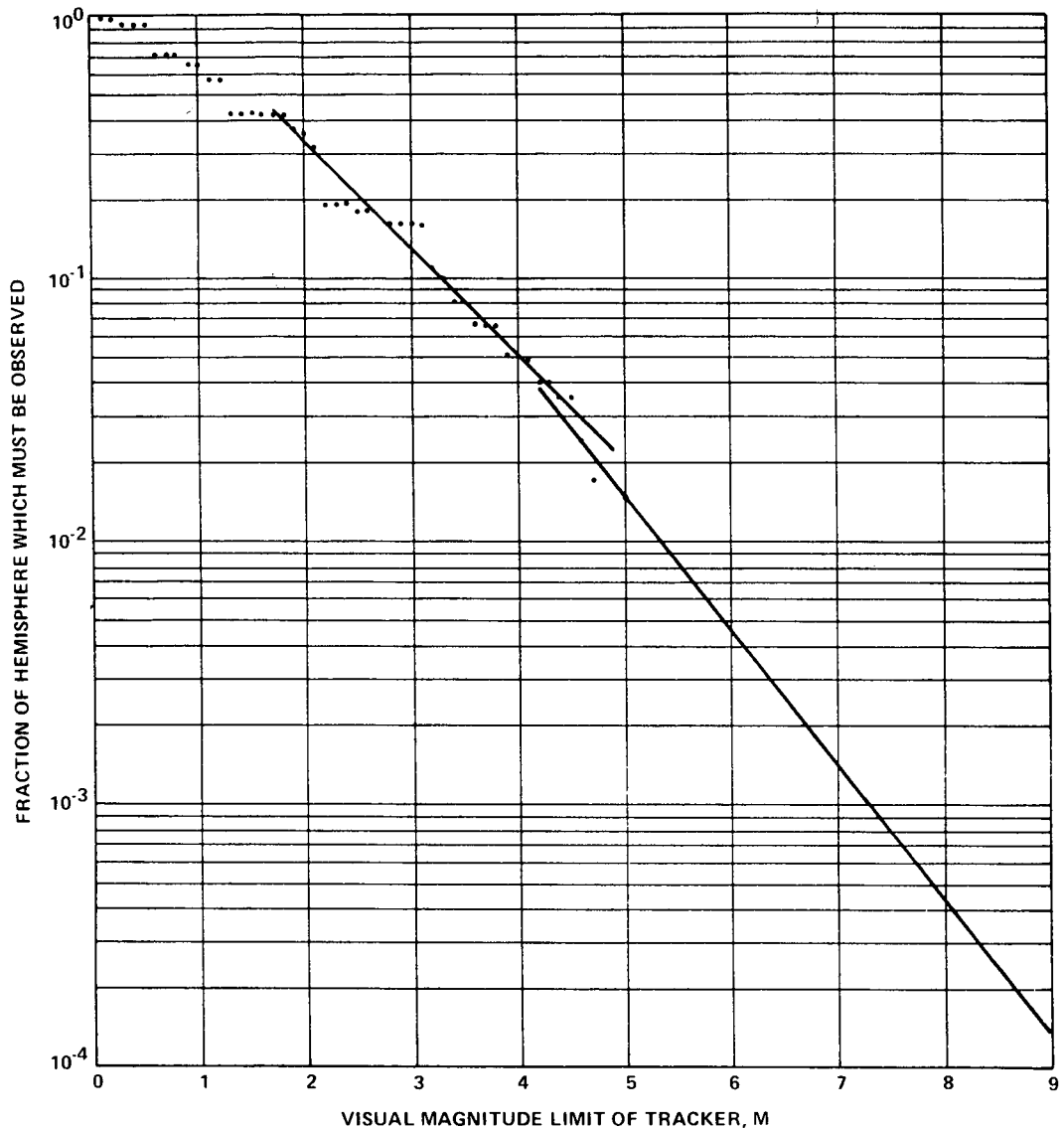
Using the data of Figure E-11, several tracker parameters can be related if typical tracker performance is known. The basic theory of the image dissector indicates that, for two similar trackers operating at a given required minimum signal-to-noise ratio, the required diameters, D_1 and D_2 , of the optical systems are approximately related to the required bandwidths, B_1 and B_2 , and the received starlight powers, P_1 and P_2 , in the following way:

$$\frac{D_1}{D_2} = \left(\frac{B_1}{B_2} \frac{P_2}{P_1} \right)^{\frac{1}{2}}, \quad (108)$$

where P is related to stellar magnitude, M , by

$$\log_{10} \left(\frac{P_1}{P_2} \right) = (100)^{\frac{1}{5}} (M_2 - M_1) .$$

For any values of B_1 and P_1 , the value of D_1 can vary widely as a function of tracker design, being particularly dependent on signal detection and modulation schemes, spectral range, and optical system losses. A careful survey of existing star trackers indicated that the best available state-of-the-art is fairly represented by a hypothetical tracker for which $D_1 = 2.0$ in., $B_1 = 1.0$ Hz, and $M_1 = +4.0$. With these values and the data of Figure E-11, it is possible to graph D as a function of tracker limiting magnitude M and, hence, of field of view diameter. Figure E-12 shows the required D as a function of



the FOV for a bandwidth of 0.33 Hz. Any tracker for which the point (D, FOV) lies above the curve of Figure E-12 will gather sufficient starlight to maintain an acceptable signal-to-noise ratio at this bandwidth. The bandwidth chosen is believed to be suitable for HEAO-C control. However, a tracker for which the FOV exceeds 10 degrees may contribute excessive pointing error due to nonlinearities; this establishes the right-hand boundary of the shaded region of "permissible design." Also, a tracker with an optical system diameter exceeding 7 inches may be unacceptably heavy, in which case the shaded region

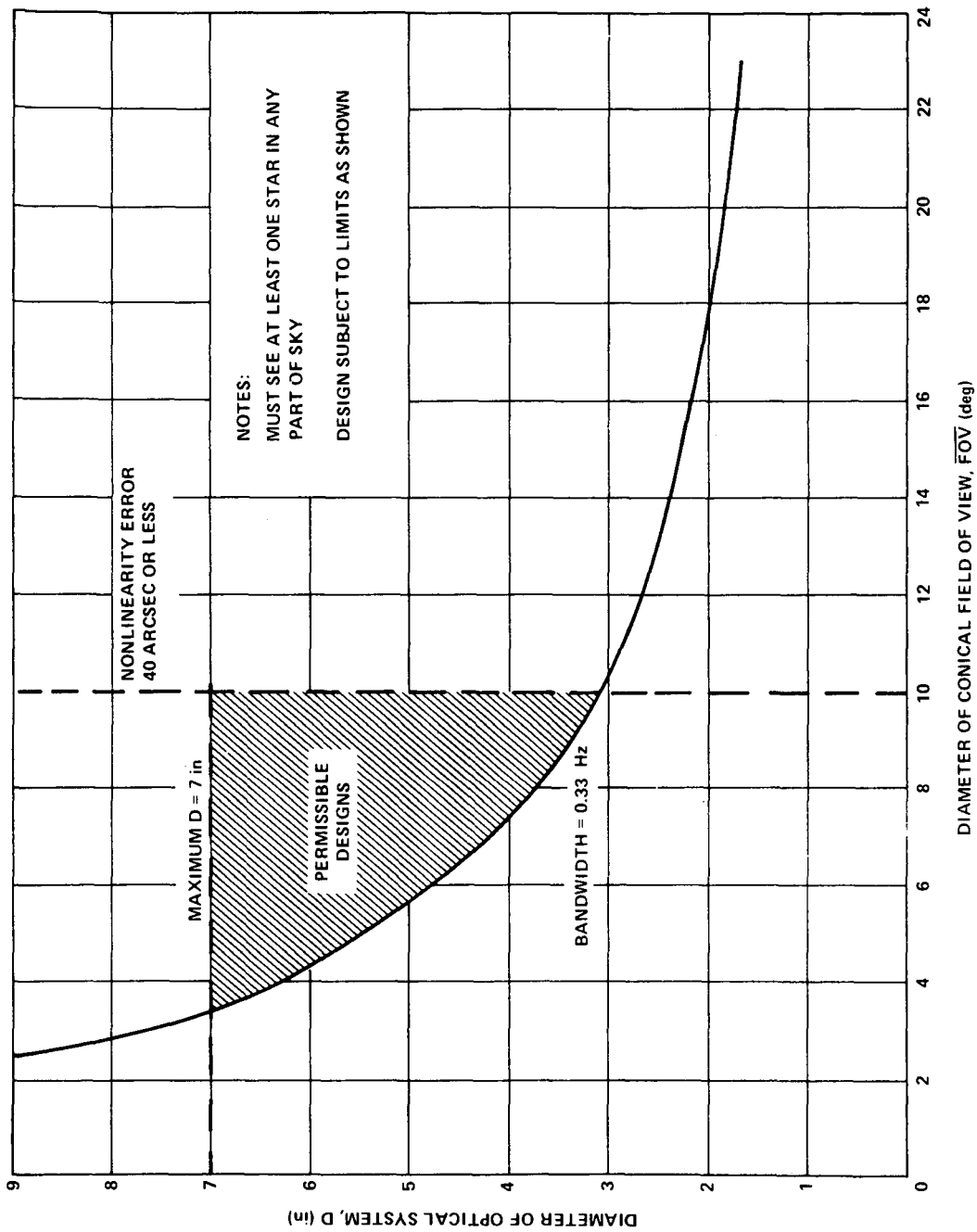


Figure E-12. Permissible fixed tracker designs.

has an upper boundary as shown. A tracker for which the point (D, FOV) lies within the shaded region is expected to detect at least one trackable star in any pointing direction, assuming the curve of Figure E-11.

It must be emphasized that Figure E-12 is based on the assumptions outlined above and that different assumptions would reshape and displace, though probably not enlarge, the shaded region of permissible designs. The small size of the region suggests that fixed tracker designs are restricted within fairly narrow limits and have little growth capability.

The picture is quite different for the gimballed tracker. Analysis shows that gimbaling rates and star acquisition will not require an instantaneous FOV larger than a few tenths of a degree in diameter; however, the effective FOV for purposes of star availability is as great as the gimbal freedom. Thus, the right-hand boundary of the shaded region of Figure E-12 may be moved to the right as much as 100 degrees, providing a very large range of permissible designs. Reliance on faint stars and a large star catalog is no longer necessary and tracker sensitivity to magnitude +2.0 or +3.0 is sufficient.

The analysis up to this point tends to indicate that a gimbal tracker selection would be desirable. However, the fixed head tracker has advantages in the areas of reliability, operational simplicity, cost, weight, and power. Because of the attractive features of the fixed tracker, further investigation was performed to determine the characteristics of a fixed tracker suitable for the HEAO-C mission.

Figure E-13 presents empirical data obtained from a star tracker manufacturer that relate the field of view diameter to visual magnitude of the stars. It was assumed that +6 visual magnitude stars would be the cutoff level for selecting a star tracker sensitivity due to the increased number of stars and noise problems present for any dimmer star sensitivity. From the 98 percent probability curve of Figure E-13, a +6 magnitude star sensitivity requires a 6 degree diameter field of view. Contacts with star tracker suppliers indicated that for the 6 degree FOV, the worst case edge tracking error will be 30 arc seconds or less, which meets the requirements of HEAO-C. Such designs are in progress using approximately a 3.5 inch diameter optical system.

In general, the most critical areas for star availability are near the galactic poles. The curve of Figure E-13 showing the average field of view diameter required to see at least one star versus visual magnitude near galactic poles indicates that for +6 magnitude stars, a 3.5 degree diameter field of view is required. The 6 degree FOV selected provides acceptable margin for the galactic pole region.

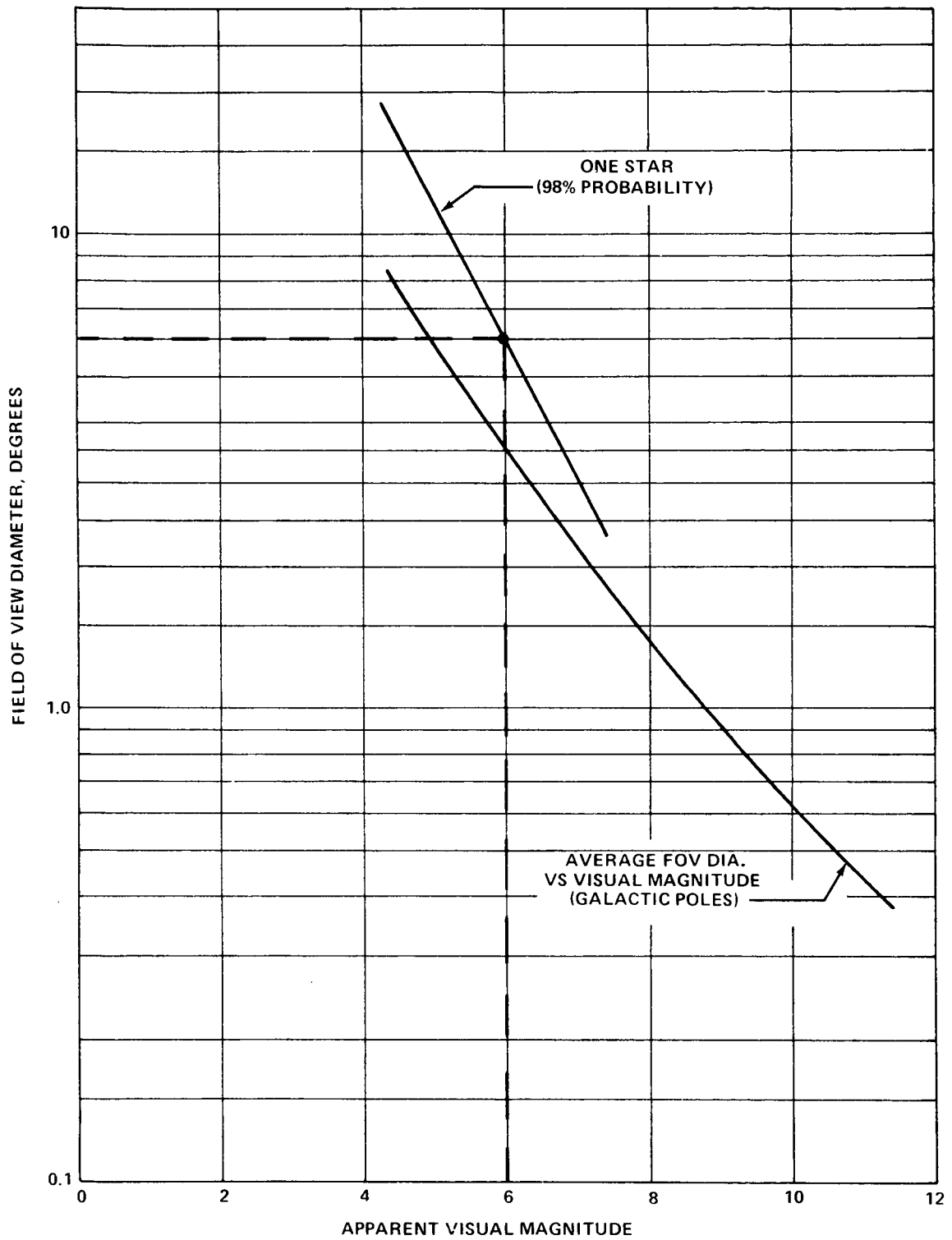


Figure E-13. Tracker field-of-view versus star magnitude relations.

To confirm the decision to use a 6 degree circular field of view and a tracker sensitive to +6 or brighter visual magnitude stars, a star search program was developed and is described briefly in the following section and in detail in another document.¹ A summary of the results show that for any look direction on the celestial sphere the probability of any one tracker seeing at least one star is 95 percent, while a fix, where one star per tracker is acquired, occurs 91 percent of the time.

HEAO-C Star Search Program

The selection of the baseline configuration of fixed head star trackers (FHSTs) requires the following trade studies:

- Field-of-view — Must be large enough to provide sufficient reference stars but minimized to reduce basic errors.
- Sensitivity — Must be sensitive enough to provide sufficient reference stars but minimized to reduce noise, saturation levels, and the number of stars to be identified.
- Configuration — Must provide star references for all pointing directions, redundancy, and backup operational modes.

To select the baseline star tracker systems and configurations and to confirm that reference stars would be available for all celestial orientations, a digital computer star search program was devised. The source of the star data was a catalog compiled by the Smithsonian Astrophysical Observatory containing approximately 259 000 stars. For HEAO-C purposes, all +6 visual magnitude or brighter stars were selected from this catalog in compiling a special star catalog for the star search program. After elimination of some stars of variable magnitude and ill-defined characteristics, the final catalog consisted of 4827 stars of +6 visual magnitude or brighter.

The four coordinate systems used are illustrated in Figure E-14. A reference coordinate system (x_r , y_r , z_r) is body fixed with x_r aligned to the sun and y_r aligned with the experiment optical axis. The orientation of each star tracker is specified by the components of a unit vector in the reference coordinate system in the direction of the tracker line-of-sight.

1. Weiler, W. J.: HEAO Star Tracker Search Program. To be published as a NASA Technical Memorandum by Program Development, George C. Marshall Space Flight Center.

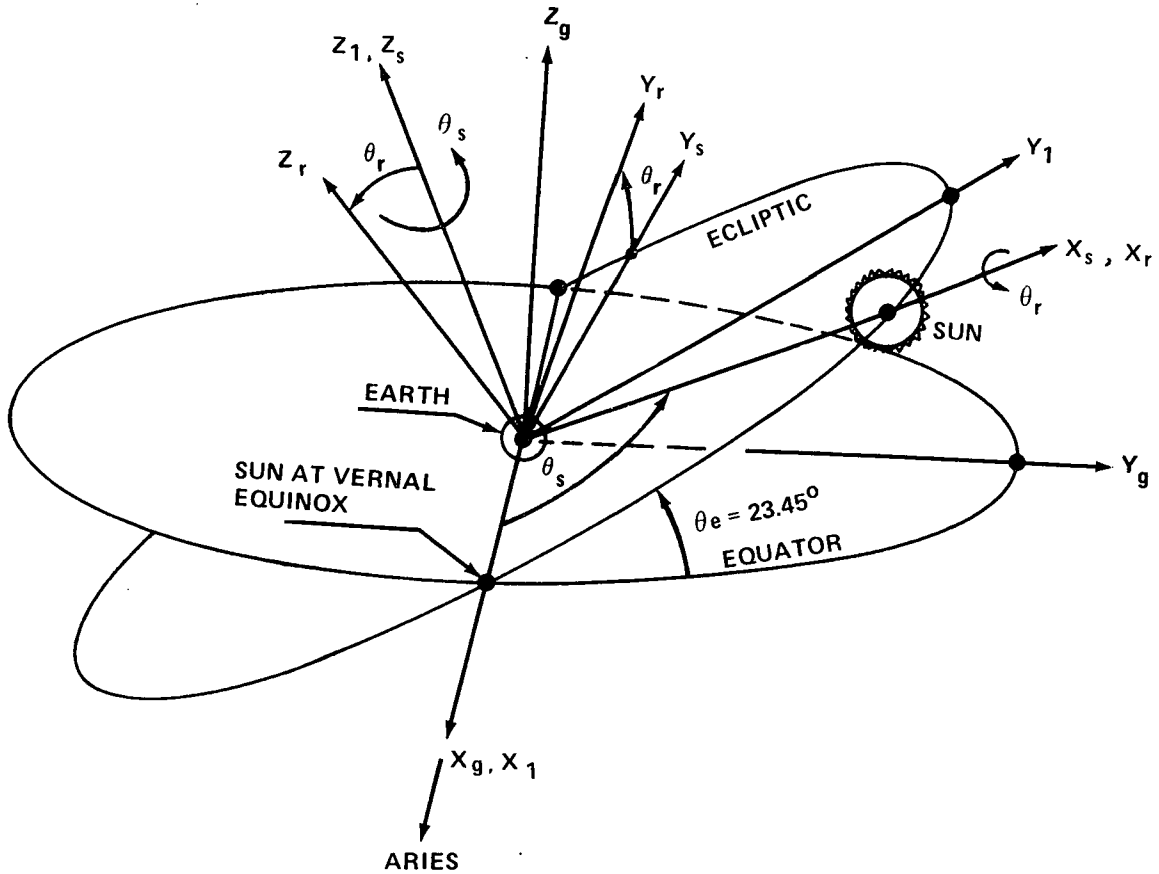


Figure E-14. Star search coordinate systems.

A solar fixed coordinate system (x_s, y_s, z_s) has x_s directed from the earth to the sun in the ecliptic plane and z_s perpendicular to the ecliptic plane in a northward direction.

An inertial ecliptic coordinate system (x_1, y_1, z_1) has x_1 directed from the earth along the line of ascending nodes (Aries) and $z_1 = z_s$ perpendicular to the ecliptic plane. θ_s is a measurement of the time of year from the vernal equinox.

A geocentric inertial system (x_g, y_g, z_g) has $x_g = x_1$ pointing to Aries with z_g perpendicular to the equatorial plane in a northward direction.

The x_1, y_1, z_1 system is rotated through the angle θ_e , 23.45 degrees, from the x_g, y_g, z_g system about the $x_g = x_1$ axis. The x_r, y_r, z_r system is rotated through an angle θ_r from the x_s, y_s, z_s system about the $x_s = x_r$ axis. The star catalog has its stars defined in the x_g, y_g, z_g systems in terms of a right ascension from the x_g axis and a declination above or below the equatorial plane. The star search is carried out in this x_g, y_g, z_g system.

Figure E-15 describes the general flow of the program. At the start, the data for that case are read in. The input data include the number of star trackers, the tracker FOV diameter, the initial and final sun angles, the increment size for the sun angle ($\Delta\theta_s$), rotation increment size about the sunline ($\Delta\theta_r$), and the unit vector direction components for each star tracker and its limiting visual magnitude. The program starts at the initial sun angle (θ_s initial) with vehicle rotation (θ_r) at zero. By coordinate transformations, the right ascension and declination of the look direction of each star tracker are found, and a search is carried out to determine the number of stars that are within the field of view of each tracker. A bookkeeping routine stores the results from which output data will be computed. The vehicle is then rolled about the sunline by an amount $\Delta\theta_r$, and the new look directions for each tracker are computed and the star search is repeated. This continues until a full revolution about the sun line has been completed. The data summarizing the search for this sunline orientation are printed, the sunline is incremented by an amount $\Delta\theta_s$, and the process is repeated. This procedure continues until the final sun angle has been acquired. Final data are then printed, and the program goes to the next case, if any, or terminates.

At the start of each case, the program prints out the number of stars found in the star catalog and all of the case input data. At the completion of the search for each sun angle, the following data summarizing the results of this sun angle are printed:

- Sun angle.
- Percent fix (Percent of look directions for which at least one star was seen in two or more trackers simultaneously).

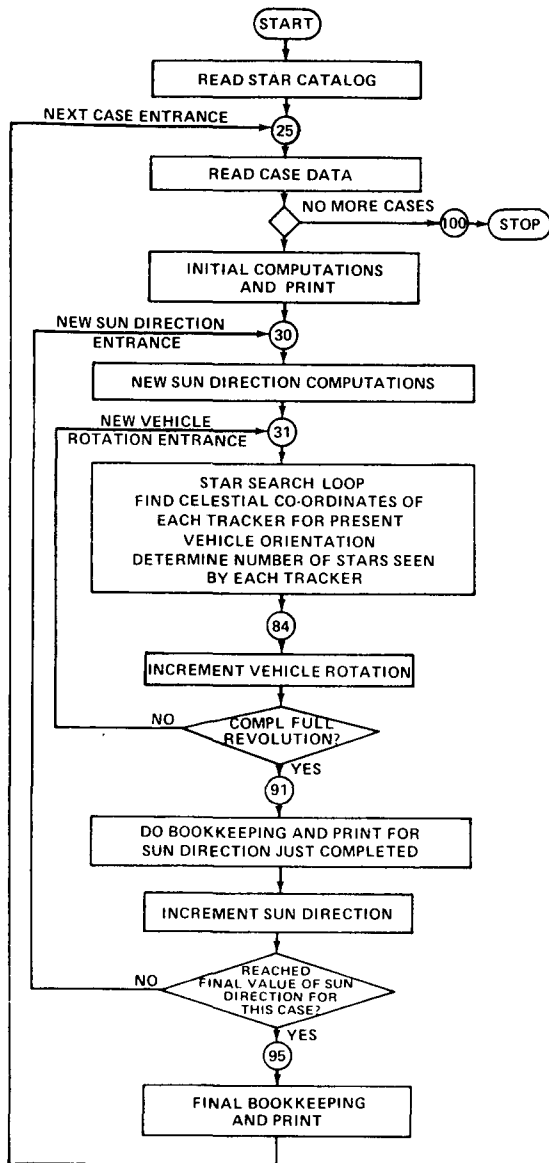


Figure E-15. Star search flow diagram.

along the x-axis and one tracker along the y-axis, the following results were obtained:

- Percent coverage for each tracker — 95 percent.
- Percent fix (two trackers — 1 star/tracker) — 91 percent.

- Each tracker -
 - Number,
 - Percent coverage (Percent of look directions this tracker saw at least one star),
 - Average number of stars seen per look direction,
 - Greatest number of stars seen at any one look direction.

At the completion of each case, the program prints the following data:

- Total number of look directions.
- Percent fix over the entire case.
- For each tracker-identical data to the sun angle print, but computed over the entire case.

For the baseline star tracker configuration using a star tracker design with a 6 degree diameter circular field of view, sensitive to +6 visual magnitude or brighter stars, and arranged to have one tracker

- Average number of stars per look direction — 3.4.
- Greatest number of stars seen by one tracker — 20.

Figures E-16 and E-17 provide plots of the star-empty look directions. Each point plotted indicates an experiment pointing direction in which a fix could not be obtained. In general, these directions are concentrated in the galactic polar regions but are separated to an extent that the probability appears to be low that an experiment pointing direction and one of these star-empty directions will coincide.

The worst case condition exists when no stars are available within the radius of the field of view of the star tracker aligned to the experiment optical axis. This would require using gyros alone, or the digital sun sensors and the y-axis tracker to sense spacecraft motions, with possible pointing accuracy degradation in this mode. A potential alternate configuration that would ease this situation is one in which the x-axis tracker is offset a few degrees from the experiment optical axis. For this case a slight roll about the experiment axis will displace the star tracker with respect to the celestial sphere and will bring reference stars into view.

An additional tracker that has its look direction in the x-y plane and midway between the baseline trackers provides three-star-tracker coverage. This case was simulated with a 98.9 percent fix in which one star was present in each of at least two trackers for any celestial pointing direction.

In conclusion, the baseline star trackers and baseline configuration provide ample coverage of the celestial sphere. Readily implemented alternates exist if further study indicates that greater coverage must be attained.

Alternate Sensors

1. Gimbal Star Tracker (GST). A first alternate to the baseline is the GST. The following are advantages of a GST over the FHST:

- Large effective FOV.
- Smaller instantaneous FOV.
- Smaller pointing error.

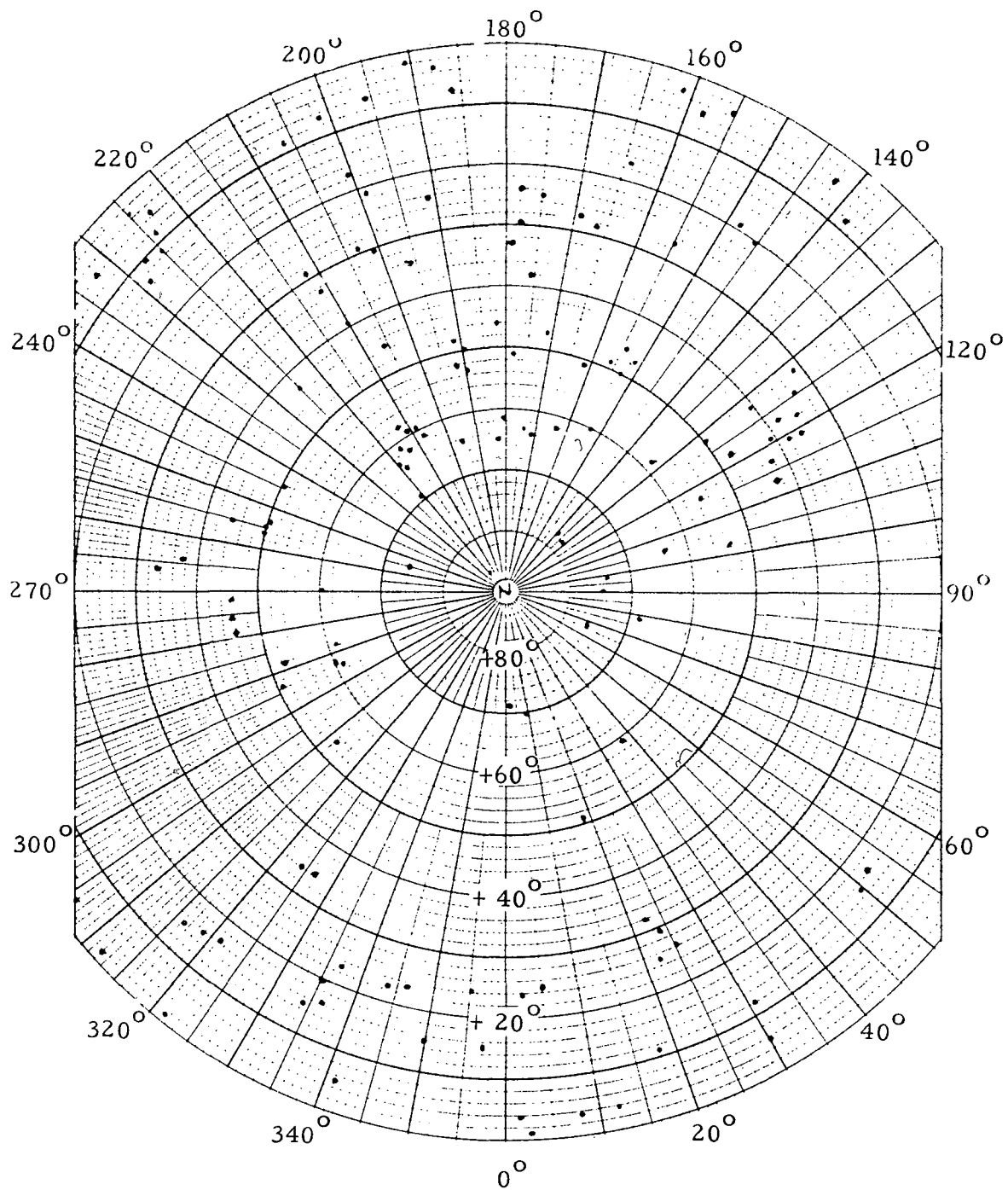


Figure E-16. Star-empty look directions (northern hemisphere).

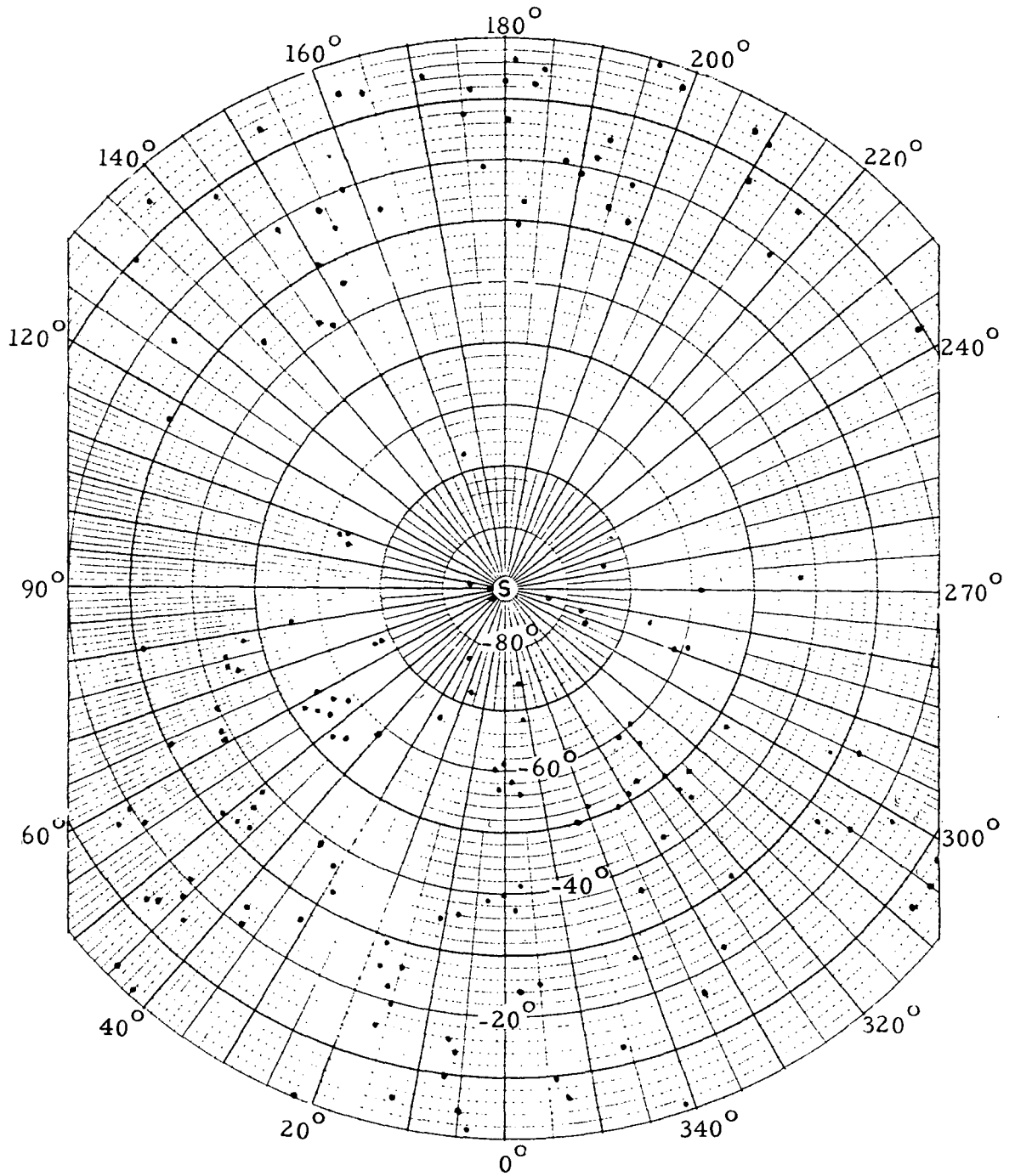


Figure E-17. Star-empty look directions (southern hemisphere).

- Lower noise equivalent angle.
- Improved pointing resolution.

Disadvantages of the GST are as follows:

- Operational complexity.
- Reliability.
- Gimbal dynamics.
- Gimbal angle encoder.
- Cost weight and power.

The larger effective field of view due to the gimbal freedom essentially eliminates the star availability problem. Also, the use of brighter navigation stars with a corresponding reduction in noise error becomes feasible. A reduction in the star identification complexity results when the brighter stars are used due to the reduction in the number of stars that must be manipulated.

Since the pointing error due to electron optics distortion increases with the size of the field of view, the smaller instantaneous FOV is a desirable feature. The smaller noise angle that is a direct result of reducing the FOV leads to better resolution and consequently improved overall pointing stability.

The operational complexity of the GST arises because of the gimbal management problem. Gimbal angles must be accurately measured to provide the necessary transformations in commanding the star tracker to acquire a given star and to read out the star coordinate data.

The added design complexity of the gimbals, gimbal components, and the gimbal control loop generally results in significant increases in cost, weight, and electrical power.

2. Reference Gyro Assembly (RGA). A number of functionally suitable gyro configuration options exist for the RGA. The following are some of these options:

- Dodecahedron (six-gyro).
- Multiple gyro skewed configurations.

- Multiple three-gyro strapdown assemblies.
- Two-degree-of-freedom gyro systems.

The tradeoff considerations are cost, system complexity, weight, reliability, and power.

The most reasonable alternate to the baseline appears to be the use of two separate three-axis gyro strapdown units. From all standpoints except reliability, this concept compares favorably with the baseline. Additional complexity must be added to obtain acceptable reliability by a cross-strapting arrangement between the individual gyros and the electronics assemblies.

Due to the mission duration, the basic gyro unit used in any of the alternate configurations should have hydrodynamic, gas-bearing supported rotors. This fact is supported by a large amount of operational data. An interesting alternate to this type of gyro is the Kearfott Gyroflex two degree of freedom gyros recently publicized in connection with aircraft stable platforms. As of this time, this gyro has not been recommended for strap-down applications and there probably are insufficient life data to warrant consideration for the HEAO. The principal attractions of the Gyroflex gyro are low cost and system simplicity.

3. Magnetometer. A three-axis magnetometer senses the geomagnetic field and produces a voltage proportional to the field strength along each axis, the polarity of the signal indicating the field direction along each axis. By comparison with a model of the geomagnetic field, taking into account the orbital parameters, the spacecraft attitude in three axes can readily be determined. Although the overall accuracy of this instrument is not high, it could be useful in attitude determination prior to the orbit adjust burn by making the acquisition of a star reference unnecessary. An additional use throughout the mission would be to provide a continuous monitoring of vehicle attitude. This has proved useful on some missions to indicate that the wrong stars were acquired.

Normally, the magnetometer would be used as a sensor in conjunction with a magnetic torquing capability and in this case can be made to serve a dual role as described. Utilization of a specific magnetometer is further described in an alternate system description in the following section.

Alternate Control Moment Gyro Configurations

The single gimbal and double gimbal control moment gyros (CMGs) are considered to be the basic building blocks for CMG system configurations. Many configurations are possible by varying the number and size of the CMGs, and by varying the relative orientations of the spin vector and gimbal axes with respect to each other and to the Observatory control axes. Each configuration has its own basic characteristics, momentum envelope, and control laws. For some configurations, multiple choice control laws exist to tailor the control system to the mission requirements.

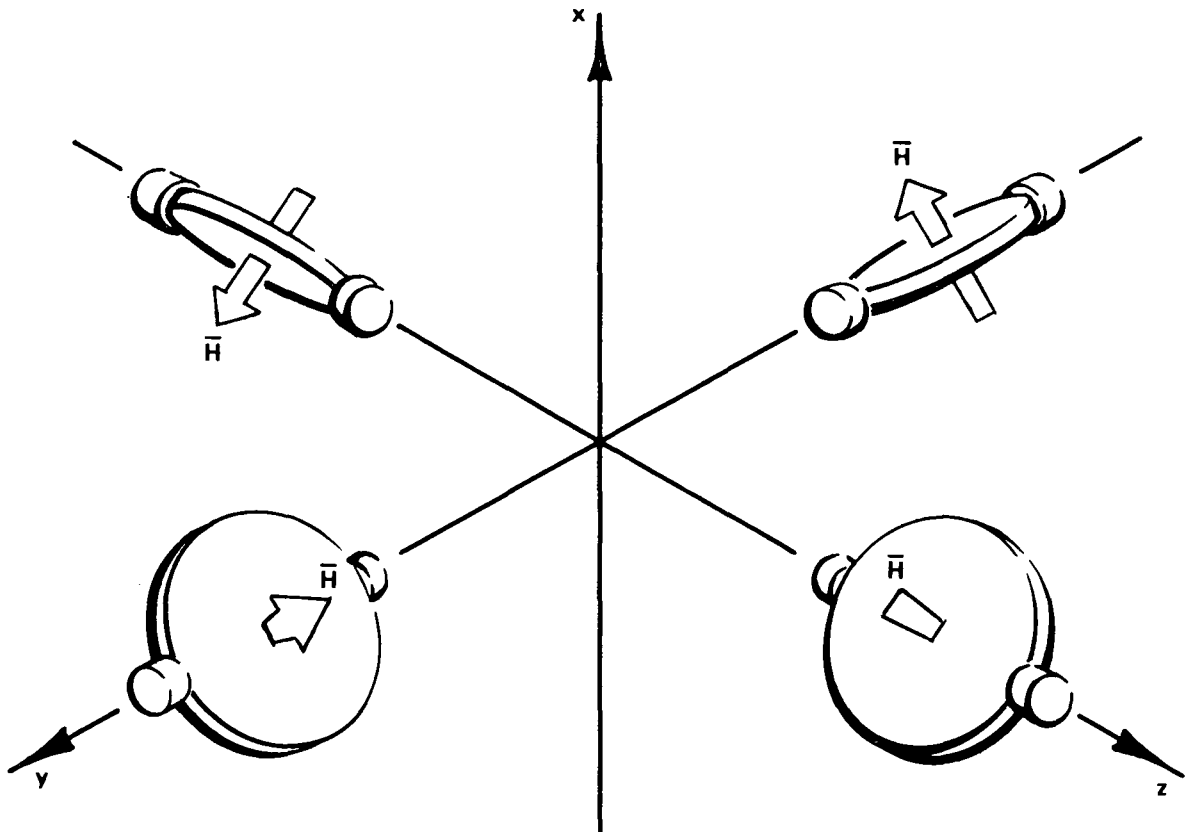
A typical four-gyro configuration that is considered an alternate for HEAO-C is the Sperry 4-FACS (4 gyro Fine Attitude Control System). A study was performed and a prototype was built under Contract NAS9-10363. Known modifications to the original system that would be required for the HEAO-C are the CMG momentum capacity, gimbal control loop design, and steering law gain constants.

Figure E-18 shows a layout schematic of the 4-FACS CMG configuration. This arrangement is very similar to the baseline 4-CMG skewed configuration. The primary differences are that in the 4-FACS system, all of the gimbal axes are aligned in one plane (the Y-Z plane as shown) and for the initial or zero momentum gimbal angles, the spin axes are tilted by an equal magnitude angle about the gimbal axes. The initial offset angle can be varied in accordance with mission needs and CMG momentum state. Another basic difference between the baseline and the 4-FACS is that, in the 4-FACS, the gimbal angles are controlled in a manner to keep the resultant vectors for paired gyros constrained to a plane. The gimbal angles for each gyro are additionally constrained to be less than 90 degrees. Generally, the gyros are sized so that the maximum angle is less than 60 degrees for a mission.

Complete details of the study and design of the 4-FACS system are contained in Reference E-9.

A number of other configuration concepts have been studied and reported in various technical documents. A final selection of a configuration and corresponding control laws for the HEAO will depend on reliability, failure capability, cost, weight, power, and ease of mechanization.

1. Scissored Pair CMG Configuration. The scissored pair CMG configuration is a possible alternate for the HEAO that has been given extensive



NOTE: THE GIMBAL AXIS OF EACH OF THE FOUR CMGs LIES IN THE y-z PLANE

Figure E-18. 4-FACS CMG configuration

analysis by several organizations. The scissored pair CMG configuration consists of six constant-speed, single-degree-of-freedom gimbaleed gyros which are used in pairs to provide three momentum vectors aligned with the three vehicle control axes. By slaving the gyros of each pair together, either electrically or mechanically, such that they are driven to equal gimbal angles, the torque produced on the vehicle is aligned along only one vehicle axis and no cross coupling occurs. This freedom from cross coupling is obtained at the expense of requiring six gyros to control three degrees of freedom, and a failure tends to negate the no-cross-coupling feature. (Additionally, a hardware implementation must be made to slave the gyros in pairs in a manner that will adjust the operation in accordance with mismatches of angular momentum and gimbal characteristics between the individual pairs of gyros.

This configuration has as its major advantages the supposed elimination of cross coupling between control axes and the simplicity of managing the gimbal commands in producing desired vehicle control torques. From a reliability standpoint, the studies have shown that, in general, the scissored pair configuration has little advantage over a four-gyro configuration. Conceivably, three gyro failures could occur and the system could still operate provided that no more than one failure per axis took place; however, the attractive feature of minimum cross coupling would be lost. (If two failures occurred, and both were on the same control axis, the system would be inoperative.) Six gyros, two per axis, are required for the system. Other systems have been conceived, and in most cases at least brought to the prototype stage, that can use six gyros in a skewed or in a planar configuration and supply a very high failure capability with a consequent substantial increase in reliability. This gain in reliability is accomplished at the expense of more sophisticated control laws requiring additional computation and failure detection implementation. Airborne computers have been advanced to the state where this additional complexity of control law implementation can be easily handled.

2. Skewed Configuration of Five or More Gyros. The predominant reason for using multiple gyro CMG system designs is that each gyro can be oriented to contribute a portion of the momentum required for each of the three control axes. The orientation can be chosen to have the momentum contribution shared equally by the gyros or in an unbalanced contribution. A choice of a particular orientation is determined by mission and spacecraft requirements.

By adding a gyro to the baseline, to make a total of five, a significant reliability improvement can be realized at the expense of somewhat increased control law and computation complexity. The cost of the additional gyro and its associated gimbal control loop may not be significantly greater than the baseline if an available design with reduced momentum capability and size can be used in all gyro positions.

Reliability and control law considerations are contained elsewhere in this document. Further study is required to assess the overall gains that might be realized by increasing the number of gyros from that of the baseline system.

Control Law Summary

1. Attitude Control Using Reaction Control System (RCS). Before beginning a discussion of the control law used in the baseline HEAO-C RCS study, it should be mentioned that the control law used is not necessarily the most suitable one for the HEAO-C. The control law as used works very well for attitude control but it is felt that during momentum dump it might have some disadvantages. It was originally felt that desaturation could be efficiently accomplished using the same logic and configuration used for attitude control. However, it has been found that momentum dumping will occur primarily about the transverse axes, so there will be a small demand on roll or X-axis control, negating the benefits of a logic with a high degree of roll mixing. Since the roll axis will have small or nonexistent accumulated secular momentum, roll mixing would cause deadband limit cycling between a pair of pitch/roll or yaw/roll engines where pitch is Z-axis and yaw is Y-axis control. Engine life would be decreased due to cycling, and small burn times would result. Pure pitch and yaw control would probably allow a longer burn time and higher Isp even though two engines would be operating simultaneously for an axis.

o

The control law used for the baseline studies is a straight line constant gain law with a gain ratio, A_1/A_0 , of 5 where $A_0 = 1$ and $A_1 = 5$. Attitude error and angular rate signals for HEAO are inputs to the control law that are multiplied by A_0 and A_1 before being summed to generate the commanded torques; thus,

$$\left. \begin{aligned} \delta_x &= A_{0x} \psi_x + A_{1x} \dot{\phi}_x \\ \delta_y &= A_{0y} \psi_y + A_{1y} \dot{\phi}_y \\ \delta_z &= A_{0z} \psi_z + A_{1z} \dot{\phi}_z \end{aligned} \right\} \cdot \quad (109)$$

Then, according to whether an engine controls pitch/roll or yaw/roll, the command torques are mixed and the resulting signals are applied to the signal modulators, the outputs of which supply the signals for engine excitation as shown in Figure E-19. The engine nomenclature is defined in the section, "Attitude Sensing and Control System Performance Simulations." The modulators simulated were simply a plus or minus deadzone limiter (i. e., no special modulation law was built into the modulators).

The control law used for the baseline study mixes roll in all eight of the reaction jets, resulting in equal control in both directions about each axis.

If roll were not mixed in the pitch axis, or the yaw axis, then two engines would have to be fired per axis to avoid introducing roll. Besides wasting fuel, the spacecraft would have excessive control in both pitch and yaw. Because the baseline configuration lends itself to signal mixing so well, it was decided to mix roll everywhere possible to avoid the unneeded large control torques. From an attitude control limit cycle viewpoint, the single engine firings that result are much more efficient than if roll were not mixed.

The primary advantage to mixing roll with pitch and yaw is the equal use of all eight engines for control allowing cycle life and throughput life for each engine to be increased due to less usage. If a law were used that pairs engines to fire simultaneously, the cycle life and throughput life would be decreased due to inefficiency, from an attitude control viewpoint.

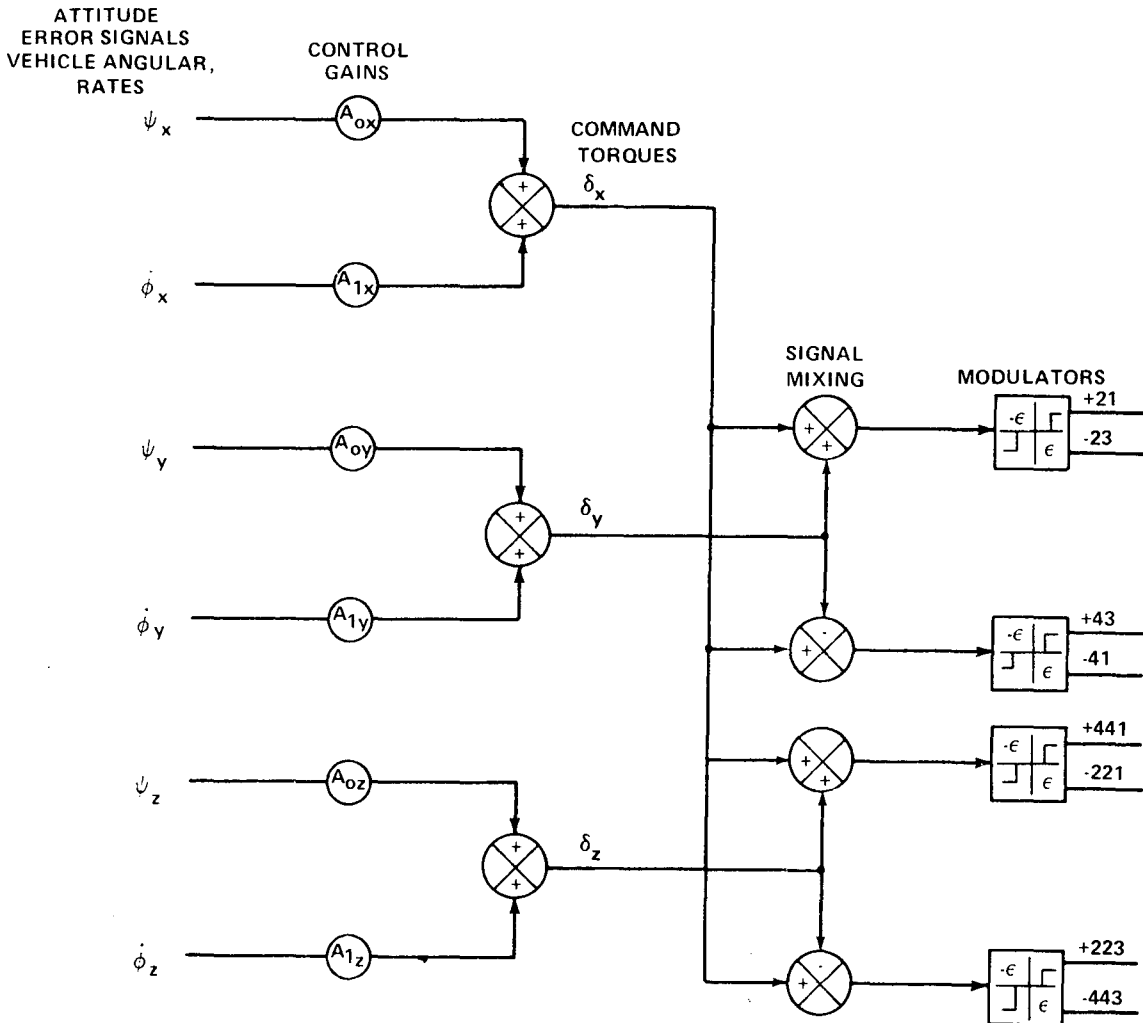


Figure E-19. The RCS control law used in the baseline studies.

In summary, the present baseline control law works very well during RCS attitude hold but it is questionable if the same law would be desirable for momentum dumping, the prime fuel consumer. One alternative would be to retain the present law, or a similar one, during attitude control and switch to a second dump law during momentum dumping. To avoid the added complexity of two laws, another alternative would be pure yaw control while mixing roll only on the pitch engines (small roll momentum). There will be some fuel wasted due to inefficient use of the engines during RCS attitude control but it is felt that the efficiency during CMG desaturation will be increased.

Control Laws for the Alternate RCS. As a first effort, it was decided to mix roll wherever possible with pitch and yaw in a manner similar to the baseline control law (Fig. E-19). The engine nomenclature is defined in the section, "Attitude Sensing and Control System Performance Simulations." The gain ratio, A_1/A_0 , remained at 5 and the command torques remained the same; only the signal mixing was different. The result, as expected, gave a somewhat inefficient control in that opposing roll engines frequently fired because one polarity of roll was handled by the pitch engines and the other polarity was handled by the yaw engines. Because of the inefficiency, a second law was devised that does not mix roll directly with pitch or yaw but the desirable feature of single engine firings in the roll axis is retained.

As shown in Figure E-20 the command torques are generated in the same manner as the other laws but there is no mixing of the command torques. This allows pitch and yaw to be controlled by a single engine firing in each direction; this capitalizes on the advantage offered by the alternate system, i. e. long single engine burns. To avoid the use of two-engine control in either direction in the roll axis, the polarity of the pitch and yaw signals is applied to the roll channel to pick the single roll engine that will best contribute to pitch or yaw control. Hence, while roll is controlled by a single engine, pitch or yaw is also aided. Since the pitch and yaw inertias are much higher than the roll inertia, resulting in shorter burns for control, no banging should occur due to a change in the polarity of the pitch or yaw errors. That is, roll should be back within its deadzone long before pitch or yaw is driven across its deadzone. The only possibility for two roll engines to fire simultaneously exists when the pitch or yaw signals are exactly zero. This is an extremely remote possibility and only single engine roll actuations are expected.

This second control law, Figure E-21, was found to lend itself to attitude control very well although a large number of actuations can accumulate on one engine since each pitch and yaw direction has only one prime controller whereas the baseline system has two per direction. The law will lend itself to momentum dumping very well though since long single engine burns will be

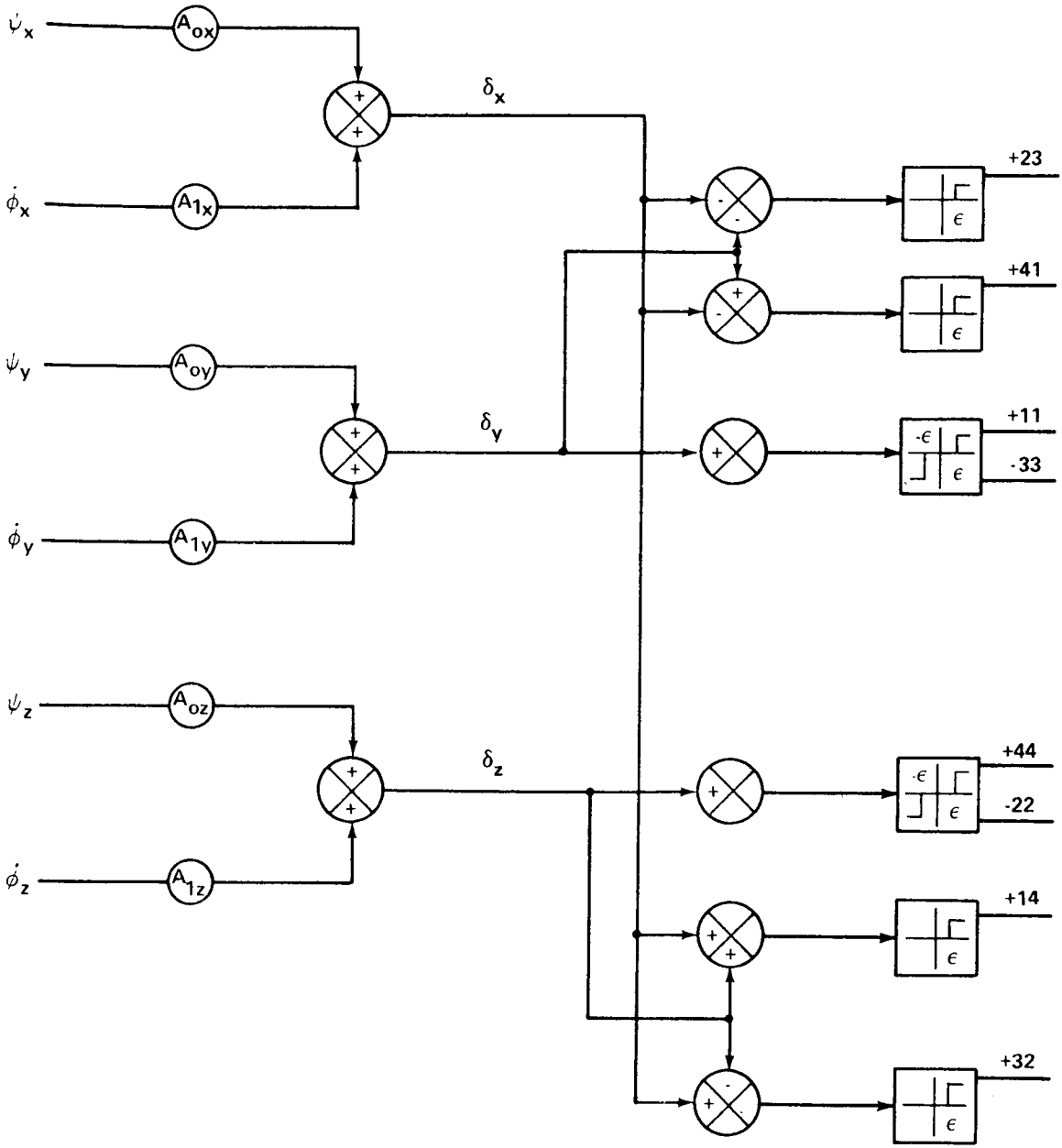


Figure E-20. The first RCS control law used in the alternate HEAO-C.

allowed in the pitch and yaw axes while the roll axis is easily controlled by separate engines. Since the momentum about the roll axis is expected to be very low, the separate roll control is again a desirable trait.

The alternate RCS configuration in conjunction with this second control law seems to offer several advantages over the baseline system, as

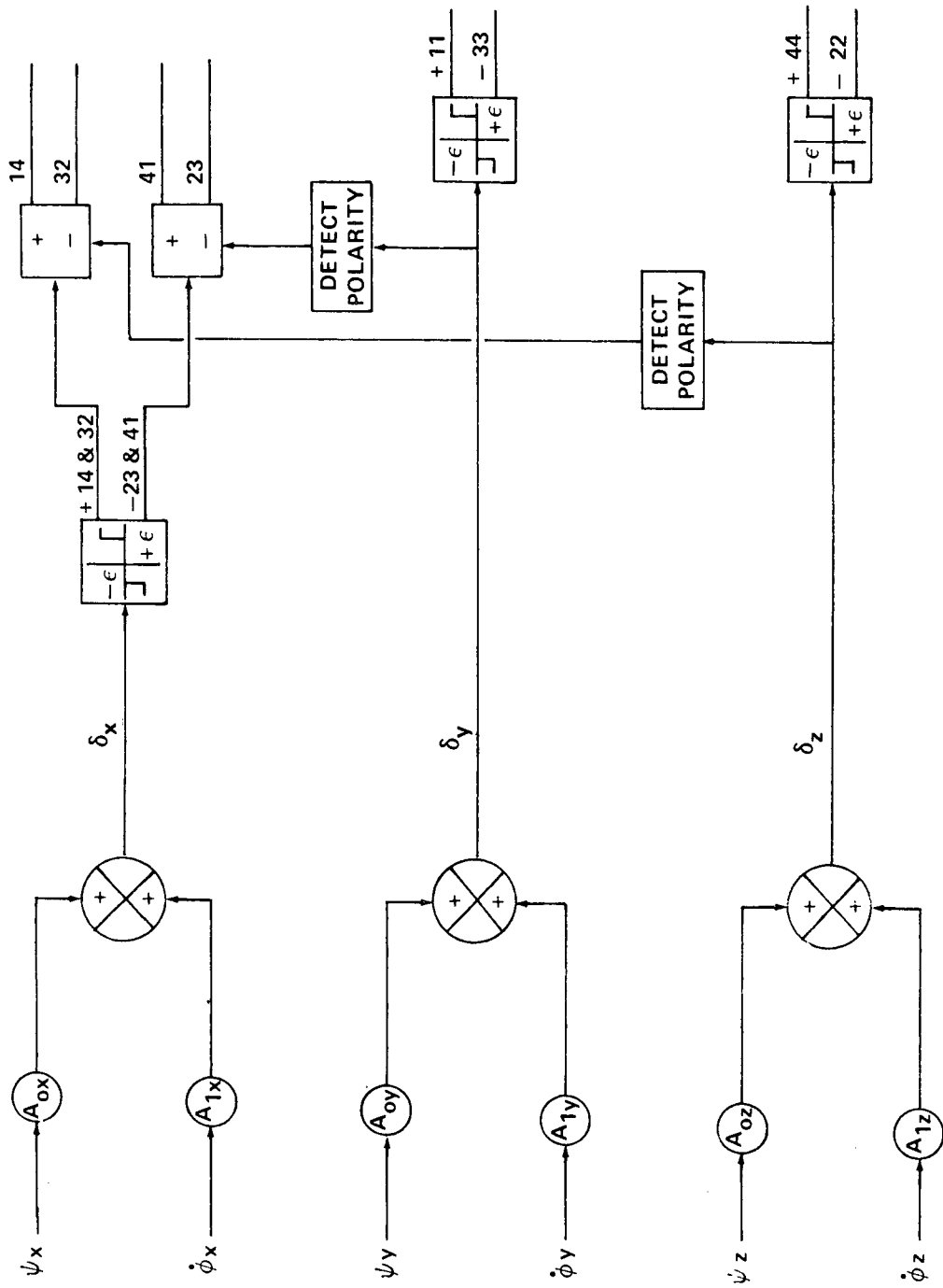


Figure E-21. Final control law for the alternate RCS configuration.

just mentioned. The main drawbacks, of course, will be the higher throughput, since only four engines are primarily used for pitch and yaw control. As mentioned previously, a requalification of the engines may be required before they could be used in the alternate system.

2. Attitude Control Using CMGs. Based on previous study results [E-8 and E-10] CMGs offer several advantages over reaction wheels especially from a power and weight viewpoint. Moreover, based on hardware availability [E-9 and E-11], there are several single-degree-of-freedom CMGs that are sized appropriately for the HEAO-C spacecraft, both from a torque and momentum viewpoint. For these reasons, single-degree-of-freedom CMGs have been baselined for HEAO-C. To provide continued operation capability when one CMG fails, at least four CMGs must be utilized. However, more than four may be dictated by reliability considerations to achieve the required two year lifetime. The CMG system selected by Bendix for the HEAO-A [E-11] seems to satisfy the HEAO-C requirements and has been baselined as the HEAO-C momentum exchange system. The same CMG developed for HEAO-A and -B should be utilized for HEAO-C to provide commonality between HEAO Missions A, B, and C and to realize the maximum development cost benefits. Figure E-1 illustrates the CMG arrangement relative to vehicle reference axes. Each CMG momentum vector is restricted to a plane that is skewed relative to the vehicle $Y_r - Z_r$ plane by the angle β ; the four planes form a pyramid whose apex is aligned with the vehicle X_r -axis; and each gimbal axis, X_c , is perpendicular to its associated plane as shown. The configuration is symmetrically skewed about the X_r vehicle axis so that none of the gimbal axes are parallel and none are parallel to a vehicle axis. As a result, each CMG can contribute momentum along each axis of the vehicle. In the event of one CMG failure, the remaining three CMGs provide the three degrees of freedom required for attitude control.

Once the CMG configuration has been selected, the second general problem area is closure of the attitude control loop through the momentum exchange system by gimbaling the CMGs in response to the attitude error signals. The logic and error signals which are used to drive the CMG gimbals are defined as the CMG steering law. The steering law must be selected such that the CMG torque produced closely approximates the desired vehicle control torque that is needed to maintain the vehicle's specified orientation. The first task that must be done prior to deriving a CMG steering law is to relate the CMG momentum and torque to the vehicle control axes. The momentum of each CMG must be projected into body control axes and summed to obtain the total CMG system momentum. In carrying out the required operations, several coordinate systems must be defined.

For any single gimbaled CMG, a coordinate system in which the CMG momentum is always constant along one axis (Figure E-22) is defined as follows:

i_c unit vector along the gimbal axis X_c

j_c unit vector along the momentum axis Y_c

k_c unit vector along the torque axis Z_c

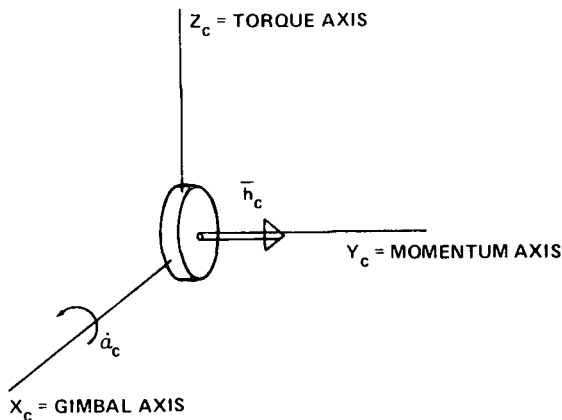


Figure E-22. CMG coordinate system.

The CMG coordinate system moves as the gimbal is varied with respect to the spacecraft body axes. Therefore, the momentum is always aligned with the Y_c -axis and the gimbal rate vector with the X_c -axis.

The torque produced by the c th CMG obeys the vector cross product law and always is aligned with the Z_c -axis. In the CMG constant momentum system, the gimbal rate $\dot{\alpha}_c$, momentum h_c , and the torque \dot{h}_c can be

written in vector form as follows:

$$\dot{\alpha}_c = \dot{\alpha}_c i_c \quad , \quad (110)$$

$$\bar{h}_c = h_c j_c \quad , \quad (111)$$

and

$$\dot{\bar{h}}_c = \dot{\alpha}_c \times \bar{h}_c = \dot{\alpha}_c h_c (i_c \times j_c) = \dot{\alpha}_c h_c k_c \quad . \quad (112)$$

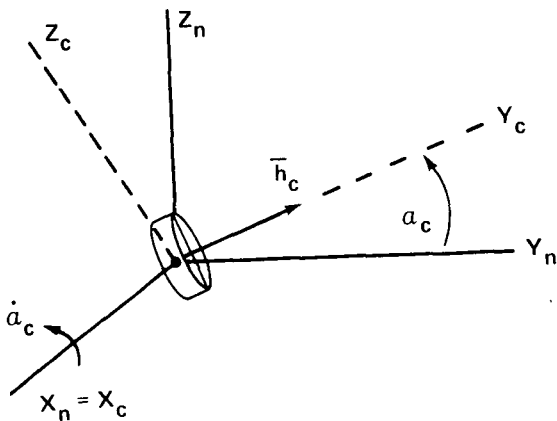
A second CMG system is defined by setting the CMG gimbal angle to zero or to a position which nulls out the total momentum of all CMGs. Such a reference, illustrated in Figure E-23, is defined as the CMG null coordinate system. When the gimbal angle is zero, the CMG null system is identical to

the CMG constant momentum system. The CMG null system is related to the constant momentum system by the rotation α about the gimbal axis which is constant in either system. The subscript n denotes the null coordinate system for a particular CMG. In vector matrix form the transformation between the two systems is written as:

$$\tilde{X}_c = A_{cn} \tilde{X}_n, \quad (113)$$

where

$$\tilde{X}_c = \begin{pmatrix} X_c \\ Y_c \\ Z_c \end{pmatrix}, \quad \tilde{X}_n = \begin{pmatrix} X_n \\ Y_n \\ Z_n \end{pmatrix}, \quad \text{and } A_{cn} = \begin{bmatrix} 1 & 0 & 0 \\ 0 & C\alpha_c & S\alpha_c \\ 0 & -S\alpha_c & C\alpha_c \end{bmatrix}.$$



The manner in which the two CMG reference systems have been defined permits the matrix A_{nc} to hold for any single-degree-of-freedom CMG. However, the mounting of each CMG is unique.

Each CMG has its own null coordinate system uniquely defined relative to the spacecraft body axes by the CMG mounting arrangement, the desired momentum envelope, and the number of CMGs. For each CMG, a matrix transformation A_{nr} must be derived to relate the spacecraft reference axis to the CMG null coordinates. The relation may be written as

$$\tilde{X}_n = A_{nr} \tilde{X}_r, \quad (114)$$

where the subscript r denotes the body axis reference frame. The relation between body and CMG constant momentum systems is obtained by

$$\tilde{X}_c = A_{cn} \tilde{X}_n = (A_{cn} A_{nr}) \tilde{X}_r = G_{cr} \tilde{X}_r \quad , \quad (115)$$

where

$$G_{cr} = \begin{bmatrix} g_{11}^c & g_{12}^c & g_{13}^c \\ g_{21}^c & g_{22}^c & g_{23}^c \\ g_{31}^c & g_{32}^c & g_{33}^c \end{bmatrix} .$$

The elements of G_{cr} are obtained by matrix multiplication of A_{cn} and A_{nr} and must be derived for each CMG. The letter c would take on the number assigned to a specific CMG. Since the transformations in this case are orthogonal the inverse is identical to the transpose, which is denoted by a star superscript; hence,

$$\tilde{X}_r = G_{cr}^* \tilde{X}_c \quad . \quad (116)$$

Use of transformation (115) yields the following equations for the c th CMG gimbal rate, momentum, and torque in-body axes:

$$\dot{\alpha}_c = \dot{\alpha}_c (g_{11}^c i_r + g_{12}^c j_r + g_{13}^c k_r) \quad , \quad (117)$$

$$h_c = h_c (g_{21}^c i_r + g_{22}^c j_r + g_{23}^c k_r) \quad , \quad (118)$$

and

$$\dot{h}_c = \dot{\alpha}_c h_c (g_{31}^c i_r + g_{32}^c j_r + g_{33}^c k_r) \quad . \quad (119)$$

The equations for total momentum and torque from m CMGs is obtained by summing the vector components:

$$\bar{H} \text{ (CMG)} = \sum_{c=1}^m \bar{h}_c = h_x i_r + h_y j_r + h_z k_r \quad (120)$$

and

$$\dot{\bar{H}} \text{ (CMG)} = \sum_{c=1}^m \dot{\bar{h}}_c = \dot{h}_x i_r + \dot{h}_y j_r + \dot{h}_z k_r \quad (121)$$

Due to environmental forces acting on an orbiting spacecraft, the CMG momentum vectors will deviate considerably from their null positions. In most orbits in which the spacecraft is inertially oriented, momentum tends to accumulate in some direction due to biased environmental forces. Under these conditions, the CMG momentum becomes concentrated in this direction until no further momentum can be obtained from the CMG system. This condition is referred to as CMG saturation. To desaturate the CMGs, a torque must be applied to the vehicle such that the CMGs are driven back either to their null position or some bias level by trying to counteract the applied torque.

a. Four-Skewed CMG Configuration. To develop a CMG steering law, the transformations, equation (115), must be derived for each CMG which relates its torque and momentum to spacecraft reference axes. The four-skewed CMG configuration, baselined for HEAO-C, is illustrated in Figure E-24. Each CMG is shown at its null position and the geometry between the CMG null and spacecraft reference coordinates is illustrated. At the null position, the momentum of CMG Number 1 and Number 3, as well as that of CMG Number 2 and Number 4, cancel. The transformations are carried out by first rotating negatively about each Y_n axis by the angle β which aligns the transformed X_n' axis with the X_r reference axis. The next rotation is about the once transformed $X_n' = X_r$ axis until the coordinates are aligned as follows: 0 about X_1' , 270 degrees about X_2' , 180 degrees about X_3' , and 90 degrees about X_4' . The results are summarized for each CMG in the form of equation (114) as follows.

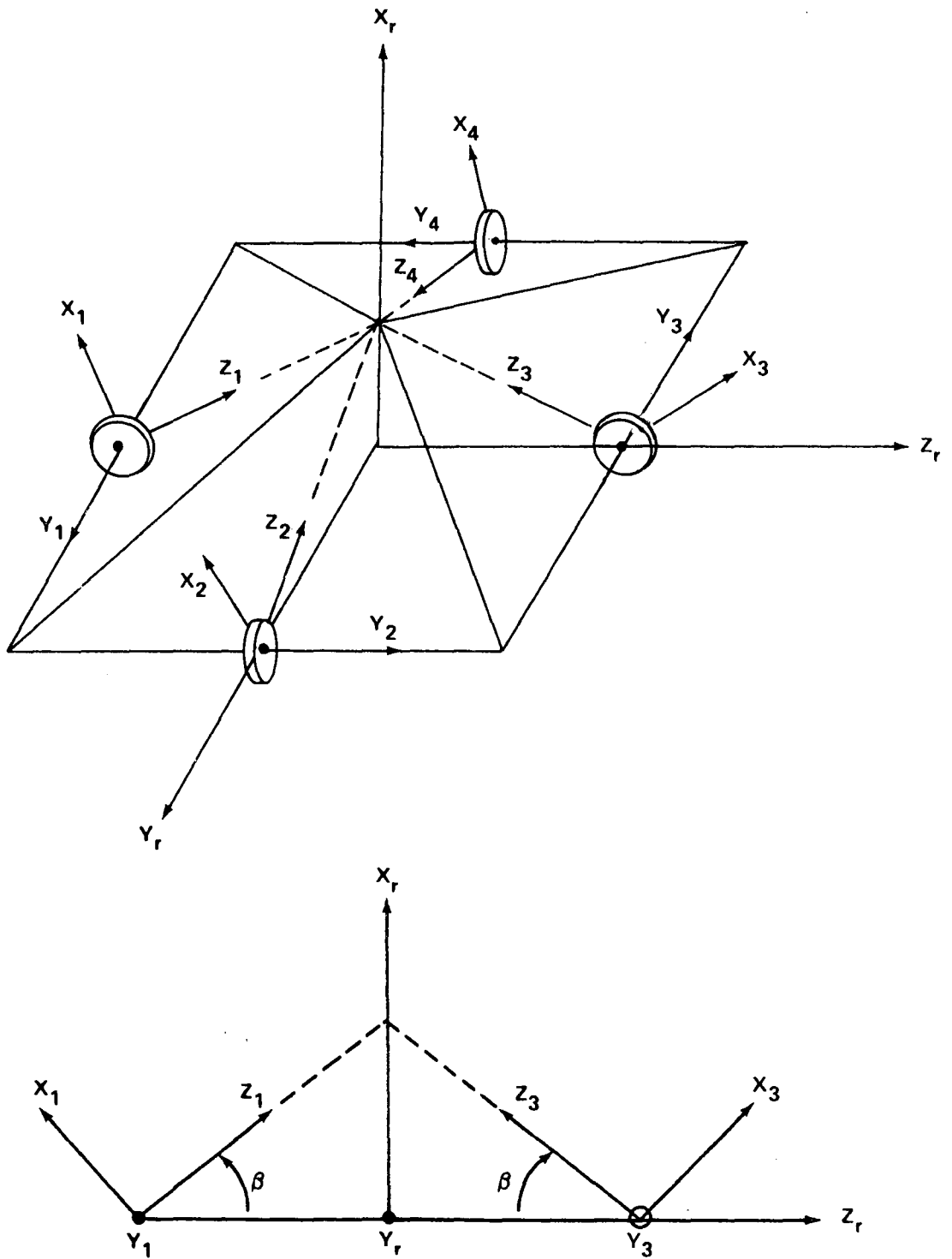


Figure E-24. Skewed CMG geometry and null coordinates.

$$\tilde{X}_1 = \begin{bmatrix} C\beta & 0 & -S\beta \\ 0 & 1 & 0 \\ S\beta & 0 & C\beta \end{bmatrix} \tilde{X}_r, \quad n = 1 \quad (122)$$

$$\tilde{X}_2 = \begin{bmatrix} C\beta & S\beta & 0 \\ 0 & 0 & 1 \\ S\beta & -C\beta & 0 \end{bmatrix} \tilde{X}_r, \quad n = 2 \quad (123)$$

$$\tilde{X}_3 = \begin{bmatrix} C\beta & 0 & S\beta \\ 0 & -1 & 0 \\ S\beta & 0 & -S\beta \end{bmatrix} \tilde{X}_r, \quad n = 3 \quad (124)$$

$$\tilde{X}_4 = \begin{bmatrix} C\beta & -S\beta & 0 \\ 0 & 0 & -1 \\ S\beta & C\beta & 0 \end{bmatrix} \tilde{X}_r, \quad n = 4 \quad (125)$$

As given by equation (113), the transformation between spacecraft reference and CMG constant momentum coordinates is

$$\tilde{X}_c = \begin{bmatrix} 0 & 0 & 0 \\ 0 & C\alpha_c & S\alpha_c \\ 0 & -S\alpha_c & C\alpha_c \end{bmatrix} \tilde{X}_n, \quad n = 1, 2, 3, 4 \quad (126)$$

Equation (115) is obtained by substituting equations (122), (123), (124), and (125) into equation (126) and carrying out the matrix multiplications with $c = n$.

For four-skewed CMGs, the transformations between body and CMG constant momentum axes are summarized below.

CMG Number 1

$$\tilde{\mathbf{X}}_1 = \mathbf{G}_{1r} \tilde{\mathbf{X}}_r, \quad \mathbf{G}_{1r} = \begin{bmatrix} C\beta & 0 & -S\beta \\ S\beta S\alpha_1 & C\alpha_1 & C\beta S\alpha_1 \\ S\beta C\alpha_1 & -S\alpha_1 & C\beta C\alpha_1 \end{bmatrix} \quad (127)$$

CMG Number 2

$$\tilde{\mathbf{X}}_2 = \mathbf{G}_{2r} \tilde{\mathbf{X}}_r, \quad \mathbf{G}_{2r} = \begin{bmatrix} C\beta & S\beta & 0 \\ S\beta S\alpha_2 & -C\beta S\alpha_2 & C\alpha_2 \\ S\beta C\alpha_2 & -C\beta C\alpha_2 & -S\alpha_2 \end{bmatrix} \quad (128)$$

CMG Number 3

$$\tilde{\mathbf{X}}_3 = \mathbf{G}_{3r} \tilde{\mathbf{X}}_r, \quad \mathbf{G}_{3r} = \begin{bmatrix} C\beta & 0 & S\beta \\ S\beta S\alpha_3 & -C\alpha_3 & -C\beta S\alpha_3 \\ S\beta C\alpha_3 & S\alpha_3 & -C\beta C\alpha_3 \end{bmatrix} \quad (129)$$

CMG Number 4

$$\tilde{\mathbf{X}}_4 = \mathbf{G}_{4r} \tilde{\mathbf{X}}_r, \quad \mathbf{G}_{4r} = \begin{bmatrix} C\beta & -S\beta & 0 \\ S\beta S\alpha_4 & C\beta S\alpha_4 & -C\alpha_4 \\ S\beta C\alpha_4 & C\beta C\alpha_4 & S\alpha_4 \end{bmatrix} \quad (130)$$

Utilizing body to CMG transformations, the momentum for each CMG can be written in body coordinates [equation (118)] as

$$\left. \begin{aligned} \bar{h}_1 &= h_1 j_1 = h_1 (S\beta S\alpha_1 i_r + C\alpha_1 j_r + C\beta S\alpha_1 k_r) \\ \bar{h}_2 &= h_2 j_2 = h_2 (S\beta S\alpha_2 i_r - C\beta S\alpha_2 j_r + C\alpha_2 k_r) \\ \bar{h}_3 &= h_3 j_3 = h_3 (S\beta S\alpha_3 i_r - C\alpha_3 j_r - C\beta S\alpha_3 k_r) \\ \bar{h}_4 &= h_4 j_4 = h_4 (S\beta S\alpha_4 i_r + C\beta S\alpha_4 j_r - C\alpha_4 k_r) \end{aligned} \right\} . \quad (131)$$

The total CMG momentum is the vector sum of all CMG momentum vectors [equation (120)]; thus,

$$\bar{H} = \sum_{c=1}^4 \bar{h}_c = h_x i_r + h_y j_r + h_z k_r \quad , \quad (132)$$

where

$$h_x = S\beta (h_1 S\alpha_1 + h_2 S\alpha_2 + h_3 S\alpha_3 + h_4 S\alpha_4) \quad ,$$

$$h_y = h_1 C\alpha_1 - h_3 C\alpha_3 + C\beta (h_4 S\alpha_4 - h_2 S\alpha_2) \quad ,$$

and

$$h_z = h_2 C\alpha_2 - h_4 C\alpha_4 + C\beta (h_1 S\alpha_1 - h_3 S\alpha_3) \quad .$$

As previously stated, the CMG momentum in reference coordinates will be used as the basis for momentum management to prevent CMG saturation and to make the CMGs operate about their null positions. The components of equation (132) are zero when the gimbal angles are zero. However, there are other combinations of gimbal angles which also produce a null momentum condition.

Using equations (127) through (130), the individual CMG torques [equations (112) and (119)] are obtained in reference coordinates as follows:

$$\dot{\mathbf{h}}_1 = \dot{\alpha}_1 h_1 (S\beta C\alpha_1 \mathbf{i}_R - S\alpha_1 \mathbf{j}_R + C\beta C\alpha_1 \mathbf{k}_R) \quad , \quad (133)$$

$$\dot{\mathbf{h}}_2 = \dot{\alpha}_2 h_2 (S\beta C\alpha_2 \mathbf{i}_R - C\beta C\alpha_2 \mathbf{j}_R - S\alpha_2 \mathbf{k}_R) \quad , \quad (134)$$

$$\dot{\mathbf{h}}_3 = \dot{\alpha}_3 h_3 (S\beta C\alpha_3 \mathbf{i}_R + S\alpha_3 \mathbf{j}_R - C\beta C\alpha_3 \mathbf{k}_R) \quad , \quad (135)$$

and

$$\dot{\mathbf{h}}_4 = \dot{\alpha}_4 h_4 (S\beta C\alpha_4 \mathbf{i}_R + C\beta C\alpha_4 \mathbf{j}_R + S\alpha_4 \mathbf{k}_R) \quad . \quad (136)$$

The total CMG torque, equation (121), is obtained by summing the contributions from each CMG:

$$\dot{\mathbf{H}} = \sum_{c=1}^4 \dot{\mathbf{h}}_c = \dot{h}_x \mathbf{i}_R + \dot{h}_y \mathbf{j}_R + \dot{h}_z \mathbf{k}_R \quad , \quad (137)$$

where

$$\dot{h}_x = S\beta (\dot{\alpha}_1 h_1 C\alpha_1 + \dot{\alpha}_2 h_2 C\alpha_2 + \dot{\alpha}_3 h_3 C\alpha_3 + \dot{\alpha}_4 h_4 C\alpha_4) \quad ,$$

$$\dot{h}_y = -\dot{\alpha}_1 h_1 S\alpha_1 - \dot{\alpha}_2 h_2 C\beta C\alpha_2 + \dot{\alpha}_3 h_3 S\alpha_3 + \dot{\alpha}_4 h_4 C\beta C\alpha_4 \quad ,$$

and

$$\dot{h}_z = \dot{\alpha}_1 h_1 C\beta C\alpha_1 - \dot{\alpha}_2 h_2 S\alpha_2 - \dot{\alpha}_3 h_3 C\beta C\alpha_3 + \dot{\alpha}_4 h_4 S\alpha_4 \quad .$$

Equation (137) can be arranged in the vector matrix form

$$\begin{bmatrix} \dot{h}_x \\ \dot{h}_y \\ \dot{h}_z \end{bmatrix} = \begin{bmatrix} h_1 S\beta C\alpha_1 & h_2 S\beta C\alpha_2 & h_3 S\beta C\alpha_3 & h_4 S\beta C\alpha_4 \\ -h_1 S\alpha_1 & -h_2 C\beta C\alpha_2 & h_3 S\alpha_3 & h_4 C\beta C\alpha_4 \\ h_1 C\beta C\alpha_1 & -h_2 S\alpha_2 & -h_3 C\beta C\alpha_3 & h_4 S\alpha_4 \end{bmatrix} \begin{bmatrix} \dot{\alpha}_1 \\ \dot{\alpha}_2 \\ \dot{\alpha}_3 \\ \dot{\alpha}_4 \end{bmatrix} \quad (138)$$

In compacted notation, equation (138) is written as

$$\dot{\tilde{H}} = C \dot{\tilde{\alpha}} \quad , \quad (139)$$

where C is a 3 by 4 matrix and $\dot{\tilde{H}}$ and $\dot{\tilde{\alpha}}$ are column vectors. Notice that the columns of C are vectors directed along each CMG torque axis, Z_c .

Since there are four torque vectors, the columns are linearly dependent.

In the foregoing sections, the momentum and torque potentials for the baseline four-skewed CMG configuration have been developed relative to the spacecraft reference axes. The next steps are to select a skew angle and to examine several candidate steering laws.

b. Skew Angle and Momentum Capacity. The foregoing equations have been derived without selecting a specific value for the CMG skew angle β , which has been assumed to be equal for all CMGs. Several factors enter into the selection of β : (1) Momentum capacity per axis and total momentum envelope, (2) Control torque capability around the null position, (3) Alignment of each gimbal axis to provide the independent degrees of freedom required for three-axis control. When one CMG has failed, the remaining three CMGs must be able to control the vehicle without degrading performance. With this in mind, a skew angle of 45 degrees would provide the greatest angular distance between gimbal rate vectors and between reference and gimbal axes. The CMG system would, therefore, provide the best operational capability with one CMG out. If the skew angle were 90 degrees, control torques could be attained about each reference axis but the X_r axis would have twice the momentum storage capacity as the other two axes. Moreover, with one CMG out, severe cross coupling would result on the X_r axis by trying to command only a Y_r or Z_r torque. For example, if h_1 were out, with β equal 90 degrees, only CMG

Number 3 could produce a Y_r axis torque, but that torque could not be produced without also torquing the X_r and Z_r axes.

The skew angle could be selected to give equal torque capability per axis near the CMG null position. By setting the gimbals to some predetermined upper limit (depending on the CMG torque motor characteristics) and setting the sign to give maximum torque per axis, equation (137) at the null position reduces to the following equations:

$$\left. \begin{aligned} \dot{h}_x (\text{max}) &= 4h S\beta \dot{\alpha}_1 \\ \dot{h}_y (\text{max}) &= 2h C\beta \dot{\alpha}_1 \\ \dot{h}_z (\text{max}) &= 2h C\beta \dot{\alpha}_1 \end{aligned} \right\} . \quad (140)$$

Equating maximum torque components produces

$$\tan(\beta) = 0.5 \quad . \quad (141)$$

A skew angle of 26.6 degrees, therefore, provides equal torque per axis capability near the CMG null position. However, the momentum envelope is not symmetric and, as the gimbals vary, the torque capability per axis does not stay equal. Since the gimbals may become rather large if momentum is dumped infrequently, equal torque per axis at the CMG null does not appear to be a good criterion for selecting the skew angle.

A more logical approach is to select the skew angle so that the CMG momentum envelope is spherical, that is, equal momentum capacity per axis. By setting the gimbals to values which produce maximum momentum per reference axis, equation (132) reduces to the following equations:

$$\left. \begin{aligned} h_x (\text{max}) &= 4h S\beta \\ h_y (\text{max}) &= 2h (1 + C\beta) \\ h_z (\text{max}) &= 2h (1 + C\beta) \end{aligned} \right\} . \quad (142)$$

Equating maximum momentum components produces

$$2 S\beta = 1 + C\beta \quad . \quad (143)$$

By squaring each side and eliminating $S^2\beta$ by trigonometric identity, the following quadratic equation is obtained:

$$5 C^2\beta + 2 C\beta - 3 = 0 \quad . \quad (144)$$

The solution of equation (144) gives a skew angle of 180 or 53.1 degrees. However, 180 degrees is a false solution since the X_r axis momentum would be zero. Table E-4 gives the maximum momentum capacity per axis for several skew angles and CMG momentum values. With a skew angle of 53.1 degrees and a unit CMG momentum of 250 ft-lb-sec, each axis has a CMG momentum potential of 800 ft-lb-sec for control purposes. A skew angle of 28.1 degrees gives twice as much momentum on the Y_r and Z_r axes as on the X_r axis, whereas 45 degrees gives 150 ft-lb-sec less on the X_r axis as compared to the transverse axis. Based on the foregoing analysis, a skew angle of either 45 or 53.1 degrees is recommended for HEAO-C.

c. CMG Gimbal Control. When the CMG gimbal angles are moved, a corresponding change occurs in the momentum relative to the body axes. By definition, torque is the time rate of change of angular momentum. Therefore, the spacecraft is acted upon by a torque when the CMG gimbal angles are changing. One basic objective, and general problem area, is the derivation of the CMG gimbal rate commands to torque the vehicle with the CMGs in some desirable manner providing control of the angular motions as well as stability. In general, a spacecraft control law is derived as a linear combination of sensor outputs such as rate gyros, sun sensors, star trackers, etc., which have been weighted by a constant gain on each output. The gains are selected to give the desired vehicle response and stability characteristics. Ideal control would be obtained if the torque called for by the vehicle control law could be produced by the CMGs. The control law is typically derived with respect to the spacecraft reference axes and may be written in the following general vector form:

$$\bar{T}_c = T_{cx} i_r + T_{cy} j_r + T_{cz} k_r \quad . \quad (145)$$

TABLE E-4. MAXIMUM MOMENTUM CAPABILITY FOR FOUR-SKEWED CMGs (ft-lb-sec)

h/ CMG	$\beta = 0$ deg		$\beta = 28.1$ deg		$\beta = 45$ deg		$\beta = 53.1$ deg		$\beta = 90$ deg	
	h_x	$h_y = h_z$	h_x	$h_y = h_z$	h_x	$h_y = h_z$	h_x	$h_y = h_z$	h_x	$h_y = h_z$
25	0	100	47	94	71	85	80	80	100	50
50	0	200	94	188	141	171	160	160	200	100
100	0	400	188	376	283	966	320	320	400	200
250	0	1000	470	940	707	854	800	800	1000	500
500	0	2000	940	1880	1414	1707	1600	1600	2000	1000

The basic objective is the derivation of a CMG gimbal control law providing an approximately of the CMG torque and the torque specified by the spacecraft control law.

The standard approach is to equate the total change in CMG angular momentum $\dot{\bar{H}}$, equation (121), to the desired torque \bar{T}_c . The vector components are equated with a negative sign and arranged in the following vector matrix form:

$$\begin{bmatrix} T_{cx} \\ T_{cy} \\ T_{cz} \end{bmatrix} = \begin{bmatrix} \\ \\ \\ \end{bmatrix} \begin{bmatrix} \dot{\alpha}_1 \\ \dot{\alpha}_2 \\ \cdot \\ \cdot \\ \cdot \\ \dot{\alpha}_n \end{bmatrix} \quad (146)$$

The 3 by n matrix must be inverted to obtain a general solution for the CMG gimbal rate commands. Several problems are obvious: (1) With four or more CMGs, the linear system is underdetermined, meaning that when the equations are consistent, there is an infinite number of solutions (there are only three equations but n unknowns); (2) For some gimbal angles, the system is known to be inconsistent and not all sets of gimbal angles producing inconsistency have been determined (for some gimbal angle combinations no solution exists); (3) These considerations and the algebra involved make a general solution almost impossible without resorting to a digital computer.

A second approach is to restrict the range of the CMG gimbals and assure small deviations from the CMG null positions. In such a case, small angle approximations are used, $\sin \alpha = \alpha$ and $\cos \alpha = 1$, and the equations are linearized. The gimbal rates are solved so that cross coupling between axes is eliminated. The resultant solution, however, is valid only for small CMG angular excursions from its null position. At this point in the CMG control system design, each individual designer will have or devise his own method for selecting a CMG steering law. Several candidate steering laws were derived and compared on the basis of their effectiveness in

producing the desired actuator response as well as their complexity in implementing each scheme. Each steering law was derived for the four-skewed CMG momentum exchange system which has been baselined for HEAO-C.

For the four-skewed CMG configuration, there are three equations (components of the CMG torque vector) and four unknowns (four CMG gimbal rates). To obtain an exact solution, a constraint equation or relation between the unknowns is needed. For each constraint or assumption that is made, a different solution will be obtained for the gimbal rates. Whatever the solution, it is referred to as the CMG steering law. Several candidate steering laws were derived and compared on the basis of their effectiveness in producing the desired control torque. Each was derived for the four-skewed CMG configuration which has been baselined for HEAO-C, and each was implemented in digital simulations. The following were candidate steering laws:

1. Constant gain.
2. Maximum contribution.
3. Psuedo inverse.
4. The Bendix summation of three gimbal inverses.
5. The BECO² momentum vector distribution.
6. The G. E.³ transpose with torque feedback.

Because of the large quantity of data, complete derivation and simulation results for each steering law are not included in this appendix. A separate NASA report is being prepared to present a comparison of each steering law and simulation results for HEAO-C, including magnetic momentum management for the CMGs. However, Table E-5 contains a brief comparison of candidate steering laws.

Each steering law was compared on the basis of complexity, accuracy, mathematical singularities, failure adaption, performance after failure, and growth potential. No attempt was made to weigh the importance

-
2. Teledyne Brown Engineering Company
 3. General Electric

TABLE E-5. CMG STEERING LAW COMPARISON

Law	Complexity	Accuracy	Singularity	Failure Adaption	Performance After Failure	Rating
Constant Gain	1	5	1	6	6	19
Max Contribution	2	4	1	1	5	13
Pseudo Inverse	4	1	4	1	1	11
Σ (3 Gimbal)	6	3	6	4	1	20
H-Distribution	5	2	5	5	1	18
Transpose with Torque Feedback	3	4	1	1	5	14
<p>Evaluation: 1 through 6, low numbers best. Recommend pseudo inverse for HEAO-C.</p>						

of each comparative factor and the ratings shown in Table E-5 are somewhat subjective. The context in which the comparative factors were used is as follows:

Complexity	The mathematical manipulations and logic required for implementation.
Accuracy	The pointing and jitter performance obtained through simulations.
Singularity	Combinations of gimbal angles which can cause zeros in the denominator of the steering law, hence, program divergence.
Failure Adaption	The corrective actions that must be taken in the event of a CMG failure; in particular, changes in the steering law.
Performance After a Failure	Pointing and jitter performance with one CMG out.
Growth Potential	Minimum modifications required to accommodate more than four CMGs.
Gyro-Hang-Up	A combination of gimbal angles which prevent the desired torque from being produced: (1) singularities, (2) saturation, (3) cannot input attitude error through the steering law, and (4) the commanded torque is perpendicular to the instantaneous CMG torque vector ($\dot{\mathbf{H}} \cdot \bar{\mathbf{T}}_c = 0$).

The constant gain steering law is derived by assuming small gimbal angles and assuming that the CMGs operate similar to scissored pairs. As implied by name, the constant gain steering law contains constants which can easily be implemented on an analog computer. It is the simplest of all

laws but is valid for gimbal angles within ± 90 degrees. It contains no singularities. With one CMG failed, the CMG null position must be redefined and a new constant gain steering law derived which is valid about the new null position. After a failure the gimbal angles tend to become larger and the performance degrades.

The maximum contribution is derived by assuming that each CMG operates independently. The gimbal rate of each CMG is commanded to produce as much as possible of the desired torque. In complexity, it compares favorably with the constant gain steering law. Excellent performance is obtained as long as the gimbal angles remain small. However, as the gimbal angles become large, gyro-hang-up conditions are approached and the performance is degraded due to cross coupling torques. There are no singularities in the maximum contribution steering law and no changes are required for failure adaption. With only three CMGs operating, the performance is degraded due to cross coupling CMG torques.

The pseudo inverse steering law basically minimizes the norm between gimbal rates, and is based on the work of R. Penrose [E-12]. A 3 by 3 matrix inversion is required to get the inverse, along with several matrix multiplications. It represents the ultimate accuracy in performance. With one CMG failed, the pseudo inverse reduces to an exact inverse without program modifications, and its performance is not degraded. The pseudo inverse is recommended for HEAO-C.

The Bendix summation of three gimbal solutions is much more complex than any of the other candidate steering laws [E-11]. Basically, the CMG torque vectors are arranged in combinations of three. There are four possible combinations, each having an exact inverse. The solutions to each combination are summed to produce the steering law. It is not known what the equivalent constraint equation would be or what, if anything, is being minimized. The Bendix law introduces several singularities that are inherent only to their scheme. Singularity detection and avoidance techniques are required which compound the complexity. Failure detection and corrective actions are required. However, after a failure only one of the three gimbal inverses would be used, in which case the steering law reverts to an exact inverse and the performance improves. The Bendix steering law is not recommended for HEAO-C, or for HEAO-A.

The BECO H-distribution [E-13] is derived by assuming a constraint between the gimbal rates that tends to distribute the CMG momentum so that gyro-hang-ups are avoided. In addition to a constraint equation, a

4 by 4 matrix must be inverted, increasing its complexity. It performed well in simulations; however, complete reprogramming is required to accommodate a CMG failure. With one CMG out, supposedly the exact inverse would be used, improving performance.

The G. E. transpose with torque feedback [E-14] is a variation of the maximum contribution steering law. Basically, each CMG is commanded individually with the CMG torque signal being fed back to prevent over-control and provide stability. It is more complex than the maximum contribution with about the same performance capabilities. Both the maximum contribution and G. E. steering laws offer maximum growth potential. As more CMGs are added, the cross coupling between CMGs becomes less and the performance improves. The main objection to this type steering law is that the system bandwidth varies as a function of the CMG gimbal position.

As long as the gimbal angles stay small, as with continuous momentum dump against the earth's magnetic field by electromagnets, all steering laws performed approximately equally. As the gimbal angles become large, there are significant differences in performance. These differences are due to the ability of the steering laws to cope with singularities, gyro-hang-up, and cross coupling CMG torques. Based on a comparison of the candidate steering laws for HEAO, the pseudo inverse is recommended for HEAO-C. As an alternate, the maximum contribution should be considered, especially if more CMGs were added for greater reliability over the two year mission.

Brief derivations of the two steering laws are given in the following paragraphs.

d. The Pseudo Inverse Steering Law. By equating the desired control torque, T_c , [equation (145)] to the CMG torque, \dot{H} , the vector-matrix equation [equation (146)], becomes

$$-\tilde{T}_c = \dot{\tilde{H}} = C(\tilde{h}\dot{\alpha}) \quad (147)$$

where C has been normalized by factoring out h_i , $i = 1, 2, 3, 4$. The matrix C is a 3 by 4 whose inverse must be obtained to solve the gimbal angular rates as functions of the desired control torque. However, since there are four unknowns but only three equations, a general solution, if one exists, is not unique. Therefore, one must resort to a pseudo inverse.

Reference E-12 gives the conditions and theory for finding a unique pseudo inverse which for a nonsingular matrix reduces to the conventional inverse. The pseudo inverse is given by

$$F = C^* (C C^*)^{-1} \quad . \quad (148)$$

The steering law then becomes

$$\tilde{h}(\alpha) = -C^* (C C^*)^{-1} \tilde{T}_c = -F \tilde{T}_c \quad , \quad (149)$$

where a superscript asterisk represents the transpose of a matrix and minus one the general inverse of a matrix. The elements of C have been defined by equation (138) for the baseline CMG configuration. To obtain the inverse, the determinant of $C C^*$ must be calculated. Since there are several combinations of gimbal angles that could make the determinant go to zero, a software limit could be inserted in the computer routine to prevent the singularity from causing program divergence. That is, whenever $|C C^*| < \epsilon$, a very small number, the determinant is set equal to ϵ . Since mathematical manipulations required to obtain the pseudo inverse are too complicated to perform without a digital computer, the elements of equation (149) will be developed only to the extent required for calculations. Most digital subroutines for matrix inversion accept the elements of the matrix to be inverted and give as outputs the elements of the inverse matrix. Let

$$D = C C^* \quad (150)$$

and

$$E = D^{-1} \quad . \quad (151)$$

The normalized elements of C are obtained from equation (138) from which the elements of D are calculated as shown in the following:

$$D_{11} = C_{11}^2 + C_{12}^2 + C_{13}^2 + C_{14}^2$$

$$D_{12} = C_{11} C_{21} + C_{12} C_{22} + C_{13} C_{23} + C_{14} C_{24}$$

$$D_{13} = C_{11} C_{31} + C_{12} C_{32} + C_{13} C_{33} + C_{14} C_{34}$$

$$D_{21} = D_{12}$$

$$D_{22} = C_{21}^2 + C_{22}^2 + C_{23}^2 + C_{24}^2$$

$$D_{23} = C_{21} C_{31} + C_{22} C_{32} + C_{23} C_{33} + C_{24} C_{34}$$

$$D_{31} = D_{13}$$

$$D_{32} = D_{23}$$

$$D_{33} = C_{31}^2 + C_{32}^2 + C_{33}^2 + C_{34}^2 \quad .$$

As indicated above, the matrix D is skew symmetric.

The elements of D are inputs to a digital matrix inversion routine to obtain the elements of E as outputs. Multiplying the elements of E by C* gives the elements of F, a 4 by 3 matrix, as shown below.

$$F_{11} = C_{11} E_{11} + C_{21} E_{21} + C_{31} E_{31}$$

$$F_{12} = C_{11} E_{12} + C_{21} E_{22} + C_{31} E_{32}$$

$$F_{13} = C_{11} E_{13} + C_{21} E_{23} + C_{31} E_{33}$$

$$F_{21} = C_{12} E_{11} + C_{22} E_{21} + C_{32} E_{31}$$

$$F_{22} = C_{12} E_{12} + C_{22} E_{22} + C_{32} E_{32}$$

$$F_{23} = C_{12} E_{13} + C_{22} E_{23} + C_{32} E_{33}$$

$$F_{31} = C_{13} E_{11} + C_{23} E_{21} + C_{33} E_{31}$$

$$F_{32} = C_{13} E_{12} + C_{23} E_{22} + C_{33} E_{32}$$

$$F_{33} = C_{13} E_{13} + C_{23} E_{23} + C_{33} E_{33}$$

$$F_{41} = C_{14} E_{11} + C_{24} E_{21} + C_{34} E_{31}$$

$$F_{42} = C_{14} E_{12} + C_{24} E_{22} + C_{34} E_{32}$$

$$F_{43} = C_{14} E_{13} + C_{24} E_{23} + C_{34} E_{33} \quad .$$

Utilizing the elements of the pseudo inverse matrix, the CMG steering law is obtained by expanding the elements of equation (149) as follows:

$$\left. \begin{aligned} \dot{\alpha}_1 &= -(F_{11} T_{cx} + F_{12} T_{cy} + F_{13} T_{cz})/h_1 \\ \dot{\alpha}_2 &= -(F_{21} T_{cx} + F_{22} T_{cy} + F_{23} T_{cz})/h_2 \\ \dot{\alpha}_3 &= -(F_{31} T_{cx} + F_{32} T_{cy} + F_{33} T_{cz})/h_3 \\ \dot{\alpha}_4 &= -(F_{41} T_{cx} + F_{42} T_{cy} + F_{43} T_{cz})/h_4 \end{aligned} \right\} \cdot \quad (152)$$

As noted previously, the columns of C are CMG torque vectors for each CMG. It can be rigorously proven that when any three are colinear the determinant of C^* goes to zero, producing a singularity in the steering law. There appear to be a large number of gimbal angle combinations that could produce singular conditions. However, in digital simulations, the only singular conditions which prevented proper operation of the steering law were those which also corresponded to CMG saturation. Therefore, singularity detection and/or avoidance schemes do not appear to be necessary for the pseudo inverse steering law.

When a CMG fails, it is acceptable to set the failed gyro elements to zero. The failed CMG must be identified and the column corresponding to the failed CMG set to zero. The pseudo inverse routine need not be reprogrammed. With one CMG out, however, C reduces to a 3 by 3 matrix whose inverse can be obtained without resorting to the pseudo inverse procedure.

The advantage of the pseudo inverse steering law is that most of the time the exact torque needed for attitude error correction can be obtained through the CMGs without any cross coupling. Also, the total CMG momentum envelope can be utilized for control purposes. Possible disadvantages are the complexity of implementing the pseudo inverse matrix inversion routine and contingency modes for CMG failures. An onboard digital computer would be required to implement the pseudo inverse steering law.

e. The MSFC Maximum Contribution Steering Law. A second and somewhat novel approach is to command each CMG separately based on its ability to contribute to the desired control torque. The criteria are to consider each CMG independently and to command its gimbal rate so that as much as possible of the desired control torque is produced. If no part of the control torque can be produced, the gimbal position is not moved. Since each CMG can produce a torque only about its torque axis as defined by k_c , the desired control torque \bar{T}_c will be projected into the CMG constant momentum coordinates and that portion aligned with k_c will be used as a basis for commanding the CMG gimbal rate. Using the transformation G_{cr} , the desired torque, as defined by the control law, in CMG coordinates is as follows:

$$\bar{T}_c = t_{cx} i_c + t_{cy} j_c + t_{cz} k_c \quad , \quad (153)$$

where

$$t_{cx} = g_{11}^c T_{cx} + g_{12}^c T_{cy} + g_{13}^c T_{cz} \quad ,$$

$$t_{cy} = g_{21}^c T_{cx} + g_{22}^c T_{cy} + g_{23}^c T_{cz} \quad ,$$

and

$$t_{cz} = g_{31}^c T_{cx} + g_{32}^c T_{cy} + g_{33}^c T_{cz} \quad .$$

Previously, the torque produced by the c th CMG was defined as

$$\dot{h}_c = \alpha_c h_c k_c \quad . \quad (154)$$

By equating elements of $\dot{\bar{h}}_c$ and $-\bar{T}_c$, the CMG gimbal rate command is obtained as

$$\dot{\alpha}_c = -t_{cz}/h_c = -(g_{31}^c T_{cx} + g_{32}^c T_{cy} + g_{33}^c T_{cz})/h_c \quad (155)$$

By defining the angle between \bar{T}_c and k_c as γ , the vector scalar product is

$$\bar{T}_c \cdot k_c = g_{31}^c T_{cx} + g_{32}^c T_{cy} + g_{33}^c T_{cz} = T_c C\gamma \quad ; \quad (156)$$

therefore,

$$\dot{\alpha}_c = -T_c C\gamma/h_c \quad (157)$$

Note that equation (156) is the projection of the desired control torque on the k_c axis. That portion of \bar{T}_c which is perpendicular to the CMG torque axes is given by

$$T_c S\gamma = T_c (1 - C^2\gamma)^{\frac{1}{2}} \quad (158)$$

and cannot be obtained by gimbaling the c th CMG at any time. Since $T_c C\gamma$ contains basically magnitude information without polarity, the expanded scalar product form should be used for the CMG gimbal commands. Each CMG is commanded individually, regardless of its angular position, based on its ability to contribute to the desired torque vector. The problems associated with the generalized inverse CMG control law have been avoided. For a specified CMG system configuration, however, the transformation between body and CMG coordinates must be derived and evaluated at each time step.

If the components of G_{cr} from equations (127) through (130) are substituted into equation (155), with $c = 1, 2, 3, 4$, the following equations are obtained for the gimbal rate commands for four-skewed CMGs:

7 (A)

$$\left. \begin{aligned} \dot{\alpha}_1 &= -(\mathcal{S}\beta C\alpha_1 T_{cx} - S\alpha_1 T_{cy} + C\beta C\alpha_1 T_{cz}) / h_1 \\ \dot{\alpha}_2 &= -(\mathcal{S}\beta C\alpha_2 T_{cx} - C\beta C\alpha_2 T_{cy} - S\alpha_2 T_{cz}) / h_2 \\ \dot{\alpha}_3 &= -(\mathcal{S}\beta C\alpha_3 T_{cx} + S\alpha_3 T_{cy} - C\beta C\alpha_3 T_{cz}) / h_3 \\ \dot{\alpha}_4 &= -(\mathcal{S}\beta C\alpha_4 T_{cx} + C\beta C\alpha_4 T_{cy} + S\alpha_4 T_{cz}) / h_4 \end{aligned} \right\} \cdot \quad (159)$$

Assuming equal momentum per CMG, the steering law can be arranged in the following vector matrix form:

$$\dot{\tilde{\alpha}} = A \tilde{T}_c / h \quad . \quad (160)$$

As previously shown by equation (139), the CMG torque with equal momentum per CMG is

$$\dot{\tilde{H}} = h C \dot{\tilde{\alpha}} \quad . \quad (161)$$

By comparing the elements of A and C, the matrix A equals the negative transpose of C; that is,

$$A = -C^* \quad . \quad (162)$$

Hence, the CMG steering law shown in equation (159) is equivalent to a transpose type steering law. The important characteristics of this type steering law are no mathematical singularities, no matrices to invert, and easy implementation of the equations for the CMG gimbal rates. Its undesirable characteristic is that the control system gain through the CMGs is not constant. Control authority about each vehicle axis varies as the gimbal angles are moved from their null position and, in general, the desired torque is not obtained. Assuming that each CMG is capable of producing the desired torque at a particular instant of time, it is possible to get four times the torque asked for by the control law. The redeeming facts are that movement of the CMGs is restricted by physical characteristics such as drive motors and gearing and that the computational cycles of the control computer are fast. Before the CMGs can move very far from a given position, the momentum deficiency is recomputed and a new desired torque is defined, thus preventing

the CMGs from producing more control than was originally needed. However, at each instant of time, each CMG will be maximizing its contribution to the desired control torque.

Assuming small gimbale angles, the CMG torque per vehicle axis, equation (137), reduces to the following equations:

$$\left. \begin{aligned} \dot{h}_x &= h S\beta (\dot{\alpha}_1 + \dot{\alpha}_2 + \dot{\alpha}_3 + \dot{\alpha}_4) \\ \dot{h}_y &= h C\beta (-\dot{\alpha}_2 + \dot{\alpha}_4) \\ \dot{h}_z &= h C\beta (\dot{\alpha}_1 - \dot{\alpha}_3) \end{aligned} \right\} \cdot \quad (163)$$

Substitution of equations (159) into equations (163) results in the following equations:

$$\left. \begin{aligned} \dot{h}_x &= -4 S^2\beta T_{cx} \\ \dot{h}_y &= -2 C^2\beta T_{cy} \\ \dot{h}_z &= -2 C^2\beta T_{cz} \end{aligned} \right\} \cdot \quad (164)$$

To obtain unity of gain through the CMG system with the CMGs at their null position, either the desired torque components, T_c , or the steering law must be normalized by dividing by the appropriate sine and cosine function of the skew angle. If one chooses to normalize the steering law, those terms with T_{cx} are divided by $4S^2\beta$ and those terms with T_{cy} or T_{cz} are divided by $2C^2\beta$. The maximum contribution steering law ensues from the normalization of equations (159) as follows:

$$\left. \begin{aligned} \dot{\alpha}_1 &= (-C\alpha_1/4h S\beta) T_{cx} + (S\alpha_1/2h C^2\beta) T_{cy} - (C\alpha_1/2h C\beta) T_{cz} \\ \dot{\alpha}_2 &= (-C\alpha_2/4h S\beta) T_{cx} + (C\alpha_2/2h C\beta) T_{cy} - (S\alpha_2/2h C^2\beta) T_{cz} \\ \dot{\alpha}_3 &= (-C\alpha_3/4h S\beta) T_{cx} - (S\alpha_3/2h C^2\beta) T_{cy} + (C\alpha_3/2h C\beta) T_{cz} \\ \dot{\alpha}_4 &= (-C\alpha_4/4h S\beta) T_{cx} - (C\alpha_4/2h C\beta) T_{cy} - (S\alpha_4/2h C^2\beta) T_{cz} \end{aligned} \right\} \cdot \quad (165)$$

Once specified, the skew angle is constant. By making the following definitions,

$$\left. \begin{aligned} K_a &= -1/4h S\beta \\ K_b &= -1/2h C\beta \\ K_c &= K_b/C\beta \end{aligned} \right\} , \quad (166)$$

the maximum contribution steering law can be written as follows:

$$\left. \begin{aligned} \dot{\alpha}_1 &= K_a C\alpha_1 T_{cx} - K_c S\alpha_1 T_{cy} + K_b C\alpha_1 T_{cz} \\ \dot{\alpha}_2 &= K_a C\alpha_2 T_{cx} - K_b C\alpha_2 T_{cy} - K_c S\alpha_2 T_{cz} \\ \dot{\alpha}_3 &= K_a C\alpha_3 T_{cx} + K_c S\alpha_3 T_{cy} - K_b C\alpha_3 T_{cz} \\ \dot{\alpha}_4 &= K_a C\alpha_4 T_{cx} + K_b C\alpha_4 T_{cy} + K_c S\alpha_4 T_{cz} \end{aligned} \right\} . \quad (167)$$

The maximum contribution CMG steering law has been used rather intensely in the HEAO-C simulations with four-skewed CMGs. Very satisfactory pointing performance was obtained in the cases simulated. Although there are no singularities in the maximum contribution steering law, those gimbal positions which cause gyro-hang-up also prevent a component of the desired torque from being fed through the steering law. For example, assuming CMG saturation in the x-axis direction with all gimbal angles at 90 degrees, no torque can be produced in the x-axis direction, $\dot{h}_x = 0$. Concurrently, the desired torque component T_{cx} cannot drive the CMG gimbals through the steering law; the coefficients of T_{cx} in equation (165) are zero. However,

gyro-hang-up conditions are, in general, dependent on the CMG configuration and are not necessarily associated with the ability to command through the steering law. Consider the gyro-hang-up condition $\alpha_1 = 90$ degrees, $\alpha_2 = 0$ degrees, $\alpha_3 = -90$ degrees, and $\alpha_4 = 0$ degrees. The z-axis CMG torque, h_z , is zero but the CMGs are not saturated and, also, the z-axis command T_{cz} cannot be fed through the steering law. The implication is that for the transpose type steering law, gyro-hang-up conditions also correspond to gimbal positions which prevent a commanded torque component from driving the CMG gimbal angle rates. The situation, however, is instantaneous. No gimbal position combination has been found that prevents more than one torque component from being fed through the steering law. The other two components should quickly drive the CMGs out of the gyro-hang-up condition, unless it also corresponds to CMG saturation.

Linear Analysis of HEAO-C Control Systems

1. Equations of Motion and System Linearization. The pertinent equations describing HEAO-C behavior are listed below.

Euler Equations of Motion⁴

$$I_x \dot{\omega}_x = T_{gx} + T_{mx} - (I_z - I_y) \omega_z \omega_y + \dot{h}_x - \omega_y h_z + \omega_z h_y \quad (168)$$

$$I_y \dot{\omega}_y = T_{gy} + T_{my} - (I_x - I_z) \omega_x \omega_z + \dot{h}_y - \omega_z h_x + \omega_x h_z \quad (169)$$

$$I_z \dot{\omega}_z = T_{gz} + T_{mz} - (I_y - I_x) \omega_y \omega_x + \dot{h}_z - \omega_x h_y + \omega_y h_x \quad (170)$$

CMG Angular Momentum

$$h_x = S\beta (h_1 S\alpha_1 + h_2 S\alpha_2 + h_3 S\alpha_3 + h_4 S\alpha_4) \quad (171)$$

$$h_y = h_1 C\alpha_1 - h_3 C\alpha_3 - C\beta (h_2 S\alpha_2 - h_4 S\alpha_4) \quad (172)$$

4. The sign of the CMG torque components has been selected as positive to correspond to a positive gimbal rate command.

$$\dot{h}_z = h_2 C \alpha_2 - h_4 C \alpha_4 + C \beta (h_1 S \alpha_1 - h_3 S \alpha_3) \quad (173)$$

CMG Torque

$$\dot{h}_x = S_\beta (h_1 \dot{\alpha}_1 C \alpha_1 + h_2 \dot{\alpha}_2 C \alpha_2 + h_3 \dot{\alpha}_3 C \alpha_3 + h_4 \dot{\alpha}_4 C \alpha_4) \quad (174)$$

$$\dot{h}_y = -h_1 \dot{\alpha}_1 S \alpha_1 + h_3 \dot{\alpha}_3 S \alpha_3 - C \beta (h_2 \dot{\alpha}_2 C \alpha_2 - h_4 \dot{\alpha}_4 C \alpha_4) \quad (175)$$

$$\dot{h}_z = -h_2 \dot{\alpha}_2 S \alpha_2 + h_4 \dot{\alpha}_4 S \alpha_4 + C \beta (h_1 \dot{\alpha}_1 C \alpha_1 - h_3 \dot{\alpha}_3 C \alpha_3) \quad (176)$$

CMG Gimbal Angle Rates, Constant Gain Steering Law

$$\dot{\alpha}_1 = K_a T_{cx} + K_b T_{cz} \quad (177)$$

$$\dot{\alpha}_2 = K_a T_{cx} - K_b T_{cy} \quad (178)$$

$$\dot{\alpha}_3 = K_a T_{cx} - K_b T_{cz} \quad (179)$$

$$\dot{\alpha}_4 = K_a T_{cx} + K_b T_{cy} \quad (180)$$

CMG Gimbal Rates, Transpose Steering Law

$$\dot{\alpha}_1 = (S \beta C \alpha_1 T_{cx} - S \alpha_1 T_{cy} + C \beta C \alpha_1 T_{cz})/h \quad (181)$$

$$\dot{\alpha}_2 = (S \beta C \alpha_2 T_{cx} - C \beta C \alpha_2 T_{cy} - S \alpha_2 T_{cz})/h \quad (182)$$

$$\dot{\alpha}_3 = (S\beta C\alpha_3 T_{cx} + S\alpha_3 T_{cy} - C\beta C\alpha_3 T_{cz})/h \quad (183)$$

$$\dot{\alpha}_4 = (S\beta C\alpha_4 T_{cx} + C\beta C\alpha_4 T_{cy} + S\alpha_4 T_{cz})/h \quad (184)$$

Magnetic Torque

$$T_{mx} = M_y B_z - M_z B_y \quad (185)$$

$$T_{my} = M_z B_x - M_x B_z \quad (186)$$

$$T_{mz} = M_x B_y - M_y B_x \quad (187)$$

Magnetic Dipole Moments

$$M_x = K_{mx} (B_y h_z - B_z h_y)/B^2 \quad (188)$$

$$M_y = K_{my} (B_z h_x - B_x h_z)/B^2 \quad (189)$$

$$M_z = K_{mz} (B_x h_y - B_y h_x)/B^2 \quad (190)$$

$$B^2 = B_x^2 + B_y^2 + B_z^2 \quad (191)$$

Euler Angle Rates (1, 2, 3 sequence)

$$\dot{\phi} = (\omega_x C\psi - \omega_y S\psi)/C\theta \approx \omega_x \quad (192)$$

$$\dot{\theta} = \omega_y C\psi + \omega_x S\psi \approx \omega_y \quad (193)$$

$$\dot{\psi} = \omega_z - \dot{\phi}S\theta \approx \omega_z \quad (194)$$

The equations can be simplified and linearized as follows. Neglecting cross products of the form $\omega_i \omega_j$ and $\omega_i h_j$ and using the approximations indicated in equations (192) through (194) yields the following equations for equations (168) through (170):

$$I_x \ddot{\phi} = T_{gx} + T_{mx} + \dot{h}_x \quad , \quad (195)$$

$$I_y \ddot{\theta} = T_{gy} + T_{my} + \dot{h}_y \quad , \quad (196)$$

and

$$I_z \ddot{\psi} = T_{gz} + T_{mz} + \dot{h}_z \quad . \quad (197)$$

Applying small angle approximations to equations (171) through (176) and letting $h_1 = h_2 = h_3 = h_4$ results in the following equations:

$$h_x = hS\beta (\alpha_1 + \alpha_2 + \alpha_3 + \alpha_4) \quad , \quad (198)$$

$$h_y = hC\beta (\alpha_4 - \alpha_2) \quad , \quad (199)$$

$$h_z = hC\beta (\alpha_1 - \alpha_3) \quad , \quad (200)$$

$$\dot{h}_x = hS\beta (\dot{\alpha}_1 + \dot{\alpha}_2 + \dot{\alpha}_3 + \dot{\alpha}_4) \quad , \quad (201)$$

$$\dot{h}_y = -hC\beta (\dot{\alpha}_2 - \dot{\alpha}_4) \quad , \quad (202)$$

and

$$\dot{h}_z = hC\beta (\dot{\alpha}_1 - \dot{\alpha}_3) \quad . \quad (203)$$

Equations (181) through (184) can be linearized by small angle approximations to obtain

$$\dot{\alpha}_1 = (S\beta T_{cx} + C\beta T_{cz})/h \quad , \quad (204)$$

$$\dot{\alpha}_2 = (S\beta T_{cx} - C\beta T_{cy})/h \quad , \quad (205)$$

$$\dot{\alpha}_3 = (S\beta T_{cx} - C\beta T_{cz})/h \quad , \quad (206)$$

and

$$\dot{\alpha}_4 = (S\beta T_{cx} + C\beta T_{cy})/h \quad . \quad (207)$$

Substitution of the above results into equations (201) through (203) yields

$$\dot{h}_x = 4S\beta^2 T_{cx} \quad , \quad (208)$$

$$\dot{h}_y = 2C\beta^2 T_{cy} \quad , \quad (209)$$

and

$$\dot{h}_z = 2C\beta^2 T_{cz} \quad . \quad (210)$$

Substitution of equations (177) through (180) into equations (201) through (203) yields

$$\dot{h}_x = 4hS\beta K_a T_{cx} \quad , \quad (211)$$

$$\dot{h}_y = 2hC\beta K_b T_{cy} \quad , \quad (212)$$

and

$$\dot{h}_z = 2hC\beta K_b T_{cy} \quad . \quad (213)$$

The magnetic torque relations [equations (185) through (191)] are equivalent, in vector form, to

$$\begin{aligned} \bar{T}_m &= \bar{M} \times \bar{B} = \frac{K_m}{B^2} \{ (\bar{B} \times \bar{h}) \times \bar{B} \} \\ &= - \{ \bar{B} (\bar{B} \cdot \bar{h}) - \bar{h} (\bar{B} \cdot \bar{B}) \} \frac{K_m}{B^2} \quad . \end{aligned} \quad (214)$$

Note that the constraint $K_{mx} = K_{my} = K_{mz} = K_m$ has been applied. For purposes of linear analysis, only the second vector term in equation (214) will be retained; hence, equations (185) through (187) simplify to

$$T_{mx} = K_m h_x \quad , \quad (215)$$

$$T_{my} = K_m h_y \quad , \quad (216)$$

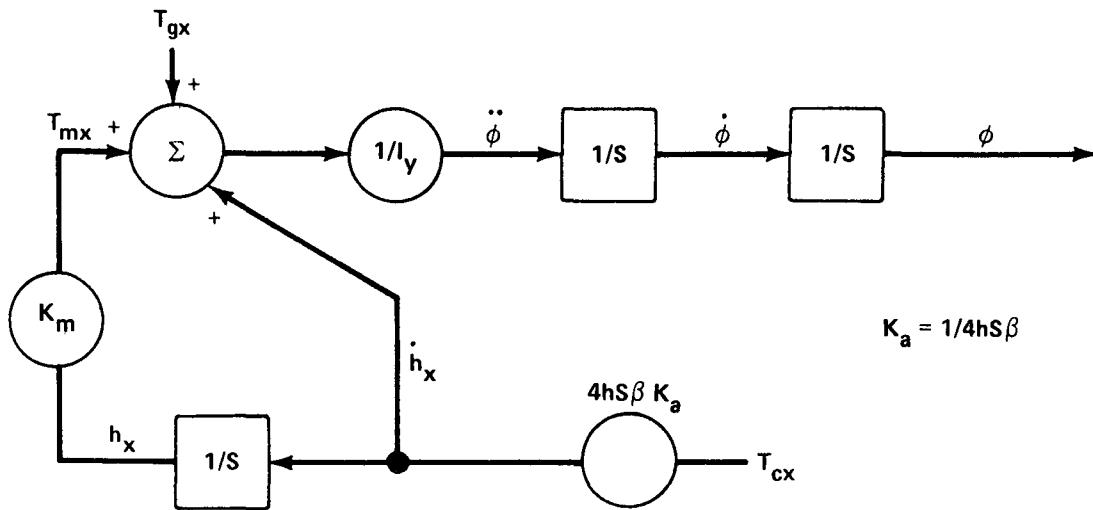
and

$$T_{mz} = K_m h_z \quad . \quad (217)$$

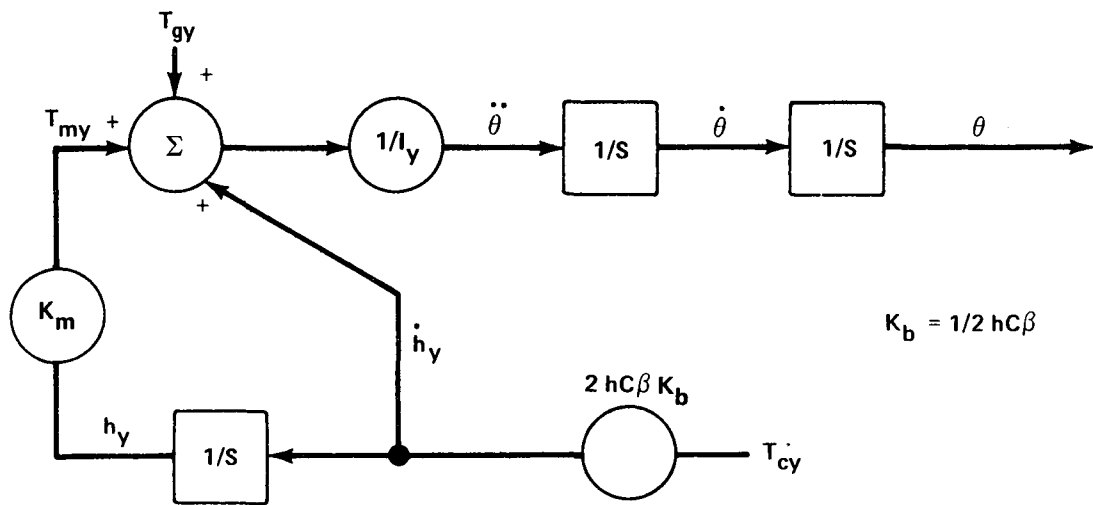
It is evident from the linearized equations [equations (195) through (217)] that the three axes can be decoupled and single axis linear models can be developed for both the constant gain and transpose steering law versions. These models are shown in Figures E-25 and E-26.

It is apparent from these linear models that the significant differences between the linearized models of the two control laws are

$$\dot{h}_x = T_{cx} \quad (218)$$



X AXIS



Y AND Z AXIS

Figure E-25. HEAO single axis linear models constant gain steering law.

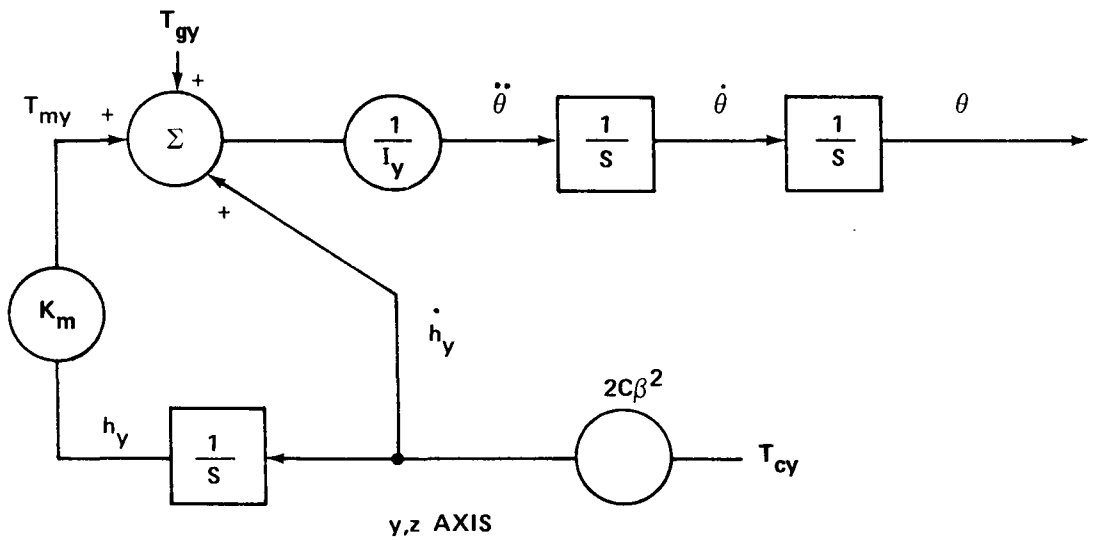
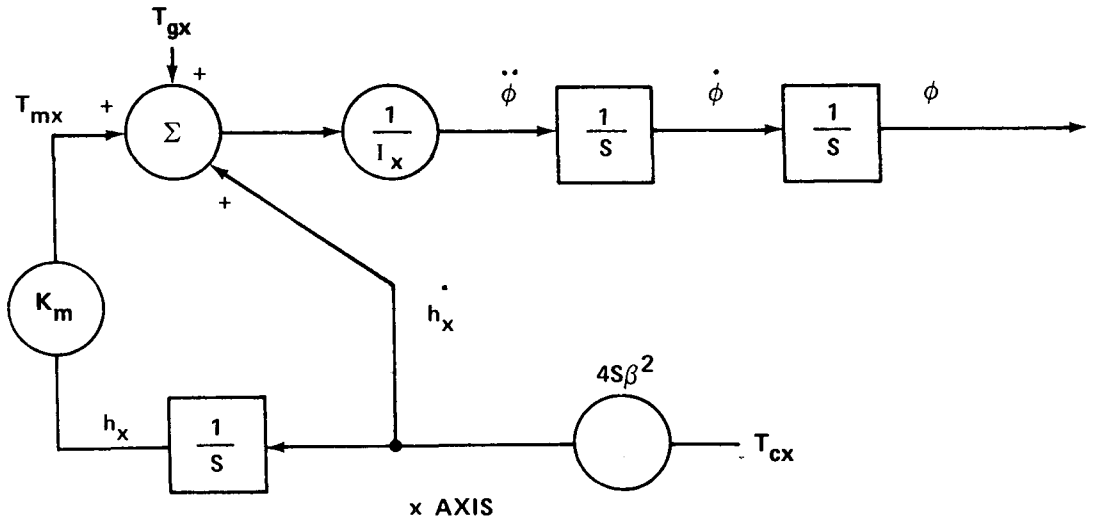


Figure E-26. HEAO single axis linear models transpose steering law.

$$\dot{h}_y = T_{cy} \quad (219)$$

and

$$\dot{h}_z = T_{cz} \quad (220)$$

for the constant gain steering law and

$$\dot{h}_x = 4S\beta^2 T_{cx} \quad (221)$$

$$\dot{h}_y = 2C\beta^2 T_{cy} \quad (222)$$

and

$$\dot{h}_z = 2C\beta^2 T_{cz} \quad (223)$$

for the transpose steering law.

The control torques T_{cx} , T_{cy} , and T_{cz} are developed by means of CMGs commanded by a control law of the following form:

$$\begin{aligned} T_{cx} &= K_{-1x} \int (\phi \text{CMD} - \theta) dt + K_{0x} (\phi \text{CMD} - \phi) + K_{1x} \dot{\phi} \\ T_{cy} &= K_{-1y} \int (\theta \text{CMD} - \theta) dt + K_{0y} (\theta \text{CMD} - \theta) + K_{1y} \dot{\theta}, \quad (224) \\ T_{cz} &= K_{-1z} \int (\psi \text{CMD} - \psi) dt + K_{0z} (\psi \text{CMD} - \psi) + K_{1z} \dot{\psi} \end{aligned}$$

where K_{-i} , in some cases, may be zero.

By substituting equations (215) through (220) into equations (195) through (197), the linearized system equations become

$$I_x \ddot{\phi} = T_{gx} + K_m \int T_{cx} dt + T_{cx} \quad , \quad (225)$$

$$I_y \ddot{\theta} = T_{gy} + K_m \int T_{cy} dt + T_{cy} \quad , \quad (226)$$

and

$$I_z \ddot{\psi} = T_{gz} + K_m \int T_{cz} dt + T_{cz} \quad (227)$$

for the constant gain steering law case. By substituting equations (215), (216), (217), (221), (222), and (223) into equations (195), (196), and (197), the linearized system equations become

$$I_x \ddot{\phi} = T_{gx} + K_m 4S^2\beta \int T_{cx} dt + 4S^2\beta T_{cx} \quad , \quad (228)$$

$$I_y \ddot{\theta} = T_{gy} + K_m 2C^2\beta \int T_{cy} dt + 2C^2\beta T_{cy} \quad , \quad (229)$$

and

$$I_z \ddot{\psi} = T_{gz} + K_m 2C^2\beta \int T_{cz} dt + 2C^2\beta T_{cz} \quad (230)$$

for the transpose steering law case. T_{cx} , T_{cy} , and T_{cz} are defined in equation (224).

In either case it is seen that the magnetic control system is arranged to supply a controlling torque, T_m , which is the scaled integral of the CMG supplied control torque. It is seen that, in addition to providing an additional torque source, the magnetic controller can provide integral control either in addition to integral control already included in T_c ($K_{-1} \neq 0$) or, in the case where $K_{-1} = 0$, integral control is supplied solely by the magnetic torque.

An additional feature of this mechanization which is not obvious from a cursory inspection of equations (225) through (230) is that, by proper selection of the control constants K_m , K_{-1} , K_0 , and K_1 , the additional magnetic torque capability can be utilized to "dump" accumulated CMG momentum in addition to providing added integral control.

Advantages of this magnetic-plus-CMG mechanization are as follows:

- By providing integral control, greater pointing accuracy in the face of low frequency disturbance torques is achieved without incurring the penalties of large system bandwidth requirements.
- The CMG momentum dump capability provided by the magnetic torque can result in smaller CMGs, or a simpler linear CMG steering law and/or reduced reaction jet control system fuel requirements.
- In the case of CMG failure, the magnetic torque can automatically process the remaining CMGs to a new null position, thus simplifying controller software or mode changing logic.

From the above control law description it can be seen that four basic control systems can be considered applicable to the problem. These are shown in Figure E-27 for the constant gain steering law case.

System I, in Figure E-27, illustrates a position plus rate feedback law without a magnetic torquing loop. In this system, control is accomplished solely by the four-skewed CMGs.

System II includes the addition of the magnetic torquing loop.

System III illustrates control by CMG with added integral feedback.

System IV includes CMG plus magnetic control with integral feedback.

The block diagrams in Figure E-27 represent the constant gain steering law case but comparison of equations (208) through (210) with equations (211) through (213) indicates that they can also represent the

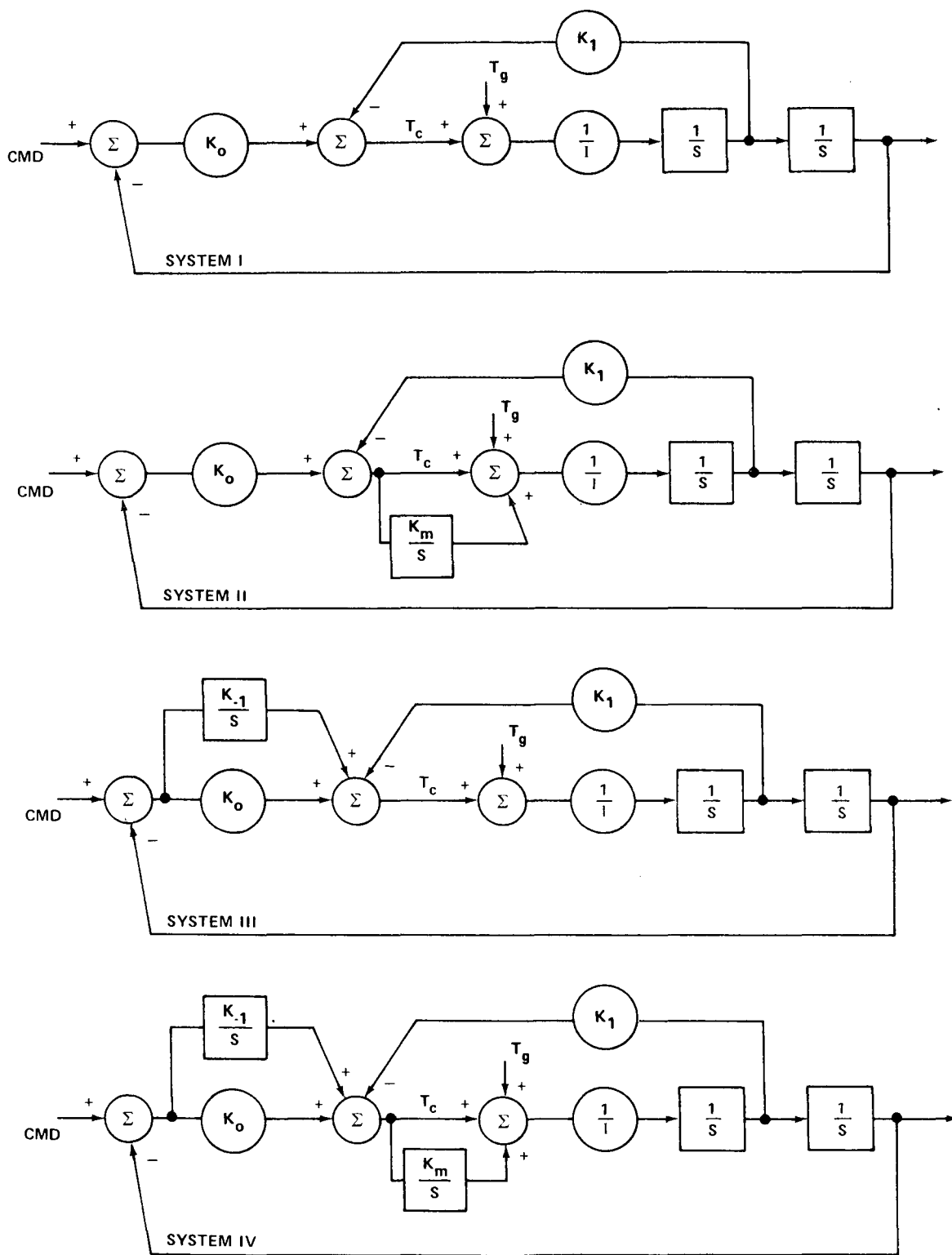


Figure E-27. Linear system configurations.

transpose steering law case by designating the control law gains as K_{-1}' , K_0' , and K_1' for the transpose steering law case. Thus, the following equations are developed for an X-axis model:

$$K_{-1}' = K_{-1}/4S^2\beta \quad , \quad (231)$$

$$K_0' = K_0/4S^2\beta \quad , \quad (232)$$

and

$$K_1' = K_1/4S^2\beta \quad ; \quad (233)$$

and for a Y- or Z-axis model the equations below are used:

$$K_{-1}' = K_{-1}/2C^2\beta \quad , \quad (234)$$

$$K_0' = K_0/2C^2\beta \quad , \quad (235)$$

and

$$K_1' = K_1/2C^2\beta \quad . \quad (236)$$

2. Linear System Analysis.

a. System I. From the block diagram in Figure E-27, the open loop transfer function G is

$$G(s) = \frac{\frac{K_0}{I}}{S \left[S + \frac{K_1}{I} \right]} = \frac{\frac{K_0}{K_1}}{S \left[\frac{I}{K_1} S + 1 \right]} \quad (237)$$

The closed loop transfer function ϕ/ϕ_{CMD} is

$$\frac{\phi(s)}{\phi_{\text{CMD}}(s)} = \frac{\frac{K_0}{I}}{S^2 + \frac{K_1}{I}S + \frac{K_0}{I}} = \frac{1}{\frac{I}{K_0}S^2 + \frac{K_1}{K_0}S + 1} \quad (238)$$

System error from disturbance torques is given by

$$\frac{\phi_e(s)}{T_g(s)} = \frac{1}{IS^2 + K_1S + K_0} = \frac{\frac{1}{K_0}}{\frac{I}{K_0}S^2 + \frac{K_1}{K_0}S + 1} \quad (239)$$

Error due to cyclical disturbance torques, such as gravity gradient torques, is obtained by substituting $j\omega_0$ for S in equation (239). (ω_0 for the HEAO missions is approximately 0.0022 rad/sec):

$$\left| \theta_e \right|_{\text{max}} = \frac{\left| T_g \right|_{\text{max}}}{-I\omega_0^2 + jK_1\omega_0 + K_0} \approx \frac{\left| T_g \right|_{\text{max}}}{K_0} \quad (240)$$

Errors due to bias disturbance torques are obtained via the Laplace transform final value theorem:

$$\phi_{\text{ess}} = \frac{T_{g_s}}{K_0} \quad ,$$

where ϕ_{ss} is the steady state error due to a bias torque T_g .

It is of interest in CMG sizing studies to determine CMG gimbal angle response due to disturbance torques. From Figure E-27, System I, it can be seen that

$$\frac{T_c(s)}{T_g(s)} = \frac{K_1S + K_0}{IS^2 + K_1S + K_0} \quad (241)$$

Control moment gyro gimbal angle, α , is determined from T_c for the constant gain case by

$$\alpha_i = \frac{T_{cx}}{4h \sin \beta} \quad (\text{X-axis}) \quad (242)$$

and

$$\alpha_i = \frac{T_{cy}}{2h \cos \beta} \quad (\text{Y-axis}) \quad (243)$$

where α_i is the gimbal angle of one CMG operating on a particular axis.

Substituting T_{cx} for T_c in equation (241) yields the following results:

$$\frac{\alpha_i(s)}{T_{gx}(s)} = \frac{K_1 S + K_0}{4h \sin \beta S (IS^2 + K_1 S + K_0)} \quad (244)$$

If T_{ax} is a cyclical gravity gradient torque of magnitude T_g and frequency ω_0 , then substitution of $j\omega_0$ for S yields

$$\left| \alpha_i \right| \approx \frac{\left| T_a \right|}{\omega_0 4h \sin \beta} \quad (245)$$

for an X-axis CMG and

$$\left| \alpha_i \right| \approx \frac{\left| T_a \right|}{\omega_0 2h \cos \beta} \quad (246)$$

for a Y- or Z-axis CMG. Equations (245) and (246) also apply to the transpose steering law case.

Control system design for the System I configuration consists of selection of a suitable K_0 and K_1 . This can be accomplished by the following steps:

1. Select K_0 , by means of equation (240), to meet the specified error criterion due to the anticipated cyclical gravity gradient torque. Figure E-28 is a graphical presentation of equation (240) utilizing convenient physical units.

2. Select K_1 to assure adequate damping of the system characteristic equation [equation (238)].

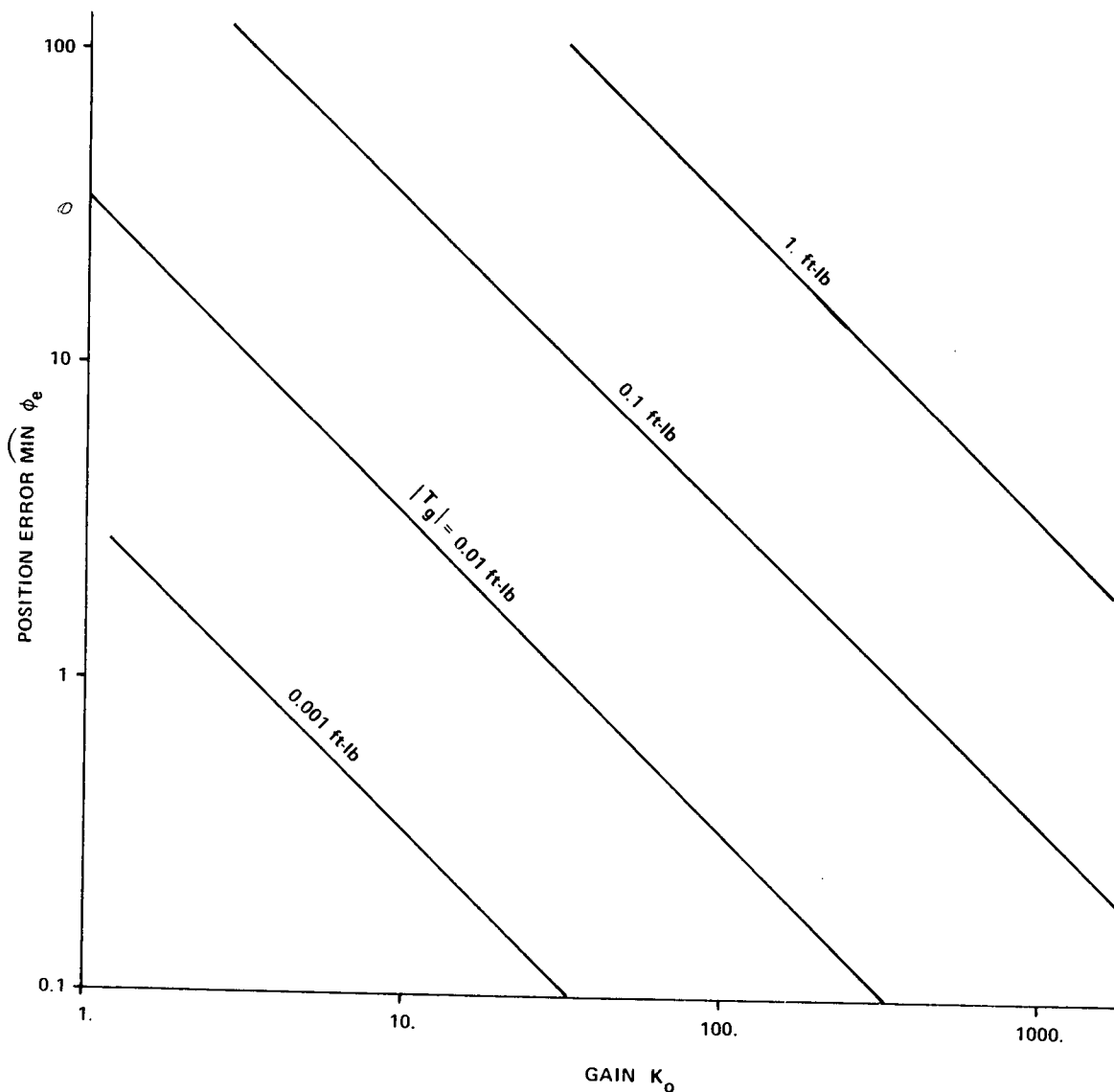


Figure E-28. System I, position gain versus position error due to disturbance torques.

Figure E-29 is a design chart to aid in selecting K_1 . When K_0 is selected, a root with desired damping (usually 0.7) is plotted at the intersection of the circle corresponding to K_0/I and the radial line, $\zeta = 0.7$. A vertical line from the root position intersects the horizontal scale at $K_1/2I$. The circles intersect the vertical scale at the system undamped natural frequency, $\omega_n = \sqrt{K_0/I}$, and a horizontal line through the root intersects the vertical scale at the system damped natural frequency or closed loop bandwidth.

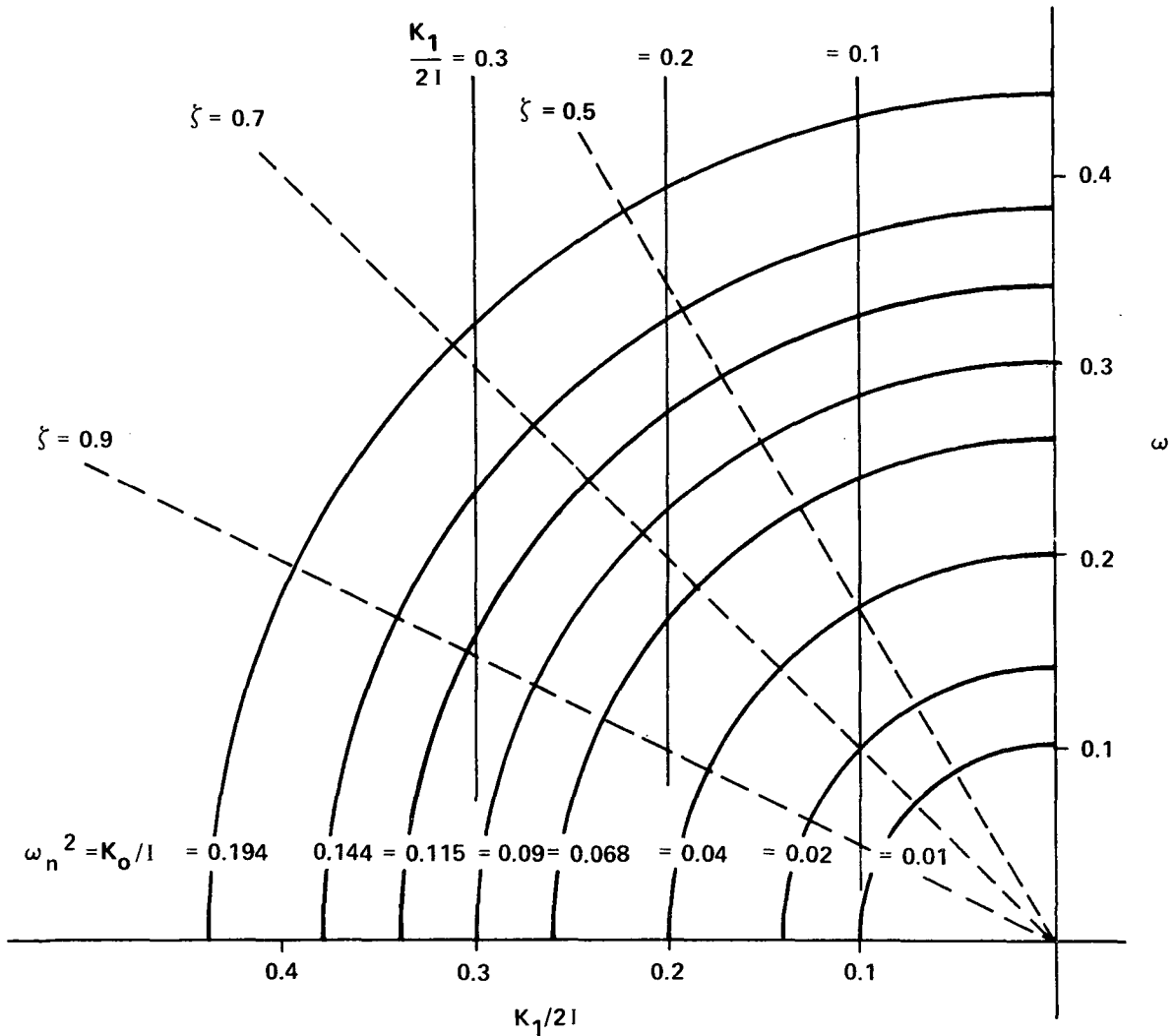


Figure E-29. System I, design — analysis chart.

If the resultant system bandwidth is unsatisfactory, a redesign can be attempted in the following manner:

Extend a horizontal line from a new bandwidth to a desirable root location ($\zeta = 0.7$). A vertical line from this root location establishes $K_1/2I$ and the nearest circle through the root location established K_0/I . The value of K_0 thus derived can be entered in the chart of Figure E-29 to reestablish position error versus disturbance torque criteria. A sample set of design values for a typical HEAO vehicle is shown in Table E-6.

TABLE E-6. SYSTEM I DESIGN EXAMPLES

I (slug-ft ²)	ω_n	ζ	Constant Gain		Transpose		$ T_d $ (ft-lb)	ϕ_e (arc min)
			K_0	K_1	K'_0	K'_1		
83 000	0.25	0.7	5157.	29 100.	X-axis 2010.	X-axis 11 350.	0.15	0.1
					Z-axis 7170.	Z-axis 40 400.		
2 600	0.115	0.7	34.4	418	Y-axis 48.8	Y-axis 582.	0.001	0.1

b. System II. From the block diagram in Figure E-27, the open loop transfer function, G , is

$$G(s) = \frac{K_0 (S + K_m)}{S [IS^2 + K_1S + K_m K_1]} = \frac{\frac{K_0}{K_1} \left(\frac{S}{K_m} + 1 \right)}{S \left[\frac{IS^2}{K_m K_1} + \frac{S}{K_m} + 1 \right]} \quad (247)$$

The closed loop transfer function is as follows:

$$\phi/\phi_{CMD} = \frac{K_0 [S + K_m]}{IS^3 + K_1S^2 + (K_m K_1 + K_0) S + K_0 K_m}$$

$$= \frac{\frac{S}{K_m} + 1}{\frac{IS^3}{K_0K_m} + \frac{K_1S^2}{K_0K_m} + \left(\frac{K_m K_1 + K_0}{K_0K_m}\right) S + 1} \quad (248)$$

System error due to disturbance torques is given by

$$\frac{\phi_e(S)}{T_g(S)} = \frac{S}{IS^3 + K_1S^2 + (K_m K_1 + K_0)S + K_m K_0} \quad (249)$$

System error due to bias torques is zero and error due to cyclical torques at frequency ω_0 and amplitude $|T_g|$ are found by substituting $j\omega_0$ for S to get

$$|\phi_e| \approx \frac{|T_g| \omega_0}{K_m K_0} \quad (250)$$

Control moment gyro gimbal angle response due to disturbance torques can be determined from

$$\frac{T_c(s)}{T_g(s)} = \frac{SK_0 \left(\frac{K_1}{K_0} S + 1\right)}{IS^3 + K_1S^2 + (K_m K_1 + K_0)S + K_m K_0} \quad (251)$$

and, for the constant gain case, α_i is given by equation (242) or equation (243). Then, by substituting $j\omega_0$ for S the following results are obtained:

$$|\alpha_i| \approx \frac{|T_g|}{K_m 4h \sin \beta} \quad (252)$$

for the X-axis and

$$|\alpha_i| \approx \frac{|T_g|}{K_m 2h \cos \beta} \quad (253)$$

for the Y- or Z-axis. These equations also apply to the transpose steering law case.

A control system design procedure for a system of this type consists of, first, selecting $K_m k_0$ to meet accuracy requirements specified by equation (250). The remaining parameters are selected to achieve adequate stability and time domain response characteristics. This design process is aided by certain relations and approximations described next. System stability is assured if

$$K_1(K_m K_1 + K_0) > K_0 K_m \quad , \quad (254)$$

which is Routh's criterion applied to the cubic denominator of equation (248). A much simpler stability criterion which is sufficient, but not necessary, is

$$K_1 > K_m \quad . \quad (255)$$

An assumption which aids in design is that if K_m is small (<0.05), then the real root of equation (248) lies between 0 and K_m .

Approximate the real root as zero, then an approximation of the remaining quadratic is

$$S^2 + \frac{K_1 S}{I} + \frac{K_m K_1 + K_0}{I} \quad . \quad (256)$$

The two remaining roots can be selected for adequate system response from the design chart in Figure E-29 where, in this case,

$$\omega_n^2 \approx \frac{K_m K_1 + K_0}{I} \approx \frac{K_0}{I} \quad (257)$$

and

$$\frac{K_1}{2I} = \zeta \omega_n \quad (258)$$

Subsequently, the selected values of K_m , K_0 , and K_1 can be substituted in equation (248); then the exact roots can be obtained. Figure E-30 is a plot of equation (250) in convenient units which facilitates selection of $K_m K_0$ to meet accuracy specifications.

Table E-7 shows the results of this design procedure applied to the HEAO spacecraft. K_m is arbitrarily selected to be either 0.01 or 0.001. Then, by use of Figure E-30, $K_m K_0$ is selected to maintain ϕ_e below 0.1 min in the face of the indicated disturbance torque. A trial set of values for K_0 and K_1 is obtained from Figure E-29, and then the trial solution is checked by accurately factoring equation (248). If the exact solution is sufficiently close to the approximated solution and the approximate resultant bandwidth (ω_n) is satisfactory, the design is complete.

Although system stability is assured if equation (254) or equation (255) is satisfied, relative stability and the effects on stability of variations of the system parameters, K_m , K_0 , and K_1 , should be analyzed. This can be accomplished by a root locus analysis as illustrated in Figures E-31, E-32, and E-33. Here the first case in Table E-6, where $I = 83\,000$, $K_m = 0.01$, $K_0 = 1250$, $K_1 = 14\,770$, is the nominal condition and each of the parameters, K_m , K_0 , and K_1 , is varied, in turn, above and below the nominal value. It is seen in Figures E-31, E-32, and E-33 that considerable variation of parameters is permissible without adversely affecting stability.

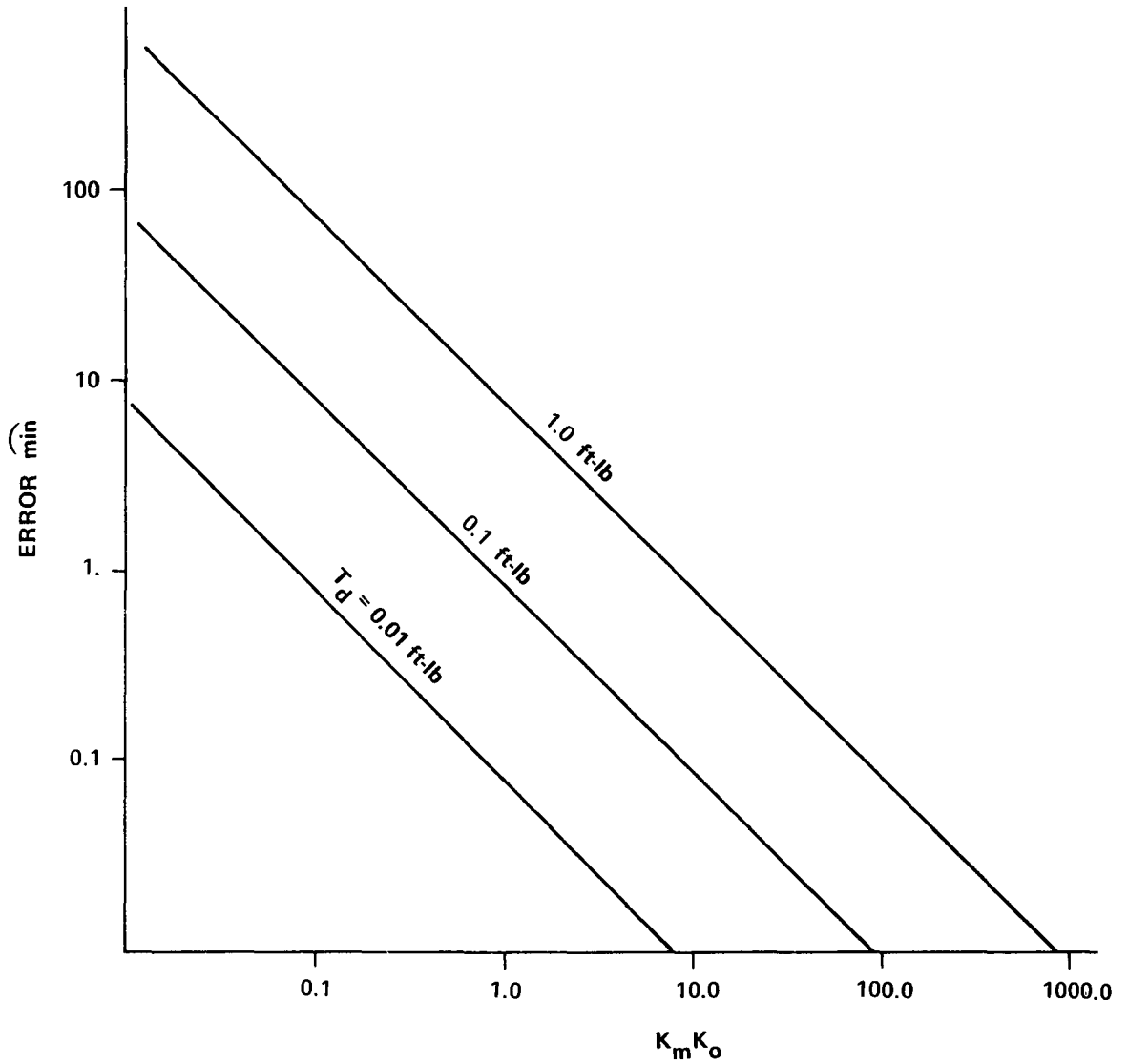


Figure E-30. System II, error due to cyclical torques.

c. System III. From the block diagram in Figure E-27, the open loop transfer function, G , is

$$G(s) = \frac{K_0 s + K_{-1}}{s^2 [I s + K_1]} = \frac{K_{-1}}{K_1} \frac{\frac{K_0 s}{K_{-1}} + 1}{s^2 \left[\frac{I}{K_1} s + 1 \right]} \quad (259)$$

TABLE E-7. SYSTEM II DESIGN EXAMPLES

I (slug-ft ²)	Exact		Approx.		Constant Gain		Transpose		T _y (ft-lb)	φ _e (arc min)
	ω _n	ζ	ω _n	ζ	K ₀	K ₁	K ₀	K ₁		
83 000	0.123	0.68	0.127	0.7	1250.	14 770.	X-axis	X-axis	0.15	0.1
							488.	5760.		
2 600	0.055	0.58	0.053	0.7	7.55	193.	Z-axis	Z-axis	0.001	0.1
							1740.	20 500.		
83 000	0.388	0.68	0.388	0.7	12 500.	45 000	X-axis	X-axis	0.15	0.1
							4880	17 600		
2 600	0.168	0.67	0.167	0.7	75.5	608	Z-axis	Z-axis	0.001	0.1
							17 400	62 500		

K_m = 0.01

K_m = 0.001

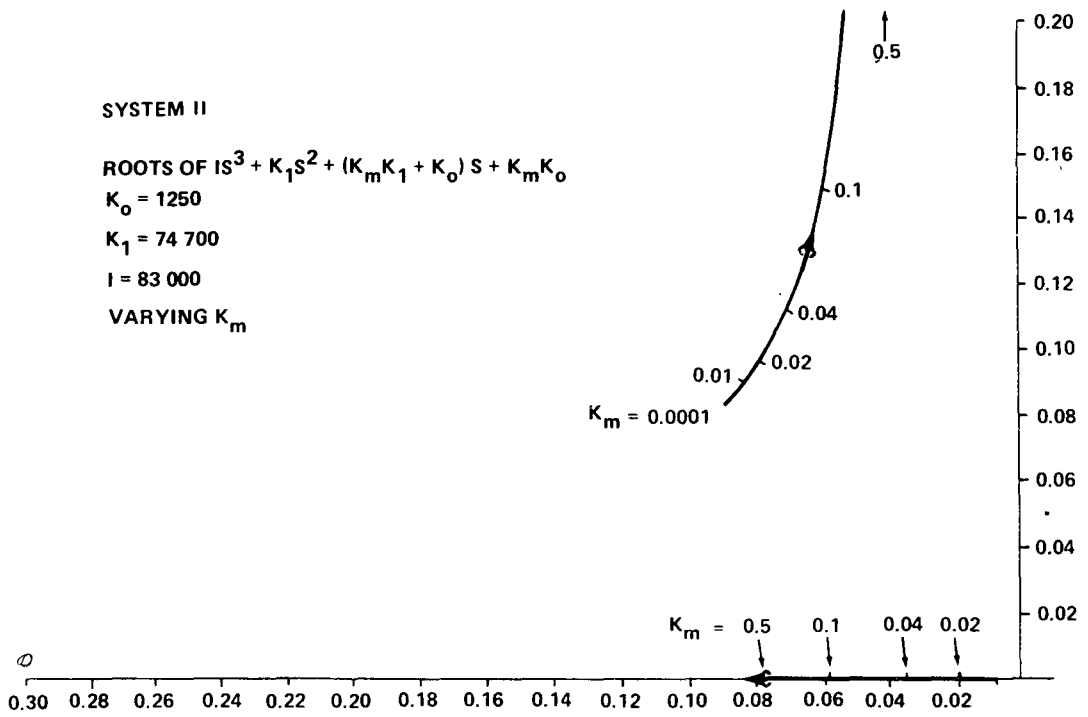


Figure E-31. System II, root locus analysis.

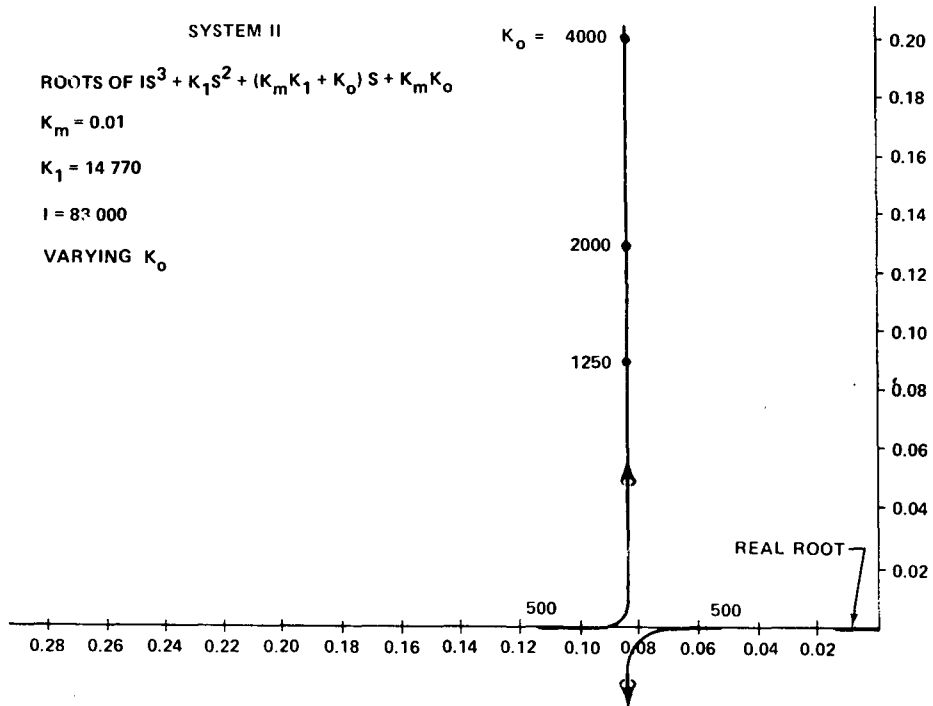


Figure E-32. System II, root locus analysis.

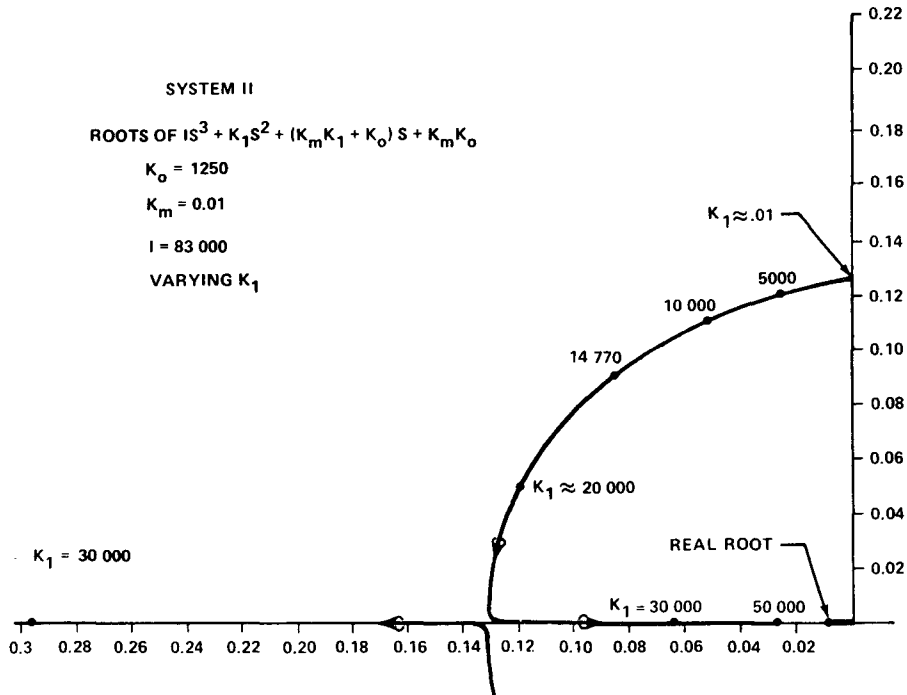


Figure E-33. System II, root locus analysis.

The closed loop transfer function ϕ/ϕ_{CMD} is

$$\frac{\phi(s)}{\phi_{CMD}(s)} = \frac{K_0S + K_{-1}}{IS^3 + K_1S^2 + K_0S + K_{-1}} \quad (260)$$

System error due to disturbance torques is given by

$$\frac{\phi_e(s)}{T_g(s)} = \frac{S}{IS^3 + K_1S^2 + K_0S + K_{-1}} \quad (261)$$

System error due to bias torques is zero. Errors due to cyclical torques at the gravity gradient frequency, ω_0 , with magnitude $|T_g|$ are found by substituting $j\omega_0$ for S to obtain

$$|\phi_e| \approx |T_g| \frac{\omega_0}{K_{-1}} \quad (262)$$

Control moment gyro gimbal angle response due to disturbance torques can be found from

$$\frac{T_c(s)}{T_g(s)} = \frac{K_1 S^2 + K_0 S + K_{-1}}{IS^3 + K_1 S^2 + K_0 S + K_{-1}} \quad (263)$$

$\alpha_i(s)$ is given in terms of $T_c(s)$ by equation (242) or equation (243). Substituting for $T_c(s)$ yields

$$\alpha_i(s) = \frac{K_1 S^2 + K_0 S + K_{-1}}{4h \sin \beta S [IS^3 + K_1 S^2 + K_0 S + K_{-1}]} \quad (264)$$

for an X-axis CMG. Gimbal angle response to a cyclical disturbance torque at the gravity gradient frequency, ω_0 , and amplitude $|T_g|$ is found by substituting $j\omega_0$ for S to obtain

$$|\alpha_i| \approx \frac{|T_g|}{\omega_0 4h \sin \beta} \quad (265)$$

for the X-axis, and in a similar manner

$$|\alpha_i| \approx \frac{|T_g|}{\omega_0 2h \cos \beta} \quad (266)$$

for the Y- or Z-axis. α_i is the gimbal angle of one CMG operating on the axis in question.

A control system design procedure for System III proceeds similarly to the procedure outlined previously for System II.

First, select K_{-1} to meet accuracy criteria specified by equation (262). The chart in Figure E-30 can aid in this choice by calling the abscissa K_{-1} instead of K_m K_0 . Next, by assuming that K_{-1} will be relatively small and one real root of the cubic in equation (260) is nearly zero, an approximation of the remaining quadratic can be obtained:

$$s^2 + \frac{K_1}{I} s + \frac{K_0}{I} \quad (267)$$

K_0 and K_1 can be selected by using the design chart in Figure E-29. It is necessary to choose a convenient ω_n and ζ (usually 0.7). In addition, the stability criterion is

$$K_1 K_0 > K_{-1} \quad , \quad (268)$$

which is Routh's criterion applied to the cubic in equation (260). The selected values for K_{-1} , K_0 , and K_1 can be substituted in equation (260) and the exact roots can be obtained. Examples of this design procedure are shown in Table E-8. The control gains in this table have been selected to produce system characteristics as nearly equivalent to those in Table E-7 as possible.

Sensitivity of a given design to variations in the parameters K_{-1} , K_0 , and K_1 can also be investigated by means of a root locus study. The design example of the top line in Table E-8 is utilized for a parameter sensitivity analysis in Figures E-34, E-35, and E-36. Each of the parameters K_{-1} , K_0 , and K_1 is varied in turn about its nominal value and the locus of the roots of the system characteristic equation [equation (260)] is plotted. Figures E-34, E-35, and E-36 illustrate that, in this case, each of the parameters can be varied in such a manner as to cause instability. However, the large variation required (gain margin) from the nominal value is also indicated and this particular example is adequately stable.

TABLE E-8. SYSTEM III DESIGN EXAMPLES

I (slug-ft ²)	Exact		Approx.		Constant Gain			Transpose				T _g (ft-lb)	φ _e (arc min)	
	ω _n	ζ	ω _n	ζ	K ₋₁	K ₀	K ₁	K ₋₁	K ₀	K ₁	K ₋₁			K ₀
83 000	0.121	0.7	0.127	0.7	11.3	1340	14 800	4.4	524	5780	X-axis	X-axis	0.15	0.1
								Z-axis	Z-axis	Z-axis	Z-axis	Z-axis		
					15.7	1865	20 600							
2 600	0.043	0.69	0.053	0.7	0.075	7.3	193	0.104	10.1	268			0.001	0.1
83 000	0.383	0.71	0.388	0.7	11.3	12 500	45 000	4.4	4880	17 600	X-axis	X-axis	0.15	0.1
								Z-axis	Z-axis	Z-axis	Z-axis	Z-axis		
					15.7	17 400	62 500							
2 600	0.167	0.7	0.167	0.7	0.075	73	610	0.104	101	847			0.001	0.1

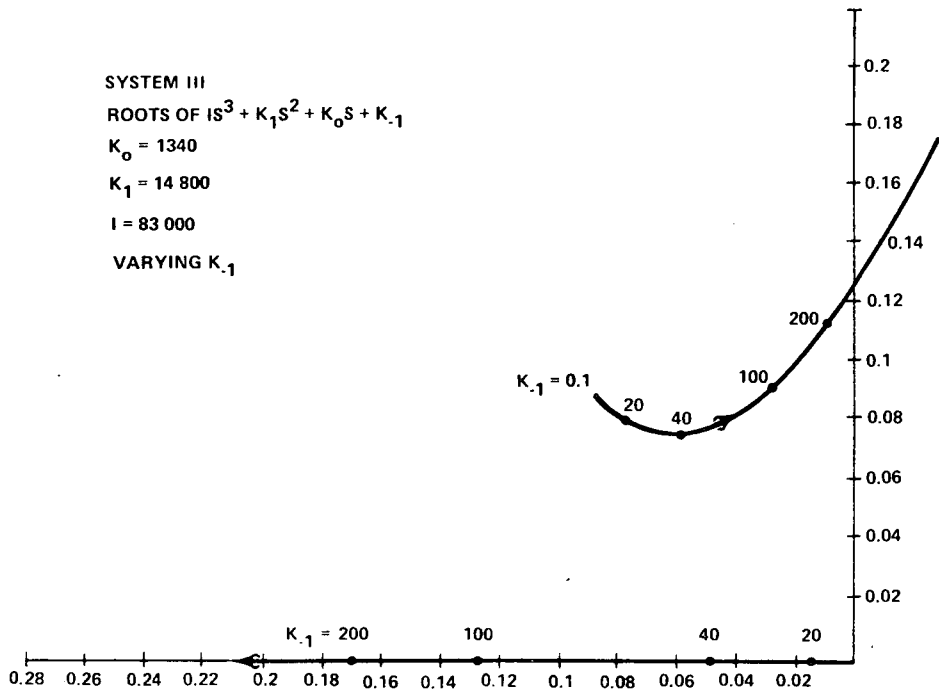


Figure E-34. System III, root locus analysis.

d. System IV. From the block diagram in Figure E-27, the open loop transfer function, G , is

$$G(s) = \frac{K_{-1} \left[\left(\frac{K_0}{K_{-1}} s + 1 \right) \left(\frac{s}{K_m} + 1 \right) \right]}{K_1 s^2 \left(\frac{I s^2}{K_1 K_m} + \frac{s}{K_m} + 1 \right)} \quad , \quad (269)$$

$$G(s) = \frac{K_0}{I} \frac{\left(s + \frac{K_{-1}}{K_0} \right) (s + K_m)}{s^2 \left(s^2 + \frac{K_1}{I} s + \frac{K_1 K_m}{I} \right)}$$

The closed loop transfer function ϕ/ϕ_{CMD} is

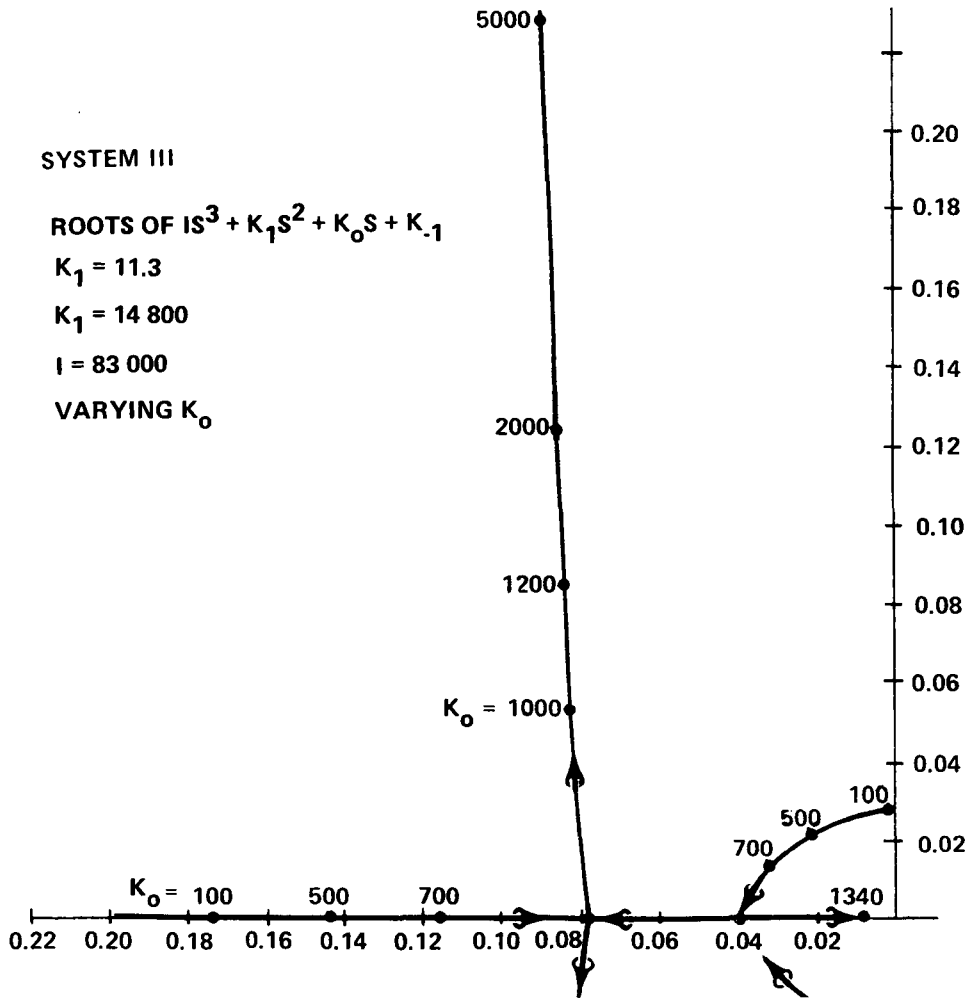


Figure E-35. System III, root locus analysis.

$$\frac{\phi(s)}{\phi_{\text{CMD}}(s)} = \frac{(K_0S + K_{-1})(K_m + S)}{IS^4 + K_1S^3 + (K_1K_m + K_0)S^2 + (K_0K_m + K_{-1})S + K_{-1}K_m} \quad (270)$$

System error due to disturbance torques is given by

$$\frac{\phi_e(s)}{T_g(s)} = \frac{S^2}{IS^4 + K_1S^3 + (K_1K_m + K_0)S^2 + (K_0K_m + K_{-1})S + K_{-1}K_m} \quad (271)$$

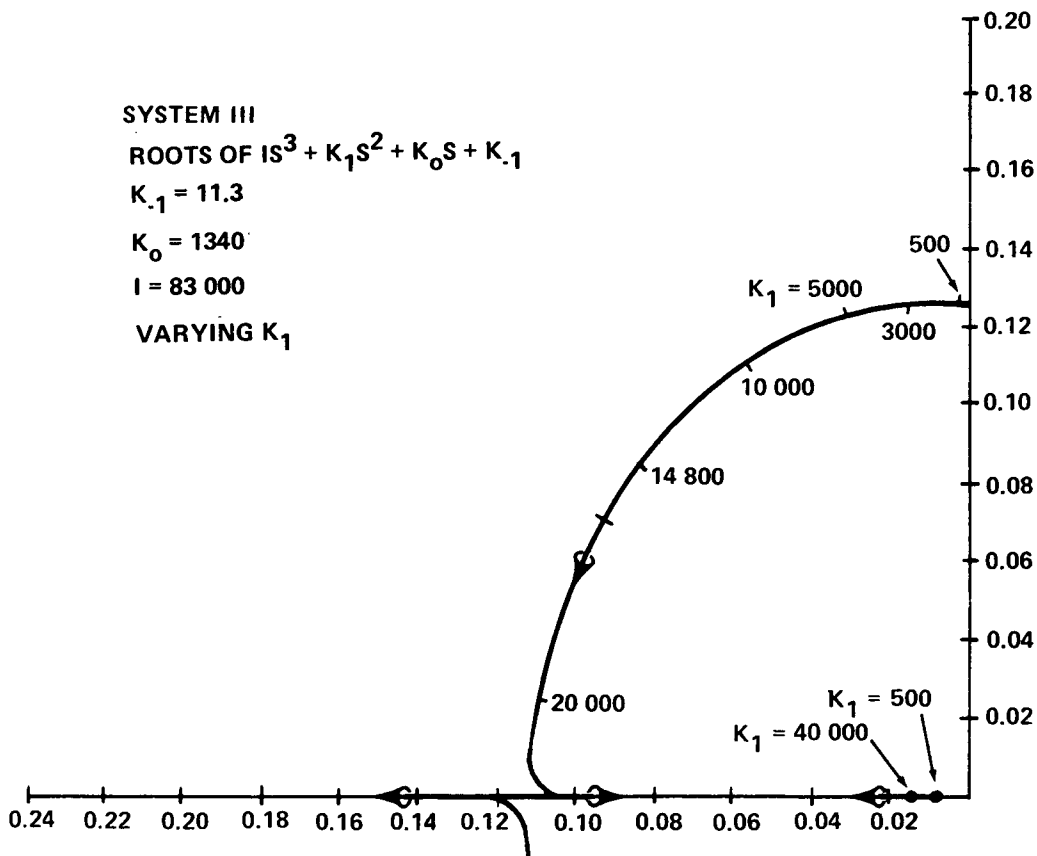


Figure E-36. System III, root locus analysis.

By use of the final value theorem, it is seen that system errors due to bias torques are zero. Errors due to cyclical torques at the gravity gradient frequency, ω_0 , with magnitude $|T_g|$ are found by substituting $j\omega_0$ for S to obtain

$$|\phi_e| \approx \frac{|T_g| \omega_0^2}{K_{-1}K_m} \quad (272)$$

Control moment gyro gimbal angle response due to disturbance torques can be determined from

$$\frac{T_c(s)}{T_g(s)} = \frac{S[K_1S^2 + K_0S + K_{-1}]}{IS^4 + K_1S^3 + [K_1K_m + K_0]S^2 + [K_0K_m + K_{-1}]S + K_{-1}K_m} \quad (273)$$

T_c is given in terms of α_i , the CMG gimbal angle, by equations (242) and (243). Substitute for T_c , let $S = j\omega_0$, and simplify to obtain

$$|\alpha_i| \approx \frac{|T_g|}{K_m 4h \sin \beta} \quad (274)$$

for an X-axis CMG and

$$|\alpha_i| \approx \frac{|T_g|}{K_m 2h \cos \beta} \quad (275)$$

for a Y- or Z-axis CMG. α_i is the gimbal angle of one CMG operating on the axis in question.

A comprehensive system design analysis has not been completed for System IV but one specific example can be used as an illustration. The example will be the large axis ($I = 83\,000$ slug-ft²). The system stability criterion is obtained by applying Routh's criterion to the quadratic denominator of equation (270) to obtain

$$K_1 (K_1 K_m + K_0) - (K_0 K_m + K_{-1}) > 0 \quad (276)$$

and

$$K_1 (K_1 K_m + K_0) - (K_0 K_m + K_{-1}) > \frac{K_1^2 K_{-1} K_m}{(K_0 K_m + K_{-1})} \quad (277)$$

as the stability criteria. A pointing accuracy of 0.1 arc min in the presence of a 0.15 ft-lb magnitude cyclical gravity gradient torque is assured, from equation (272), if

$$K_{-1} K_m \geq 0.025 \quad (278)$$

The fastest system design approach is utilization of the open loop transfer function, $G(s)$, given by equation (269) in a Bode plot synthesis technique. This is illustrated in Figure E-37. The breakpoints

$$\omega = \frac{K_{-1}}{K_0}, \quad K_m \quad \text{and} \quad \sqrt{\frac{K_1 K_m}{I}}$$

are selected to insure a stable system of adequate bandwidth. After some trial and error, the final plot of Figure E-37 is obtained. The basic parametric relationship established is

$$K_{-1} K_m = 0.025 \quad .$$

A value of 0.01 for K_m is arbitrarily selected to be compatible with magnetic system torque capability. Then, $K_{-1} = 2.5$. The gain, K_{-1}/K_1 , is set at -86 dB or 5.0×10^{-5} to insure stability. Then $K_1 = 50\,000$ and $K_0 = 500$. The resultant system as shown in Figure E-37 is adequately stable and meets accuracy specifications. However, considerable further effort is required to completely establish design guidelines for this system.

3. Conclusions. It has been established that stable practical designs of the four system types can be implemented and the necessary equations and design tools have been developed.

The two primary system performance criteria are pointing error and CMG gimbal angle due to gravity gradient disturbance torque. Table E-9 is a collection of the pertinent simplified formulae relating pointing error, ϕ_e , and gimbal angle, α_i , (for the X-axis only) to disturbance torque magnitude, T_g .

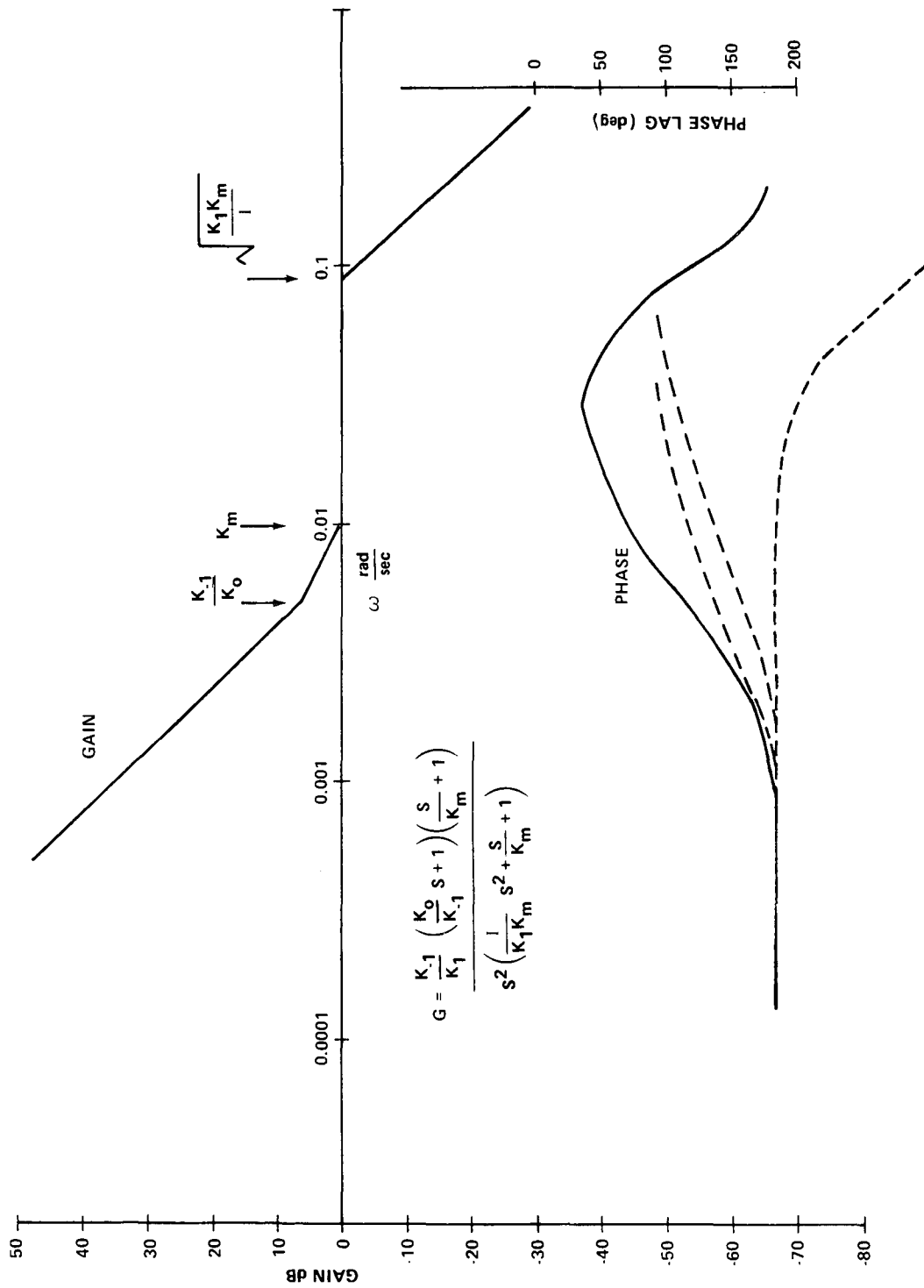


Figure E-37. System IV, design example.

TABLE E-9. COMPARISON OF SIMPLE FORMULAS FOR POINTING ERROR, ϕ_e , AND CMG GIMBAL ANGLE, α_i , DUE TO CYCLICAL DISTURBANCE TORQUES

System	I	II	III	IV
$ \phi_e $ rad	$\frac{ T_g }{K_0}$	$\frac{ T_g \omega_0}{K_m K_0}$	$\frac{ T_g \omega_0}{K^{-1}}$	$\frac{ T_g \omega_0^2}{K^{-1} K_m}$
$ \alpha_i $ rad	$\frac{ T_g }{\omega_0 4h \sin \beta}$	$\frac{ T_g }{K_m 4h \sin \beta}$	$\frac{ T_g }{\omega_0 4h \sin \beta}$	$\frac{ T_g }{K_m 4h \sin \beta}$

Pointing error for System I is a function of K_0 which implies that a large bandwidth is necessary to minimize pointing error. Systems II and III are very similar since $K_m K_0$ can be nearly equal to K_{-1} . It is apparent, from the design information on types I, II, and III, that Systems II and III can maintain the same or better pointing accuracy with less required bandwidth than System I. System IV can meet pointing accuracy requirements with even less bandwidth than Systems II or III. This is illustrated in Figure E-38 where the open loop gain versus frequency of the systems defined by the first line in Tables E-6, E-7, and E-8 is plotted. All of the systems have the same pointing error. System bandwidth can be defined as the frequency at which the open loop gain is unity. The bandwidths shown in the plots are 0.17, 0.11, and 0.11 for Systems I, II, and III, respectively. The plot in Figure E-37 illustrates a comparable System IV design with bandwidth approximately equal to 0.04 rad/sec.

A comparison of CMG gimbal angle response to cyclical disturbance torques shows that Systems I and III are equivalent. Similarly, Systems II and IV are equivalent. If K_m is larger than ω_0 (0.002), System II or IV is superior with respect to minimizing CMG gimbal angle.

Alternate System Description

1. Description. An alternate actuator system proposed for HEAO-C is composed of the four-skewed CMGs for maneuvering and attitude hold during normal operations, a cold gas RCS for control during Orbit Adjust Stage (OAS) burn and initial stabilization, and three orthogonal electromagnets for momentum management of the CMGs and for direct control torque in the event of two CMG failures. Such a system will be more reliable, weigh less, and provide greater depth of failure without degrading system performance than the RCS-CMG system baselined for HEAO-C. For long lifetime missions such as HEAO, a considerable amount of RCS fuel is required to dump the accumulated CMG momentum due to biased environmental forces. It seems only natural to consider the productive use of environmental forces such as gravity gradient or the earth's magnetic field. Previous studies for the Skylab program show that gravity gradient can be utilized to dump CMG momentum. But during dump, the spacecraft's pointing requirements must be ignored and the vehicle must be maneuvered in a specific sequence so that the gravity gradient counteracts the accumulated momentum. For HEAO, experiment viewing time takes priority and precludes the use of gravity dump. Currently, the earth's magnetic field offers the greatest growth potential for utilizing the HEAOs

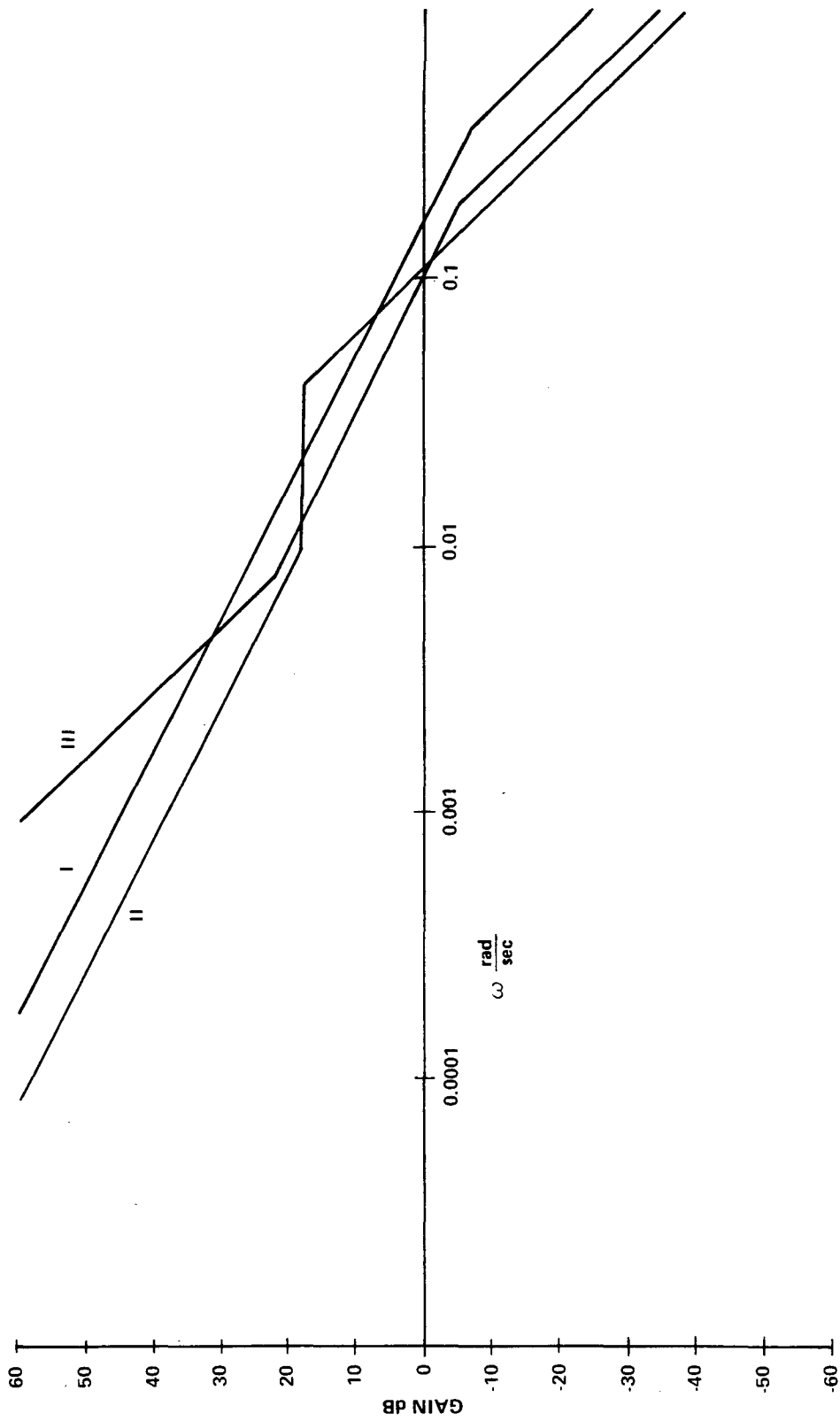


Figure E-38. Open loop gain plots for typical System I, II, and III designs.

environment for control purposes, without sacrificing experiment viewing time by imposed maneuvers or restricting the Observatory's orientation.

2. Magnetic Torquer. Basically, the advantage of utilization of controlled interactions with ambient fields is that no fuel need be carried aboard the vehicle for CMG momentum dump. However, the use of electromagnets to react against the earth's magnetic field does require additional power to drive the coils. The magnetic system proposed for HEAO consists of three electromagnets aligned orthogonally with each vehicle principal axis. When current is passed through the coils, a dipole moment (\overline{M}) is generated which reacts with the earth's magnetic field (\overline{B}) to produce a torque (\overline{T}_m). The torque produced obeys the vector cross product

$$\overline{T}_m = \overline{M} \times \overline{B} \quad . \quad (279)$$

It is apparent that the torque produced is perpendicular to both the dipole moment and the earth's field. Although limited in magnitude by the electromagnet size, the direction of this dipole can be produced in any direction. At any instant of time, the magnitude and direction of the earth's field depends on the Observatory's orbital position relative to the surface of the earth. The vector components of \overline{B} would be obtained by onboard magnetometers. The magnitude of \overline{M} varies as a function of the currents being passed through the coils at any time. To maximize the torque produced by a given current, the dipole generated should be perpendicular to the earth's field. Moreover, it is apparent that a torque cannot be produced in the direction of \overline{B} .

At some instant of time, the desired torque may be aligned with \overline{B} , in which case it cannot be produced. However, these periods are relatively short because, as the orbital position of the Observatory changes, a corresponding change occurs in the direction of the earth's field. Over any time interval during an orbit, the CMGs produce the desired torque required for fine control and the magnetic torque, if available, is used to dump the momentum accumulated in the CMGs. The magnetic system proposed for HEAO provides a torque proportional to the stored momentum. As such, it is a secondary control torque and if it cannot momentarily be produced, the vehicle performance is not degraded.

3. Magnetic Control Law. Let the CMG momentum be denoted by the vector

$$\bar{H} = h_x \bar{i} + h_y \bar{j} + h_z \bar{k} \quad . \quad (280)$$

If a proportional system is considered, the magnetic torque required to dump the CMG momenta must be proportional to \bar{H} but opposite in direction; therefore,

$$\bar{T}_m = -K \bar{H} \quad , \quad (281)$$

where K is an arbitrary constant to be determined. Equating equations (279) and (281) and taking the vector cross product of \bar{B} with both sides gives

$$\bar{B} \times (-K \bar{H}) = \bar{B} \times (\bar{M} \times \bar{B}) = B^2 \bar{M} - (\bar{M} \cdot \bar{B}) \bar{B} \quad . \quad (282)$$

The maximum torque for a given magnitude of \bar{B} and \bar{M} is obtained when \bar{M} is normal to \bar{B} , implying that $\bar{M} \cdot \bar{B} = 0$. For this case, equation (282) can be solved for \bar{M} to give

$$\bar{M} = \bar{B} \times (-K \bar{H}) / B^2 = \frac{-K}{B^2} (\bar{B} \times \bar{H}) \quad , \quad (283)$$

which gives the dipole moment required to dump the CMG momentum \bar{H} . In expanded form, the vector components of the required magnetic control law for momentum dumping are

$$\left. \begin{aligned} M_x &= (-K/B^2) (B_y h_z - B_z h_y) \\ M_y &= (-K/B^2) (B_z h_x - B_x h_z) \\ M_z &= (-K/B^2) (B_x h_y - B_y h_x) \end{aligned} \right\} \quad . \quad (284)$$

The magnetic dipole can, of course, be directly related to current and voltage. For use on HEAO, the power has been arbitrarily limited to 10 watts per electromagnet. Substituting the dipole commands into the torque equation [equation (279)] produces

$$\underline{T}_m = (-K/B^2) (\underline{B} \times \underline{H}) \times \underline{B} = [-K/B^2] (B^2 \underline{H} - \underline{B} (\underline{B} \cdot \underline{H})) . \quad (285)$$

as the magnetic torque produced to dump the CMG momentum. If \underline{H} is perpendicular to \underline{B} , then $\underline{B} \cdot \underline{H} = 0$ and the exact torque needed for momentum dump is produced. Consider the other extreme and assume that \underline{H} is aligned with \underline{B} . In this case, \underline{H} can be expressed as a constant k times \underline{B} ($\underline{H} = k \underline{B}$) and equation (285) becomes zero. That is, no magnetic torque is produced when the earth's field is unfavorable for dumping momentum. Only that portion of the desired torque which is perpendicular to the earth's field will be produced at any given time. However, momentum can be dumped on one axis at the expense of increasing momentum on another axis, but the total magnitude will always be reduced by the magnetic system.

In the event of two CMG failures, the magnetic system could be used to provide direct torque in addition to dumping CMG momentum. For direct torque control, the magnetic torque would be set equal to the desired control torque, \underline{T}_c . The desired torque is based upon attitude error signals which have been weighted by appropriate feedback gains. Normally, the CMGs would provide this torque through the CMG steering law. The dipole moment required for direct torque commands is obtained by setting $\underline{T}_m = \underline{T}_c$.

In a manner similar to that used to obtain the dipole commands for momentum dump, the dipole command for direct torque control is

$$\underline{M} = (\underline{B} \times \underline{T}_c) / B^2 . \quad (286)$$

Assuming that two CMGs have failed, the dipole commands would be a combination of those required for momentum dump and direct control. The magnetic torque would be

$$\underline{T}_m = -K \underline{H} + \underline{T}_c . \quad (287)$$

The corresponding dipole solution is

$$\bar{M} = \frac{\bar{B} \times (-K \bar{H} + \bar{T}_c)}{B^2} = \frac{-K}{B^2} (\bar{B} \times \bar{H}) + \frac{1}{B^2} (\bar{B} \times \bar{T}_c) . \quad (288)$$

Hence, the form of the dipole command changes according to the type actuation desired.

4. Electromagnet Sizing. The maximum dipole is physically limited by the shape and volume of the electromagnet, the number of turns in the coil, current passed through the coils, and physical properties of the materials used. In sizing the electromagnets, low power usage is selected over weight as a design criterion. A maximum of 10 watts per coil has been arbitrarily selected as an upper limit and the rest of the magnetic system has been sized accordingly to meet the required torque and/or momentum dump capability. The magnetic system would be installed in the OAS stage and, for this reason, the length of the electromagnet has been limited to 60 inches.

Based on simulation results for which the dipoles per axis were limited to selected values, it was found that a dipole moment for axis of 0.2 ft-lb/gauss was adequate to dump the expected secular momentum due to gravity gradient torque. However, under worst case conditions, the magnetic system could not dump all the accumulated momentum and the CMGs could saturate in approximately one day. For direct torque control, the magnetic system must produce a torque equal to or greater than that of gravity gradient, in which case a dipole moment of 0.4 ft-lb/gauss is desirable. With a properly sized magnetic system, two out of four CMGs could be failed and still maintain acceptable HEAO-C performance. For this reason, a value of 0.4 ft-lb/gauss was selected as a basis for designing electromagnets for HEAO-C. A candidate electromagnetic torquer design to meet the above specifications is included here. In this case, a Permendur core was assumed to be utilized.

The specifications for the design of the electromagnetic torquer are listed below:

- Magnetic moment, $M = 0.4 \text{ ft-lb/gauss} = 5440 \text{ amp-turn-m}^2$
- Length, $L = 60 \text{ in.} = 1.525 \text{ m}$

- Power, $p = 10 \text{ W}$

- Core Material — Permendur

$$\text{Density, } \rho_c = 8.3 \times 10^3 \text{ kg/m}^3$$

$$\text{Flux Density, } B = 20\,000 \text{ gauss}$$

$$\text{Field Intensity, } H = 18 \text{ oersted} = 1430 \text{ amp/m}$$

- Wire — Aluminum

$$\text{Density, } \rho = 2.7 \times 10^3 \text{ kg/m}^3$$

$$\text{Resistivity, } \sigma = 2.82 \times 10^{-8} \text{ ohm-m}$$

The required core volume is found in the following formula:

$$\begin{aligned} V &= \frac{4\pi \times 10^{-3} \times M}{B} = \frac{(4) \times (3.14 \times 10^{-3}) (5.44 \times 10^3)}{2.0 \times 10^4} \\ &= 0.00342 \text{ m}^3 = 209.5 \text{ in.}^3 \end{aligned} \quad (289)$$

The core diameter is given by

$$\begin{aligned} d &= \left(\frac{4V}{\pi L} \right)^{\frac{1}{2}} = \left[\frac{(4) \times (3.42 \times 10^{-3})}{(3.14) \times (6.0 \times 10^1 \times 2.54 \times 10^{-2})} \right]^{\frac{1}{2}} \\ &= 0.0535 \text{ m} = 2.11 \text{ in.} \end{aligned} \quad (290)$$

The core weight is given by

$$\begin{aligned} W_c &= \rho_c V = (8.3 \times 10^3) (3.42 \times 10^{-3}) \\ &= 28.4 \text{ kg} = 62.6 \text{ lbm} \end{aligned} \quad (291)$$

The winding weight is given by

$$W_s = \frac{4\pi H^2 L \sigma \rho V}{P}$$

$$W_s = \frac{(4.0) (3.14) [(1.43)^2 \times 10^6] (1.525) (2.82 \times 10^{-8}) (2.7 \times 10^3) (3.42 \times 10^{-3})}{1.0 \times 10^1}$$

$$= 1.02 \text{ Kg} = 2.25 \text{ lbm} \quad . \quad (292)$$

The total weight is obtained by adding W_c and W_s plus a 10 percent allowance for winding insulation and torquer cover.

$$W_t = W_c + W_s + 0.1 (W_c + W_s)$$

$$= 28.4 + 1.02 + 0.1 (28.4 + 1.02)$$

$$= 32.36 \text{ kg} = 71.4 \text{ lbm.} \quad . \quad (293)$$

The total diameter of the torquer, allowing 10 percent for insulation and covering, is obtained from

$$d_t = 2 W_s / \rho \pi d L + d + 10\%$$

$$= 2.04 / (2.7 \times 10^3) (3.14) (0.0535) (1.525) + 0.0535 + 10\%$$

$$= 0.0565 + 10\% = 0.06215\text{m} = 2.45 \text{ in.} \quad (294)$$

Table E-10 summarizes the torquer characteristics for this design.

TABLE E-10. ELECTROMAGNETIC TORQUER DESIGN DATA

	Total (1 torquer)	Total (3 torquers)
Weight, lbm	71.4	214.2
Max Power, W	10	30
Outside Diameter, in.	2.45	
Core Diameter, in.	2.11	
Core Volume, in. ³	209.5	628.5
Max Magnetic Moment, amp-turn-m ²	5 440	
Torque Produced in a 0.35 gauss field, ft-lb	0.14	0.24
Flux Density, gauss	20 000	
Field Intensity, oersted	18	
Core Material	Permendur	
Winding Material	Aluminum	

5. Location of Electromagnets. Because of the large magnetic moment capability of the electromagnets and their large size (60 inches long), an effort has been made to determine their most suitable location inside the spacecraft so that magnetic contamination will be minimized. The term "magnetic contamination" has been used to mean interference by the torquer magnetic field with the proper operation of certain experiment and subsystem components. Magnetically sensitive components must be either removed to an area of low field intensity or magnetically shielded.

The location of certain magnetically sensitive experiment components, like image detectors and aspect detectors, is fixed inside the spacecraft; however, other sensitive subsystem components (such as tape recorders, data processors, amplifiers, and transmitters) can be located inside the spacecraft where the magnetic field intensity is low. The task is, therefore, to determine the location of the three electromagnets inside the spacecraft so that the magnetic field is reduced at the location of these fixed experiment components that are sensitive to magnetic field.

Two most probable arrangements for the layout of the electromagnets inside the spacecraft have been considered. These two cases are listed below:

- Case I — Two electromagnets are located at one end of the spacecraft and the third electromagnet is located in the middle of the spacecraft as shown in Figure E-39.
- Case II — All three electromagnets are located in the OAS as shown in Figure E-40.

The OAS offers an attractive place to locate the three electromagnets for the following reasons:

- The OAS does not contain any magnetic-field-sensitive components which operate in phase with electromagnets.
- Any experiments and system components which are sensitive to the magnetic field will be located some distance away from the electromagnets.
- All the three electromagnets can be easily accommodated in the space available in the OAS.

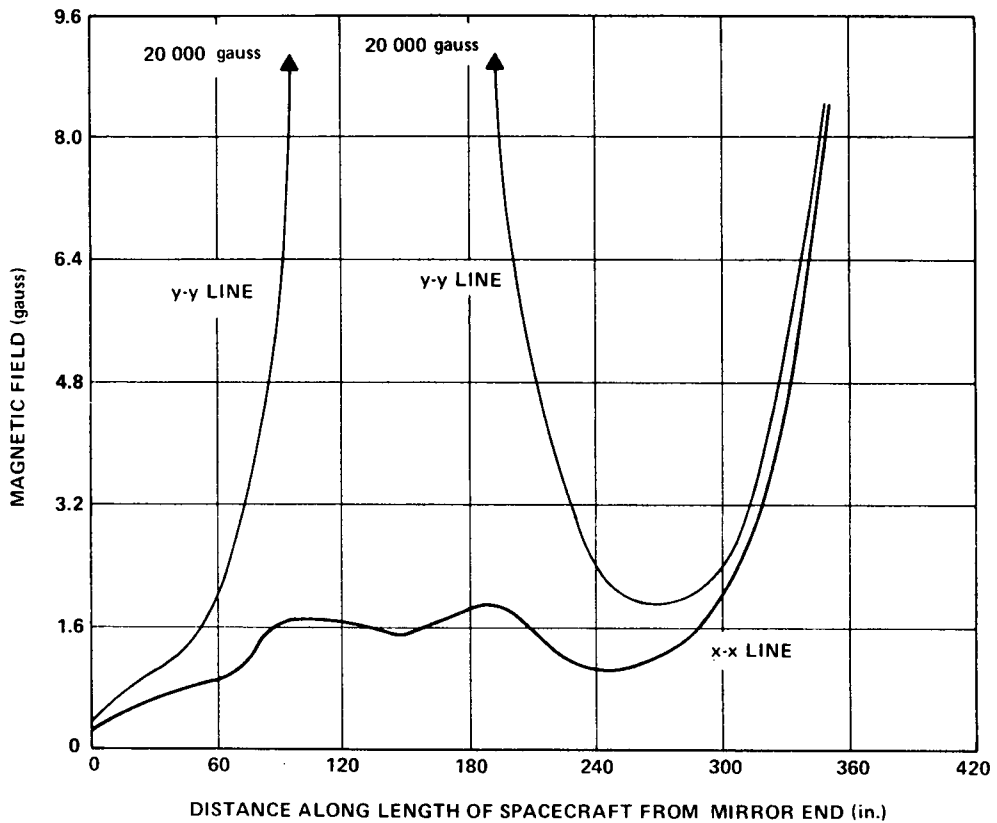
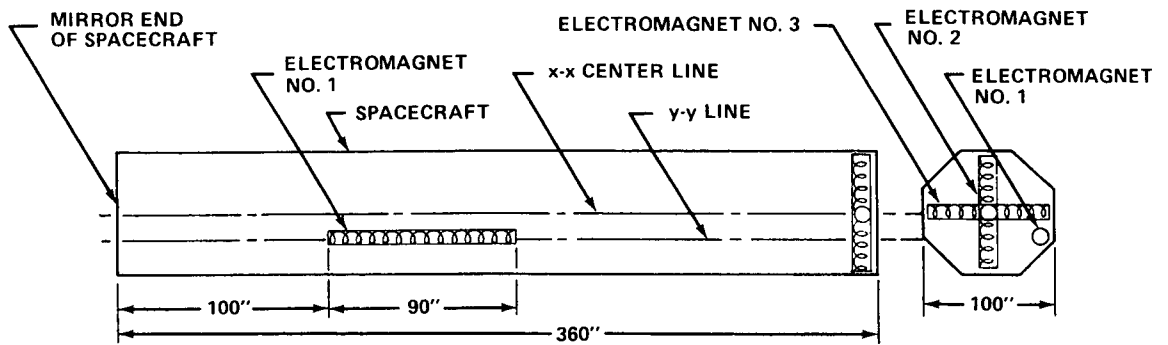


Figure E-39. Layout of the electromagnets and the magnetic field profile inside the spacecraft for Case I.

6. Magnetic Field Distribution. The magnetic field profiles inside the spacecraft resulting from the three electromagnets have been computed on the following assumptions:

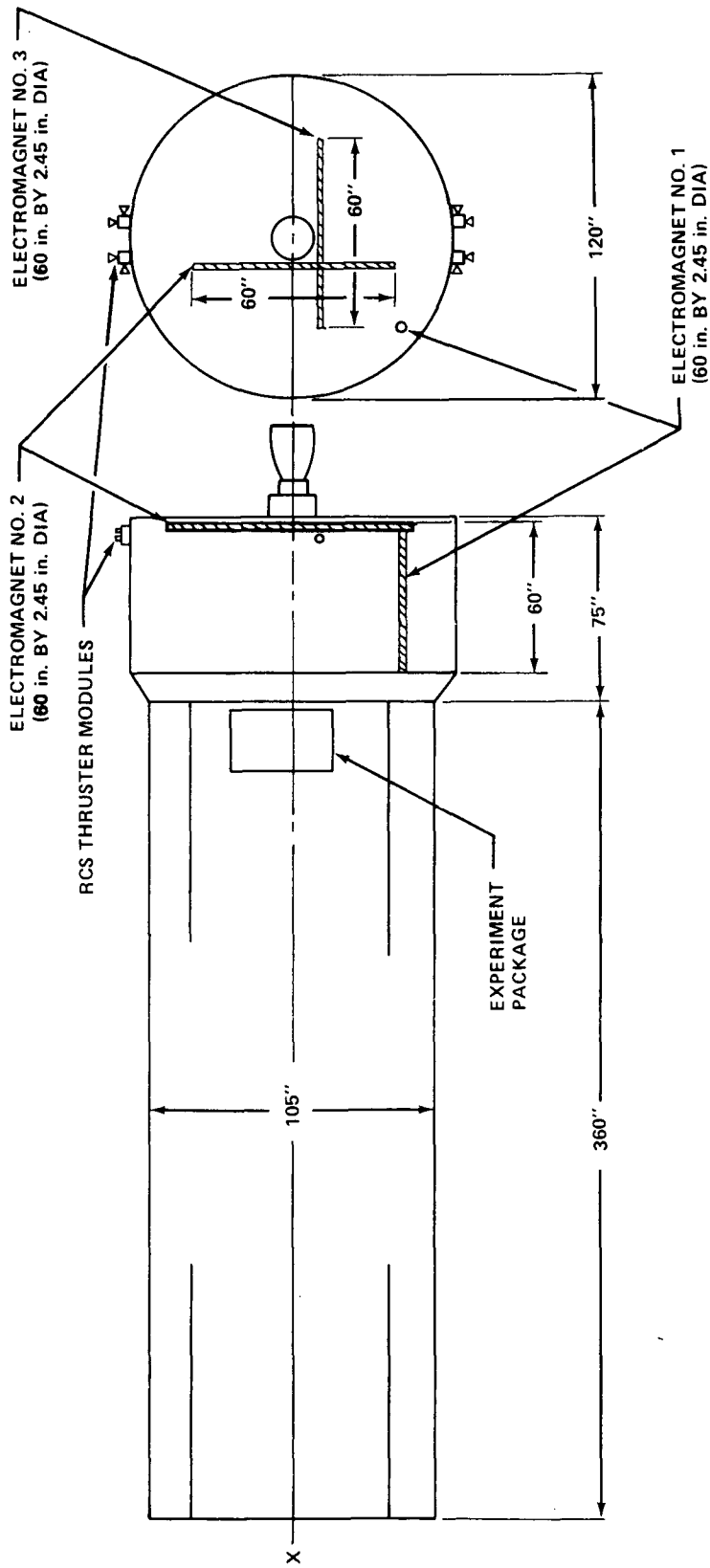


Figure E-40. Layout of the three electromagnets inside the OAS.

- All the three electromagnets are switched on and are generating the maximum magnetic moment of 5440 amp-turn-m².
- The total magnetic field at a point is the summation of the absolute magnetic fields due to individual electromagnets. In fact, the total magnetic field is the vectorial summation of the fields due to the individual electromagnets. The total field computed by this simplified approximation is only slightly higher than that obtained by the vectorial summation.
- The magnetic field due to each electromagnet has been considered equivalent to the field due to a magnetic dipole. This assumption is valid due to that large length-to-diameter ratio of the electromagnet.
- No field distortion by other spacecraft components.

The magnetic field at a point P, shown in Figure E-41, due to a dipole magnet is given by

$$|\bar{H}| = \frac{M}{2L} \left[\left(\frac{\cos \beta}{NP^2} - \frac{\cos \alpha}{SP^2} \right)^2 + \left(\frac{\sin \alpha}{SP^2} - \frac{\sin \beta}{NP^2} \right)^2 \right]^{\frac{1}{2}} \quad (295)$$

where $|\bar{H}|$ is the absolute value of field at P; M is the magnetic moment of the magnet; L is the half-length of the magnet; α, β are angles as shown in Figure E-41; and NP, SP are distances shown in Figure E-41.

The magnetic field profiles of Figures E-39 and E-42 have been computed using equation (295). An examination of Figure E-39 shows that for points lying on the y-y line and very close to the electromagnet Number 1, the field is very strong. However, the field drops very fast with distance from the electromagnet, and at a distance of about 50 inches from the end of electromagnet Number 1 and in the region between the electromagnets, the field strength is about 2 gauss. The field starts increasing again as one approaches the two electromagnets located at the end of the spacecraft. The field strength is only about 5 gauss at a distance of about 10 inches from the Number 2 and Number 3 electromagnets.

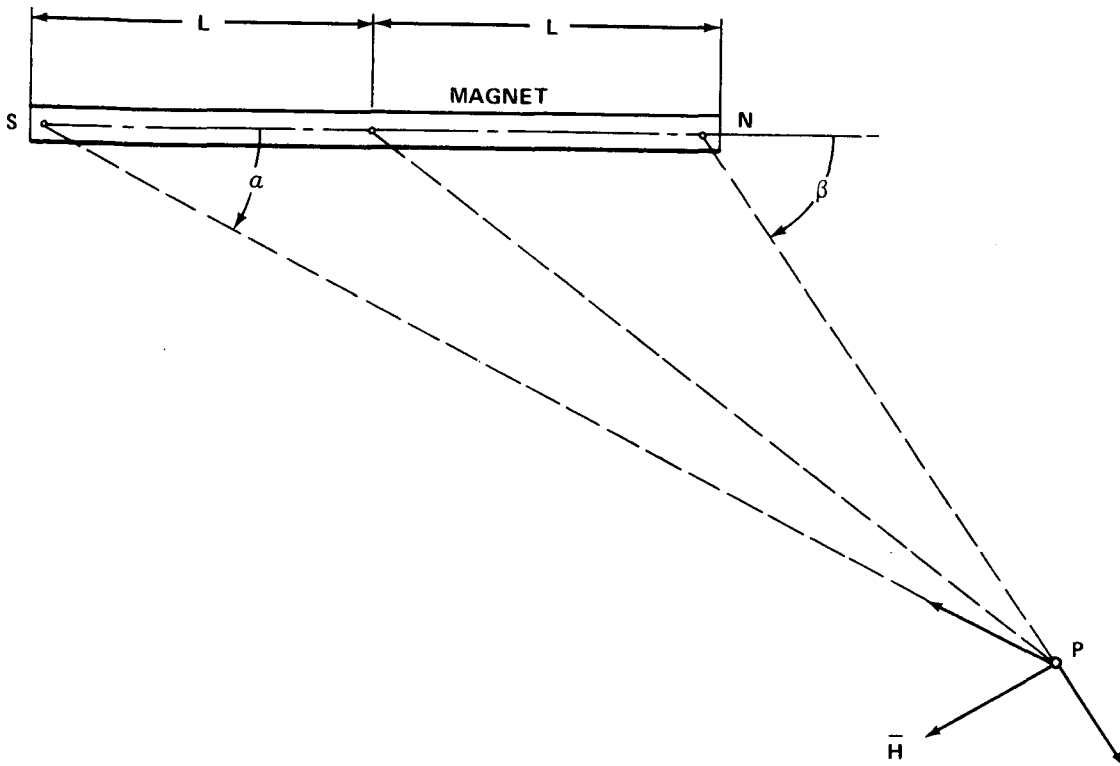


Figure E-41. Magnetic field at point P due to a dipole magnet.

For points lying on the x-x line, the field strength is below 2 gauss for over 300 inches of the spacecraft length, but it starts increasing as the Number 2 and Number 3 electromagnets are approached. The field strength for points lying in the region above the x-x line will be lower than that for the x-x line, except for the region very close to the Number 2 and Number 3 electromagnets.

From this analysis, it appears that the field in the spacecraft is small except in the vicinity of the electromagnets. It is also noted that the field on the longitudinal axis of the electromagnet and very near its end is much stronger (approximately 10 000 gauss) than the field on the axis normal to the longitudinal axis (approximately 40 gauss). Thus, magnetic-sensitive components should not be located close to the ends of the electromagnet.

An examination of the magnetic field profiles for Case II shown in Figure E-42 reveals that the magnetic field near the electromagnets is strong. However, the field drops very fast as distance from the electromagnets

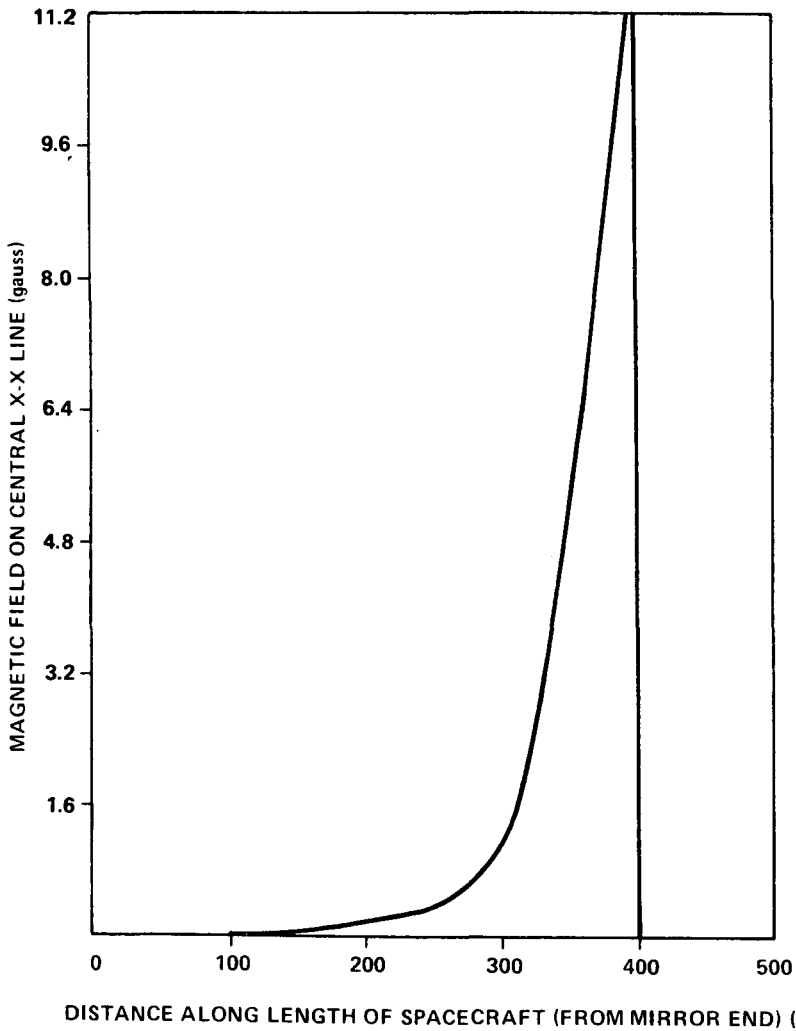
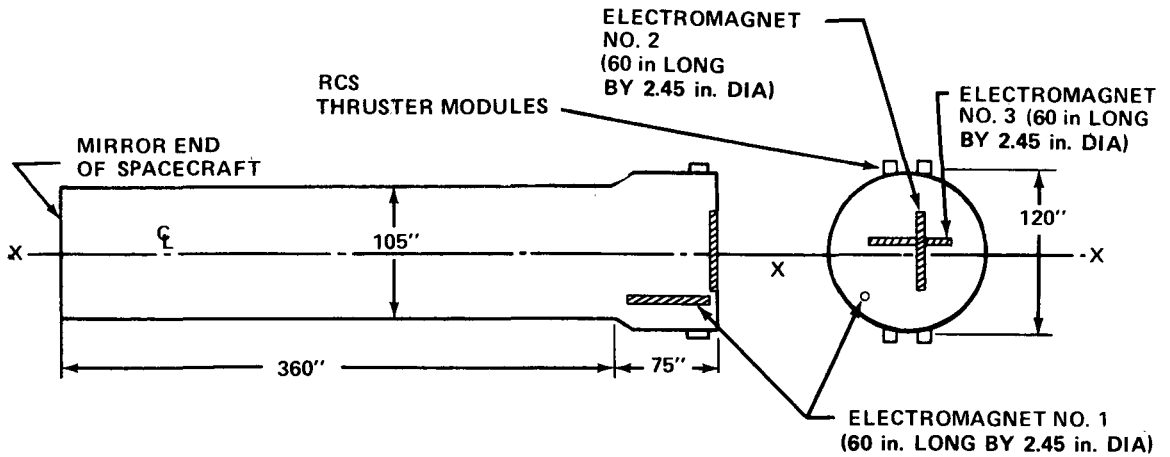


Figure E-42. Magnetic field distribution inside the spacecraft for Case II.

increases, and at a distance of about 120 inches from the center of the Number 2 and Number 3 electromagnets, the field strength is about 1 gauss.

The advantages of Case II over Case I are listed below:

- Most of the experiment and subsystem components are located far away from the electromagnets and, therefore, will operate in fields of very low intensity. This will require very little or no shielding for many components.
- The weight of the shielding required will be less than that for Case I.
- Because of the lower shielding weight required, the magnetic moment induced in the shields will also be smaller.
- If the tubes for telescopes are made of Invar, this location of the electromagnets will induce very little magnetic moment in the tubes. This will increase the performance of the electromagnets and reduce the problem of demagnetization of the Invar tubes after the electromagnets are switched off.

Because of these advantages it is recommended that the three electromagnets be located in the OAS. Case II field distribution (Figure E-42) is, therefore, used in analyzing the magnetic shielding requirements for the components.

7. Magnetic Shielding. Based on analysis and the magnetic field propagation graphs, the experiments can tolerate the magnetic field due to the electromagnets. However, if desired, some of the more sensitive experiment components can be shielded to reduce the field to even lower values near the components. Completely enclosed individual shielding of the components such as solid state detector, imaging proportional counter, etc., is not feasible because of the viewing requirements and movement of these experiments inside the telescopic tubes. Therefore, a part of the telescopic tubes which contains these experiments and where the magnetic field is higher is shielded. Therefore, boxes P and Q shown in Figure E-43 need to be shielded.

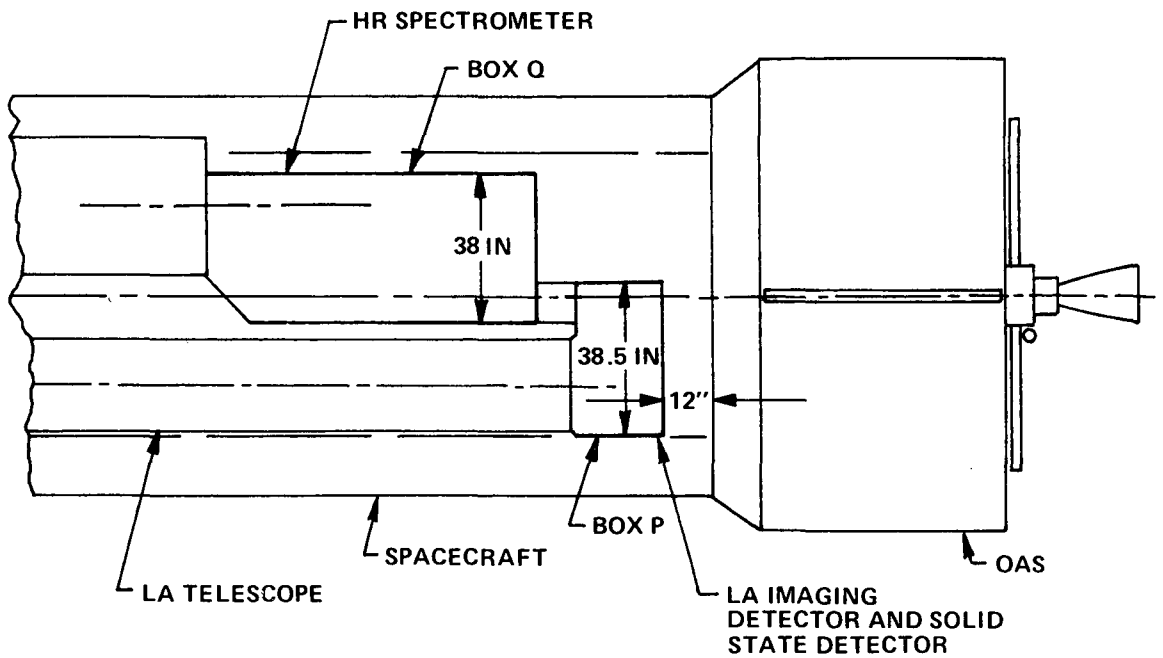
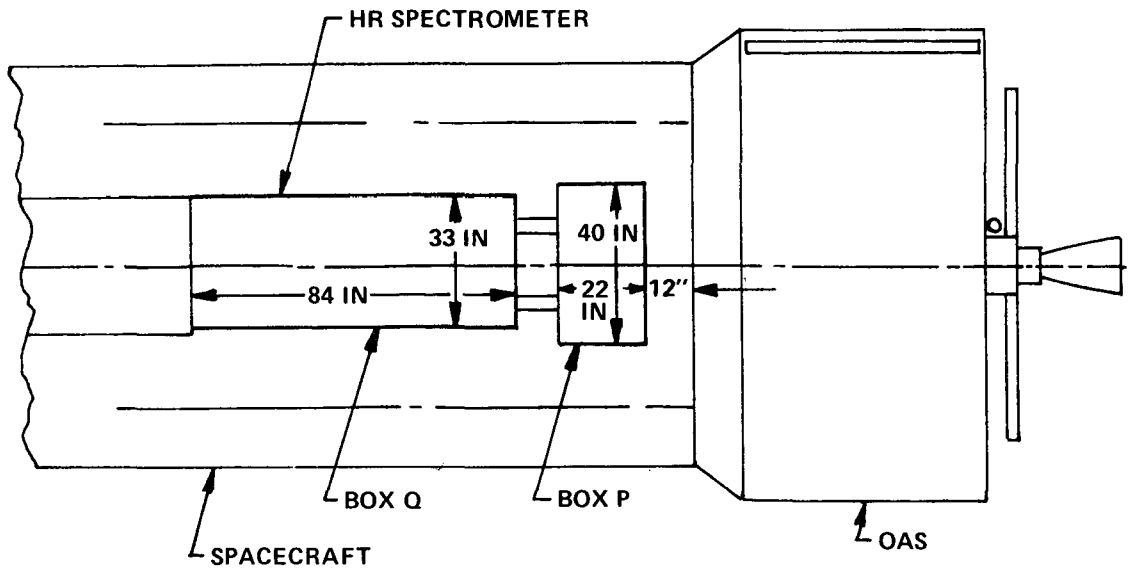


Figure E-43. Location of boxes P and Q in the spacecraft.

The dimensions of Box P when shielded are 56 inches by 28 inches by 42 inches, and the part of Box Q which is shielded is 36 inches by 50 inches

by 42 inches. The maximum field at the nearest end of Box P to the electromagnets is less than 4 gauss and, similarly, for Box Q is 2 gauss. The field at other locations in Boxes P and Q will be less than these respective values. These maximum values representing the worst fields are, therefore, used in sizing the magnetic shield.

Selecting shield mu-30 (80 percent Ni-Fe) shield material because of its high permeability (50 000 initial, 400 000 maximum) and reducing the field inside the shielded Boxes P and Q to 0.5 gauss results in a shield thickness requirements for Box P of 0.004 inch and for Box Q of 0.002 inch. The volume of the shield for Box P is 30 cubic inches and for Box Q is 14 cubic inches. The weight of the shield for Box P is about 10 lbm and for Box Q is about 5 lbm.

From Figure E-40 it is noted that RCS thruster modules are located close to the electromagnets. These RCS thruster modules contain solenoid valves which are susceptible to the magnetic field. The solenoid valves used are of stainless steel alloy and require 6000 to 8000 gauss magnetic field for normal operation. The manufacturer of these valves states that any magnetic field less than 1000 gauss will have no effect on the performance of these valves. The magnetic field produced by the three electromagnets at the location of each of the thruster modules will be less than 30 gauss. This magnetic field is low enough not to cause any interference with the normal functioning of the solenoid valves. However, these solenoid valves can be shielded to reduce the magnetic field to 1.0 gauss without any significant shielding weight penalty. Using shield mu-30 as the shielding material, the weight of the shield for 35 solenoid valves, each valve 3 inches by 2 inches, is about 1 lbm.

Table E-11 lists the amount of shielding required for various components and their desirable location in the spacecraft. The total weight of the magnetic shield required is 16 lbm.

8. Magnetic Field Effects on Components. In addition to generating a field while operating, the electromagnets may magnetize certain spacecraft components and shields. The effect of this is that these components and shields will acquire an induced magnetism which may help or oppose the electromagnet magnetic moment depending upon their location. When electromagnets are not operating, the residual magnetism in these components and shields will interact with the geomagnetic field, thereby producing a disturbance torque on the spacecraft.

An estimate of the induced magnetic moment in the shields has been made and the total induced magnetic moment is 2 amp-turn-m² under the

TABLE E-11. MAGNETIC FIELD TOLERANCES AND SHIELDING REQUIREMENTS FOR SPACECRAFT COMPONENTS

Component	Magnetic Field Strength Limit (gauss)	Desirable Location in the Spacecraft (From Mirror End of Spacecraft) (in.)	Actual Field Strength (gauss)		Shielding Weight Required (lbm)
			Without Shielding	With mu-30 Shielding	
Experiments					
Box P (Refer to Figure E-43)	10	Sta. 330 to 360	<4	0.5	10
Box Q (Refer to Figure E-43)	10	Sta. 240 to 330	<2	0.5	5
RCS					
Solenoid Valves (35 Valves)	(a)	Sta. 400 to 440	<30	1.0	1
System Components (Tape Recorder, Transmitters, Data Processors, etc.)	5	Sta. 0 to 280	<5		
Total Weight					16

a. Actual figure is not available but it is estimated that it should be less than 1000 gauss.

assumption that all the induced magnetic moments are unidirectional. This induced magnetic moment is less than 0.1 percent of the magnetic moment of the single electromagnet and, therefore, will not have any significant effect on the performance of the electromagnets.

The maximum disturbance torque produced by this induced magnetic moment in a maximum geomagnetic field of 0.40 gauss is about 0.6×10^{-4} ft-lbf. This torque is 0.1 percent of the average gravity torque, or about three orders of magnitude smaller, and, hence, is negligible.

Some additional problems will be introduced if the telescope tubes are made of Invar material, although the present concept for the baseline does not envision tubes made of Invar. The Invar material is a soft magnetic material having the following composition:

- Nickel — 34.50 to 36.00
- Carbon — 0.12 maximum
- Manganese — 0.50 maximum
- Silicon — 0.50 maximum
- Iron — Remainder .

If the tubes are annealed, they will be magnetized in the earth's magnetic field. Because of the large volume of the material involved, a significant magnetic moment will be generated by the tubes onboard the spacecraft. The consequence of this is that the generated magnetic moment will react with the earth's field to produce a disturbing torque on the spacecraft. This disturbing torque must be counteracted by the spacecraft attitude control system. If an RCS is used, additional propellant will be required. If electromagnets are used, a portion of their over-capacity will apply to this force.

If the Invar tubes are hard-drawn, they are not likely to be magnetized by the earth's magnetic field. However, if the electromagnets are placed sufficiently close to the tubes, the tubes will be magnetized by their magnetic fields.

If the three electromagnets are located in the OAS as shown in Figure E-40, the magnetic field at the end of the tubes nearest the electromagnets will be less than 4 gauss. Furthermore, the magnetic field is

nonuniform over the tubes and is very weak over most of the part of the tubes, as shown by the field distribution (Fig. E-42). Therefore, the induced magnetic moment in the tubes due to the three electromagnets will be low.

One of the advantages of using Invar tubes is that the experiment components located inside the tubes will not require shielding because the Invar tubes will act as shields.

When the electromagnet is switched off, there will be some residual magnetism left in the tubes, but it will be much less than the induced magnetic moment because Invar is a soft magnetic material and has low magnetic retentivity. The residual magnetic moment in the tubes can be reduced to a negligible amount if the electromagnet is energized in the opposite sense to produce a demagnetizing force (this is equal to the coercive force for the Invar material) for a short duration of time (1 to 2 seconds).

From the above analysis, it appears that the induced magnetic moment in the tubes due to all three electromagnets is small and can be minimized by proper mechanization of the electromagnets. Thus, it can be concluded that the degradation in the performance of the electromagnets in the presence of the Invar tubes is negligible for the special layout of the electromagnets shown in Figure E-42.

9. CMG Steering Law. With the magnetic system continuously dumping CMG momentum, several candidate CMG steering laws were simulated. In all cases, the stored CMG momentum remained near zero; consequently, the gimbal angles stay very small. Even under worst environmental torque conditions, the deviation of the angles from their null position was only about 3 degrees. As a result, all steering laws performed equally well and all produced excellent pointing and jitter performance. Since the gimbal angles stay very small, a constant gain steering law is adequate for HEAO with magnetic momentum dump. However, if rapid slewing is commanded, the gimbal angles become large during the maneuver. If HEAO is required to maneuver rapidly (for example, solar flare viewing in an antisolar direction), the maximum contribution steering law is recommended. Moreover, the maximum contribution steering law does not require any modification in the event of a CMG failure, providing fail operational capability. Assuming one CMG has failed, the magnetic system will automatically drive the remaining CMGs to a new null (zero momenta) position, without that failure being detected and without any changes being made in the software.



10. Magnetometer. A magnetometer will be required onboard the spacecraft for sensing the magnitude and direction of the geomagnetic field if a magnetic CMG desaturation system is utilized. A three-axis magnetometer will sense the geomagnetic field in the three Observatory body axes.

The magnetometers manufactured by Dalmo-Victor and used on the Orbital Astronomy Observatory (OAS) spacecraft can be used on the HEAO-C spacecraft. This fluxgate type magnetometer measures the geomagnetic field along each of the vehicle axes and converts this to a dc voltage. It weighs 6.5 lbm and requires a power of 1.76 watts. The performance characteristics are as follows:

- Range — $\pm 60\,000$ gamma (± 0.6 gauss).
- Sensitivity — 4.167×10^{-5} Vdc/gauss.
- Dimensions — 10.5 in. by 4.75 in. by 4.75 in.
- Frequency Response — 280 cycles.

The magnetometer should be located on the spacecraft where the geomagnetic field is practically undistorted due to the field of the electromagnets and induced magnetic moments. The farthest the magnetometer can be placed from the electromagnets is the mirror end of the spacecraft. At this end of the spacecraft, the magnetic field due to the three electromagnets is about 0.094 gauss. This field is about 30 percent of the average geomagnetic field of 0.32 gauss. The magnetometer will sense this field (due to electromagnets) in addition to the geomagnetic field and will, therefore, give erroneous signals. To accurately sense the geomagnetic field, the following three alternatives are possible:

- The first alternative is to calibrate the magnetometer to take into account the additional field due to the electromagnets. This will require some additional computations; also, the magnetometer may not be calibrated accurately due to the variation of the magnetic moment of the electromagnets.
- The second alternative is to mount the magnetometer on a boom. If the field due to the electromagnets at the locations of the boom-mounted magnetometer is desired to be less than 10 percent of the average

geomagnetic field (i. e. , 0.032 gauss), then the length of the boom required is about 16 feet. A boom-mounted magnetometer is not preferred because of the boom deployment problem and bending of the boom due to solar heating, etc.

- The third alternative is to sense the geomagnetic field using the magnetometer in discrete time intervals. The geomagnetic field changes very slowly as the spacecraft orbits (two cycles per orbit); therefore, it can be treated, essentially, as constant over small intervals of time (e. g. , the range of 1 minute). Thus, the geomagnetic field can be measured at an interval of 1 minute by switching off the electromagnets for short durations of time (about 5 to 10 seconds). While the electromagnets are off, the field due to the residual magnetism in the electromagnets and due to the induced magnetic moment in the shields will be very small (less than 10 percent of the maximum field) and, therefore, very little error will be introduced in the sensed geomagnetic field.

The third alternative is recommended for use because it does not require any boom and calibration of the magnetometer; also, the error introduced by using this scheme is negligible.

CMG Momentum Envelope Program

An analog computer program has been developed to determine the maximum momentum surface that a particular set of four single-degree-of-freedom skewed CMGs can generate. The CMGs are mounted so that their momentum vectors always lie in the planes of the faces of a pyramid, as shown in Figure E-44. As each CMG is gimballed, its momentum vector will rotate in the plane. No gimbal limits or gimbal rate limits are placed on the CMGs, and it is assumed that they have equal momentum. The angle of inclination of the faces of the pyramid (β) may be varied from 0 to 90 degrees.

There is always some total momentum vector \bar{H} which is the vector sum of the individual CMG momentum vectors. If the four CMGs were caused to rotate in a random fashion, the locus of the tip of the total momentum vector

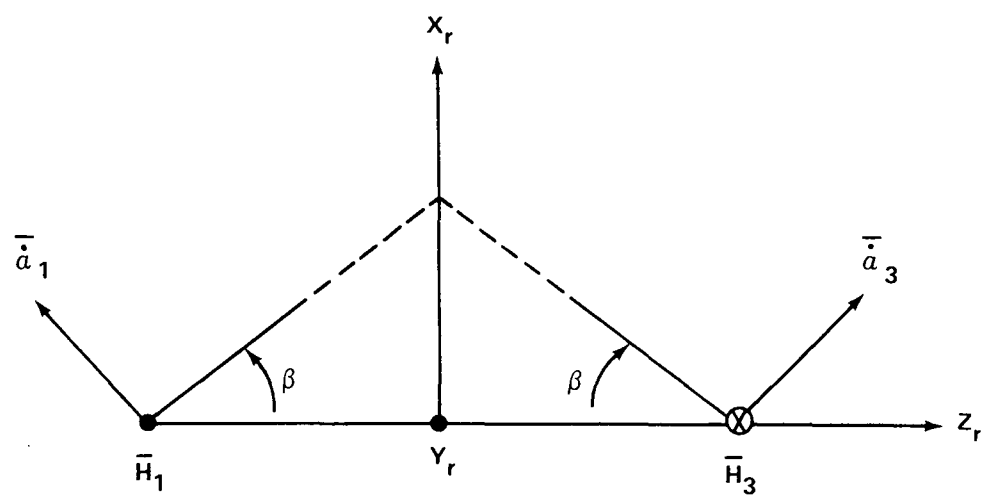
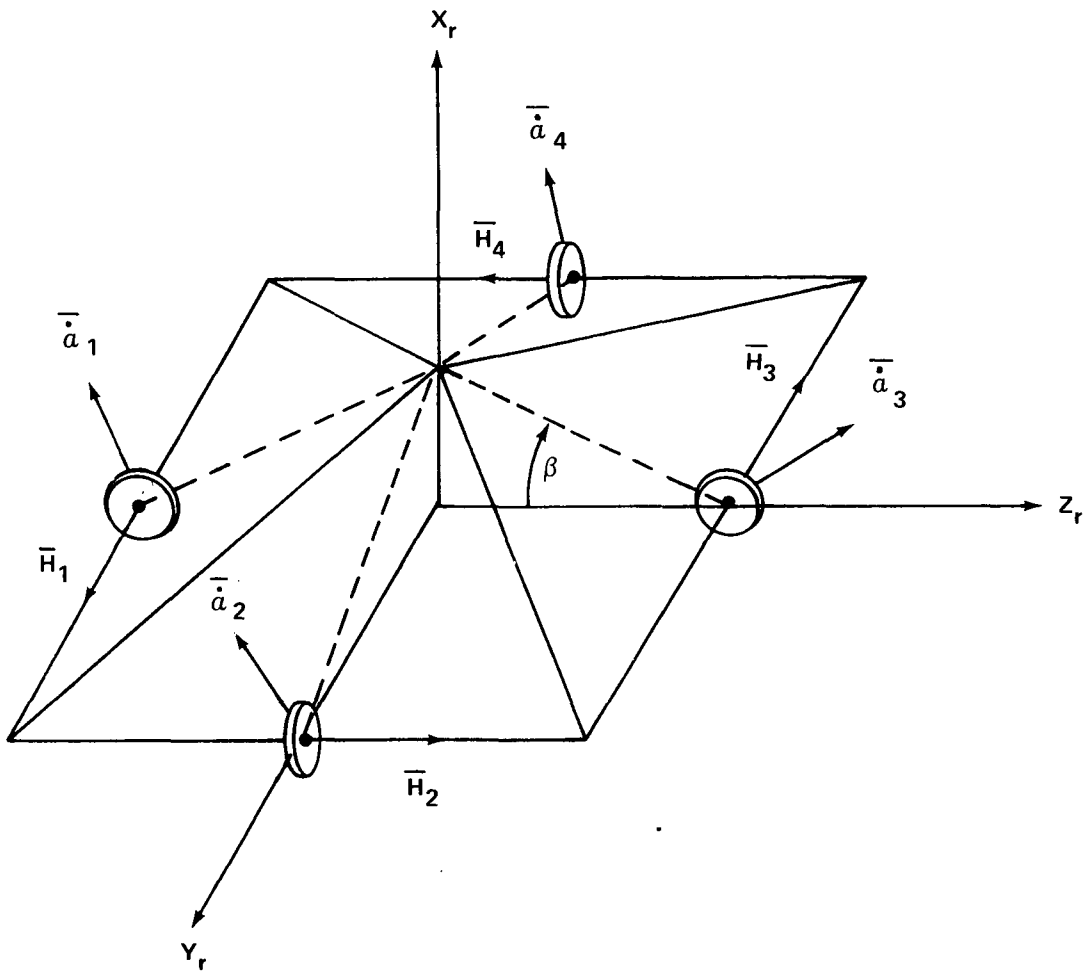


Figure E-44. CMG configuration.

would describe a solid. The boundary of this solid is the desired maximum momentum surface, or momentum envelope. This envelope is a function of the physical system and is independent of the control law used to command the CMGs. However, a control law is a necessary part of the scheme being used to generate plots of the momentum envelope. The maximum contribution control law is being used. The accuracy of the control law will determine how true a representation of the actual envelope is drawn.

The program commands a total momentum vector of greater magnitude than the system can produce. This commanded vector remains fixed in length and follows a prescribed pattern in direction. It begins pointing up the $+X_r$ -axis. It then increments through a fixed angle in the X_r - Y_r plane toward the Y_r -axis and then revolves about the X_r -axis. It continues incrementing and rotating until it reaches the $-X_r$ -axis. The control law causes the individual CMGs to rotate so as to make the total actual momentum vector follow the commanded total momentum vector. The rectangular components of the actual total momentum vector are plotted by an X-Y plotter to obtain various views of the locus of its tip. Ideally, the actual vector would follow the commanded exactly in direction, and would maintain the greatest length possible in every direction. Actually, due to sensitivity points and singularity points of the control law, there is some deviation in parallelism of the actual vector to the commanded in some regions, especially when the commanded vector becomes nearly parallel with one of the CMG gimbal axes. Thus, ideally, the lines on the figures should be interpreted as the intersection with the true momentum envelope of a series of widening cones about both the $+X_r$ - and $-X_r$ -axes, degenerating to a plane when they meet in the Y_r - Z_r plane. Actually, however, the lines deviate slightly from their ideal paths in certain regions.

One or more CMGs may be failed by setting its momentum to zero. No modification to the control law is required when CMGs are failed.

Figures E-45 through E-48 show profiles of the momentum envelopes for $\beta = 30$ degrees and $\beta = 53.1$ degrees with all CMGs operational and with one CMG failed. The figures are scaled in terms of normalized momentum where one major graph division represents one H, the momentum of one CMG. Much distortion of the surface is observed when a CMG is failed. The white areas should be interpreted as depressions in the surface, not as holes extending

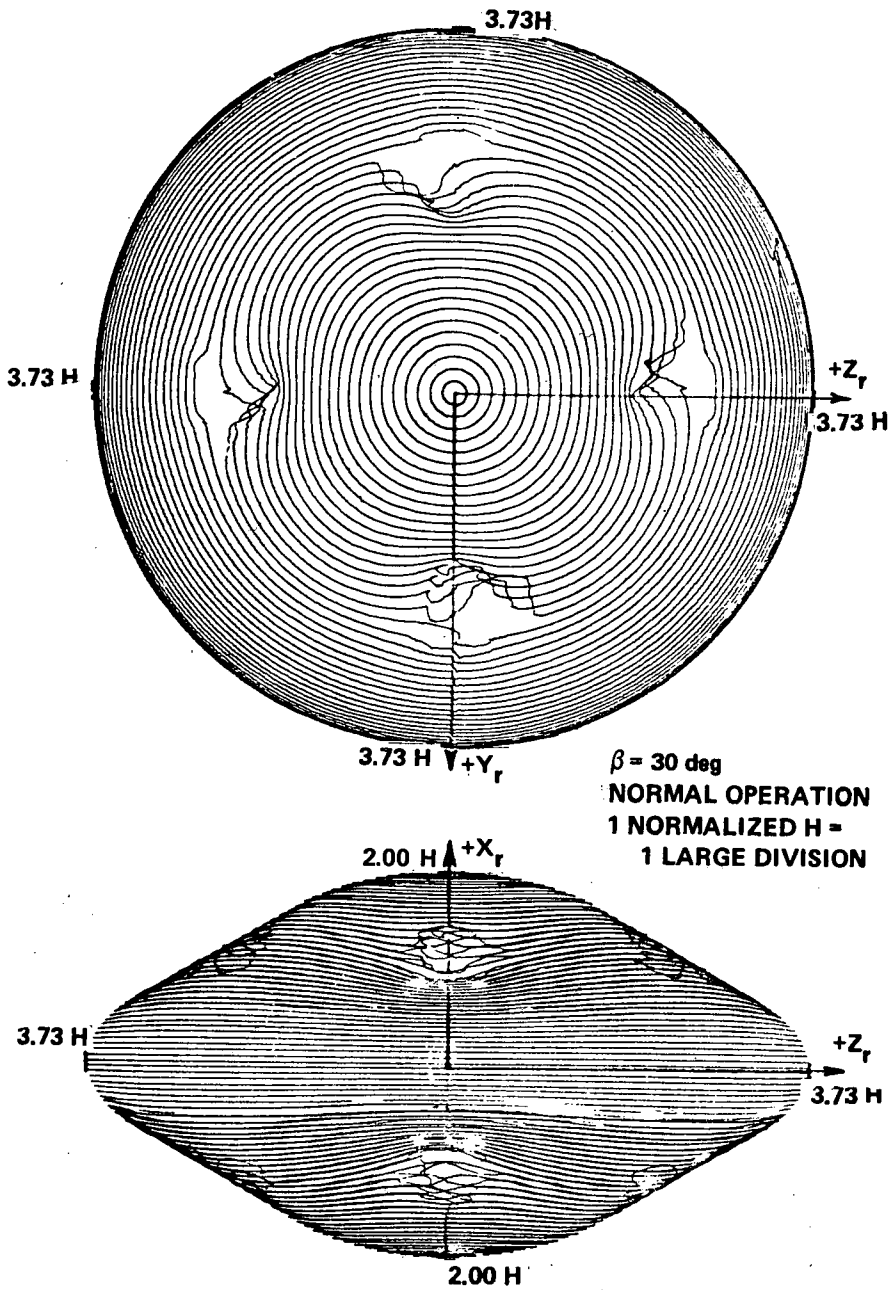


Figure E-45. Four-skewed CMGs maximum momentum envelope.

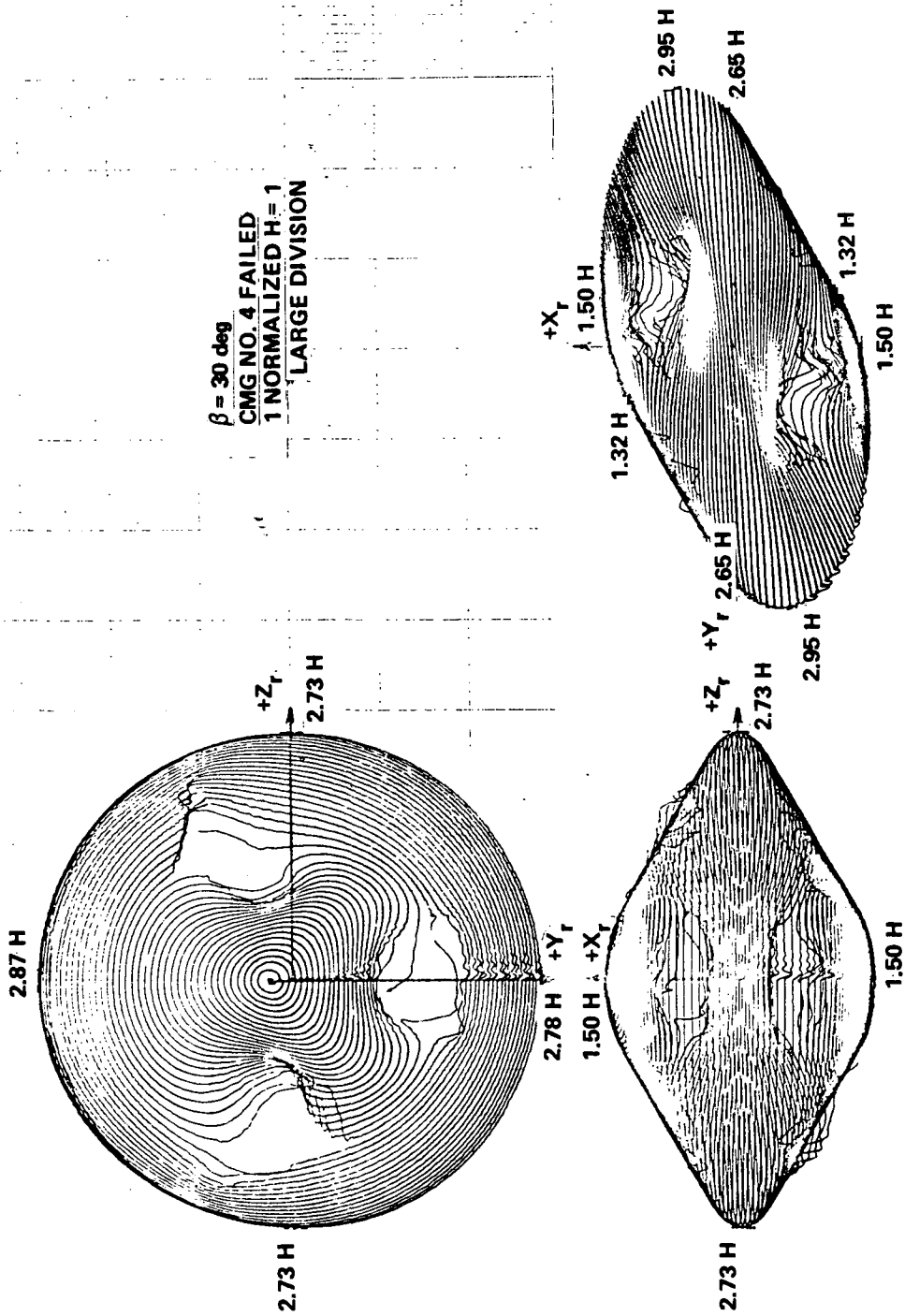


Figure E-46. Four-skewed CMGs maximum momentum envelope.

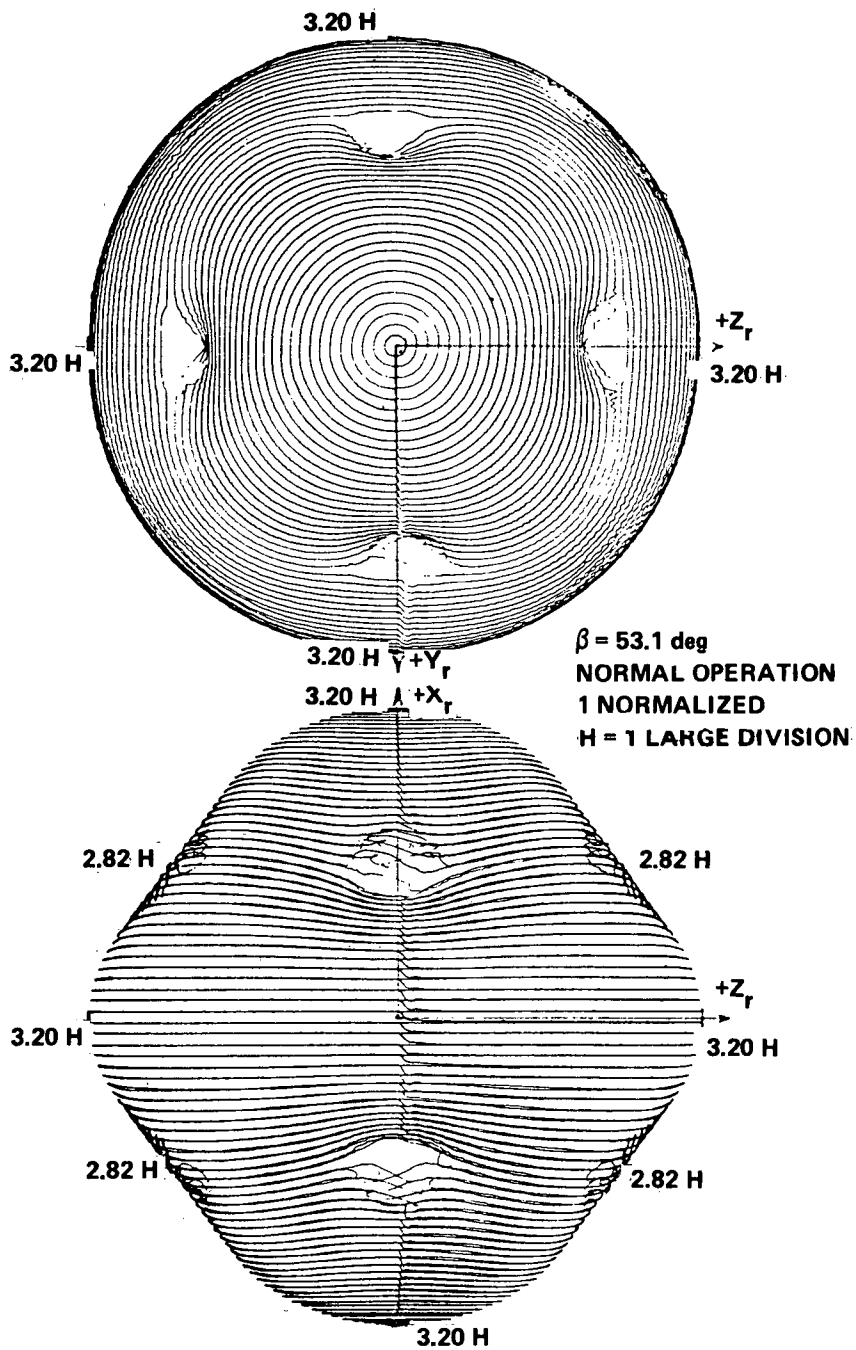


Figure E-47. Four-skewed CMGs maximum momentum envelope.

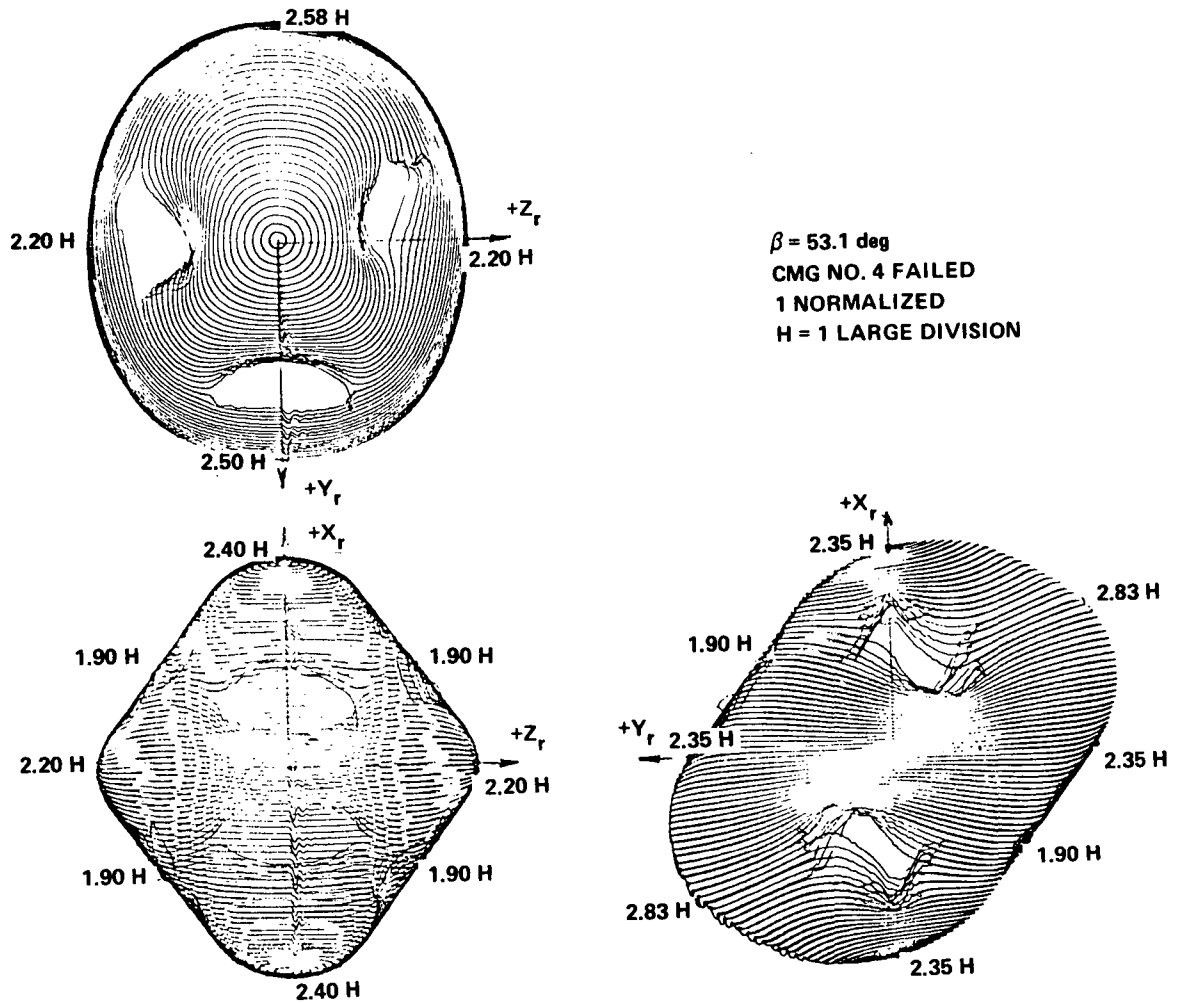


Figure E-48. Four-skewed CMGs maximum momentum envelope.

through the solid. The absence of contours in the regions is mainly due to deviation of the actual vector from the commanded because of control law sensitivity points. Depressions do exist there, and have been verified by digital computer simulations.

The numbers given on the figures were measured from the figure. Numerical values should be obtained from digital simulation. The analog results, however, are of much use in determining what areas to search out digitally to find the minimum points of the momentum envelope and are useful for visualizing the envelope for different configurations, especially under

failure conditions. The details of the simulation are given in another document.⁵

A digital version of this momentum envelope generating program has been developed. It is not presently being used because the lack of plotting facilities on available computers would necessitate plotting the momentum profiles by hand.

Pointing Capability Study of the HEAO-C Attitude Controller

In this study, the Bendix minimum modified MA-500 CMG and the baseline star tracker characteristics were used in an analog computer program to assess the pointing stability of the HEAO-C in the presence of a cyclical disturbance torque due to gravity gradient effects. The disturbance torque was estimated to be 0.07 ft-lb peak at a frequency of approximately 0.0022 rad/sec.

The general approach was to design a controller on a linear analysis basis to meet pointing accuracy specifications of less than 1 arc second in the presence of the expected torque disturbance and then to evaluate the effects of the primary system nonlinearities.

The specifications used for the study are listed below:

CMG gimbal torque motor	10 ft-lb max
Torque motor deadspace	0.22 ft-lb running 0.15 ft-lb static
Gimbal friction	0.13 ft-lb
Gimbal inertia	0.36 slug-ft ²
Gimbal inertia (effective)	3.18 slug-ft ²
CMG angular momentum	500 ft-lb-sec max
Vehicle inertia	82 650 slug-ft ²

5. Weiler, W. J.: Control Moment Gyro Momentum Profile Display. To be published as a NASA Technical Memorandum by Program Development, George C. Marshall Space Flight Center.

Star tracker saturation	±28 arc sec
Star tracker deadspace	0.2 to 10 arc sec

Figure E-49 is a simplified block diagram that was used to determine the gain constants necessary to make a unity transfer function between the gimbal rate, α , and the commanded gimbal rate, α_c . The gimbal loop has the following closed loop transfer function:

$$\frac{\dot{\alpha}}{\dot{\alpha}_c} = \frac{31.5 K}{s^2 + 100s + 31.5K} \quad (296)$$

For a damping constant of 0.7 and $\omega = 71.4$, K is 162 and the transfer function becomes

$$\frac{\dot{\alpha}}{\dot{\alpha}_c} = \frac{5100}{s^2 + 100s + 5100} \quad (297)$$

Normalizing to a unity gain form gives

$$\frac{\dot{\alpha}}{\dot{\alpha}_c} = \frac{1}{1.96 \times 10^{-4} s^2 + 1.96 \times 10^{-2} s + 1} \quad (298)$$

Figure E-50 is a block diagram of the simplified single axis analog simulation using the specified nonlinear star tracker and CMG values. The star tracker deadspace could be varied from 0.2 to 10 arc seconds and the output was saturation limited at 28 arc seconds. As previously stated, the CMG gimbal loop gains were selected to provide a unity transfer function between the commanded gimbal rate and the actual CMG gimbal rate.

The compensator network was selected to provide additional gain at the low frequency input torque disturbance (0.0022 rad/sec) to obtain a vehicle angular error of less than one arc second. The pole-zero combination shapes

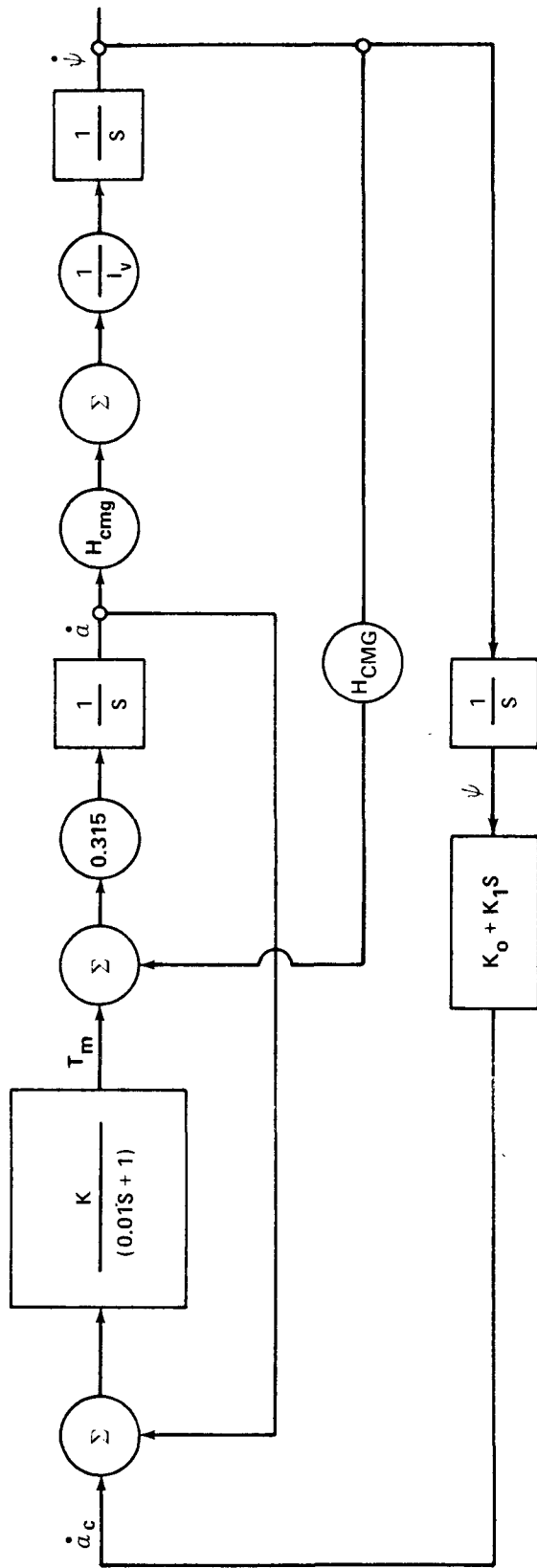


Figure E-49. Linear analysis diagram.

the frequency response to provide approximately a 12 dB gain margin. No attempt was made to optimize this compensator because it is recognized that, after better vehicle definition, terms to account for structural bending characteristics must be included to obtain a complete simulation. However, the network confirmed the concept and provided a stable system meeting the error requirement.

Figure E-51 is a recording of a run made with the star tracker deadspace set at zero and with the 0.07 ft-lb peak sinusoidally varying disturbance torque. Under this steady state condition, the vehicle angular error remains less than 0.1 arc second as predicted except for the approximate 2 arc second peaks that occur periodically. By observing the CMG gimbal angle, it can be seen that these angle disturbances occur at the time of the disturbing torque at which the gimbal torque motor must reverse torquing direction. The torque motor deadspace prevents control momentarily until the positive reverse torque occurs and the 2 arc second peak error occurs, lasting for approximately 10 seconds. Since these peaks occur four times per orbit, the total time per orbit when the pointing error exceeds the low steady state value would be about 40 seconds.

The vehicle rate has a peak value of about 0.4 arc sec/sec, which is well below the 1 arc sec/sec specification of the HEAO-C.

Limit cycles occur with this system when the disturbance torque is removed. The limit cycle has a peak value of about 2 arc seconds. Applying the disturbance torque during limit cycling stops this oscillation and returns the system to the low steady state angle condition.

Figure E-52 is a recording of a run made with a one arc second star tracker deadspace. The vehicle tends toward instability with the vehicle rate peaking at about 1 arc sec/sec periodically when the disturbance torque passes through zero. The error angle peaks more often and requires longer times to completely damp.

The baseline CMG with its specified nonlinearities can control the vehicle to a pointing stability of 5 arc seconds or better peak-to-peak in the presence of the gravity gradient effects.

The star tracker deadspace has a significant effect on stability when the tracker is used directly in the control loop. Using the star tracker to update the strapdown error calculations, as in the HEAO-C baseline concept, should eliminate the stability problem.

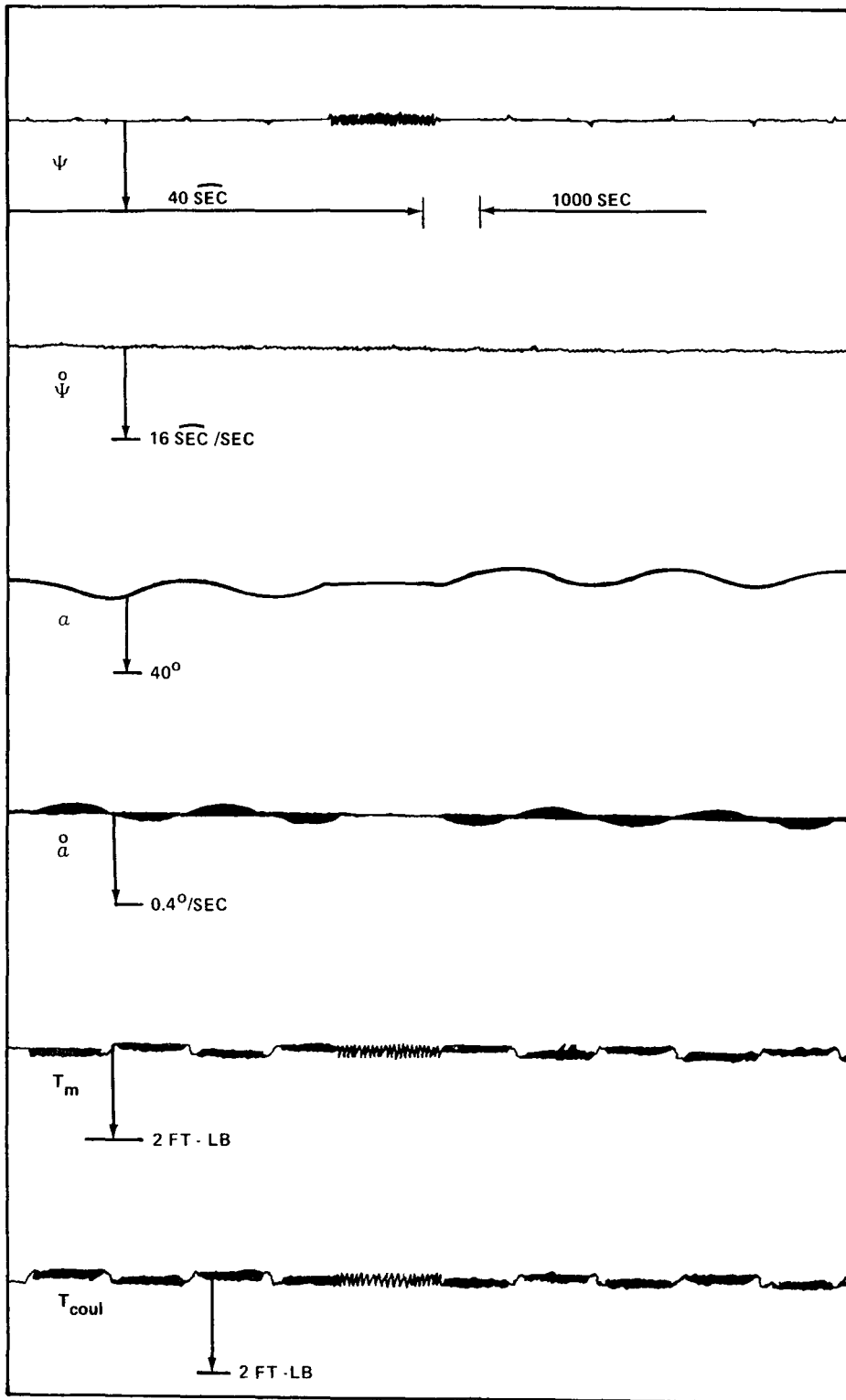


Figure E-51. Star tracker deadspace = 0 arc sec.

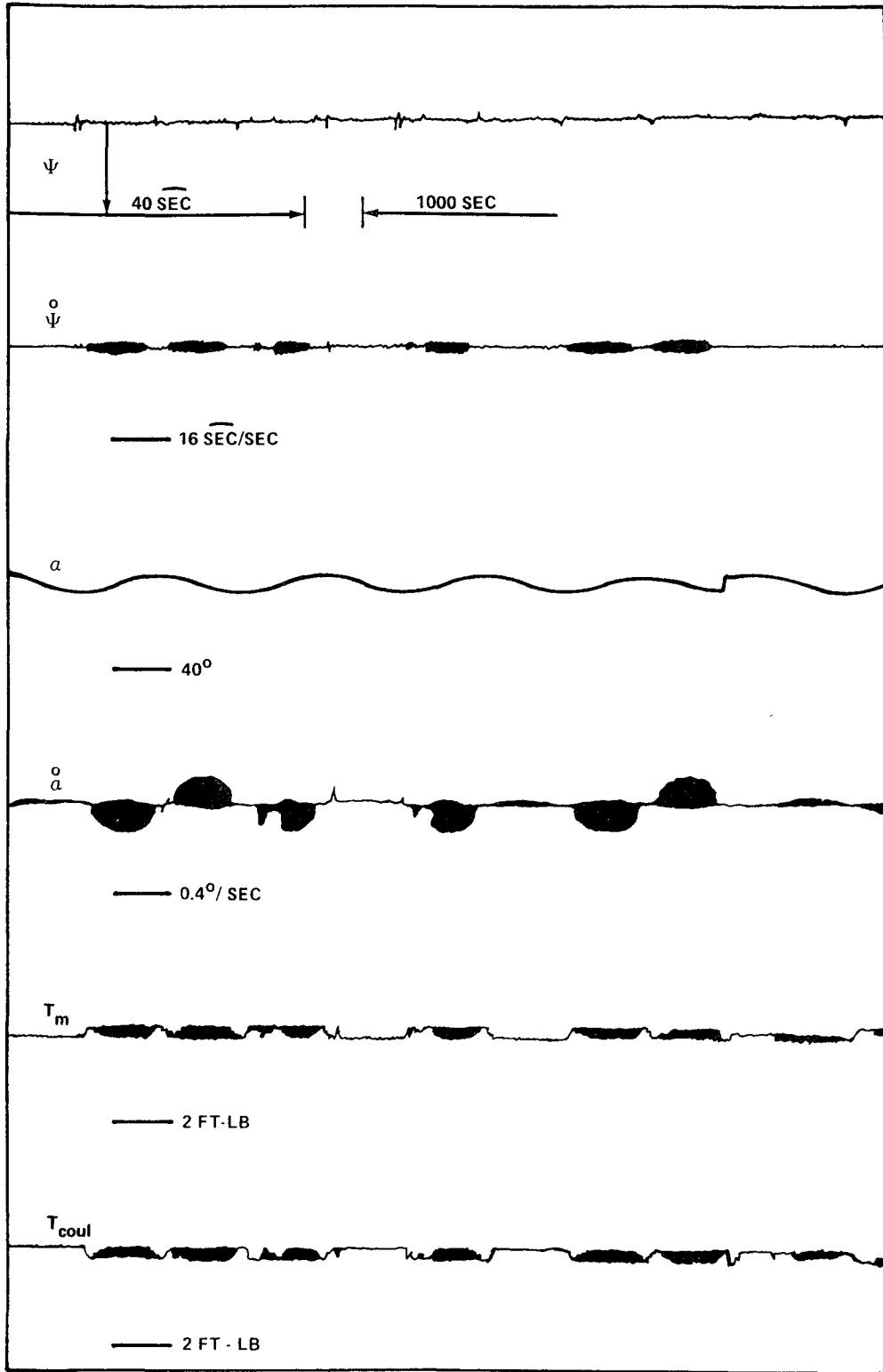


Figure E-52. Star tracker deadspace = 1 arc sec.

Optimization of the compensator and loop gain parameters should result in a more stable system; however, peak angular excursions of the type demonstrated will occur.

Attitude Sensing and Control System Performance Simulations

1. Reaction Control System Simulation. System performance studies of the baseline and alternate RCS were conducted using the thruster attitude control simulation (TACS)⁶ as the primary tool and using hand calculations secondarily.

The TACS is a digital computer program which includes space vehicle dynamics with gravity gradient, RCS engine thrust, and aerodynamic torques as vehicle disturbances. Provision is also included for RCS engine control logic changes and for changes in the RCS engine layout. Alternate system studies are relatively easy to implement in TACS.

Two coordinate systems are required in TACS. One is a quasi-inertial system with the origin at the center of the earth and the Z-axis aligned on the solar vector. The other coordinate system is a vehicle body system with its origin at the center of mass of the vehicle. It was chosen so that a reduced set of gravity gradient equations could be used.

The TACS roughly consists of four parts:

- General Equations.
- Rotational Dynamics.
- Vehicle Dynamics.
- Translational Dynamics.

A flow diagram of TACS is shown in Figure E-53.

a. General Equations. The general equations calculate parameters that are used in several or all portions of TACS. Acceleration due to gravity,

6. Brandon, Larry: A Description of the Thruster Attitude Control Simulation and Its Application to the HEAO-C Study. To be published as a NASA Technical Memorandum by Program Development, George C. Marshall Space Flight Center.

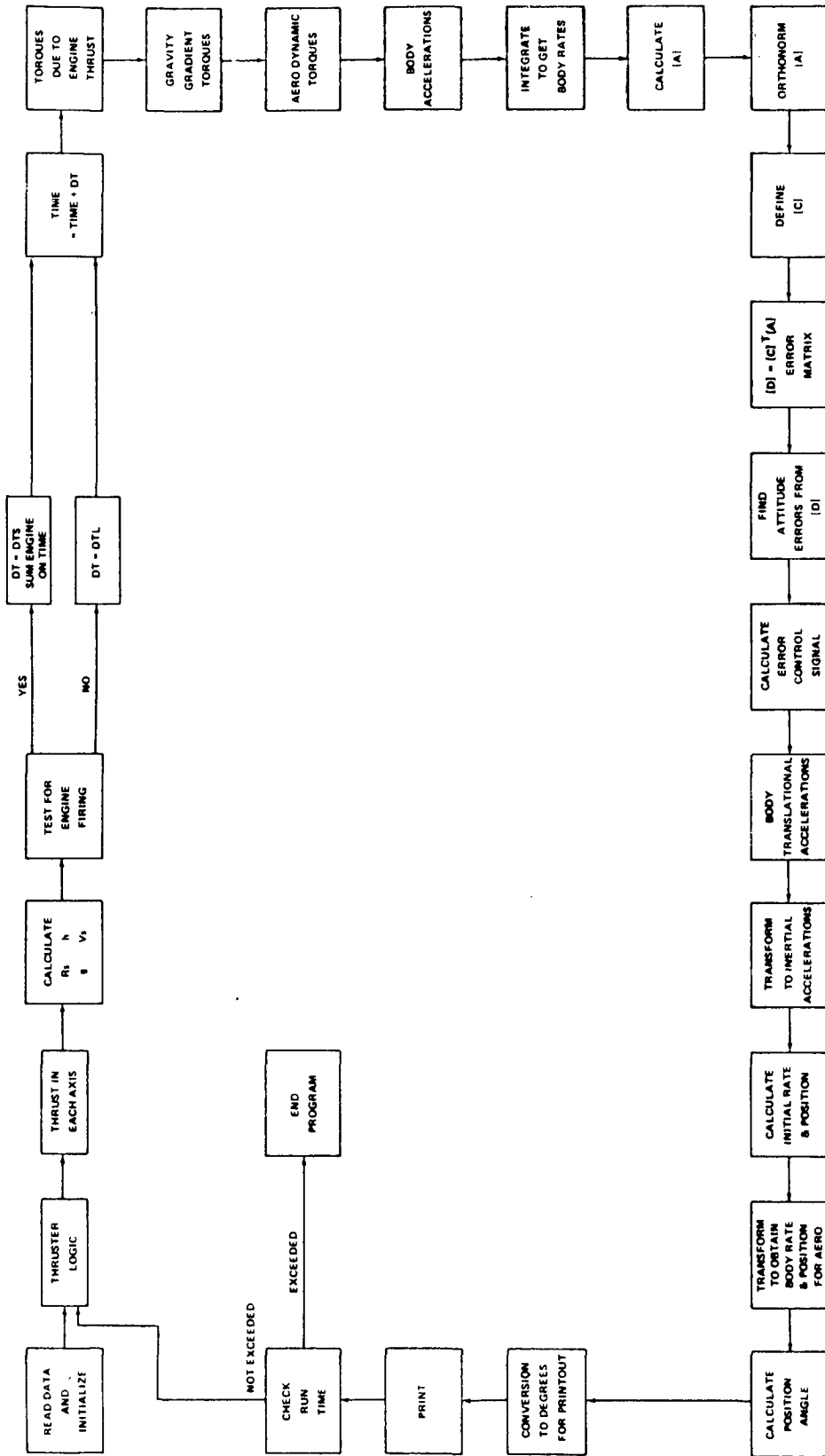


Figure E-53. TACS flow diagram.

orbital height and velocity, and vehicle position angle are the primary calculations but some initial condition calculations are also performed.

b. Rotational Dynamics. Gravity gradient and aerodynamic torques are the only forces in TACS that tend to drive the vehicle unstable. As mentioned previously the gravity gradient equations used are valid only if the body coordinate system's origin is at the center of mass.

The aerodynamic equations used in TACS are valid only for the HEAO and were taken from Reference E-15. The equations calculate aerodynamic coefficients as functions of the angle of attack and of the roll angle.

Equations for torques due to engines firing are simply lever arms times thrust.

Body angular accelerations include the effects of cross coupling caused by precession of a spinning body. The direction cosine method of determining the transformation matrix was chosen over the Euler method since the direction cosine method allows a greater degree of freedom; i. e. , rotation is not limited to 90 degrees in any axis. The matrix elements of A are obtained by integrating the rate of change of each element. These rates are calculated from previous element values and body angular rates. Trigonometric functions are avoided and a simple orthonormalization procedure is used.

c. Vehicle Dynamics. Vehicle attitude is controlled through a second direction cosine matrix C, which defines the desired attitude of the HEAO. If vehicle rotation (as in the scan mode) is desired, the matrix unit must define that rotation through trigonometric functions.

The product of the transpose of C times A is the error matrix D. By choosing the proper terms and combining them, attitude errors can be derived. The errors in these angles approach zero as the angles approach zero. The attitude errors are combined with the body angular rates using appropriate gain factors to give torque command signals.

Thruster logic is described in another part of the appendix.

d. Translational Dynamics. The orbit of the TACS vehicle is affected only by gravity and thruster firings since aerodynamic drag is ignored; for the short time of the computer runs, normally less than three orbits, this is felt to be quite acceptable. Body accelerations due to thruster firings are calculated and combined with gravitational acceleration and transformed to a

quasi-inertial space to give inertial accelerations. These are integrated twice to obtain inertial rates and position. These are then transformed back to body coordinates for use in the gravity gradient and aerodynamic equations.

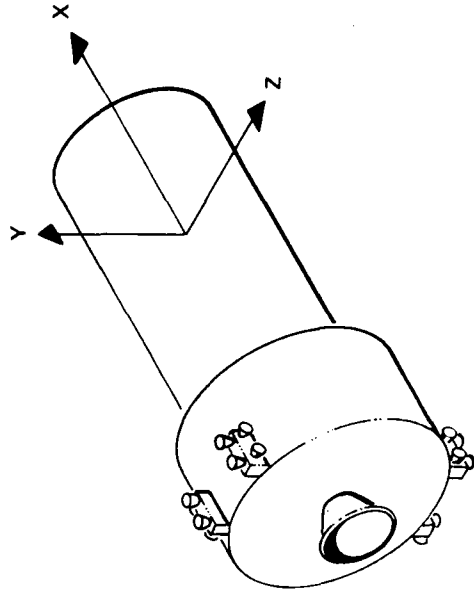
e. Simulation Results. A minimum time of 25 milliseconds was assumed for all engines for all cases except the dump mode to make comparative analysis easier. Possibly, a minimum time of 50 milliseconds would have been more realistic. To make a preliminary comparison between the baseline and alternate RCS systems, the minimum angular rates due to thruster firings were hand-calculated (Fig. E-54). Pitch and yaw rates are only slightly different in the two systems but roll is decidedly better in the baseline system. The small roll accelerations from the pitch engines allow a much finer roll control and, at the same time, the yaw engines can provide coarse roll control as needed. The baseline HEAO RCS configuration is shown in Figure E-55.

f. Baseline System. Based on the latest timeline available, simulations were run on each event possible (Table E-12). A specific impulse of 140 seconds was used in all fuel weight calculations. The first event considered was the separation of the HEAO from the launch vehicle. Separation can cause up to 3 deg/sec rate in all three axes. To remove these rates and maintain the attitude requires about 1000 pound-seconds impulse or 7.5 pounds of fuel. If attitude hold at this time is not required, a significant part of the fuel expended can be saved. It is felt that attitude hold should not be required at this time.

After acquiring rate stabilization, a maneuver of up to 90 degrees in the X and Y axes will be required for solar acquisition. Assuming a 2 deg/sec maneuver rate, a hand calculation showed an impulse requirement of about 270 pound-seconds, equivalent to 1.91 pounds of fuel, for solar acquisition. Approximately 30 engine actuations are required for the preceding events.

Vehicle control in the 140 by 250 nautical mile orbit will impose a severe demand on fuel consumption if the HEAO is parked for 30 days. The nominal stay of 4.5 orbits requires only 154 pound-seconds impulse, or a little more than one pound of fuel. A 30 day stay will require over 16 000 pound-seconds impulse, or 115 pounds of fuel. These figures reflect performance with a ± 0.5 degree deadzone. It is felt that for the parking orbit a much larger deadzone should be used, resulting in a large fuel savings. The only requirement is that the solar panels be maintained on the sunline well enough to keep the batteries charged. At this time of the mission, there are no severe demands on the batteries so loose control is possible.

HEAO-C WITH OAS	MIN. ON TIME = 0.025 sec THRUST = 5 lbf	ANGULAR ACCELERATION PER ENGINE arc sec/sec ²			ANGULAR RATE PER ENGINE ARC sec/ sec			MOMENT OF INERTIA (slug-ft ²)
		$\ddot{\phi}_x$	$\ddot{\phi}_y$	$\ddot{\phi}_z$	$\dot{\phi}_x$	$\dot{\phi}_y$	$\dot{\phi}_z$	
BASELINE	1764 OR 442.8	319.68	317.16	44.1	7.99	7.92	I _x = 2878 I _y = 69512 I _z = 70049	
				OR 11.07				
ALTERNATE	1785	319.68	317.16	44.6	7.99	7.92		



MOMENT ARM

BASELINE

L_x = 4.92 FT OR 1.23 FT

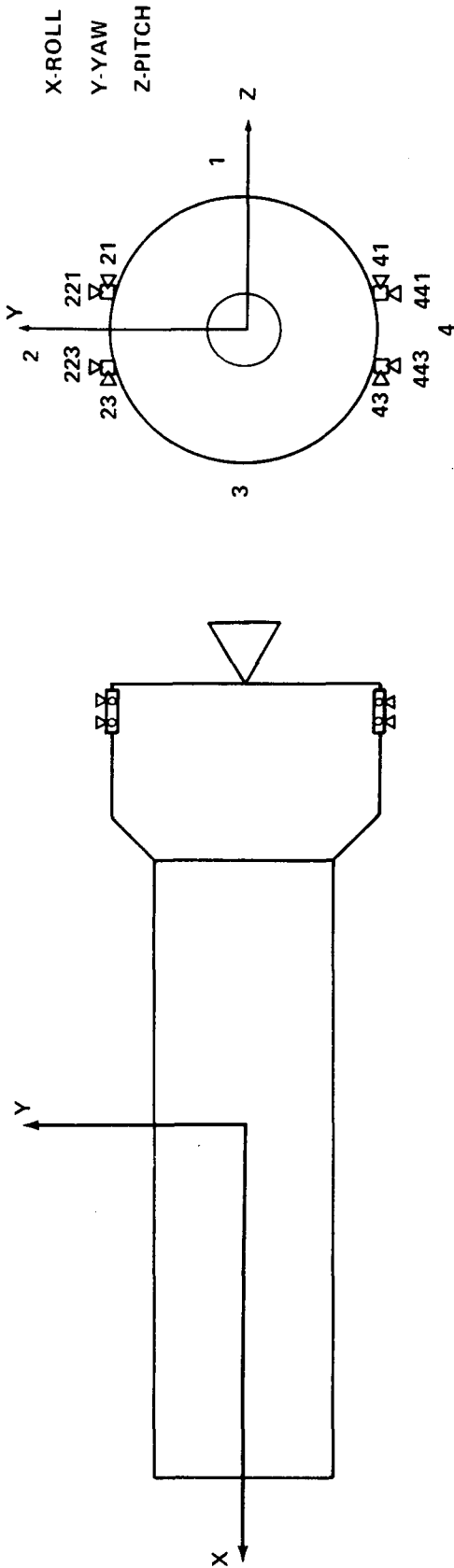
L_{y,z} = 21.5 FT

ALTERNATE

L_x = 5 FT

L_{y,z} = 21.5 FT

Figure E-54. HEAO-C thruster characteristics.



ERROR SIGNAL	21	221	223	23	41	43	441	443	43
+ PITCH							X	X	
- PITCH		X	X						
+ YAW	X				X				
- YAW				X					X
+ ROLL	X		X				X		X
- ROLL		X		X	X			X	

Figure E-55. Baseline HEAO engine layout and logic.

**TABLE E-12. HEAO-C FUEL AND IMPULSE
BUDGET FOR THE BASELINE RCS CONFIGURATION**

Event	Total Impulse (lb-sec)	Fuel Required at $I_{sp} = 140$ sec (lbm)	Worst Case Engine Cycling For an Engine	Comments
Null 3 deg/sec 3 axes	1 043. 8	7. 45	30	Includes Attitude Control
Solar Acquisition (90 deg about X and Y)	268. 0	1. 91	4	2 deg/sec max maneuver rate
Attitude Control in 140 by 250 n. mi. Orbit	153. 6 16 082. 0	1. 09 at 4. 5 Orbits 114. 8 at 30 Days	319 or 31 500	0. 244 lbm/orbit
OAS Thrust Vector Misalignment During Burn to 205 by 250 n. mi.	1 079. 5	7. 71	150	7. 5 min burn
Attitude Control in 205 by 250 n. mi. Orbit	33. 49	0. 239	70	0. 239 lbm/orbit for 1 orbit
OAS Thrust Vector Misalignment During Burn to 250 by 270 n.mi.	804. 1	5. 74	112	5. 58 min burn
Attitude Control in 250 by 270 n. mi.	51. 0	0. 364	106	0. 242 lbm/orbit for 1. 5 orbits
OAS Thrust Vector Misalignment During Burn to 270 n. mi. Circular	673. 2	4. 80	94	4. 68 min burn
Attitude Control in 270 n. mi. Orbit Until CMGs are up to Speed End of Checkout and Acquisition of X-Ray Reference	253. 3	1. 81	451	0. 245 lbm/orbit for 7. 4 orbits
CMG Momentum Dumping at 270 n. mi.	107 767	769. 7	211 090	Only 52 750 actuators per engine are expected
Totals	112 126. 99 or 128 055. 39	795. 647 or 909. 357	212 426 or 243 607	

A second prime driver in this orbit is the engine cycling consideration. If the worst case attitude is considered (X-axis 45 degrees with respect to the orbital plane), a single engine could be actuated up to 70 times per orbit. For the nominal stay, the total will be insignificant but, for a 30 day hold, the engine will be actuated over 30 000 times. Again, a looser attitude control will remedy the situation. These are worst case figures and should not be considered typical.

Aerodynamic effects show up to a small degree in the 140 by 250 nautical mile orbit, but not to any significant amount. Large aerodynamic torques may occur in more nearly circular orbits below 140 nautical miles. If such orbits are baselined, aerodynamic effects should be studied in detail.

During the OAS burn from the 140 by 250 nautical mile orbit to the 205 by 250 nautical mile orbit, the OAS thrust vector misalignment is assumed to have the worst case value of 0.5 degree. The RCS must supply a corrective impulse of 1080 pound-seconds to maintain vehicle attitude. This is about 7.71 pounds of fuel.

The nominal stay of one orbit in the 205 by 250 nautical mile orbit requires about 34 pound-seconds impulse or 0.239 pound of fuel. For one orbit, engine cycling is negligible. No contingencies were studied in this orbit.

The OAS engine is ignited again for insertion into the 250 by 270 nautical mile orbit. At worst case, this burn requires an RCS impulse of about 800 pound-seconds or 5.74 pounds of fuel. The HEAO will remain in the new orbit for 1.5 orbits, requiring an impulse of 50 pound-seconds or 0.36 pound of fuel. Engine cycling is not a problem as the worst case is slightly over 100 actuations.

The final OAS burn to the 270 nautical mile circular orbit will require almost 675 pound-seconds impulse or 4.8 pounds of fuel. This and each of the preceding two OAS burns will actuate an RCS engine about 100 times worst case. The OAS burn times were not well defined and it is felt that the numbers used were on the high side. Better definition will probably show a fuel reduction.

Once the 270 nautical mile orbit is attained the RCS will maintain attitude control for 7.4 orbits until X-ray acquisition, at which time the CMGs will be up to speed and operational. During the 7.4 orbits, approximately 250 pound-seconds impulse, or 1.8 pounds of fuel, will be

required. This indicates a fuel consumption rate of 0.245 pound per orbit. Knowing how many orbits the HEAO will make in a 1 year or a 2 year mission, one can calculate the fuel consumption for an all-RCS control system. There are approximately 5500 and 11 000 orbits for the 1 and 2 year missions, respectively. This means that 1347 pounds of fuel will be required for the 1 year all-RCS mission and 2695 pounds of fuel for the 2 year mission. These numbers would become extremely important in the case of a failure of the CMG control system.

Grumman studied an all-RCS system for the HEAO-A and -B vehicles [E-16]. Figure A3-1 on page A3-14 of their report shows about 250 actuations per orbit for the same configuration as that used in TACS for the HEAO-C study. This compares very well with TACS, 233 actuations per orbit, for the HEAO-C. It should be noted that the inertia values for HEAO-C are larger but a wider deadband (± 0.8 degree) was used in Reference E-16. From the limited number of TACS runs made with different minimum impulses, it is felt that the HEAO-C curve would be quite similar to Figure A3-1 of Reference E-16.

Once the CMGs are operating the RCSs main job will be to dump accumulated secular momentum which will be assumed to be 209 ft-lb-sec per orbit on the average. There are two ways to dump the secular momentum: first, with the CMGs in an attitude hold mode and, second, with the RCS in an attitude hold mode. In the first method the appropriate RCS engines are fired in a single burst to remove the momentum. Since the CMGs can respond at 2.5 deg/sec (10 ft-lb torque on the vehicle), there will be about a 2 degree overshoot at 20 seconds. This method is not the most efficient for the CMGs since a special CMG control law for dumping may be required. Some contractor studies have shown a large overshoot if the pointing control law is used. The RCS can be fired efficiently in that long single engine burns can be made, reducing fuel consumption and actuation rates. A pseudo error signal must be generated from a knowledge of the secular momentum distribution to ensure that the proper engines will be fired. This will require a modification to the control law during the dump mode. Assuming that a pseudo error signal can be accurately generated, a worst case actuation rate would be about 11 000 cycles over a 2 year period. Typically, it is felt that about 2800 actuations per engine would be required for 2 years.

The second method of momentum dumping places the RCS in an attitude hold mode while the CMGs are gimbaled in the most efficient and direct manner to dump the accumulated momentum. The baseline CMGs

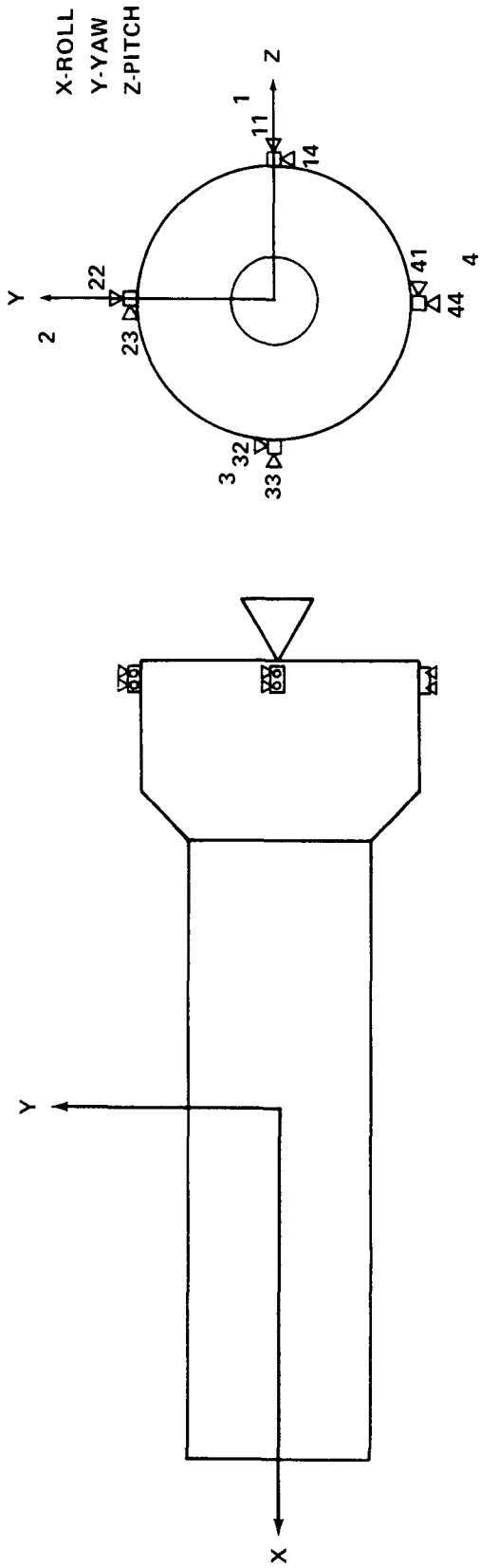
can gimbal at 2.5 deg/sec which places a 10 ft-lb torque per CMG on the HEAO. This torque causes an angular acceleration of 0.0082 deg/sec.² Assuming a minimum time of 50 milliseconds, a minimum duty cycle will result. During a typical dump of 209 ft-lb-sec of momentum, the RCS will actuate an engine 38 times to maintain pointing accuracy within ± 0.5 degree. It is felt that on the average, two engines will be firing during any particular dump; this results in 19 actuations per engine per orbit worst case. This gives a worst case actuation rate of 211 000 for a 2 year lifetime. This is high by a factor of four since, on the average, all four pairs of engines will be equally used, i. e., 52 750 actuations per engine over a 2 year period should be expected. This method of momentum dumping has two advantages. First, there does not have to be a control law modification during burn and, secondly, the vehicle remains pointed within ± 0.5 degree.

Fuel consumption should be higher in the second method, however, due to the series of small on-time engine firings versus the full-on engines in the first method. It is questionable whether the fuel savings would warrant the more difficult implementation of the first method but the problem should be studied in more detail.

In any case, momentum dumping for a 2 year period requires about 108 000 lb-sec impulse. Assuming a specific impulse of 140 seconds, 770 pounds of fuel are required. Table E-12 presents the worst case total impulse and actuation rates. Since it would not be practical to design for these worst case parameters, a design goal of 53 572 actuations per engine and total impulse of 16 373 lb-sec per engine over the 2 year period is felt to be quite adequate.

g. Alternate RCS Configuration. The alternate RCS configuration shown in Figure E-56 requires a modification to the existing hardware to place the engine modules at the 90 degree intervals. Although the cost might prohibit such a modification, it has nevertheless been studied because some advantages might be seen by using it. The two control laws described previously for the alternate system were implemented in the TACS program and run for two orbits.

The control law that mixes the roll signals directly with pitch and yaw signals proved to be highly undesirable. The vehicle can have errors so that pitch/roll and yaw/roll engines will fire simultaneously, or nearly so, in opposing roll directions. This will effectively eliminate the roll signal mix in requiring another engine burn just to correct the roll error. The simulation showed that this happened quite frequently, producing a much



ERROR	11	14	22	23	32	33	41	44
+ PITCH		X						X
- PITCH			X		X			
+ YAW	X						X	
- YAW				X		X		
+ ROLL		X			X			
- ROLL				X			X	

Figure E-56. Alternate RCS configuration.

higher fuel consumption and engine actuation rate than was actually required for control. Fuel consumption during attitude hold was increased by about 25 percent over that for the baseline system. Actuation rates also went up by a similar amount. It was decided then to implement the second law described.

The second law proved to be much better, although it was still not as efficient as the baseline system during attitude control. In the 270 nautical mile circular orbit fuel consumption increased slightly over the baseline from 0.245 lbm per orbit to 0.258 lbm per orbit. However, there was a 100 percent increase in the maximum engine cycling rate, from 61 actuations per orbit with the baseline system to 143 actuations per orbit with the alternate system. The increase in actuation rates will not appreciably affect engine cycle life unless the maximum stay time of about 30 days is used in the initial orbit and, then, only if the worst case orientation and deadband are used.

In Table E-13 the same amount of fuel is indicated for control during OAS burn for both the baseline and alternate systems. The numbers presented are hand-calculated and do not take into account any control system; only the maximum impulse possible was computed and, from this, fuel weights and maximum single engine cycles were computed. This is somewhat erroneous and it is felt that the alternate system would operate more efficiently here since opportunities for longer burn times on a single engine would arise.

The sun acquisition event will not be much different using either the baseline or alternate RCS since the proper engine burns will be determined before firing; i. e. , no error signal as such will be acted on. Therefore, the most efficient engine burn will be chosen. The control of the separation rates will make some difference but, if attitude hold is not required, the impulse required is negligible.

In any case, momentum dumping will be the primary fuel consumer and the RCS should be designed with that mode as the primary driver. Again, the same figures are reflected in both the baseline and alternate systems because a nominal impulse was hand-calculated and, from it, fuel weight and actuation rates were determined. Actually a considerable difference in fuel requirements might be seen since in the actual system the specific impulse of an engine is highly dependent on the length of each burn. An attempt will be made to add CMG dumping to the TACS program to study just this case. Until this is done, only estimates of fuel savings can be made.

**TABLE E-13. HEAO-C FUEL AND IMPULSE
BUDGET FOR THE ALTERNATE RCS CONFIGURATION**

Event	Total Impulse (lb-sec)	Fuel Required at $I_{sp} = 140$ sec (lbm)	Worst Case Engine Cycling For an Engine	Comments
Null 3 deg/sec 3 axes	1043.8	7.45	30	Includes Attitude Control
Solar Acquisition (90 deg about X and Y)	268.0	1.90	4	2 deg/sec max maneuver rate
Attitude Control in 140 by 250 n. mi. Orbit	165.9 17 374.0	1.18 at 4.5 Orbits 124.1 at 30 Days	675 or 70 632	0.263 lbm/orbit
OAS Thrust Vector Misalignment During Burn to 205 by 250 n. mi.	1 079.5	7.71	150	7.5 min burn
Attitude Control in 205 by 250 n. mi. Orbit	36.55	0.261	146	0.261 lbm/orbit for 1 orbit
OAS Thrust Vector Misalignment During Burn to 250 by 270 n. mi.	804.1	5.74	112	5.58 min burn
Attitude Control in 250 by 270 n. mi. Orbit	54.4	0.38	144	0.259 lbm/orbit for 1.5 orbits
OAS Thrust Vector Misalignment During Burn to 270 n. mi. Circular	673.2	4.80	94	4.68 min burn
Attitude Control in 270 n. mi. Orbit Until CMGs are up to Speed, End of Checkout and Acquisition of X-Ray Reference	266.9	1.90	1 058	0.258 lbm/orbit for 7.4 orbits
CMG Momentum Dumping at 270 n. mi.	107 767	769.7	422 180	Typically 105 545 Actuations per engine are expected
Totals	112 159.35 or 129 367.45	801.02 or 923.24	424 593 or 494 550	

h. Conclusions. At the present time, simulation results and some calculations have shown that the accumulated secular momentum will, primarily, be about the transverse axes (Y and Z) with very little about the longitudinal axis. Therefore, a reaction control system that most efficiently controls momentum dumping about the Y and Z axes should be chosen. Because of this consideration, it is felt that the alternate system has the better configuration.

The alternate configuration has the capability of producing long single engine pitch and yaw burns without introducing a roll torque. Therefore, on the average, a higher I_{sp} should result, saving fuel in this critical area.

At the same time, the small expected roll secular momentum can be controlled quite well due to the single engine burns in the roll axis. Pitch and yaw of course are aided when a roll engine is burned.

The baseline system is quite the opposite. If pure pitch or yaw is desired, two engines must be actuated resulting in a shorter burn time for any one control period. If two engines are not burned simultaneously, roll is introduced into the system. Since these engines are controlling pitch and yaw they often have longer burns than are required for roll control. Hence, roll is over-controlled and some banging back and forth within a pitch pair or yaw pair of engines will result. Engine life due to cycling is decreased but the throughput life is increased since each engine burns for less time. A detailed study is needed to determine if, based on the mission timeline, secular momentum is built up on one side of the pitch-yaw axes more than the other side. If it is biased toward one polarity, the baseline system may have some advantage due to decreased cycle rate and throughput; i. e. , two engines are doing what one engine must do in the alternate system. However, the momentum will probably be accumulated equally on both sides of the pitch and yaw axes, on the average. If such is the case, there should be no danger of the engines exceeding their life due to cycling although throughput may be too high.

With only four engines used in the alternate system for dumping the major part of the momentum, a simple, equal division among the engines gives 26 941 lb-sec per engine. The engines are presently qualified for only 18 000 lb-sec impulse but an engine has been demonstrated to have 27 500 lb-sec total impulse capability. This demonstration only required that the engine remain within its 3σ performance specification; therefore, further study is needed to see if a requalification would be required or if the engine already is capable of a 2 year mission in the alternate configuration.

2. Control Moment Gyro Performance Simulations. Typical baseline performance was shown in Chapter VII. The maximum pointing error under worst case conditions is 0.102 arc minutes. With the addition of electromagnets for continuous momentum dump, the performance improves by about a factor of 4, as shown in Figure E-57. With the magnetic torquers sized at 0.4 ft-lb/gauss and a magnetic loop gain, K_m , equal to 0.01 sec^{-1} , the maximum pointing error is 0.0225 arc minutes. Since momenta are being continuously dumped the stored CMG momenta stay near zero; consequently, the CMG gimbal angles, shown in Figure E-58, deviate less than 4 degrees from their null position. The coil dipoles, shown in Figure E-59, have been hard-limited to 0.4 ft-lb/gauss and commanded proportionally to the vector components of the stored CMG momentum. The dipole commands have been derived previously in this appendix. As noted in Figure E-59, the X-axis component saturates twice during the orbit. By decreasing K_m to 0.001, the coils do not saturate, but not as much momentum is dumped and a corresponding increase occurs in CMG gimbal angles. The pointing performance is relatively unchanged. However, by increasing K_m to 0.1 all the coils reach saturation values. Both the stored momenta and gimbal angles stay near zero, but the pointing performance is degraded slightly. Using still higher K_m values causes the coil dipoles to react in a bang-bang manner that produces a magnetic torque which greatly degrades the pointing performance. Based on several runs in which K_m was varied, a magnetic loop gain of 0.01 is recommended for continuous momentum dump. Figure E-60 illustrates the magnetic torque applied to the spacecraft as the result of the coil dipoles shown in Figure E-59. The components of the magnetic torque are about equal to that of gravity gradient in both magnitude and shape, indicating that the magnetic system is indeed counteracting the environmental torque, leaving the CMGs with relatively little to do. The baseline system utilizes the pseudo inverse CMG steering law.

Alternate System. Several CMG steering laws were simulated. One that shows potential for use with magnetics is the maximum contribution (MC) steering law. Using the MC, each CMG gimbal rate is commanded, as if it were the only one, to contribute as much as possible to the commanded torque. Simulations indicate that when the gimbal angles get large, certain combinations of angles can momentarily prevent the desired torque from being produced without also producing unwanted torque components that will disturb the pointing accuracy. This is indicated in Figure E-61 by run number T-68: All the CMGs are operating and no momentum is being dumped ($M_L = 0$).

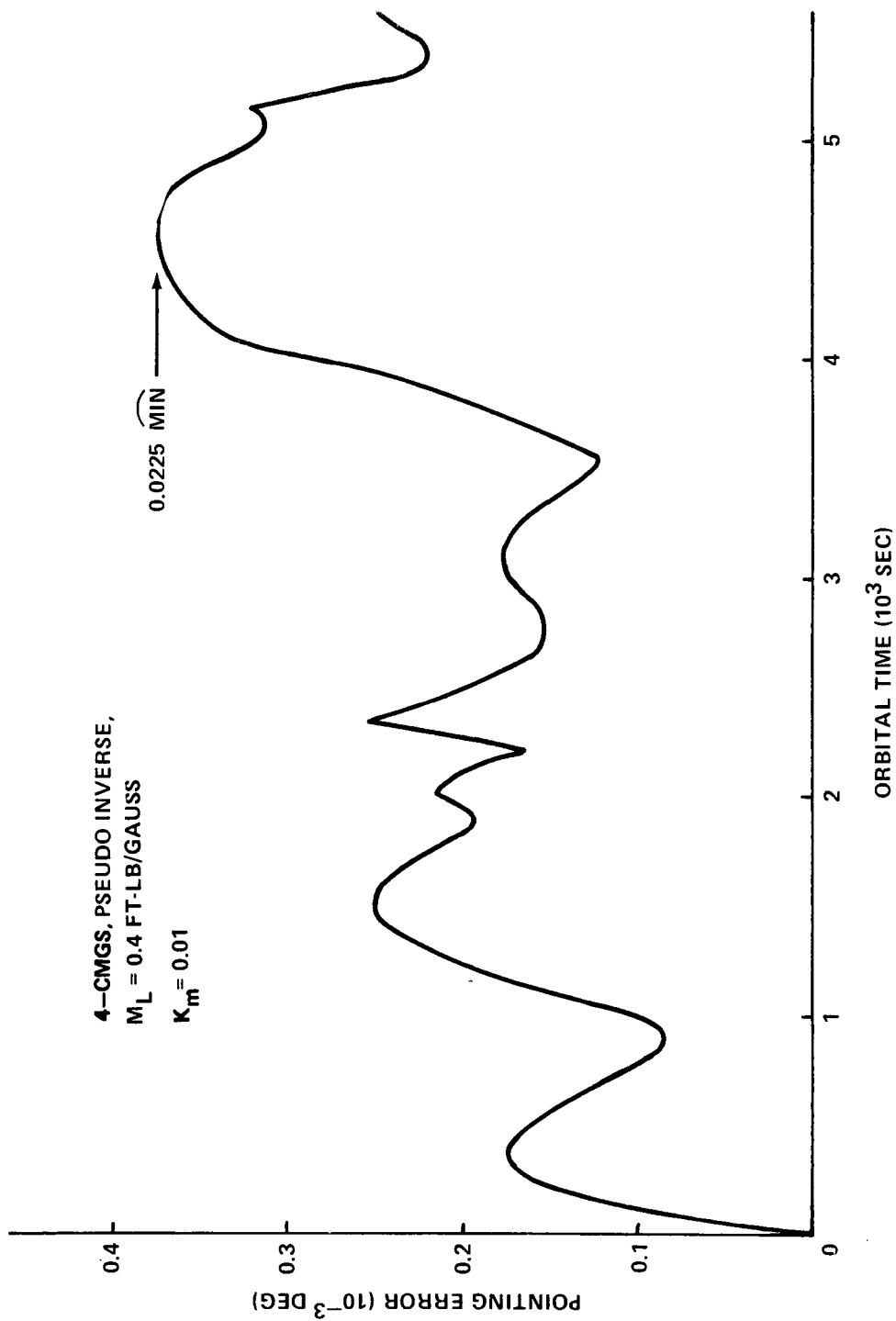


Figure E-57. Performance of pseudo inverse law magnetics.

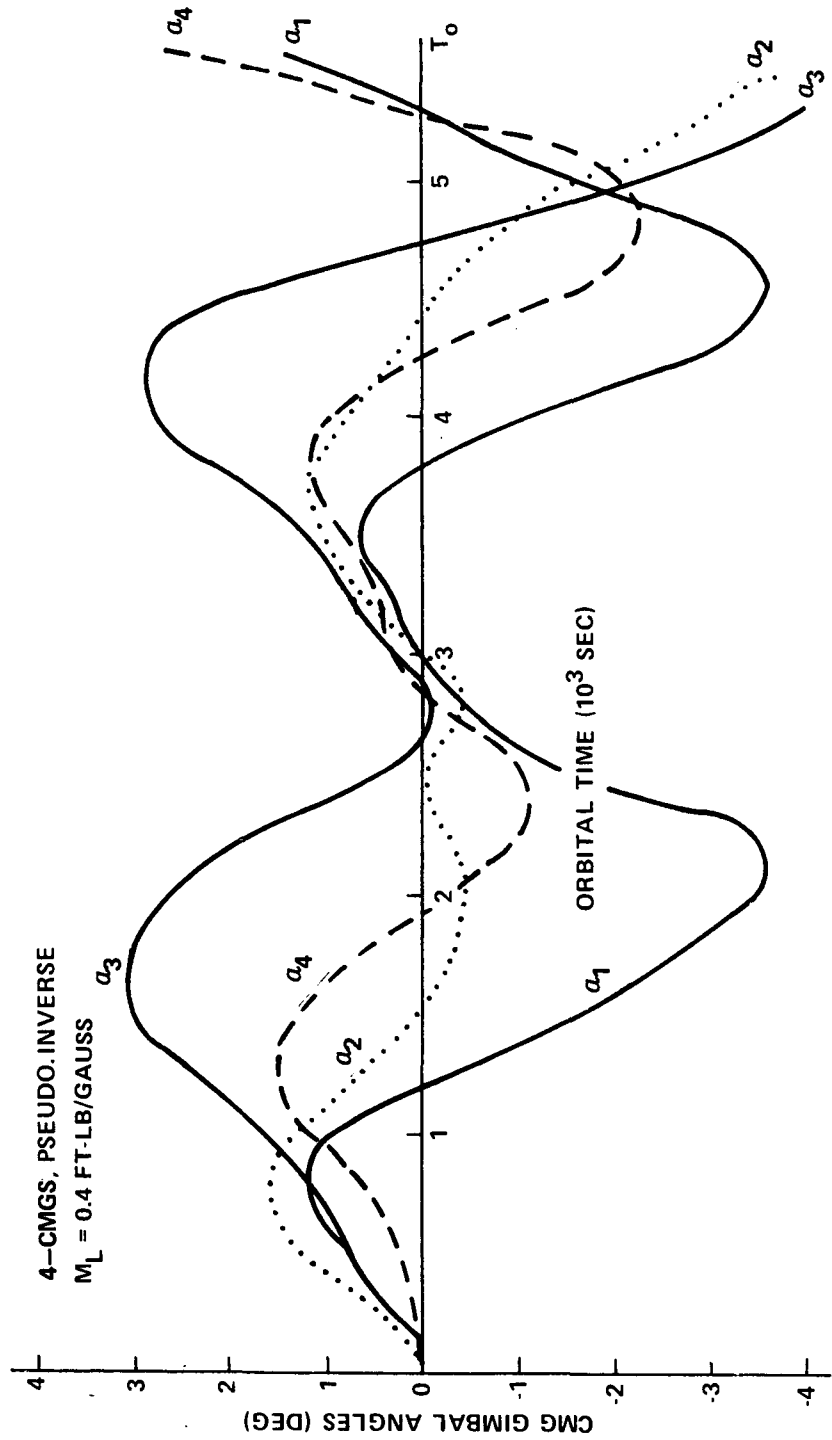


Figure E-58. CMG gimbal angles with magnetic CMG dump.

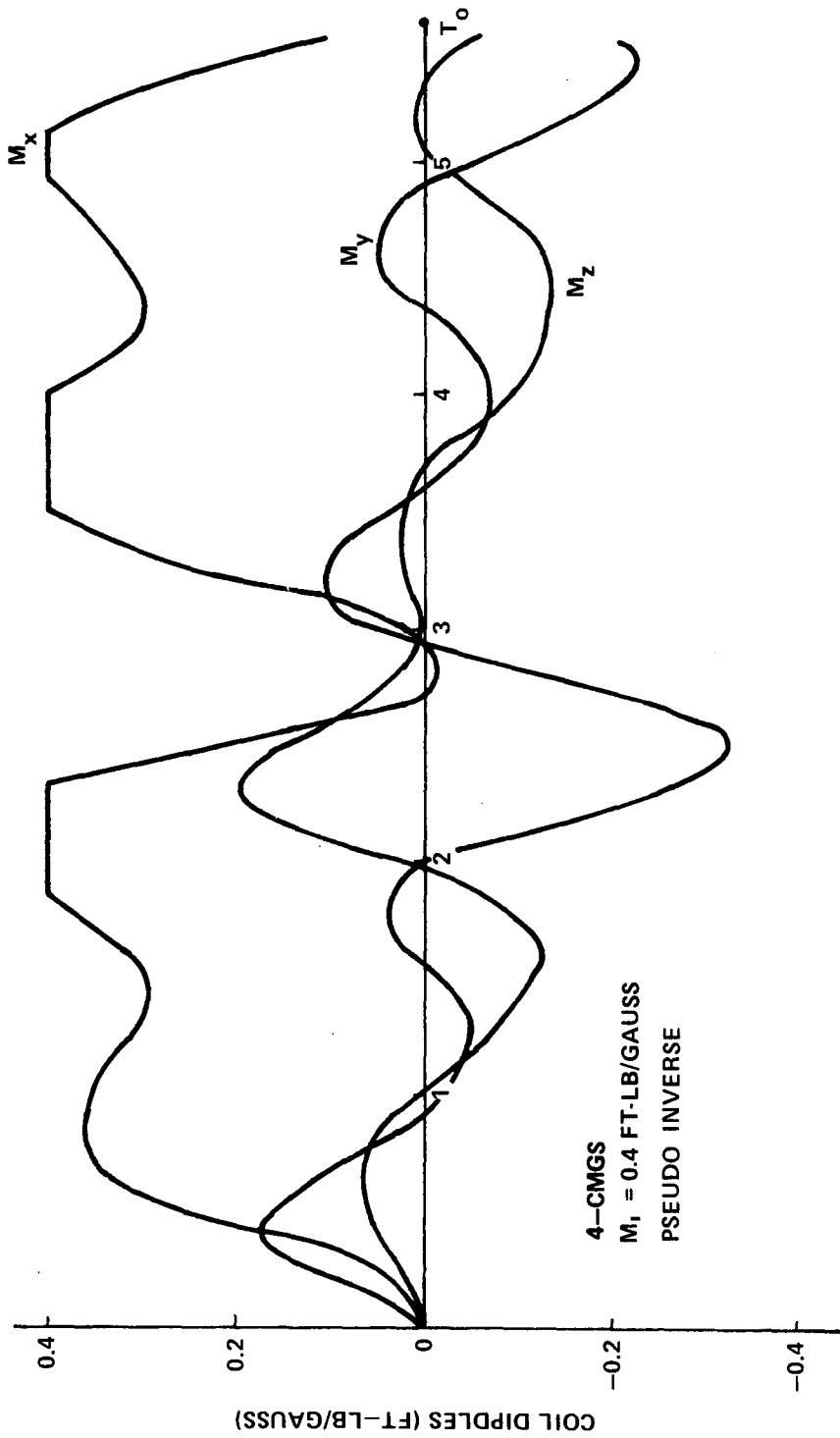


Figure E-59. Dipole moment components versus orbital time (10^3 sec).

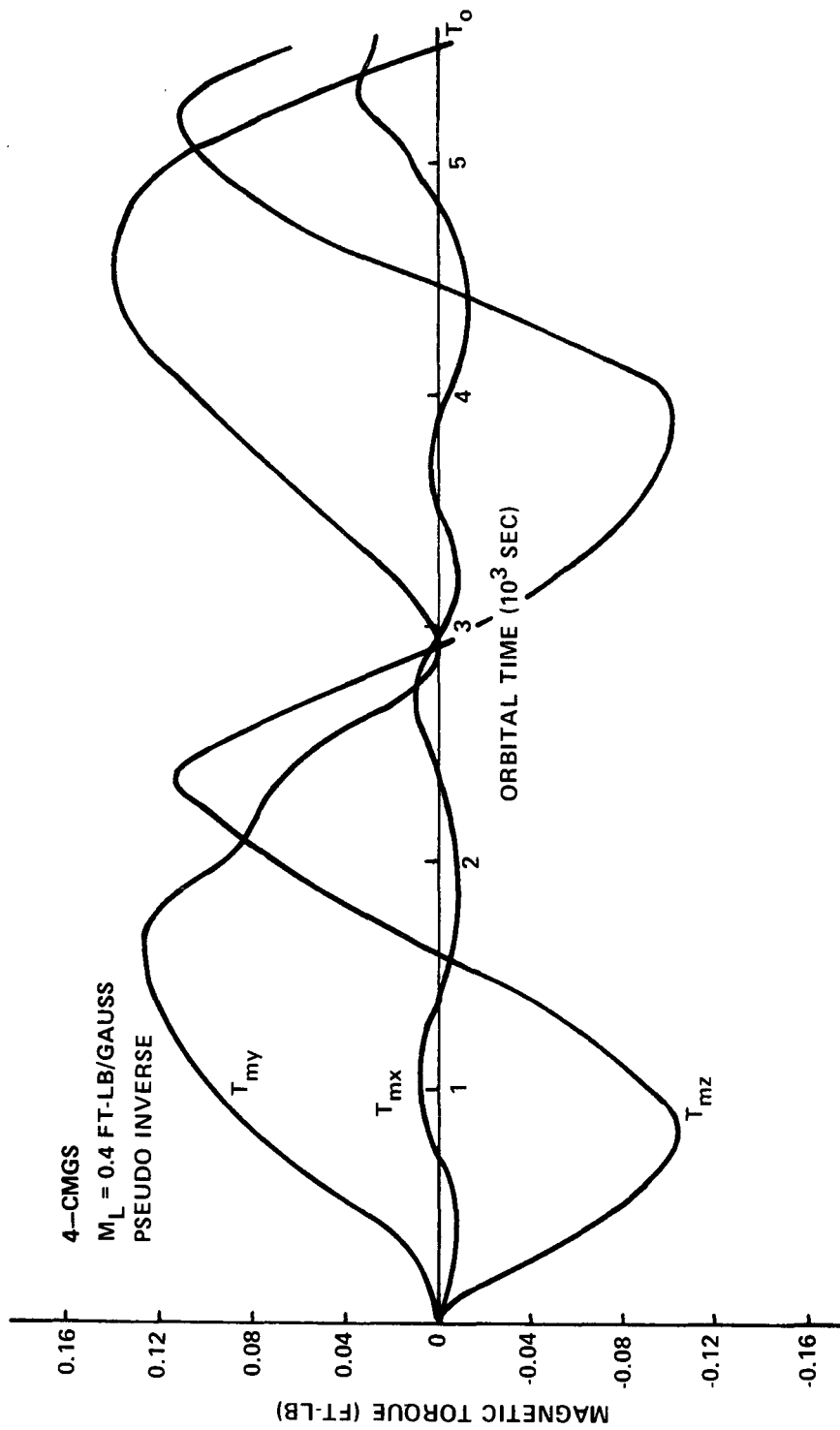


Figure E-60. Magnetic torque component to dump CMG momentum.

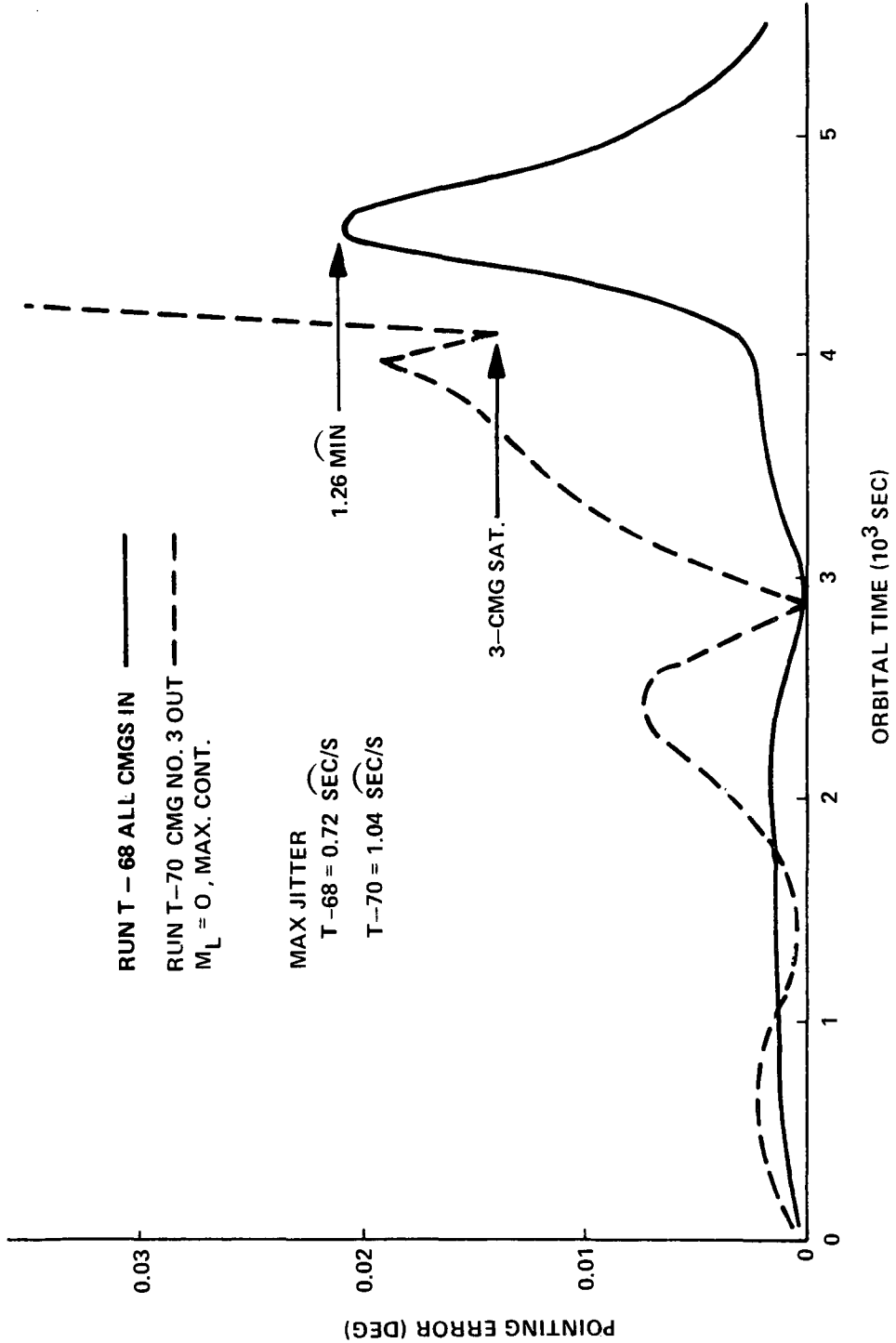


Figure E-61. Pointing performance with the maximum contribution steering law.

At 4600 seconds, the pointing error is 1.26 arc minutes, which exceeds HEAO-C pointing specifications; however, by using higher feedback gains, the error can be reduced (shown by a later run not included herein) to an acceptable value. After the peak error, acceptable performance was maintained until CMG saturation was near the two orbit time point. Near the peak attitude errors, the gimbal angles, shown in Figure E-62, change rapidly. At one orbit the third gimbal angle attains a value of 142 degrees; the other angles also deviate considerably from their null position. Since CMG Number 3 appears to be doing the most work, it was failed by setting its momentum to zero. The resulting pointing performance is also shown in Figure E-61. The remaining three CMGs saturated at 4100 seconds, after which pointing control is lost. Additional runs with the momentum per CMG raised to 500 ft-lb-sec (not shown) illustrate that the gimbal angles stay relatively small over one orbital period, even with one CMG failed, and both the pointing and jitter specifications are more than satisfied. The conclusion is that as long as the gimbal angles stay small (90 degrees), the MC steering law satisfies HEAO-C requirements. If more than four CMGs are used, the induced cross coupling effects (see Figure E-61 at 4600 sec) become less and the MC steering law performance is enhanced.

With the addition of magnetic torquers for momentum management, the pointing performance improved by a factor of 3 and the jitter by a factor of 10. As illustrated in Figure E-63, the maximum solar pointing error is 0.39 arc minutes and the maximum jitter is 0.0756 arc seconds per second. The momentum dumped by the coils is the difference between the accumulated gravity gradient, H_g , and that stored in the CMG system, H_{CMG} (Fig. E-64). Over one orbit's time, about 400 ft-lb-sec momentum was dumped magnetically. The performance is measured by three Euler angles: ϕ about the sunline (Z-axis), θ about the once transformed solar Y_s -axes (X-axis), and ψ about the twice transformed solar Z_s -axis (Y-axis). The Euler angles are depicted in Figure E-65. The solar offset angle for run T-51 is dominated by θ , the rotation about the long Observatory axis. The target pointing error is the same as that obtained with the pseudo inverse with magnetics (Fig. E-57).

Run number T-52 indicates the vehicle's performance while the magnetic system is automatically forcing the CMGs to a new null position. After failing the third CMG by setting $H_3 = 0$, the system momentum was initially biased in the antisolar direction by 250 ft-lb-sec. The magnetic torquers process the CMGs to a new null position (zero momentum), during

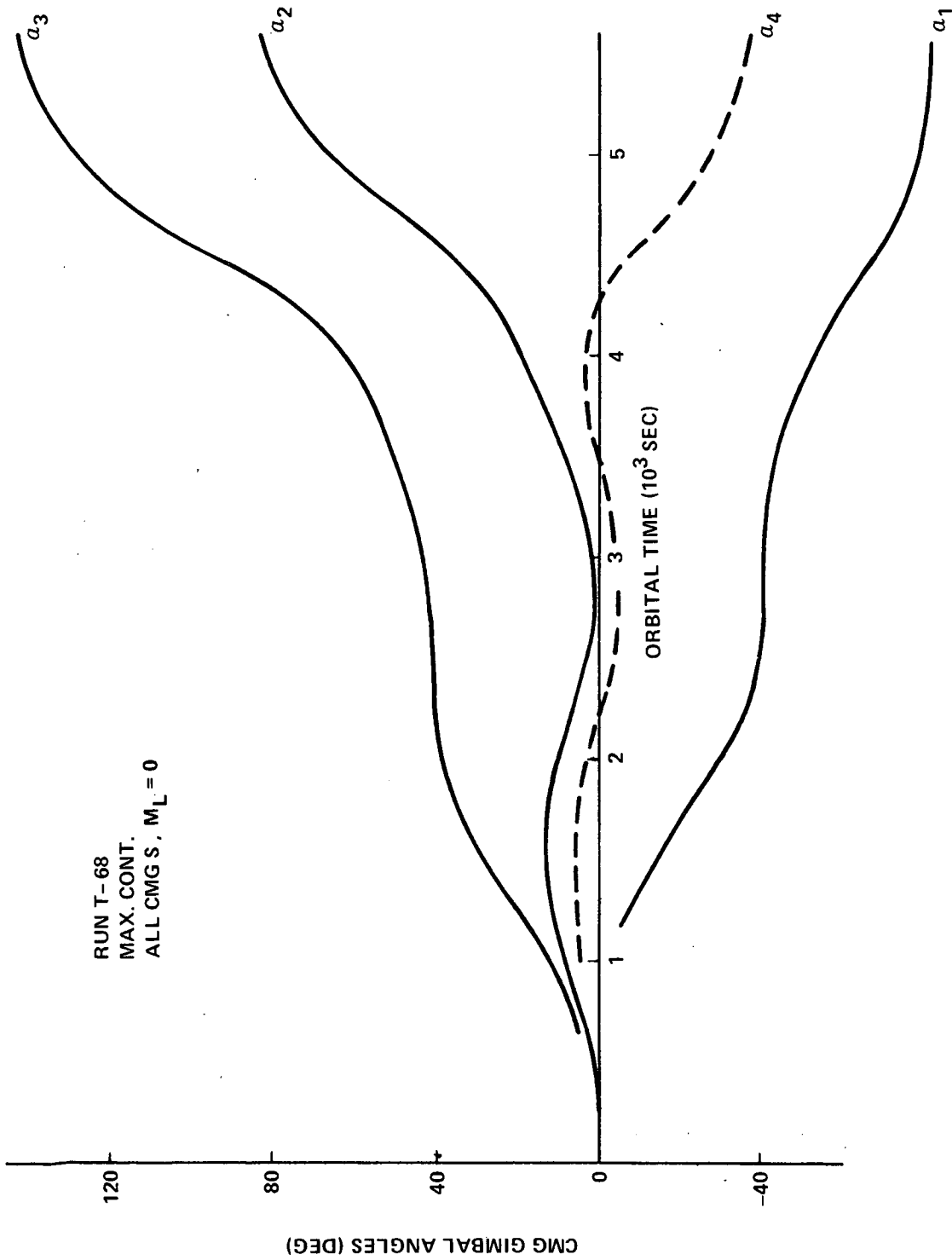


Figure E-62. CMG gimbal angles with maximum contribution steering law.

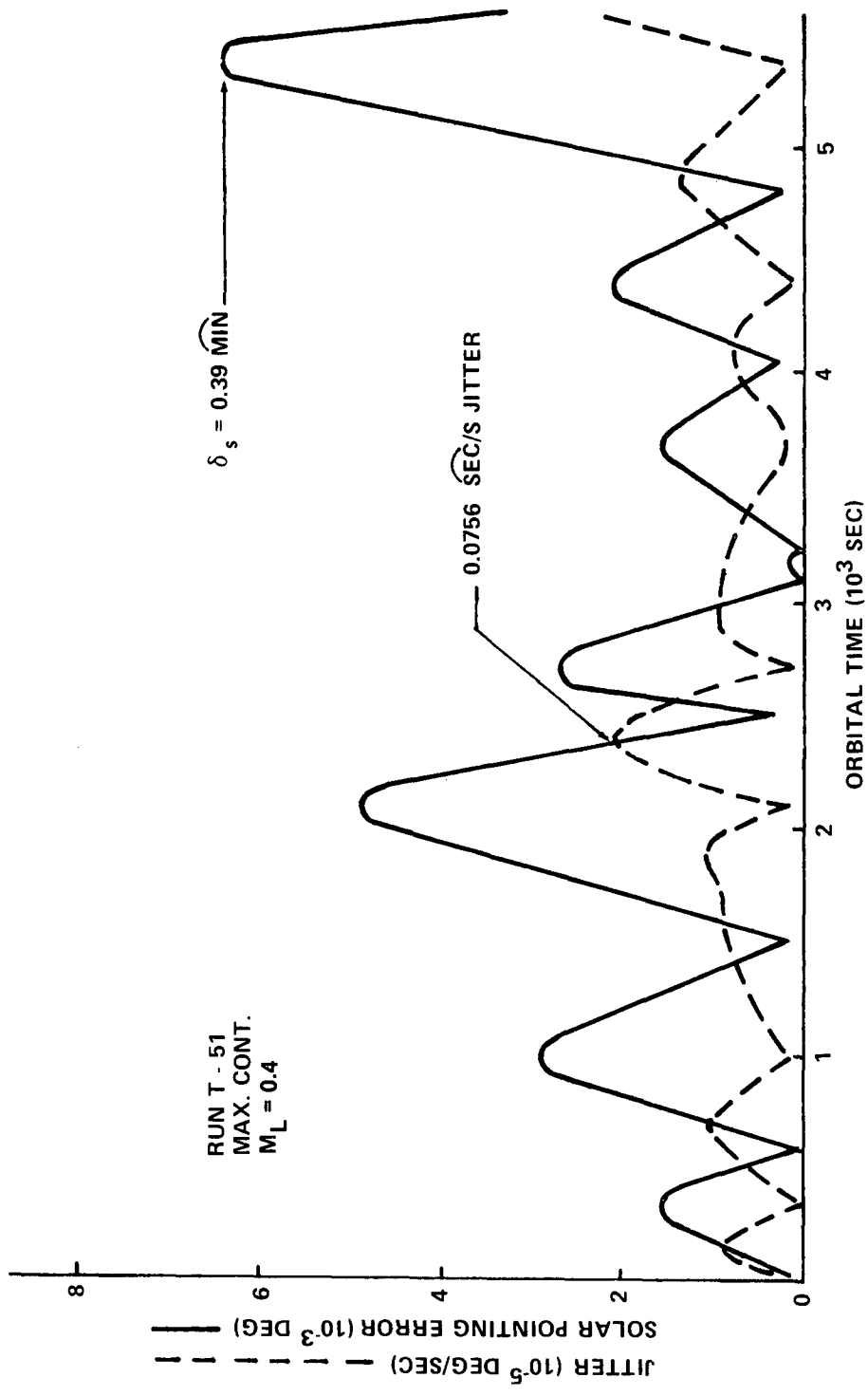


Figure E-63. Solar pointing and jitter for maximum contribution steering law with magnetic dump.

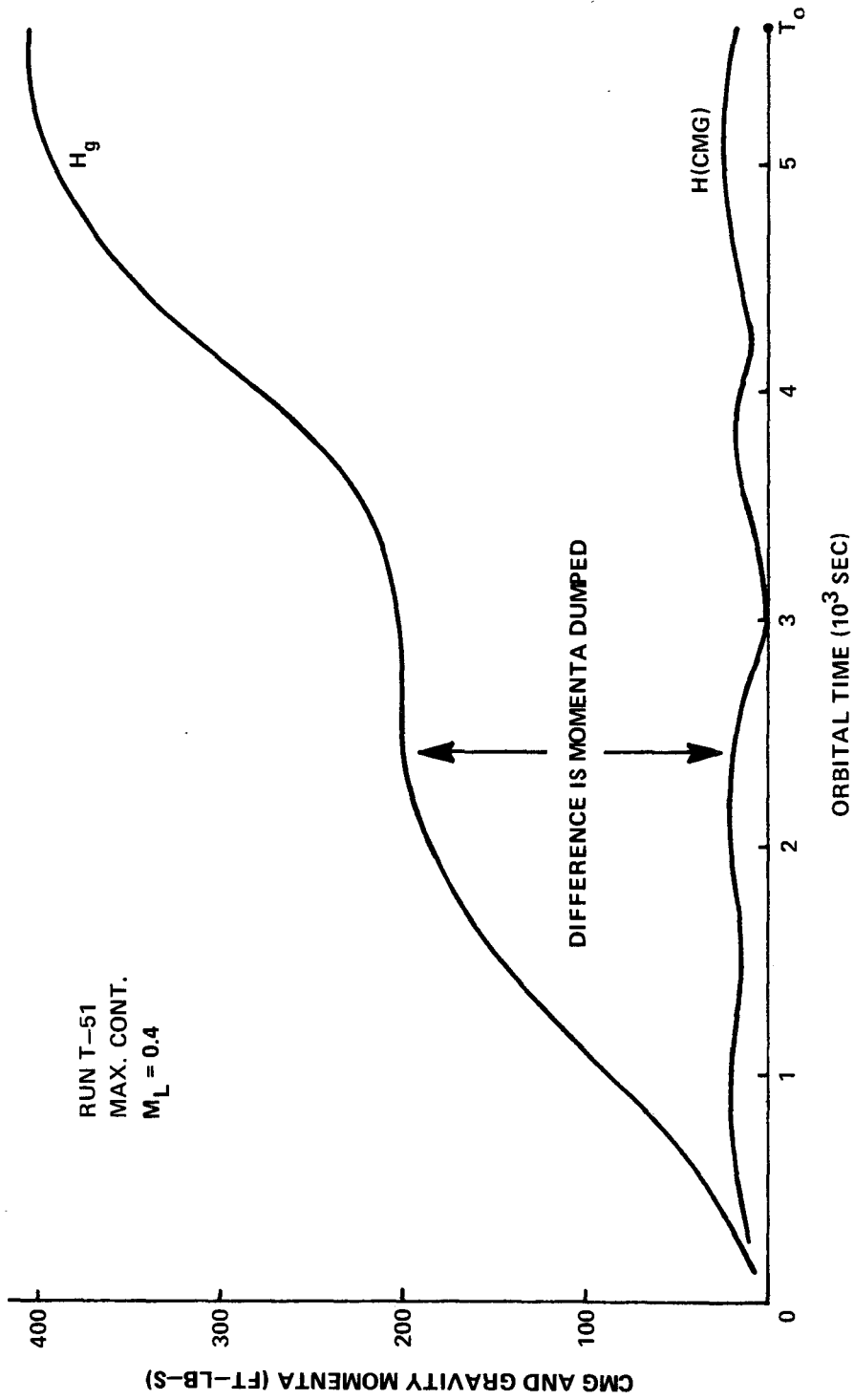


Figure E-64. Momenta dumped by electromagnets.

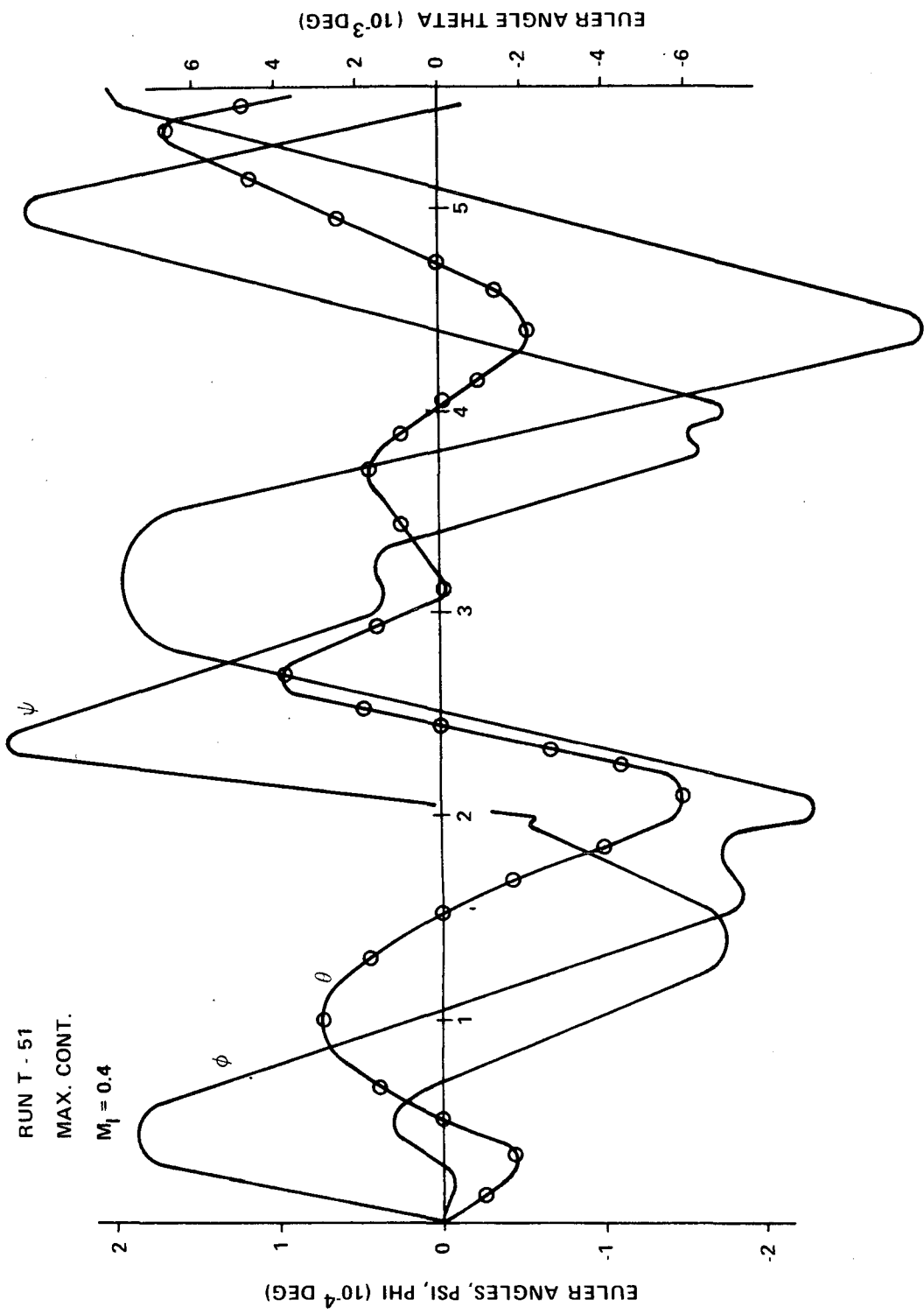


Figure E-65. Euler angles versus orbital time (10^3 sec).

which time the CMG gimbal angles move rather rapidly, disturbing the attitude of the vehicle. As noted in Figure E-66, the solar offset angle attains a peak value of 6.6 arc minutes at 1800 seconds. After finding a new null, the second orbit pointing performance is well within that required; the peak value is 0.11 arc minutes at 4300 seconds into the second orbit. The momentum dumped by the electromagnets is shown in Figure E-67, the difference between H_g and H_{CMG} . A change of 250 ft-lb-sec occurred during the search for a new null and about 400 ft-lb-sec secular gravity momentum was dumped. The dipole components on all axes initially saturate (Fig. E-68), but are operating linearly after 2000 seconds. The corresponding magnetic torque components (Fig. E-69), indicate a peak value of 0.225 ft-lb which exceeds that due to gravity. After 1800 seconds, a new CMG null was found (Fig. E-70). With $\alpha_1 = 0$, $\alpha_2 = 56.4$, and $\alpha_4 = -56.4$ degrees, the CMG momentum state is zero with respect to the spacecraft principal axis.

Additional runs with other steering laws indicate that magnetic momentum dump always keeps the CMG gimbal angles and momentum small, permitting linear operation of the steering law. The performance of any steering law is enhanced by the magnetic system. With small gimbal angles, the performance obtained by various steering laws was comparable. However, once the gimbal angles get large, the performance is usually degraded by cross coupling and nonlinear effects in the Euler equations. Only the pseudo inverse and H-distribution laws performed without degradation with large gimbal angles. Moreover, maneuvers were commanded with the CMGs near a saturation condition to illustrate the transfer of momentum from one spacecraft axis to another — one of the reasons for selecting a near-spherical CMG momentum profile for HEAO-C.

Reaction Control System

This portion of Appendix E presents a detailed discussion devoted to the design and performance aspects of the reaction engine assembly (REA) and the reaction engine module (REM) used in the baseline RCS of the HEAO-C spacecraft. Also discussed in this section are the alternate RCS concepts that were considered for the baseline HEAO-C spacecraft. These alternate concepts include the baseline RCS with an alternate REM location, manifolding the RCS tanks to the main tank of the OAS for propellant transfer, and a cold gas RCS. Other RCS analyses are also discussed in this section.

1. Reaction Engine Assembly/Reaction Engine Module Design and Performance Aspects

a. Overall Configuration. The REM is designed as a completely integrated all-welded/brazed assembly. Figure E-71 depicts the REM and

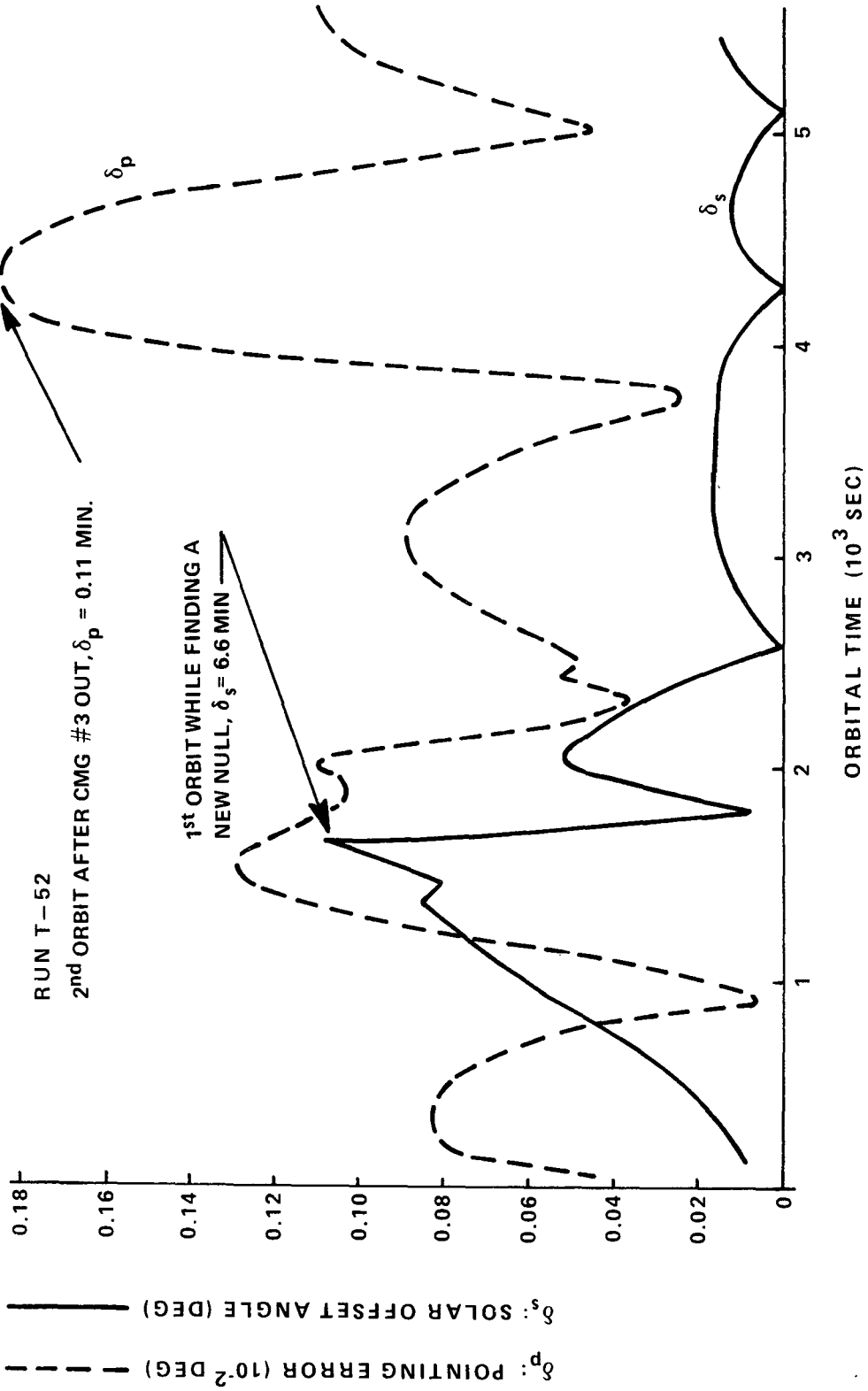


Figure E-66. Solar offset angle and pointing error.

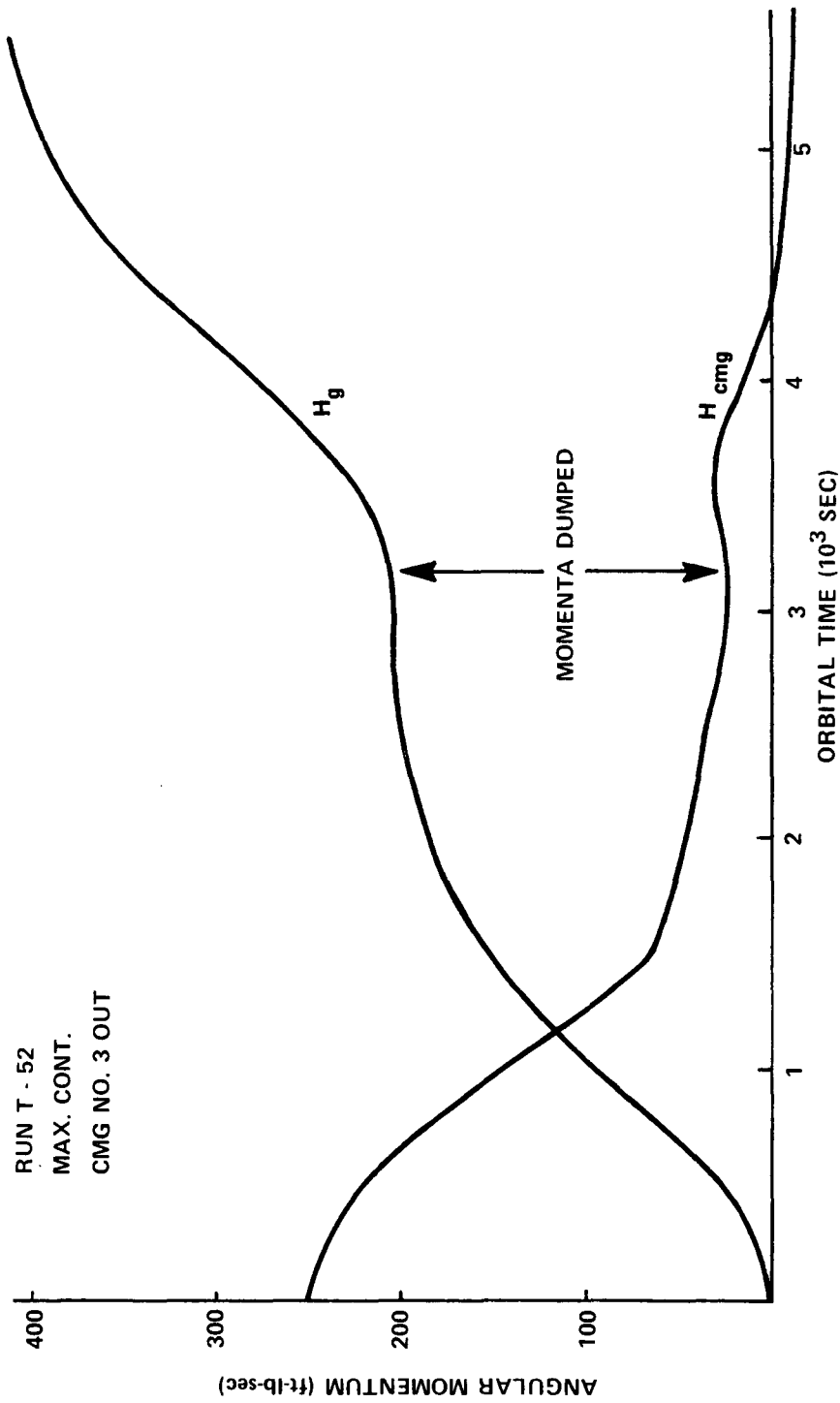


Figure E-67. Stored CMG and secular gravity momenta.

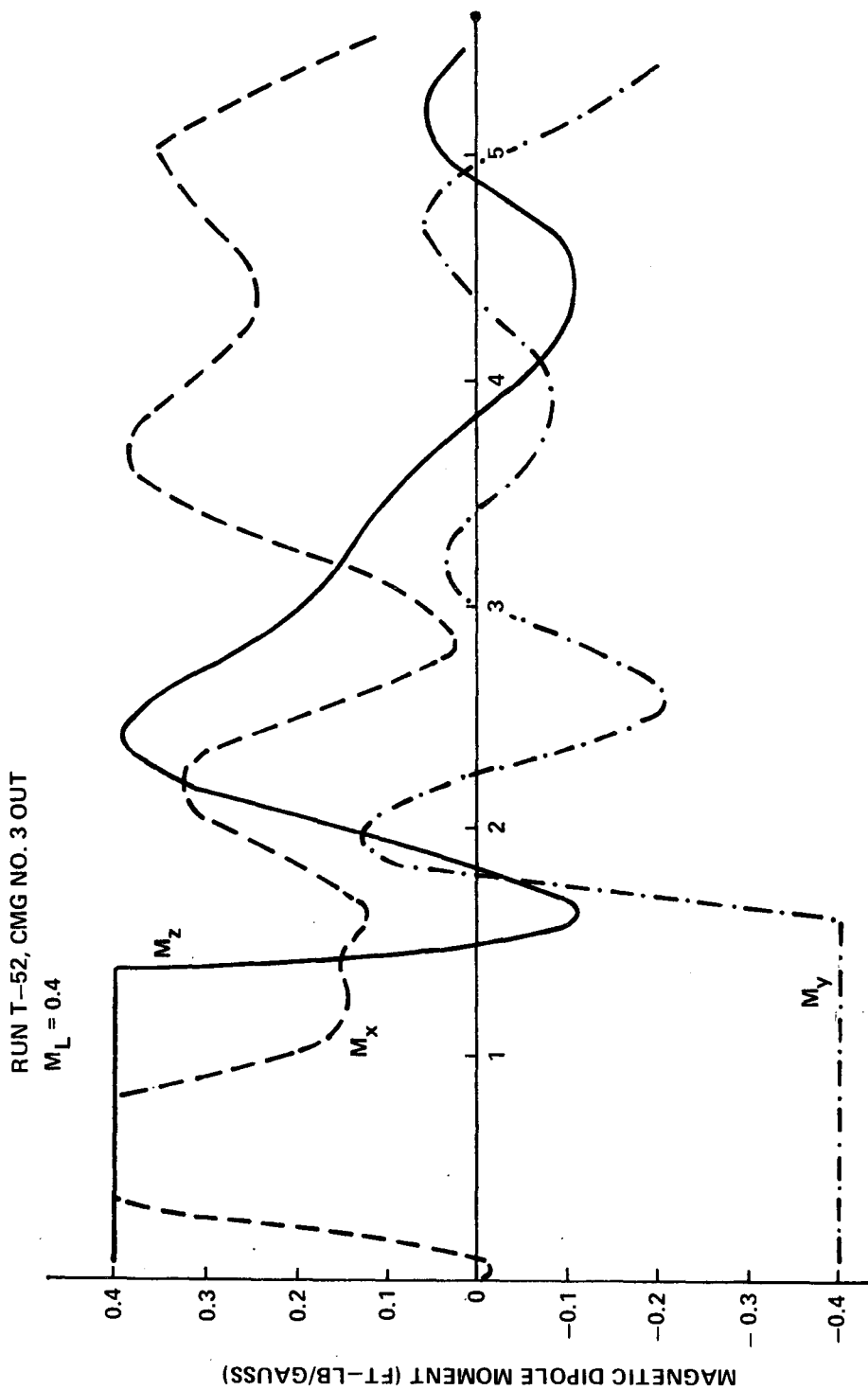


Figure E-68. Dipole components versus orbital time (10^3 sec).

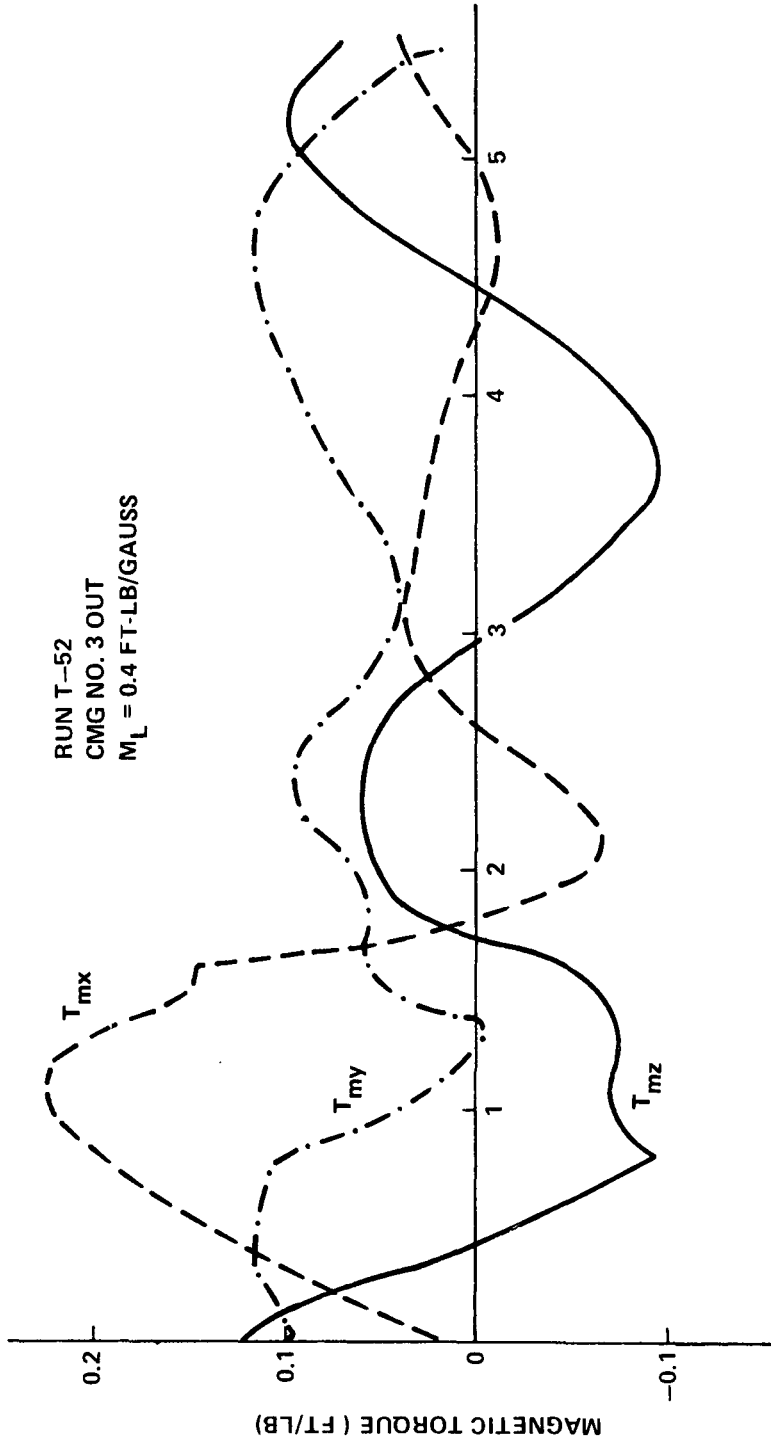


Figure E-69. Magnetic torque versus orbital time (10^3 sec).

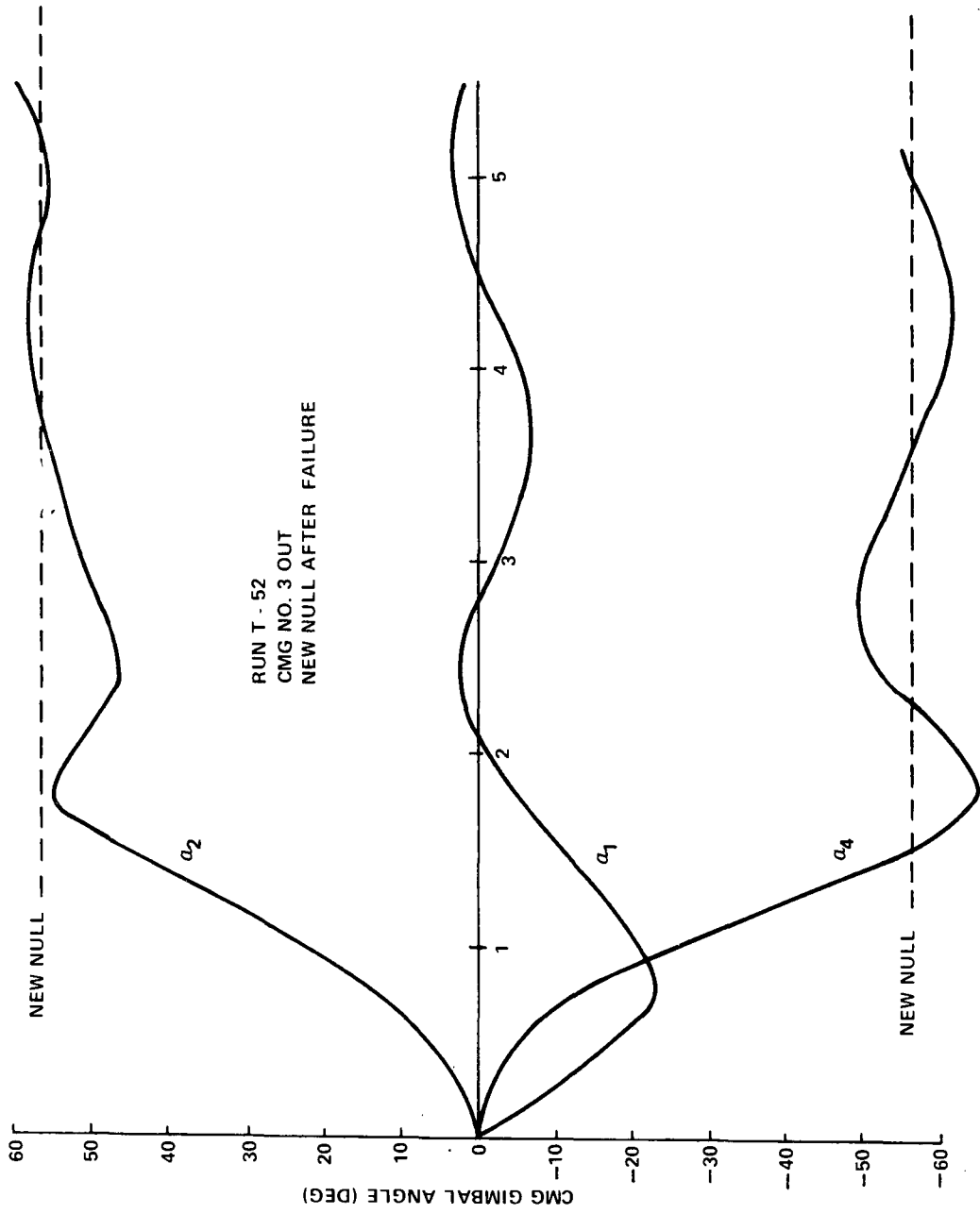


Figure E-70. CMG gimbal angle versus orbital time (10^3 sec).

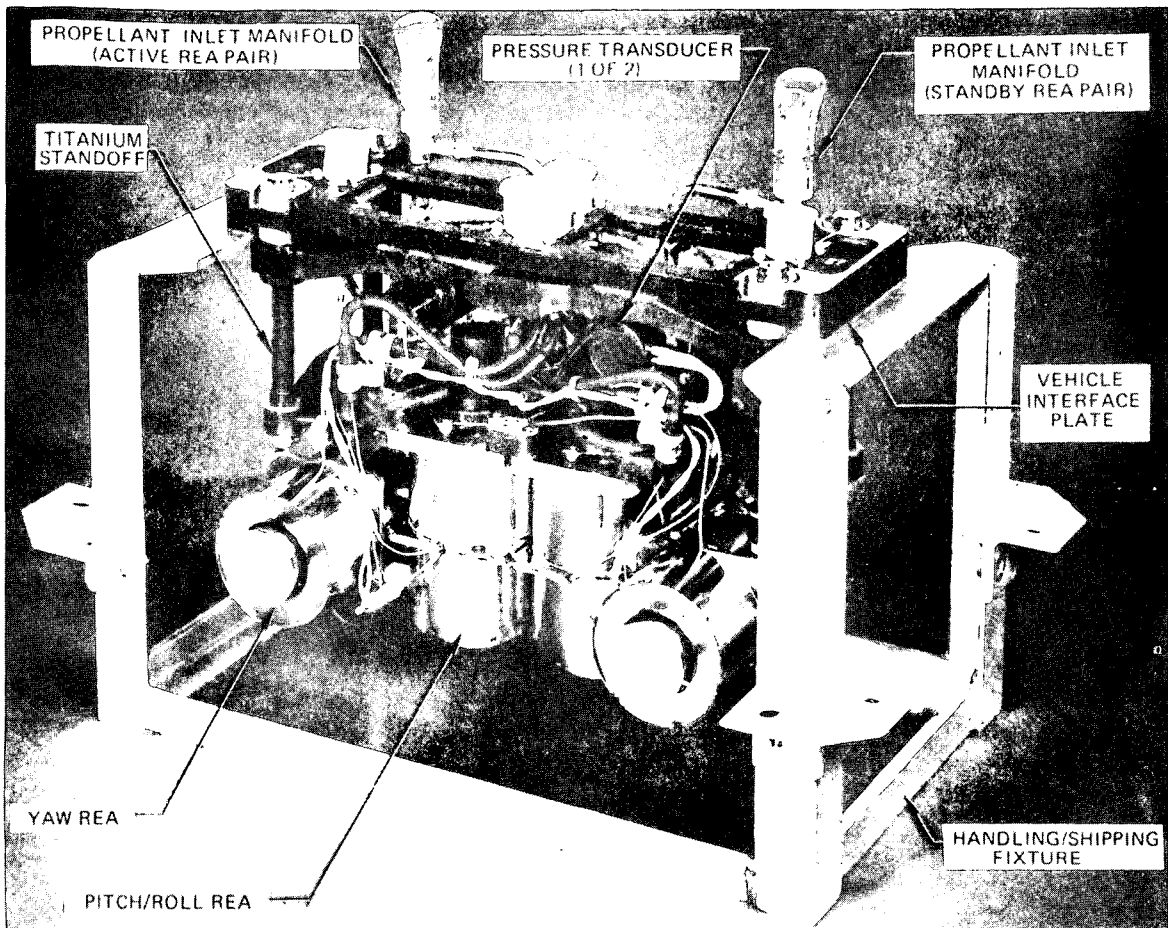


Figure E-71. Reaction engine module (REM) [E-17].

its major component parts. The REM consists of two identical subsystems, an active and a standby, independently controlled and manifolded. Each subsystem consists of one pitch/roll REA and one yaw/roll REA oriented 90 degrees apart. Each REA consists of a thrust chamber and nozzle, normally closed, direct-actuated, electrically operated thrust chamber valve (TCV) and a thermal shield assembly. Each REM contains two chamber pressure transducers, one on each of the active REAs. However, for application to the HEAO-C spacecraft, each REM will be modified to contain four chamber pressure transducers, one on each of the active REAs and one on each of the standby REAs. Each REM also contains one thermistor to monitor average valve temperature, four thermocouples to monitor chamber wall temperature, two REM plate heaters (REA valve heaters), two thermal short heaters (REA catalyst bed heaters), and two thermostats. The REM contains four separate electrical connectors, two for valve power, one for heater power,

and one for instrumentation leads. In the event of failure, the standby subsystem can perform the functions of the failed active subsystem. The REM-RCM⁷ interface consists of an interface plate casting (Fig. E-71) which provides a four-bolt hole pattern mechanical interface and a four-connector electrical interface. Shock mounts located between an interface plate and the REA mounting structure provide some thermal isolation to the vehicle, as well as attenuation of vibration and shock loads imposed by the vehicle. The interface plate vehicle, bolt hole pattern provides for left and right REMs for vehicle installation purposes, and all electrical connectors are individually keyed to insure proper electrical hookup. Once the REMs are attached to the RCM, an aerodynamic fairing is placed over them for protection during ascent through the atmosphere. This fairing is retained throughout the entire mission. Cutaways are provided in the fairing for the REA exhaust plume [E-17].

b. REA/REM Performance and Requirements. Table E-14 presents a summary of some of the REA/REM performance limits. The data presented in this table refer to the REA/REM qualification performance requirements necessary for the Lockheed SCS⁸. A requalification of the REA/REM system is necessary before it can be applied to the HEAO-C RCS. The minimum thrust of 2.5 pounds and a minimum impulse bit (MIB) of 0.15 lb-sec capability of this REA, while maintaining a pulsing specific impulse in the 125 to 205 second range, is an important characteristic that conserves fuel during desaturation of the CMGs. The pressurization system blowdown ratio, electrical pulse width, and maximum and minimum operating pressures are all integrally related with such performance parameters as thrust level repeatability, impulse bit repeatability, and impulse bit response as summarized in Table E-14 [E-17].

c. Rocket Engine Assembly Design. Figure E-72, a schematic of the REA, shows that the REA is made up of three major components: TCV, thrust chamber assembly (TCA), and heat shield assembly. The REA is an all-welded configuration, including the TCV-to-TCA interface. This all-welded approach is used in the liquid TCV inlet interface, which is prepared for brazing into the REM. As shown in Figure E-72, this inlet tube incorporates a trim orifice which is sized on the basis of the actual flow data of the REA components. The tube assembly is connected to the TCV with an Aeroquip coupling braze fitting. The REA configuration, as shown in Figure E-72, is used in the LMSC⁹ REM in the yaw/roll position; whereas, pitch/roll REAs

7. RCM — Reaction Control Module

8. SCS — Satellite Control Section.

9. LMSC — Lockheed Missiles and Space Company.

TABLE E-14. REA/REM PERFORMANCE CAPABILITIES [E-17]

Item	Data
Thrust (min)	2.5 lbf
Minimum Impulse Bit (MIB) up to 1.0 cps (max)	0.15 lbf-sec
Total Pulses per REA	175 000
Total Impulse per REA	18 000 lbf-sec
REA Minimum Electrical Pulse Width	22 msec
Specific Impulse Pulsing at 0.01 cps Steady State	125 sec 205 sec
Steady State Response Time to 1.0 lb Thrust (max)	100 msec
Response -- MIB Pulsing Percent in 50 msec Percent in 100 msec	33 60
Repeatability Impulse Bit Between Two REAs Thrust Between Two REAs	+22% +15%
Duty Cycle per REM Maximum Activity Minimum activity	Two REAs Firing Steady State for 5 min, 5 cps Pulsing per REA One REA Firing at 0.01 cps
Propellant	Hydrazine, MIL-P-26536
Environmental Temperature Range	0 to 140° F
Propellant Temperature Limits	+40 to +140° F
Operating Voltage	24.5 to 33 Vdc
Life Firing (min) Calendar	45 days 42 months After Acceptance Test

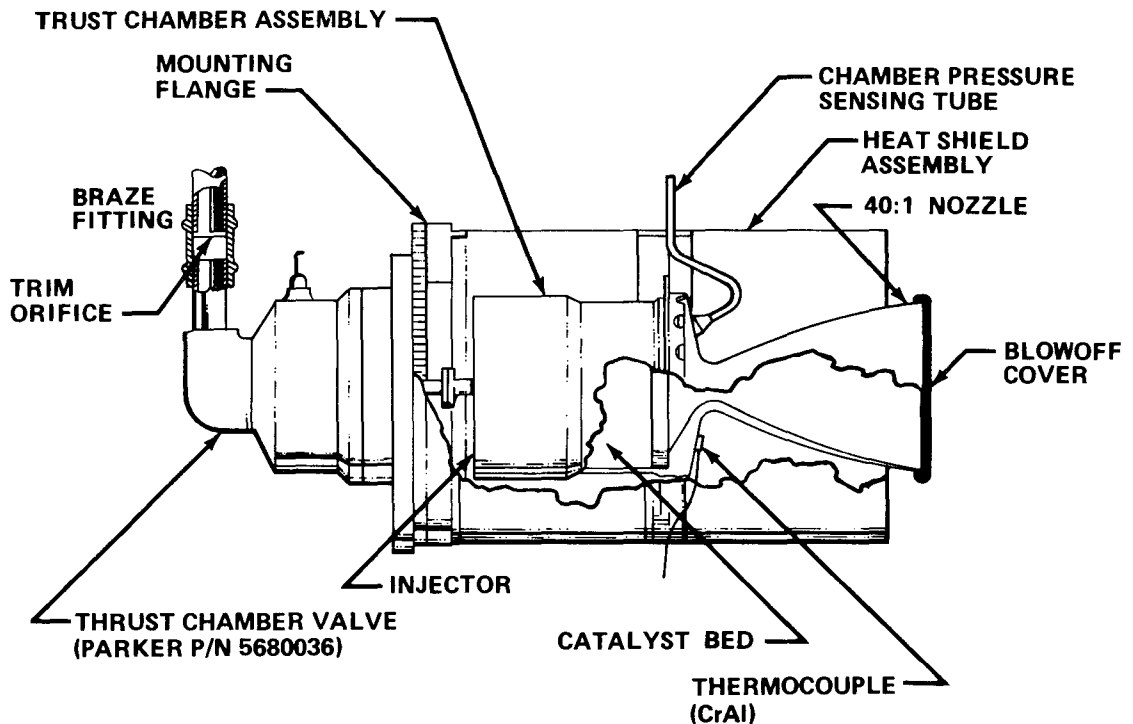


Figure E-72. Reaction engine assembly, MR-50A [E-17] .

are oriented 90 degrees to the yaw/roll REAs and incorporate a 90 degree tube/orifice assembly joined to the TCV with a 90 degree elbow braze fitting.

Figure E-72 also shows the mechanical interface mounting flange (forward heat shield flange) located at the base of the thrust chamber valve. All axial loads are transmitted from the TCA through the welded injector feed tube to the valve outlet stem and, thence, from the valve end cap to the REA mounting flange. The heat shield assembly provides lateral structural support to the TCA in addition to providing a radiation heat barrier.

Thermal control of the REA is normally maintained by extensive use of thermal control coatings. With the exception of the feed tube, the TCA exterior and the nozzle interior up to the throat are rhodium-plated. The injector feed tube/valve outlet stem and the exterior of the valve are painted with sicon black paint. The end cap of the valve (that portion which views the injector) is painted with sicon aluminum paint. Finally, the entire heat shield assembly is gold-plated on all external and internal surfaces [E-17].

d. Thrust Chamber Valve. For control of propellant flow to the thrust chamber, the REA uses an all-welded, metal-to-metal seat, normally closed solenoid valve. The valve is manufactured by the Systems Division of the Aerospace Group of Parker-Hannifin. An important design feature of the TCV is that it incorporates no sliding fits such as those required in more conventional coaxial solenoid valve designs. Consequently, the TCV is insensitive to contamination and/or thermal cycling (distortion) effects on opening and closing response and force margins (i. e. , TCV hangup or seizure is essentially eliminated).

All of the valve components which come in contact with the fluid media (hydrazine) are fabricated from 300 series stainless steel, with the exception of the magnetic circuit (solenoid shell and armature) and the poppet, which are fabricated from 430 and 17-4PH stainless steel, respectively.

Since the valve is subjected to a relatively large number of cycles, including a cycle life margin capability of 10^6 cycles, the hard-seat design was chosen over a soft-seat design. Extensive process development by Parker-Hannifin has resulted in seat/poppet surfaces which will not degrade over life and, hence, will maintain zero liquid internal leakage and a maximum gas leakage of 10 scc/hr GN_2 . Table E-15 summarizes the TCV performance/design characteristics [E-17].

e. Thrust Chamber Assembly. Table E-16 summarizes the design parameters of the REA. Monopropellant hydrazine is injected from the TCV through the feed tube and through the injection element into the Shell 405 catalyst bed. Catalyst bed dimensions were determined by use of monopropellant hydrazine design and scaling criteria developed by Rocket Research Corporation under contract to Jet Propulsion Laboratory, NAS-7-373 [E-18]. The granular Shell 405 ABSG catalyst, purchased to a Rocket Research Corporation material specification, is constrained between the catalyst bed plates and the injector face.

Prior to assembly, Haynes 25 screens are tack-welded to both sides of the bed plates to eliminate any migration of catalyst within and out of the catalyst bed. With the exception of the injector, which is Inconel, all other parts of the TCA are fabricated from Haynes 25 with the thrust chamber being machined from Haynes 25 bar including the 40:1 RAO expansion nozzle [E-17].

f. Heat Shield Assembly. The heat shield assembly consists of two gold-plated shields fabricated of 0.012 inch thick Haynes 25 sheet. These shields are rolled and the seam is electron beam welded. The forward shield is electron beam welded to the mounting flange, and the forward and aft shields

TABLE E-15. TCV PERFORMANCE/DESIGN CHARACTERISTICS [E-17]

Parameter	Requirement
Pressure Drop	14.6 ± 1.6 psid at 0.01169 lbm/sec
Internal Leakage	10 scc/hr GN ₂ max from 0 to 300 psig
External Leakage	6 × 10 ⁻⁶ scc/sec He max at 300 psig
Service Life	250 000 cycles
Response	
Opening	4.2 ± 1.0 msec at 85 psig, 35° F, and 33 Vdc
	5.1 ± 0.5 msec at 180 psig, 70° F, and 28 Vdc
	6.5 ± 1.0 msec at 215 psig, 250° F, and 24 Vdc
Closing	6.6 ± 1.0 msec at 85 psig, 35° F, and 33 Vdc
	5.5 ± 0.5 msec at 180 psig, 70° F, and 28 Vdc
	4.5 ± 1.0 msec at 215 psig, 250° F, and 24 Vdc
Operating Voltage	20 to 33 Vdc
Power Drain	29.0 W max
Pull-in Voltage	20.0 Vdc max
Drop-out Voltage	2.5 Vdc min

TABLE E-16. REA DESIGN SUMMARY [E-17]

Parameter	Data
Catalyst	Shell 405
Nozzle	
Expansion Ratio	40 : 1 (RAO)
Throat Diameter, in.	0.197
Exit Diameter, in.	1.246
Material of Construction	
[⊗] Thrust Chamber	Haynes 25 (L605)
Injector and Feed Tube	Inconel 600
Heat Shield Assembly	CRES 304 (flanges) Haynes 25 (shields)
Weight, lbm	
Heat Shield and Support	0.41
Thrust Chamber	0.39
Valve	<u>0.40</u>
Total REA	1.20
Dimensions, in.	
Thrust Chamber Diameter	1.18
Thrust Chamber Length	3.74
Thrust Chamber Valve Length	<u>1.59</u>
Total REA Length, in.	5.33

are each electron beam welded to mating discs. During REA buildup, the forward heat shield assembly, together with the thermal spacer, is bolted to the TCV following welding of the TCV to the thrust chamber. At this time, a thermocouple is welded to the convergent section of the thrust chamber and a 0.125 inch chamber pressure sensing tube is welded to the P_c adapter.

The P_c tube and thermocouple are routed through clearance holes 180 degrees apart in the heat shield discs. The aft heat shield assembly is joined to the forward heat shield assembly with four small melt-down welds on the mating discs [E-17].

g. REM Thermal Design. Development of the REM thermal design was guided by two sets of constraints. The first set, imposed by the LMSC detail specification, included the REM thermal environment range, performance requirements (impulse bit size, thrust level, etc.), desired operational duty cycles, and allowable thermal interactions with the spacecraft. The second set consisted of available enthalpy, structural requirements, and catalyst bed design requirements developed from Rocket Research Corporation's experience with hydrazine systems. Table E-17 summarizes the REM passive vehicle-imposed thermal interfaces and design constraints.

The initial design objectives envisioned passive thermal control during all operational modes at 20° F environment. Early in the program, vehicle level mission analyses indicated that operation at temperatures below 20° F and periods of complete REA inactivity were possible and would require the addition of REM plate heaters to maintain valve temperatures and thermal short heaters to maintain the catalyst beds at temperatures which would provide satisfactory steady-state start characteristics.

Operational characteristics of the firing REA are dependent upon the gas temperature and frequency of operation. The chamber temperature of the firing unit should be maintained as high as practicable for achievement of maximum performance, while allowing controlled amounts of conductive and radiative heat dissipation to maintain other REM components within acceptable operating temperatures. At the pulsing frequency of 0.01 Hz, the REA gas temperature must be sufficient to meet specified performance requirements under MIB operating conditions. Lower operational activity is limited by valve temperatures, adjacent REA cold restart capabilities, and available heater power, rather than by vehicle-imposed performance requirements.

TABLE E-17. REM-MONO THERMAL DESIGN/MANAGEMENT SUMMARY (PASSIVE) [E-17]

Design Parameter	Goal	Intent of Goal	Limiting Values	Predicted/Demonstrated Values
REA	Thermal Isolation	Maximize performance consistent with valve temperature control	Maximize pulse mode I_s	$I_s = 129$ lbf-sec/lbm
	Nozzle	Optimize	Minimum propellant consumption and heat loss	
	Maximum Bulk Hydrazine Injection Temperature	300° F	Prevent bulk boiling during injection	335° F
	Minimum Valve Temperature (Standby)	40° F	Prevent propellant freezing	35° F
	Maximum Valve Temperature	225° F	Avoid valve or propellant overheating	275° F
REM	Total Heat Rejection to Spacecraft	85 Btu/hr, Hz ≤ 0.03 225 Btu/hr, Hz > 0.03	Avoid upset of vehicle thermal control	70 Btu/hr, Hz < 0.03 168 Btu/hr at steady state
	Pressure Transducer Operating Temperature Range	0° F to 200° F	Assure instrument linearity	56.5° F to 195° F
	Minimum Chamber Temperature (Standby REAs)	40° F	Assure reliable start	20° F or less 17.1° F

The main path of heat conduction from the firing REA to other components is through the propellant feed tube. Heat conducted through the feed tube reaches the valve which is thermally linked to all other valve bodies. During minimum duty cycle modes of operation, all valve temperatures are kept above freezing by the direct interconnection. At higher duty cycles, heat dissipation by radiation from the REA surfaces to the radiation shield and to space diverts the valve thermal load. The shields are conductively isolated from the REA surfaces. The shield reradiates heat to the operating REA to increase performance and minimize heat losses to the spacecraft.

The nozzles are instrumental in the overall heat balance because of the wide range of temperatures they view during an orbital period. In sizing the various REA conductive paths, nozzle view temperature conditions are conservatively fixed. During maximum and minimum duty-cycle operations, the nozzles view +140 and -460° F, respectively.

Temperature distributions throughout the REM structure are controlled by radiation and conduction heat paths from either the active or backup pair of REAs. Conductive heat loss to the spacecraft is minimized by isolation of the REM structure from the interface plate by means of thermal standoffs. Radiation heat loss from the hot REA surface to the spacecraft is greatly reduced by the cylindrical radiation shield placed over the entire length of REA surface. At low duty cycles, the active, nonfiring, catalyst bed temperature is maintained at a level sufficient to ensure smooth ignition by a thermal wire short. For very low duty cycles, or for starts after periods of no activity, an electrical resistance heater (catalyst bed heater) is mounted to the thermal short. Electrical resistance heaters (valve heaters) are also mounted on the REM mount plate to ensure proper valve temperatures at extremely low spacecraft temperatures. One valve heater in parallel with a catalyst bed heater supplies heat to the valves and catalyst beds of the two active REAs in a REM. An identical system is provided for the standby REAs. The standby heaters are inactive as long as the active REAs are functioning. The REA valve heaters are thermostatically controlled, and one heater requires 21 watts of electrical power at 33 Vdc. The catalyst bed heaters are not thermostatically controlled but are commandable on-off, and one heater requires 3 watts at 33 Vdc.

As was just described, the REAs are clustered in the REMs for thermal management, which is a major factor in hydrazine engine life. The REAs are thermally linked, isolated, and insulated to achieve highest possible

operating temperatures. REA temperature is maintained passively by heat generated during heavy duty cycle REA activity, and the active electrical heating system is available as backup during a low REA duty cycle.

Tables E-18 and E-19 summarize the passive and active thermal management requirements and design goals, as well as the approach or results achieved. Table E-20 summarizes the entire RCS electrical power requirement [E-17].

TABLE E-18. REM-MONO THERMAL MANAGEMENT REQUIREMENTS (PASSIVE MODE) [E-17].

Condition	Hot Environment	Nominal Cold Environment	Extreme Cold Environment
REM Surroundings	+140° F	+20° F	+20° F
Propellant Supply	+140° F	+40° F	+40° F
Nozzle Exit View	+140° F	-460° F	-460° F
Duty Cycle	Variable (incl. worst case TCV temperature)	0.01 Hz (MIB)	Total impulse per orbit ≤ 1.79 lbf-sec; off times up to 2100 seconds
Number REAs Active	Two worst case	One	One or alternate firing REAs

h. REM Structural Design. The REM structural design was, of necessity, closely integrated with the thermal and performance design requirements, the envelope requirements, and the environmental requirements for vibration and pyrotechnic shock. The resultant structural design provides the necessary strength where required, yet still provides thermal isolation or thermal linkage consistent with thermal management constraints. The major element of the REM structural design is the REM mounting structure (REM plate) to which the four REAs are mounted. The two outboard REAs are used for yaw control and are mounted with their centerlines at a 90-degree angle

TABLE E-19. REM-MONO THERMAL
MANAGEMENT (ACTIVE MODEL) [E-17]

<u>Requirements</u>
1. Propellant valve temperature: $\geq 40^{\circ}\text{F}$ (min.) and $\leq 85^{\circ}\text{F}$ (max.)
2. Catalyst bed temperature (active and/or standby) sufficient to assure satisfactory REA operation.
<u>Conditions</u>
1. No REM activity
2. Any duty cycle
3. Surrounding environment: -10°F to $+20^{\circ}\text{F}$ (propellant temperature = $+40^{\circ}\text{F}$; nozzle view = -460°F)
<u>Design Approach</u>
1. Redundant REM plate (TCV) thermostatically controlled heaters
2. Thrust chamber heaters (one each REA pair)

TABLE E-20. RCS POWER REQUIREMENTS

Item	Power (watts at 33 Vdc)
REA Valve	29
REM Valve Heaters (4 active) ^a	21 per heater
REM Catalyst Bed Heater (4 active)	3 per heater
REM Instrumentation	≈ 1 per REM
Isolation Valves	108 per valve
Propellant Tank Heaters ^a	5 per tank
Propellant Tank Instrumentation	≈ 1 per tank

a. Thermostatically controlled

from the two inboard pitch/roll REAs. Each REA is identical and is a self-contained subsystem with integral thermal control and structural integrity when mounted at the valve/thermal shield mounting plate. The REM mounting structure provides a thermal linkage between all four thrust chamber valves and REAs.

Propellant is provided to each pair of REA propellant valves through a common manifold fitting which incorporates a braze tube terminus at the vehicle interface. Welded or brazed connections are used in the REM system for all propellant and pressure vessel components.

The mounting structure is attached to the vehicle through an interface plate and cage assembly consisting of four titanium standoffs. The titanium standoffs provide thermal isolation between the vehicle and the mounting structure and also provide damping to reduce shock and vibration loads applied in the two axes normal to the centerline of the standoffs. Damping of loads in the axis parallel to the standoff centerline is provided by the cage assembly, which incorporates shock isolators.

The four electrical connectors for the valve leads, heater leads, and instrumentation leads are located on the interface plate [E-17] .

i. REA Performance. Rocket engine assembly performance and requirements for the LMSC SCS mission are summarized in Table E-21. Table E-22 presents the detailed steady-state performance of the REA over the nominal REM operating range. The thrust developed by each REA varies with feed pressure as shown in Figure E-73. The thrust available for control about each vehicle axis is twice the quantities shown because two engines are available for pitch, yaw, and roll about each axis in two directions.

Pulse mode REA performance has been mapped at 0.022 second pulse width and frequencies ranging from 0.01 to 10 cps. These data (one temperature condition presented in Figures E-74 and E-75) include impulse bit, and specific impulse, respectively. The effect of electrical pulse width upon impulse bit delivered is shown in Figure E-76. The impulse bit about each axis of the vehicle is twice the quantities shown in Figure E-74 and E-76 when two engines are thrusting.

TABLE E-21. ENGINE PERFORMANCE/REQUIREMENTS [E-17]

Parameter	Performance
Specific Impulse, Steady State	
Nominal Initial	232.5 lbf-sec/lbm
Nominal Final	226.7 lbf-sec/lbm
Minimum Required	205 lbf-sec/lbm
Total Impulse	18 000 lbf-sec
Total Number of Pulses	175 000
Duty Cycle	0.004 cps to steady state (5 min)
Pulse Width	22 msec to steady state
Vibration (Random)	37.9 g rms
Operating Temperature	+40° F to +140° F

Pulse mode REA response is measured during each MR-50A REA acceptance test at feed pressures of 233 and 117 psia as percent total impulse delivered at specific times. The duty cycle of this test is 0.1 cps, with a pulse width of 0.022 second (0.22 percent duty cycle). Based upon qualification and acceptance test results of end item REAs to date, the minimum observed pulse mode response is approximately 60 percent in 50 milliseconds and 70 percent in 100 milliseconds from valve signal for these conditions [E-17].

j. Conclusions. The REM just described is flight-qualified for a Lockheed program. The REM is an extremely sophisticated design which meets stringent thermal, performance, and structural requirements. The resultant design, being totally welded and brazed, is a compact, fully integrated module with no external seals or fittings. The subject REM, which incorporates four complete REAs, has been subjected to an extensive development and qualification program for Lockheed's application, which included a continuous orbital life test covering all mission temperature, duty cycle, and feed pressure conditions.

TABLE E-22. REA PERFORMANCE SUMMARY
NOMINAL OPERATING CONDITIONS [E-17]

Parameter	Units	Initial	Final
Feed Pressure	psia	233	117
Propellant Temperature	° F	70	70
Chamber Pressure	psia	103.6	59.8
Mass Flow Rate	lbm/sec	0.02413	0.01403
Characteristic Exhaust Velocity	ft/sec	4264	4228
Thrust Coefficient		1.753	1.725
Altitude Thrust	lbf	5.61	3.18
Specific Impulse	lbf-sec/lbm	232.5	226.7
Ammonia Dissociation	%	63.5	65.3
Exhaust Gas Temperature	° F	1623	1597

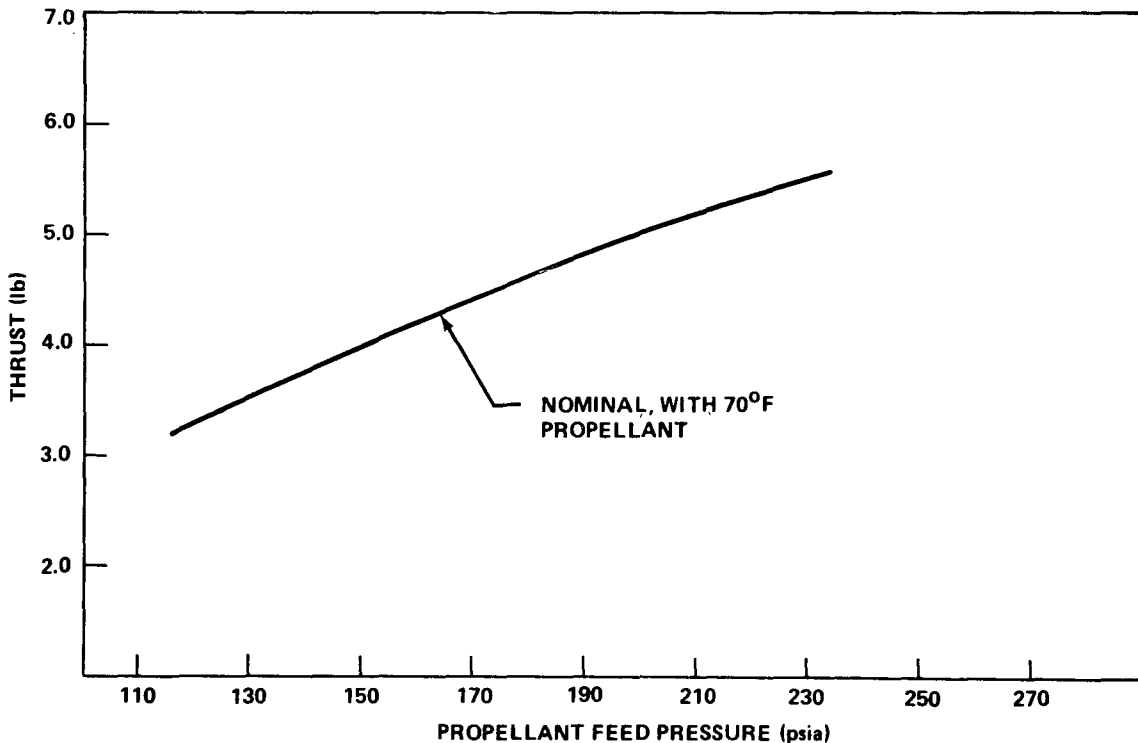


Figure E-73. MR-50A REA thrust as function of propellant feed pressure [E-17].

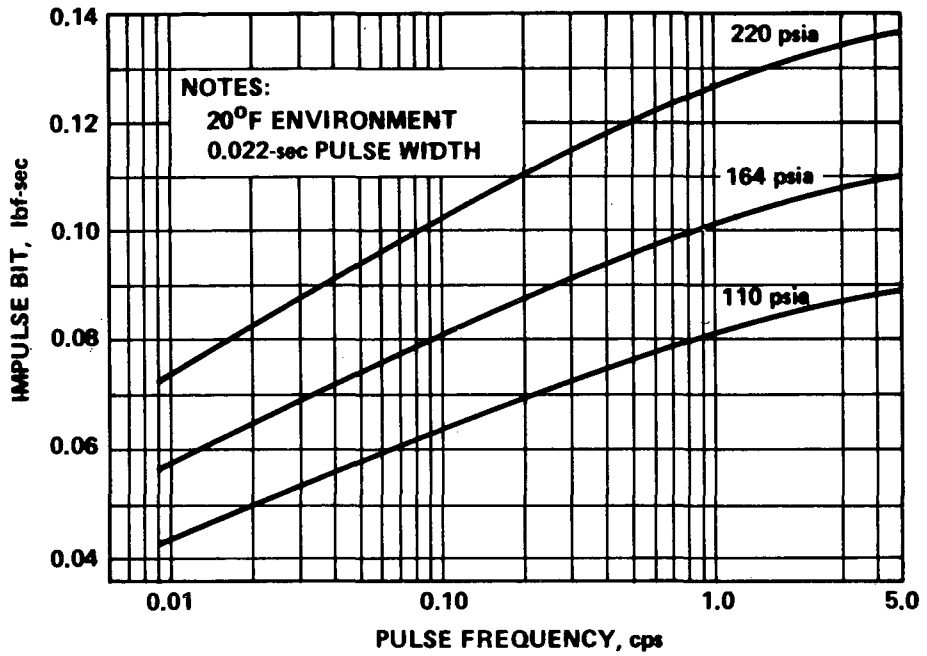


Figure E-74. MR-50A REA impulse bit as a function of pulse frequency [E-17].

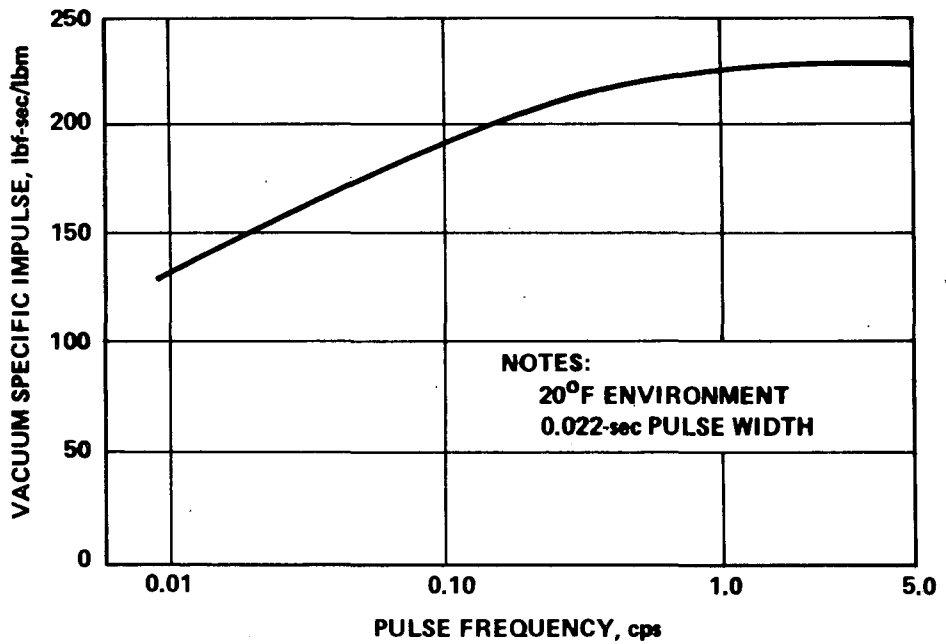


Figure E-75. MR-50A REA vacuum specific impulse as a function of pulse frequency [E-17].

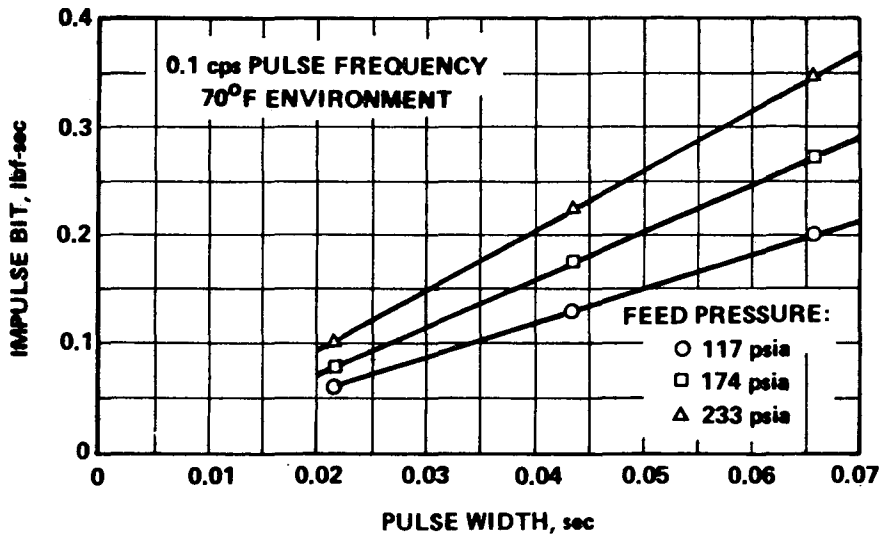


Figure E-76. MR-50A REA impulse bit as a function of pulse width [E-17] .

The achievement of such an integrated design requiring extended orbital life demonstration is not necessarily straightforward. Once developed and qualified, however, such a module affords an extremely clean vehicle interface, because roll, yaw, and pitch thrusters; associated instrumentation; structural mounts; and passive and active thermal control systems are contained in one package requiring minimum maintenance and providing essentially direct plug-in capability to the vehicle [E-17] .

2. Alternate Reaction Control System Concepts for the Baseline

HEAO-C Spacecraft. This section summarizes and describes three alternate RCS concepts that were considered for the baseline HEAO-C spacecraft. First, the concept of an alternate location of the REMs on the RCM for the baseline HEAO-C RCS is discussed. Second, the concept of manifolding the RCS tanks to the main tank of the OAS for propellant transfer is discussed. This concept demonstrates the growth capability of the baseline HEAO-C RCS should the propellant budget increase. Third, a cold gas RCS for the HEAO-C spacecraft is discussed.

a. Baseline HEAO-C RCS Alternate REM Location. Figure E-77 presents a layout of the major components of this system. This RCS is identical to the baseline HEAO-C RCS, except the REMs are relocated at 90 degree intervals around the circumference of the RCM. The REM location points lie on the RCM on the spacecraft $\pm Y$ and $\pm Z$ coordinate axes. For the baseline

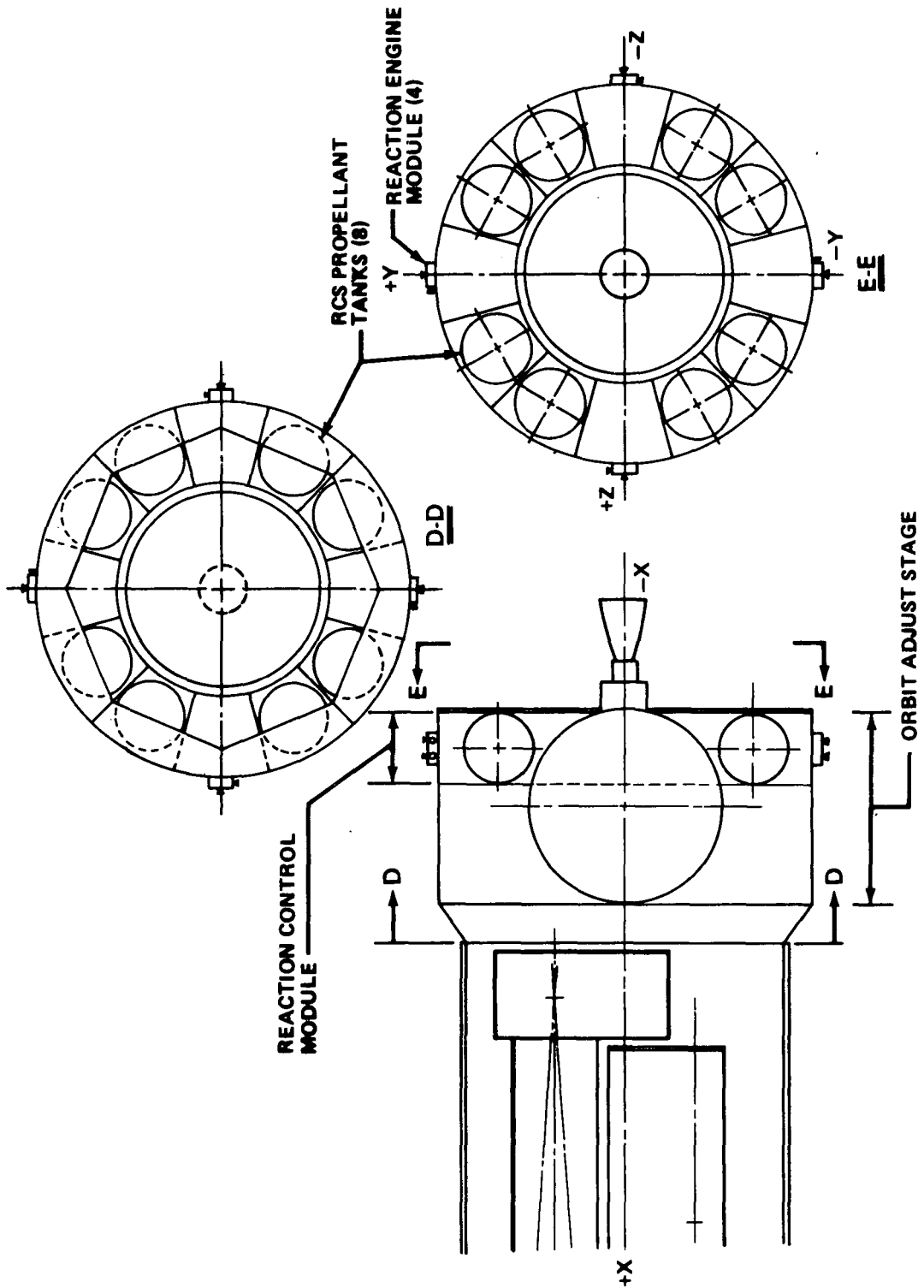


Figure E-77. Layout of alternate baseline RCS major component locations.

RCS, the REMs are located on the RCM one foot from the Y plane along the +Z and -Z axis and on the $\pm Y$ sides of the spacecraft. The primary driver in selecting the baseline concept was that the concept already exists on the Lockheed SCS, and modifications such as placing the REMs at 90 degree intervals around the RCM would result in higher cost. However, the cost involved in relocating the REMs is not expected to be of significant magnitude, and the 90 degree interval concept does have some advantages which are discussed later.

The baseline configuration is advantageous in providing cleaner firing logic, and in most cases, one REA is pulsed to effect a combined pitch/roll or a yaw/roll maneuver. To perform a pure pitch or a pure yaw maneuver with the baseline concept, two REAs have to be fired simultaneously. This results in twice the thrust and essentially half the burn time as would be required with the 90 degree configuration, in which one REA is fired to perform the same maneuver. In the case of the 90 degree configuration, a roll component vector cannot be effected by firing a pitch or a yaw REA. A plus or minus roll maneuver is accomplished by firing an appropriate REA or coupled pair of REAs configured only to perform that maneuver (see Figure E-77).

The 90 degree configuration is advantageous in that a REA is fired for longer periods of time when performing a maneuver, which results in better performance and more efficient utilization of the REAs. Longer REA burn times increase the operating temperature of the REA which, in turn, delivers a higher specific impulse, thus minimizing the amount of propellant needed to perform a particular maneuver. Higher REA operating temperatures also have a significant effect on increasing the REA catalyst bed lifetime. A control analysis has indicated that a RCS thrust level of five pounds or less in all planes is sufficient to maintain attitude control during the mission. This also includes control during the OAS burns, assuming a worst case main engine misalignment and other disturbing torques. From a thermal point of view, the 90 degree configuration may present a problem since one of the REMs will always be on the cold side of the spacecraft. This particular REM could demand much activity from its active thermal control system. However, from a propulsion efficiency point of view, the 90 degree configuration appears to be best.

In a follow-on Phase B study, it is suggested that a detailed trade-off analysis be performed between the baseline concept and the 90 degree configuration to determine which is better. This analysis should include such

parameters as cost, propulsion efficiency, REA lifetime, and thermal requirements.

b. RCS/OAS Main Tank Manifold. The RCS/OAS main tank manifold concept is also identical to the baseline RCS, except that four tanks are used instead of eight and the RCS is manifolded to the main propellant tank of the OAS. The main propulsion system of the OAS also utilizes monopropellant hydrazine, and a RCS/OAS propellant manifold allows the REMs to be supplied with propellant from either the main tank or the RCS tanks. Propellant transfer from the main tank to the RCS tanks can also be accomplished by this concept.

Figure E-78 presents an isometric layout of the manifold concept. The purpose of this concept is to demonstrate the propellant growth capability available should the RCS propellant budget for the HEAO-C mission increase. As was discussed in Chapter VII of the baseline report, nine bays are available in the RCM, each of which could house a propellant tank. Eight tanks are required to contain the propellant needed for the baseline RCS; however, should the propellant requirement increase slightly, a ninth tank could be added to the system. Should the propellant requirement increase beyond the capacity of being contained in nine propellant tanks, or should more propellant redundancy be required for reliability purposes, then it is suggested that the additional propellant be located in the main tank of the OAS with propellant transfer available to the RCS.

When operating in a blowdown, pressure-fed mode, the maximum propellant loading of the main tank of the OAS is 2910 pounds. Of this 2910 pounds, approximately 1200 pounds are allocated for use during the OAS burns to put the HEAO-C spacecraft into the proper orbit. The remaining 1710 pounds are available for RCS use. The OAS pressurizing gas is nitrogen, and the initial pressure is 310 psia at the 2910 pound propellant loading. As propellant is used, this pressure decreases, and at propellant depletion the tank pressure is 100 psia. The OAS propellant tank does not employ any diaphragms for the propellant/pressurization system. Gas-free propellant feed under zero-g conditions is insured by a system of collection and feed galleries leading to the tank outlet. These galleries consist of two rings oriented 90 degrees to each other which conform to the inside wall of the tank. These rings intersect each other at the top and bottom, or outlet, of the tank. Propellant is collected, held, and transported through these galleries to the tank outlet by surface tension forces in the propellant. As shown in Figures E-78 and E-79, the RCS/OAS propellant manifold line connects to the main propulsion system

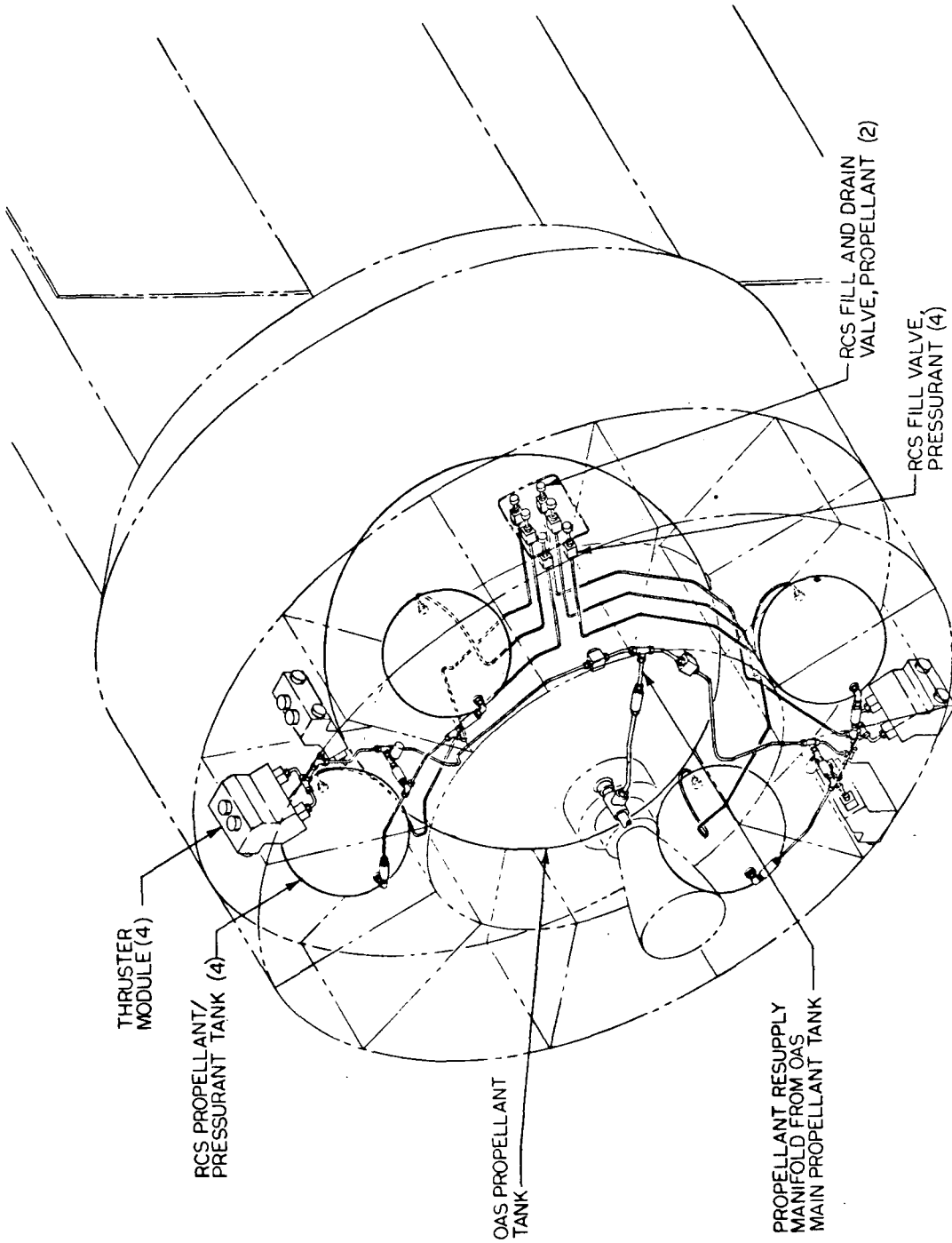


Figure E-78. RCS/OAS maintank manifold isometric layout.

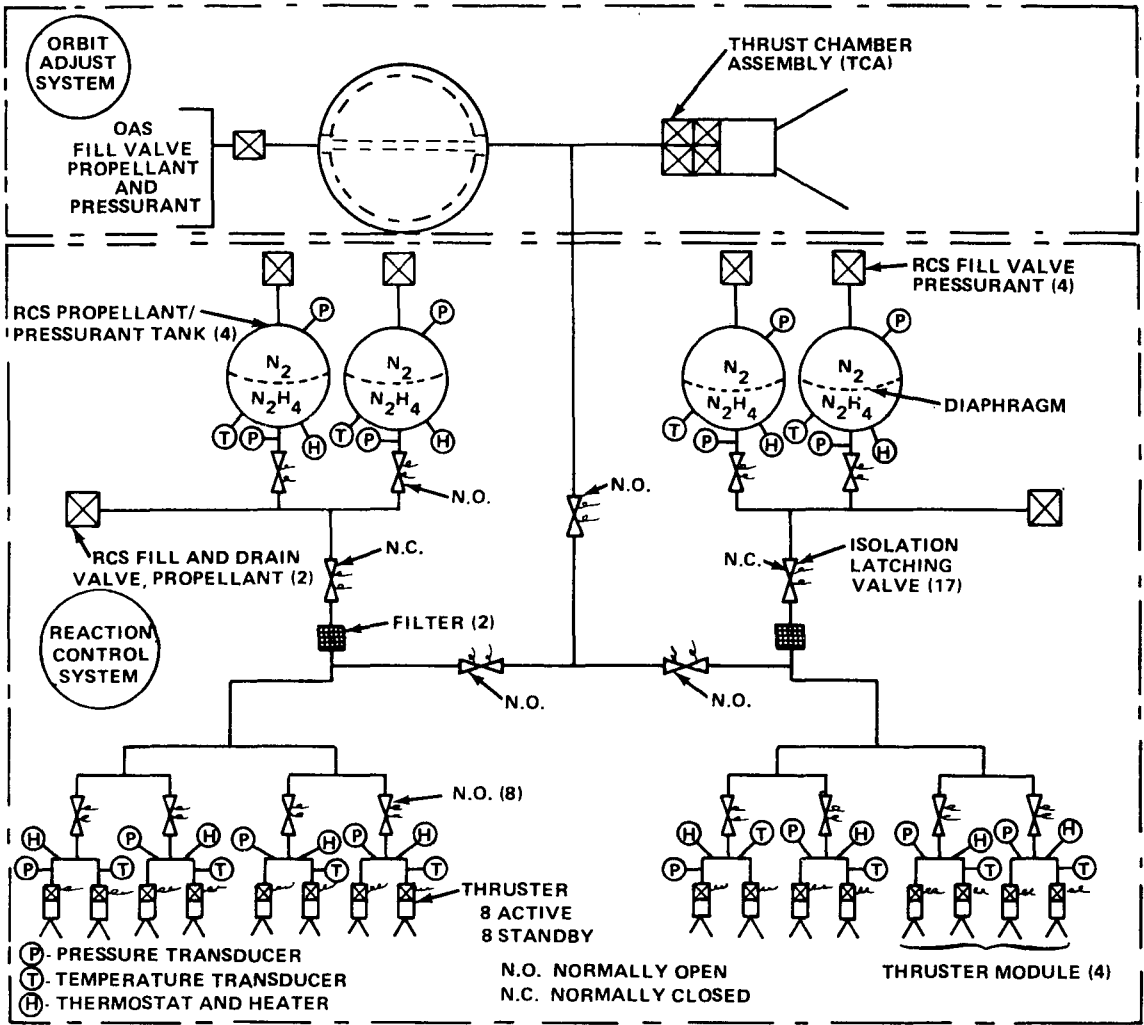


Figure E-79. System schematic of the RCS/OAS main tank manifold concept.

propellant supply line between the OAS propellant tank and the main engine valves. Flight experience has demonstrated that the surface tension propellant collection system performs well. Propellant transfer from the main tank to the RCS tanks is a backup mode available on the Lockheed SCS; this process has also been demonstrated in flight.

Figure E-79 presents a functional schematic of the RCS/OAS main tank manifold concept, and a weight statement for this concept is presented in Table E-23. The functional operation of this system is explained as follows.

TABLE E-23. RCS/OAS MAIN TANK MANIFOLD
CONCEPT WEIGHT SUMMARY

Item	Component Weight (lb)
GN ₂ Fill and Drain Valve (4)	1.00
Propellant Fill and Drain Valve (2)	0.60
Isolation/Shutoff Valve (17)	10.20
Tank, Including Thermostats and Heaters (4)	69.00
Pressure Transducer, Other Than REM (16)	4.80
Temperature Transducer, Other Than REM (4)	0.56
Filter (2)	0.50
REM, Including Thermostats and Heaters, Instrumentation, and Other Associated Equipment (4)	36.00
Plumbing	<u>10.00</u>
System Dry Weight	132.66
Propellant N ₂ H ₄	412.00
Pressurant GN ₂	<u>9.33</u>
Total System Weight	553.99

Additional Propellant Weight is Carried in the Main Tank

As was mentioned previously, approximately 1710 pounds of hydrazine could be provided in the OAS propellant tank for use by the RCS. In addition, four RCS tanks are also available to supply 412 pounds of propellant. Unlike the Lockheed SCS, the propellant in the main tank is not used to resupply the RCS tanks as they become depleted, even though the system can be operated in this manner. The primary functional operation of this system is to utilize

the propellant in the main tank by feeding propellant to the REMs through the manifold feed line (see Figure E-79). The RCS tanks are isolated from the system by closed isolation valves and are on standby as a redundant system should a main tank failure necessitate isolating that part from the RCS. The four RCS tanks are also available should the main tank deplete its propellant supply before the mission is completed. Four RCS tanks should provide the RCS propellant backup capability of completing one year of the mission, assuming no failures. The number of RCS tanks in this system can be expanded to nine should the amount of propellant needed increase. The function of the RCS tanks is identical to the baseline; i. e., there are two banks of tanks, each bank and each tank is capable of being isolated, and propellant transfer from one unit to the other is possible.

The initial use of propellant out of the main tank instead of the RCS tank was chosen because this method is believed to be more reliable than transferring propellant from the main tank to the RCS tanks. The transferring of propellant involves the cycling of isolation valves as well as tank diaphragms which has a tendency to lower the reliability of the system.

c. A Cold Gas RCS/Magnetic Torquer Concept. The use of magnetic torquers for continuous CMG desaturation has been proposed as an alternate control concept for the HEAO-C spacecraft. The magnetic torquers become effective after the OAS burns, and attitude control during these burns is provided by a cold gas thruster system. The design of this cold gas thruster system is similar to the one used as a backup to the hydrazine system on the Lockheed SCS. The cold gas system can also be expanded for use as a backup system for the magnetic torquers to provide a large impulse capability for a particular maneuver. The configuration described utilizes components and systems of LMSC flight-qualified hardware.

Figure E-80 presents an isometric layout of the cold gas/magnetic torquer system as proposed for the HEAO-C spacecraft. This cold gas attitude control system is based on the use of tetrafluoromethane (CF_4), qualified hardware, and the flight-proven reliability of similar Agena systems. Freon-14 was chosen because of its high density, relative inertness, and low critical temperature. It is also readily available without requiring special storage or handling procedures. A functional schematic of the system is shown in Figure E-81. The system is comprised of two 5382 cubic inch gas storage tanks (each with a thermal management system), a dual-level pressure regulator, two triple configured thrust valves, a manual fill valve, and

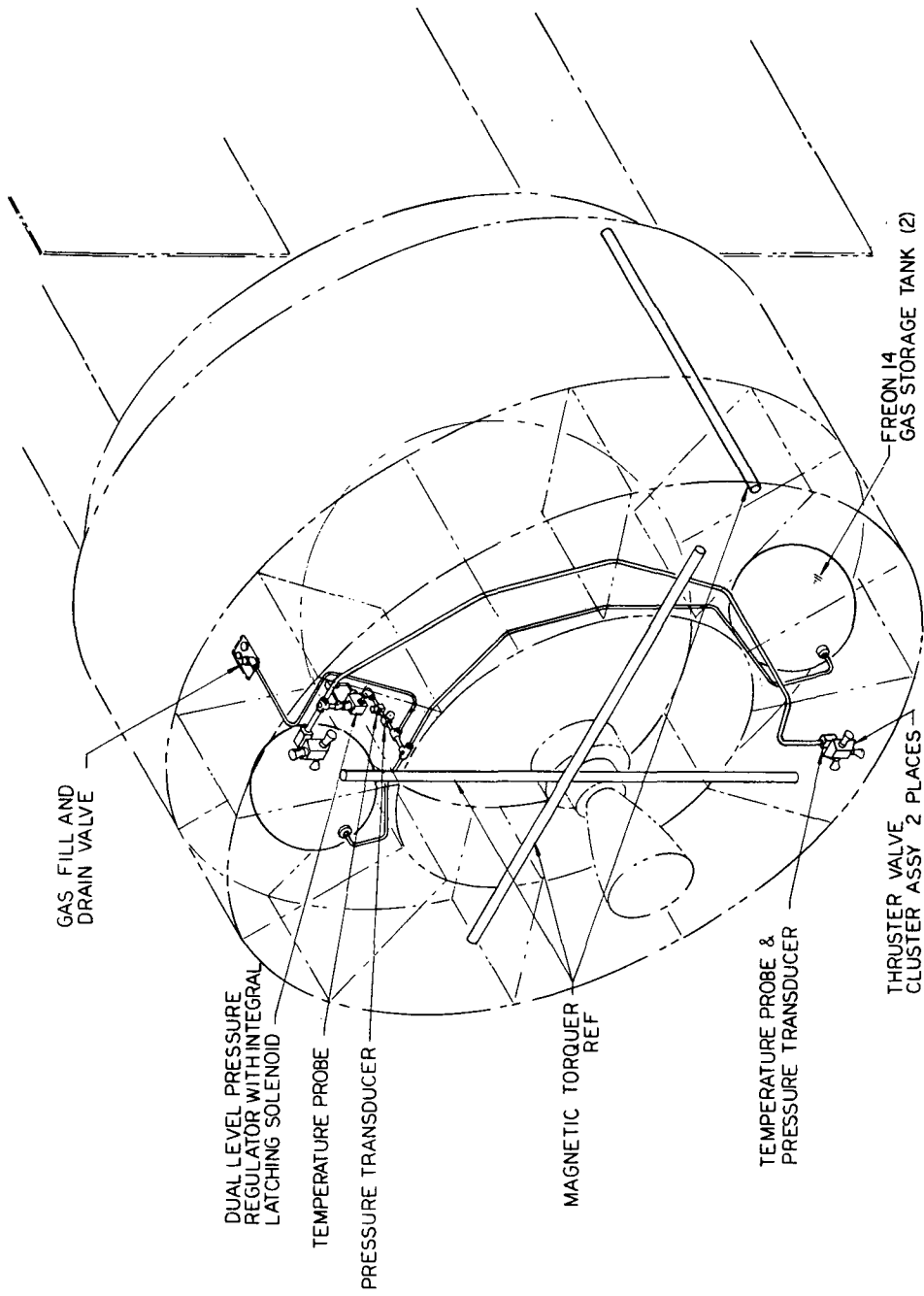


Figure E-80. Cold gas RCS/magnetic torquer isometric layout.

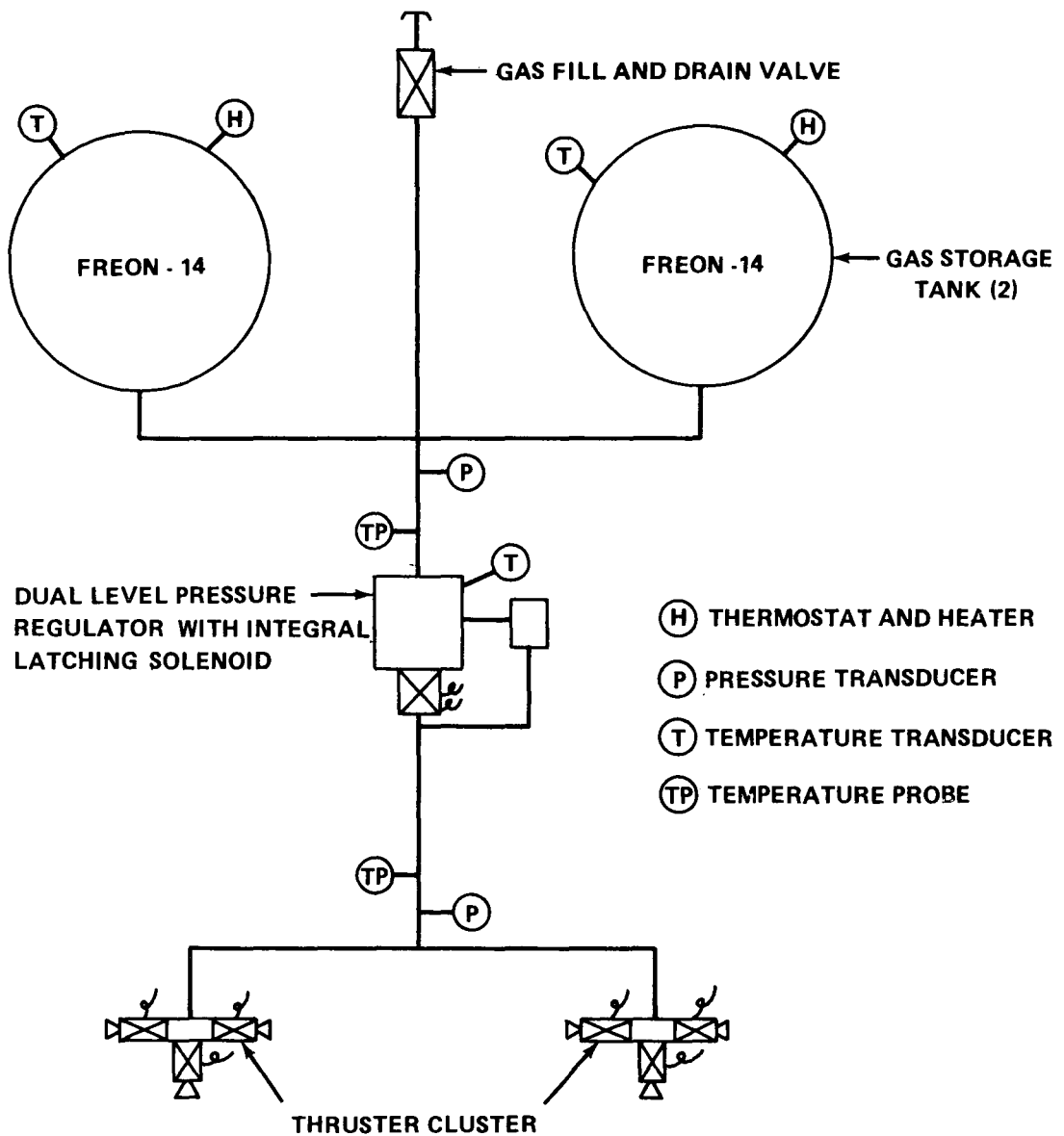


Figure E-81. System schematic of the cold gas RCS [E-19] .

instrumentation required for checkout and diagnostic purposes. The pressure regulator contains an integral latching type solenoid valve which isolates gas flow to the thrust valves until commanded open by ground command. This valve is also capable of being commanded closed. The tank thermal management system permits heating the gas in the 160° F to 185° F range. The thrust

valve is a direct acting solenoid with a convergent-divergent nozzle attached to the outlet of the valve to provide efficient conversion of gas energy into thrust. A nominal specific impulse for this system is in the range of 37 seconds to 45 seconds plus, depending on the temperature of the gas.

The regulator output pressure and thrust valves are designed to permit two different thrust levels from the same system. Thrust level capabilities with the dual-level regulator are 10 pounds and 0.5 pound. During periods of large perturbations or vehicle disturbances, such as occur during the OAS main engine burns, the high thrust level maintains control of the vehicle. The low thrust permits operation during normal limit cycling to counteract small torque disturbances on the vehicle. The low thrust level is also available as an aid to the magnetic torquer system. The system provides 5500 pound-second minimum impulse using an isentropic blowdown and 165 pounds of Freon-14 gas. The system is capable of 7250 minimum pound-seconds by loading to maximum system capability (290 lb) using an isentropic blowdown rate of usage. System maximum capability increases to 12 900 pound-seconds using isothermal blowdown rates. The loading and unloading of control gas are accomplished by means of a manually operated fill valve. The fill valve incorporates redundant seals when in the flight-ready configuration.

Brazed type plumbing connections are used through the system to assure leak-tight seals. The system is designed for a two to one safety factor (design burst pressure to maximum operating pressure) to permit complete access to the vehicle by personnel in the immediate area. This also allows manual connections and final checkout after ground support equipment has been removed, rather than using fly-away type umbilical couplings. The system is capable of several weeks of hold in a ready condition on the pad prior to launch.

The system weight, excluding the gas, is approximately 135 pounds.

The flexibility and alternatives of the present SCS are extensive. As shown in Figure E-82, a total of nine additional bays could be used for gas storage tanks. Qualified high pressure isolation valves are available which permit designing redundant systems with the capability of transferring control gas from one system to the other. The isolation valves can also isolate the pressure regulator and thrust valve from the storage tanks. The amount of gas available with 11 tanks used in conjunction with the 0.5 pound thrust level provides a large amount of backup impulse capability for the magnetic torquers [E-19] .

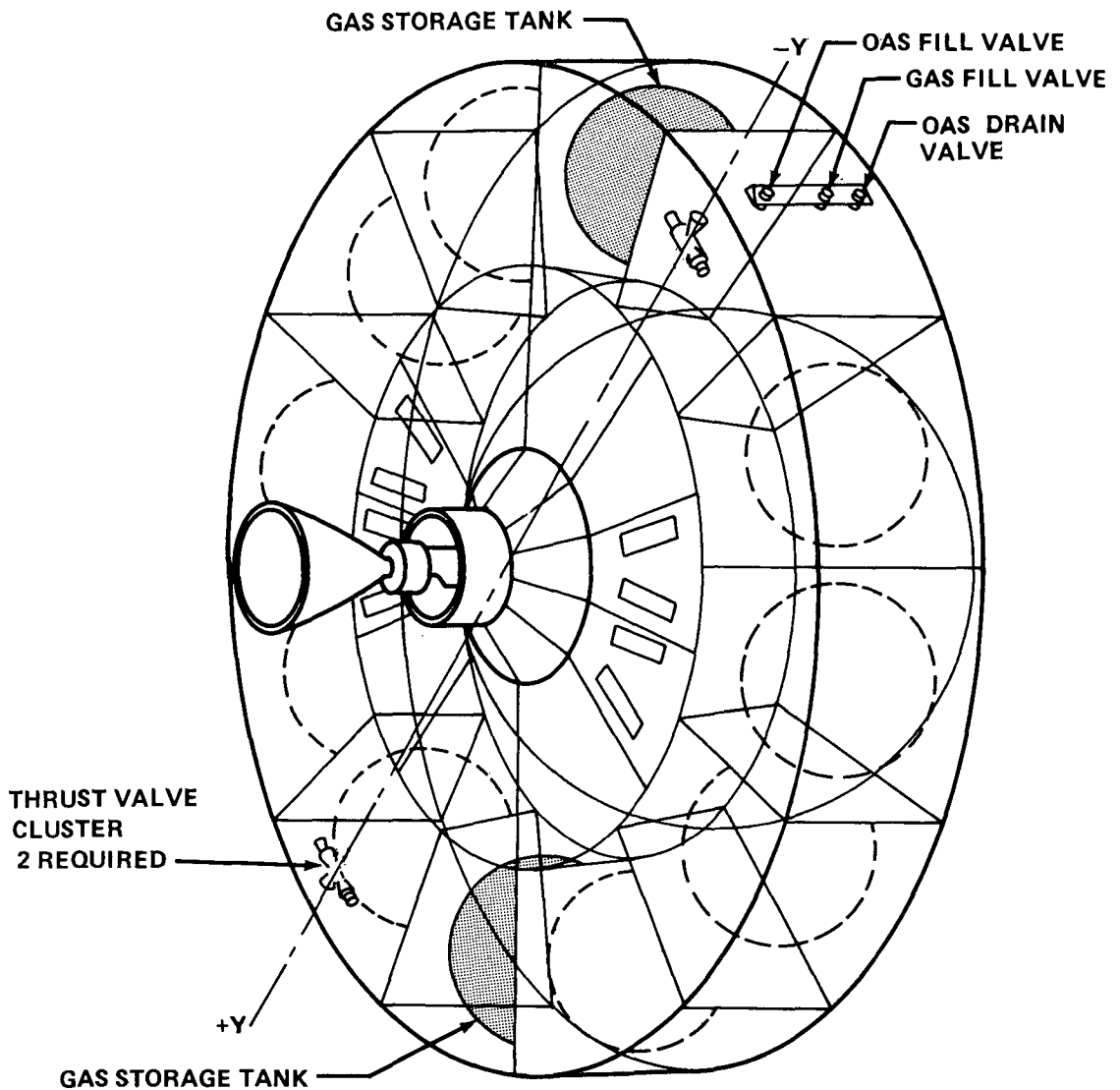


Figure E-82. Alternate cold gas RCS concept [E-19] .

3. Reaction Control System Concepts for Alternate HEAO-C Spacecraft. This section presents a summary of some of the HEAO-C spacecraft concepts and associated RCS concepts that were configured early in the HEAO-C study.

Figure E-83 presents a HEAO-C concept that was configured before the ground rule was established that the OAS would remain attached. With the OAS detached, this concept utilizes a subsystem module located aft of

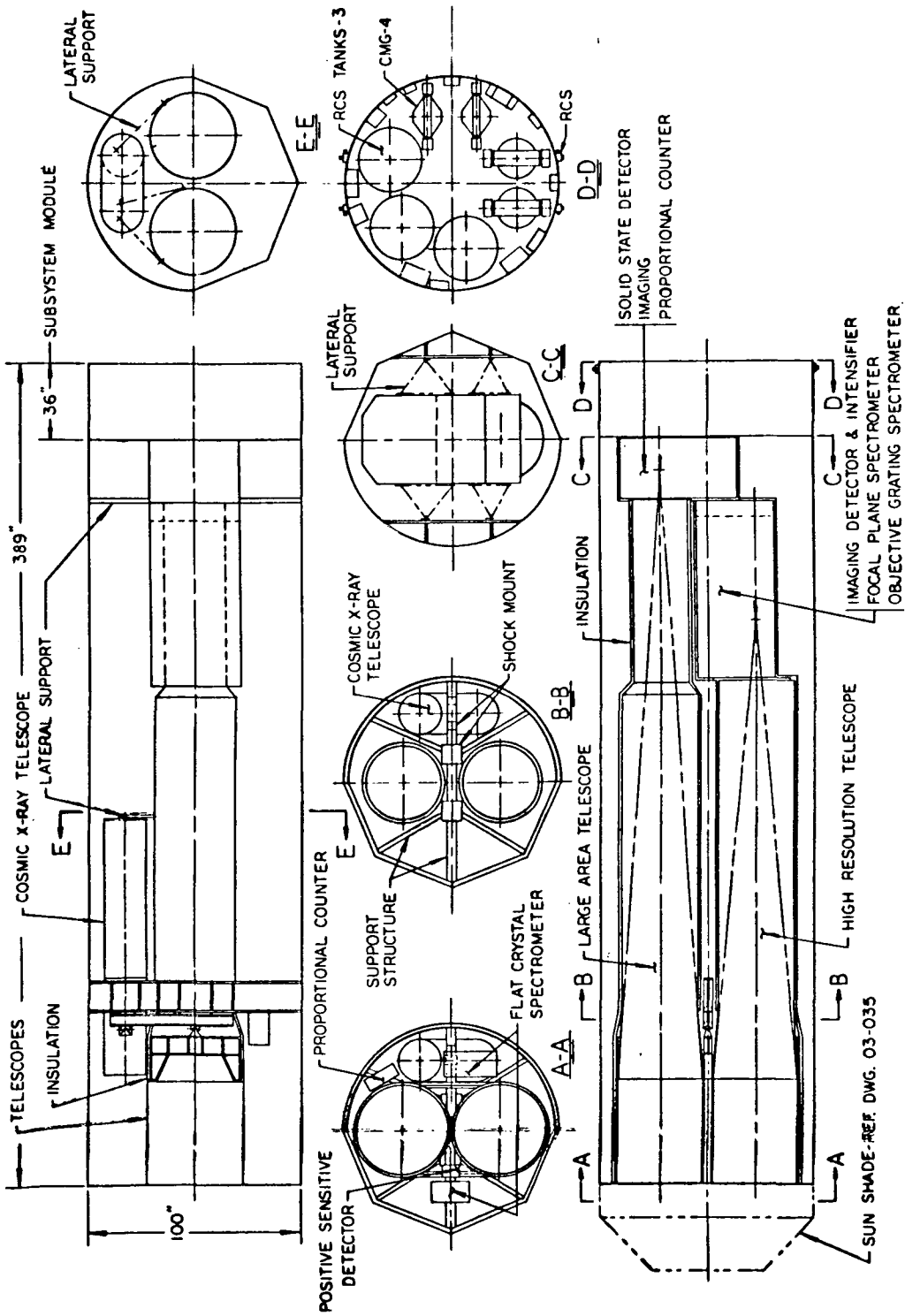


Figure E-83. HEAO-C spacecraft concept with subsystem module.

the spacecraft. This module contains most of the major subsystem components such as the CMGs, batteries, RCS tanks, and REMs. The REMs and their location concept on the spacecraft are identical to those used on the Lockheed SCS and the baseline RCS for the HEAO-C spacecraft.

Figure E-84 presents the same concept as Figure E-83 except that a subsystem module is not used and the subsystem component locations are distributed throughout the spacecraft. The RCS components and number are the same. The tanks are located more forward, close to the center, of the spacecraft, and the REM location concept is the same, except that they have been rotated 90 degrees because, otherwise, the spacecraft configuration would not allow symmetry.

Figure E-85 presents a functional schematic of the RCS used in the spacecraft concepts shown in Figures E-83 and E-84. The RCS is a mono-propellant hydrazine system utilizing three blowdown pressure-fed tanks. The three tanks are manifolded on both the propellant and pressurant sides of the tanks, and solenoid isolation valves are provided on both sides of each tank for isolation purposes in case of failure. There is no redundancy in propellant. The REMs and the plumbing concept are identical to that of the Lockheed SCS. The active thrusters are on a single manifold, and the standby thrusters are also on a single manifold. Should one of the active REAs fail, the entire set of active thrusters is isolated and the standby thrusters are, then, activated. The propellant tank used in this concept is the same as that used for the RCS on the Martin Transtage. However, this tank utilizes a diaphragm material designated as EPR-132. This diaphragm is not compatible with hydrazine over long periods of time, and the tank will have to be requalified with a diaphragm material that is more compatible, such as EPT-10. The tank will also have to be qualified with tank heaters. Table E-24 presents some characteristics and data associated with this tank. Table E-25 presents a weight statement for this RCS.

Figure E-86 presents another HEAO-C configuration that was considered during the study. With the OAS detached, the hydrazine RCS associated with this concept consists of six tanks and four REMs attached to the aft section of the spacecraft. Due to a change in spacecraft mass characteristics from the two previous concepts, the amount of propellant needed for the two-year mission decreased. The tanks and REMs used in this RCS are identical to those used in the baseline RCS for the HEAO-C spacecraft. However, the REMs are located at 90 degree intervals around the circumference of the

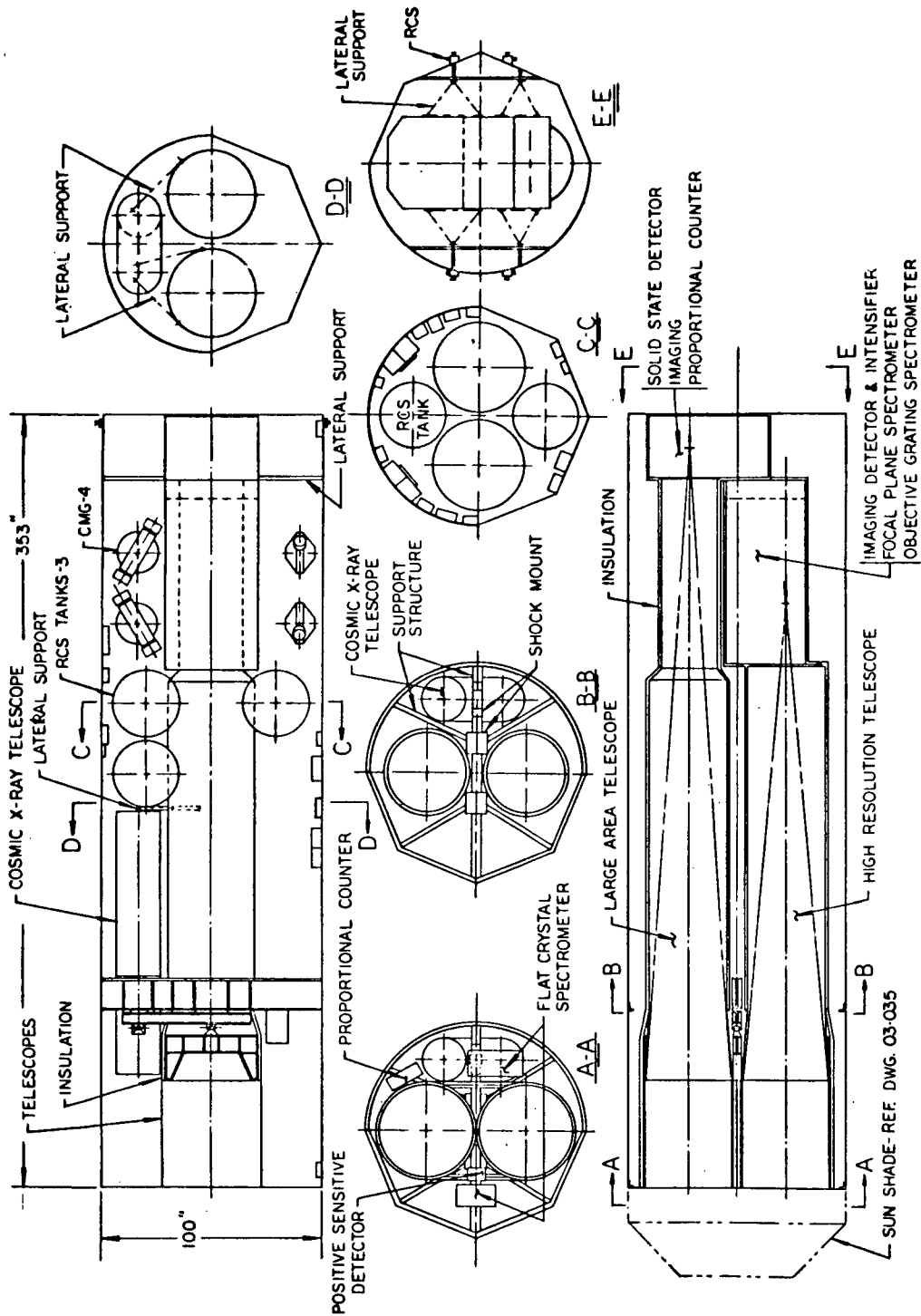


Figure E-84. HEAO-C spacecraft concept without the subsystem module.

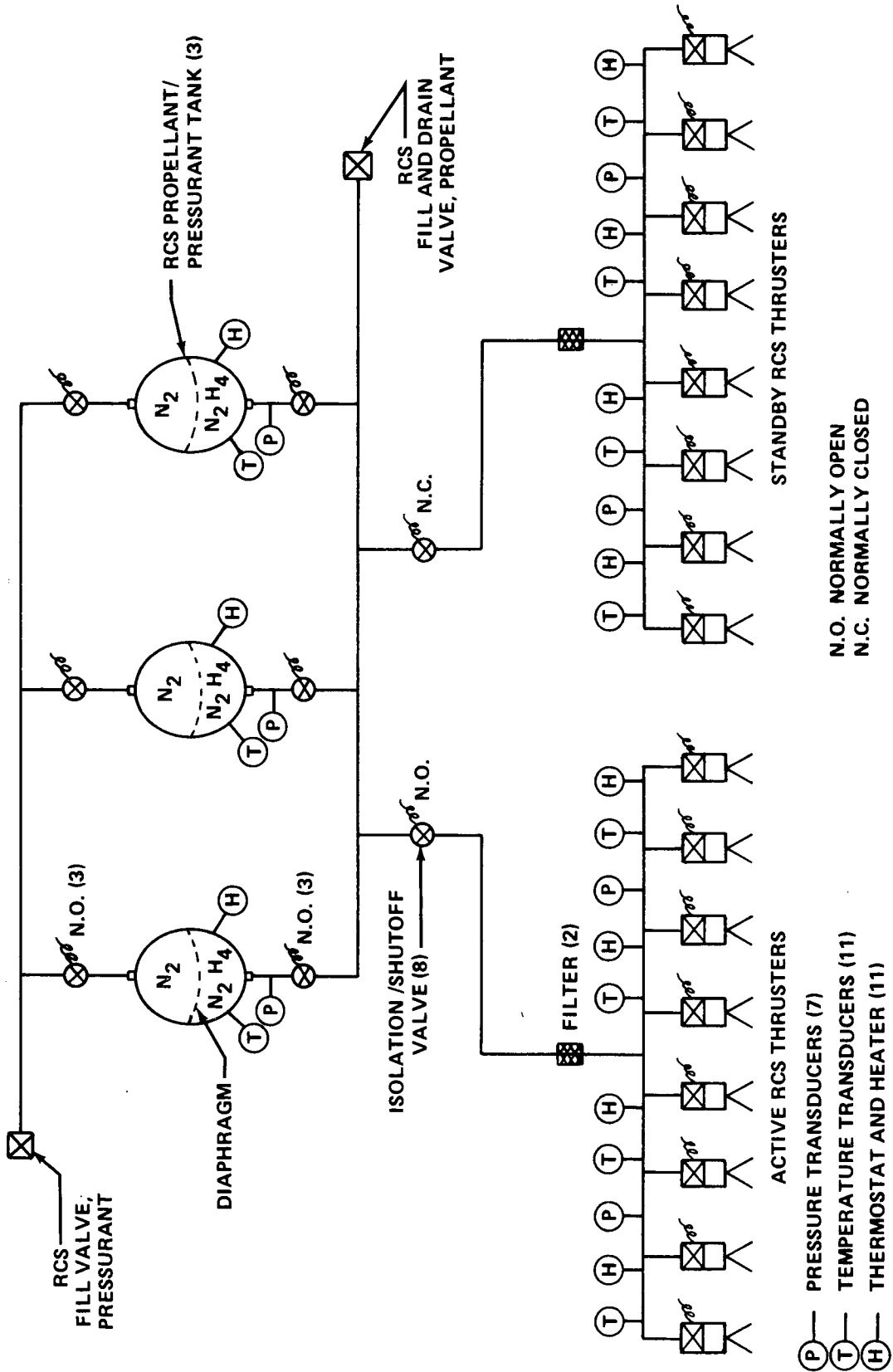


Figure E-85. System schematic of alternate HEAO-C spacecraft RCS with and without the subsystem module.

TABLE E-24. ALTERNATE RCS PROPELLANT TANK DATA

Parameter	Data
Manufacturer	PSI and Martin
Dimension	28.8 in. by 35.4 in.
Volume	14 928 in. ³
Development Status	Qualified
Program Used On	Transtage (Martin)
Operating Pressure	400 psia Blowdown range (264 psia to 110 psia)
Proof Pressure	600 psig
Burst Pressure	800 psig
Weight	54.5 lb.
Diaphragm Material	EPR-132

TABLE E-25. ALTERNATE RCS WEIGHT SUMMARY

Item	Component Weight (lb)
GN ₂ Fill and Drain Valve	0.25
Isolation/Shutoff Valve (8)	4.80
Tank (3)	163.50
Pressure Transducer (7)	2.10
Temperature Transducer (11)	1.54
Thermostat and Heater (11)	2.75
Propellant Fill and Drain Valve	0.30
Filter (2)	0.50
Thruster Module (4)	36.00
Plumbing	<u>10.00</u>
System Dry Weight	221.74
Propellant N ₂ H ₄	800.00
Pressurant GN ₂	<u>15.00</u>
Total System Weight	1036.74

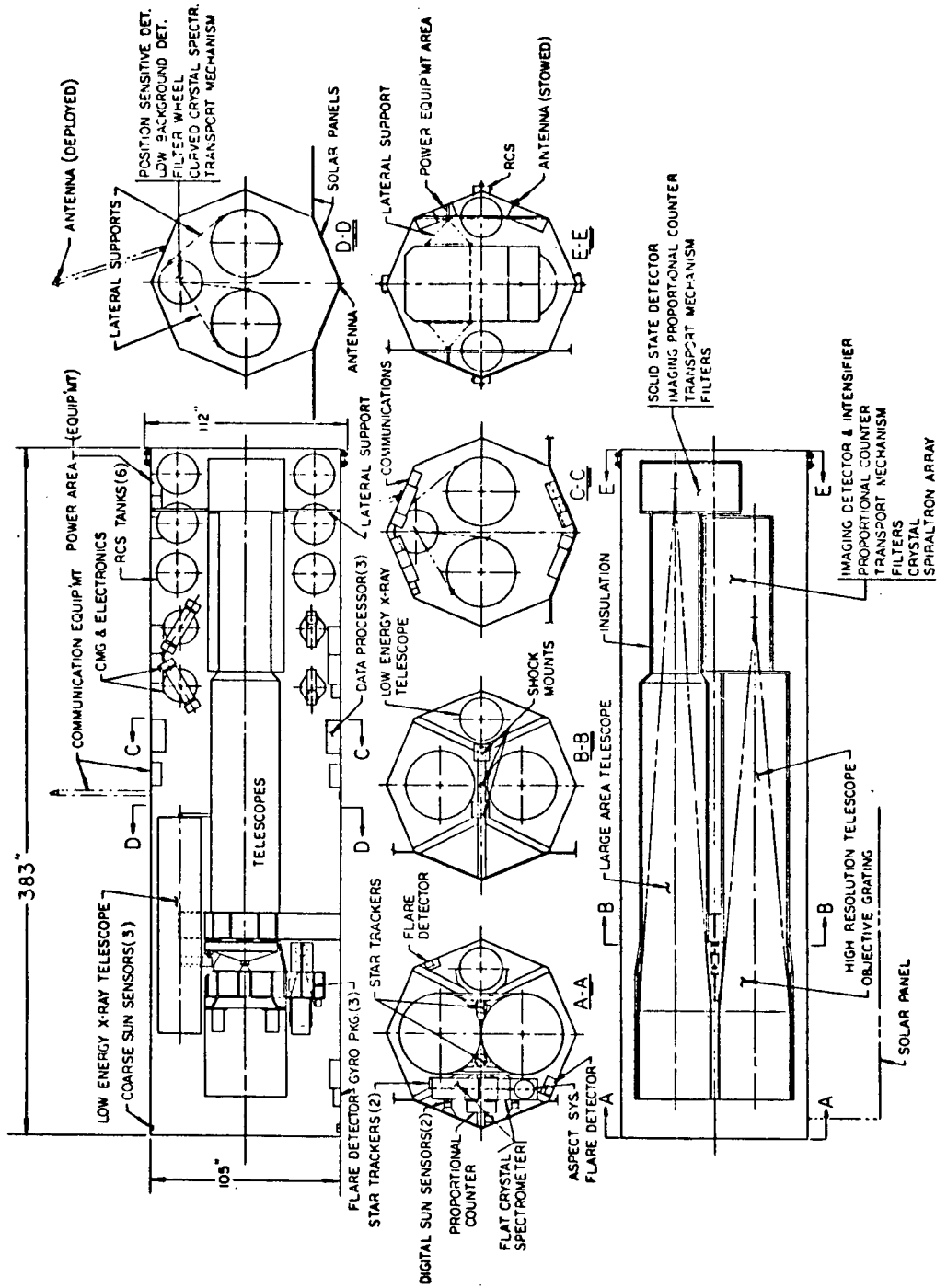


Figure E-86. Alternate HEAO-C spacecraft concept.

spacecraft. Figure E-87 presents a functional schematic of this system, and its operation is identical to that of the baseline RCS for the HEAO-C spacecraft. Table E-26 presents a weight statement for this RCS.

TABLE E-26. ALTERNATE RCS WEIGHT SUMMARY

Item	Component Weight (lb)
GN ₂ Fill and Drain Valve (6)	1.50
Isolation/Shutoff Valve (17)	10.20
Tank (6)	103.50
Pressure Transducer (20)	6.00
Temperature Transducer (22)	3.08
Thermostat and Heater (14)	3.50
Propellant Fill and Drain Valve (2)	0.60
Filter (2)	0.50
Thruster Module (4)	36.00
Plumbing	<u>10.00</u>
System Dry Weight	174.88
Propellant N ₂ H ₄	600.00
Pressurant GN ₂	<u>14.00</u>
Total System Weight	788.88

4. Other Reaction Control System Analyses. This section is a discussion of certain RCS topics that were considered during the HEAO-C study. Some of these topics were given more indepth consideration than others.

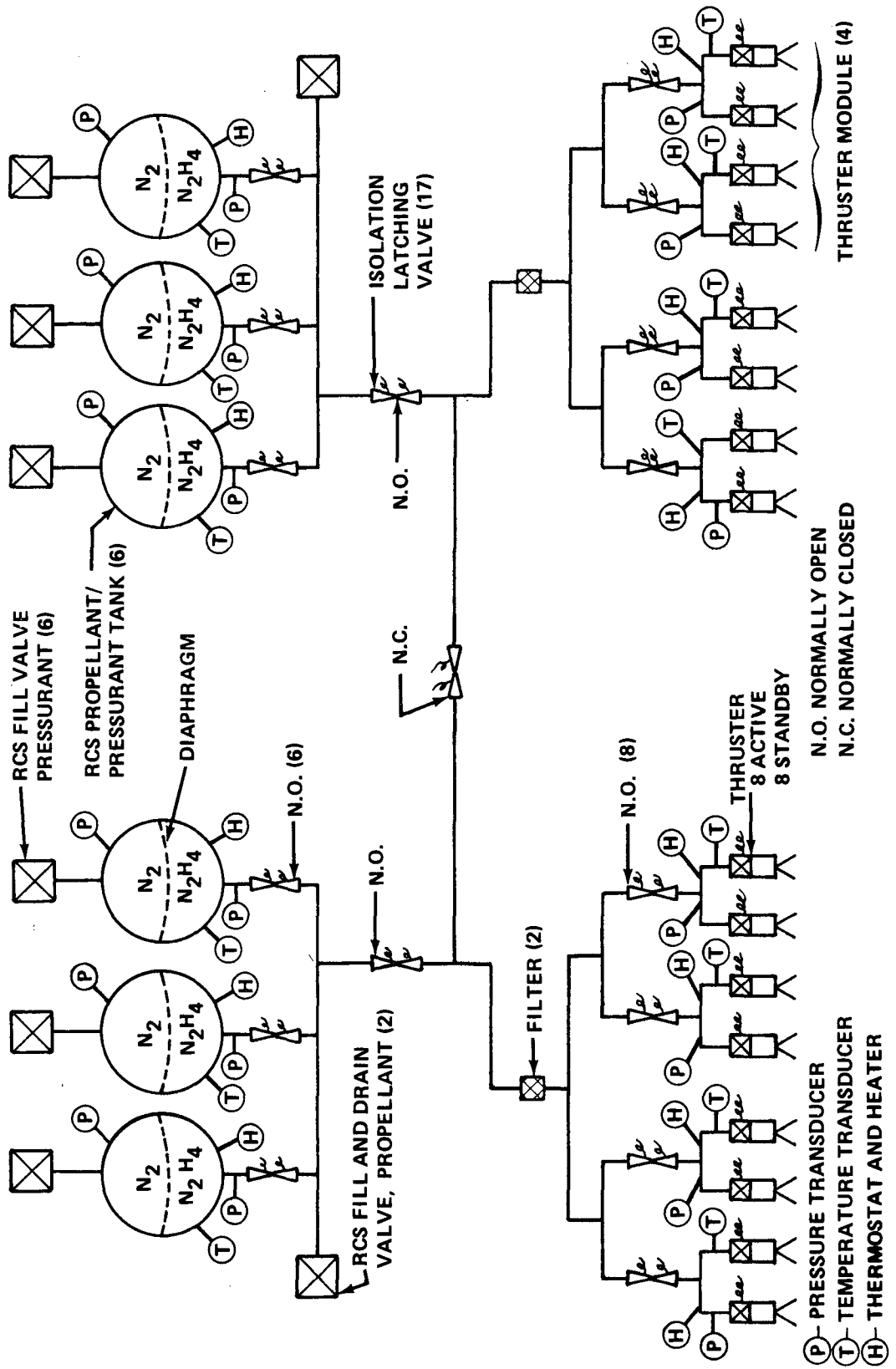


Figure E-87. System schematic of the alternate HEAO-C spacecraft RCS.

a. Other Thrusters. The type of RCS considered was always monopropellant hydrazine with the exception of the cold gas/magnetic torquer concept. The reason for this, established in the HEAO-A and B Phase A report [E-15], was that a monopropellant hydrazine system can meet the HEAO-C 2 year total impulse requirement and, yet, maintain a lightweight, simple, and reliable system capable of providing average performance and a relatively clean exhaust. However, a literature survey was conducted to determine the hydrazine thrusters that were available for consideration for the HEAO-C spacecraft. Some of these thrusters are listed in Table E-27. Thrusters of small thrust magnitude (0.1 pound or less) were considered in hopes that they could be used as a backup to the CMGs and yet maintain the stringent point requirements of the HEAO-C spacecraft. CMG desaturation without excessive jitter is also desirable such that the taking of data would be uninterrupted during desaturation. However, it was determined that generally, as the thruster size and associated thrust magnitude decreased, the thruster lifetime or total impulse capability also decreased. A thruster with a thrust magnitude of 0.1 pound or less that could satisfy its required impulse necessary when used for desaturating the CMGs over the 2 year HEAO-C mission lifetime could not be found.

TABLE E-27. MAJOR HYDRAZINE THRUSTERS CONSIDERED FOR THE HEAO-C SPACECRAFT

Thrust Level	Manu- facturer	Develop- ment Status	Programs Used On	Qualified For		Weight
				Cycles	Impulse	
0.1 lb	Hamilton Std.	Near Quali- fied Status	Proposed for ATS F/G	100 000	6 000 lb-sec	0.85 lb
0.5 lb	Rocket Research	Quali- fied	HPM (Classi- fied)	Low 20 000	7 300 lb-sec	1.4 lb
5.0 lb	Rocket Research	Quali- fied	P-95 (Classi- fied Lockheed)	175 000	18 000 lb-sec	1.6 lb
5.0 lb	Hamilton Std.	Quali- fied	Intelsat IV (Hughes)	100 000	100 000 lb-sec	1.4 lb

Rocket Research Corporation's MR-50A thruster and associated REM appeared to be the best qualified system available to apply to the HEAO-C RCS requirements. The requirement to maintain commonality with HEAO-A and -B was the driver in the selection of this thruster system. During their Phase B study on HEAO-A and -B, Grumman chose a modified Rocket Research REM for use in the RCS for these spacecraft. Since the HEAO-C concept is similar to Grumman's configuration for HEAO-A and -B, the Rocket Research REM was also chosen as the baseline thruster system for the HEAO-C spacecraft. The alternate thruster survey was then deleted.

b. Blowdown Versus Pressure Regulated Pressurization System. During the HEAO-C study, consideration was given to providing the baseline RCS tanks with an external regulated pressurization system, rather than operating in the blowdown mode. The advantages in providing an external regulated pressurization system for the RCS tanks result in a constant thrust level throughout the mission and, also, the propellant necessary can be contained in fewer tanks. The thrust is constant because the feed pressure is always constant. Since the propellant tanks can be filled to almost maximum capacity, the number of tanks necessary is essentially half that needed when operating in the blowdown mode. For a given propellant loading, the weight is essentially the same for each system.

The disadvantages in providing an external regulated pressurization system for the baseline RCS are as follows: The RCS has not been qualified with such a system and qualification testing would be necessary; the blowdown concept has been flight-qualified and has flown on Lockheed's SCS; and the additional components (such as tanks, valves, and regulators) necessary for the regulated system cause the system to be more complex and less reliable than the blowdown concept. Because of the disadvantages associated with the regulated system, the blowdown concept was retained for the baseline RCS for the HEAO-C spacecraft.

c. Catalyst Bed Lifetime. Because of the concern about the lifetime capability of the Shell 405 catalyst used in the REA of the baseline HEAO-C RCS, we contacted several companies that had tested small monopropellant hydrazine thrusters.

Rocket Research Corporation's MR-50A thruster chosen for the baseline HEAO-C RCS has been qualified to the following specifications:

Total Actuations	175 000 cycles
Total Impulse	18 000 lb-sec
Min Pulse Width	22 msec
Extreme Duty Cycle	5 min steady state burn and pulsing to 10 cps

Over several qualification tests of this thruster, the average catalyst bed loss by weight has been measured to be from 2 to 3 percent.

Hamilton Standard has tested a five pound thrust monopropellant hydrazine engine to qualification for 113 000 pulses (200 000 has been demonstrated) which included 30 cold starts. Pulses were 125 msec on and 875 msec off. The catalyst bed degradation during the qualification test was measured to be between 5 and 10 percent by weight. Hamilton Standard has also tested this same type engine for a two hour steady-state burn without shutdown.

During this investigation, it was learned that a minimum number of cold starts would prolong the life of the catalyst bed. It was also learned that if a monopropellant hydrazine thruster were allowed to operate long enough, such that the catalyst bed temperature approached that of steady-state conditions, the catalyst bed would retain a high temperature for several hours. If, for HEAO-C orbital conditions, a thruster is allowed to fire twice (evenly spaced) during an orbit such that the catalyst bed approaches steady-state operating temperatures, cold starts will be eliminated. According to TRW, if the catalyst bed temperature drops below 150° F, a cold start will occur when the engine is fired.

In conclusion, catalyst bed lifetime is inherent with engine design. The engine will have to be qualified to meet the HEAO-C RCS engine requirements. To prolong the catalyst bed lifetime, the number of cold starts must be minimized or deleted, if possible. Several ways to minimize cold starts are to use electric heaters, to insulate the thruster such that the catalyst bed will retain most of its heat between firings, and to minimize the time between firings. As has been previously discussed, the REM used on the baseline HEAO-C RCS has been designed to provide both of these active and passive thermal conditions. Loss of the catalyst is not due to chemical effects; rather it is caused by mechanical abrasions that occur due to thermal cycling.

d. Contamination Due to Thruster Exhaust. A literature survey was conducted to obtain information about the potential contamination threat associated with the exhaust of a hydrazine RCS. The Air Force Rocket Propulsion Laboratory has done some testing with hydrazine thrusters to determine the effects of exhaust contamination, and Hittman Associates has also done some analysis in this area.

The products of combustion in the exhaust of a hydrazine thruster are gaseous ammonia (NH_3), nitrogen (N_2), and hydrogen (H_2). Small traces of hydrazine and bits of Shell 405 catalyst may be found in the exhaust but, with the engine operating under proper conditions, these constituents of the exhaust should be very small or nonexistent. These exhaust products are very clean and, generally, tests thus far have indicated that they are not a serious contamination threat to a spacecraft. Tests have shown that ammonia deposits on optical surfaces and solar cells actually increase the transmittance of light through them.

Care should be taken in determining the method of installation and the location of star trackers or other apparatus that require visible light for operation in relation to the thrusters on the HEAO-C spacecraft. This is necessary since a large portion of the visible light entering an apparatus through a plume can be blocked. The placement of apparatus upon the HEAO-C spacecraft in relation to the thrusters is also important when considering plume impingement with resulting thermal effects upon the apparatus as well as the spacecraft.

Since the HEAO-C spacecraft has extremely sensitive surfaces and instruments in the form of experiments and optical surfaces, some contamination concern must still be maintained and further investigation is recommended. Not only should this investigation involve the exhaust of a hydrazine RCS, but other potential contaminants that might be onboard the spacecraft. Should the exhaust of a hydrazine thruster prove to be a serious contamination threat, a considerable design impact upon the HEAO-C spacecraft attitude control system could result.

REFERENCES

- E-1. Davis, Billy G.: A Discussion of Orbital Workshop Orientation and Gravitational Effects. NASA TM X-53829, May 5, 1969.
- E-2. Spacecraft Gravitational Torques. NASA SP-8024, May 1969.
- E-3. Spacecraft Aerodynamic Torques. NASA SP-8058, January 1971.
- E-4. Spacecraft Radiation Torques. NASA SP-8027, October 1969.
- E-5. Lockheed Missiles and Space Company: Environmental Torques on Spacecraft. Report No. A783101, NASA Contract No. NAS8-20082, Huntsville Research and Engineering Center, Huntsville, Alabama, August 1966.
- E-6a. Spacecraft Magnetic Torques. NASA SP-8018, March 1969.
- E-6b. Spacecraft Mass Expulsion Torques. NASA SP-8034, December 1969.
- E-7. Teledyne Brown Engineering Company: HEAO-C Experiments and Transport Mechanisms. Report No. SE-PD-1310, NASA Contract No. NAS8-20073, Huntsville, Alabama, March 1971.
- E-8. Teledyne Brown Engineering Company: Conceptual Design of a Spacecraft for the High Energy Astronomy Observatory (HEAO) Mission C. Report No. SE-MSFC-1257, NASA Contract No. NAS8-26003, Huntsville, Alabama, November 1970.
- E-9. Sperry Flight System Division: Fine Attitude Control System, Final Report. NASA Contract No. NAS9-10363, Phoenix, Arizona.
- E-10. Greensite, A. L.: Analysis and Design of Space Vehicle Flight Control Systems. Spectrum Books, New York, 1970.
- E-11. Bendix Corporation: HEAO Phase B Study Final Report, Volume I — System Summary and Description, March 1971.
- E-12. Penrose, R.: On the Generalized Inverse of a Matrix. Proc. Cambr. Phil. Soc., 1955.

REFERENCES (Concluded)

- E-13. Teledyne Brown Engineering Company: HEAO-C Baseline Attitude Sensing and Control Systems Description. Report No. SE-PD-1340, NASA Contract No. NAS8-20073, Huntsville, Alabama, July 1971.
- E-14. Folgate, K.: Control Moment Gyro Control Laws. Technical Memo 1K31-1, General Electric Company, Philadelphia, Pennsylvania, January 1969.
- E-15. Conceptual Design of a High Energy Astronomy Observatory, Volume I and Volume II. NASA TMX-53976, Program Development, Marshall Space Flight Center, February 16, 1970.
- E-16. Grumman Aerospace Corporation: High Energy Astronomy Observatory, NASA Phase B Final Study Report; Vol. II — Design Definitions/Engineering Analysis, Appendix. NASA Contract No. NAS8-26272, April 1971.
- E-17. Smith, W.W., et al.: Development and Design Aspects of a Five-Pound-Thrust RCS Rocket Engine Module. AIAA Paper No. 70-654, June 15, 1970.
- E-18. Schmitz, B.W.; Williams, D.A.; Maybee, D.; and Smith, W.W.: Design and Scaling Criteria for Monopropellant Hydrazine Rocket Engines and Gas Generators Employing Shell 405 Catalysts. AIAA Paper No. 66-594, June 1966.
- E-19. Benton, H.R. and Crozier, R.D.: Cold Gas Thruster Attitude Control Systems for the Satellite Control Section. Lockheed Paper.

TABLE OF CONTENTS

	Page
Electrical Power Subsystem Analyses	F- 1
1. Electrical Power Subsystem Performance Model	F- 1
2. System Performance Factors	F- 6
Solar Cells and Coverslides	F- 9
1. Solar Cell Selection	F- 9
2. Coverslides	F-12
3. Solar Cell Characteristics	F-16
a. Solar Cell Coefficients and Design Factors	F-16
b. Cell Characteristics as a Function of Mission Conditions	F-19
Solar Array Analysis	F-22
1. Baseline Configuration and Area	F-22
2. Initial Calculations	F-24
3. Baseline Solar Panels	F-26
a. Size Constraints	F-26
b. Substrate and Configuration	F-28
c. Cell Arrangement	F-28
4. Orientation and Temperature Studies	F-31
a. Orientation Model	F-31
b. Array Temperature Relationships	F-33
5. Parametric Performance Studies for the Baseline	F-40
6. Baseline Solar Array Performance	F-45
a. Characteristic Ratings	F-45
b. Array Performance Variations with Earth Seasons	F-49
c. Array Performance for Abnormal Conditions	F-52

TABLE OF CONTENTS (Continued)

	Page
7. Solar Array Tradeoffs	F-55
a. Alternate No. 1 Solar Array	F-55
b. Alternate No. 2 Solar Array	F-56
c. Tradeoff Summary	F-62
Deployment Tradeoffs	F-62
1. Tradeoff Studies and Evaluation Criteria	F-62
2. Alternate Deployment Concepts	F-64
a. Direct Drive	F-64
b. Linkages	F-64
c. Cable Drives	F-66
d. Linear Extender	F-66
e. Tension Springs	F-66
f. Torsion Springs	F-66
3. Cinching Release and Latch Mechanisms	F-66
a. Torque Tube Release	F-66
b. Cammed Catch	F-67
c. Baseline Cinching and Release	F-68
d. Latching Concepts	F-68
Energy Storage Subsystem	F-71
1. Requirements and Ratings	F-71
2. Battery Tradeoffs	F-74
3. Baseline Battery Assembly	F-79
4. Battery Control Subsystem	F-81
a. General Description	F-81
b. Battery Characteristics for Control	F-83

TABLE OF CONTENTS (Continued)

	Page
5. Battery Charger Assemblies	F- 86
a. Requirements	F- 86
b. Baseline Design	F- 86
Power Conditioning Concepts	F- 89
1. Power Conditioning Subsystem	F- 89
2. Converter-Regulator Concepts	F- 90
a. Transformerless Boost-Buck Regulator	F- 90
b. Magnetic Amplifier Regulators	F- 92
c. Transformer-Coupled Buck-Boost Regulator	F- 92
Cabling Studies	F- 95
1. Cable Optimization for HEAO-C Baseline	F- 95
2. Distribution Cable Estimates	F-103
3. Derivation of Cable Optimization Equation	F-103
Preliminary Specification for HEAO Electrical System	F-108
1. General System Requirements	F-108
a. Function	F-108
b. Reliable Features	F-109
c. Power Characteristics	F-109
d. Spacecraft System Grounding	F-109
e. Interference Control	F-111
f. Corona Supression	F-111
g. Interface Connectors	F-111
h. Protection of Electrical Circuits and Electronic Devices	F-112

TABLE OF CONTENTS (Concluded)

	Page
2. Electrical Power Subsystem Requirements	F-113
a. Solar Cell Array Subsystem	F-114
b. Battery Charging Subsystem	F-119
c. Power Conditioning Subsystem	F-121
d. Batteries	F-122
3. Electrical Distribution and Control Subsystem	F-125
a. Introduction	F-125
b. Distribution	F-125
c. Load Control	F-126
d. Circuit Protection	F-126
e. Measurements	F-126
References	F-127
Bibliography	F-127

LIST OF ILLUSTRATIONS

Figure	Title	Page
F-1.	EPS performance model	F- 2
F-2.	Energy storage requirements	F- 4
F-3.	Sensitivity of required solar array power to load and sunlight period.	F- 7
F-4.	Effect of occultation period on system performance factor.	F- 7
F-5.	Candidate solar cells	F- 9
F-6.	Initial performance comparison of 2 ohm-cm and 10 ohm- cm solar cells	F-10
F-7.	Comparison of radiation effect on types of solar cells. . . .	F-11
F-8.	Reference solar cell characteristics for HEAO-C	F-13
F-9.	Coverslide characteristics.	F-15
F-10.	Reflectance effects on solar cell performance	F-20
F-11.	Performance of initial array design for 15 degree orien- tation as a function of time in sunlight	F-27
F-12.	Solar panel weight versus substrate thickness	F-29
F-13.	Array orientation model	F-32
F-14.	Typical variations of array incidence angles with scanning	F-34
F-15.	Effect of stacking factor on array maximum temperature .	F-36
F-16.	Average body section temperature variations with incidence and stacking factors	F-37

LIST OF ILLUSTRATIONS (Continued)

Figure	Title	Page
F-17.	Maximum wing temperature dependence on incidence and deployment angles.	F-38
F-18.	Average temperature of array wings for various deployment and incidence angles	F-39
F-19.	Baseline array body section power capabilities	F-40
F-20.	Array body parametric performance curves as a function of tilt orientation	F-41
F-21.	Array body parametric performance curves as a function of roll orientation.	F-42
F-22.	Power performance curves for a solar array wing.	F-43
F-23.	Parametric performance curves for both wings.	F-44
F-24.	Baseline array EOM performance rating	F-46
F-25.	Rated V-I characteristics for baseline array wings	F-46
F-26.	Rated V-I characteristics for baseline solar array body sections	F-47
F-27.	Solar array power — voltage loss	F-48
F-28.	Variations of occultation time.	F-50
F-29.	Angle of sunline to orbit plane variations	F-51
F-30.	Off-sun pointing capability for selected seasonal periods.	F-53
F-31.	Baseline solar array output with wings undeployed for tilt orientations	F-54

LIST OF ILLUSTRATIONS (Continued)

Figure	Title	Page
F-32.	Baseline solar output with wings undeployed for roll orientation	F-54
F-33.	Alternate No. 1 array configuration.	F-55
F-34.	Power capability curves for alternate No. 1 array	F-57
F-35.	Body section performance for alternate No. 1 array.	F-58
F-36.	Power versus orientation for alternate No. 1 array	F-59
F-37.	Alternate No. 1 array power growth capability	F-60
F-38.	Solar array alternate No. 2 configuration.	F-60
F-39.	Performance of alternate No. 2 array	F-61
F-40.	Alternate deployment concepts	F-65
F-41.	Torque tube release mechanism	F-67
F-42.	Cammed catch release mechanism	F-68
F-43.	Drag link latch.	F-69
F-44.	Spring clip latch.	F-70
F-45.	Spring-bolt latching scheme	F-70
F-46.	Battery cycle life versus depth of discharge	F-73
F-47.	Battery capacity required for HEAO-C.	F-74
F-48.	Energy-volume-mass characteristics for battery assemblies	F-75

LIST OF ILLUSTRATIONS (Concluded)

Figure	Title	Page
F-49.	Comparison of battery cells, assemblies, and ratings . . .	F-77
F-50.	Discharge characteristics for Ni-Cd cell	F-80
F-51.	Off-sun pointing capability of HEAO-C baseline	F-82
F-52.	Long-term performance of battery assemblies with matched and unmatched cells	F-84
F-53.	Cell divergence during charge-discharge cycle	F-85
F-54.	Battery capacity retention characteristics	F-85
F-55.	Charger response to third electrode signal	F-88
F-56.	Transformerless boost-buck regulator	F-91
F-57.	Magnetic amplifier coupled regulators	F-93
F-58.	Baseline regulator efficiency characteristics	F-96
F-59.	Characteristics of stranded-insulated wire	F-97
F-60.	Simplified transmission cable diagram	F-99
F-61.	Electrical system cabling model	F-104

LIST OF TABLES

Table	Title	Page
F-1.	Silicon Solar Cell Specification	F- 12
F-2.	Coverslide for Solar Cells	F- 14
F-3.	Solar Cell Characteristics at Typical Mission Conditions	F- 22
F-4.	Comparison of Solar Array Configurations for HEAO-C Requirements	F- 63
F-5.	HEAO-C Energy Storage Requirements	F- 71
F-6.	Specifications for Typical Battery Cells (Secondary Nickel-Cadmium)	F- 76
F-7.	Typical Battery Assembly Characteristics	F- 76
F-8.	Comparison of Battery System Weights	F- 79
F-9.	Wire Characteristics and Optimum Current Type C6, Class N	F- 98
F-10.	Primary Transmission Cable Summary Without Redundancy	F-102

APPENDIX F. ELECTRICAL SYSTEMS

Electrical Power Subsystem Analyses

1. Electrical Power Subsystem Performance Model. Except for some instrumentation and possibly a few command input signals, the electrical interfaces of the electrical power system (EPS) are normally satisfied via the electrical distribution and control subsystem. The load and voltage requirements discussed in Chapter VIII were considered to be at the specific subsystem or experiment load. Therefore, the electrical system loads and losses were added to the load requirements established so that the EPS requirements and performance could be analyzed.

The load requirements were considered preliminary, lacking the detailed definition that affects electrical system requirements. To account for the state of definition and to allow for some growth in requirements, a contingency factor of approximately 20 percent was added. Growth of power requirements late in the study reduced the contingency to about 14 percent.

Several EPS concepts are possible to meet the given requirements within the general constraints of Chapter VIII for a solar array battery system. The number of subsystem arrangements possible is rather limited, but there are many concept variations pertaining to major assembly concepts and methods of implementing basic hardware. Some of the variations and alternates to the baseline EPS are discussed in this appendix.

The baseline EPS system is described by the simplified diagram of Figure F-1. Based on analyses of similar satellite systems and previous studies, efficiency factors, as denoted on the diagram, were derived for the basic parts of the subsystem. The requirements and performance of the energy storage and solar array subsystems have been analyzed on the basis of this subsystem model.

To sustain the spacecraft loads during the dark periods (occultation) of the orbit, the battery subsystem must convert stored electrochemical energy into electrical power and supply the loads through the discharge path losses. The output energy requirement is determined by:

F-1

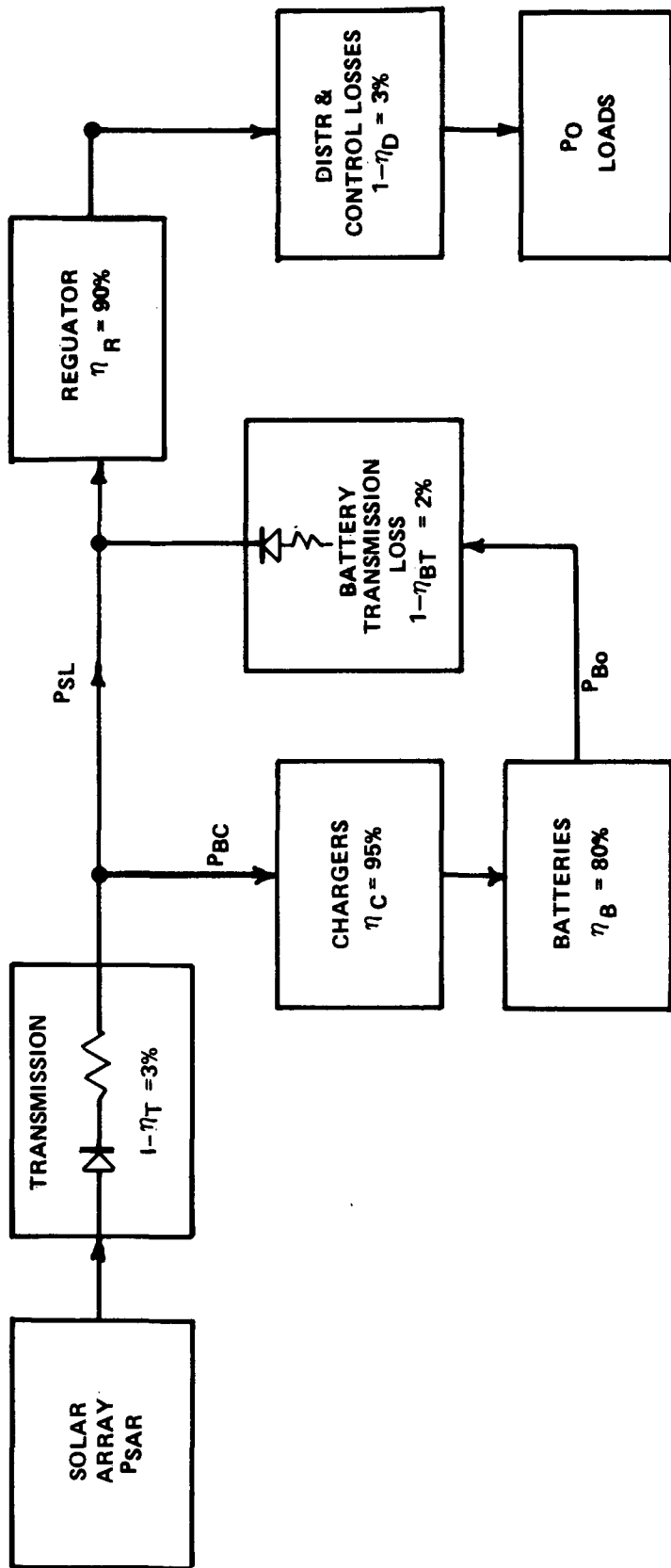


Figure F-1. EPS performance model.

$$W_{Bo} = \frac{P_o \cdot t_d}{(\eta_{BT})(\eta_R)(\eta_D)} \text{ watt-hours } ,$$

where

W_{Bo} = Energy delivered by batteries in watt-hours.

P_o = Average load power required in watts.

t_d = Occultation period in hours.

η_{BT} = Efficiency of transmission from battery to distribution center.

η_R = Efficiency of regulators.

η_D = Efficiency of distribution of power to the loads.

For the design load of 722 watts and the maximum dark period of 35.8 minutes, the battery energy required is:

$$W_{Bo} = 504 \text{ watt-hours } .$$

The average power required of the batteries, found by dividing W_{Bo} by t_d , is:

$$P_{Bo} = 845 \text{ watts } .$$

Figure F-2 shows how the energy storage requirement varies with the load for the range of occultation periods possible for the orbital parameters defined for HEAO-C.

The primary power for the system must be furnished by the solar array during sunlight periods. The array must supply loads through the primary system losses and must also furnish power to recharge batteries. The energy balance of the system must be maintained to sustain continuous operation since the batteries and solar array operate at different times and for different periods. The array must be sized for this energy balance. Referring to Figure F-1, the average solar array power needed to supply the load is:

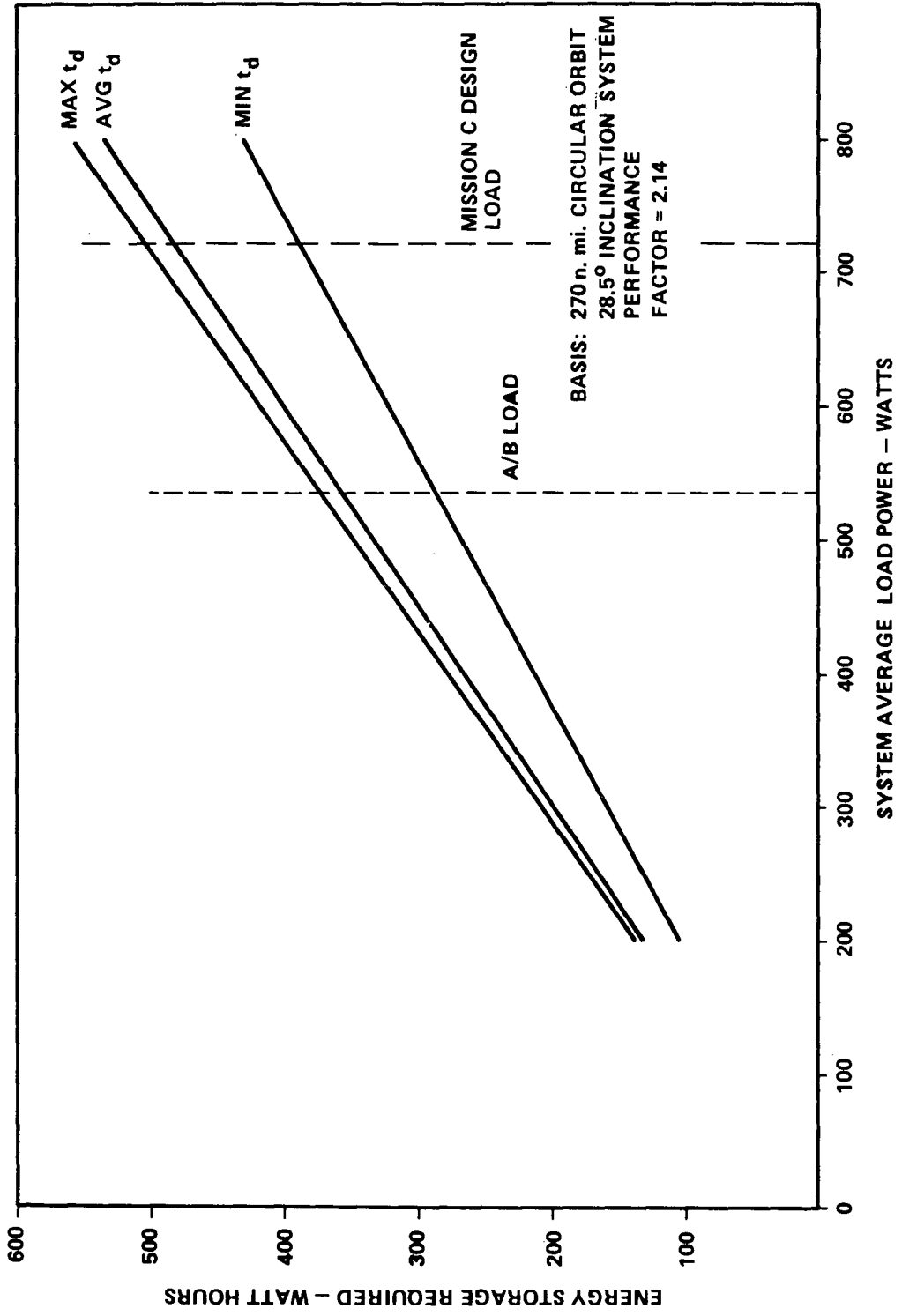


Figure F-2. Energy storage requirements.

$$P_{SL} = \frac{P_o}{(\eta_D)(\eta_R)(\eta_T)} \text{ watts}$$

where all symbols have been defined except η_T which is the primary power transmission efficiency.

The average solar array power required to replenish the energy storage subsystem is:

$$P_{SB} = \frac{P_{BC}}{\eta_T} \text{ watts}$$

where P_{BC} is the average recharge power, in watts, to chargers.

The total required solar array power is then:

$$P_{SAR} = P_{SL} + P_{SB} \text{ watts} .$$

The power P_{SB} may be determined in terms of output energy, the battery recharge efficiency, η_B , the charger efficiency, η_C , and the sunlight time, t_S .

Rewriting the above equation, then, gives the condition for energy balance:

$$P_{SAR} = \frac{P_o}{\eta_D \cdot \eta_R \cdot \eta_T} + \frac{W_{Bo}}{\eta_T \cdot \eta_C \cdot \eta_B \cdot t_S} \text{ watts} .$$

Substituting for W_{Bo} and for $t_d = t_o - t_S$ gives:

$$P_{SAR} = \frac{P_o}{\eta_T \cdot \eta_R \cdot \eta_D} \left(1 + \frac{t_o - t_S}{\eta_{BT} \cdot \eta_B \cdot \eta_C \cdot t_S} \right) \text{ watts}$$

$$P_{SAR} = 1549 \text{ watts}$$

for the HEAO-C orbital conditions of 270 n. mi. altitude, 28.5 degree inclination and maximum occultation of 35.7 minutes. The system design must provide,

as a minimum, the average power denoted by P_{SAR} throughout the mission and for all specified pointing conditions that are considered to be continuous for several orbits. Considering variations in load and sunlight-to-darkness ratios, Figure F-3 shows the sensitivity of the required power, P_{SAR} , as a function of these.

2. System Performance Factors. The power system performance factor, M_s , is a typical figure of merit used to define power performance of solar array-battery systems and is not to be confused with system efficiency although efficiency is a factor. M_s is defined as the ratio of the generated, raw, average power to the delivered, conditioned power. Since energy storage is involved, this factor is also a function of sunlight and darkness times. For a given system concept, performance factors can be stated for given mission and load requirements. Similar factors can be given for the resultant designs where design margins, degradation, etc., have been accounted in the solar array size. For the HEAO-C baseline EPS, the performance factor is computed for the maximum occultation time of 35.7 minutes.

$$M_s = \frac{P_{SAR}}{P_o}$$

where

P_{SAR} = Required solar array power (avg.) in watts

P_o = Output or load power in watts.

M_s = 2.14 .

Figure F-4 shows how the performance factor would vary if the solar array design were based on shorter periods of darkness possible for the mission.

The energy efficiency of the primary (solar power) system (Fig. F-1) is the product of the distribution, regulation/power conditioning, and transmission subsystem efficiencies symbolized as follows:

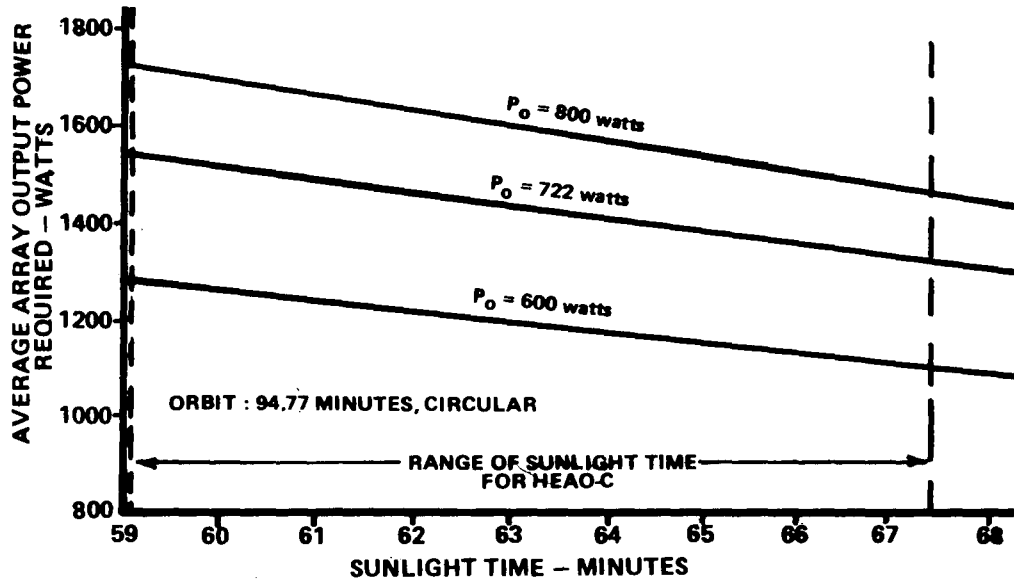


Figure F-3. Sensitivity of required solar array power to load and sunlight period.

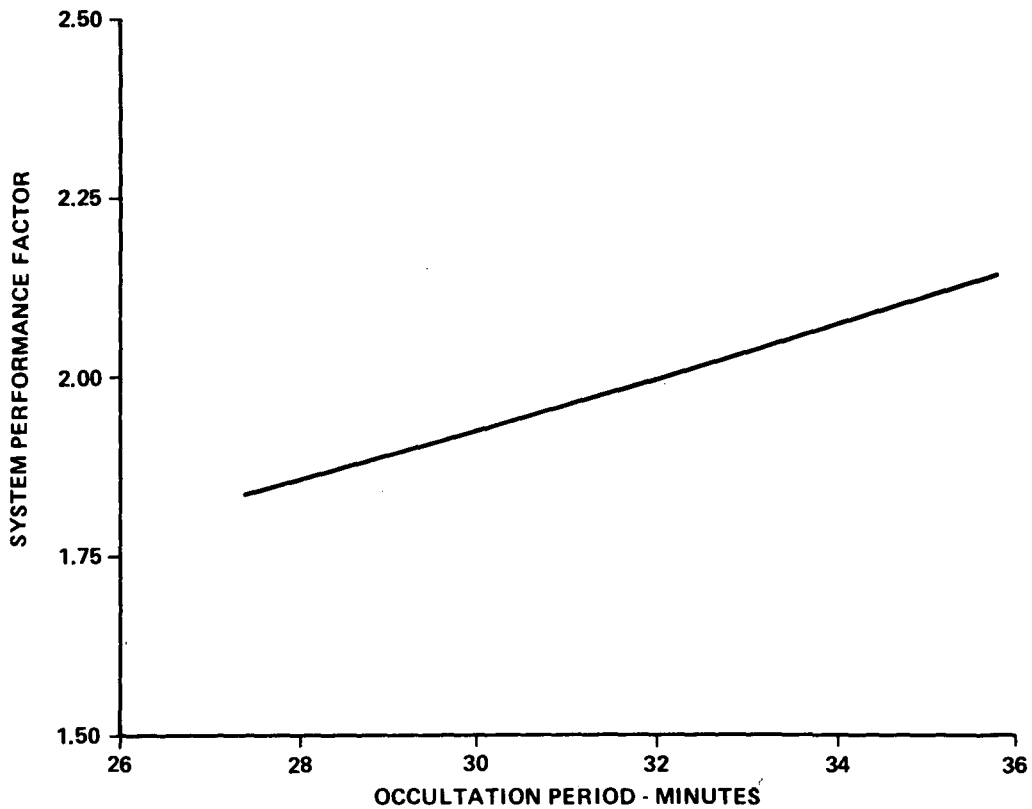


Figure F-4. Effect of occultation period on system performance factor.

$$\eta_{PS} = \eta_D \cdot \eta_R \cdot \eta_T \quad .$$

Substituting HEAO EPS values gives:

$$\eta_{PS} = 84.7 \text{ percent} \quad .$$

The secondary system (energy storage) efficiency, η_{SS} , is the product of battery, charger, and battery transmission efficiencies, or:

$$\eta_{SS} = \eta_C \cdot \eta_B \cdot \eta_{BT}$$

$$\eta_{SS} = 74.5 \text{ percent} \quad .$$

The average efficiency of the overall system, η_S , is determined as follows:

$$\eta_S = \frac{W_o}{W_{in}} = \frac{P_o \cdot t_o}{\frac{P_o \cdot t_S}{\eta_{PS}} + \frac{P_o \cdot t_d}{\eta_{PS} \cdot \eta_{SS}}}$$

where

W_o = Output energy to the loads for the entire orbital period, t_o , in watt-hours.

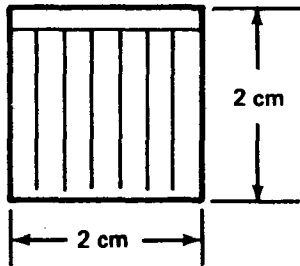
W_{in} = Input energy delivered by the solar array for the sunlight period, t_S , in watt-hours.

Substituting system efficiency values from above and using the minimum sunlight orbit case determines the lowest system efficiency:

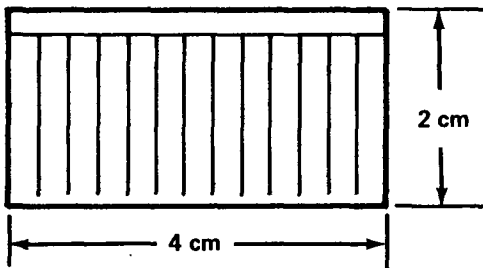
$$\eta_S = 75.3 \text{ percent} \quad .$$

Solar Cells and Coverslides

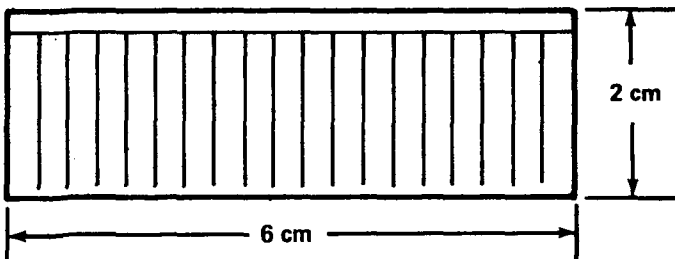
1. Solar Cell Selection. Tradeoff studies and laboratory tests of solar cell performance and costs have shown that silicon N on P cells offer the best power for a given area and a reasonably good radiation resistance for low altitude orbits. Candidate solar cell types (Fig. F-5) were limited to those used on Skylab. Investigation of manufacturing trends shows that the previous 1 by 2 cm and 2 by 2 cm sizes, considered standards, are being replaced by 2 by 4 cm and possibly 2 by 6 cm sizes, respectively. The larger cells have become cost competitive with the smaller ones, making them most attractive for larger solar array requirements such as HEAO. The larger cells offer convenience in panel fabrication and improved power performance because of better utilization of array panel area.



N/P 7 - 14 ohm-cm
Ag Ti SOLDER DIPPED CONTACTS
120 mA @430 mV @28°C AMO



N/P 1-3 ohm-cm
Ag Ti SOLDER SIPPED CONTACTS
232 mA @475 mV @28°C AMO



N/P 7 - 14 ohm-cm
Ag Ti SOLDER DIPPED CONTACTS
360 mA @430 mV @28°C AMO

Figure F-5. Candidate solar cells.

Since the cost of cells having a base resistivity of 2 ohm-cm is roughly the same as the 10 ohm-cm type, the tradeoff depends on initial performance and how well each type sustains performance under radiation exposure. Figure F-6 compares the initial performance of the two cell types.

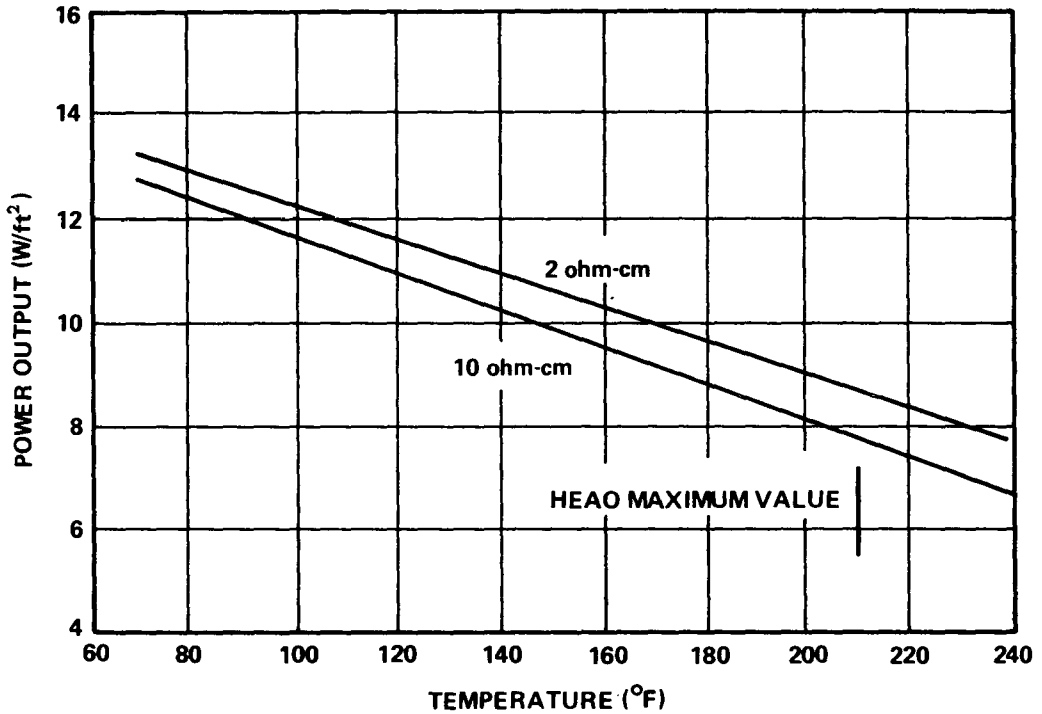


Figure F-6. Initial performance comparison of 2 ohm-cm and 10 ohm-cm solar cells.

The 10 ohm-cm cells are more resistant to radiation and are the best selection for high radiation belt applications. However, for the HEAO orbits, the radiation levels are low and the degradation of the 2 ohm-cm cells will be relatively low. Since the initial performance of the 2 ohm-cm cells is significantly higher, the radiation effects for 2 years in 200 to 270 n.mi. orbits does not degrade these cells enough to cause their performance to fall below that of 10 ohm-cm cells. The relative performance of the two types of cells in a low orbit radiation environment is shown by Figure F-7.

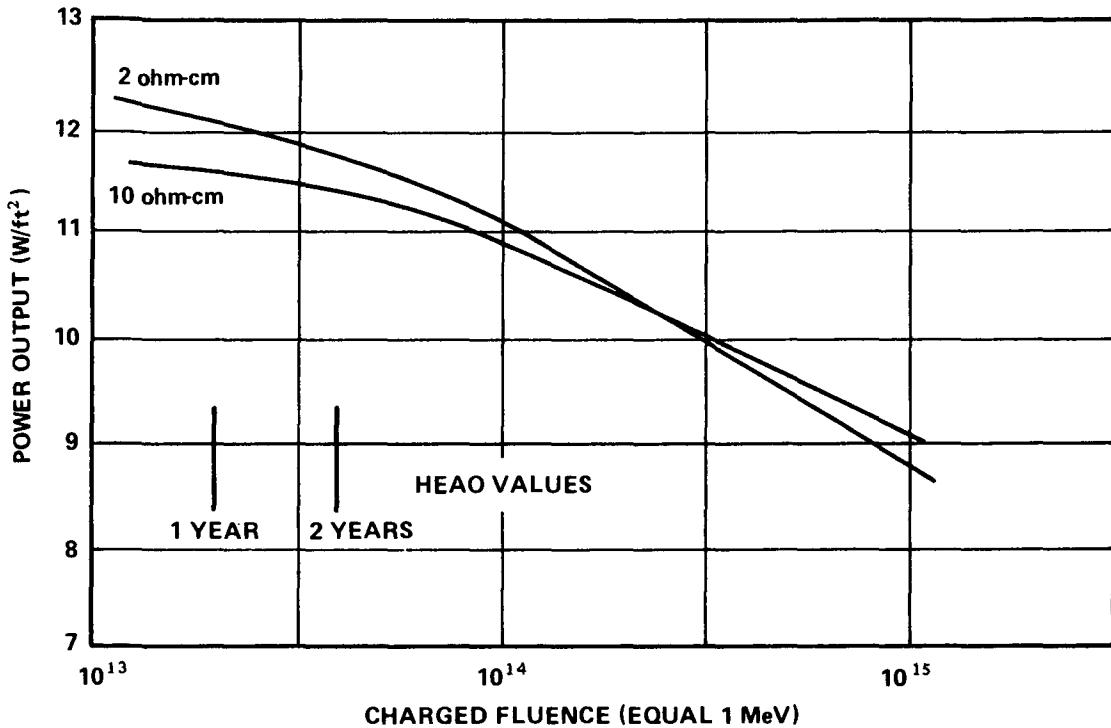


Figure F-7. Comparison of radiation effect on types of solar cells.

Cost analyses in terms of watts per dollar indicate that production yields of 2 ohm-cm cells in the range of 10.5- to 11.0-percent efficiency are the most economical. Therefore, the solar cell selected for the HEAO baseline is a silicon, N on P, 2 ohm-cm type, 2 by 4 cm size, with a nominal 11.0-percent efficiency rating.

Selecting a specific size cell does not restrict the performance analyses made herein. It may be assumed that the equivalent performance could be obtained for other cell sizes by scaling in proportion to the cell area.

The solar cell baseline for HEAO-C is described by Table F-1.

Figure F-8 shows the voltage-current characteristics of the reference solar cell (bare) at the beginning-of-life (BOL). These characteristics represent the average of the upper 25 percent of 200 cells tested. Samples were taken from lots typical of those being delivered for the OWS solar array. The best cell tested had an efficiency of 11.4 percent, while the worst cell had 10.1 percent.

TABLE F-1. SILICON SOLAR CELL SPECIFICATION

Type	N-on-P Silicon
Base Resistivity	2 ohm-cm
Size	2 × 4 cm
Thickness	14 ± 2 mils
Contacts	Ag-Ti (Solderless)
Effective Area	7.7 cm ²
Efficiency @ AMO, 28° C	11.0%
Open Circuit Voltage, V _{oc}	0.587 volt
Short Circuit Current, I _{sc}	284 milliamps
Max. Power Voltage, V _m	0.460 volt
Max. Power Current, I _m	261 milliamps

Losses are incurred and the cell characteristics are changed upon assembly of solar panels because of the addition of coverslides and increased series resistance. The characteristics are further changed by exposure to radiation and micrometeorites, by changes in thermal characteristics of the assembly, by temperature variations, and by variations in light intensity or angle of incidence.

2. Coverslides. The HEAO solar array design is based on the use of coverslides on each solar cell, a standard practice. Several manufacturers offer a variety of materials, optical coatings, and thickness — properties that determine the characteristics of the coverslide. Typical materials are fused silica, quartz, and high-quality glass often referred to as microsheet. Typical coatings are: (1) antireflective — to reduce reflection losses, (2) ultraviolet rejection (blue filter) to eliminate the undesirable part of the spectrum, (3) infrared rejection (red filter) — to reduce thermal burden, and (4) a combination of blue-red filters. Standard thicknesses range from 6 to 60 mils, depending upon application.

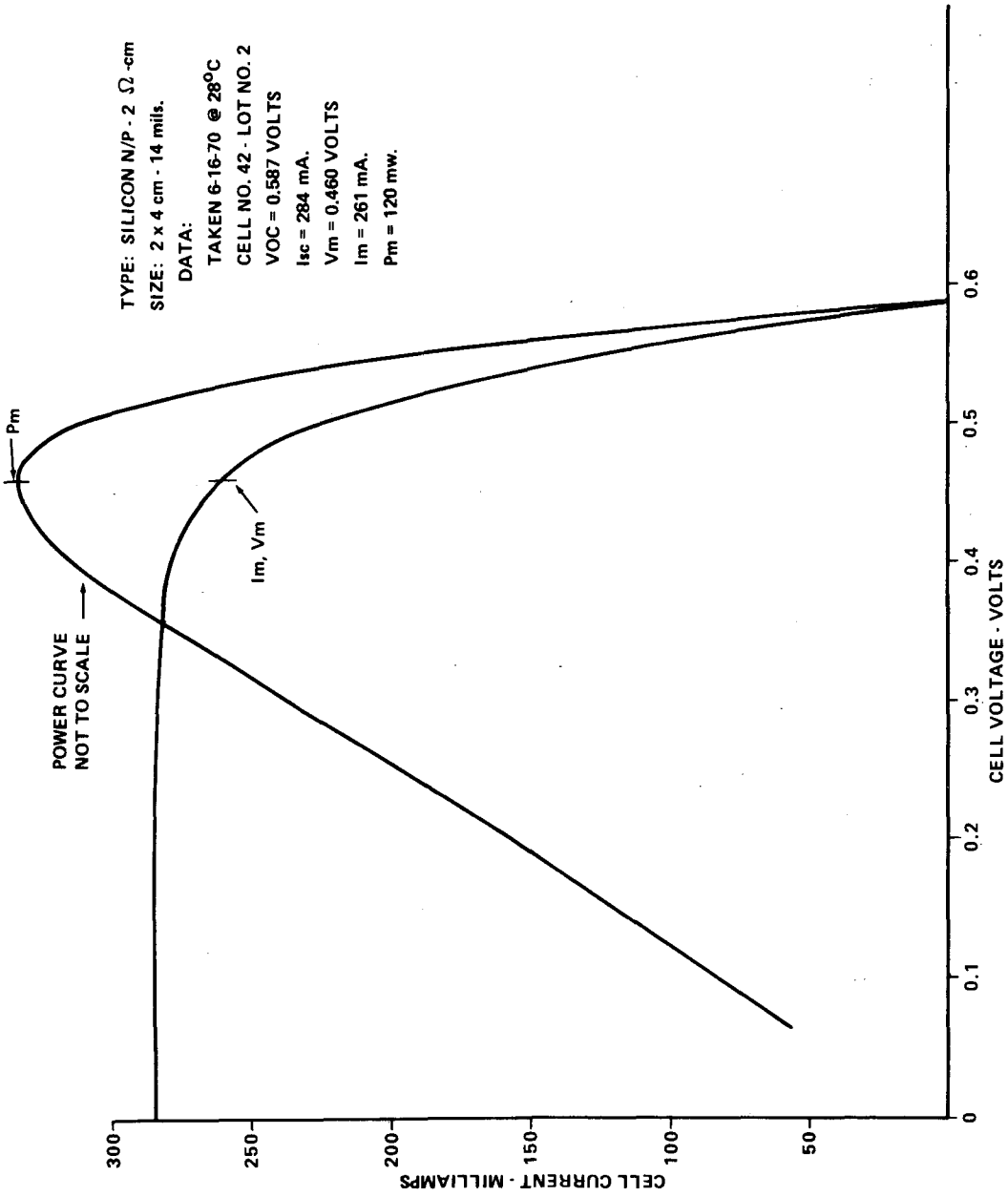


Figure F-8. Reference solar cell characteristics for HEAO-C.

Coverslides offer several benefits to solar array performance. They improve the thermal characteristics to obtain higher power output, reduce cell degradation from space radiation, and offer some protection against micro-meteorite damage.

Previous study tradeoffs (1) showed that coverslides with anti-reflective coatings were desirable. The estimates and analyses of radiation environment for the low altitude orbits indicated that the thin, 6-mil slides provided adequate radiation resistance and lower array weight. The blue filter types offer better overall performance, freedom from sensitivity to orientation angles, and lower cost compared to the blue-red combinations. The micro-sheet types are cheaper but they more than double transmission losses and their optical-thermal properties degrade more for a given time in space when compared to fused silica or quartz. Although microsheet was favored in earlier studies because of low initial cost, degradation and relative losses need to be considered with cell costs and design confidence before an optimum selection can be made. This is particularly true where coverslides represent a rather small part of the total array design, fabrication, and integration cost. For this reason, the higher performance, fused silica coverslides were selected as the baseline for this study.

The coverslide specifications are given in Table F-2. Figure F-9 shows typical transmittance and reflectance characteristics of the blue filter coverslide specified.

TABLE F-2. COVERSLIDE FOR SOLAR CELLS

Common Name	Blue Filter Coverslide
Size	$4 \times 1.88 \times 0.05$ cm
Material	Fused Silica
Mfg. Type (Typical)	Corning 7940
Ultraviolet Rejection Coating Antireflective Coating	Below $0.410 \pm 0.015\mu$ Less than 2% reflection from 0.575 to 0.675μ
Transmission Losses	Overall losses less than 4% above 0.450μ
Thermal Properties:	(On 2 ohm-cm solar cell)
Absorbance, α	0.78 ± 0.01
Emittance, ϵ	0.82 ± 0.02 @ 100°C
$\Delta\epsilon/\Delta T$	$\sim 3.64 \times 10^{-4}$ per $^\circ\text{C}$

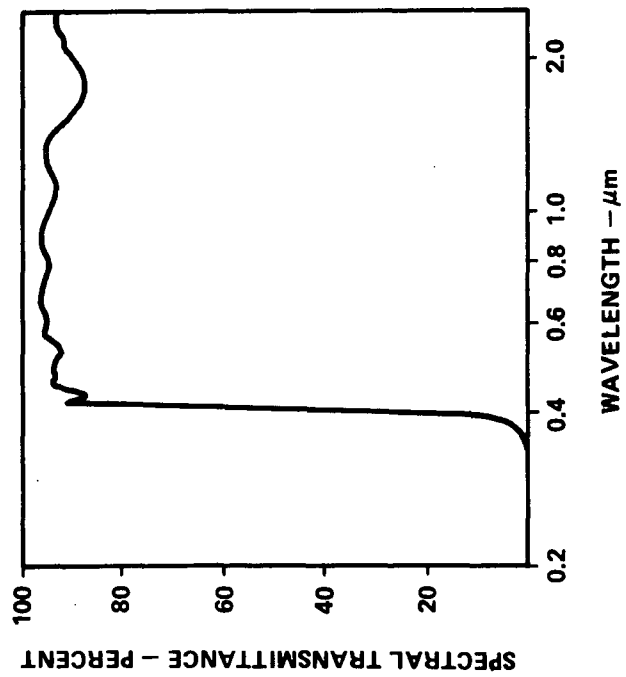
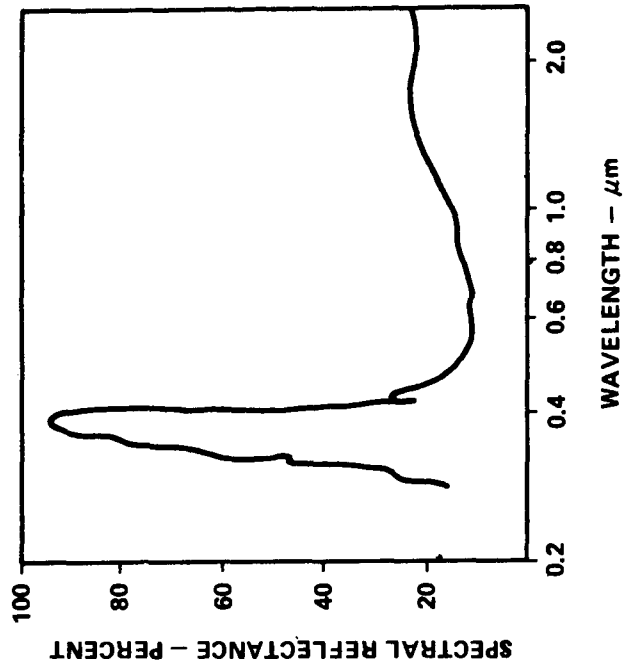


Figure F-9. Coverslide characteristics.

The effects of the coverslides on solar cell performance is discussed in the following section.

3. Solar Cell Characteristics

a. Solar Cell Coefficients and Design Factors. Solar cell characteristics and ratings are specified under conditions recognized as standards by the industry for test and acceptance purposes. A bare cell is rated at the standard performance test conditions of $28^{\circ} \pm 2^{\circ} \text{C}$ temperature and light source calibrated for air mass zero (AMO) intensity and spectral distribution. The light intensity specified is 140 milliwatts per cm^2 . Power and efficiency ratings are based on the total energy of the solar spectrum as an input but only on the effective area (excludes contact area) of the cell. The angle of incidence is within 1 degree of normal to the cell.

To analyze the solar array performance for conditions and variations imposed by the mission, the initial cell characteristics must be adjusted. The coefficients and factors used to correct the solar cell characteristics for the HEAO-C mission are defined as follows:

1. Fabrication loss — The loss in performance incurred by assembling cells into modules. Primarily, these losses are caused by coverslides, series resistance, and mismatch of cell characteristics. A total 5 percent loss allowance has been made which gives a power efficiency correction, η_f , of 0.95.

2. Mismatch and calibration error — Difficulty with accurate calibration and measurement of light sources, standards, and cell characteristics often leads to erroneous predication of array performance. No loss has been assigned for these factors in this study.

3. Degradation — Experience has shown that solar cell performance degrades with time in space. Degradation can be attributed to damage caused by particle and ultraviolet radiation, micrometeorite damage, and deterioration of contacts. Such effects are not well understood on a combined basis, and the environment cannot be accurately predicted because of random variations. Therefore, an allowance of 4 percent per year loss is not considered too conservative for a 2 year mission. The efficiency correction for degradation, η_{rad} , was 0.96 per year.

6. Reflectance — Solar cell ratings are based on a light intensity of 140 mW/cm² (AMO) incident on the cell with an incidence angle of 0 degrees; i. e., the plane of the cell is perpendicular to the light vector. Since the effective intensity varies as the cosine of the angle of incidence, the cell output can be expected to vary in the same manner except for large angles of incidence, where surface reflection decreases the effective input energy. As the incidence angle increases, the reflectance of the coverslide and cell increases, causing the cell output to decrease more than prescribed by the cosine law. Neglecting coverslide coatings the variation in front surface reflectance is described by the Fresnel formula:

$$\rho(\phi) = \frac{1}{2} \left[\frac{\tan^2(\phi - \phi^1)}{\tan^2(\phi + \phi^1)} + \frac{\sin^2(\phi - \phi^1)}{\sin^2(\phi + \phi)} \right] \quad (1)$$

where

ϕ = Angle of incidence in degrees

ϕ^1 = Angle of refraction in degrees.

The angle of refraction is defined by Snell's law:

$$\phi^1 = \arcsin \frac{(\sin \phi)}{n} \quad (2)$$

where

n = index of refraction

~ 1.46 for coverslides specified.

The energy transmitted to the solar cell can then be expressed in terms of energy transmitted at 0 degrees incidence as follows:

$$S(\phi) = S(0) \left[\frac{1 - \rho(\phi)}{1 - \rho(0)} \right] \cos \phi \quad (3)$$

Figure F-10a shows the variation of theoretical reflectance and the predicted effective intensity [equation (3)] as a function of the incidence

angle, for a solar cell covered with a coverslide. The coverslide coatings add to the reflection effect causing the cell performance to deviate from that predicted by the intensity curve of Figure F-10b. Measured cell output as a function of incidence angle shows that the cell outputs can be lower than that predicted by the Fresnel formula. Such deviations are shown by Figure F-10b. For all practical design purposes, however, the theoretical prediction is satisfactory because differences in refraction index and coatings can account for the small differences given by the specific example shown.

It may be noted from Figure F-10 that the losses due to reflectance are insignificant for incidence angles lower than 45 degrees.

b. Cell Characteristics as a Function of Mission Conditions. The initial characteristics and design coefficients were inserted into a computerized mathematical model for silicon solar cells to derive characteristics for various design point conditions. The model produces V-I characteristic curves for simultaneous variations of input conditions such as temperature, orientation, intensity, and environmental effects. A typical example of corrections made to obtain an EOM operating characteristic is described below, using small case letters to signify parameters on a cell basis, and using primes to signify initial reference values, listed in Table F-1.

The rated maximum power produced by the cell, p'_m , can be defined as:

$$p'_m = v'_m \cdot i'_m = S' \cdot \eta' \cdot \eta_a \cdot A_c \cos O^\circ \text{ (at } T = 28^\circ\text{C)},$$

where v'_m and i'_m are the initial, rated voltage and current, and

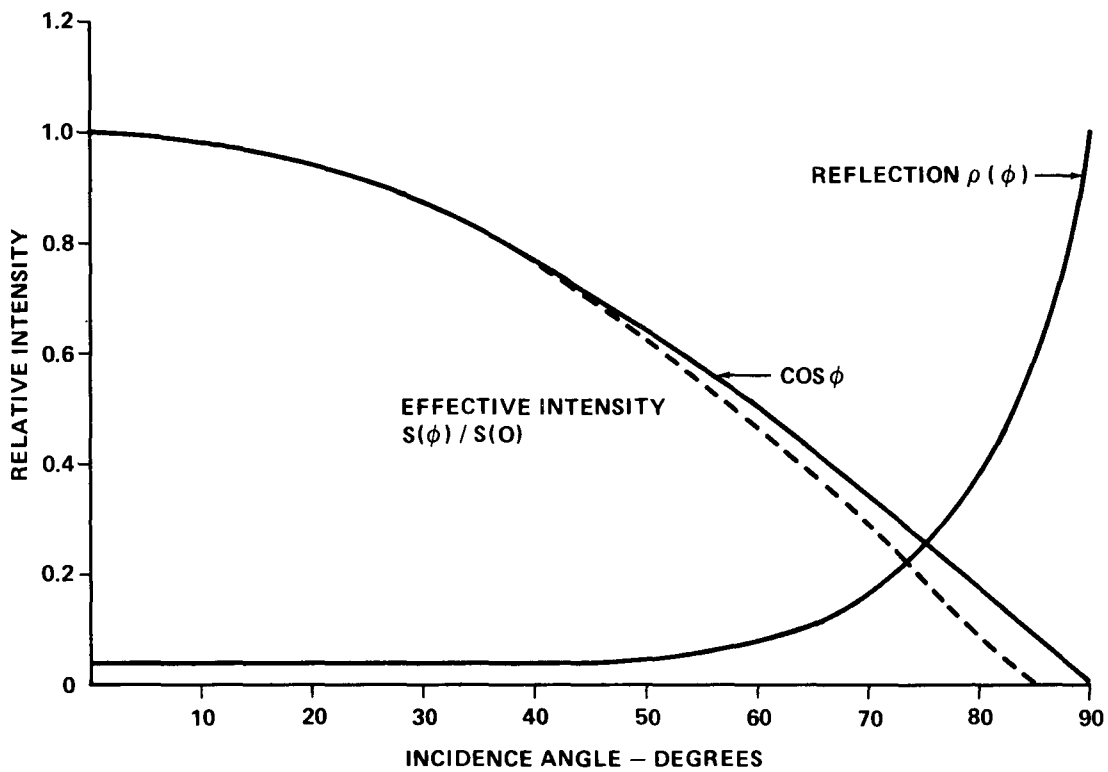
$$S' = \text{Standard intensity } 139.5 \text{ mW/cm}^2.$$

$$\eta' = \text{Rated cell efficiency.}$$

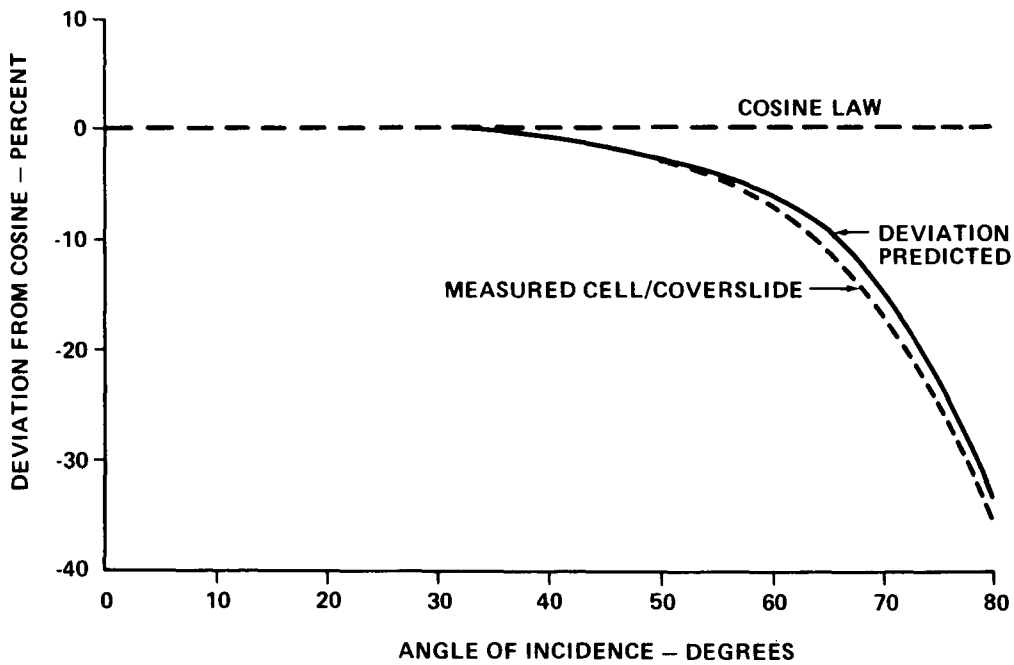
$$\eta_a = \text{Ratio of effective area to cell area.}$$

$$A_c = \text{Cell area in cm}^2.$$

The maximum power for an EOM condition is defined by the characteristics that exist at the given condition and the defined coefficients:



a. PREDICTED EFFECTS



b. DEVIATIONS FROM COSINE LAW

Figure F-10. Reflectance effects on solar cell performance.

10 ④

$$p_m = v_m \cdot i_m = f(p'_m)$$

$$p_m = S \cdot \eta_{\text{EOM}} \cdot \eta_a \cdot A_c \cos \phi \left[\frac{1 - \rho(\phi)}{1 - \rho(0)} \right] (1 + K_p \Delta T) .$$

In terms of the initial conditions, and assuming an oriented case in space (i. e., incidence angle $\phi = 0$), the equations become:

$$p_m = S \cdot \eta' \cdot \eta_a \cdot A_c \cdot \eta_f \cdot \eta_{\text{rad}}^2 (1 + K_p \Delta T)$$

or

$$p_m = \frac{S}{S'} p'_m (\eta_f \cdot \eta_{\text{rad}}^2) (1 + K_p \Delta T) = \frac{S}{S'} f(v'_m \cdot i'_m)$$

where

S = EOM effective solar intensity in mW/cm^2 .

η_f and η_{rad} = Efficiency corrections for fabrication and degradation.

K_p = Temperature coefficient for power.

ΔT = $T - T_{\text{rated}} = T - 28^\circ\text{C}$.

T = Temperature of the condition in $^\circ\text{C}$.

To adjust the voltage and current characteristics for the same EOM condition, an appropriate portion of the fabrication and degradation losses must be allocated to current and to voltage. Noting that these losses primarily affect short circuit current, the following allocations were used:

$$\eta_f = 0.996_{(v)} \cdot 0.954_{(i)} = 0.95$$

$$\eta_{\text{rad}} = 0.97_{(v)} \cdot 0.95_{(i)} = (0.96)^2 = 0.92 .$$

The resultant correction for voltage, η_v , is then 0.967, and for current, η_i , is 0.906.

The short circuit current, i_{sc} , may then be found for the same EOM condition as follows:

$$i_{sc} = (\eta_i \cdot i'_{sc}) \left(\frac{S}{S'} \right) (1 + K_{sc} \cdot i'_{sc} \cdot \Delta T)$$

where K_{sc} is the temperature coefficient for current.

The open circuit voltage, v_{oc} , adjusted for degradation and temperature is determined as follows:

$$v_{oc} = (\eta_v \cdot v'_{oc}) (1 + K_{oc} \Delta T)$$

where S is not greatly different from S' , and K_{oc} is the temperature coefficient for v_{oc} .

The current, i_m , and the voltage, v_m , can be determined in the same manner as i_{sc} and v_{oc} using the appropriate coefficients from 3. a. of this subsection.

Table F-3 gives oriented cell characteristics for a few typical mission conditions.

TABLE F-3. SOLAR CELL CHARACTERISTICS AT TYPICAL MISSION CONDITIONS

Time (yr)	Temp (° C)	V_{oc} (V)	I_{sc} (mA)	V_m (V)	I_m (mA)	P_m (mW)	S (mW/cm ²)
BOL	28	0.585	273	0.458	261	114.0	140
1	60	0.503	277	0.382	252	96.3	143
2 (EOM)	70	0.460	265	0.354	241	85.5	140

Solar Array Analysis

1. Baseline Configuration and Area. The final baseline solar array has been described in Chapter VIII and was illustrated by Figure VIII-3. The basic configuration of the baseline did not change during the study, although the panel size and stacking factor were adapted to the HEAO-C requirements established.

The octagonal spacecraft dimensions, groundruled from previous studies, were 360 inches long with 105 inches O.D. maximum at the corners and a side width of approximately 40 inches. Since groundrules did not permit multiple-folded wings, the area limit on the solar array was essentially that of four sides of the regular octagon. The basic configuration initially selected as the baseline is shown in Figure VIII-4. This configuration was selected because:

- Initial load requirements were much greater than determined during the study.
- It provided a larger growth potential than the alternates.
- It permitted lower cell density and lower temperature for body mounted panels.

It should also be noted that the baseline configuration requires the Z-axis to be through the corners. The deployment angle, δ , required to orient the array wings toward the sun is 67.5 degrees.

Alternate configurations are feasible and are discussed in this appendix. Also, these were confined to the spacecraft configuration specified.

The four areas, A_1 , A_2 , A_3 , and A_4 (Fig. VII-4), indicate that the solar array is divided into four parts designated as sections. Each section is composed of several panels. The nonmoveable sections are referred to as "body sections." The deployed (flip-out) sections are called "wings." The limiting area of each side is 40 in. by 360 in. = 14 400 in.² or 100 ft². Subtracting an allowance for panel spacing, corner spacing, and mounting hardware reduces the maximum area per side available for solar panels to 97 ft².

The total solar cell area for each array section was approximated initially as follows:

A_1, A_2, A_3, A_4 = Cell area per section denoted.

$A_1 = A_4$, and $A_2 = A_3$ for symmetry.

A_S = Area per side available for solar panels.

m_f = Mounting factor (allowance for mounting hardware and panel border).

= ratio of area available for cells to A_S .

sf = Stacking factor = ratio of cell area to that available for cells (sf_w used for wing section, sf_b used for body sections).

The cell area for the wings initially was:

$$A_1 = A_4 = (mf)(sf_w) A_S = (0.97)(0.89) 97$$

$$A_1 = A_4 = 83.7 \text{ ft}^2 \text{ or } 7.78 \text{ m}^2.$$

For the body sections:

$$A_2 = A_3 (mf)(sf_b) A_S = 0.97 (0.35) 97$$

$$A_2 = A_3 = 32.9 \text{ ft}^2 \text{ or } 3.06 \text{ m}^2.$$

The above factors were later corrected after considering practical panels and solar cell arrangements to:

$$A_S = 96.25.$$

$$mf = 0.949.$$

$$sf_w = 0.903.$$

$$sf_b = \text{Variable from 0 to 0.66 (temperature limit)}.$$

The stacking factor, representing the solar cell density, was limited for the body sections to keep the temperature below the 100°C limit set for reliable operation of cell assemblies.

2. Initial Calculations. Initial solar array performance calculations were made on the basis of maximum power characteristics of cells to determine approximate array area requirements to meet the electrical requirements. It was established earlier that the design load of 722 watts average requires the solar array to deliver 1549 watts based on the system performance factor of 2.14 for the orbit with the maximum occultation period of 35.7 minutes.

At EOM (2 years), the array must continuously support the system loads for the 15 degree off-sun pointing of the spacecraft. Short term performance for 30 degree pointing is also required. To meet these design conditions, the total array area required may be approximated by the following equation:

$$A_t = \frac{P_{SAR}}{(sf) (mf) S \cos \phi \cdot \eta \cdot \eta_f \cdot (\eta_{rad})^y (f_r) [1 + K_p (T - 28^\circ)]}$$

where all symbols have been defined except:

y = Length of mission (years).

f_r = Correction for reflection if incidence angle ϕ exceeds 45 degrees.

η = Solar cell efficiency corrected for effective area.

The above equation assumes that the entire array lies in the same plane and has a common temperature. The baseline, however, has panels in three planes. Therefore, the power produced by each section is determined, and neglecting small losses due to voltage differences, the section powers are summed to obtain the total array output. Since both wing sections lie in the same plane computations are simplified by considering them together so that the solar array output power is defined by:

$$P_{sa} = 2 P_w + P_2 + P_3$$

where P_w is the power produced by one wing and P_2 and P_3 represent the power of the two body sections.

Using the areas and factors defined in subparagraph 2. above, these requirements were iterated with the configuration constraints and preliminary thermal data to apportion cell areas to the four array sections. Since the baseline configuration provided adequate area to support this load, the wing sections were assigned the high, 90 percent stacking factor (consistent with normal panel fabrication techniques) because they would operate at a lower temperature and a higher efficiency than the body sections would if they had the same stacking factor. The initial baseline set the stacking factor for the body section at 35 percent.

An example of the initial calculation results is given in Figure F-11. The total output of the array, having wings with a 90 percent stacking factor and body sections with a 35 percent stacking factor, is shown as a function of the time in sunlight. The performance indicated is based on the temperature profiles given in Chapter VII for the 15 degree off-sun orientation. It may be observed that the power produced with these stacking factors is considerably higher than required. The pronounced effect of temperature on solar array performance is also indicated by Figure F-11. The "cold" array emerging from darkness at about 0.45 hour produces approximately 1000 watts more than at the end of the sunlight period, where it has become heated.

Later computer runs, using V-I characteristics, were made to determine array performance for some of the established design cases. Other stacking factors were considered for the body sections to adjust the solar array performance to the design requirements. It should be noted further that time did not permit iteration of all array cases with a thermal analysis. Therefore, simplified scaling equation and curves were used to determine solar array temperatures for cases other than initial baseline cases. As shown later, all scaling was referenced to the baseline thermal data discussed in Chapter VI to obtain relative comparison to the baseline performance. The later studies used design factors consistent with the baseline solar panels.

3. Baseline Solar Panels

a. Size Constraints. It has been shown that the baseline solar array consisted of four areas: two wing sections and two body mounted sections. The octagonal configuration and the dimensional limits placed on the baseline structure not only fix the ultimate array area and power but, also, influence the practical modularization of the array into panel assemblies. Commonality with solar panel configurations defined in Phase B studies of HEAO A/B missions also influenced the selection of solar panel dimensions that have been baselined. The maximum panel length considered practical in these earlier studies was approximately 120 inches, being influenced by the panels planned for the Skylab. Since the spacecraft length is 360 inches without sun shield, the length of each array section was divided into three parts. Allowing for mounting and deployment clearance, the maximum panel length will be about 119.5 inches. Although the envelope indicates that each side of the octagon can be about 40 inches, the panel width must be at least 1 inch less to allow for hinges, mounting, and deployment hardware. The panel thickness was constrained to about 0.75 inch by the inner structural envelope and an allowance for the thickness of the thermal covering on the spacecraft. Panel thickness and hinges turned out to be critical limits on the panel design dimensions.

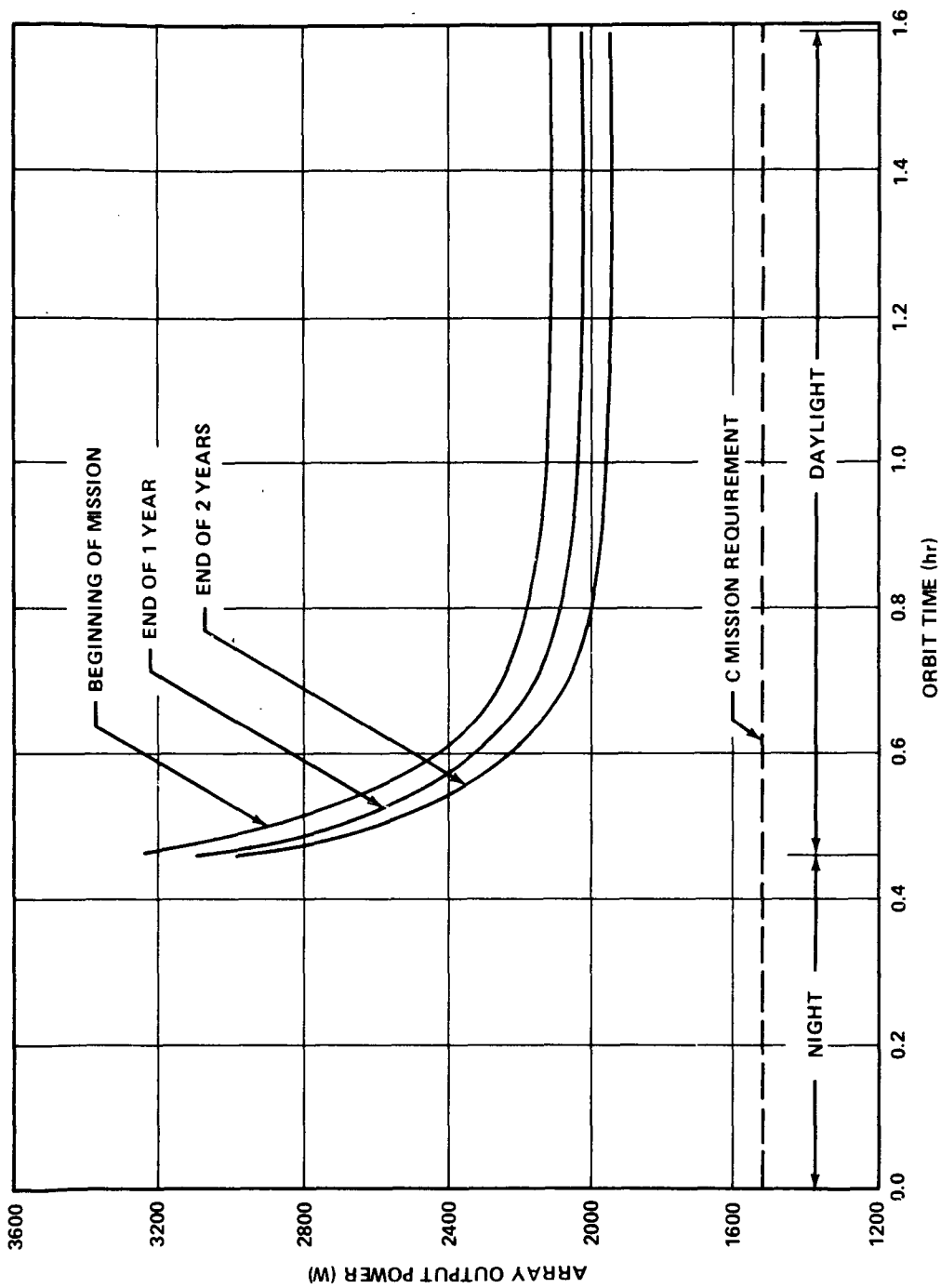


Figure F-11. Performance of initial array design for 15 degree orientation as a function of time in sunlight.

Considering practical subassemblies and arrangements of cells also influences the panel size for efficient area utilization. The reverse is also true — panel dimensions influence practical series — parallel arrangements that can lead to off-optimum voltage arrangements.

b. Substrate and Configuration. The solar array panels for HEAO-C consist of solar cell modules, connections and wiring, adhesives, and insulation materials mounted on an 0.7 inch aluminum honeycomb substrate. Aluminum, U-shaped channels, inserted in the honeycomb to frame the panel, provide smooth edges and additional rigidity. Each panel is 119.2 inches long and 38.2 inches wide which meets the spacecraft configuration constraints and provides an area optimized for a 90 percent stacking factor after allowance was made for border and mounting hardware. One wing section panel was shown in Figure VIII-10.

Structural and dynamic characteristics of the panel are discussed in Chapter V. These studies indicated that the original substrate thickness of 0.375 inch was inadequate to meet launch conditions. Therefore, the baseline was changed to 0.7 inch thickness. The weight penalty for this increase was very small. Figure F-12 shows the sensitivity of panel weight to substrate thickness. Panel weight is dominated by face-sheet thickness and adhesives.

The baseline solar panel weight is 36.1 pounds. Figure VIII-10 shows a cross section of the panel and gives a detailed weight breakdown for the parts and materials involved. Body section panels with a 35 percent stacking factor would weigh 31.6 pounds.

For design commonality, the same dimensions and physical design were used for the body mounted panels except that no hinges and release attachments are necessary. Should iteration of requirements show that no body mounted cells are needed, the body mounted panels should be eliminated and replaced with the appropriate thermal coverings.

The same panel designs are considered practical for the alternate array configurations analyzed in this appendix and for the A/B missions.

c. Cell Arrangement. It has been shown that each section of the array was divided into three panels by the selection criteria used for sizing. Iteration of practical cell arrangements with area available panels, described earlier in this appendix, led to determination of the panel dimensions which allows an area of 36.8 by 118.2 inches (28 300 cm²) for solar cells. The

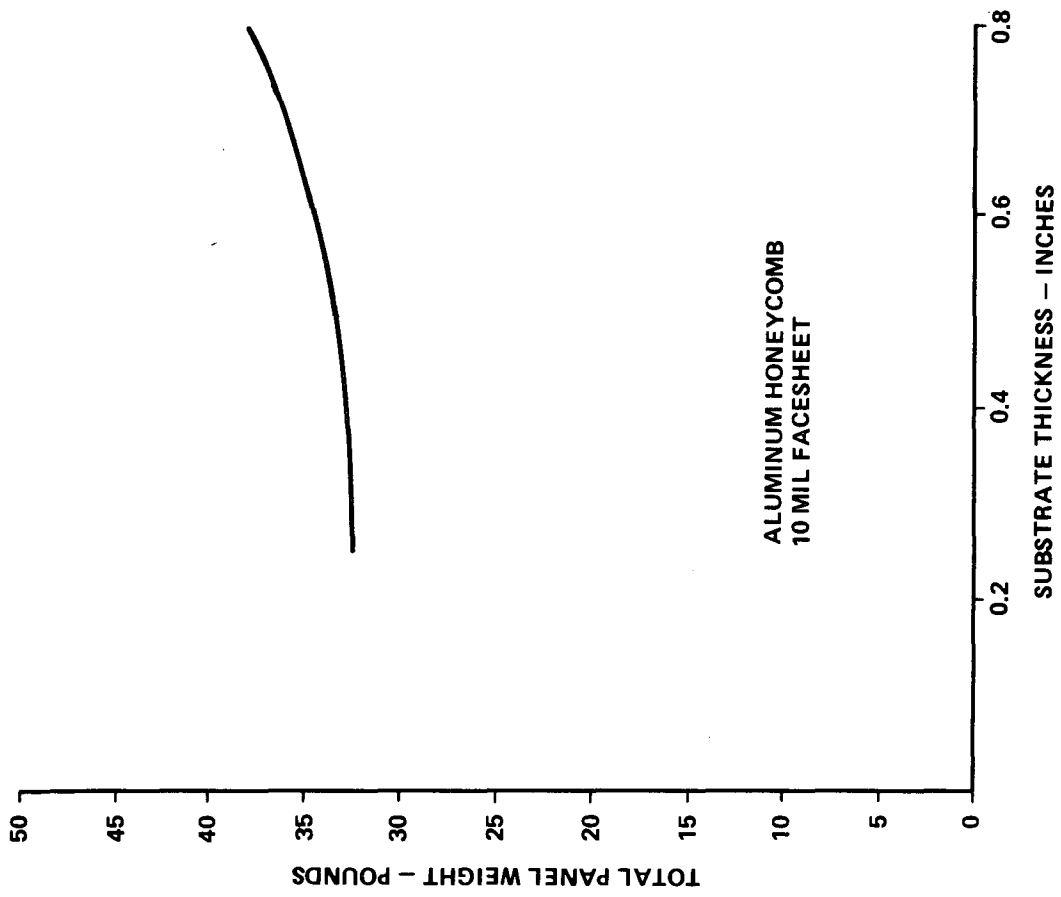


Figure F-12. Solar panel weight versus substrate thickness.

mounting allowance for the panel (not the same as the mf used before) is $36.8 \times 118.2 \div 38.2 \times 119.2 = 0.949$. Using the final stacking factor for wing panels $sf_w = 0.903$, the cell area per panel, A_{pc} , is:

$$\begin{aligned} A_{pc} &= 1/3 A_1 = 1/3 A_4 = (mf_p)(sf_w) A_p \\ &= 0.949 (0.903)(29\ 200) \\ A_{pc} &= 25\ 520\ \text{cm}^2. \end{aligned}$$

The number of cells per panel is then:

$$\text{Number of cells} = \frac{A_{pc}}{A_c} = \frac{25\ 520}{8}$$

$$\text{Number of cells} = 3190 .$$

To use the more efficient stepdown (bucking) converter principles for battery chargers sets a minimum voltage on the primary solar power buses which is above the voltage of the battery under charge plus the voltage drop needed across the charger. For HEAO-C, the minimum at the charger is estimated at 36.5 volts. Allowing for transmission and diode drops, the minimum array voltage is 38.0 volts. The minimum number of solar cells in series can then be determined for design load and temperature conditions using the solar cell V-I characteristics. The minimum cell voltage at maximum power expected for the application is 0.35 volt which requires at least 108 series cells.

Consideration of panel dimensions and thermal conditions leads to an arrangement with the cells connected in series across the width of the panel to minimize the detrimental effects of temperature gradients that can be expected across the panel. Such problems are discussed in References F-2 and F-3. Only central conditions were specifically analyzed, thermally, for the solar array in this study. The panel width limits the number of cells in series in one row to 44. Along the length, 73 rows of cells can be mounted with the proper spacing. Considering symmetry and practical locations for termination of cell modules influences the selection of cell grouping that permits 110 series cells in two and one-half rows. A total of 29 series groups would then be permissible in 73 rows with the last row containing only 22 cells.

Based on practical sizes of submodules and modules that can be easily handled and assembled at once, the electrical arrangement and groupings that best use the panel area are shown by Figure VIII-11. For the baseline design, a wing panel requires 10 solar cell assemblies (3190 cells) to achieve the prescribed 90 percent stacking factor. A 42 percent stacking factor is needed to mount the 1540 cells required on the body section panels.

4. Orientation and Temperature Studies. Studies were made to establish orientation and temperature data needed for later array performance analyses. Array performance depends on the simultaneous orientation and temperature conditions of each panel. The temperature is a function of orbital and pointing conditions.

a. Orientation Model. A computer program written for attitude and control studies was used to analyze the effects of varying the spacecraft orientation and the orbital parameters possible for the mission. The configuration model and symbols used for orientation studies are shown in Figure F-13. A space-fixed coordinate system, designated by capitals X, Y, Z, is used as a reference for defining the sunline and spacecraft positions. The small letters, x-, y-, and z-axes, represent the spacecraft coordinates. The corresponding axes of the two coordinate systems coincide when the spacecraft is at its reference position.

With reference to Figure VIII-4, the orientation angle, ϕ_0 , is defined as the angle between the sunline, S, and the z-axis of the spacecraft. Since the wings are perpendicular to the z-axis, the normal vector, N_1 , in Figure F-13 represents the vector normal to the wings. Thus, the orientation angle, ϕ_1 , for the wings is the same as ϕ_0 , in this case; the orientation specified for the spacecraft, ϕ_1 , differs from ϕ_0 only if the wing deployment angle is allowed to be different from the 67.5 degree baseline.

Planes 2 and 3 have the same relationship to plane 1 in Figure F-13 as the wings have to sections 2 and 3 in Figure VIII-4. Therefore, the sunlight angle of incidence of the body sections is defined by angles ϕ_2 and ϕ_3 of the model. The term "tilt" infers that the z-axis moves off the sunline by tilting the x-axis toward or away from the sunline. The term "roll" means the x-axis remains essentially perpendicular to the sunline and the vehicle rolls the z-axis off the sunline. Letting angles ψ and Θ be 0, the roll motion is simulated by fixing the body and then varying the angle β . A scanning mode may be simulated by setting different combinations of β and Θ and then letting ψ vary.

STIMULATED CONFIGURATION
FOR HEAO-C SOLAR ARRAY

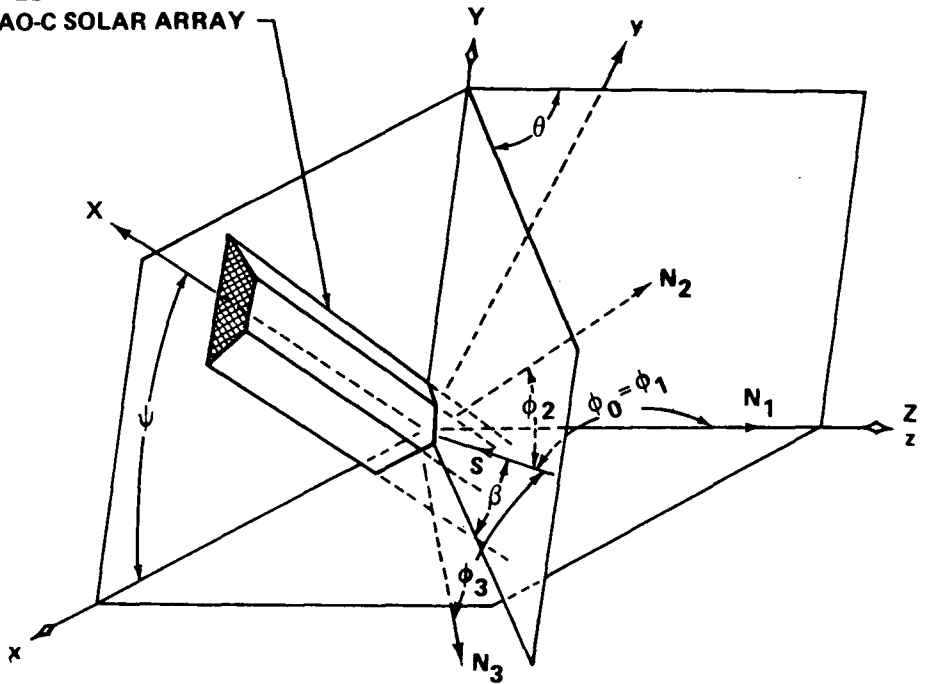


Figure F-13. Array orientation model.

The cosine of the incidence angles for the various array sections may be derived from Figure F-13 by obtaining the dot product of vector, S , and the vectors, N_1 , N_2 , and N_3 , normal to the planes representing the solar array sections, as follows:

$$\hat{N}_1 = |N_1| (o + j_o + k \cos o \text{ degree})$$

$$\hat{S} = |S| (\cos \beta \sin \Theta + j \sin \beta + k \cos \beta \cos \Theta)$$

then

$$\cos \phi_1 = \hat{N}_1 \cdot \hat{S} = \cos \beta \cos \Theta.$$

Similarly,

$$\begin{aligned} \cos \phi_2 = \hat{N}_2 \cdot \hat{S} = & \sin 22.5 \text{ deg} (\cos \beta \sin \Theta \sin \psi + \sin \beta \cos \psi) \\ & + \cos 22.5 \text{ deg} (\cos \beta \cos \Theta) \end{aligned}$$

$$\cos \phi_3 = \hat{N}_3 \cdot \hat{S} = \sin 337.5 \text{ deg} (\cos \beta \sin \psi \sin \Theta + \sin \beta \cos \psi) \\ + \cos 337.5 \text{ deg} (\cos \beta \cos \Theta) .$$

NOTE: ϕ_1 will equal ϕ_0 for all cases where the deployment angle, δ , of Figure VIII-4 is fixed at 67.5 degrees.

Typical variations of the body section incidence angles, ϕ_2 and ϕ_3 , are shown for an example scanning mode (ψ varies) in Figure F-14.

The computer routines simulating orbital and seasonal variations may be related to the above functions, permitting simultaneous numerical solution for any specified mission and pointing condition. The incidence angle functions determined may then be inserted into a program which determines the power produced by each section of the array and the total power in accordance with the following equations:

$$P_w = A_s (mf)(sf_w) S \cos \phi_1 [f(r)] (\eta) \eta_f (\eta_{\text{rad}})^y [1 + K_p (T_1 - 28 \text{ deg})]$$

$$P_2 = A_s (mf)(sf_b) S \cos \phi_2 [f(r)] (\eta) \eta_f (\eta_{\text{rad}})^y [1 + K_p (T_2 - 28 \text{ deg})]$$

$$P_3 = A_s (mf)(sf_b) S \cos \phi_3 [f(r)] (\eta) \eta_f (\eta_{\text{rad}})^y [1 + K_p (T_3 - 28 \text{ deg})]$$

and the total array power, P_{SA} , is:

$$P_{SA} = 2 P_w + P_2 + P_3 .$$

The temperatures required for solution, and their dependence on other functions and design factors, are discussed in the next subsection.

b. Array Temperature Relationships. The thermal analysis of the solar array was based on the initial baseline parameters below:

Wing stacking factor = 90 percent

Body stacking factor = 35 percent

Deployment angle (wing) = 67.5 percent

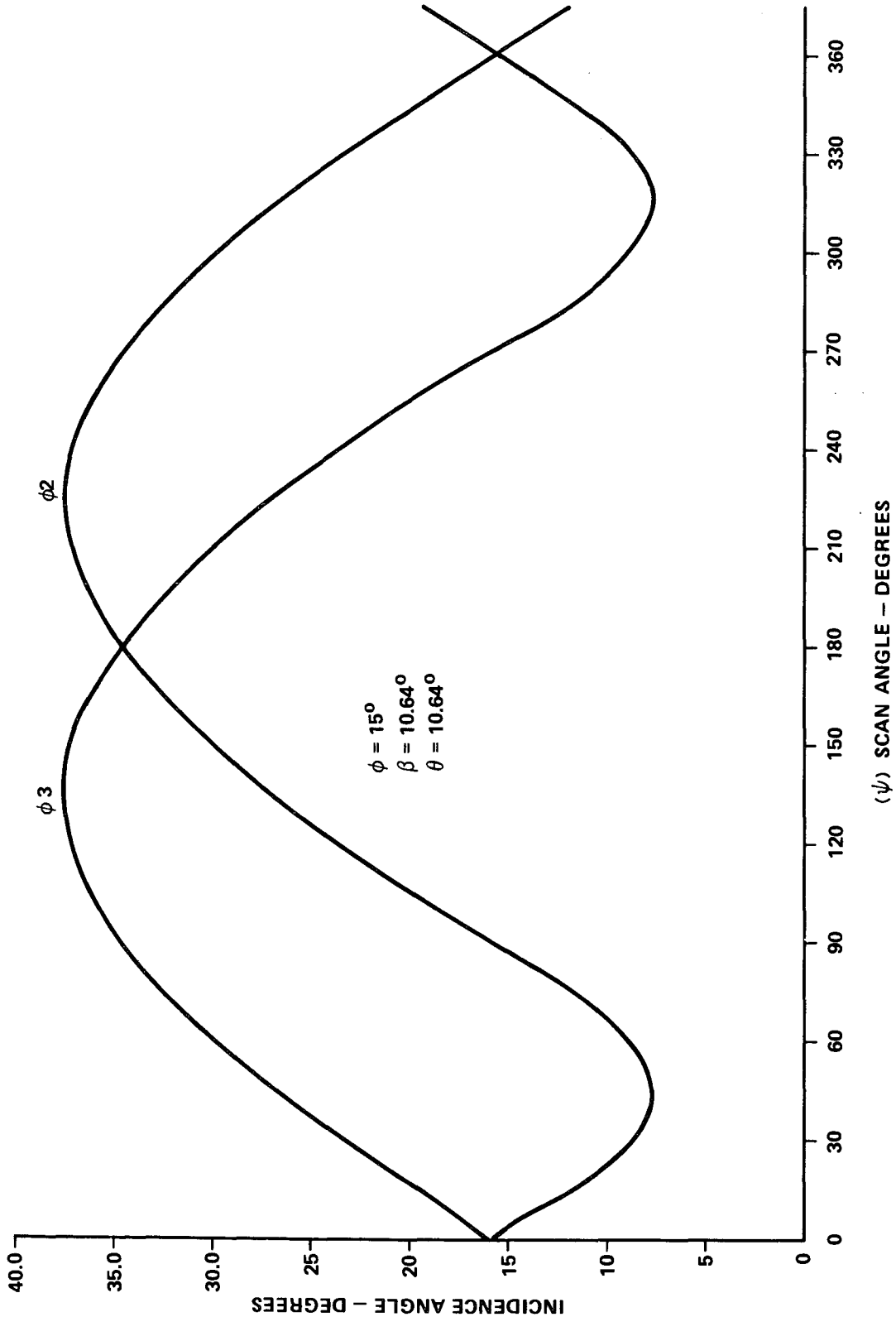


Figure F-14. Typical variations of array incidence angles with scanning.

$$\text{Cell, } \alpha/\epsilon = 0.78/0.83$$

$$\text{Other surface, } \alpha/\epsilon = 0.35/0.85$$

To analyze a wide range of orientations and stacking factors, the thermal control group supplied simplified, theoretical, thermal balance equations that could be used to adjust maximum temperatures for different stacking factors. These equations describe temperature equilibrium with radiative heat transfer and neglect such things as conductance, albedo, etc. However, when these are referenced to the baseline temperature profiles, obtained by the more rigorous thermal analysis in Chapter VI, reasonably accurate predictions may be expected.

Prediction of body-mounted temperatures, peak and average, were made using Figure F-15. The curve labeled theoretical was derived from radiative heat transfer equations and describes a free body in a nonconducting medium. The corrected curve gives the maximum predicted temperature after the theoretical curve is referenced to baseline thermal profiles. It should be noted that a substantial variation of solar constant, S , exists with mission time, which is expected to decrease the predicted temperatures because "hot" case orbit data were used. Solar intensity variations caused by solar activity have been neglected. Figure F-15 is for an orientation of 0 degree which is equivalent to body panel incidence angles, ϕ_2 and ϕ_3 , of 22.5 degrees. It may be observed that a maximum stacking factor that can be used on the body section is about 65 percent if the 100°C temperature limit for the solar cell assemblies is not to be exceeded. Present requirements do not require high stacking factors.

Average temperatures, related to the maximums, were derived for orbital maximum and minimum sunlight periods. The temperature, which was averaged over the sunlight period of the orbit for body section solar panels with various stacking factors, is shown as a function of light incidence angle in Figure F-16.

The effects of varying the solar array deployment angle on solar array temperature was studied in Reference F-2. Thermal data from this reference and from previous Phase A studies were used to derive parametric temperature curves, scaled to the baseline, for deployment variations.

Figure F-17 relates maximum panel temperature to deployment and incidence angles. As the deployment angle is increased, the panel temperatures decrease. The variation shown occurs because the heat-sink temperature

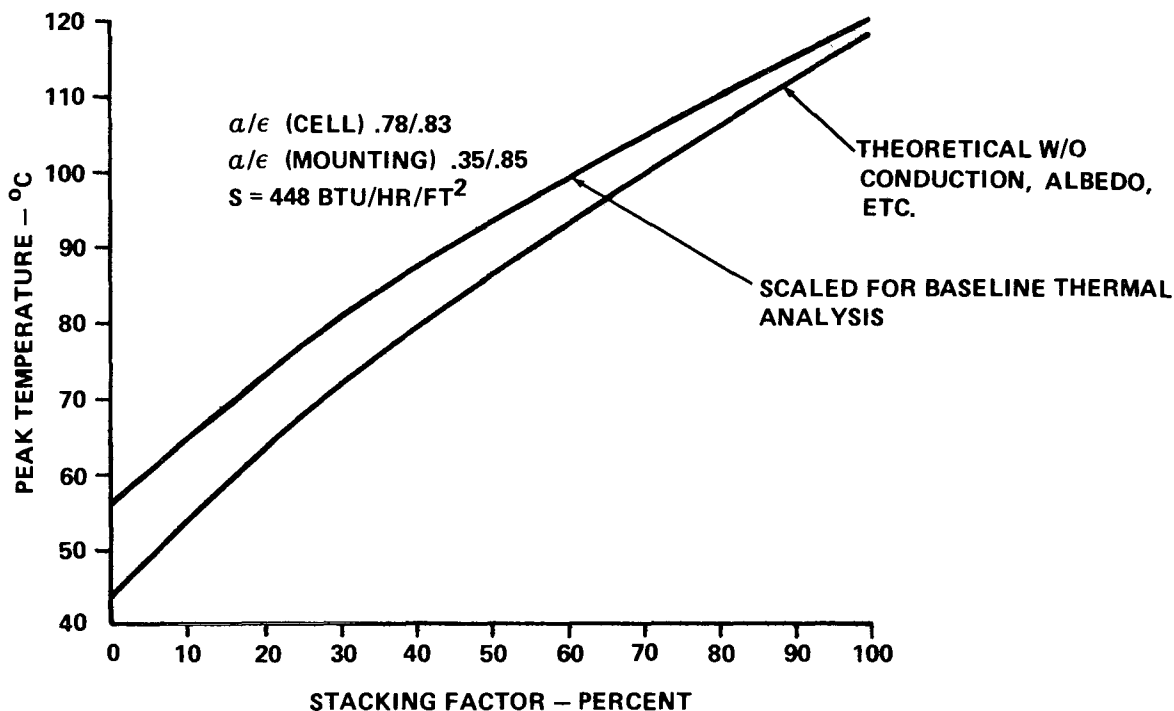


Figure F-15. Effect of stacking factor on array maximum temperature.

for the rear of the solar panel is dependent on the reradiation from the spacecraft and the amount of body surface viewed by the panels. This decreased peak temperature, obtained with larger deployment angles, is one of the reasons the baseline array configuration was selected. A possible undesirable aspect is that the decreased maximum temperature results in faster thermal transient; however, the increased power available outweighs any expected degradation.

Figure F-18 shows the variation of solar array wing average temperature with variable incidence and deployment angles. This curve shows that there is no particular advantage in exceeding the baseline 67.5-degree deployment angle. This figure was used to develop data for the average power capability of the wing panels.

It should be noted that both average and peak temperature curves are for the average, central location on the wings. Temperature gradients across the wings are recognized, but these will not be as severe for the baseline as they would be for the alternate configurations discussed later.

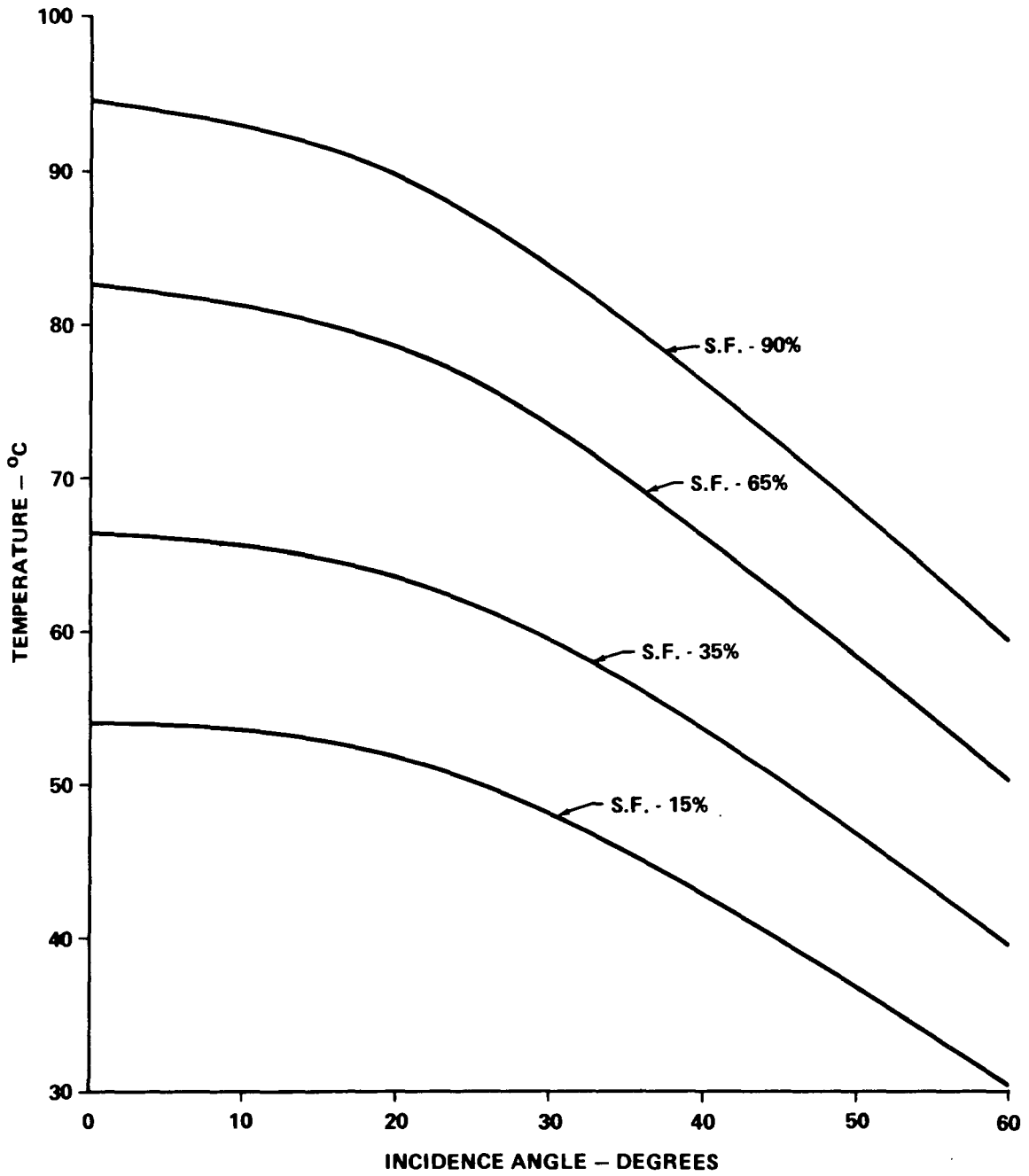


Figure F-16. Average body section temperature variations with incidence and stacking factors.

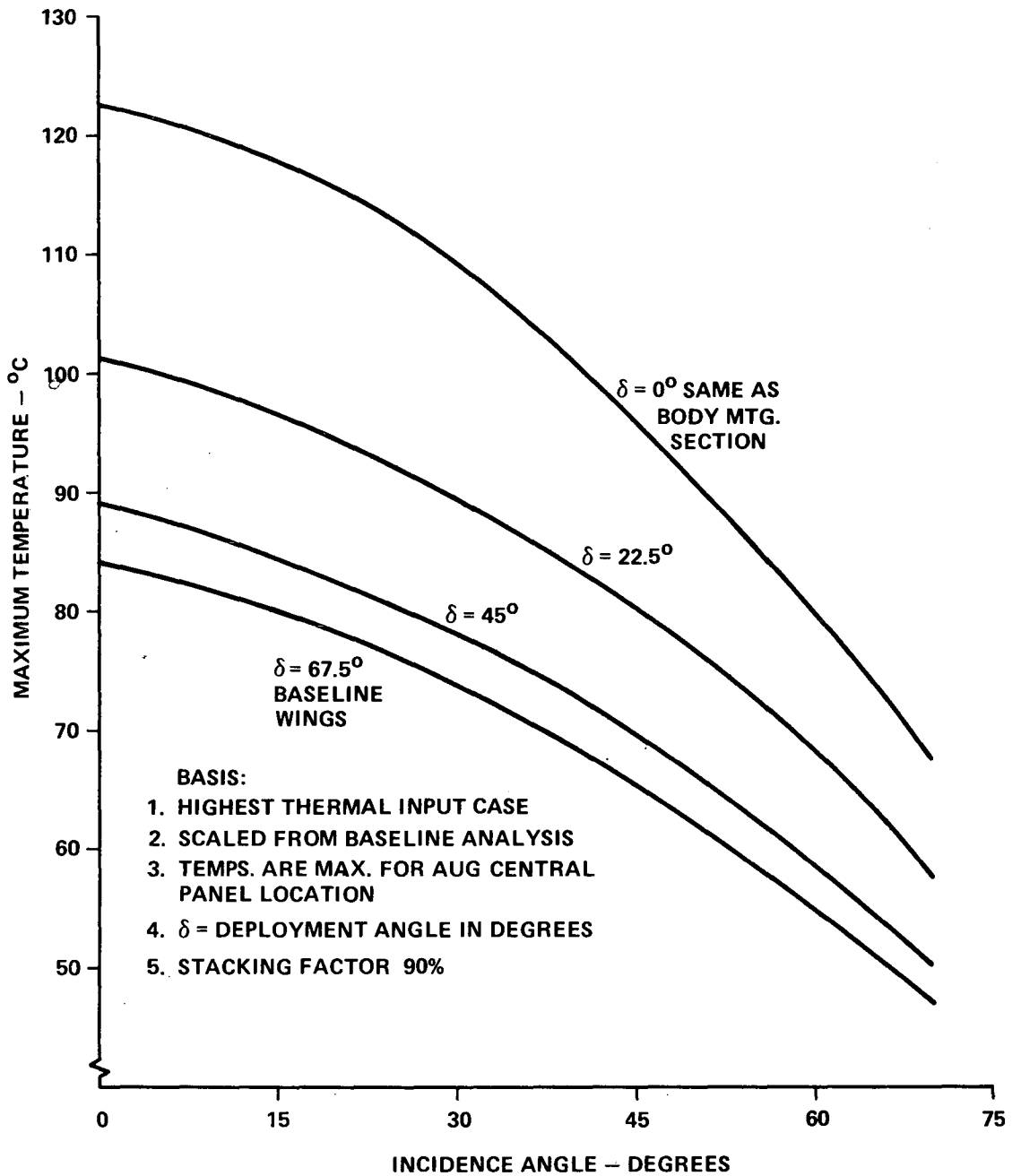


Figure F-17. Maximum wing temperature dependence on incidence and deployment angles.

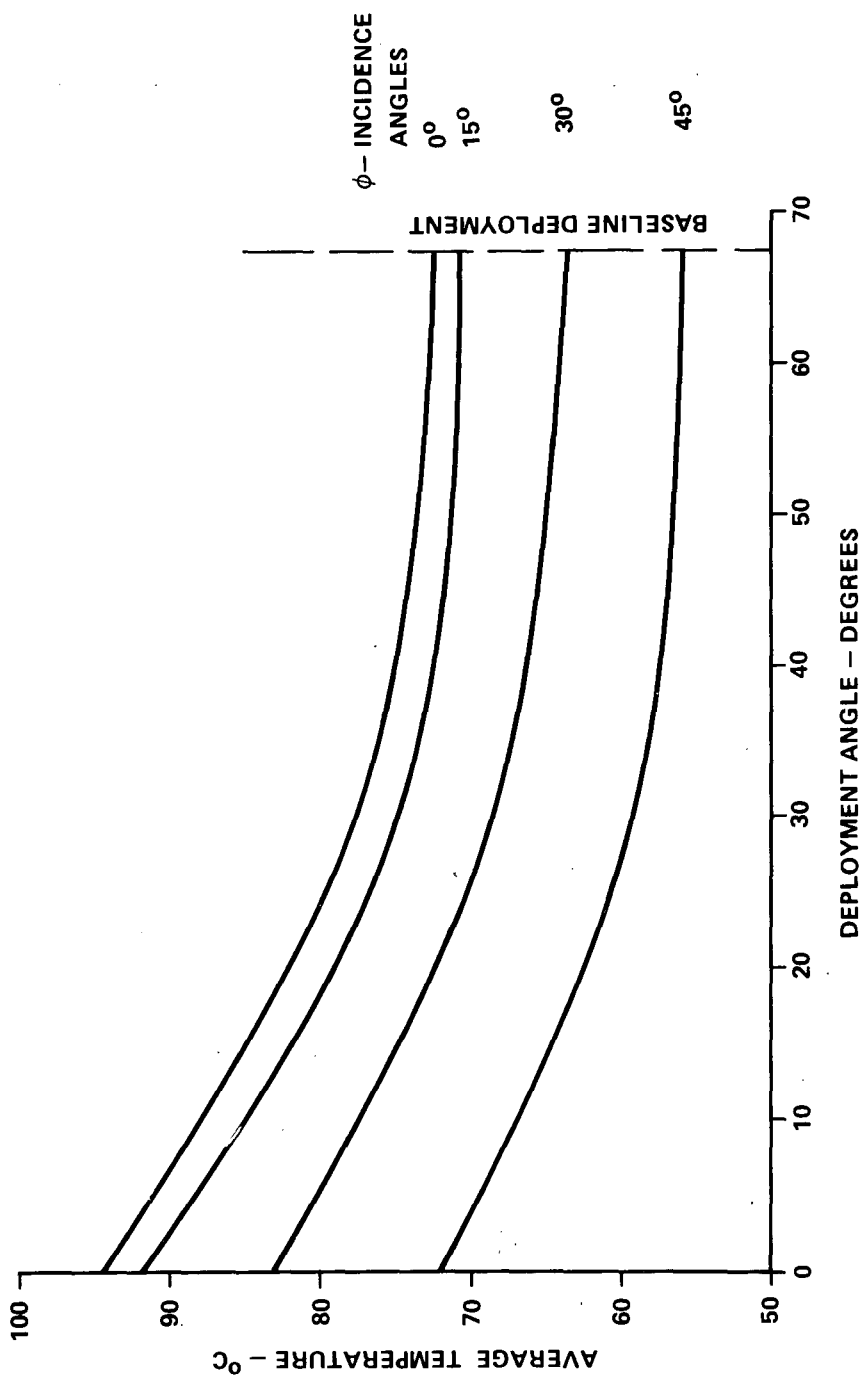


Figure F-18. Average temperature of array wings for various deployment and incidence angles.

5. Parametric Performance Studies for the Baseline. To determine the baseline design, the basic configuration was parametrically analyzed for several stacking factors and for at least three orientations covering the range specified for the mission. Deployment angle and orientation effects on performance were assessed in a similar manner.

Figure F-19 illustrates performance of the body mounted portion of the array. The initial array assumed a 35 percent stacking factor (SF) on the body. Under the nominal, maximum, continuous off-sun pointing conditions (15 degrees), 600 watts are available, dropping to 540 watts at the maximum off-sun angle of 30 degrees. Later studies indicated that the 35 percent stacked panel was in excess of requirements and the final baseline body has approximately a 15 percent SF. This yields 240 watts average at a 15 degree angle and 210 watts at a 30 degree angle. The potential for power growth of the array is evident. Figures F-20 and F-21 illustrate the effects of tilt and roll orientation on the body mounted section with parametric curves for various SFs. The power under these conditions remains adequate for baseline requirements. It should be noted that although incidence angles for the two body sections are widely different in these two figures, the sum of the outputs of both sections is essentially the same for roll and tilt within the range of interest.

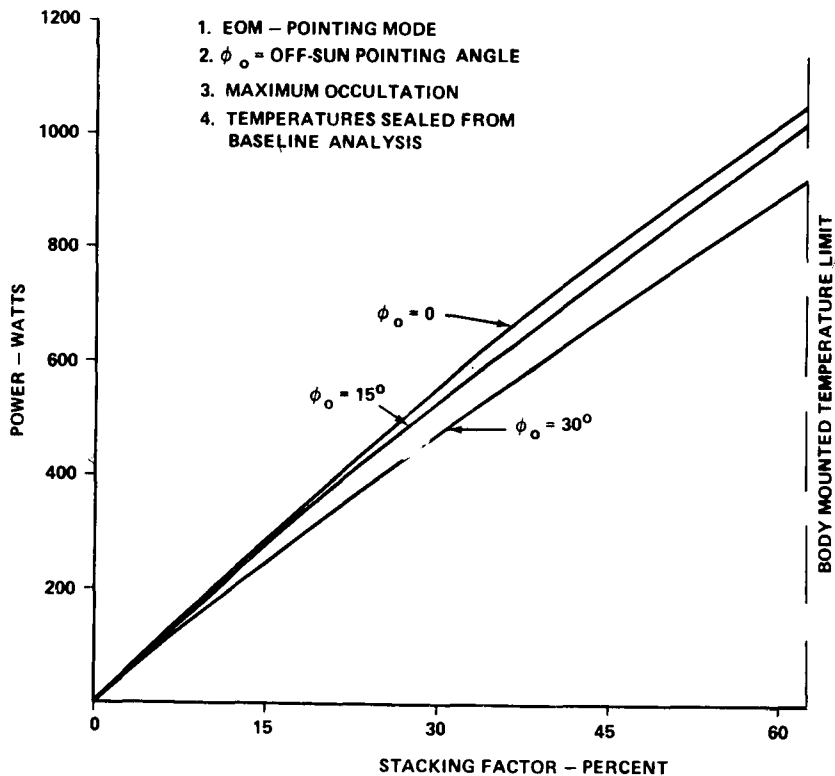


Figure F-19. Baseline array body section power capabilities.

BASIS:

1. E O M - POINTING MODE
2. TEMPERATURE SCALED FROM BASELINE ANALYSIS
3. ϕ_0 ANGLE FOR X-AXIS TILTED TOWARD SUN ONLY

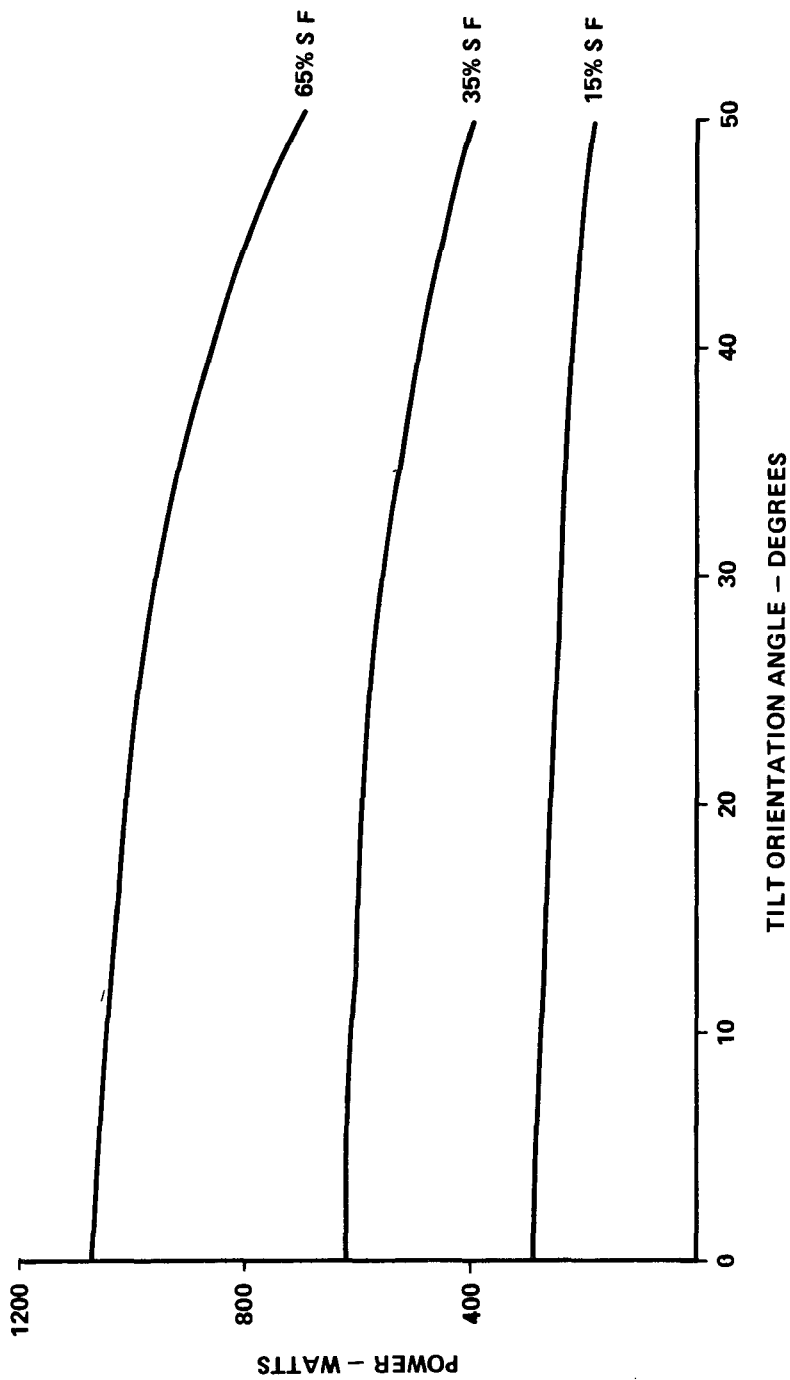


Figure F-20. Array body parametric performance curves as a function of tilt orientation.

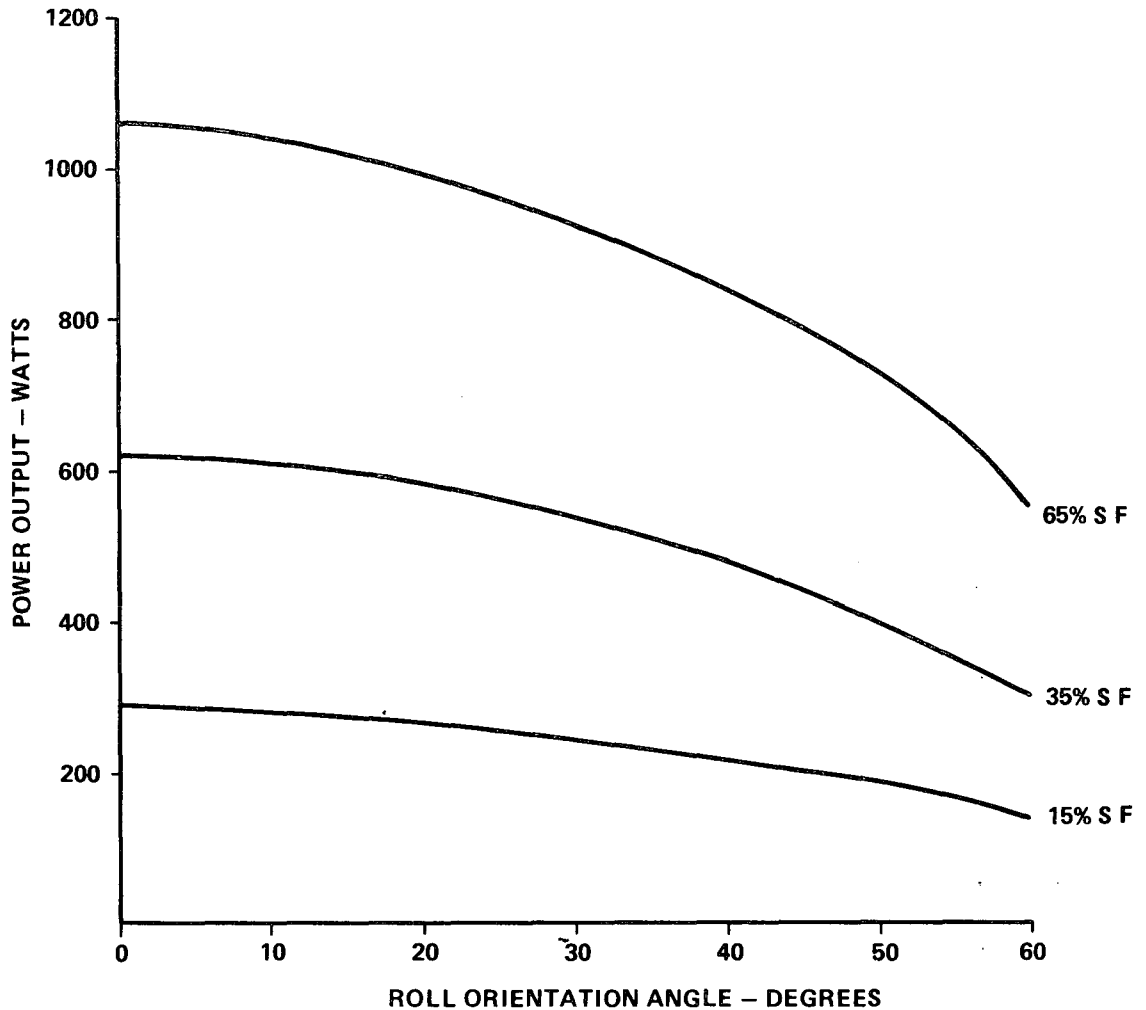


Figure F-21. Array body parametric performance curves as a function of roll orientation.

Parametric power performance curves are given for one wing (3 panels) of the array in Figure F-22. The wing output for several spacecraft orientations is shown as a function of the deployment angle.

Figure F-23 is a chart showing the performance of both wings as a function of roll and tilt orientations and for several deployment angles to illustrate the beneficial effects of the baseline 67.5 degree deployment. Note that to about 20 degree orientation, the total wing power could supply HEAO-C requirements. The total power capability of the HEAO-C array is approximately the sum of the wing and body section powers.

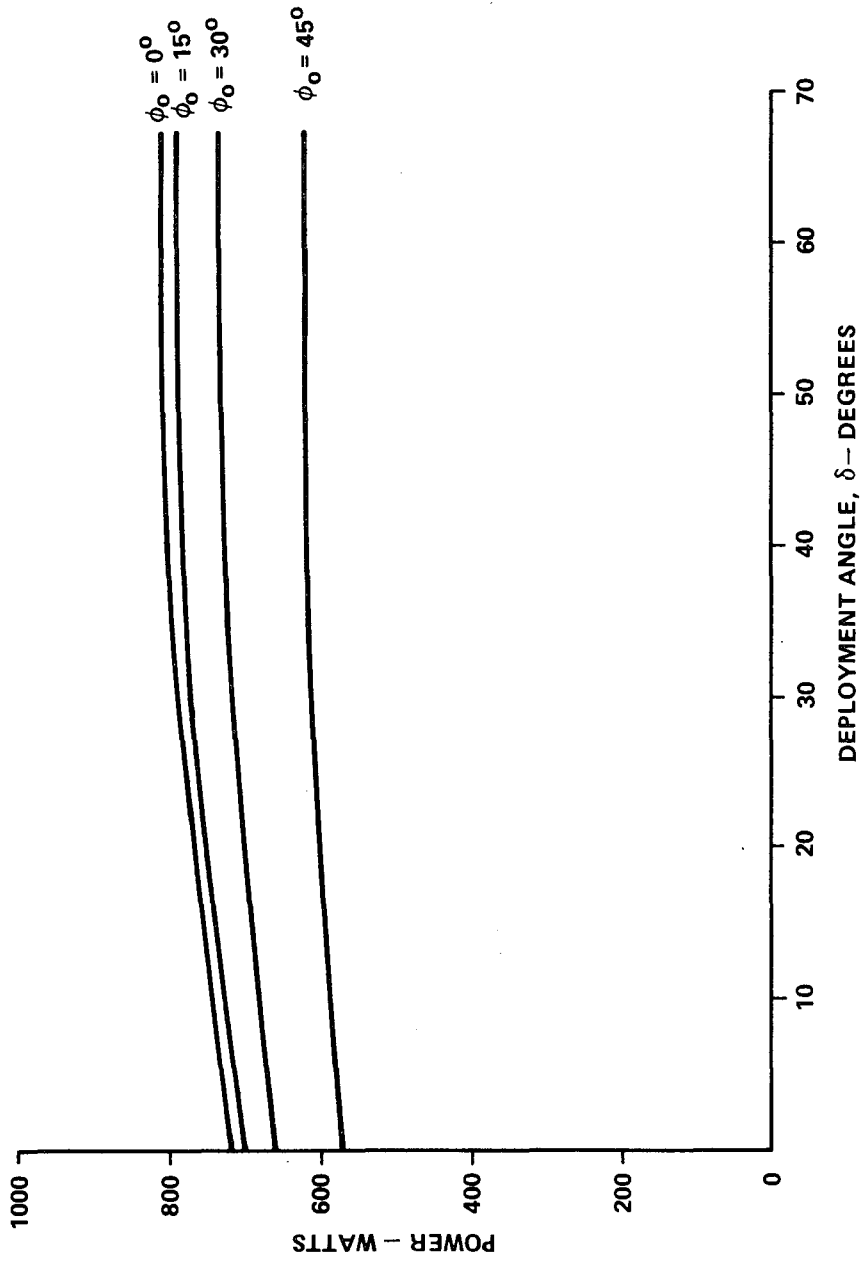


Figure F-22. Power performance curves for a solar array wing.

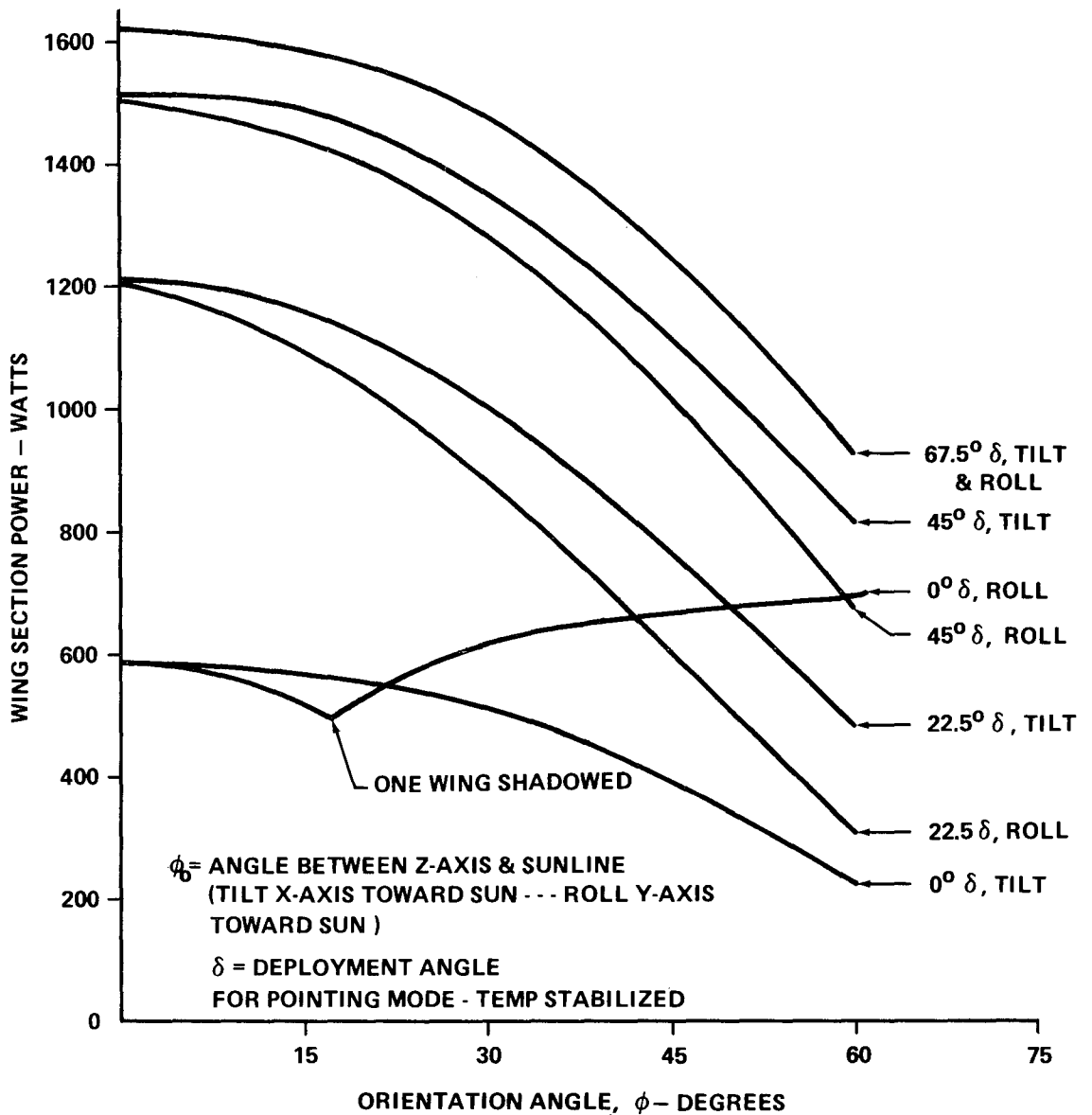


Figure F-23. Parametric performance curves for both wings.

In the conceptual and early design studies there have been assumptions about power requirements of some components or operational duty cycles on others, which may result in future reduction or growth of HEAO-C power requirements. Experience indicates that growth is the more likely, and the design work has included study of the impact of power growth. Several methods

of dealing with increased requirements are available: additional solar array area, careful scheduling of peak loads, or reducing power of other components. For the HEAO-C baseline, an increased solar array area appears to be no problem in dealing with reasonable variations in the load. The fact that the 15 percent stacking factor of the body mounted panels could be increased to 65 percent indicates a source of substantial power growth.

Figure VIII-7 shows the power growth capability for the baseline solar array configuration for the EOM 15 degree pointing design case. Sufficient area is available to increase the average power rating of the array to 2570 watts (unconditioned). This would support a continuous output load of about 1200 watts. Changes in energy storage and regulation equipment would be required for significant power increases above the present design level.

6. Baseline Solar Array Performance

a. Characteristic Ratings. From the foregoing parametric analyses, a final, conservative design for the baseline solar array was selected, keeping the basic configuration the same as that initially selected. The array then will consist of six wing panels (three per wing) with a 90 percent stacking factor, and two body panels (one per section) having an equivalent stacking factor of 15 percent on a section basis. The individual body panels will have a stacking factor of half that of one wing panel. The EOM power characteristics which define the design rating of the final baseline array are shown in Figure F-24. Notice that this array has the capability of satisfying mission requirements even though one panel should fail to deploy.

The performance and ratings of the baseline solar array and panels were discussed in Chapter VIII.

Good system design and the design of regulation, battery charging, and distribution equipment require a thorough knowledge of voltage-current (V-I) characteristics as well as power performance for the various environmental and operating conditions. For instance, chargers and regulators are designed to use the high power available from the cold array at the beginning of the sunlight period. Typical V-I characteristics for the sections of the array were obtained from computer runs. These characteristics are given for the baseline array wings in Figure F-25. Typical BOL and EOM characteristics are shown for several operating temperatures with the spacecraft z-axis oriented to the sun. Similar characteristics are illustrated for the body sections of the array in Figure F-26.

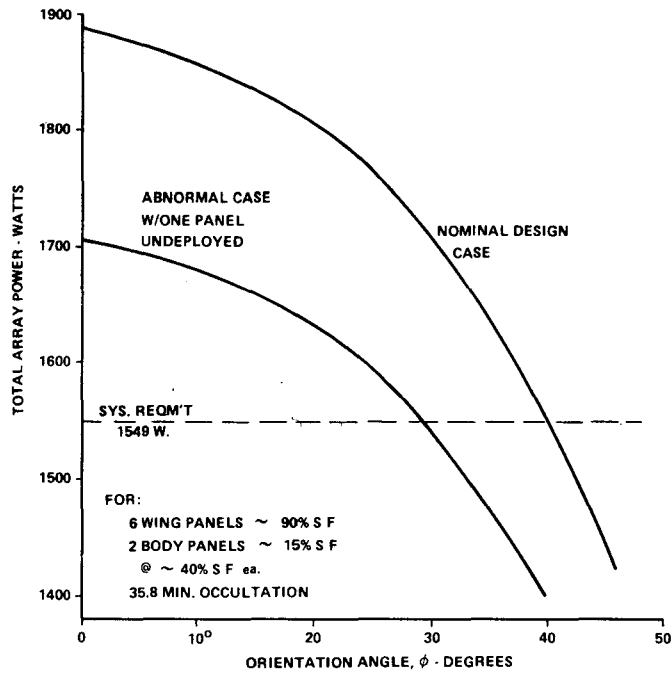


Figure F-24. Baseline array EOM performance rating.

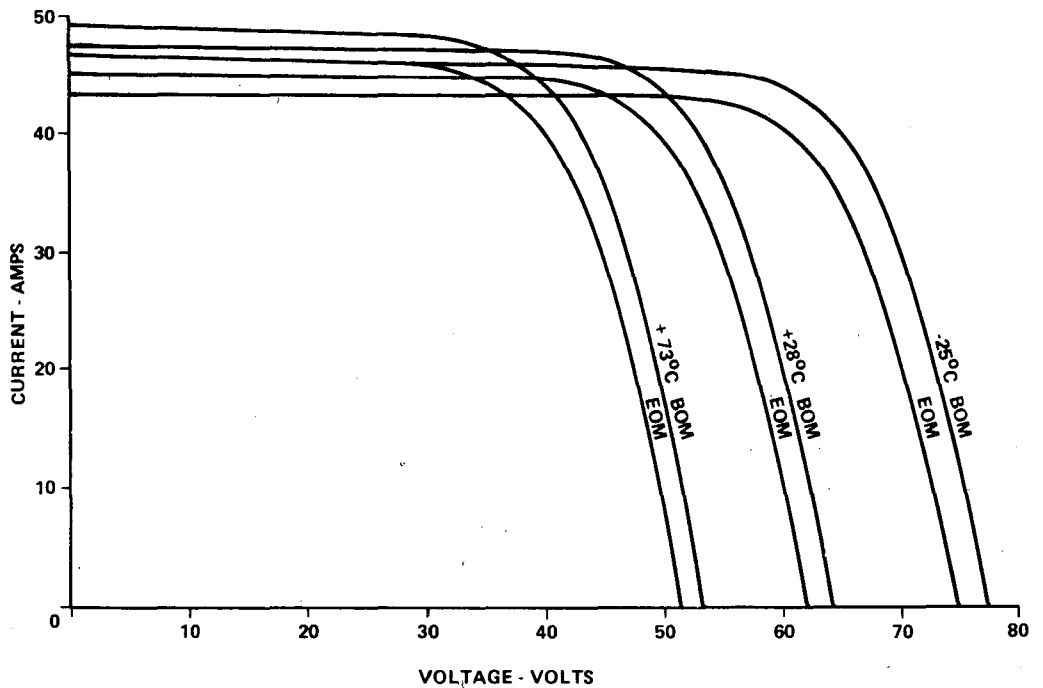


Figure F-25. Rated V-I characteristics for baseline array wings.

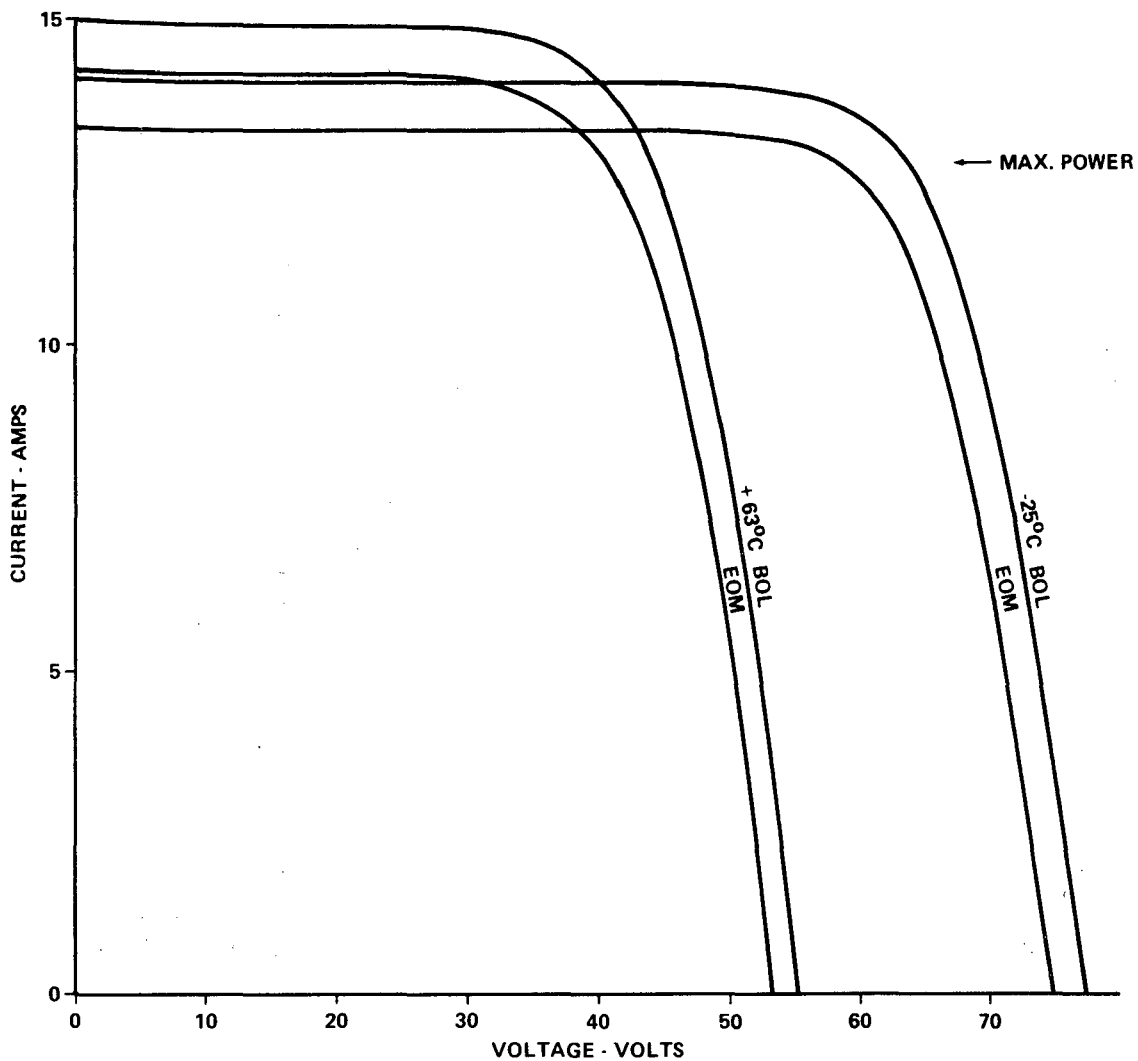


Figure F-26. Rated V-I characteristics for baseline solar array body sections.

The fact that all array panels do not operate at the same temperature was investigated using V-I curve data. Performance derating or a small power loss is incurred by the temperature and orientation differences. For the nominal operating modes and design pointing limits, it was found that the voltage mismatch was rather small; the maximum appeared to be 2.5 volts. Figure F-27 shows a typical example of the power loss that may occur because of mismatched V-I characteristics. This loss was slightly less than 1 percent for the cases investigated. The effects of temperature gradient across the wings were not included; however, these are not expected to be large.

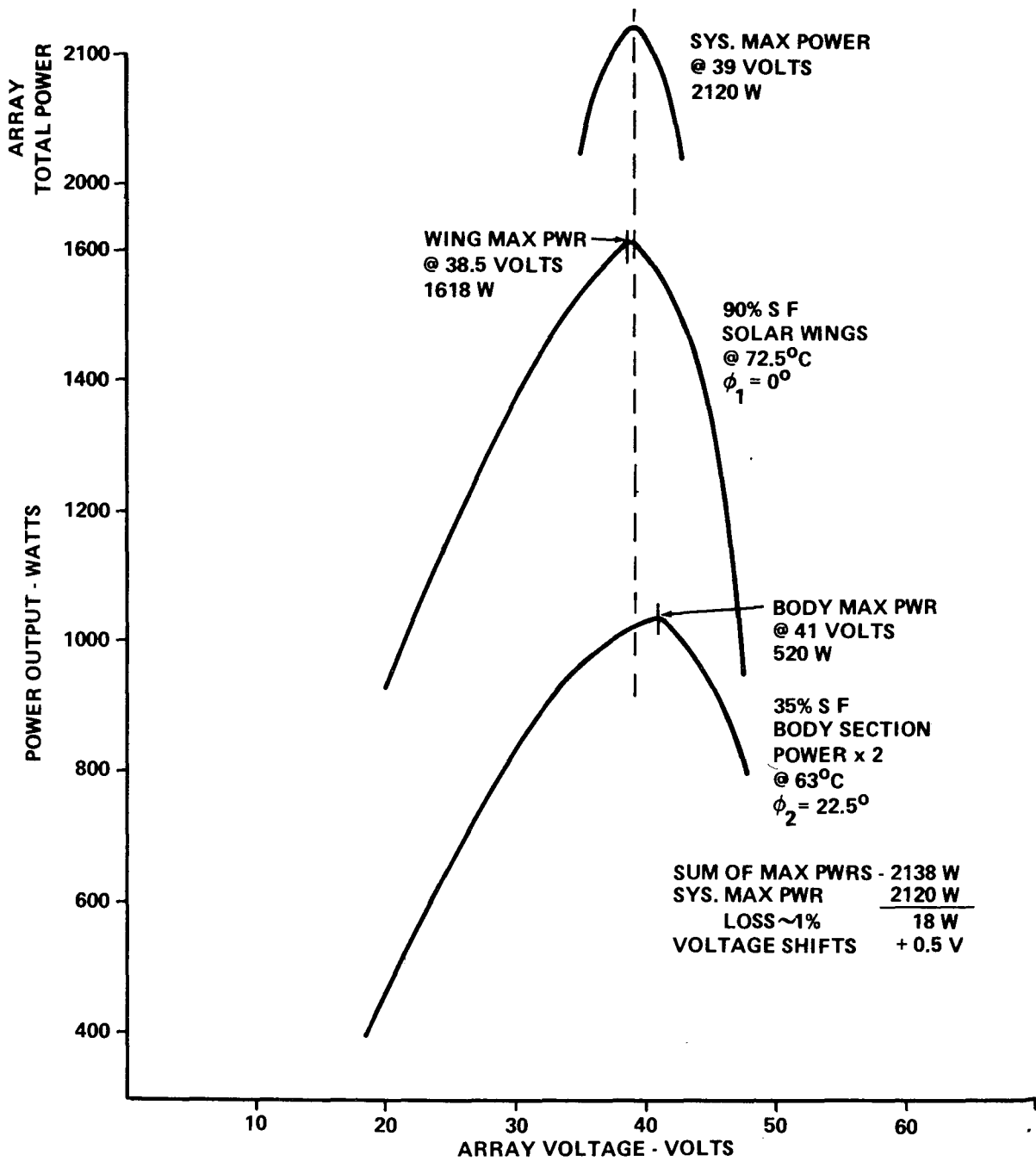


Figure F-27. Solar array power — voltage loss.

b. Array Performance Variations with Earth Seasons. The orbital parameters derived for the specified HEAO-C mission, discussed in Chapter III, were used to obtain profiles of the occultation (dark) period of the specified orbit as a function of the seasons of the earth for two widely different, but typical, launch cases. These profiles, shown in Figure F-28, apply to a launch at winter solstice ($\lambda = 90$ degrees) and to a launch at the vernal equinox ($\lambda = 0$ degree). The angle λ completes a 360 degree cycle in 365 days. The angles, Ω , shown refer to the orbital plane position with respect to the sun at the time of launch. The values of Ω were selected so that the initial orbit would have the maximum occultation period for the equinox launch (equivalent to the cold temperature case). The initial orbit of the winter solstice launch has the minimum occultation period (equivalent to the hot temperature case). Although occultation variations appear random, they are directly related to corresponding β angle (angle sunline makes to the orbital plane) variations that are plotted for the same launch cases in Figure F-29. A computer program supplied by the attitude control group was used to obtain these figures. It may be observed that the β angle has short-term cycles whose period varies between ~ 40 and 60 days. Orbital regression causes these short-term variations. The occultation profiles in Figure F-28 show that the maximum occultation (35.7 minutes) occurs frequently, while the shortest possible dark period (27.4 minutes) rarely occurs. It occurred only once (at 0 day — winter solstice) in the two cases analyzed. Comparing the two figures shows the reason for this. When β passes through 0 degree, a condition for maximum occultation occurs. Since β passes through zero frequently for the specified orbit, the average occultation period on a yearly basis is close to the maximum. To obtain minimum occultation, maximum β must occur at $\lambda \cong 90$ or 270 degrees. This coincidence is very infrequent. The average dark period as determined by Figure F-28 was between 33.3 and 33.4 minutes.

The average was used to determine average depth-of-discharge ratings for batteries. The foregoing profiles were also used to assess the EPS and solar array performance needed to account for seasonal variations in the prescribed mission.

Since rigorous thermal analysis was not possible within the study period for all seasonal variations of the mission, hot-and-cold-case temperature profiles given in Chapter VI were used to obtain the range of solar array temperatures expected with seasonal changes. Linear extrapolation was used to determine intermediate condition temperatures. With these data, a cursory assessment (the final baseline solar array) provides adequate power during off-sun pointing beyond the requirements. The EOM design rating is the minimum because it includes nominal worst-case conditions. The array provides a design margin of 282 watts for the 15 degree pointing case. Higher performance

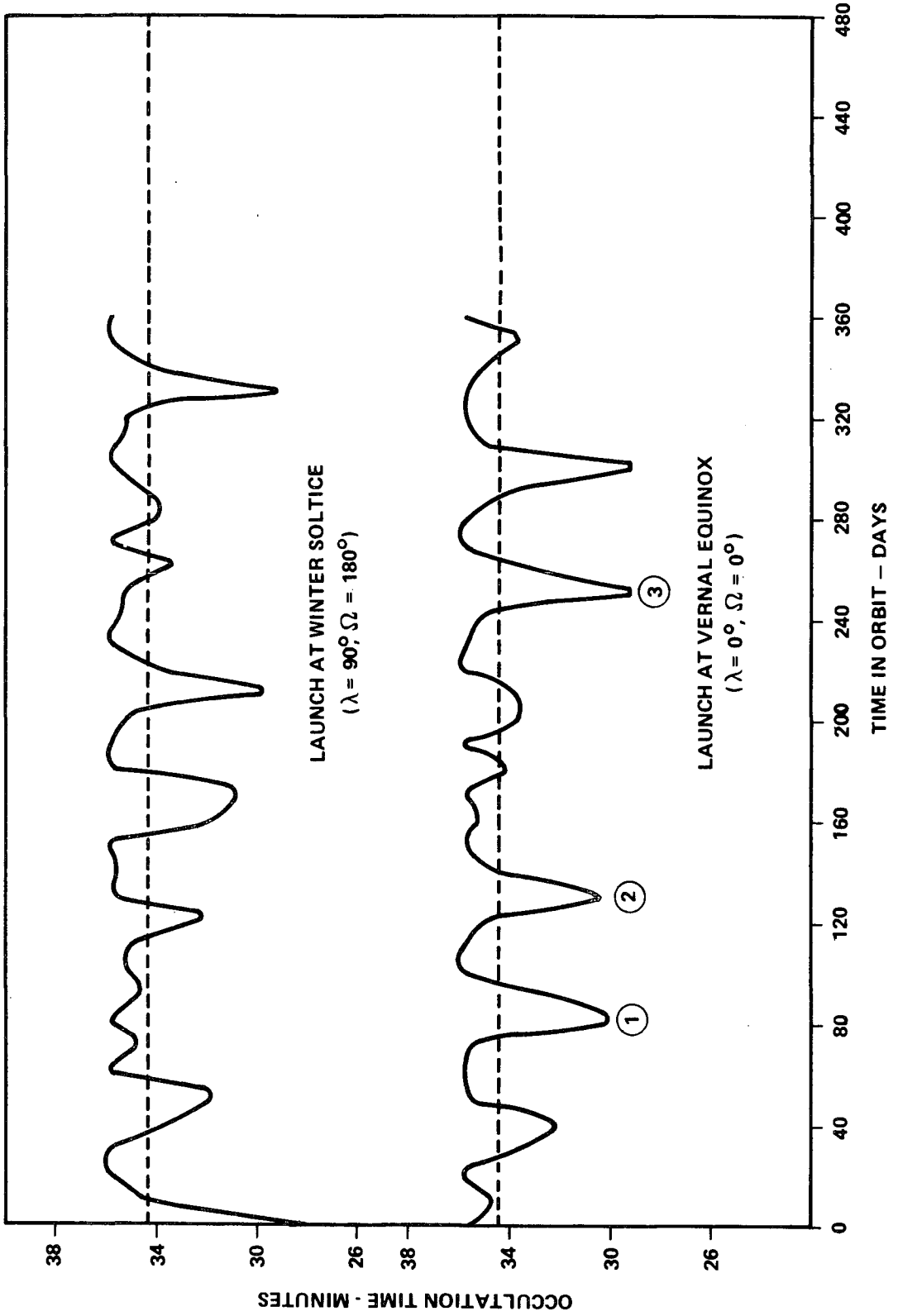


Figure F-28. Variations of occultation time.

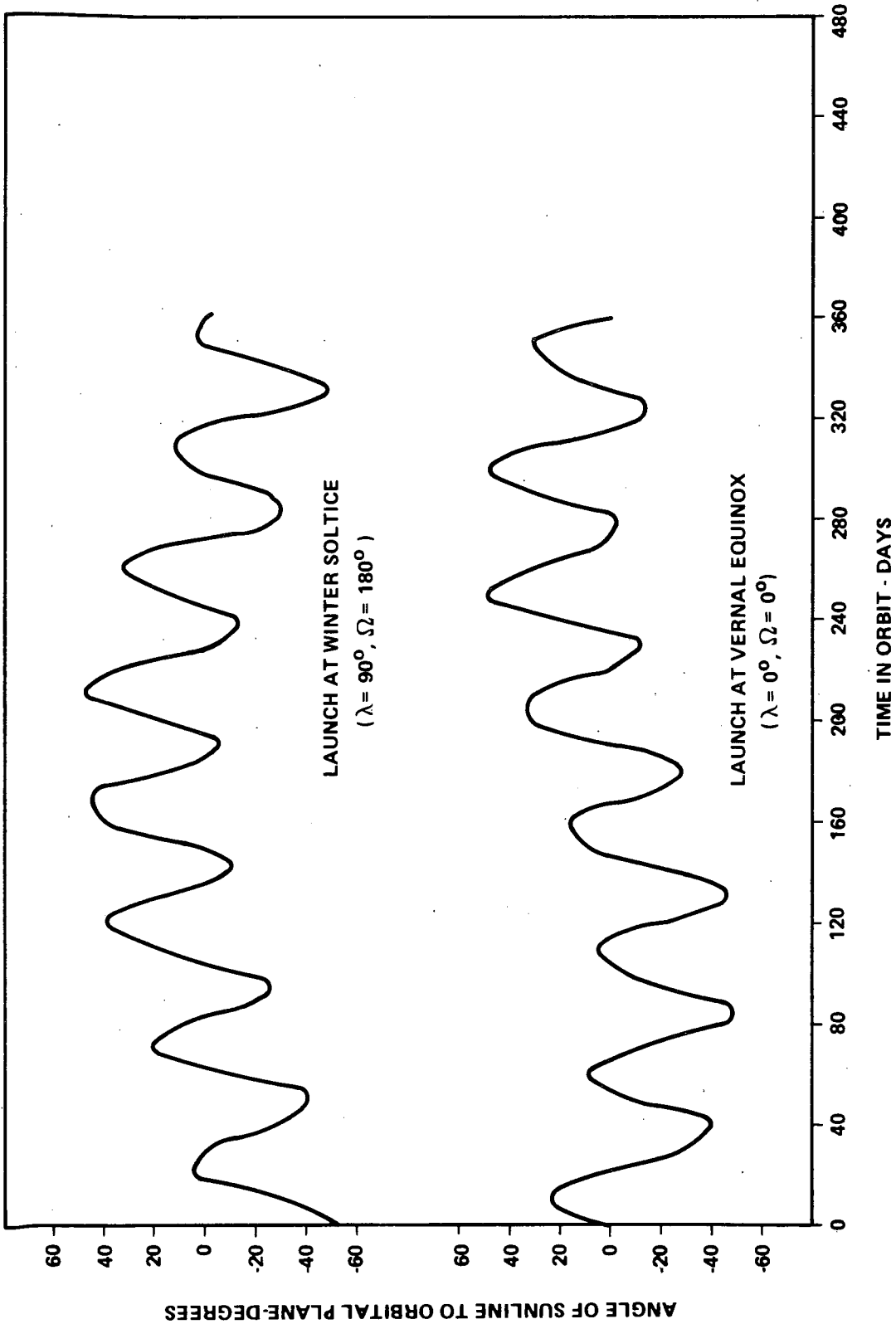


Figure F-29. Angle of sunline to orbit plane variations.

will be available earlier in the mission. Greater off-sun-pointing capabilities will exist for certain intervals when maximum sun orbits occur. The time these periods occur will depend on the exact launch conditions; for example, the launch at vernal equinox case given in Figure F-28 is used to show this additional capability. Notice that four periods of about 12 days each occur in the year where the dark period is less than 32 minutes. The system performance is determined for the first three periods [denoted (1), (2), (3)], assuming that the case represents the last year of the mission. The power allowance for degradation is an appreciable part of the additional capability to be shown; therefore, the situation will improve during the first year of the mission. Figure F-30 shows the power available from the final baseline array for the subject periods. The system requirement of 1444 watts reflects the better system performance factor during these periods. The continuous off-sun pointing permissible will be at least 47 degrees for period (1), 45 degrees for period (2), and 40 degrees for period (3). Reference to the EOM design rating performance (Fig. F-24) shows that the capability of 40 degrees off-sun pointing during the minimum sunlight (maximum occultation) orbit is equal to case (3) and almost as good as cases (1) and (2). This is because the variations in the solar intensity with the seasons are approximately compensated by opposing temperature variations.

c. Array Performance for Abnormal Conditions. The HEAO-C subsystems are to be designed for very high reliability and confidence. The solar array deployment mechanisms are no exception even though they are probably the most vulnerable part of the solar array. Redundant release bolts, each having redundant initiation and channels for firing, assure reliable deployment. However, to select the stacking factor to be used for the final baseline, curves (Fig. F-24) were plotted for maximum design conditions, considering that one wing panel had not deployed. Figure F-24 shows that for this extreme situation an array having body sections with about 15 percent stacking factor can fulfill the load requirements at the EOM 30 degree pointing case. Therefore, the initial baseline was changed to have only two body panels equivalent to a 15 percent stacking factor for the whole body section.

Off nominal cases at the BOL were also investigated. Considering that delays in orbital adjust phase maneuvers might occur or that a long waiting period might be necessary before command access is available from tracking stations, the BOL performance of the solar array was determined for the case where both wings are yet undeployed. Figures F-31 and F-32 show array capabilities under such conditions for various roll and tilt orientations. These curves indicate that the undeployed array can support a load of about 400 watts. These curves were used further to assess the battery discharge requirements and limitations for this abnormal operational mode.

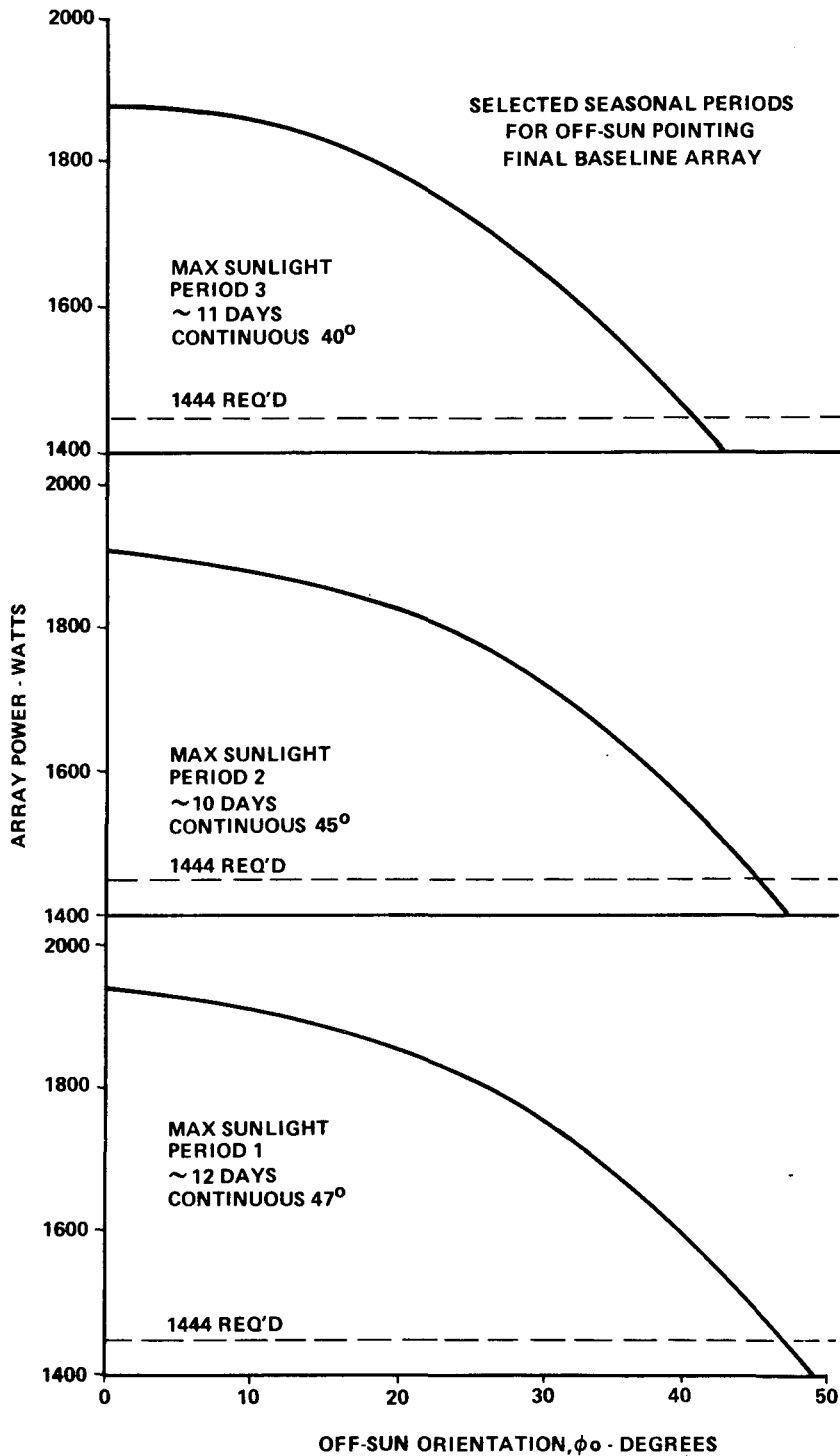


Figure F-30. Off-sun pointing capability for selected seasonal periods.

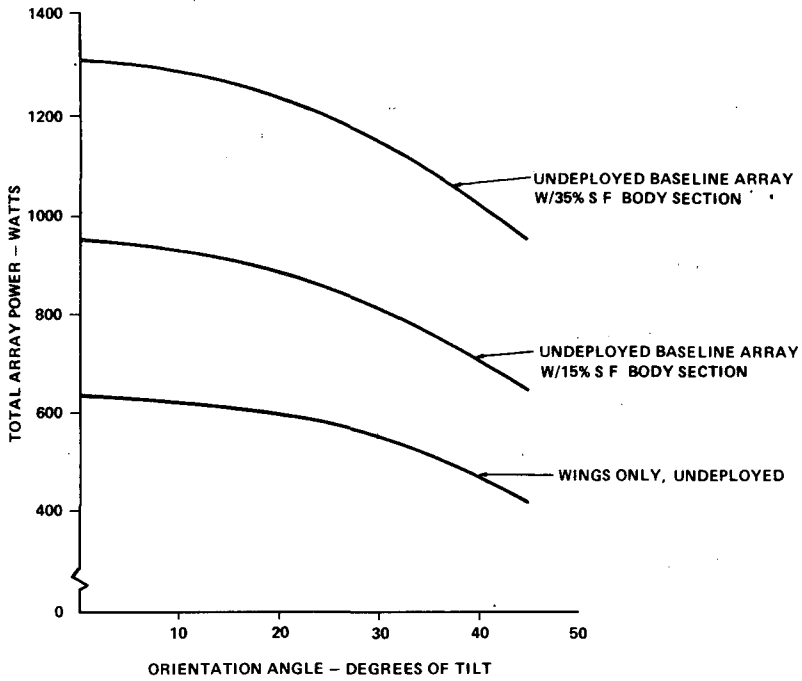


Figure F-31. Baseline solar array output with wings undeployed for tilt orientations.

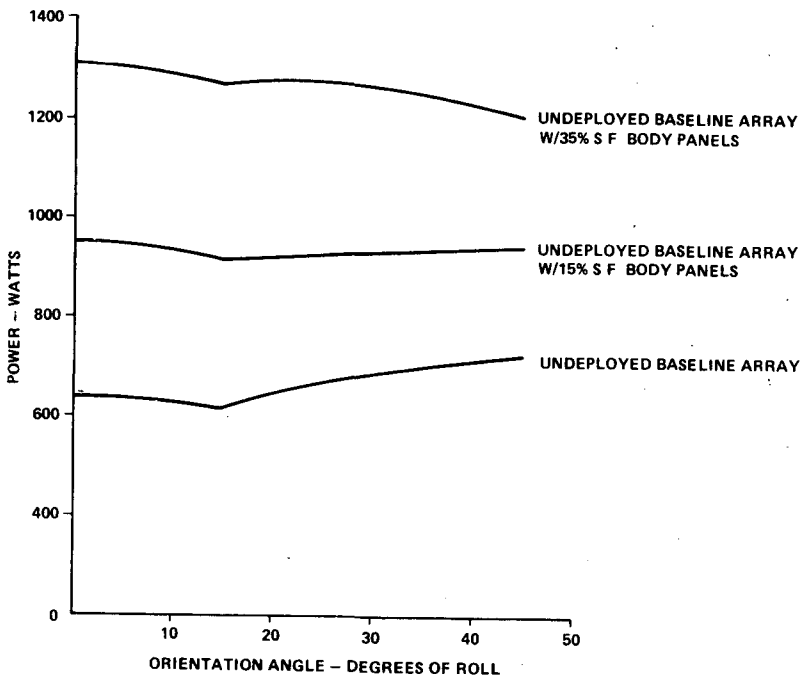


Figure F-32. Baseline solar output with wings undeployed for roll orientation.

7. Solar Array Tradeoffs. Chapter VIII describes the baseline solar array and discusses the performance and variations possible with various mission conditions and design selections. Two alternate configurations, (No. 1 and No. 2) were analyzed with respect to HEAO requirements. The configuration alterations are concerned only with changing the position of the spacecraft Z-axis and the corners on which the wing panels are to be hinged. The same spacecraft dimensions are used; therefore, the baseline wing panels are useable on the alternate configurations. It was not considered feasible to increase the stacking factor used for the wings; therefore, the alternate cases are principally limited by the cell area available on two wings.

a. Alternate No. 1 Solar Array. The basic configuration designated as alternate No. 1 solar array is shown in Figure F-33. It can be seen that alternate No. 1 has the Z-axis through one of the sides of the octagonal spacecraft and the deployment angle is 45 degrees to orient the wings perpendicular to the Z-axis. This configuration has the advantage of being easily analyzed since all sections of the array are in the same plane. Its disadvantages compared to the baseline are (1) its growth limited to the area of three sides rather than four for the baseline, and (2) body and wing sections for the same stacking factors will have higher temperature and decreased efficiency. The body section runs at higher temperatures because it is sun oriented; the wings have higher temperatures because of the smaller deployment angle.

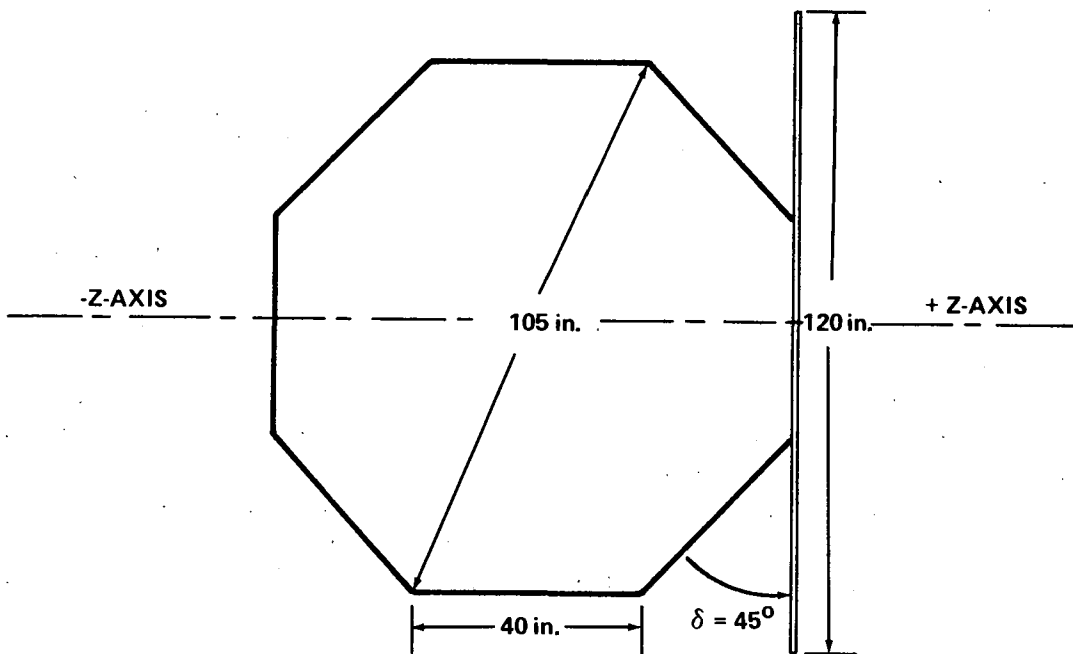


Figure F-33. Alternate No. 1 array configuration.

Power capability performance curves for the alternate No. 1 array are shown in Figure F-34. These curves cover the same EOM design cases used for the baseline concept. The body section performance as a function of stacking factor is shown in Figure F-35 for three orientation angles. Comparison with baseline curves will show that the alternate body section output is somewhat less than half that of the initial baseline at corresponding stacking factors.

The total array performance for alternate No. 1 configuration is shown in Figure F-36 as a function of orientation and for 0, 15, and 35 percent stacking factors for the body section. It is readily seen that the alternate configuration has the capability of performing the HEAO-C mission even though the solar cells operate less efficiently. If HEAO-C power requirements do not increase, it would be recommended that this alternate be considered for the baseline because it is simpler. The approximate growth capability for alternate No. 1 array is shown for the EOM, 15 degree pointing case in Figure F-37. The maximum temperature limit occurs at a lower stacking factor than for the baseline; however, the maximum 2075 watts indicated is considered quite adequate for growth contingencies.

To be equivalent to the baseline array, alternate No. 1 would need the 35 percent stacking factor for the body section. This is equivalent to about 5 percent more solar cells on an overall array basis.

b. Alternate No. 2 Solar Array. The second alternate configuration for the solar array is shown by Figure F-38. This alternate uses no body mounted panels; an analysis was based primarily on the use of wing panels described for the baseline.

The deployment angle, δ , required to orient the wings for alternate No. 2 is 22.5 degrees. Figure F-17 shows that the maximum temperature for this configuration is approximately 102°C at a 0 degree incidence angle. This is slightly above the 100°C temperature limit set for solar cells which indicates the panel would have a marginal reliability for a 2 year mission. A small reduction in the stacking factor could reduce the temperature to acceptable limits but the power capability would also be reduced correspondingly. A stacking factor of about 82 percent would provide an adequate temperature reduction. The power output performance for alternate No. 2 solar array is shown in Figure F-39 for end-of-mission conditions and for the design orientation cases used for baseline panels. It may be noted that this version does not supply enough power to satisfy the design load established for HEAO-C. Therefore, performance curves for the 82 percent stacking factor design are not warranted. This is caused by the increased temperature incurred by the

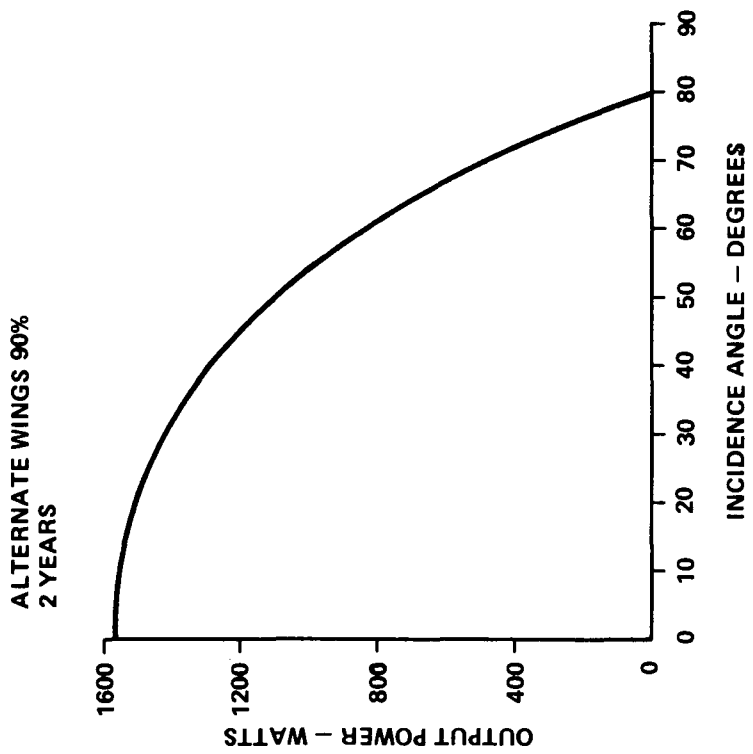
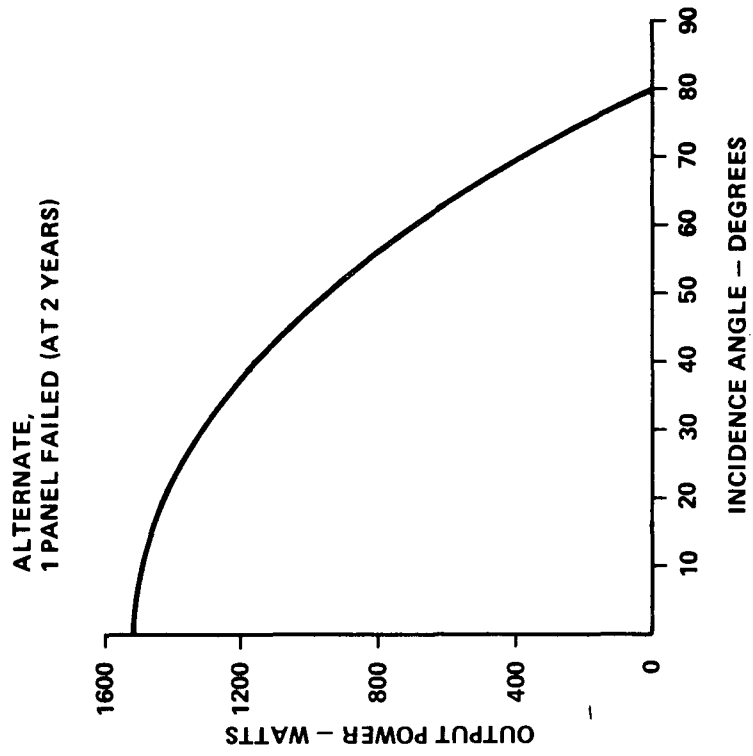


Figure F-34. Power capability curves for alternate No. 1 array.

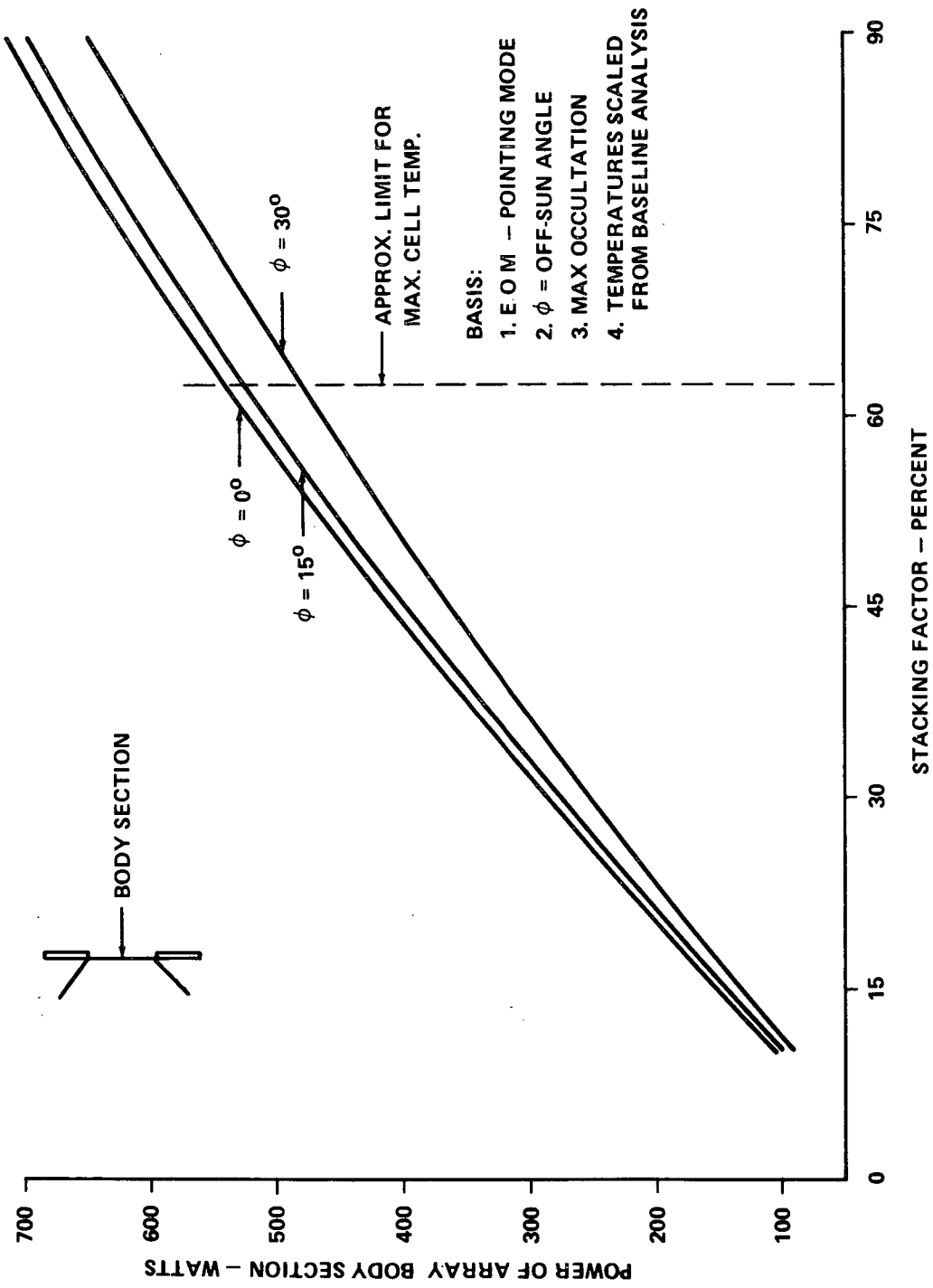


Figure F-35. Body section performance for alternate No. 1 array.

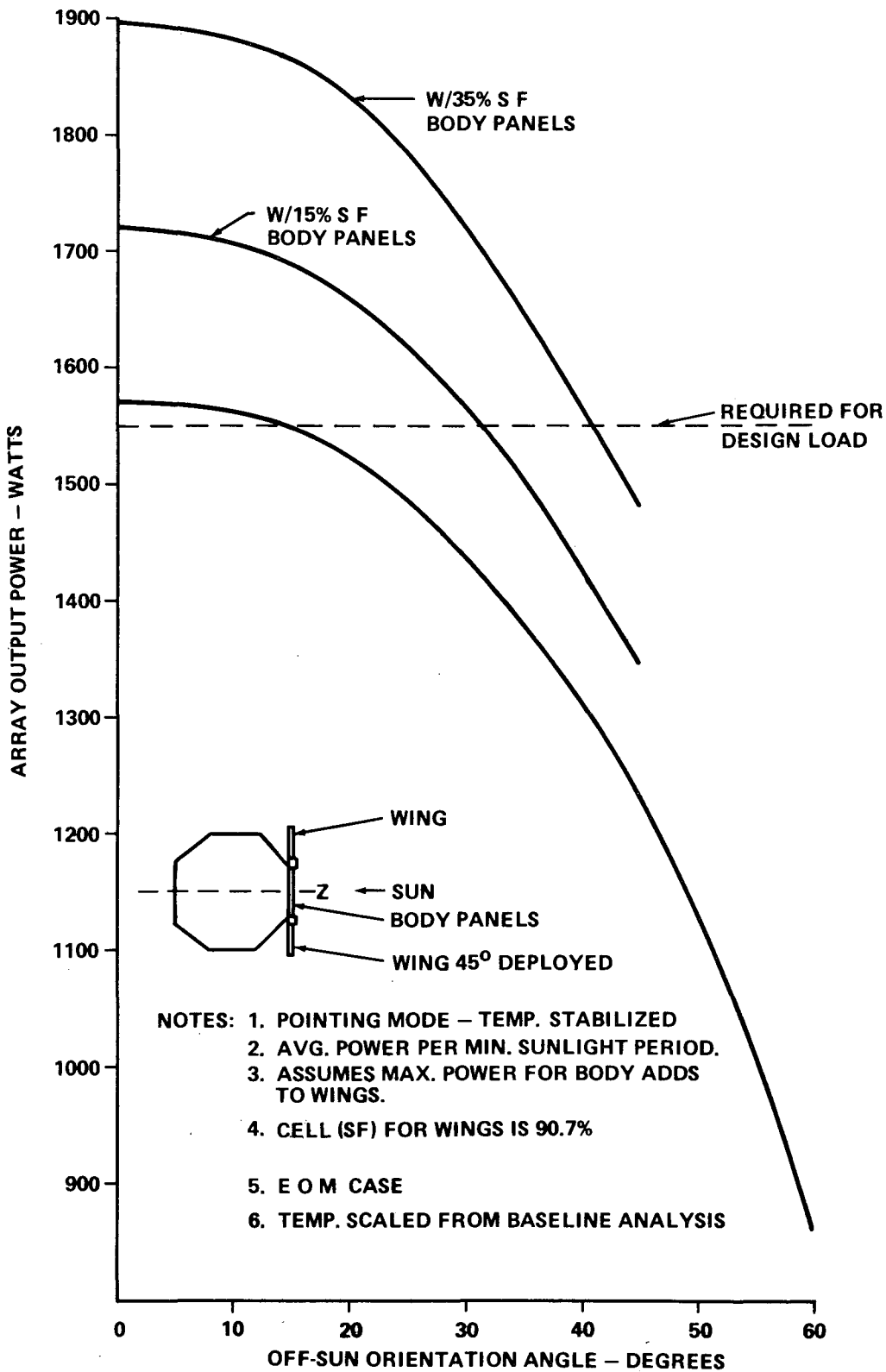


Figure F-36. Power versus orientation for alternate No. 1 array.

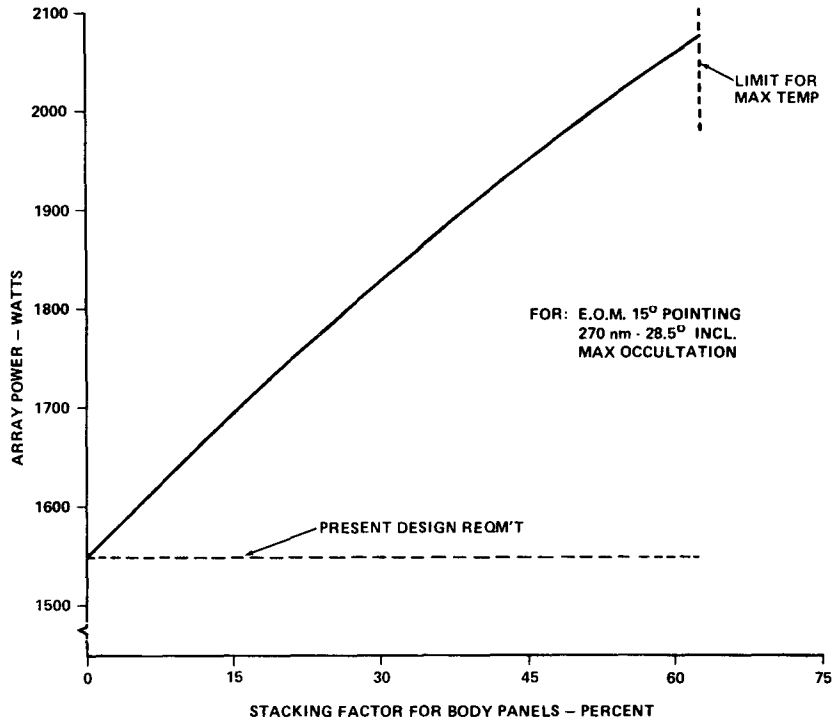


Figure F-37. Alternate No. 1 array power growth capability.

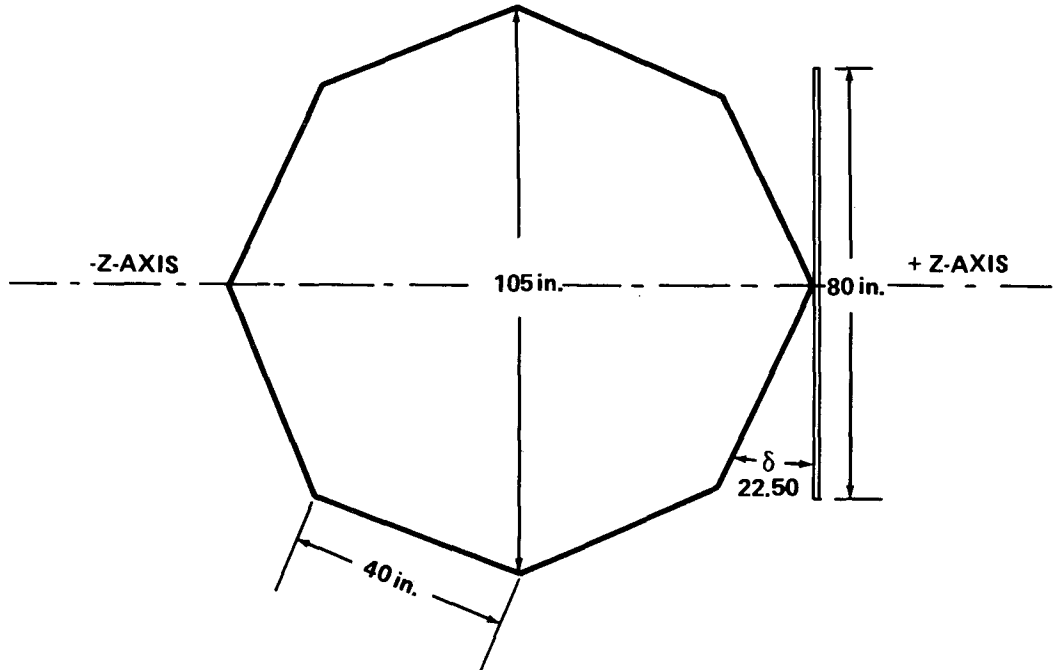


Figure F-38. Solar array alternate No. 2 configuration.

small deployment angle which makes the wings more like body mounted panels as compared to the baseline and to alternate configuration No. 1. Although this configuration could be adequate for smaller load requirements, it is not recommended for HEAO because it incurs higher temperature, it has poorer efficiency, and it is area and power limited and offers no growth potential.

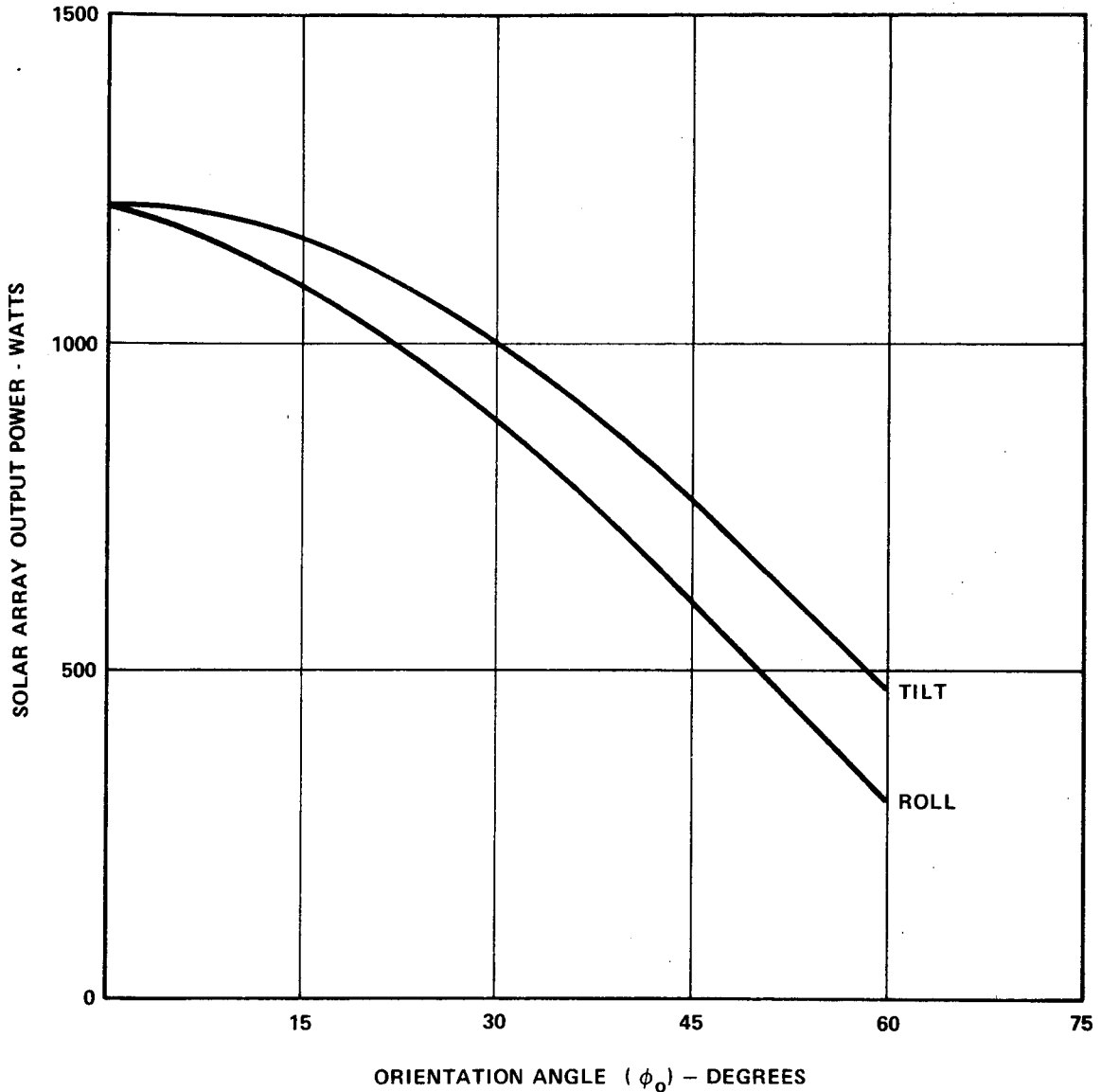


Figure F-39. Performance of alternate No. 2 array.

c. Tradeoff Summary. A brief summary of the tradeoff study results is given in Table F-4. The two alternate configurations are compared to the baseline on the basis of HEAO-C requirements. The table shows that the baseline and alternate No. 1 designs were adjusted to deliver about the same power (1835 watts versus 1860 watts at 15 degree pointing). The alternate required a higher stacking factor on the body section, and about 5 percent more cells to be equivalent. Because of the higher panel temperature and its lack of body area the second alternate did not meet the requirements.

Alternate No. 2 could support a 537 watt spacecraft load. If the body stacking factors for the baseline and alternate No. 1 were increased to the 62 to 65 percent limit, the baseline would support a 1200 watt load and the alternate would support 965 watts. It is again noted the baseline wing panel design was used on the alternate configurations.

Deployment Tradeoffs

1. Tradeoff Studies and Evaluation Criteria. Investigation of power requirements and availability for the HEAO spacecraft led to the conclusion that for Mission C, a deployable array was necessary. The alternate array configurations also required wing deployment. Several concepts for the deployment were considered, and the selected method is described in Chapter VIII.

In addition to schemes for deploying single panels, initial consideration was given to methods of deploying an entire wing, or both wings simultaneously.

Subsequent considerations were given to such things as array reliability/redundancy requirements, complexity, installation weight, volume and power penalties, individual mechanism reliability, and commonality for alternate array configurations. From these, criteria were established to evaluate tradeoffs and to select a baseline. Briefly, the deployment concepts were evaluated on the following bases:

- Deployment mechanisms should be easily adapted to all array configurations considered.
- Devices must be simple, reliable, and adaptable to redundancy concepts.

TABLE F-4. COMPARISON OF SOLAR ARRAY CONFIGURATIONS FOR HEAO-C REQUIREMENTS

Tradeoff	Baseline ^a		Alt. No. 1 ^b		Alt. No. 2 ^c	
Pointing Angle (deg)	15	30	15	30	15	30
Design Load (W)	722	722	722	722	722	722
Array Watts Req'd	1549	1549	1549	1549	1549	1549
Array Design Rating	1835	1698	1860	1720	1150	
Load Margin	135	70	151	81	Inadequate	
Continuous Pointing Rated Config. (deg) One Panel Undeployed (deg)	40		42		N/A	N/A
	30		29		N/A	N/A
Max. Load Growth Possible at 15 deg, EOM (W)	1200		965		537	

- a. Body section with ~ 15 percent stacking factor.
- b. Alternate No. 1 has a 35 percent stacking factor for the body section.
- c. Exceeds 100°C solar panel temperature. Has no body section.

- Deployment concept should not impose high weight or power penalties.
- Baseline and alternate array wings would each consist of three identical panels — aluminum honeycomb substrates ~ 119 by 38 by 0.7 inches weighing about 35 pounds.
- Each wing panel would be separately deployed.
- Deployment mechanisms must be compatible with vibration, shock, and temperature conditions, and with reliable release and latching concepts.
- Panel retraction is not required.

2. Alternate Deployment Concepts. The alternative deployment methods are basically illustrated in Figure F-40 as they would apply to alternate array No. 1; however, most are equally applicable to the baseline or alternate No. 2 arrays.

a. Direct Drive. The power required for drive motors would be approximately 2.5 watts each, and the number of motors depends on the configuration selected. Since deployment occurs once, power is not considered a critical requirement. However, it is higher than required for other schemes. The weight of each motor is approximately 0.75 to 1.0 pound, not an excessive weight penalty. However, it did not appear to be the lightest approach because it requires gears and other devices for adaption to the baseline structural configuration and constraints. It also did not eliminate the need for constraints and release mechanisms.

This approach is better adapted to deploying entire wings. It is considered rather complex and expensive for deploying six panels separately. Its potential advantages were that it offered compact, controllable operation and it offered retractability (not required).

b. Linkages. The linkage concept shown also requires drive mechanisms such as motors. The mechanism shown is not applicable under the criteria established. It applies to deploying several panels with one device. It would also be more complex or require unwarranted space within the spacecraft if it were applied to the baseline configuration. This would be next to the heaviest approach.

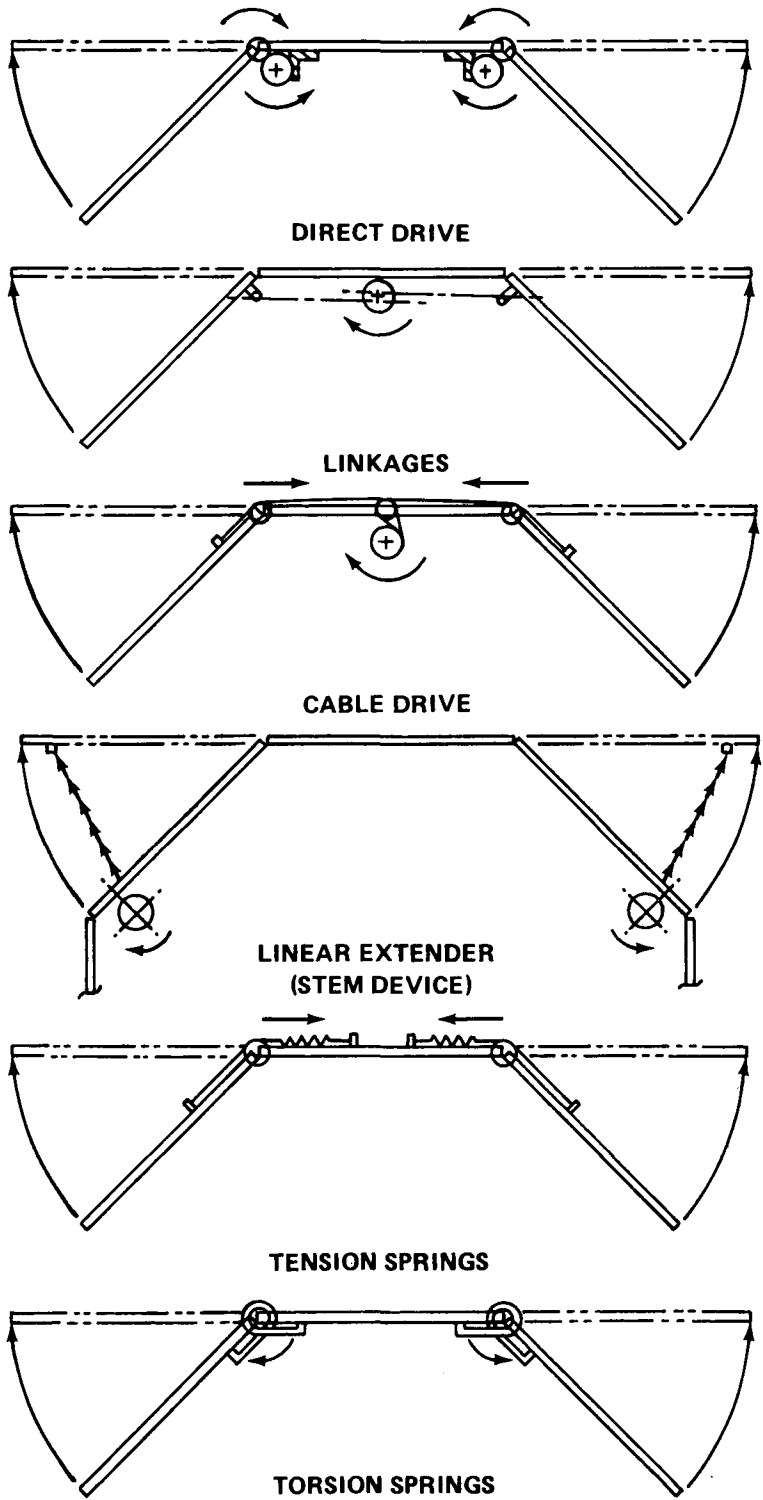


Figure F-40. Alternate deployment concepts.

c. Cable Drives. The cable drive approach offers the same advantages as the linkage concept and it would be somewhat lighter. However, it was also discarded as not applicable to deploying individual panels. In addition to the disadvantages of the linkage approach, it requires attachments on the forward side of the panels. This would complicate panel design and influence the layout of the body sections. This approach appeared to be the least reliable.

d. Linear Extender. Linear extenders offer good mechanical efficiency and positive control for deployment and retraction. However, they are considered to be complex, expensive, and the heaviest approach. Compared to spring approaches, this extender concept requires power and considerable internal space.

e. Tension Springs. The tension spring concept was discarded in favor of the torsion spring concept since its advantages were the same but it had more disadvantages. It required access through or attachment to the outer surface of the body section and it complicates panel layout because of forward side attachments.

f. Torsion Springs. The torsion spring method shown is very close to the selected baseline. It is considered to be the best alternate. The approach offers compact, lightweight, reliable operation. It is a simple, low-cost approach easily adapted to the array configurations. Like the other concepts, it requires constraint and release mechanisms. It is not retractable and it requires dampers.

Compared to the baseline, it is slightly more complex because of the number of springs and hinge adjustments needed. The baseline combines the concept with the torque tube concept illustrated in Figure F-41 to provide better mounting rigidity, vibration resistance, and hinge alignment. Use of springs and dampers eliminates the need for the motor indicated. The torque tube is not used for cinching in the baseline.

3. Cinching Release and Latch Mechanisms.

a. Torque Tube Release. Figure F-41 shows a cinching mechanism which mechanically latches the panels in place during launch. It consists of simple latches and eyes. Drive is by means of a motor or the torque rod. This approach could be used for cinching and releasing the entire wing (three panels) with one actuation mechanism. It offers the advantage of one drive mechanism being able to release multiple cinch points needed for a reliable, vibration-resistant mounting of large panels.

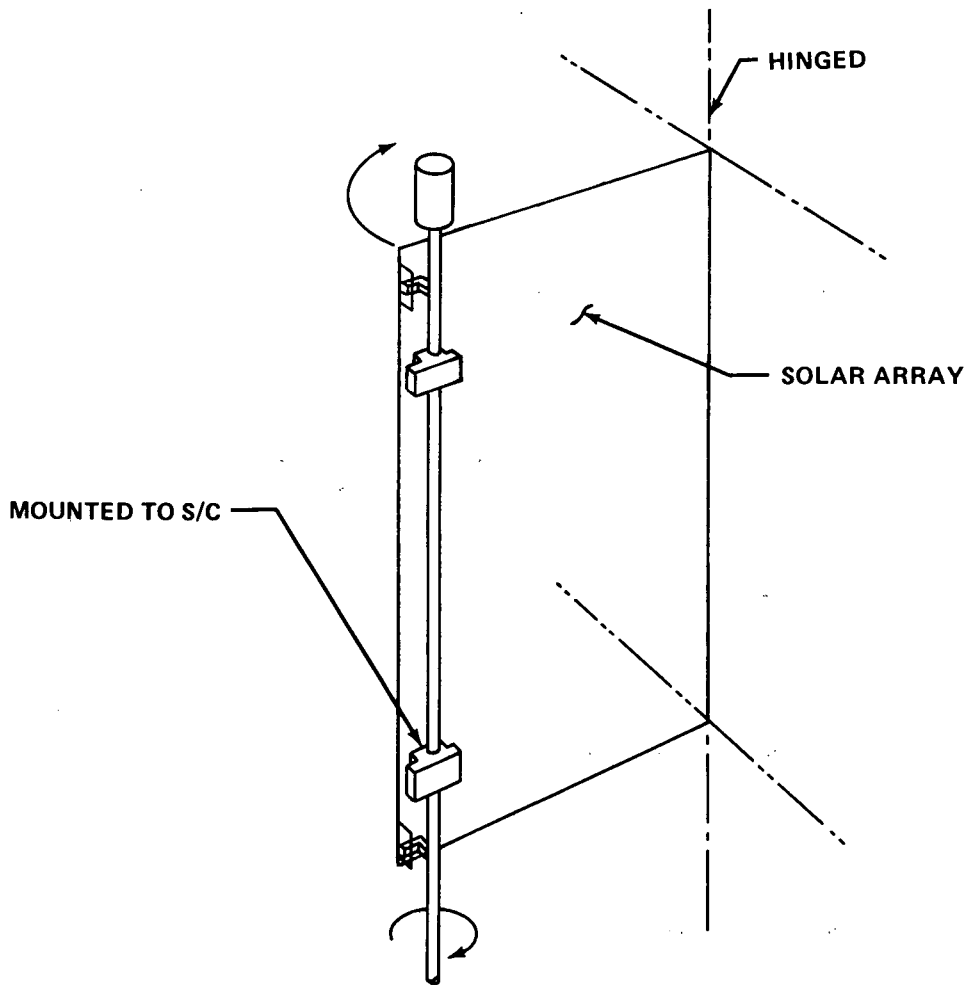


Figure F-41. Torque tube release mechanism.

The torque tube-motor technique was considered heavy, complex, and too expensive for cinching six panels as required by the baseline.

b. Cammed Catch. Figure F-42 shows another cam-type latch. A motor or linear actuator would pull the cable, releasing the latch. All latches on one wing could use the same actuator. Multiple motors would be expensive. Pyrotechnic actuators would be used for redundancy purposes instead.

The cammed catch approach was considered complex and not highly reliable. Loading springs would probably be needed to attain tight cinching, considering the hinge and location tolerances for the solar panel, the release devices, and the cinch pins. Considerable linear motion is required of the actuator. The location of the actuators and the alignment of drive rods were considered difficult for the subject concept.

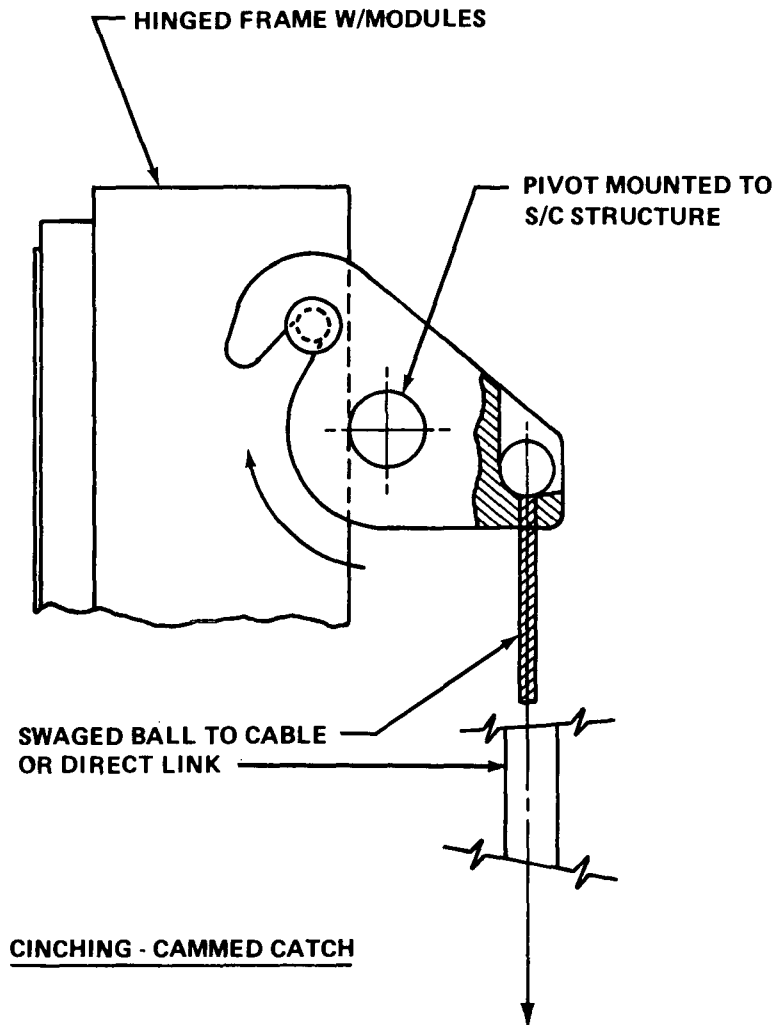


Figure F-42. Cammed catch release mechanism.

c. Baseline Cinching and Release. The cinching and release mechanisms discussed in Chapter VIII for the baseline are pyrotechnic bolts. These are based on the cinching principle of a snug-fitting bayonet pin, placed in coincident holes, located in adjacent stationary and moveable members. The pyrotechnics sever the pins to release the moveable member. There are many applicable assemblies that have been designed for cinching and release applications. This approach was baselined because: (1) it has an extensive test and flight history, (2) it has simplicity and proven reliability, and (3) it is economical and offers qualified designs.

d. Latching Concepts. Although positive stops are required for deployment, the need for latching the deployed panels has not been ascertained for the baseline. Such a requirement depends on the maneuvering forces exerted

and the stiffness and damping provided by the deployment mechanisms. Latches will be avoided if analyses show they are not necessary for maintaining array position. Latches add to the complexity and weight of the system.

Should latching be required, there are several concepts applicable. Figures F-43 through F-45 show three latch candidates. The drag link concept illustrated in Figure F-43 is considered the heaviest, the most volume consuming, and the most expensive approach. The spring clip approach, illustrated by Figure F-44, is the simplest and lightest. However, it may be difficult to adapt this concept to the baseline deployment and hinge arrangements. As shown in Figure F-45, the spring-loaded bolt scheme is also a good contender. It is slightly heavier and more complex than the spring clip approach. Another possibility is the use of a spring-loaded, cam catch similar to that in Figure F-42. The drive rod and actuator would not be required unless retraction was desired.

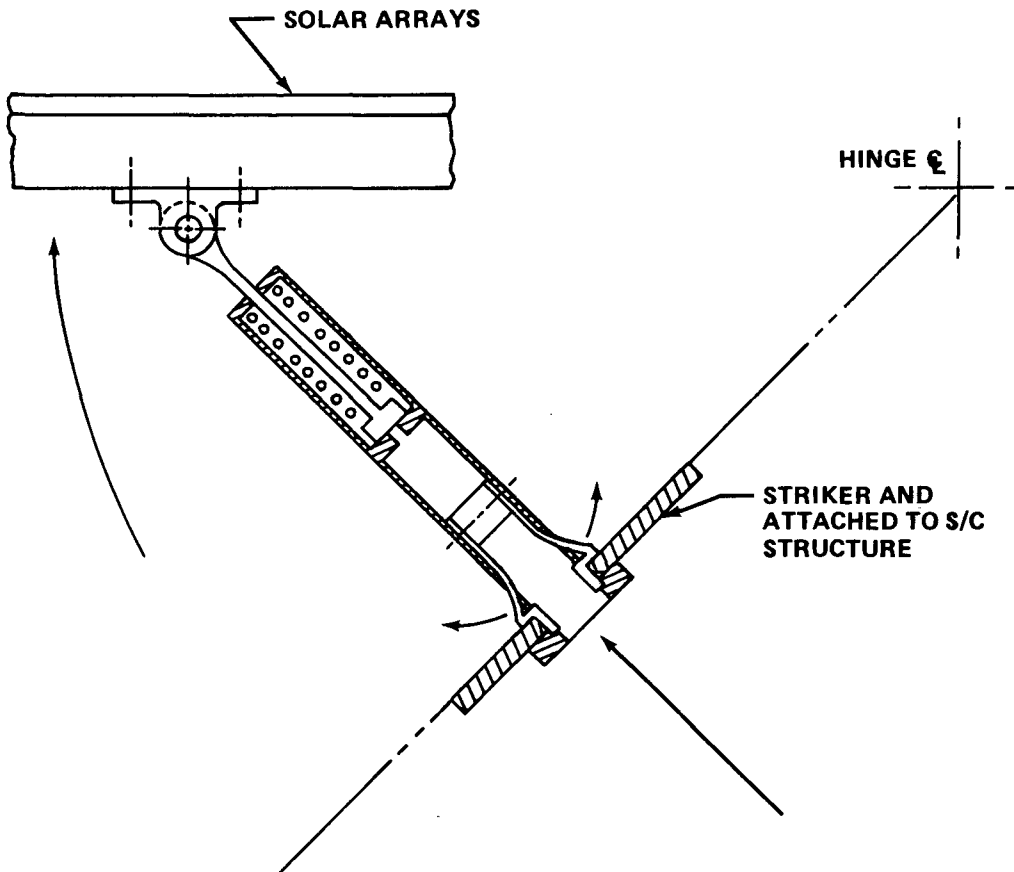


Figure F-43. Drag link latch.

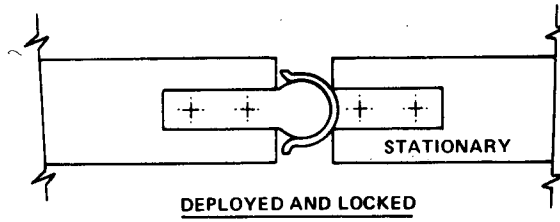
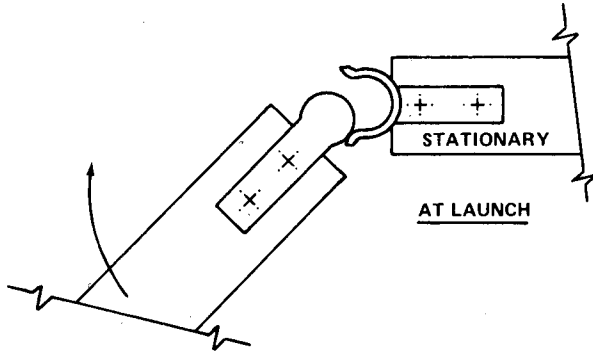


Figure F-44. Spring clip latch.

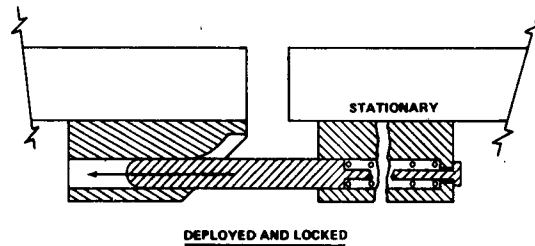
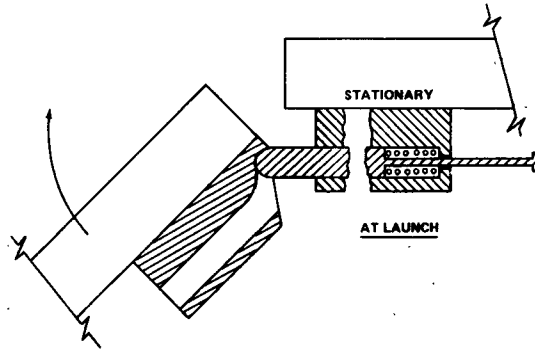


Figure F-45. Spring-bolt latching scheme.

Energy Storage Subsystem

1. Requirements and Ratings. It was shown earlier in this appendix that the baseline electrical system had an efficiency of 85.5 percent when operating from battery power. It was also shown that the energy and secondary power requirements vary with the load and occultation period of the orbit. Table F-5 shows the range of average requirements established for the batteries during orbital operations.

TABLE F-5. HEAO-C ENERGY STORAGE REQUIREMENTS

Occultation Period	Maximum (35.8 min.)	Average (34.3 min.)	Minimum (27.4 min.)
System Req'm'ts (Avg)	Energy Power	Energy Power	Energy Power
HEAO-C Load 633 Watts	440 W-h 740 W	423 W-h 740 W	352 W-h 740 W
Design Load 722 Watts	502 W-h 845 W	483 W-h 845 W	390 W-h 845 W
Min. Discharge Voltage: 24 Vdc Nominal — 22 Vdc Extreme			
Temperature: 10 ± 5°C Nominal			
Cycle Life: 11 080 Cycle for 2 years at 270 n. mi.			

The rationale for selecting Ni-Cd-type batteries was given in Chapter VIII. Additional comments are as follows:

- The very high energy, electrochemical couple of a zinc-silver oxide battery is more hazardous from an energy density and gassing point of view. Migration characteristics limit separator life. The short recharge period available in earth orbit does not permit charge currents to be limited to safe values if appreciable energy is taken from the battery. Thus, good secondary Ag-O₂ batteries are not available for more than a few hundred cycles.

- Silver-cadmium has some of the characteristics of Ag-O₂ types, although not as severe. They may be considered for missions below 10 000 cycles; however, they also must have longer recharge time than is available at 270 n. mi. if reliable operation is to be obtained. In addition, the watt-hour efficiency of Ag-O₂ cells is about 10 percent lower than Ni-Cd even though they have a higher specific energy (W-hr/lb).

Considering the reliability requirements, the cycle life required, the test data, and the data from previous satellite applications led to the conclusion that Ni-Cd batteries can satisfy HEAO-C requirements providing the following precautions are taken:

- Keep the depth-of-discharge low (below 15 percent).
- Keep the temperature in the range of 5° to 15°C.
- Effect good control on manufacturing, testing, and acceptance.
- Use matched cells and assure compatible, reliable charge control
- Do not specify cell configurations for which the manufacturer has not demonstrated considerable previous success.

Reliability, test, and cycle life data from manufacturers reports, from extensive MSFC test data on Pegasus and ATM cells, NAD-Crane reports produced for NASA, and from References F-2 and F-3 were reviewed to establish reliability, performance, and cycle life predictions for the HEAO-C mission. Figure F-46 represents a reasonable average of the wide range of data available for predicting cycle life of batteries to operate in a low earth orbit. The figure indicates that for HEAO-C conditions, the cycle life will exceed 16 000 cycles. The effect of temperature on battery life is quite evident. The 0°C curve approaches the 25°C curve beyond 40 percent DOD, primarily because the current rates are higher which makes the evolution of hydrogen more likely at the lower temperature. Such conditions quickly degrade plate-separator assemblies and hydrogen buildup will over-pressurize the cells.

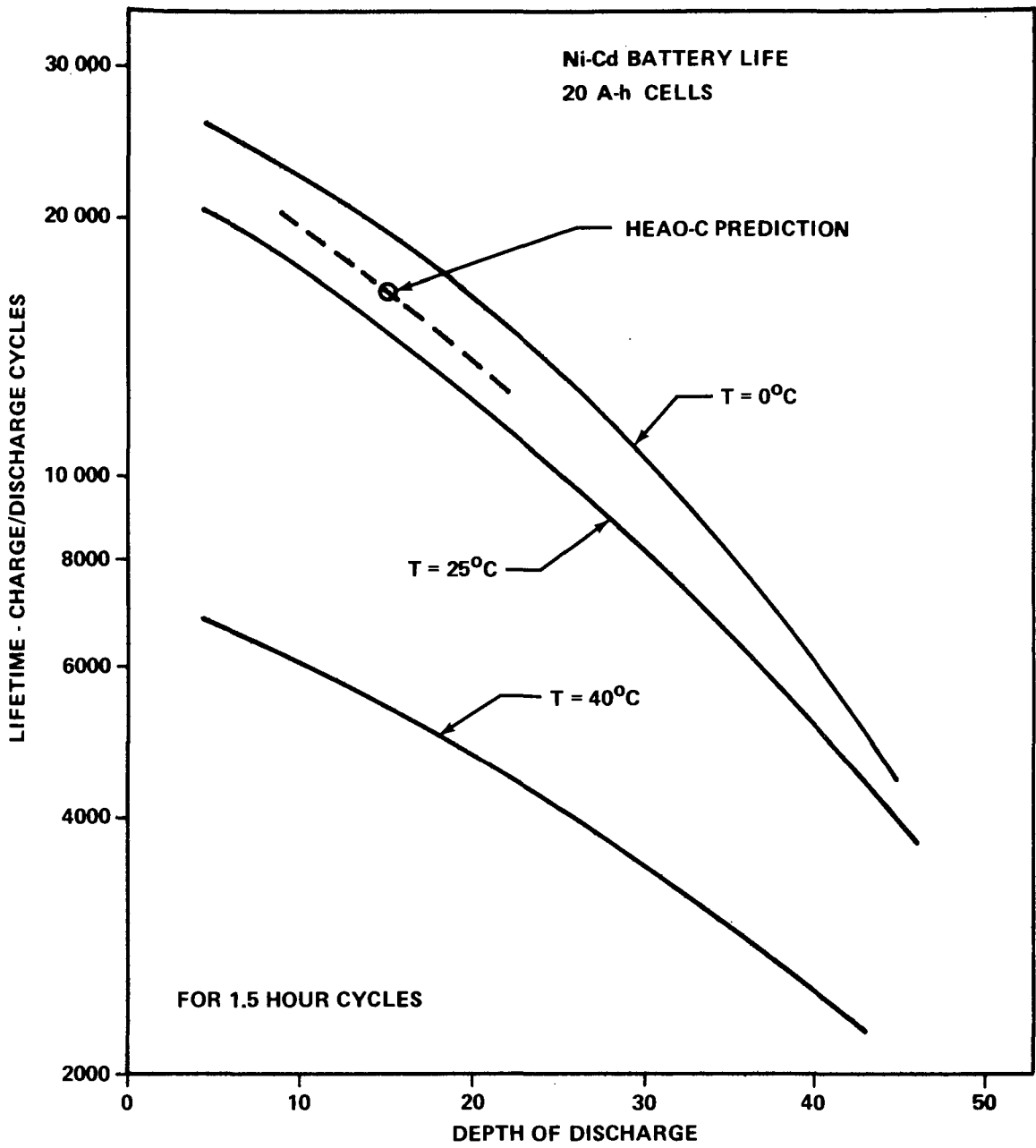


Figure F-46. Battery cycle life versus depth of discharge.

Selecting the 15 percent depth-of-discharge as a limit, the minimum battery capacity required for the mission can be determined from Figure F-47 which shows the battery energy capacity required as a function of depth of discharge (DOD) based on the design load and average orbital condition. As indicated, a minimum capacity of 3168 watt-hours is required at 15 percent DOD.

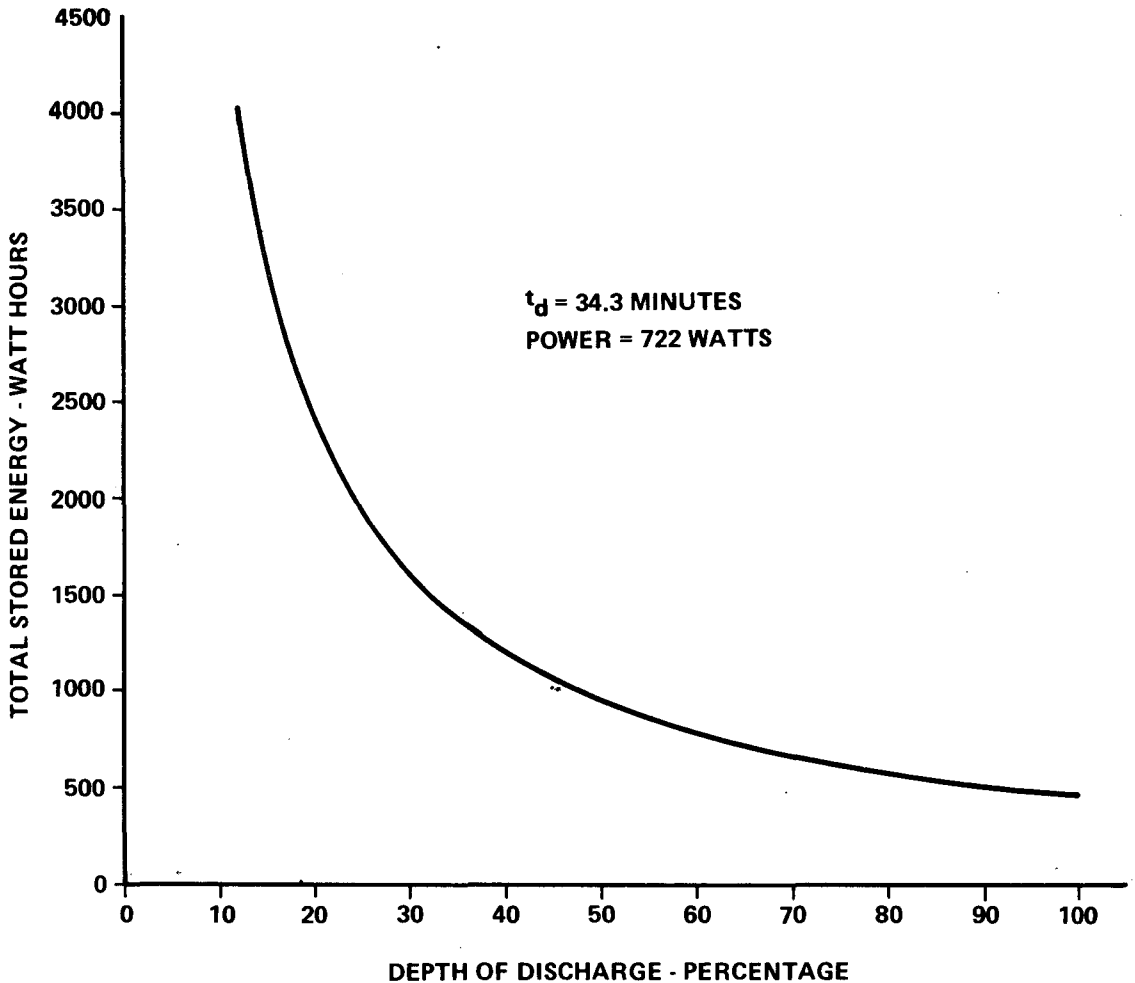


Figure F-47. Battery capacity required for HEAO-C.

2. Battery Tradeoffs. The battery tradeoff considerations mentioned earlier set the range of interest for cell sizes between 15 and 30 ampere-hours. Considering also complexity and weight, the range of interest for the number of battery assemblies was between 4 and 8.

Applicable cell data were determined from manufacturer's ratings for space proven cells. Typical rating and sizes for 15, 20, and 30 ampere-hour cells are given in Table F-6. Cell dimensions vary with the manufacturer; however, the volumes and energy density are very close to the same. Successful, previous applications were surveyed to derive the assembly characteristics shown in Table F-7.

Preliminary tradeoffs, based on Tables F-6 and F-7 and with the capacity and DOD constraints, were made to determine an optimum cell and assembly configuration. Figure F-48 shows the approximate relationship of energy-to-mass and energy-to-volume with rated capacity of typical battery assemblies. An expanded vertical axis is used to show the variations. As may be expected, the larger cell sizes have higher performance factors because housing and other hardware are a smaller fraction of the total weight and volume. The differences are rather small, indicating that significant size or weight penalties will not be incurred by different cell sizes if assembly configurations can be tailored close to the system requirements.

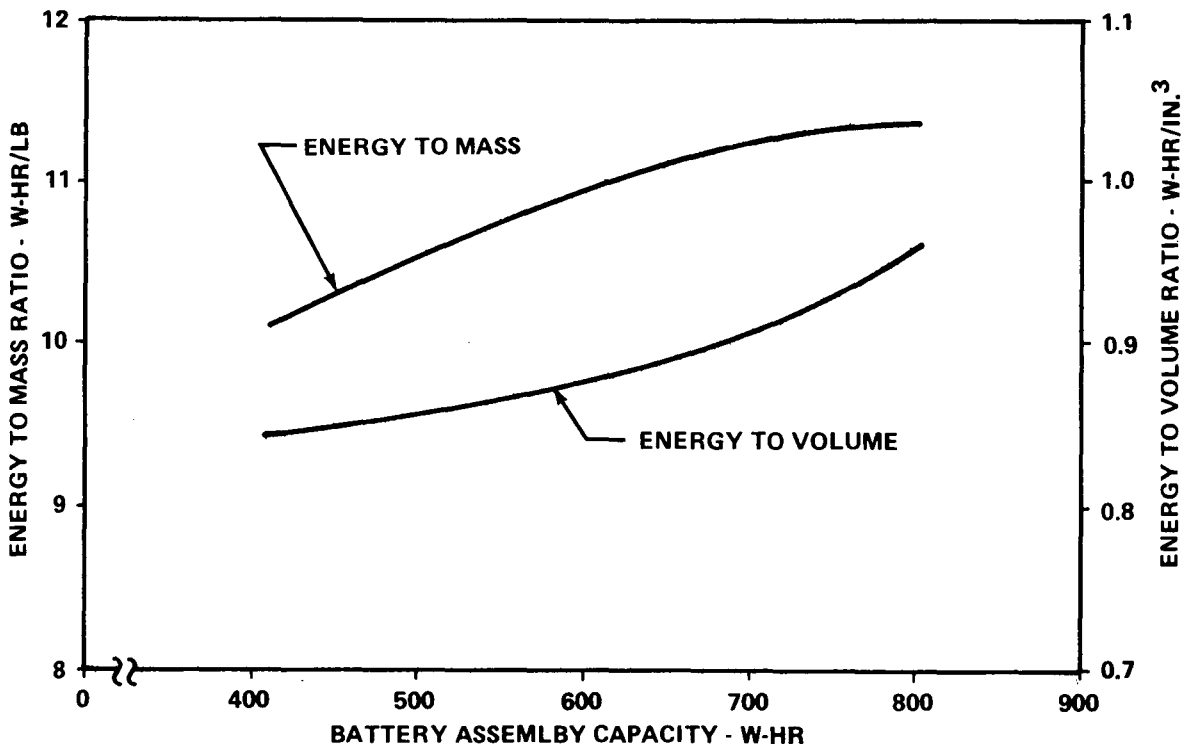


Figure F-48. Energy-volume-mass characteristics for battery assemblies.

TABLE F-6. SPECIFICATIONS FOR TYPICAL BATTERY CELLS (Secondary Nickel-Cadmium)

Cell Rating (amp-hr)	Cell Voltage at 25°C	Energy Capacity (watt-hr)	Cell Dimension (in.)			Cell Volume (in. ³)	Cell Weights (ounce)
			Width	Length	Height		
15	1.25	18.75	2.42	1.00	6.90	16.7	25.4
20	1.27	25.4	3.18	1.03	6.62	21.7	32.0
30	1.28	38.4	3.19	1.46	6.38	29.6	44.8

TABLE F-7. TYPICAL BATTERY ASSEMBLY CHARACTERISTICS

Cell Rating (amp-hr)	No. of Cells Required	Assembly Capacity (watt-hr)	Assembly Dimensions (in.) ^a			Volume (in. ³)	Weight (lb) ^b	Performance Factor	
			Length	Width	Height			watt-hr/lb	watt-hr/in. ³
15	22	413	12.69	5.12	7.63	490	41	10.1	0.843
20	22	559	13.10	6.67	7.40	646	52	10.8	0.865
30	21	807	16.91	6.93	7.17	840	72	11.2	0.962

a. Approximately 0.020 in. allowed between cells for insulation, thermal shims, connections, etc.

b. Weight allowances for housing, connectors, and wiring.

Figure F-49 shows the rated capacity of various assemblies of cells for the three cell sizes (15, 20, and 30 ampere-hour) as a function of the cells per assembly. The right vertical axis shows the number of assemblies required for the HEAO-C, 483 watt-hour requirement with a 15 percent DOD limit. The rating of each assembly is read on the left vertical axis. Since all combinations between assemblies 4 and 9 are feasible in capacity, the compromising application needs are considered as follows:

- A lower number of cell assemblies is desirable from a charge control and thermal standpoint. The undesirable aspects of lower number of cells is an increase in the number of assemblies and an increase in losses, especially diode losses.

- Reliability and redundancy, requiring more assemblies, increase complexity and the housing and cable weight. The range of 4 to 8 assemblies was considered reasonable.

- Higher numbers of cells tends to improve efficiency and lower the number of assemblies, but the charge control becomes more critical caused by masking of the weaker cells. For this reason, the number of series cells was limited to 24.

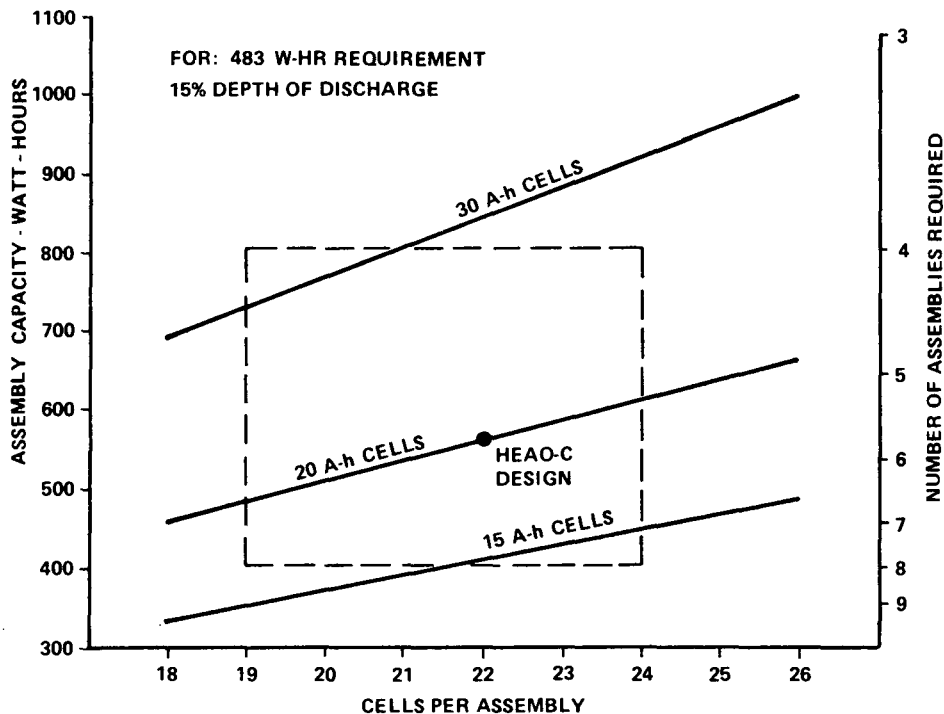


Figure F-49. Comparison of battery cells, assemblies, and ratings.

The boundary limits are shown as dashed lines on Figure F-49. Within the 4 to 8 assembly range which is considered practical, the only good 30 ampere-hour cell assembly would be the 21-cell version because the 30 ampere-hour curve crosses the 4 assembly line very near the 21-cell mark. Fewer cells, within the range, would be off-optimum because the curve lies between the 4 and 5 assembly lines; therefore 5 assemblies would be required for the 18-, 19-, and 20-cell, 30 ampere-hour batteries. The inflexibility of the large size cells is obvious for the energy domain of HEAO-C because each cell represents a large increment.

Similar reasoning for the 15 ampere-hour cell assemblies indicates that the cell increments are small and that higher assembly numbers are needed. Since the 15 ampere-hour curve crosses the 24-cell line just beyond 7, the number required would be 8 for 22-, 23-, and 24-cell configurations. The 22-cell assembly would be closest to optimum. Again, the flexibility within the HEAO region is restricted.

The 20 ampere-hour sizes are centrally located in Figure F-49 and, therefore, offer the greatest versatility for optimum adaption to small variations in HEAO-C requirements. All cell configurations in the region 19 to 24 are practical. This size appears to offer the best compromise of reliability and redundancy with complexity and cabling penalties because it centers around six assemblies. It also satisfactorily meets the cell limits.

Because assembly weights are not continuous, the system weights for the assembly cell combination within the region established (19 to 24 cells and 4 to 8 assemblies) are tabulated in Table F-8.

Referring to Table F-8, the 4-assembly, 21-cell configuration of 30 ampere-hour cells has the lowest weight but is on the line limited by reliability/redundancy. The next size is on the lower cell limit line and weighs more than the lighter 20 ampere-hour configurations. Six other configurations would be selected before the most weight competitive 15 ampere-hour size.

Favoring the reliability and cell limit considerations led to the selection of the conservative 20 ampere-hour cell configuration of 6 assemblies with 22 cells each. The off-optimum weight penalty for the conservative selection is 24 pounds. Other advantages of this selection are (1) the lower weight per assembly makes handling and installation more reliable than for a 72 pound assembly, and (2) it will be easier to assure a good thermal and charge control design for the smaller cells and assemblies.

TABLE F-8. COMPARISON OF BATTERY SYSTEM WEIGHTS

Cell Size		15 amp-hr	20 amp-hr	30 amp-hr
Configuration		System Weight (lb)		
No. Assy's	No. Cells			
4	21	N/A	N/A	288 ^a
5	19	N/A	N/A	317
	20	N/A	N/A	335
6	22	N/A	312 ^a	424
	23	N/A	329	N/A
	24	N/A	341	N/A
7	19	N/A	315 ^a	
	20	N/A	331	N/A
	21	N/A	348	N/A
8	22	328	433	N/A
	23	342	N/A	N/A
	24	357	N/A	N/A

a. Lowest weight configurations.

3. Baseline Battery Assembly. The battery assembly for the EPS baseline, shown by Figure VIII-16, has the 13 by 6.6 by 7.25 inch dimensions and will weigh 52 pounds. It consists of a magnesium alloy (stainless steel alternate) housing, 22 series connected cells, connectors, sensors, insulators, and thermal shims. All cells are hermetically sealed, Ni-Cd-type cells in stainless steel containers. Each cell is nominally rated for 20 ampere-hours, and is qualified and space proven. Typical rated discharge characteristics for several temperatures are given for the baseline cell in Figure F-50.

11 ②

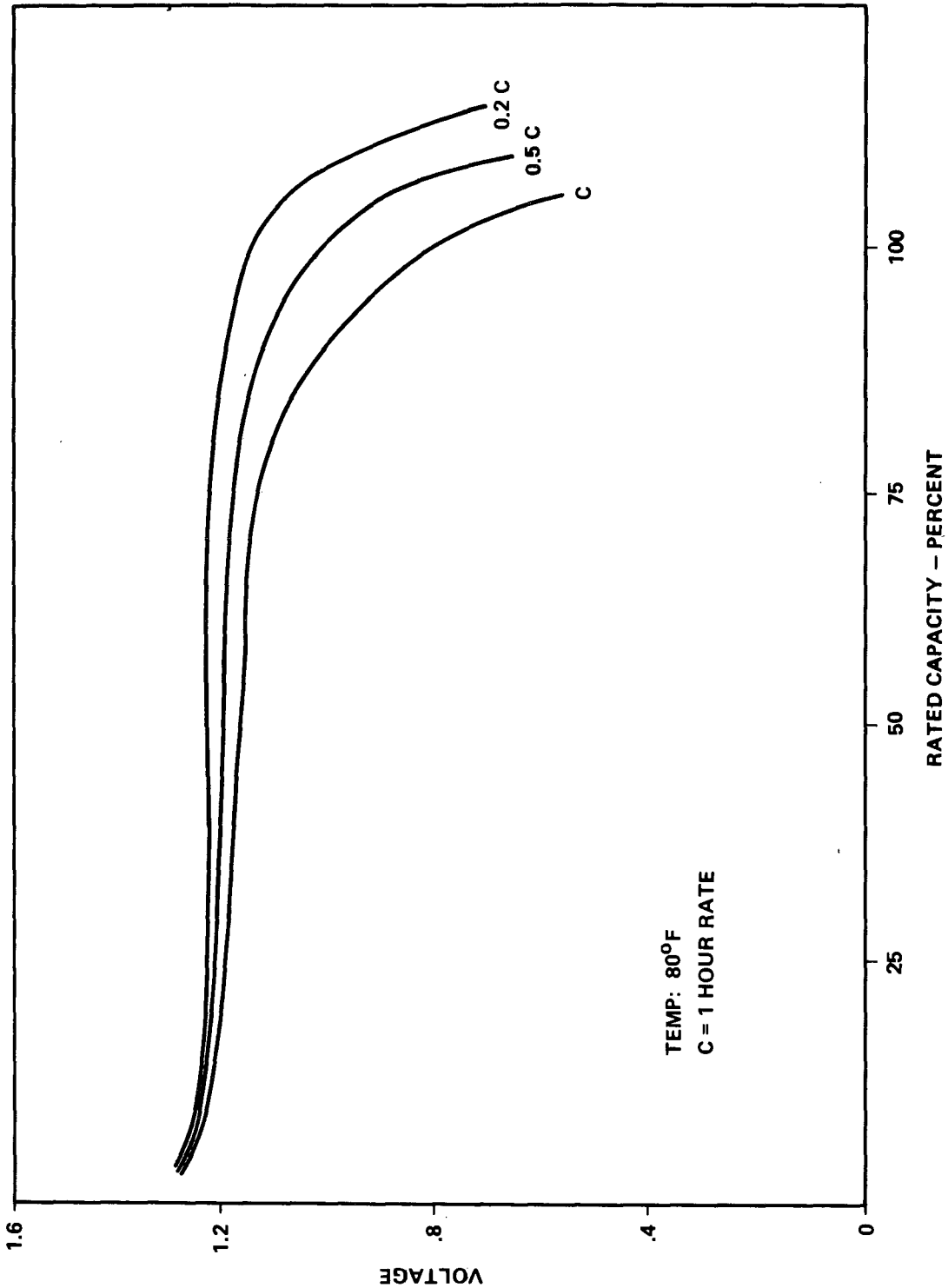


Figure F-50. Discharge characteristics for Ni-Cd cell.

Three of the cells in each assembly are third electrode types that can supply signals to stop charge when fully recharged. Redundant connections and temperature sensors for control and instrumentation are provided. The schematic diagram for an assembly is given by Figure VIII-18 showing the cell connection, sensors, and the operational and test connectors.

The assembly is designed for maintaining close temperature control, $10 \pm 5^\circ \text{C}$, and will satisfy all other environmental requirements. Each assembly is nominally rated for 20 amperes, 24 to 29 Vdc output at the 1 hour discharge rate. The minimum capacity rating will be 560 watt-hours. Recharge will be strictly controlled. The maximum charge rate and voltage will be limited to 15 amperes and 33 Vdc, respectively.

Six battery assemblies are used in the system to furnish 3220 watt-hour capacity to meet all system needs, to fulfill redundancy requirements, and to limit the average DOD below the 15 percent limit set. The 14 percent DOD rating resulting from the design assures an ample cycle life of over 16 000 cycles as compared to the 11 080 cycles required.

Additional ratings and characteristics are specified in the subsection of this appendix, entitled "Electrical Requirements," and are established for the HEAO equipment.

Performance analyses were run for the total installation of base-line batteries in conjunction with the solar array to determine the limits for continuous off-sun pointing. The number of orbits allowable for continuous off-sun pointing is plotted as a function of the off-sun pointing angle in Figure F-51. The worst occultation period was assumed. The 50 percent depth-of-discharge limit indicated was the maximum considered safe during the last year of the mission. All operating points below and to the left of the curve are permissible. However, for the sake of reliability, this mode of operation is not recommended.

4. Battery Control Subsystem

a. General Description. The importance of good battery control has been discussed in Chapter VIII. Protection against excessive discharge is equally important. The battery controls and charger assemblies are discussed only for some of the major design criteria and charger concepts because this is a rather complex, extensive subject if all the subtle, but highly important, details are covered.

OFF-SUN POINTING CAPABILITY OF HEAO-C BASELINE EPS

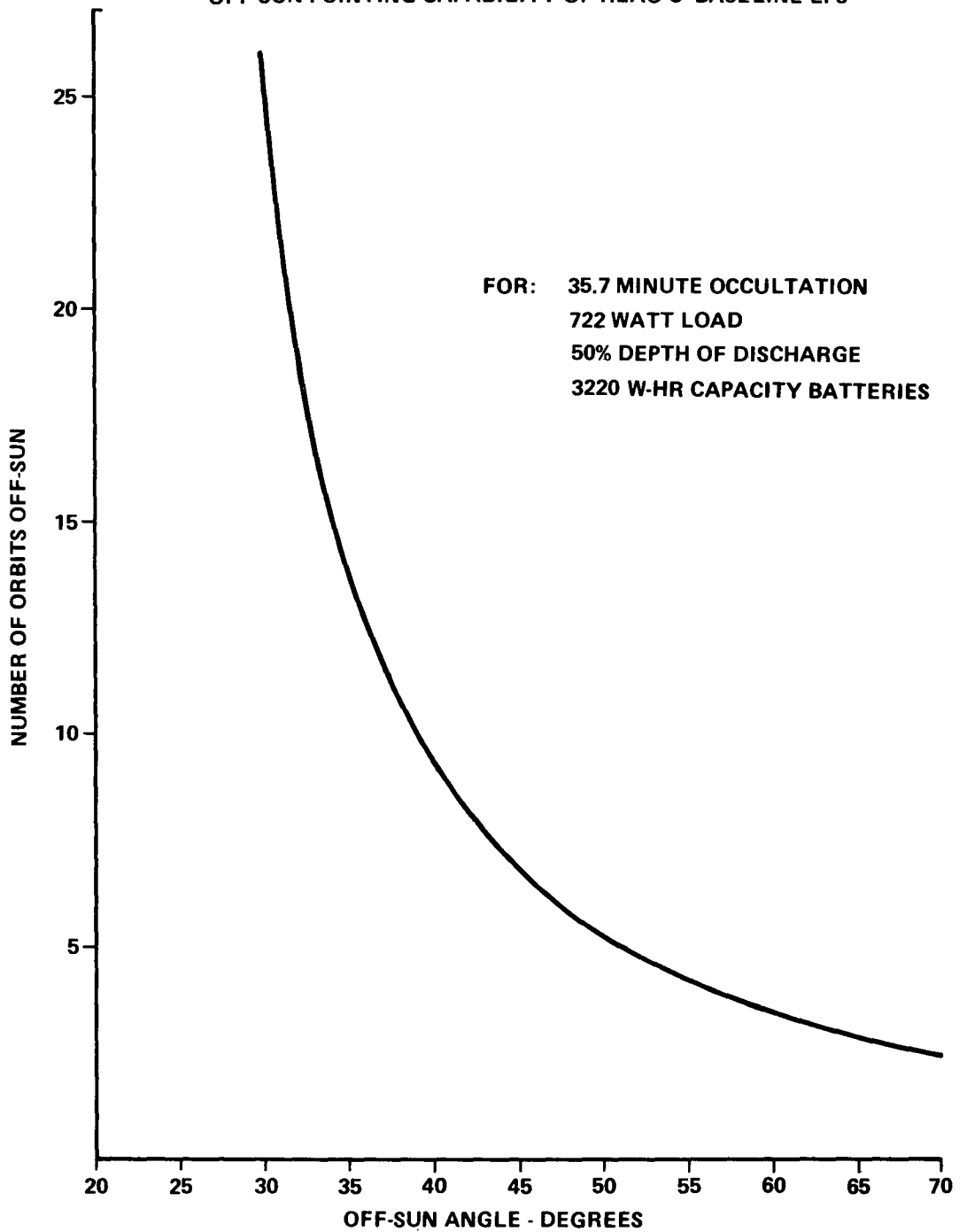


Figure F-51. Off-sun pointing capability of HEAO-C baseline.

As indicated previously, each of the six battery assemblies will have a dedicated charger control; therefore, six charger assemblies are required in the baseline system. Not all of the charge control subsystem is included in the six-charger assemblies; remote sensors in the solar power distributors, in the battery assemblies, and the sensors and overload protection in the ECAs are parts of the charge control network. The charger assemblies are the primary control units and are the only assemblies that interface with the battery assemblies.

Each charger is located near the battery to assure short cables. The battery charge input and the discharge output of the battery are routed through the charger. Battery instrumentation for control and telemetry is also routed through the charger assemblies. Each charger interfaces with a solar power distributor and an ECA, providing redundant access to input power channels from the solar array and sensors. The charger directs battery output power over redundant lines to the secondary power buses in the ECA.

Under nominal conditions, discharge will be limited to less than the rated 20 amperes and to a low voltage limit of 24 Vdc. Provisions are made for limit overrides via ground command if abnormal system conditions occur. An excessive battery temperature of 45° C during charge will interrupt charging, and 55° C will remove the battery from the bus if at least two other battery assemblies are functioning.

b. Battery Characteristics for Control. The detail characteristics of batteries have, in the past, varied with manufacturers, styles, and configurations, and, as evidenced by wide variations in test data, even with the same cell lot. Rigid NASA specifications have been created to curtail some of the randomness in cell performance. Such controls are to be affected for HEAO. Long-term cycle test data, illustrated in Figure F-52, show the effect of using matched and unmatched cells in an assembly.

Typical over-charge current and voltage limits were shown for a Ni-Cd cell in Figure VIII-19. The characteristics must be recognized by the charger for reliable control. On the average, voltage characteristics are multiplied by 22 series cells for the HEAO assembly; however, because of possible mismatch and cell differences, the charger must be designed to assure that all cells remain within their limits, not just the average assembly value. Violation of such limits on any cell leads to early termination of the assembly life. Cell variations with charge, shown by Figure F-53, were obtained from ATM cell tests. The sensitivity of control parameters to temperature was indicated by Figure VIII-17. Such variations must be compensated.

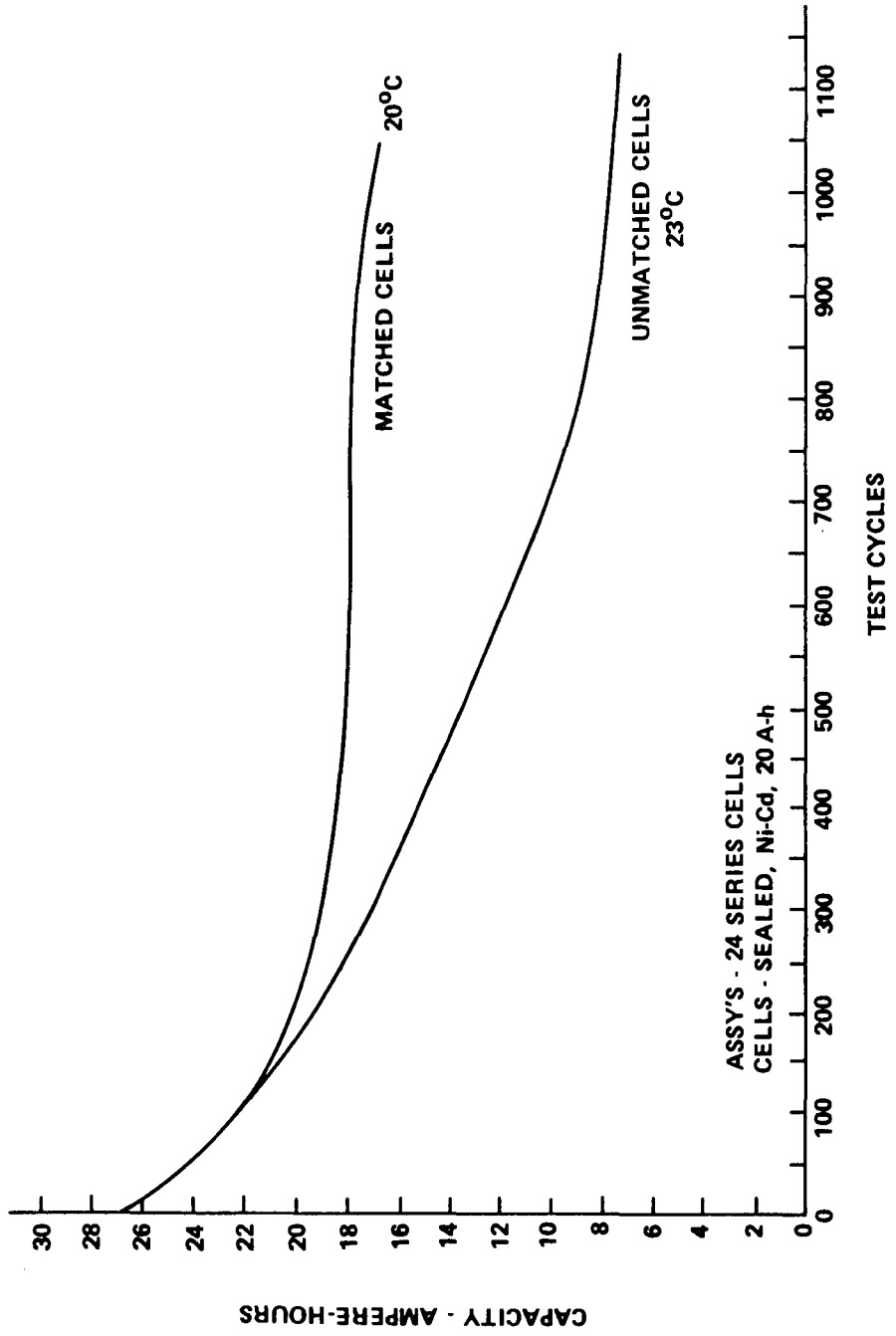


Figure F-52. Long-term performance of battery assemblies with matched and unmatched cells.

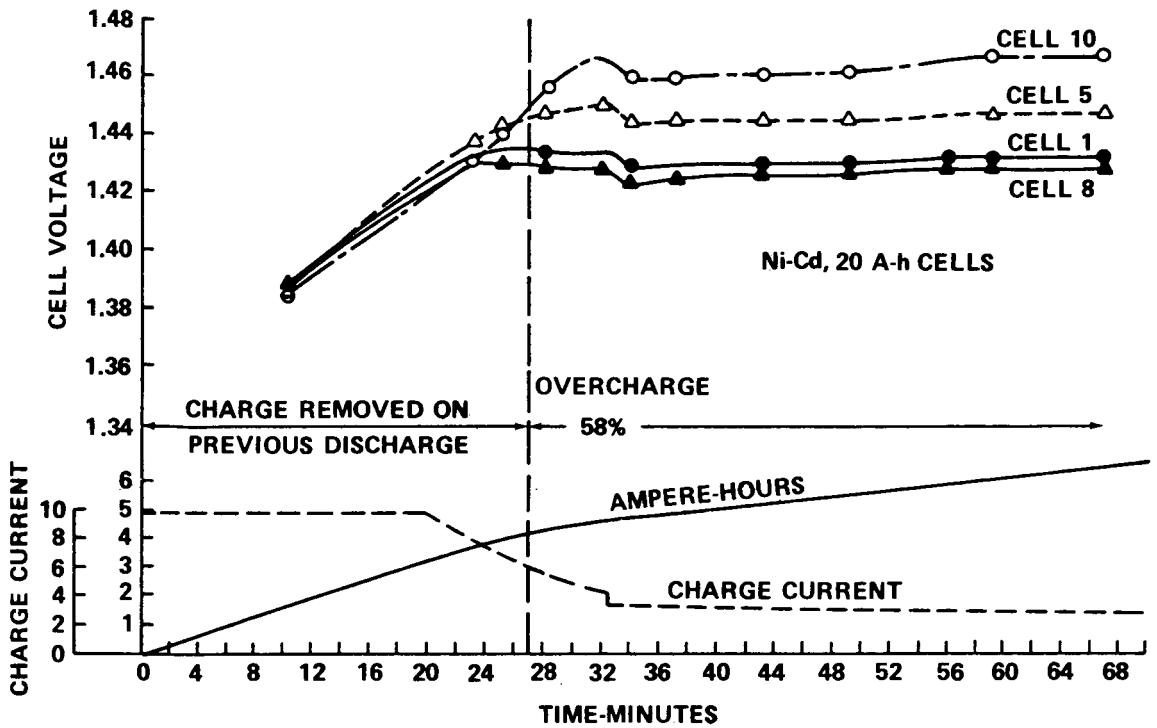


Figure F-53. Cell divergence during charge-discharge cycle.

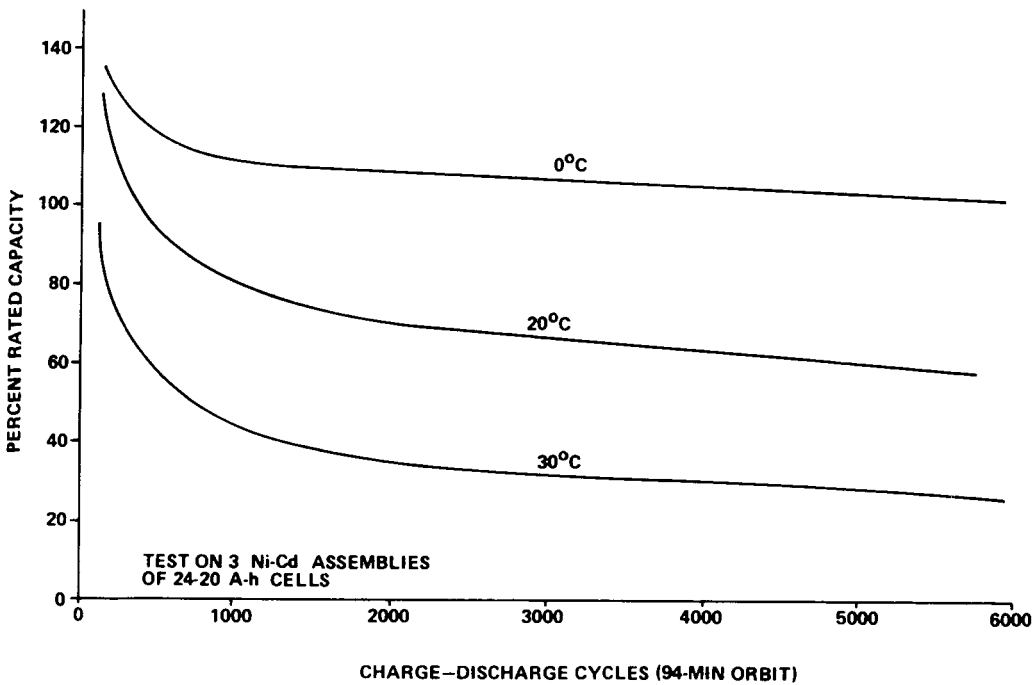


Figure F-54. Battery capacity retention characteristics.

The performance improvements resulting from maintaining a low battery temperature are illustrated by the cycle life test results (Fig. F-54). Capacity retention is very important to mission success.

The charge voltage will be temperature-compensated and limited to 33 volts maximum. Charge rates will be limited to less than 15 amperes. The average charge current required per orbit per battery is approximately 3.1 amperes.

5. Battery Charger Assemblies

a. Requirements. Each of the battery charger assemblies must maintain its battery in good operational condition for 2 years. Most of the specific requirements have been discussed previously. The assemblies are briefly summarized as follows:

- Accommodate the battery characteristics discussed above.
- Be consistent with the system reliability and redundancy requirements.
- Receive solar array power at voltages between 38 and 78 Vdc.
- Sense primary bus conditions and avoid overloading the bus.
- Limit the charge current to less than 15 amperes and normally deliver an average current between 3 and 5 amperes.
- Limit the charge voltage to 33 Vdc and provide output between 22 and 33 volts as needed.
- Be rated for over 400 watts.
- Monitor charge, discharge, and battery conditions.
- Receive control signals and compensate the output accordingly.
- Terminate charge as soon as possible to avoid degradation and thermal burden.
- Provide instrumentation for remote power management.

b. Baseline Design. The battery charger design meets the above requirements and recognizes the battery and system characteristics. In selecting the baseline, previously used charger designs and basic converter circuitry tradeoffs were considered. The selected design is 95 percent efficient and

provides the essential redundancy features. It uses qualified, conservatively rated components and subassemblies. The charger ratings were summarized in Table VIII-16.

The charger is a nonisolated, step-down, static-switching converter, basically consisting of controlled semiconductor switches, magnetic and electrostatic energy storage devices, and electronic control components. As indicated in Figure VIII-18, power transistors are used to accomplish conversion and to control the output. Magnetic chokes and capacitors provide the necessary energy storage. Logic and amplifier circuitry, consisting of resistors, diodes, transistors, and capacitors, control the power switches in accordance with the input control signals received. Low-pass filter sections are provided to meet the system EMI and RFI requirements.

Normally, the charger input appears as a constant power load, the level being determined by the battery. The input impedance is modified by the control signals as the battery or system demands. The charger replenishes the energy drawn from the battery and furnishes additional power to compensate for the losses incurred by battery inefficiency. The output of the charger is a variable that is adapted to the battery characteristics.

The charger has a modified constant current and a constant voltage output characteristic which is adjusted by the control signals received. The control signals are received from internal and remote sensors. The battery current, voltage, and ampere-hours are monitored internally. Remote signals received are battery temperature and third electrode cell signals from the battery assembly, and signals for the V-I characteristics of the solar array bus from the solar power distributor.

Without array power tracking feedback, the charger would limit the initial charge current to about 12 amperes. High rates are permissible when the battery is discharged and when the battery temperature is in the proper range. Normally, with six batteries requiring charge, the peak power tracking feedback will limit the initial charger current for each battery to 5 or 6 amperes when the array is cold. As the array heats and the power available decreases, the charger will reduce the charge current so that the spacecraft loads are supplied first. The charge current is also reduced when the battery detectors indicate a reduction is needed. The current, voltage, and temperature are interdependent in this mode to adjust to the specific characteristics of the battery. When the temperature dependent voltage reaches a preset level, the charge voltage drops 0.5 volt. The current is reduced and the charger operates in a constant voltage mode until cutoff is initial by third electrode signals or redundantly by the ampere hour detector.

Figure F-55 illustrates the charger response to the signal from the third electrode cells. At about 13 minutes, charge begins; the charge current rises to the limit and remains. The voltage climbs as the battery is

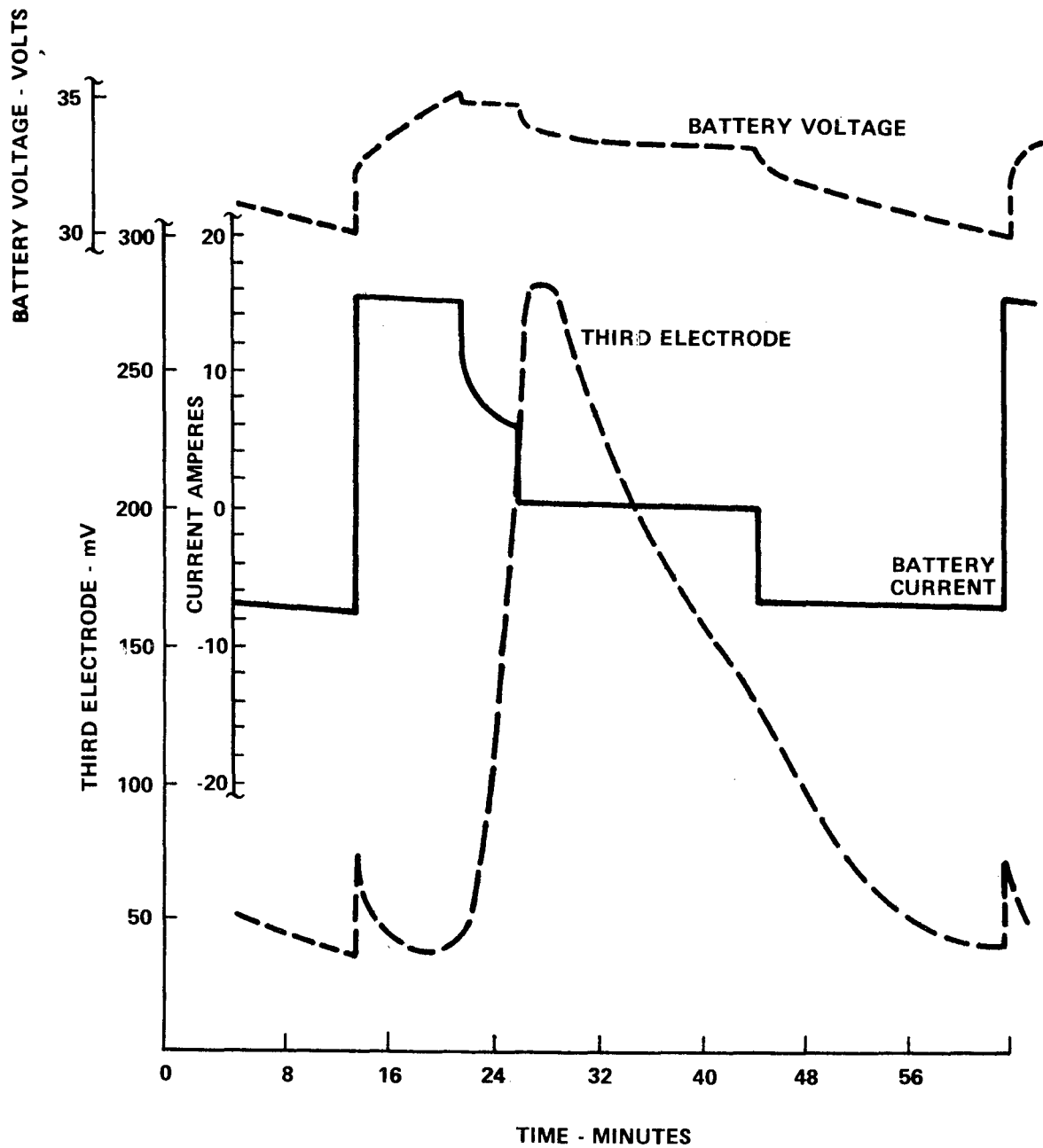


Figure F-55. Charger response to third electrode signal.

charged. At the voltage level which is indicating the battery is nearing full charge, the voltage drops back slightly causing the charge current to decrease significantly. The charger maintains a constant voltage until the sharply rising third electrode signal indicates full recharge. This occurs at about 24 minutes in the example shown. The charger then terminates the charge (0 current output).

The ampere-hour meter clocks the battery output and input during the entire cycle. When the output and the losses have been resupplied, the meter furnishes an output that is used to terminate the charge also. The ampere-hour meter also furnishes battery charge-discharge status information to the telemetry subsystem for transfer to the ground. This information enables control of batteries and chargers from the ground.

Recombination electrodes within the cells permit a high charge rate over a wide temperature range, and these electrodes avoid the hazard of hydrogen pressure buildup. These electrodes also enhance the characteristics of the third electrode. The charge, however, provides charge rate limiting or shutdown capabilities for abnormal battery conditions. Temperature limit sensors in the battery signal charge limits if the battery is too cold or charge termination if it is too hot. Additional discussion of charger characteristics is given in Chapter VIII.

Power Conditioning Concepts

1. Power Conditioning Subsystem. The HEAO-C electrical system concepts, discussed in Chapter VIII, indicated that the power conditioning subsystem handled and conditioned all the power delivered to the spacecraft loads. Most of this subsystem is contained within the four regulator assemblies provided. Several sensors and the on-off controls required are remotely located in the ECAs. The remote sensors provide for remote regulation at the bus, standby and power sharing operations, backup fault protection, and redundant operational modes.

The baseline provides highly efficient operation based on reliable principles and proven components and subassemblies. Avoiding new or novel approaches, several basic regulator concepts were analyzed before choosing the baseline. Only static, dc-to-dc converters with regulation were studied. Boost-buck (or stepup-stepdown) types are applicable for output power condition because high voltage is received from the solar array during part of the orbit while low voltage is provided by the batteries. Stepdown types are applicable to chargers.

The converter-regulator concepts considered were as follows:

- An all semiconductor, boost-buck type without transformers.
- A magnetic amplifier-controlled type.
- A transformer coupled buck-boost type with integrated circuit controls.

2. Converter-Regulator Concepts

a. **Transformerless Boost-Buck Regulator.** The arrangement of components in a voltage regulator circuit determines whether it is a stepup or stepdown regulating device. The components in Figure F-56 arranged inside the dotted line marked "boost" accomplish the stepup voltage regulation. The same components in the "buck" portion of the regulator accomplish a stepdown in voltage to control regulation.

The control signal S_1 for the boost part of the regulator determines the voltage at the point marked V_2 according to the equation,

$$V_2 = V_1 \left[\frac{t_{(on)}}{t_{(off)}} + 1 \right].$$
 An understanding of this technique may be found by

referring to a text on voltage-doubling circuits. If $t_{(on)}$ is equal to $t_{(off)}$, the voltage at point V_2 will be twice the input voltage, neglecting circuit losses. If the pulse train is a controlled variable duty cycle, then stepup voltage regulation of the desired output can be accomplished.

Depending on the nature of the control signals, the "buck" portion of the regulator can be operated as a series dissipative regulator or as a switching regulator. As a series dissipative regulator, L_2 and C_2 may not be required. Normally the series dissipative approach would not be recommended since it is less efficient and reliable than the switching mode regulator approach. An application for this regulation scheme would be to use only the boost part as a stepup regulator. For example, it could be used with a battery system having an output that varies from 18 to 27 volts to produce 28 volts constant output. This approach requires fewer cells to achieve the desired output voltage than a "down" regulator and is lighter than the more conventional transformer method of boosting the voltage. This approach would merit consideration if weight of the EPS became a critical factor. However, it does not provide the desired dc isolation of the source from the load.

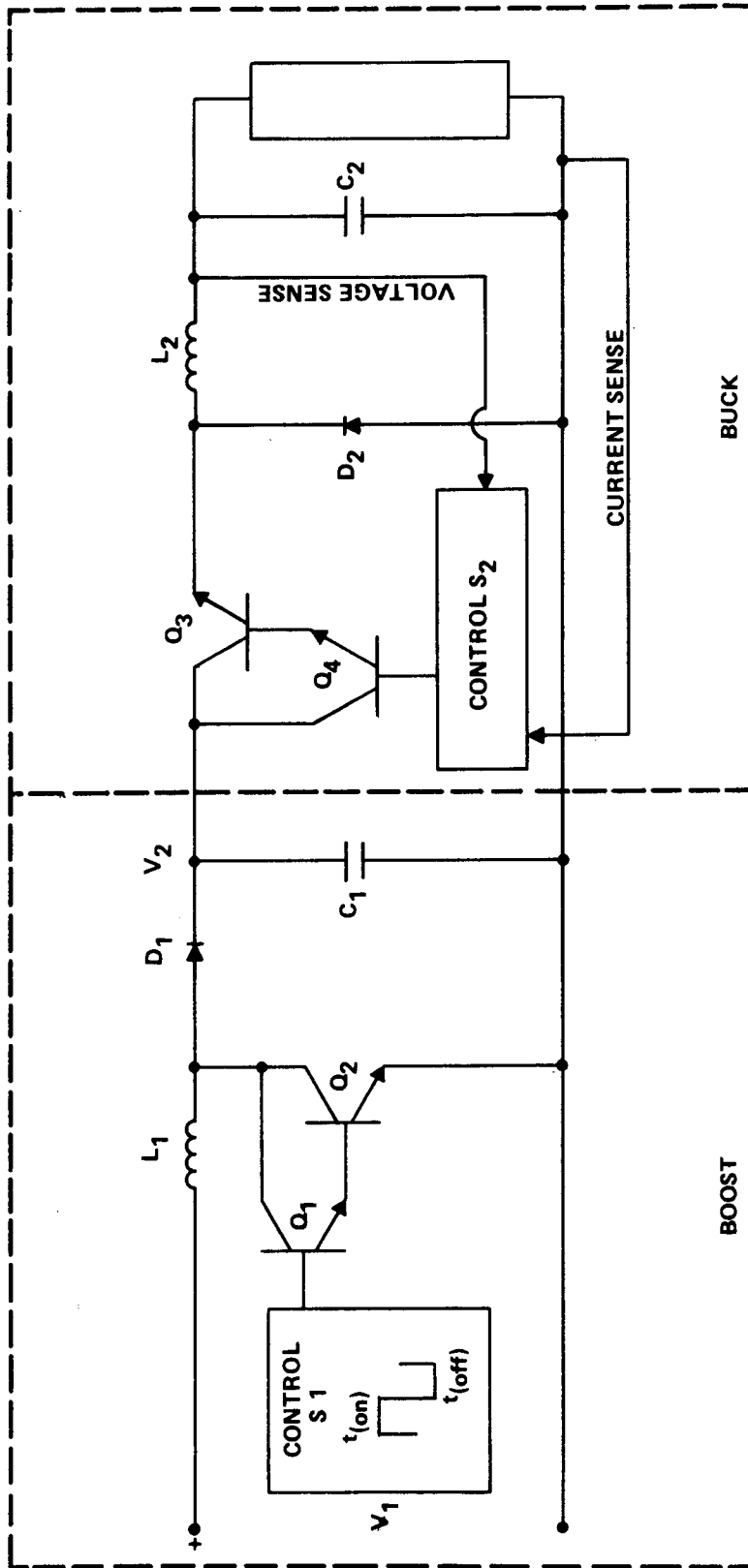


Figure F-56. Transformerless boost-buck regulator.

b. Magnetic Amplifier Regulators. The magnetic amplifier is a rugged, reliable device for controlling current and voltage in an EPS. It is superior to low-level, integrated circuit controls when the application imposes a high radiation environment. Power transistors perform satisfactorily if sufficient base drive is used to compensate for the beta reduction. Magnetic amplifier approaches are particularly attractive if there is an ac source.

There are several versions of the magnetic amplifier type of regulator. Only the magnetic amplifier-coupled types (i. e., use for control) were considered here. Types feeding directly into rectifiers and filters are also feasible.

A block diagram of the subject regulator is shown in Figure F-57 (a). It consists of the magnetic amplifier, associated amplifier components, and an oscillator to supply ac for the gate windings. As mentioned, the amplification could be accomplished with magnetic components. For the types considered, the output marked E_{in} can be used to control either of the power sections shown as Figure F-57 (b) or F-57 (c).

The magnetic amplifier has three control windings in addition to its gate (excitation) windings: (1) a control winding is used to control the output voltage of the regulator, (2) another winding provides overload (short-circuit) protection, and (3) another provides feedback to control the amplifier gain. The effect of feedback on the amplifier performance is illustrated by Figure F-57 (d). The slope of the curves indicates the gain. With feedback, it takes less change in control current to accomplish a given change in output than it does without feedback. A single stage of power amplification, following the magnetic amplifier, is adequate to meet the HEAO regulator requirements.

Since the mission does not impose high radiation requirements this concept was not chosen because it is heavier and requires a larger assembly volume. It also has a slower response and usually a higher output dynamic impedance.

c. Transformer-Coupled Buck-Boost Regulator. The transformer-coupled, buck-boost regulator was baselined for HEAO-C. It is simpler than the type described in Paragraph a. above, and is lighter and more efficient than type b. It provides dc isolation between the power source and the loads which is very important from a system reliability and EMI standpoint.

Figure VIII-22 shows the basic elements of the baseline regulator. The diagram indicates that the control circuits, power transistors,

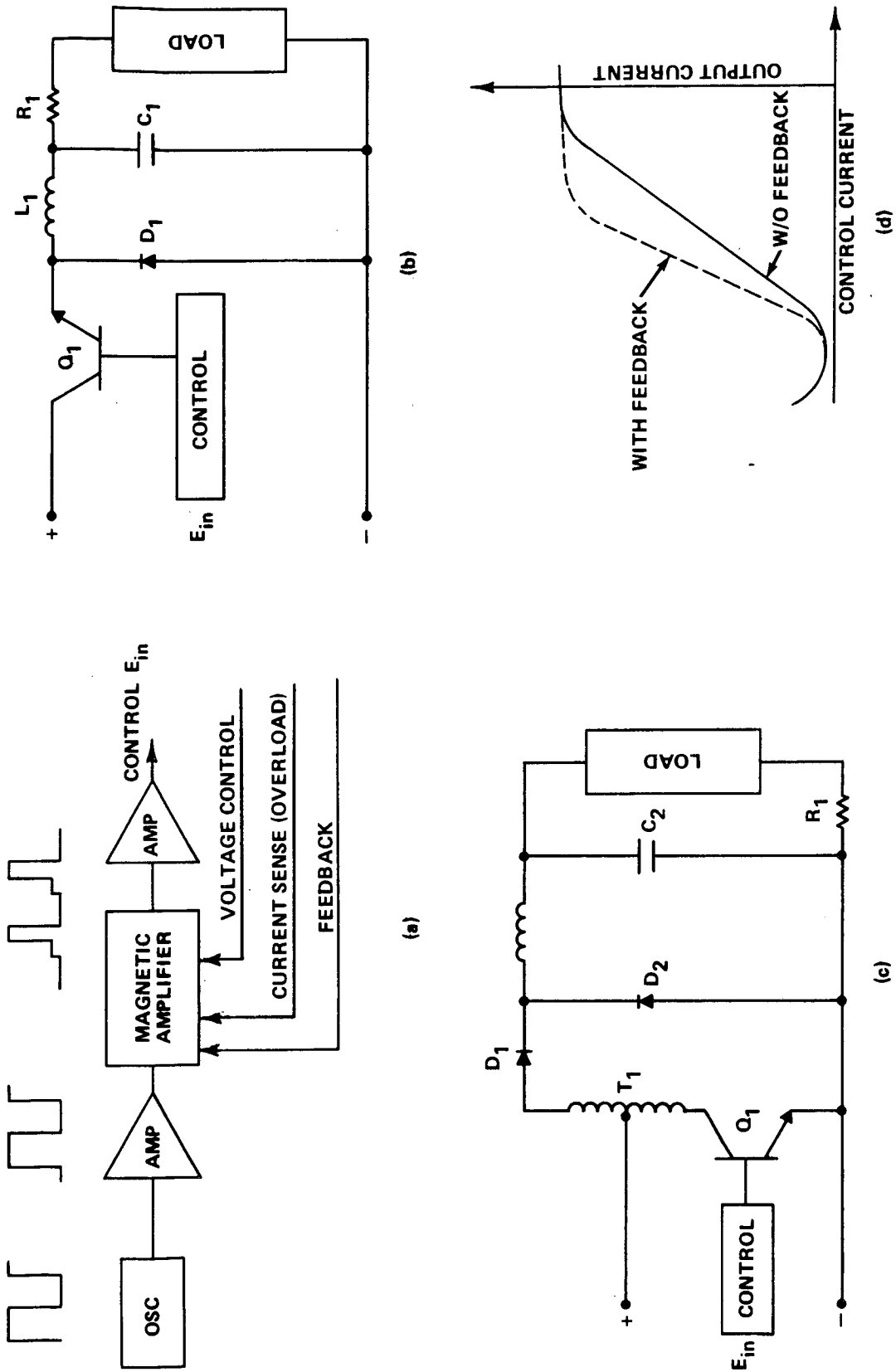


Figure F-57. Magnetic amplifier coupled regulators.

diodes, and filter capacitor are redundant and individually fused so that failures are self-clearing. A prime requirement is that the regulator must be capable of parallel operation and have the ability to load share and maintain output voltage regulation.

The regulator has a power capability of 400 watts continuous and 450 watts under peak conditions. In normal operation, the regulator will have a current capability of 14.3 amperes at 28 volts. At 16.2 amperes, the regulator will start current limiting to zero voltage at short circuit as illustrated in Figure VIII-23. This feature inherently protects the primary source.

Power division between the regulators is accomplished by a combination of voltage sensors and current limiting. Each regulator has a current-limiting sensor to limit its maximum power output capability or its share of full load power. The regulators are connected to a tapped resistor across the output for voltage sense. The regulator connected to the highest point supplies load power. As load power is applied, the output voltage will decrease until the cut-in point of the second regulator is reached. At this point, both regulators will share the load without either operating in a current limiting mode. The slope of the voltage drop, cut-in point will decrease at a rate of 0.03 volt per ampere of output load current. In this arrangement, the voltage regulators operate more efficiently. Another mode of operation is to connect the regulators to the same voltage sense points in the ECAs. In this configuration, paralleled regulators share equal amounts of the output power. The regulators are connected to the power buses in such a manner that, upon command, any regulator can be connected to either of the redundant output buses.

Figure VIII-23 illustrates the output characteristics of the regulator. More precise voltage regulation is easy to obtain; however, some slope to the output voltage characteristic is desirable for easier load sharing. For normal operation, only two of the four regulators will be on. Under peak power demands, all regulators will be on. The regulators are rated so that two units will satisfy the system requirements. Operational mode switching is accomplished in the ECA. Command override provisions have been made for automatically operated protective devices.

The output of the voltage regulator varies from 28 to 27.5 volts as illustrated in Figure VIII-23(a).

When the full load is achieved on regulator 1, the redundant unit is automatically placed on line and both units share the load without current-limiting. If the output of either regulator is shorted or both regulators are overloaded they will current limit according to the curves as shown.

The efficiency of the regulator is very good, but a higher efficiency could be achieved if the input to the regulator was for a more limited voltage range. The efficiency of the regulator is approximately 90 percent at full load as shown by Figure F-58(a). The characteristic is typical of electrical power equipment; at low load, the efficiency decreases because control losses are relatively constant. The efficiency is shown as a function of input voltage in Figure F-58(b). It is almost constant for the higher input voltages. The semiconductor drops cause the decrease at the lower end. As indicated by both curves, the control power and coupling transformer losses remain approximately the same for all conditions of regulator operation. The input voltage ranges of 22 to 29 and 38 to 80 volts are not difficult to handle with semiconductors or transformers; however, increased transformer losses are incurred. System voltage requirements over 100 volts decrease reliability and impose cost penalties on semiconductors and capacitors.

The reliability and efficiency of the baseline regulators are adequate. Isolation and simplicity of operation are achieved. The ratings and characteristics were summarized in Chapter VIII.

Cabling Studies

1. Cable Optimization for HEAO-C Baseline. The formula for optimizing cable weights with power loss for a given system is developed later in this appendix. This is a good preliminary design approximation; however, the cable sizing must also be evaluated against voltage regulation limits, temperature rise variations, current carry specifications, and network arrangements that influence cable selections. Knowing the typical design and performance parameters for a given type of system, such as the solar array-battery for HEAO and the load requirements, the current density for transmission and distribution cables which obtains a minimum system weight can be determined from the following:

$$\text{Optimum current density} = \frac{I}{A} = \left(\frac{\sigma}{r} \times \frac{\Delta P_s}{\Delta W_t} \right)^{\frac{1}{2}}$$

where

I = Load current in amperes.

A = Transmission or distribution cable conductor cross-sectional area (in.²).

r = Resistivity of the conductors [ohm-(in.)²/in.].

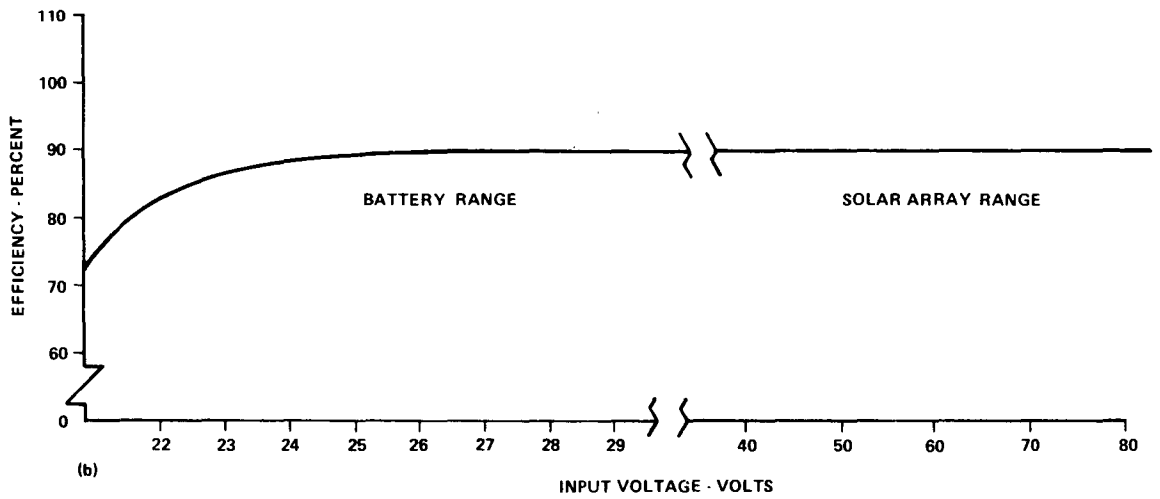
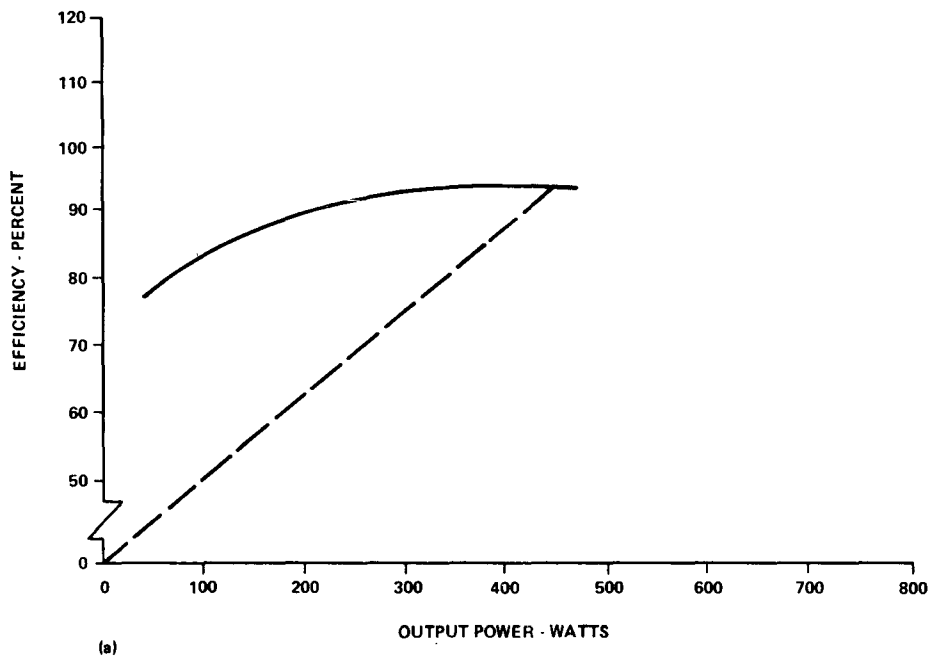


Figure F-58. Baseline regulator efficiency characteristics.

σ = Specific weight of cable in pounds per cubic inch of conductor.

$\left(\frac{\Delta P_s}{\Delta W_t}\right)$ = The source (solar array) power increase gained by an increase in system weight (watts/lb).

The solution of the equation is much easier, but less accurate, if handbook values of resistivity of copper (0.68×10^{-6} ohm-in.²/in.) and of the specific weight of copper (0.32 lb/in.³) are used only. These parameters can be obtained from MSFC or MIL specifications to include the effects of stranded conductors, temperature, and insulation used for aerospace wire and cables. This complicates the solution because insulation type and dimensions heavily influence weight, volume, and area, and these vary with conductor size and rating.

The resistivity and specific weights were calculated for conductor sizes AWG-26 to AWG-10 using MSFC SPEC 40M39513A data for Type C6 Class N wire. The resistivity was essentially constant at an average of 0.75×10^{-6} ohm-in.²/in. The specific weight, however, decreases as the conductor size increases as shown in Figure F-59. Note the specific weight is per conductor volume, not total volume. Since various size cables can be expected in a transmission network, the specific AWG-16 weight was selected a nominal value for determining the optimum current density.

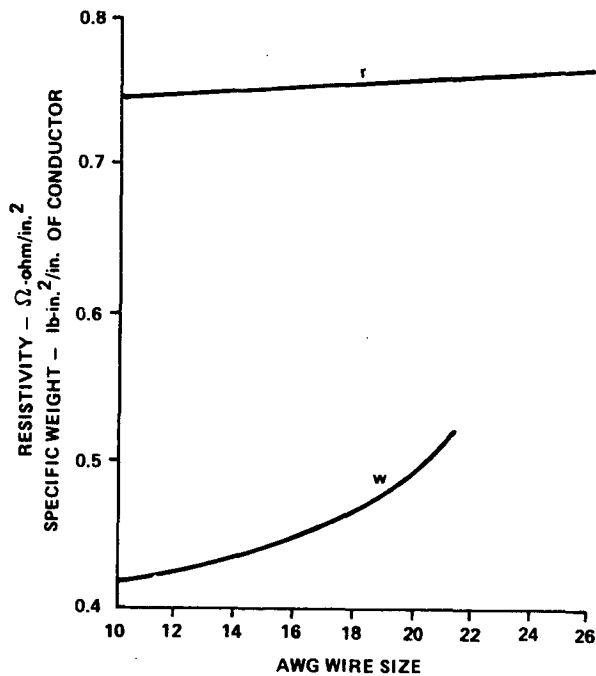


Figure F-59. Characteristics of stranded-insulated wire.

Using specific HEAO design data, the power-to-weight ratio was obtained for the solar array. The array consists of six wing panels and two body panels having a total weight of about 270 pounds. The array produces 1618 watts at EOM under the high temperature and 15 degree orientation design conditions. Assuming linear change in power with respect to weight, the power divided by array weight gives $\left(\frac{\Delta P_s}{\Delta W_t}\right) = 6 \text{ watts/lb.}$

The optimum operating current density is then computed:

$$\text{Optimum } \frac{I}{A} = \left(\frac{0.447 \times 6.0}{0.75 \times 10^{-6}}\right)^{\frac{1}{2}} = 1890 \text{ amps/in.}^2$$

Multiplying the above value by the cross-sectional area of several conductor sizes gives the optimum current for that size wire if used in the HEAO transmission subsystem. The optimum current and other wire characteristics are tabulated for several wire sizes in Table F-9.

TABLE F-9. WIRE CHARACTERISTICS AND OPTIMUM CURRENT, TYPE C6, CLASS N

AWG Size	Cond. Area (cir. mils)	Insulated Diameter (mils)	Ohms ^a per 1000 ft	Pounds per 1000 ft	Optimum Current (amps)	Volt Drop (mV/ft)
24	475	25	25.1	2.65	0.70	17.6
22	754	32	15.5	3.82	1.14	17.70
20	1216	40	9.79	5.58	1.79	17.50
16	2426	58	4.76	10.82	3.60	17.15
12	6088	91	1.88	24.80	9.03	16.98

a. R at 20° C.

$$R_t = R_{20} [1 + 0.00385 (t - 20)]$$

It may be noted that the optimization equation gives current densities that would produce about the same voltage drop for the various wire sizes. Also, for the specific optimum currents listed, all are within the current carrying rating of the sizes shown except that size AWG-24 is close to its maximum rating.

Referring to Figure F-60, the simplified diagram showing half of the transmission subsystem, Table F-9 values may be used to determine optimum cable sizes for the HEAO EPS. The cables between the solar array and the solar power distributor, represented by R_1 , must have at least twice as many conductors as the number of solar assemblies on half of the array (one positive and one negative). Since the conductor must handle the current of one cell assembly, it must carry a nominal 0.74 ampere at EOM and a short circuit current of 0.85 ampere at BOL. The conductor size that has an optimum current larger than 0.74 is AWG-22. Therefore, AWG-22 size conductors should be selected for the solar array cables if the voltage drop and power loss requirements of the system are satisfied. This will be assessed later.

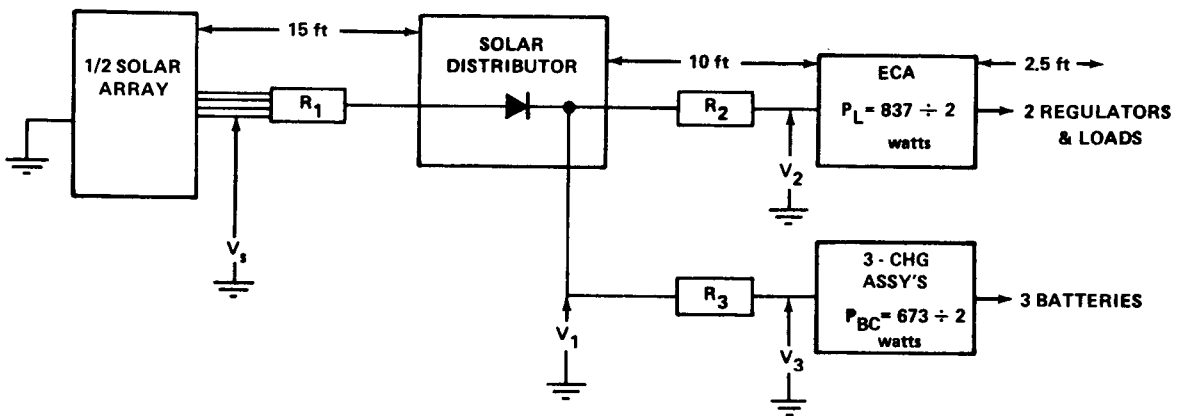


Figure F-60. Simplified transmission cable diagram.

The cables between the solar distributor and the ECA, represented by R_2 (Fig. F-60) need only two conductors, therefore, neglecting redundancy. It will be shown later that the current required by each ECA is 11.54 amperes. This would require a conductor size larger than shown by Table F-9. For cable flexibility and redundancy reasons, two size AWG-12s per leg (4 conductors per cable) were selected.

The battery charger load shown is separated into three parts, giving a current of 3.07 amperes each. Size AWG-16 conductors should satisfy the battery cable requirements.

Having selected conductor sizes, the voltage drops and power losses must be assessed to assure they meet the system design requirements. Again, Figure F-60 is used for this assessment.

Lumped resistances, R_1 , R_2 , and R_3 , represent the cable resistances of three major sections of the transmission network. The distances shown between assemblies are approximate, typical cable runs that were determined by scaling the HEAO-C equipment layout drawings. The source voltage is V_s at the solar array, and the output voltages (inputs to ECA and chargers) are shown as V_2 and V_3 . The loads shown were determined from the EPS analysis. The blocking diodes within the solar distributor have been assigned a voltage drop of $v_d = 0.8$ volt.

Of the output voltages, V_3 has the most critical limit (minimum) because stepdown conversion is desired in the chargers. A minimum V_3 of 36.5 volts then determines the voltage regulation needed for a given solar array output. Transmission requirements will be assessed for worst design limit cases of minimum V_s of 38.5 volts and maximum current values. Using minimum, V_s and V_3 , the maximum cable voltage drop permissible may be determined:

$$V_{\text{loss}} = (V_s - V_d) - V_3 \text{ volts}$$

or

$$V_{\text{loss}} = I_1 R_1 + I_3 R_3 = 1.2 \text{ volts} \quad .$$

The voltage drop, V_3 , for the battery charger cables can be determined by:

$$V_3 = \left(\frac{2r_3 \cdot l_3 \cdot P_{bc}}{V_3} \right) \text{ volts}$$

where

r_3 = Conductor resistance (ohms/1000 ft).

l_3 = Length of battery charger cables (ft).

P_{bc} = Power required by charger (kW).

V_3 = Minimum voltage permissible for battery charger (volts).

Substituting values from Table F-9 and Figure F-59,

$$V_3 = \frac{2(4.76)(10)[(0.673 \div 2) \times 3]}{36.5} \text{ volts}$$

$$V_3 = 0.292 \text{ volts (drop) .}$$

Total $I_3 = 0.22$ amperes. The voltage output at the diodes would then be:

$$V_1 = V_3 + v_3 = 36.79 \text{ volts .}$$

The current, I_2 , to the PCUs is then found from:

$$V_1 = I_2 R_2 + V_2 = I_2 R_2 + \left(\frac{P_2}{I_2} \right)$$

$$I_2 = \frac{V_1 \pm \left(V_1^2 - 4R_2 P_2 \right)^{\frac{1}{2}}}{2R_2}$$

and for 2 No. AWG-12s, $R_2 = \frac{(1.88 \div 2) 10}{500} = 0.0188 \text{ ohm}$

$$I_2 = 11.3 \text{ amps}$$

$$V_2 = 36.58 \text{ volts}$$

and the drops,

$$v_2 = 0.213 \text{ volts}$$

Then,

$$I_1 = I_2 + I_3 = 20.52 \text{ amperes .}$$

For the baseline array, one solar distributor services 33 equivalent solar cell assemblies (4 panels). Therefore, the resistance, R_1 , consists of 33 AWG-22 circuits in parallel. Thus,

$$R_1 = \frac{(2 \times 15)(15.5 \div 1000)}{33} = 0.0141 \text{ ohm .}$$

The voltage drop across the solar array cables, R_1 , is then

$$V_1 = 20.52 \times 0.0141 = 0.289 \text{ volt} .$$

Adding the voltage drops, V_1 , V_d , and V_3 , to the charger input voltage, $V_3 = 36.5$ volts, gives:

$$V_s = 36.5 + 0.292 + 0.8 + 0.289$$

$$V_s = 37.87 \text{ volts}$$

which is less than the 38.5 volt minimum provided by the array design. Therefore, the voltage-drop requirements have been satisfied and the cable conductors have been selected that provide very near optimum weight for the given EPS.

Based on the foregoing technique, design parameters for the various power transmission cables are summarized for the baseline EPS in Table F-10.

TABLE F-10. PRIMARY TRANSMISSION CABLE SUMMARY
WITHOUT REDUNDANCY

Cable Designation	Quantity	Conductors		Line Drop (volts)	Power Loss (watts)	Approx. Weight (lb)
		AWG Size	No. Per Cable			
Array/Solar Distr.	8	22	29	0.289	11.9	15.5
Distr./Bat. Chg.	6	16	2	0.292	5.3	1.3
Distr./ECA	2	12	4	0.213	4.8	2.0
ECA/Regulator	4	12	4	0.053	1.2	1.0
Total Cables	20			0.48/ 0.55	23.2	19.8
Diodes	66			0.78	32.1	1.4
Total Transmission				1.26/ 1.33	55.3	21.2

2. Distribution Cable Estimates. The same procedure as shown for transmission cabling can be applied to the selection of distribution cabling. Different specific values, however, are called for because the weight penalties incurred by providing power conditioning and batteries to sustain dark-period operation reduce the watts per pound ratio of the power source. Considering only the HEAO equipment for power generation will give a specific power source rating of about 1.5 watts per pound. Also, a smaller size conductor, AWG-20, should be considered as a nominal size for determining the specific conductor weights. Inserting these values into the equation for optimum current density gives:

$$I/A = \left(\frac{0.486 \times 1.5}{0.75 \times 10^{-6}} \right)^{\frac{1}{2}} = 1974 \text{ amps/in.}^2$$

This current density can then be used as a guide for initial selection of conductor sizes for the various segments of the distribution network.

Cabling used for HEAO shall conform to the MSFC-SPEC-40M39513 for wire and shall have a minimum rating of 250 volts. In general, 600-volt insulation should be used for external cabling because better reliability is afforded by the higher abrasive resistance and ruggedness. Cable jackets should be used in location where wire may be subject to abuse. Should detailed design indicate that some cables require shielding, these cables shall conform to MSFC-SPEC-40M39582.

Insulation materials shall be rated for at least 200° C. Such materials shall also conform to the outgassing requirements established by MSFC-SPEC-50M02442.

In general, miniature, circular connectors in accordance with MSFC-SPEC-39569 shall be used. Should cases arise where other types or shapes of connectors are required, these should meet equivalent performance and qualification status requirements.

3. Derivation of Cable Optimization Equation. Given an electrical system (Fig. F-61) that is composed of a power source (power generation, ancillary devices, housing structure and mounting) and electrical distribution or transmission cabling delivering power to the loads, determine the optimum distribution rating and weight.

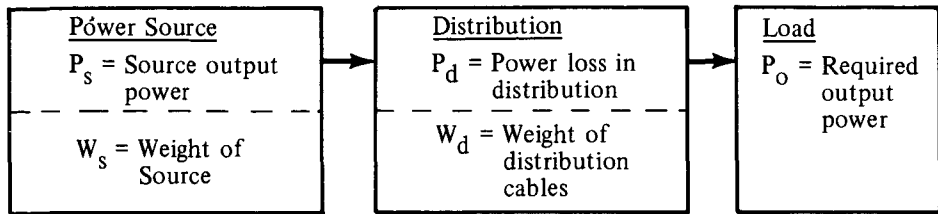


Figure F-61. Electrical system cabling model.

The power demand on the EPS is P_o , prescribed by vehicle load requirements. It is assumed that P_o has been accurately determined as a minimum nominal rating and that it remains a fixed requirement. Since losses are incurred by distribution, the power source must be sized to furnish both the load power and the distribution losses; i. e. ,

$$P_s = P_o + P_d \quad (4)$$

where

P_s = Power source output power (watts).

P_o = EP output power to the loads (watts).

P_d = Power loss in distribution (watts).

The system weight required to furnish P_o is the sum of the source and distribution weights,

$$W_t = W_s + W_d \quad (5)$$

where

W_t = Total system weight (lb).

W_s = Power source weight (lb).

W_d = Distribution system weight (lb).

The figure of merit or power-to-weight ratio, M , of the system is defined by equation (6):

$$M = \frac{P_o}{W_t} = \frac{P_s - P_d}{W_s + W_d} \quad (6)$$

Since finite, positive weights are required to generate and to deliver power, optimum performance is obtained when M is a maximum. Since P_o is constant, this occurs when the combined weights, $W_s + W_d$, are at a minimum. Therefore, differentiating M with respect to weight and setting the result equal to zero will define the point of optimum performance. Rearranging equation (6) and differentiating gives:

$$\frac{d}{dW_t} (M) = \frac{d}{dW} \left(\frac{P_o}{W_s + W_d} \right)$$

where $P_o = \text{constant} > 0$.

Setting equal to zero for maximum

$$\frac{d(M)}{dW_t} = \frac{P_o (dW_s + dW_d) - 0}{(W_s + W_d)^2} = 0 \quad (7)$$

$$dW_s + dW_d = 0$$

and

$$dW_s = -dW_d \quad .$$

Thus, the optimum performance is obtained when the change in distribution weight is equal and opposite to the change in power source weight. Note that a change in power loss was defined as the same change in power source output for this problem and, therefore, the general expression for optimum power/weight performance in terms of significant variations (Δ 's) is:

$$\frac{\Delta P_s}{\Delta W_s} = - \frac{\Delta P_d}{\Delta W_d} \quad (8)$$

To determine useable functions for equation (8), assume the primary variation in distribution weight pertains to selection of wire and cable sizes and that distribution gear, boxes, and installation weight are essentially determined by the output circuitry requirements and are relatively constant in the range of P_o to be investigated. For this case, this weight is fixed and is not part of the tradeoff. However, it could be accounted for if distribution equipment ratings and weights are related to power, losses, and system changes.

Connector losses and voltage drops are normally very small and are neglected. This neglect is further compensated for by the fact that percentage drops are usually specified to be the same for the various connector pin ratings. Other factors affecting optimization are: (1) regulation (voltage drop) which must be investigated for conformance to system standards established, (2) voltage rating which affects the size of switchgear and insulation, and (3) the redundancy philosophy.

Only cabling parameters have been considered in this derivation. The power loss in distribution in terms of cable parameters and weights is next determined on a single conductor basis.

The power loss in a conductor for a given load current is:

$$P_d = I_o^2 R \text{ watts,} \quad (9)$$

where

I_o = Load current (amperes)

R = Conductor resistance (ohms).

The conductor resistance may be expressed as,

$$R = r \frac{L}{A} \text{ ohms,} \quad (10)$$

where

r = Resistivity of the conductor (ohm-in.²/in. or ohm-cm²/cm).

L = Length of conductor (in. or cm).

A = Cross-sectional area of conductor (in.² or cm²).

For an initial condition of R_1 , the initial power loss is then defined as follows:

$$P_{d1} = I^2 R_1 = \frac{r L I^2}{A} \quad (11)$$

Increasing the conductor area increases weight, but decreases power loss. For a ΔA increase, the resultant power loss is

$$P_{d2} = \frac{I^2 r L}{A + \Delta A} \quad (12)$$

and the change in power loss is then,

$$\Delta P_d = P_{d2} - P_{d1} = r L I^2 \left(\frac{1}{A + \Delta A} - \frac{1}{A} \right)$$

$$\Delta P_d = - \frac{I^2 r L \Delta A}{A(A + \Delta A)} \quad (13)$$

The distribution weight may be defined as:

$$W_d = \sigma L A \text{ lb} , \quad (14)$$

where

σ = Specific weight of wire (lb/in.³ or lb/cm³).

L = Length (in. or cm).

A = Cross-sectional area (in.² or cm²).

For an area change of ΔA , the change in weight is given by

$$\Delta W_t_d = \sigma L \Delta A \quad (15)$$

The power loss as a function of distribution weight is then given by combining equations (13) and (15),

$$- \frac{\Delta P_d}{\Delta W_d} = \frac{r I^2}{\sigma A(A + \Delta A)} \quad (16)$$

The next step is to determine, for each candidate power source to be investigated, the power to weight ratio typical for the power level being investigated; i. e. , divide the source power by its weight. Assuming that the power rating changes linearly with weight in the range of interest, the source deltas can be determined by equation (17):

$$\frac{\Delta P_s}{\Delta W_s} = \frac{P_s}{W_s} \quad (17)$$

where ΔW_s is the change in power source weight (lb) required to effect a given change in generated power, ΔP_s (watts).

Specific solutions are obtainable for each candidate power source by equating equations (16) and (17) in accordance with equation (8) as follows:

$$\frac{\Delta P_s}{\Delta W_s} = \frac{r I^2}{\sigma A(A + \Delta A)} \quad (18)$$

In the limit, as ΔA approaches 0, the optimum operation required is determined; i. e. ,

$$\text{Optimum } I/A = \left(\frac{\sigma}{r} \cdot \frac{\Delta P_s}{\Delta W_s} \right)^{\frac{1}{2}} \text{ (amps/in.}^2 \text{ or amps/cm}^2 \text{)} \quad (19)$$

Equation (16) gives the optimum operating current density. Therefore, the system is weight optimized when distribution conductor sizes are selected for the computed current density. It is again noted (from previous distribution consideration) that the solution gives the theoretical optimum and does not necessarily conform to voltage regulation requirements. Such requirements tend to penalize the system weight.

Preliminary Specification for HEAO Electrical System

1. General System Requirements

a. **Function.** The HEAO electrical system shall provide the power generation, conditioning, control, and distribution support for the HEAO payload, spacecraft systems, and the orbit adjust stage. The integral spacecraft

power systems shall provide power from prelaunch operations, "switch to internal power, "through the 2 year lifetime of the spacecraft. Provisions shall be made for ground-supplied power before this time. The power system shall be so designed that there will be no single-point failure that would result in loss of the spacecraft/module or loss of the primary mission objective.

b. **Reliable Features.** The electrical system shall incorporate reliable features or devices for (1) protection against internal and external overloads and faults, (2) overvoltage and undervoltage protection, (3) reverse current protection, and (4) fault isolation. The design shall be based on conservative derating factors for component parts, especially for power semi-conductors, switching and fault isolation devices, and capacitors. In general, such devices should be operated between 30 and 50 percent of their nominal power and voltage ratings.

c. **Power Characteristics.** The power system shall be designed to minimize power requirements. The output steady-state voltage shall be 28 ± 2 percent Vdc at power supply. This voltage shall not go below or above the steady-state voltage more than 3 volts and return to steady-state voltage within 100 milliseconds. The total ac component of bus-noise voltage shall not exceed 1.0 volt peak-to-peak for all frequencies from 20 Hz to 20 kHz. Transient voltage shall not exceed ± 50 volts with a pulse width not greater than 10 microseconds.

d. **Spacecraft System Grounding**

(1) **General.** Grounding of all electrical/electronic circuitry shall be accomplished in a controlled manner so as to provide adequate voltage references while preventing ground currents from flowing and interacting with other circuits. To achieve this, a single-path-to-ground (structure), i. e., only one path from any point in a circuit to ground, shall be utilized throughout the entire system to the maximum extent practicable.

The static case ground shall be brought out through an individual connector pin or terminal and shall be connected to the module structure, per bonding specification MIL-B-5087B.

(2) **Single-Point-Ground (SPG).** All power sources, with common returns, shall be grounded at one point only at any given time. The lead length from main power bus to SPG shall be capable of carrying any fault current which may occur. The SPG shall not be used intentionally as a normal circuit-current-carrying path.

(3) Vehicle Ground Point (VGP). Secondary power supplies (dc-to-dc converters or transformer isolated supplies) may be used to isolate circuitry from the main power bus. Where secondary power supplies are used, the following requirements shall apply:

- Secondary power supplies which connect directly to circuitry in two or more subsystems, components, or enclosures shall be grounded to structure through a VGP with a resistive value not exceeding 10 000 ohms.

- A secondary power supply connected directly to circuitry which is contained completely within a single enclosure may be isolated from structure.

- Secondary power supplies shall have 1 megohm isolation between the primary and secondary circuitry before external electrical connection. Several secondary power supplies may use the same VGP or different VGPs.

- The dc resistance between VGPs as well as between VGPs and each SPG shall be kept to a minimum value through the use of continuous metal or the use of joints in accordance with MIL-B-5087B.

(4) Load Isolation. Each load which is connected to the main power bus shall have a minimum dc resistance of 50 megohms at 50 volts between power input leads and unit case before external electrical connection.

(5) Control and Signal Circuit Grounding. Control and signal circuitry shall be isolated 50 megohms or greater at 50 Vdc from chassis, rack and structure except for a single dc patch to ground in accordance with Paragraph c. above. Radio frequency grounding or bypassing of circuit returns may be necessary to achieve a low reference potential for circuits with pulses having rise and fall times shorter than 10 microseconds.

(6) Circuit Shield Grounding. The method of grounding of circuit ground shields shall depend on the intended usage, such as RF as given below.

(7) RF Circuit Shielding. The RF circuit shielding is repetitive pulses and CW above 50 kHz or pulses with rise and fall times less than 10 microseconds, but not including television signals or CW and pulsed CW above 5 MHz. Shields on all wire segments (coaxial or other) carrying RF or

connected to circuits susceptible to RF shall be as a minimum requirement, RF grounded (capacitor bypassed) at both ends and along the length of shield as practical. The only ground connection which shall be dc (directly) grounded is at one end of the shield. All shield grounds shall be attached to the basic structure or internal to their respective chassis, but they shall not cause the power bus dc single-patch-to-ground to be violated.

When bonding straps are used to meet the EMI requirements, wire shields shall be carried through the connector of the using equipment and grounded to the inside of the case as close to the connector as possible. The length from connector to ground shall not be greater than 2 inches internally. All other shielded wires shall have their shields grounded at one end only. If the shield is designed to exclude signals, it shall be grounded at the receiving end. If the shield is designed to retain a signal, it shall be grounded at the source end. If triaxial cable is used, ground one shield at one end and the other shield at the other end.

e. Interference Control. The negative return shall be isolated from the chassis ground, and shall be brought out through individual connector pins, except that signal returns which are unsusceptible to EMI may share a common return. The physical distance between circuit supply and return should be minimized and, wherever possible, they should be twisted pair wires. The spacecraft hardware shall be designed to avoid permanent and residual magnetic fields wherever possible. The interference levels and design shall comply with either MIL-I-6181D or MIL-STD-461A.

f. Corona Supression. Electrical and electronic systems and components of spacecraft hardware shall be designed so that proper functioning will not be impaired by corona discharge and shall not be a source of interference which adversely affects the operation of other equipment under any of the required operating conditions.

Where adverse corona effects are avoided by pressurizing or evacuating a component, the seals used shall be capable of maintaining the required internal pressure throughout the useful life of the hardware. When adverse corona effects are avoided in unsealed components by restricting operation to space-vacuum conditions, the ability of the equipment to reach the required vacuum in the planned time shall be demonstrated.

g. Interface Connectors. All electrical connectors used on spacecraft interface shall be configured to prevent being connected to accessible connectors other than the one intended.

(1) Pin Assignment and Pin or Socket Selection. Redundant paths provided to comply with reliability requirements shall be routed through separate connectors.

Where practical, positive and negative electrical circuits shall not be routed through adjacent pins of a connector if a short circuit between them would constitute a loss of spacecraft hardware.

(2) Connector Use. Cable connections of spacecraft hardware shall be designed so that pin and socket connectors are properly used to prevent power from shorting to ground. They also shall be designed to protect personnel both when connected and disconnected.

h. Protection of Electrical Circuits and Electronic Devices

(1) Overload Protection. The positive dc input line from the spacecraft to the experiment hardware shall have overload protection. Experiments-supplied redundant power sources shall have each source individually protected with either a fuse or circuit breaker.

(2) Electronic Devices. Electronic devices used in spacecraft hardware shall incorporate protection against reverse polarity overloads of other improper electrical inputs during qualification, acceptance, and other tests, if such inputs could damage the devices in a way that would not be immediately and unmistakably apparent. If it is impractical to incorporate adequate protection as a part of the device, protection shall be provided externally by groundbase equipment at the interface between the device and the ground test equipment.

(3) Moisture Protection. Electrical connectors, wiring junctions, and all electrical and electronic devices used shall be environmentally sealed or otherwise positively protected against moisture.

(4) External Wire Bundle and Harness Protection. All wire bundles, harnesses, and cables external of the spacecraft black boxes shall conform to MSFC Drawing 40M39582. Routing and installation of all wire bundles, harnesses, and cables shall be specified on the drawings. Special precautions shall be taken to prevent damage as a result of extreme temperature conditions, chafing, or any other conditions that may result in damage.

(5) Debris Protection. Flight hardware shall be designed so that malfunctions or inadvertent operation cannot be caused by exposure to conducting or nonconducting debris or foreign materials floating in a gravity free state.

Electrical circuitry, including buses, shall be designed and fabricated to prevent unwanted current paths being produced by such debris.

Critical electrical items shall be provided with suitable containers, potting, or epoxy coating.

2. Electrical Power Subsystem Requirements. The function of the electrical power generation subsystem is to convert solar energy to electrical energy, store energy for use when solar energy is not available, and supply conditioned electrical power to the electrical distribution and load control networks. The EPS shall meet the following requirements:

- The electrical power subsystem shall consist of a solar cell array, batteries, battery chargers, voltage regulators, controls, instrumentation, and networks required to provide the HEAO mission power requirement. This system will be an integral spacecraft system and will be mounted to the basic spacecraft structure.

- The solar cell array shall rely upon spacecraft attitude control for orientation. Subsystem commands will be processed by the HEAO command system and monitored data processed by the telemetry system. The subsystem must be mechanically, electrically, and thermally integrated into the spacecraft to optimize overall spacecraft life and performance. Wherever practical, the subsystem design shall utilize materials, parts, and associated processes that have been proven on other space projects, giving due consideration to the present state-of-the-art, cost schedules, and test and reliability requirements.

- The systems, subsystems, and component parts designed and manufactured under this specification shall conform to accepted standards of spacecraft design and shall be constructed and finished in a manner indicative of good workmanship. Particular attention shall be given to neatness, cleanliness, and thoroughness of all processes and operations involving assembly and finishing of all items.

- The electrical power subsystem must supply full payload and energy storage power for all mission modes during the mission life. Mission modes identified include prelaunch test and checkout, launch and orbit acquisition through array deployment, nominal mission orbital operation, and nonsolar-oriented special operations. The system will be capable of supplying an orbital average electrical power requirement of 722 watts at the end of the mission, provide sufficient energy to recharge the batteries to full capacity after an orbital eclipse discharge, and be initially designed to include a 20 percent power capability growth factor. In addition to this average power requirement, the system shall have capability to supply the mission timeline and peak power requirements.

- The subsystem shall be capable of operation during selected degraded orbits. The subsystem shall be designed to supply the above-specified load power requirements with inclinations of the solar cell array of up to 30 degrees from normal sunlight incidence. In addition, the subsystem will be capable of sustaining a maximum number of limited duration (540 minutes for worst case) experiment pointing operations, resulting in spacecraft Z-axis excursion beyond 30 degrees from the sunline, and meet the end-of-life requirements.

a. Solar Cell Array Subsystem

(1) Baseline Definition. The solar cell array system collects sunlight incident on the array, converts a portion of the energy to electricity, and dissipates the remainder as heat. The electrical power generated in the array is concentrated and transferred by electrical networks to load regulating and energy storage subsystems.

The HEAO solar array shall consist of foldout sections which are to be deployed following the launch phase of the mission. The configuration shall be compatible with that of the spacecraft. In a stowed condition, the array shall not violate the launch envelope constraints set forth for the spacecraft atop the launch vehicle.

In a stowed condition, the solar cell side of the panels shall face outward from the spacecraft.

The solar cell array shall be electrically divided into separate power sources such that loss of any one source will still permit successful mission operation. The array will have no single-point failure capable of degrading output power below that required for a successful mission. Redundant wiring and connectors will be provided throughout.

Cell assemblies shall be electrically connected in series and parallel combinations with redundant electrical interconnectors. High redundancy is desired in the design, and the specific design shall be of an accepted and space-flight-proven character. The series-parallel cell arrangement and cell interconnection techniques shall require approval of the government before incorporation. The number of solar cells in series should be such that minimum and maximum voltage for efficient operation of the battery chargers and voltage regulators are not exceeded, and to minimize the effects of potential solar cell reverse biasing and heating. The number of solar cells in parallel in a string assembly shall be limited to the equivalent of three 2 by 4 cm cells in parallel. The number of series cells shall not exceed 125.

Materials used in the array systems shall not liberate corrosive gases or fumes, nor shall they liberate fumes which would be detrimental to the performance of the solar array system or the health of any person nearby, nor shall they liberate any substance which may redeposit on any neighboring surfaces. Adhesives shall be selected in accordance with MSFC Drawing 50M02442.

The solar cell array system must be capable of surviving without damage from the environment, test conditions, and operating modes anticipated from manufacture through end of mission. In addition, the solar cell array subassemblies shall have a shelf life sufficient to ensure successful operation in the event of a schedule slippage.

As determined by electrical power subsystem studies, additional features shall be incorporated to enable "Dark I-V" testing (without exposing solar cell to sunlight) of the solar array and to provide for power inputs from electrical system.

NOTE: If a design is used in switching solar panels in or out of the power system, or if possibly some shadow might fall across the solar panels such as that from an antenna, special attention should be given to screening individual solar cells to prevent back emf which would cause an avalanche condition.

(2) Performance. The baseline solar array subsystem shall be established in accordance with the following requirements: (1) Deliver at the end-of-mission the array power, and simultaneously, (2) resupply the batteries with energy for the conditions specified in the following paragraphs.

NOTE: Subsystem losses and inefficiencies shall be subtracted from the contingency allowance.

The end-of-mission power rating of the array shall be based on the following conditions:

- Two-year mission with allowance for degradation.
- Distance to the sun of 1 AU.
- Orbital sunlight period of 59.1 minutes.
- Periods of off-sun pointing of 30 degrees from axis normal to array.
- Design temperature specified is approximately 93° C.

(3) Configuration. The baseline solar array subsystem shall typically consist of panels of solar cells, cabling and connections, temperature and deployment sensors, diodes and isolation, and the provisions for array stowage, release, and deployment. Unique requirements of the array configuration and elements are defined in tradeoff studies.

Each panel of the solar array shall consist of modules which are electrically and physically separable.

(4) Array Stowage, Release, and Deployment. Dependable materials and simple, easily aligned hinges shall be used. Hinge and alignment tolerances shall be such that no panel distortion is incurred and that freezing or sticking will not hinder deployment.

Simple deployment devices, such as springs, shall be used to extend the array sections. Positive stops and holding mechanisms shall be used to fix the array position after deployment. Panels shall be properly cushioned and securely constrained against the side of the spacecraft during the vehicle launch phase. The design shall assure that the panels will not be distorted and that the array will safely endure the shock, vibration, and acoustic environment specified for launch.

Proven, highly reliable release devices shall be used. These devices shall have redundancy features which will permit initiating release by at least two independent means. Redundant, independent channels and electrical devices shall be provided to release the solar array. The primary method of deployment shall be from onboard devices, such as timers and electrical interlocks. The backup method shall be by ground command.

(5) Solar Panels and Modules

(a) Definitions. A solar panel is defined as that structure and solar cell module group which stows and/or deploys as a rigid single unit of fixed geometry.

A solar cell module is defined as that series/parallel matrix of cells which produces the total array voltage and which is a portion of, or fit onto, the solar panel substructure.

(b) Substrates. Solar panel substrate shall be of low-mass construction such as aluminum honeycomb, consistent with the rigidity/cell support requirements under the various mission environments.

The panel size shall be optimized for the application considering module replacement, etc.

The surfaces of the substrate shall be properly conditioned for the application of paint and for cell-mounting material. The rear surface of the panels shall be painted with a stable paint having good thermal properties. The paint must resist degradation because of the space environment.

Cell assemblies, electrical terminals, and conductors shall be insulated from the substrate. The insulation shall be rated for a minimum 250 Vdc. The insulation resistance between electrical parts and the substrate shall be greater than 1000 megohms.

(c) Solar Cells and Coverslides. In addition to normal production and acceptance testing and inspection, the contractor shall verify, on a significant sample basis, cell characteristics pertinent to design and performance evaluation. Cells shall be of the type, date, and make to be used for HEAO. Examples of characteristics to be verified are temperature coefficients, leakage, covered and uncovered spectral response, transmission, cutoff, and thermal absorption and emissivity characteristics of covered cells.

Single crystal silicon solar cells of the N-on-P type shall be used. The minimum base resistivity shall be 2 ohm-cm. The nominal cell size shall be either 2 by 2, 2 by 4, or 2 by 6 cm. The cells shall have multiple grids and minimum effective area of 95 percent. High-quality, silver-titanium contacts which resist degradation and have good mechanical strength shall be used. All cells shall be tested at the same voltage (near expected maximum power point) and graded for output performance at $28^{\circ} \pm 2^{\circ} \text{C}$ using a solar simulator calibrated for AM-O light intensity and spectral distribution through the use of a JPL standard solar cell. The current shall be specified at a particular voltage near the maximum power point voltage to obtain the needed cells with the best performance to cost ratio within the limits hereof.

The average of delivered cells shall have an output equivalent to a standard efficiency of 10.6 percent or more. The minimum efficiency cell shall have an output not less than 9.8 percent.

Sufficient quantities of covered cells and submodules shall be tested for their performance at nominal and worst-case temperatures predicted for the solar array.

Cells shall be covered with good quality coverslides that are sized for the cell selected. The coverslides shall have a thickness of no less than 6 mils and shall have both an antireflective coating and a filter coating with a cutoff of 0.400 ± 0.015 micron.

(d) Cell Arrangement and Interconnections. Cell interconnections shall be carefully designed for the cell size, the material used, and compatibility with cell contacts. Potential stresses incurred by thermal cycling of the panels shall be duly considered and minimized. Interconnects shall have adequate stress relief features. Materials shall be selected to minimize work-hardening and to provide good conduction and bonding characteristics.

The interconnects shall provide a minimum of two attachments to each cell it services if 2 by 4 cm cells are used, and four attachments for each cell it services if 2 by 6 cm cells are used.

A cell assembly or group shall be a complete series string of cells or cell submodules (paralleled) which operate as a single electrical unit between isolated positive and negative terminals provided on the module. Redundant terminals for each cell group shall be provided on the HEAO solar modules.

Cell assemblies shall be fabricated and mounted on the substrate with a flat lay-down, non-overlapping technique.

(6) Solar Power Distribution. Each panel of the solar array shall be separately cabled. The cable shall accommodate the output conductors and temperature sensors. The number and size of cell assemblies per group will determine the number and size of power conductors per cable. The minimum number of conductors shall be limited by failure mode per reliability considerations on the number of cell assembly per groups that are interconnected without isolation, individual diode ratings, and cabling complexity. In all cases, conductors shall be appropriately sized for the current and low-voltage drop.

Provisions shall be made to effect the necessary interfaces between the solar array and the spacecraft EPS subsystems and for diodes, solar buses, protective and control devices, and checkout provisions for the array. Particular attention should be given to providing access for dark characteristics checkout between blocking diodes and the array panels.

Measurements. Provisions shall be made to monitor the solar cell array temperature and relay this information to the ground.

b. Battery Charging Subsystem

(1) Definition. Battery charging system shall consist of battery charging units capable of adequately recharging sealed nickel cadmium batteries to replace the energy used during the dark phase of each orbit. There shall be a separate charger for each battery. The charger shall include provisions for maximum utilization of solar array output power and for battery state of charge control and indication.

(2) Performance. Each battery controller shall be designed and sized to safely handle the peak and transient loads TBD that will be expected of a given battery. In addition, the protection and fault isolation equipment shall be designed to reliably function when subjected to conditions in excess of the above peaks to be specified.

The charger shall maintain full operating capability for all anticipated test and operational environments from assembly, qualification testing, prelaunch, and launch throughout the required mission.

Array power or GSE power only shall be used to energize the charger regulator and its control circuits. No battery power shall be used to energize any charger circuit excluding ampere-hour circuitry. During each orbital cycle, the charger shall be capable of feeding power to the external regulator or load bus and of charging the battery, provided sufficient array power is available. The power consumption of the charger shall be the minimum practicable for all natural combinations of operational and environmental conditions specified herein.

The charger shall be designed such that the generation of radio interference and the vulnerability of the system to radio interference shall be controlled to the maximum practical extent. Mutual interference between units of the system shall not prevent satisfactory operation of the system specified herein.

(3) Construction. The charger shall consist of a positive means of regulating charging power into the battery. The construction shall be fail safe in that any failure in any one modular regulator unit shall leave the charger operational. All requirements as specified herein apply to the composite regulator. A number of modules in excess of those required to provide maximum power shall be provided for redundancy. The quantity of redundant modules shall be determined by the vendor and shall be subjected to MSFC approval. For other required elements in the charger, modular construction may be utilized where performance and reliability are enhanced.

The dc power to the charger will be furnished from the output of a solar array.

(4) Charge Control. The charging shall ensure that the recharge fraction does not exceed 110 percent at 10° C. The charge control shall be spaceflight proven and shall be subject to government approval. Trickle charge shall not be used.

The charger shall cease charging the battery whenever the thermistors in the battery senses a 30° + 0° , -4° C battery temperature but a command override shall be provided. This tolerance shall include the thermistor tolerance. Stopping of charging shall not prevent the battery from feeding power to the external regulator through the charger when the charger regulator voltage drops because of insufficient array power.

Temperature sensing for charging control will be provided by thermistors in the battery. The charger shall contain all circuits associated with the thermistors. Voltage sensing for charging control shall be accomplished at the battery input terminals by means of duplicate sensing leads.

The duplicate thermistors and voltage-sensing leads shall be furnished to minimize the loss of voltage or temperature sensing of the battery. Loss of a single thermistor, or either or both of its leads, or loss of one negative or positive, or both a negative and a positive voltage sensing lead, shall not cause the charger to stop functioning properly.

Each battery charge controller shall be required to provide an individual battery assembly with the controls, protection, and accommodations specified as follows:

- Assure maximum charge voltage does not exceed the hydrogen evolution potential in any cell.
- Limit battery charging current to less than nominal "C" rate.
- Compensate the charge rate and voltage as a function of battery temperature and, as applicable, other battery sensors.
- Remove the battery from the bus if its temperature exceeds 30° + 0° , -4° C.

- Remove the battery from the bus if excessive charge rate occurs or if the average cell discharge voltage drops below 1.1 volts to avoid cell voltage reversal.

- Protect against reverse currents under such conditions as a cell short, etc.

- Provide controls for servicing redundant buses individually or together.

- Provide means of minimizing internal faults and positive protection/isolation of battery or internal faults from the power source and the output buses.

- Provide means for implementing subsystem checkout and remote control of batteries via the command system. Capability to override automatic controls shall also be provided.

(5) Measurements. The battery current and voltage, control status, temperature, and state of charge shall be measured and the necessary interfaces for telemetry monitoring provided.

c. Power Conditioning Subsystem

(1) General. The voltage regulating subsystem shall accept electrical energy from the electrical power subsystem power sources and transform it to the power quality specified for input to the power distribution system.

(2) Performance. Each voltage regulator shall provide a regulated steady-state voltage of 28 ± 2 percent volts to the power distribution system. The regulator shall be capable of accepting various input voltages as determined by the power source. The regulator shall maintain the specified tolerances as the load varies from no load to full load. The response time of the regulator shall be sufficient to hold the output voltage within the specified tolerance. The regulator output voltage ripple shall not exceed TBD voltage peak-to-peak.

Protective circuitry between each regulator shall be used. The minimum acceptable regulator efficiency shall be 88 percent as measured from input to output terminals. The regulator shall be capable of operating in an unregulated mode under low-input voltage conditions, and shall not sustain

damage as a result of this condition. In the event that the input voltage drops below the output voltage, no reverse current shall be permitted to flow to the regulator voltage source.

Regulator operation shall be fail-safe. The regulator shall accept externally supplied commands for control. The regulator under selected operating conditions shall be automatically disabled.

(3) Power Sharing. The regulators shall be controlled together in a manner such that each regulator furnishes an equal portion of the loads.

(4) Measurements. Selected signal indications of the operational status of the regulator shall be provided for power control and flight analysis.

d. Batteries

(1) General. The HEAO batteries shall normally store electrical energy during the sunlit portion of the orbit and discharge during the eclipsed portion of the orbit. However, capability shall be provided for other modes of operation such as launch and system startup, orbit transfer, and off-solar vector pointing. There shall be a minimum of four batteries. Sufficient power and capacity shall be available so that the 2 year mission can be completed with the loss of one battery. The batteries shall be nickel-cadmium rechargeable batteries capable of satisfying the present estimated load of 722 watts (including 20 percent growth factor) for a minimum mission life of 2 years and/or a minimum of 12 000 cycles. The maximum normal cyclic depth of discharge is 15 percent. Design depth of discharge is subject to MSFC approval.

(2) Performance. The battery capacity and voltage shall be chosen to optimize battery power capability, capacity, and reliability at the end of the mission.

Cyclic life tests with at least two batteries for a minimum of 6000 cycles shall be conducted to demonstrate performance capabilities of the battery assemblies and charge control techniques.

Cells of the same production lot as the flight battery cells shall be stored under controlled environment (less than 15° C) to be used for post-test comparative performance analysis.

(3) Construction. Each battery assembly shall be complete battery of single cells connected in series. Each battery assembly shall be packaged in a separate housing. The battery housing shall be sturdily constructed of corrosion resistant materials, especially suited for battery construction which conforms to materials standards established for HEAO. To minimize environmental testing, the assembly shall be designed with a 1.5 safety margin to assure that the battery will survive without damage, the extremes of environments specified for the mission. The housing shall afford rigid containment of the cells under most severe environmental/operational conditions, accounting for the tolerances of cell and assembly materials dimensions. The structure shall not permit detrimental deformation of cells that might result from internal pressure and temperature variations. In addition, the structure shall provide rigid cell constraint from internal pressure of at least 100 psig.

High quality, thermally stable insulation materials shall be used between cells and between cells and assembly housing. The electrical insulation shall be rated for at least 250 volts dc. The electrical insulation resistance to case shall be 10 megohms or greater, at 250 volts dc.

The battery shall be provided with external electrical power receptacle which is permanently attached to the battery case. The receptacle shall be per MSFC Drawing 40M39569A.

All battery assemblies shall have a separate connector or provisions for monitoring cell voltage within the assembly.

Low-loss, highly conductive interconnections between cells shall be provided. The contractor shall justify his method of bonding (welding, brazing, and soldering) interconnections to cell terminals. The interconnections shall be designed to minimize stresses or work hardening that might result from dimensional tolerances or temperature variations.

The battery assembly shall be designed for easy, safe-handling, testing, and installation. Provisions shall be made to minimize hazards to personnel or spacecraft equipment (sharp edges, electric arcing, etc.). Provisions for protecting batteries against electrical, mechanical, and thermal damage shall be assured for all phases of the program such as storage, charging or discharging, handling, installation, testing. Special attention should be given to protection of connections, thermal surfaces, and mounting surfaces. Except for the external connector pins (which shall be protected), no exposed electrical terminals or conductors shall be permitted. A battery assembly shall have a protective cover to prevent inadvertent damage or contamination of the cells and sensors.

The battery assemblies shall be manufactured, tested, inspected, and accepted in accordance with specifications that conform to the reliability and quality assurance provisions established for HEAO. Such specifications shall also include process and procedure controls unique to space quality batteries.

(4) Thermal Design. The battery assembly shall be designed for good heat dissipation considering abnormal loading conditions and possible ambient environment variations. The assembly shall have thermal control provisions to keep the hottest spot on the warmest cell within 3° C of the housing temperature. The thermal design shall be verified by appropriate tests.

(5) Storage. All flight model batteries and spares are to be stored in a safe condition and in a controlled environment. The storage and handling plan shall be approved by the government.

(6) Measurements. A minimum of three redundant temperature-sensing devices shall be included in the battery assembly for charge control, high temperature cutoff, and telemetry. The sensing device to measure battery current is in the charge control assembly. Other sensing devices, to be determined by the contractor, shall be reliable proven devices for battery applications.

(7) Battery Cells

(a) Construction. The cells to be used in the HEAO battery assemblies shall be hermetically sealed or high pressure vented secondary nickel-cadmium type cells of competent manufacture. The cell cases shall have a sturdy, stainless-steel container with the cover welded to the enclosure. Special attention shall be given to the inside dimensions and tolerances of the case, to packing density of plates and separators, and to the constraint and physical support that the case assembly provides for the plates/separators and internal connections.

All cells and/or batteries shall be conditioned for use and scaled. The cell case shall be the primary pressure vessel of each cell and the battery case the primary pressure vessel of each battery and shall be capable of withstanding the proof pressure as specified herein.

Proof pressure is the test pressure to which all components are subject with no detrimental deformation allowed. Cell proof pressure is defined as 1.5 times the maximum cell case relief valve pressure setting. Detrimental deformation is deformation which impairs normal cell operation and shall be defined by the vendor. No electrolyte leakage shall occur at proof pressure.

During normal operating conditions and environments, venting of cells and/or batteries shall not be allowed. If venting occurs, caused by some malfunction or failure in equipment, venting provisions shall allow the escape of gas only; venting of liquid electrolyte shall not be permitted under any conditions.

(b) Matching. Accepted, delivered cells shall be constrained, carefully conditioned, cycled for at least 30 cycles, and matched to close tolerances before battery assembly. The contractor shall define such procedures, selection criteria, and unacceptable limits with government approval. Cells differing in cycle life more than 10 cycles shall not be assembled together. Any cell or battery assembly having more than 500 cycles of testing shall not be used in the flight system. Cells or battery assemblies having experienced discharge rates greater than the "C" rate or having been exposed to temperatures beyond -40° or $+40^{\circ}$ C shall not be permitted in the flight system.

Cells failing prescribed acceptance or matching tests shall not be considered for assembly. In addition, subsequent to cell test, should any cell show evidence of abuse, leakage, terminal or insulator damage, or physical deformation, it shall be eliminated.

(c) Storage and Handling. The care, precautions, and protection of cells during storage, handling, and testing shall conform to the requirements established for a flight battery assembly.

3. Electrical Distribution and Control Subsystem

a. Introduction. The electrical distribution subsystem shall provide load control, protection, and delivery of power to user equipment. This subsystem shall distribute the power from the sources to the experiment loads and housekeeping loads. The power furnished to critical loads and experiments shall be supplied by redundant power sources and networks designed so that after the failure of one source and/or network, the system shall maintain full operational capability. This redundancy shall be achieved by bus switching, and/or diode isolation of buses furnishing the same load, and/or providing multiple distribution.

b. Distribution. Regulated power will be distributed to the loads as required. The power buses shall furnish 28 ± 2 percent volts to the experiments and spacecraft subassemblies. The electrical system distribution loss shall not exceed 3 percent of the total power distributed, and the maximum bus voltage drop from source to load shall be less than 1 volt. Provisions shall be made for accepting ground power for electrical system test during prelaunch checkout.

c. Load Control. The subsystem control shall provide the capability of powering up or down the distribution buses during flight or with ground power, selectively switching the bus sources, and routing the power. Automatic control of the distribution system shall be used, but ground command shall override the automatic system. In the event of a load failure and/or network failure, provision shall be made to remove the failed load and/or network from the electrical system. In addition, the electrical distribution and control subsystem shall provide capability to switch out any experiment or unnecessary load during different modes of operation throughout the mission from the ground.

d. Circuit Protection. The protective circuitry shall be designed to ensure the safe and reliable operation of the electrical system and to prevent fault propagation and fault damage to other parts of the system. The protection system shall consist primarily of circuit breakers to remove the threat of short circuit high currents, but this does not preclude the use of any other protective circuitry where required, justified, and approved by MSFC.

e. Measurements. The electrical distribution and control subsystem shall be monitored to provide ground indication of the status of each bus, switching circuitry, and the state of the protection circuitry both inflight and during ground checkout. Continuous voltage and current monitoring capability of all power buses shall be provided. Inflight information shall be capable of use within the power control system and for telemetry to the ground for system evaluation.

REFERENCES

- F-1. Space Environment Criteria Guidelines for Use in Space Vehicle Development. NASA TMX-53957, Second Edition, August 26, 1970.
- F-2. Grumman Aerospace Corporation: High Energy Astronomy Observatory. Volume II, NASA Contract No. NAS8-26272, April 1971.
- F-3. TRW, Systems Group: HEAO Phase B Final Report. Volume II, NASA Contract No. NAS8-26273, April 1971.

BIBLIOGRAPHY

Lockheed Missiles and Space Company: HEAO Orbit Adjust Stage and Associated Hardware Definition. LMSC Report A989276, NASA Contract NAS8-26492, May 21, 1971.

TABLE OF CONTENTS

	Page
INTRODUCTION	G- 1
RELIABILITY ANALYSES	G- 1
1. Observatory System	G- 1
2. Attitude Sensing and Control	G- 3
3. Electrical Power System	G-18
4. Communications System	G-23
5. Data Handling System	G-27
6. Reaction Control System	G-32
CONCLUSIONS AND RECOMMENDATIONS	G-39
DEGRADED MODE ASSESSMENT	G-40
RELIABILITY VERSUS COST ASSESSMENT	G-48
REFERENCES	G-51

LIST OF ILLUSTRATIONS

Figure	Title	Page
G-1.	ASCS reliability model	G- 5
G-2.	ASCS equipment locations	G- 7
G-3.	Magnetic coil system reliability model	G- 9
G-4.	EPS reliability block diagram	G-19
G-5.	Battery charger reliability model	G-23
G-6.	Communication system reliability model	G-24
G-7.	Transmitter reliability model	G-26
G-8.	DHS reliability model	G-28
G-9.	Tape recorder block diagram	G-31
G-10.	Tape recorder block diagram (condensed)	G-33
G-11.	Reliability model: Four tape recorders	G-34
G-12.	Reliability model: Three tape recorders	G-35
G-13.	RCS schematic	G-36
G-14.	Mission/Data Worth	G-42
G-15.	Reliability versus Δ cost	G-48

LIST OF TABLES

Table	Title	Page
G-1.	HEAO-C Reliability Numerics Summary	G- 2
G-2.	HEAO-C Equipment Failure Rates	G- 4
G-3.	ASCS Reliability Numerics Summary	G- 6
G-4.	Magnetic System Failure Rate Data	G- 8
G-5.	HEAO-C Transfer Assembly Part Count	G-11
G-6.	RGA Configuration Reliability Comparisons	G-16
G-7.	EPS Reliability Numerics Summary	G-18
G-8.	Communication System Reliability Numerics Summary. . .	G-25
G-9.	DHS Reliability Numeric Summary	G-27
G-10.	RCS Reliability Numerics Summary	G-32
G-11.	Two Year Propellant Block Failure Rates	G-38
G-12.	Cumulative Mission/Data Worth	G-43
G-13.	Degraded Mode Analysis Guidelines	G-44
G-14.	Degraded Mode Assessment	G-45
G-15.	Reliability Versus Δ Cost Data (2 Year Lifetime)	G-49

APPENDIX G. RELIABILITY ANALYSIS

Introduction

The design approach in the study was to plan for a reliability of 0.95 for one year, to determine what the corresponding reliability would be for two years, and to assess the cost impact of raising the reliability to 0.90 at the end of two years. It was desired to perform a "classical" reliability analysis on the Observatory subsystems to be able to compare the results from the HEAO-A and -B studies. In performing this analysis, the same component failure rates from those studies were utilized wherever a similar component existed in the HEAO-C design, unless there was some indication that the failure rates should be changed.

The reliability of experiments and the Orbit Adjust Stage (OAS) were not assessed during the study due to lack of information about their reliability. Also, it was assumed for the purpose of this study that the reliability of the thermal control system and structures was very high, and would not have as significant an effect on the overall Observatory reliability as would the other systems. The results of this analysis appear below. An assessment was made of the capability of the Observatory to perform in degraded modes of operation, and an assessment was also made of the cost penalty for increasing reliability beyond that of the baseline Observatory. These assessments are documented in succeeding paragraphs.

Reliability Analyses

1. Observatory System. In the analyses described here, a failure is any event which severely reduces either the quality or quantity of experimental data. The meaning of "severe reduction" is interpreted according to the function of the equipment being analyzed. Experiment and launch phase reliability and the reliability effects of the additional system integration hardware necessitated by redundancy (checkout and fault isolation) have not been assessed. The first and last of these require further definition before a reasonably realistic reliability estimate can be made, and time/manpower constraints did not permit an estimate of launch phase reliability.

A critical-function no-single-point-failure criterion, two-year life potential, 0.95 one-year reliability, maximum practical use of existing equipment, and commonality with the phase B HEAO-A and -B were the goals

used to guide the baseline HEAO-C design. No attempt to optimize the resulting preliminary design was made.

Table G-1 summarizes the subsystem reliability analyses (five-digit numbers are used to demonstrate system sensitivity and do not reflect equipment data confidence).

TABLE G-1. HEAO-C RELIABILITY NUMERICS SUMMARY

Subsystem	Reliability	
	1 yr	2 yr
Attitude Sensing and Control (ASCS)	0.94520	0.81024
Electrical Power (EPS)	0.99199	0.94403
Communications (COMM)	0.99963	0.99792
Data Handling (DHS)	0.98890	0.95895
Reaction Control (RCS)	0.99739	0.92948
Baseline	0.92446	0.68035
Alternate 1	0.96188	0.76363
Alternate 2	0.96717	0.83899

As shown here, the baseline does not meet the one year goal of 0.95. The principal impediment to higher reliability is the ASCS control moment gyro (CMG) assembly. Alternate 1 is obtained from the baseline by deletion of one of the four baseline tape recorders and addition of one CMG. Alternate 2 is obtained from the baseline by deletion of one tape recorder and the RCS and addition of a cold gas system for attitude control prior to CMG spin-up and a magnetic coil system for CMG momentum desaturation. Data received from the Leach Corporation substantiates a higher recorder reliability than was obtained earlier in the study. Use of three recorders was recommended by TRW Systems, Inc., in Reference G-1 and four by Grumman Aerospace Corp. (GAC) in Reference G-2.

Apart from the CMGs, other equipment of concern from the reliability standpoint are the following: batteries, the ASCS transfer assembly, tape recorders, RCS thrusters, and fuel tank bladders. Concern with the last two items extends only to requalification for a two year life. The tape recorder estimate is thought to be reasonably accurate, but will change slightly as additional details are taken into account. Additional component information has made possible the use of a deterministic reliability model in place of the Monte Carlo model used in the HEAO-A and -B phase B studies. The ASCS transfer assembly requires further definition before a realistic reliability estimate can be made, although a preliminary estimate is given below. While the battery assembly reliability is thought to approach the estimates given below, not much credence should be given the actual numbers. The problems encountered with the battery estimates, and discussions of the other concerns, are covered in the subsystem analyses below. Most of the failure rate data used are given in Table G-2. Additional failure rate data used for the transfer assembly and the magnetic system are given in Section 2 and a breakdown of the tape recorder failure rate is given in Section 5. These data agree, for the most part, with those used by HEAO-A and -B phase B contractors. Listing of specific vendor equipment is provided, where possible, to document failure rate sources and does not necessarily indicate equipment selection preferences. Failure rate reductions of 10:1 and 30:1 have been used for standby status of electronic and mechanical equipment, respectively, where appropriate.

2. Attitude Sensing and Control. A summary of this analysis is given in Chapter VII, Section F. The ASCS block diagram is repeated here as Figure G-1. Table G-3 is an expanded version of Table VII-14 of Chapter VII, Section F. Locations of the ASCS equipment are shown in Figure G-2.

The transfer and WASS assemblies reliabilities have not been factored into the ASCS reliabilities. The transfer assembly is not sufficiently defined to permit a realistic reliability estimate, while the WASS assembly is a convenience item.

In addition to the baseline reliabilities, the effects of certain modifications to the baseline are shown by Table G-3. The first, or minimum modification, is the addition of a fifth CMG. The CMG assembly then has one and two year reliabilities of 0.99303 and 0.95796, which are considerably better than those of the baseline four-CMG assembly. The next line of the table shows the ASCS reliabilities with the five-CMG assembly, and

TABLE G-2. HEAO-C EQUIPMENT FAILURE RATES

Equipment	Failure Rate (ppmh)	Source	Remarks
Wide Angle Sun Sensor (WASS)	0.692	GAC	BDX 1818787
WASS Electronics	0.68	GAC	BDX
Digital Sun Sensor (DSS)	0.10	GAC	Adcole 15380
DSS Electronics	8.65	GAC	
Fixed-Head Star Tracker and Electronics (FHST)	3.33	ITT ^a	Dual Mode Tracker
Inertial rate-integrating gyro and Electronics (IRIG)	5.07	TRW	Nortronics
ASCS Processor	37.39	GAC	GI-K7G
CMG	11.14	BDX ^b	BDX-900 (Honeywell)
Solar Cell	0.447	PD-DO-EP ^c	HDC-501 = 33.47)
Solar Cell Blocking Diode	0.044	TRW	BDX-MA-500
Battery	8.47	NAD, Crane ^d	2 x 4 cm
Charger	4.8	ATM ^e	Derived by BECO
Regulator	11.1	ATM	
Panel Deployment Mechanism	P _s = 0.9947	TRW	
Power Control Unit	3.88	BECO ^f	Estimate based on piece part count of preliminary design.
Electrical Integration Unit	1.5	BECO	Estimate based on piece part count of preliminary design.
Antenna	0.13	TRW	
Antenna Deployment Mechanism	P _s = 0.9947		Assumed similar to solar panel deployment mechanism.
Receiver	10.4	TRW	Motorola
Transmitter	5.2	TRW	Transponder
Phase Shift Keyed (PSK) Demodulator	1.788	TRW	
Frequency Multiplexer (MUX)	1.147	TRW	
Remote MUX	1.2	PD-DO-EC ^c	
Plated Wire Command Memory	11.22	Motorola	
Command Processor	10.0	BECO	CDC 469
Clock	3.0	GAC	
Format Generator	5.0	GAC	
Read-Only Memory (ROM)	0.28	S&E-QUAL ^g	
Tape Recorder Control Unit	5.0	GAC	
Remote Decoder	1.8	GAC	
Pulse Code Modulator Encoder	9.0	GAC	
Tape Recorder	8.917	Leach	Leach 2000; See Figure G-2; value adjust for duty cycling
RCS Electronics	1.63	GAC	
RCS Fill Valve (leakage)	0.01	TRW	
Tank	0.07	TRW	
Bladder	0.33	TRW	
Isolation Valve (leakage)	0.01	TRW	Carleton Control Corp. latching solenoid valve
Temperature Transducer (leakage)	0.005	TRW	
Pressure Transducer (leakage)	0.005	TRW	
Filter (leakage)	0.024	TRW	
Thruster	0.7 PPMC	GAC	Rocket Research Corp. MR-50A

a. International Telephone and Telegraph

b. Bendix Aerospace Corp.

c. Preliminary Design Office, Program Development, Marshall Space Flight Center

d. Naval Ammunition Depot, Crane, Ind.

e. Apollo Telescope Mount

f. Teledyne Brown Engineering

g. Quality and Reliability Assurance Laboratory, Science and Engineering, Marshall Space Flight Center

TABLE G-3. ASCS RELIABILITY NUMERICS SUMMARY

Assembly	Reliability	
	1 yr	2 yr
Transfer	0.98969	0.97949
WASS	1.00000	0.99999
Celestial Reference (CRA)	0.99954	0.99818
X-FHST	0.99954	0.99820
DSS	0.99690	0.98826
FHST/DSS	1.00000	0.99998
Processor	0.99407	0.96354
Reference Gyro Assembly (RGA)	0.99684	0.98780
CMG	0.95428	0.85284
Baseline ASCS	0.94520	0.81024
5-CMG	0.99303 ^a	0.95796
ASCS	0.98358 ^b	0.91011
HEAO-C	0.96198 ^c	0.76421
6-CMG	0.99904	0.98904
ASCS	0.98953	0.93964
HEAO-C	0.96780	0.78900
Scissored Pairs	0.97426	0.90851
ASCS	0.96498	0.86313
HEAO-C	0.94379	0.72476
Magnetics × 4-CMG	0.99888 × 0.99700	0.99761 × 0.98063
ASCS	0.98640	0.92942
HEAO-C	0.96728	0.83963
Magnetics × 5-CMG	0.99888 × 0.99965	0.99761 × 0.99575
ASCS	0.98903	0.94375
HEAO-C	0.96984	0.85258

- a. One year reliability of the 5-CMG Assembly
- b. One year Reliability of the ASCS with a 5-CMG Assembly
- c. One year Reliability of the HEAO with a 5-CMG Assembly

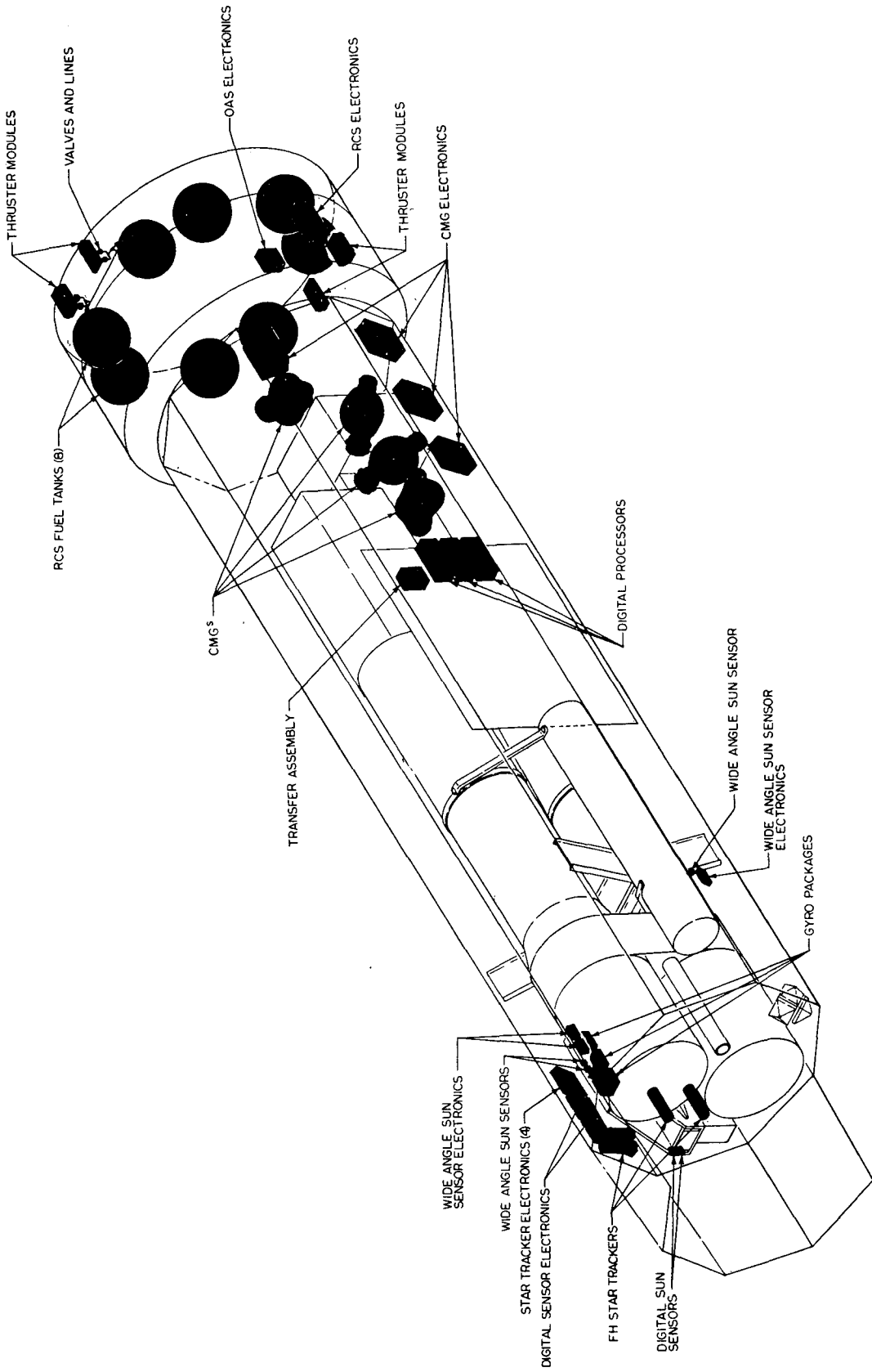


Figure G-2. ACS equipment locations.

12 (4)

the next, the HEAO-C reliabilities. The next modification, addition of a sixth CMG, effects only a minor additional overall improvement, and the use of the six-CMGs in a "scissored pair" arrangement of paired CMGs on each of three orthogonal axes, with one failure per axis permitted, drops the overall one year reliability below the required 0.95. Examination of the HEAO-C layouts indicates sufficient room within the spacecraft envelope to accommodate one or two additional CMGs. Use of five or more smaller CMGs has been suggested. In this case it is thought that three CMGs may be unable to provide the necessary torque capability, so that any failure rate improvement would be offset by a lower depth-of-failure tolerance.

Other than simply adding CMGs, reliability improvement may be obtained by use of a magnetic coil system for CMG momentum desaturation. Only two CMGs are then required for attitude control. A block diagram for such a system is given in Figure G-3 and corresponding failure rates are given in Table G-4. It should be emphasized that these failure rate data apply to the magnetic system used on Orbital Astronomical Observatory (OAO). Hence, the reliabilities shown for the magnetic system should be considered only as indicative of what may be achieved with a magnetic system.

TABLE G-4. MAGNETIC SYSTEM FAILURE RATE DATA

Equipment	Failure Rate (PPMH)	Source	Remarks
Magnetometer (per axis)	0.3	GAC	Dalmo-Victor. 6.5 lb, 1.76 W, 28 Vdc.
Coil Driver	0.702	BECO	Based on piece part count
Magnetic Coil	0.04	BECO	Dalmo-Victor Spec. No. AV-252CS-57 10.1 lb, 2.9 W, 28 Vdc. (HEAO- C coil wt. approx. 50 lb)

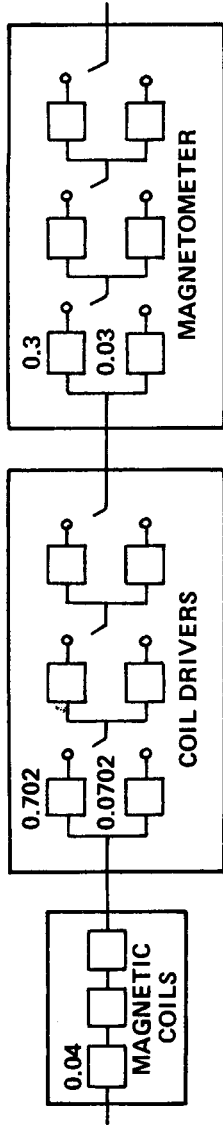


Figure G-3. Magnetic coil system reliability model.

One drawback of the magnetic system configuration proposed is that each coil is a potential single-point failure. Considering the low failure rate of such coils, generally, and the HEAO-C coil weight estimate of approximately 50 lb, complete redundancy is probably unnecessary. Use of redundant coil windings is probably the best solution. One possibility which does not appear to have been considered is the use of four coils in a skewed configuration. Such a configuration could be implemented with only a minor software impact and the additional weight and power requirements of a single coil and its drivers.

A cold gas system would be used for attitude control from launch vehicle separation to completion of CMG spin-up if a magnetic system were used. Since this system would be used only briefly at the start of the mission and has not been defined in detail, no reliability estimate was attempted.

Discussions of the procedures used to generate the reliability numerics above, together with failure definitions, will be given below. It will be convenient to have the experiment viewing direction regarded as the +X-axis with the nominal sun direction being the +Z-axis. Rotations about the X, Y, and Z axes will then be referred to as roll, pitch, and yaw, respectively.

As remarked earlier, the transfer assembly is not sufficiently defined to permit a realistic reliability estimate. The functions of this assembly are redundancy management and implementation of the RCS thruster control law for contingency mode operation. Table G-5 describes the piece part count determined by GAC in the phase B HEAO-A and -B studies wherein the transfer assembly was assigned the functions of processor and gyro failure isolation and implementation of the contingency mode thruster control law, and the derivation of an effective failure rate for the purpose of a tentative reliability estimate. As additional redundancy management schemes are defined and implemented via this assembly, the reliability estimate will decrease but can be raised again by use of circuit-level redundancy and high reliability parts. This is possible since the transfer assembly is unique to HEAO-C.

The 0.1 duty-cycle K-factor in Table G-5 is used to effect a 10:1 failure rate reduction for standby status. If an exponential reliability formula is assumed,

$$R(t) = \exp(-\lambda_{\text{effective}} \times t),$$

the reliabilities shown in Table G-3 are obtained.

TABLE G-5. HEAO-C TRANSFER ASSEMBLY PART COUNT

Part	Type	Quantity (N)	Failure Rate, (PPMH)	Duty Cycle Factor	KN
Resistor	RNR-1%	100	0.0009	1.00	0.09
Relay	DPT Latching	50	0.1	0.1	0.5
Operation Amplifier	LM101	40	0.12	0.1	0.48
Gate	SN 5400	12	0.03	0.1	0.036
Gate	SN 54121	6	0.03	0.1	0.018
Capacitor-Ceramic	CK06	52	0.003	0.1	0.0156
Capacitor-Tantalum	CS13	6	0.016	0.1	0.0096
Zener	IN751A	16	0.005	0.1	0.0080
Diode	IN645	42	0.002	0.1	0.0084
Resistor	RNR-1%	180	0.0009	0.1	0.0162
					λ effective = 1.1818 (PPMH)

The function of the WASS assembly is to provide the sun aspect information required to bring the spacecraft +Z-axis to within approximately 30 degrees of the sun line, so that the sun will fall within the 64 degree by 64 degree DSS field of view (FOV). Two WASSs are installed with their FOVs centered on the +Z-axis, and a third looks along the -Z-axis (Fig. G-2). In the normal sun acquisition mode, only one of the +Z WASS electronics units is powered; the -Z WASS electronics unit is also powered. The two WASSs being used then cover 4π steradians, permitting sun location regardless of the spacecraft orientation. Should the primary +Z WASS (or its associated electronics) fail, it can be replaced by the backup unit. Should both +Z WASSs (or the -Z WASS) fail, the sun can still be located (with a roll maneuver when required). Thus, the WASS assembly functional capability is maintained so long as one WASS (and its electronics) is unfailed. Although this capability is required only during the sun acquisition mode entered after launch vehicle separation, and whenever the attitude reference is lost, one +Z WASS electronics unit can be powered continuously to provide redundant attitude information. Since the sensor itself is always "powered" (see Chapter VII Section B), the reliability model shown in Figure G-1 is applicable. As a detail, it is noted that once both +Z WASSs have failed, no purpose would be served by powering the -Z WASS electronics at all times, so the model chosen is slightly pessimistic. The applicable formula, assuming a 10:1 failure rate reduction for standby electronics, is

$$R(t) = e^{-\lambda t} \left[e^{-2\lambda' t} + \frac{\lambda + 2\lambda'}{\lambda'} (1 - e^{-\lambda' t}) e^{-\lambda' t} + \frac{(\lambda + \lambda')(\lambda + 2\lambda')}{2\lambda'^2} (1 - e^{-\lambda' t})^2 \right]$$

where

$$\lambda = 0.692 + 0.68 = 1.372 \text{ (PPMH)}$$

$$\lambda' = 0.692 + 0.068 = 0.76 \text{ (PPMH)}$$

The argument that the WASS is a convenience item proceeds along the following lines. Each DSS has a 64 degree by 64 degree FOV. Should no WASS be available, roll the spacecraft 180 degrees. If the sun is not located during this roll, pitch the craft 60 degrees and repeat the roll. If the sun is not located, then a third pitch-roll maneuver will locate the sun.

Considering that the WASS (and associated electronics) units are simple, relatively inexpensive, and highly reliable, use of the DSSs as WASS backups is not justified. Moreover, the DSS assembly can be regarded as a convenience item for sun acquisition. Should the DSSs not be available, the vehicle +Z-axis can be brought to within approximately 0.1 degree of the sun line using the WASS assembly. Yawing the spacecraft and using the FHSTs as star mappers will permit a celestial reference acquisition. The vehicle will then be in a pointing mode, and transfer to the desired target can be accomplished in the usual manner under gyro control.

If neither the DSSs or WASSs were available, sun acquisition would be more complicated. One possibility would make use of the solar array power output. With the panels undeployed (as would be the case immediately after launch vehicle separation) and, hence, at an angle to each other, a certain amount of directional information would be available in one axis. With the panels deployed, only the angle between the +Z-axis and the sun line could be determined. Since the power curve is relatively flat near its maximum point, this angle measurement could not be very accurate, and the yaw-scan maneuver (described above) required to obtain a celestial reference would then be complicated by the uncertain orientation of the scan plane with respect to the celestial sphere. Thus, deletion of both the WASS and DSS cannot be recommended, and operational efficiency is an argument for both.

The DSS and FHST are two-axis sensors. The X-axis FHST provides pitch and yaw attitude information, the Y-axis FHST gives roll and yaw information, and the DSS yields pitch and roll information. Thus, the DSS outputs can be used to malfunction-detect the roll output of the Y-axis FHST and pitch output of the X-axis FHST. When the RGA is taken into account, a complete malfunction detection/identification scheme using output comparison of dissimilar instruments can be constructed. Since the pointing stability requirement is less stringent in roll than in pitch and yaw, the DSS can maintain pointing capability (possibly with a slight pointing stability performance degradation) through its roll output if both Y-axis FHSTs fail. The pitch output, however, is not sufficiently precise to maintain pointing capability within specifications if both X-axis FHSTs fail. These considerations lead to the reliability structure depicted in Figure G-1 for the CRA consisting of the DSSs and FHSTs.

Both the X- and Y-axis FHST pairs are operated in a "one plus standby" manner. With a 10:1 failure rate reduction, the applicable reliability formula is

$$R_{\text{FHST}}(t) = e^{-\lambda t} \left(11 - 10 e^{-\lambda t/10} \right) .$$

The DSS electronics unit are operated similarly. Defining the "online" and "standby" failure rates

$$\lambda = 0.1 + 8.65 = 8.75 \text{ (PPMH)}$$

$$\lambda' = 0.1 + 0.865 = 0.76 \text{ (PPMH)}$$

the DSS/electronics reliability formula is

$$R_{\text{DSS}}(t) = e^{-\lambda t} \left[e^{-\lambda' t} + \frac{\lambda + \lambda'}{\lambda} (1 - e^{-\lambda' t}) \right] .$$

For independent events A and B,

$$\text{Pr}(A + B) = \text{Pr}(A) + \text{Pr}(B) - \text{Pr}(A) \text{Pr}(B) ,$$

so that the DSS/FHST assembly reliability is given by

$$R_{\text{DSS/FHST}} = R_{\text{FHST}} (1 - R_{\text{DSS}}) + R_{\text{DSS}}$$

and the CRA reliability is then found as

$$R_{\text{CRA}} = R_{\text{FHST}} R_{\text{DSS/FHST}} .$$

An unobstructed FOV for both the sun sensors and star trackers is a requirement. Locating the Y-axis FHSTs forward of the spacecraft envelope, as shown in Figure G-2, ensures that an undeployed or partially deployed solar

panel will not block their FOVs. A cutout in the sun shade allows for the DSS FOVs. The size of the cutout is minimized by placing these sensors as close as possible to the shade.

The processor assembly consists of a primary and two standby units. With a 10:1 failure rate reduction for standby status, the reliability formula is derived as

$$R(t) = e^{-\lambda t} [(55e^{-\lambda t/10} - 120) e^{-\lambda t/10} + 66] .$$

The quoted failure rate of 37.39 PPMH represents the best values obtainable with existing equipment of the required capability. This figure could be reduced by resort to large scale integration (LSI) technology, but this would entail a new development. If only two processors were used in a primary and standby configuration, the processor assembly reliability would be approximately the same as that of the baseline CMG assembly, i.e., approximately 0.95 for one year. Hence, the third processor is necessary if the overall 0.95 one year reliability goal is to be met. One requirement of the type of redundancy used in this instance is that of processor self-test capability.

The RGA consists of one pair of IRIGs on each of three orthogonal axes. Each pair is utilized in the "primary and standby" configuration. Accordingly, the reliability formula is

$$R(t) = e^{-3\lambda t} (11 - 10e^{-\lambda t/10})^3 .$$

The gyro selected is the Nortronics GI-K7G, a scaled-down version of the Nortronics GI-T1-B gyro used in a ground alignment application in the Minuteman ICBM (see Chapter VII, Section B). The failure rate of 5.07 PPMH quoted by TRW does not appear to have been adjusted for the HEAO environment.

Growth potential for the RGA can be realized by adding additional gyros or resorting to a skewed gyro configuration such as the dodecahedral RGA now in development [G-3 and G-4]. Two versions of the dodecahedral RGA can be

envisioned. In the first, one of the six gyros is kept in unpowered standby until the first failure occurs. This configuration is denoted by 3/(5+1) in Table G-6. The second (3/6) configuration keeps all unfailed gyros online. Both configurations require three unfailed gyros to maintain functional capability. The first two failures are detected by a voting scheme¹ and the third by monitoring the internal states (wheel speed, temperature, etc.) of the remaining gyros. Table G-6 compares the reliabilities of these configurations to the baseline at six month intervals, assuming a gyro failure rate of 5.07 PPMH and ignoring switching effects. There is little reliability difference between the dodecahedral RGA configurations. Advantages of these RGAs over the baseline include higher reliability and internal self-test capability (voting of dissimilar instruments is not required to detect gyro failures).

TABLE G-6. RGA CONFIGURATION RELIABILITY COMPARISONS

Month	3/ (5 + 1)	3/6	Baseline
6	0.999997	0.999997	0.999198
12	0.999957	0.999950	0.996843
18	0.999799	0.999767	0.993017
24	0.999411	0.999318	0.987797

With RCS CMG momentum desaturation, three CMGs are required for attitude control. Accordingly, configurations of four, five, and six CMGs, including scissored pairs, were considered. With magnetic desaturation, two CMGs are required, and configurations of four and five CMGs were considered. The respective reliability formulas are as follows:

$$R_{3/4}(t) = P^3 (4-3P) \quad ,$$

$$P_{3/5}(t) = P^3 [(6P-15) P + 10] \quad ,$$

-
1. Steincamp, James W.: Strapdown Inertial Measurement Unit (IMU) Sensor Malfunction Detection and Rate Estimation. MSFC IN-DO-E-70-1, 1970.

$$R_{3/6}(t) = P^3 \left\{ [(-10P + 36) P - 45] P + 20 \right\} ,$$

$$R_{SP}(t) = P^3 (2-P)^3 ,$$

$$R_{2/4}(t) = P^2 [(3P-8) P + 6] ,$$

$$R_{2/5}(t) = P^2 \left\{ [(-4P + 15) P - 20] P + 10 \right\} ,$$

where $P = e^{-\lambda t}$.

There seems to be sufficient volume within the spacecraft envelope to accommodate one or two additional CMGs. The failure rate of 11.14 PPMH quoted for the Bendix MA-500 CMG can most likely be reduced slightly, but the expected reduction does not lead to a large reliability increase. The CMG assembly reliability can also be increased by holding redundant CMGs in unpowered standby status until failures occur. Again, the reliability increase is not large. Use of smaller CMGs with lower failure rates has been suggested. Failure rates would be somewhat less, but the lower torque capability of the smaller CMGs would offset this by reducing the allowable depth of failure. This last comment may not apply if a magnetic momentum desaturation system is used. Simulation results indicate a lower torque capability requirement with such a system.

As remarked earlier, failure rates for the HEAO-C magnetic CMG momentum desaturation system were assumed to be similar to those of the OAO system. Accordingly, the reliabilities given here should be considered only as indicative of those achievable with a magnetic system. A block diagram of a possible system is given by Figure G-3, and the failure rates are listed in Table G-4. The coil reliability formula is simple $e^{-3\lambda t}$, and the formulas for the coil drivers and magnetometer axial sensors are identical, namely,

$$R(t) = e^{-3\lambda t} (11 - 10e^{-\lambda t/10})^3 .$$

The system reliability is the product of these three reliabilities. Reliability growth can be realized by use of redundant coil windings (which also eliminates the potential single point failures of the system shown) and/or four coils in a skewed configuration.

3. Electrical Power System. The EPS reliability block diagram given by Figure G-4 shows the solar array as configured for the initial baseline. Table G-7 summarizes the results of the reliability calculations for this baseline. Late in the study, certain changes to the solar panel layout were made. These changes, described below, should have no significant effect upon the results.

TABLE G-7. EPS RELIABILITY NUMERICS SUMMARY

Assembly	Reliability	
	1 yr	2 yr
Solar Array	0.99983	0.99983
Power Regulator	0.99703	0.98081
Power Control	0.99888	0.99568
Electrical Integration	0.99915	0.99664
Battery/Charger	0.99708	0.97010
Baseline EPS	0.99199	0.94403

The initial baseline solar array consisted of six deployable panels and body-mounted cells electrically equivalent to two of the deployable panels. Initial power output at the design reference condition (15 degrees off sun line) was 2365 watts with a constant requirement of 1549 watts. A 4 percent output degradation for each of the two years was assumed. For reliability purposes, this array may be considered to consist of eight standard panels, six of which are deployable. The bolt-cutters, two of which are allowed for each panel, determine the reliability of the panel deployment mechanism. Since only one bolt-cutter need operate for the panel to be deployed, the deployment mechanism reliability is

$$P_1 = 0.9947 (2.0 - 0.9947) = 0.99997 \text{ ,}$$

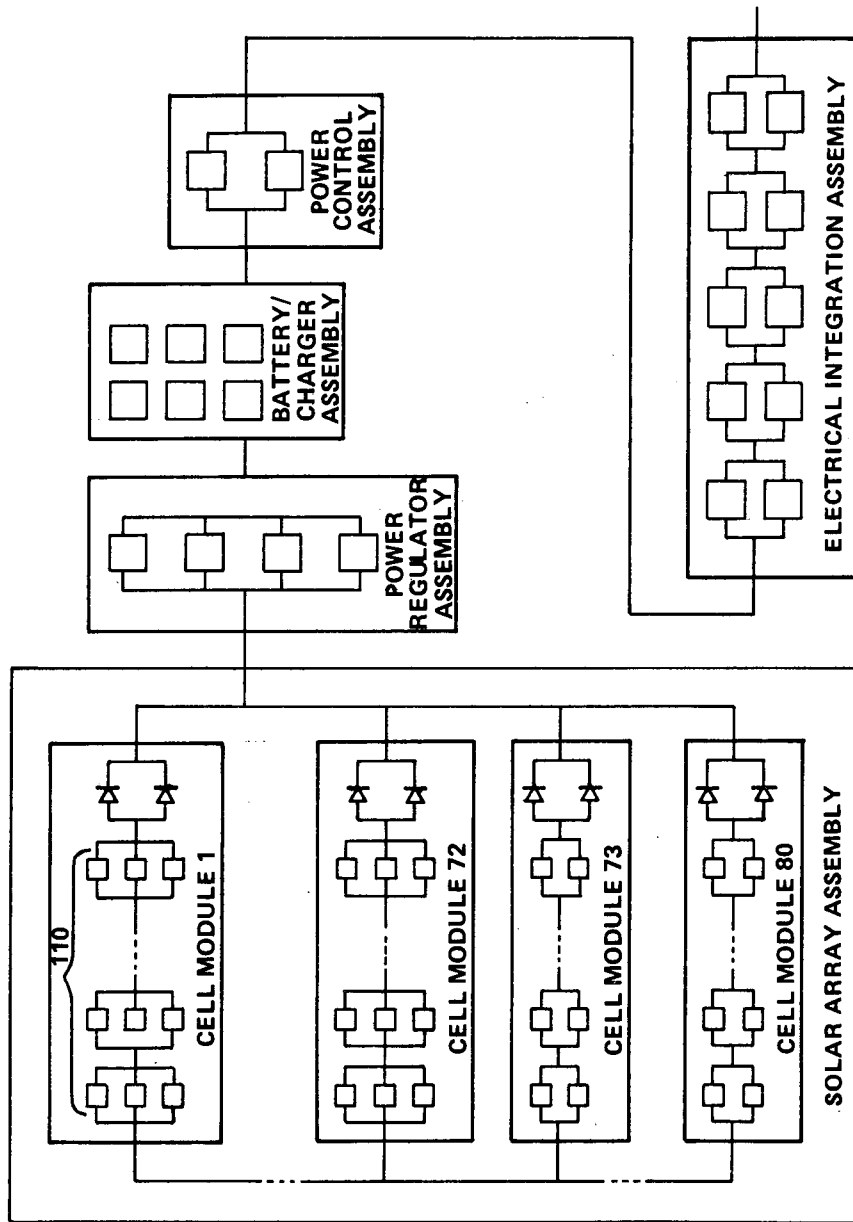


Figure G-4. EPS reliability block diagram.

where 0.9947 is the bolt-cutter reliability. The probabilities of deploying exactly six and exactly five panels are

$$P_6 = P_1^6 = 0.99983$$

and

$$P_5 = 6P_1^5 (1-P_1) = 1.6852 \times 10^{-4} .$$

Each of the eight standard panels contains nine modules which consist of a series arrangement of 110 units of three cells in parallel followed by two blocking diodes in parallel, and one module in which the number of parallel cells in each unit is reduced to two. The solar cell failure rate, based on a pessimistic loss estimate of 100 of the 25520 cells in one year, is 0.447 PPMH. The blocking diode failure rate quoted by TRW is 0.044 PPMH. The blocking diode unit reliabilities are computed by the formula

$$R_d(t) = e^{-\lambda t} (2 - e^{-\lambda t}) .$$

We can assume that the power decrease due to isolated cell failures is negligible, so that only failure of a complete module is of concern. The reliability of a three-cell unit is obtained from

$$R_3(t) = \sum_{k=0}^2 \binom{3}{k} P^{3-k} (1-P)^k ,$$

where $P = e^{-\lambda t}$, and the reliability of the 330-cell modules is therefore given by

$$R_{\text{mod}}(t) = R_3^{110}(t) R_d(t) .$$

Assuming the power output of the 220-cell modules to be two-thirds that of the 330-cell modules, the initial power outputs of these modules are 20.39 and 30.58 watts, respectively. The one and two year outputs of the larger module are then 29.45 and 28.27 watts. The power margins at these times are 722.3 and 621.5 watts. These margins will not be exhausted by failures so long as not more than 19 of the 330-cell modules fail during the first year or 16 during the first two years. The corresponding probabilities, which cannot be distinguished from unity by a careful calculation, are given by

$$R(n) = \sum_{k=0}^n \binom{72}{k} R_{\text{mod}}^{72k} (1-R_{\text{mod}})^k ,$$

where $n = 19$, or $n = 16$. Doubling the failure rate does not change the results. Since the model followed here is pessimistic, it is concluded that the reliability of the solar array is essentially constant and not less than that of the probability that all six panels deploy.

After this report was written, the number of solar cells was reduced to bring the beginning-of-life array power output down to 2015 watts. Examination of the reliability calculations carried out for the baseline array strongly suggests that these changes will have no significant impact on the conclusion that the array reliability is not less than the probability that all six panels deploy, particularly in view of the fact that about 100 watts of power can still be obtained from an undeployed panel at the reference condition.

The power regulator assembly consists of four identical units, two being required for satisfactory performance. While this is a load-sharing arrangement, the substantial derating used makes possible the use of the 2-of-4 binomial formula. The reliabilities are then determined from

$$R(t) = \left((3e^{-\lambda t} - 8) e^{-\lambda t} + 6 \right) e^{-2\lambda t} .$$

The power control assembly consists of two identical units. Again, load-sharing effects are negligible and the reliabilities are then given by

$$R(t) = e^{-\lambda t} (2 - e^{-\lambda t}) .$$

The electrical integration assembly consists of 10 identical units arranged as five serial pairs, which leads to the reliability formula

$$R(t) = e^{-5\lambda t} (2 - e^{-\lambda t})^5 .$$

The battery/charger assembly consists of six battery/charger units, three being required for satisfactory performance. While there is considerable confidence that an adequate battery/charger assembly can be designed (and the analysis which follows indicates an adequate reliability for the baseline design), the nature of the available failure rate data raises doubts about the mathematical models used by the Phase B HEAO-A and -B contractors. The simple model described below, used with ATM data, is intended to yield pessimistic reliability estimates.

The principal difficulty encountered in battery reliability analyses is that an adequate model must allow for a cell failure rate increasing in some manner with the accumulated number of charge/discharge cycles and with depth of discharge, for cell reversal phenomena governed by cell capacity loss statistics, and for wearout. While considerable battery test data were accumulated during the course of this study, it was not obvious that satisfactory quantification of these variables would be possible. Hence, the simple model described below was used.

A 70 percent utilization factor was used to obtain an adjusted charger failure rate λ_c for daylight operation, and the battery failure rate λ_b was adjusted by assuming a load sharing factor of $6/n$, n being the number of unfailed batteries. The model chosen has the dependency diagram given by Figure G-5.

If $P_i(t)$ denotes the probability that exactly i battery/charger units fail in time $(0, t)$, then

$$P_0(t) = e^{-\lambda_1 t} ,$$

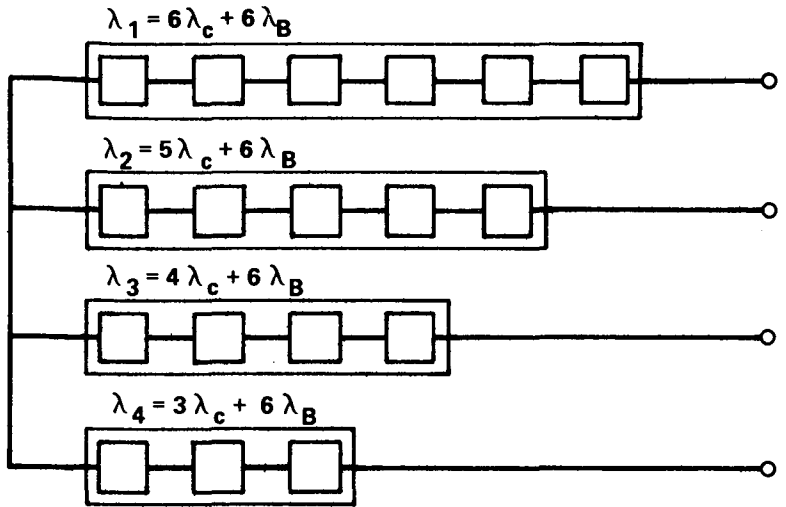


Figure G-5. Battery charger reliability model.

$$P_1(t) = \frac{\lambda_1}{\lambda_c} (e^{-\lambda_2 t} - e^{-\lambda_1 t}) ,$$

$$P_2(t) = \frac{\lambda_1 \lambda_2}{\lambda_c^2} \left(\frac{1}{2} e^{-\lambda_3 t} + \frac{1}{2} e^{-\lambda_1 t} - e^{-\lambda_2 t} \right) ,$$

$$P_3(t) = \frac{\lambda_1 \lambda_2 \lambda_3}{\lambda_c^3} \left(\frac{1}{6} e^{-\lambda_4 t} - \frac{1}{2} e^{-\lambda_3 t} + \frac{1}{2} e^{-\lambda_2 t} - \frac{1}{6} e^{-\lambda_1 t} \right) ;$$

and the reliability is given by

$$R(t) = \sum_{i=0}^3 P_i(t) .$$

4. Communications System. The communications subsystem reliability block diagram is given by Figure G-6. Table G-8 summarizes the results of this analysis.

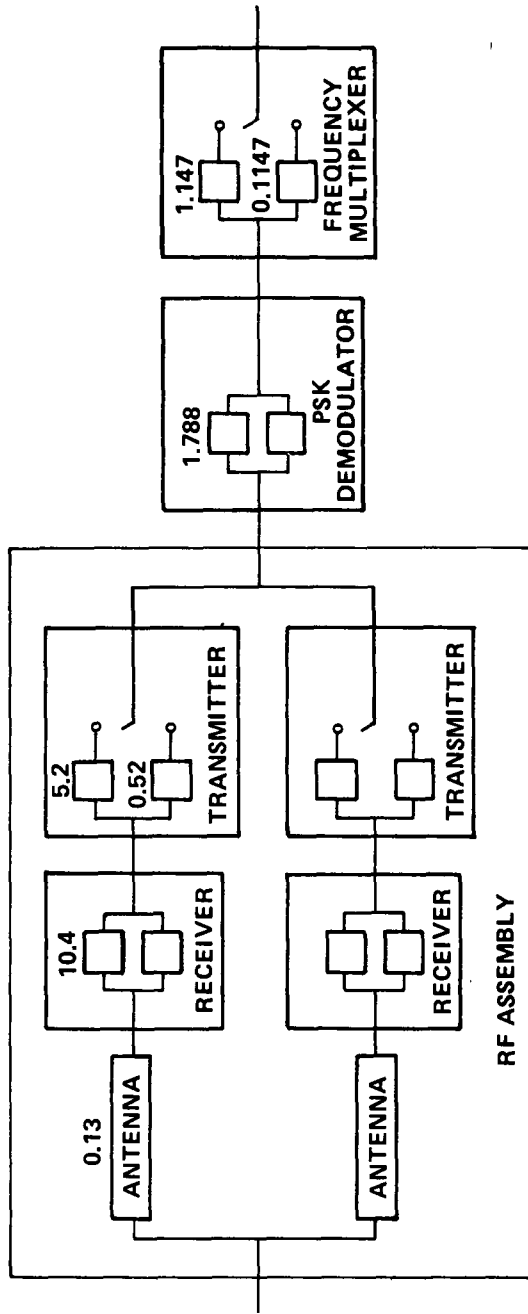


Figure G-6. Communication system reliability model.

TABLE G-8. COMMUNICATION SYSTEM RELIABILITY NUMERICS SUMMARY

Assembly	Reliability	
	1 yr	2 yr
Radio Frequency (RF)	0.99992	0.99909
Antenna Deployment	0.99997	0.99997
Antenna	0.99886	0.99772
Receiver	0.99240	0.97221
Transmitter	0.99996	0.99985
PSK Demodulator	0.99976	0.99905
Frequency MUX	0.99994	0.99978
Baseline Communications System	0.99963	0.99792

The antenna deployment mechanism is similar to that used for the solar panels: a spring-loaded boom with redundant bolt-cutters as actuators. Since only one of the two bolt-cutters need operate to deploy the antenna, the deployment probability is

$$P_D = 0.9947 (2 - 0.9947) = 0.99997$$

The antenna reliability is simply

$$R_{ANT}(t) = e^{-\lambda t}$$

The two receivers in each RF unit are operated continuously, with one

required for operation of the unit. The receiver reliability formula is then

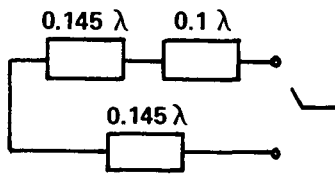
$$P_{RCVR} = e^{-\lambda t} (2 - e^{-\lambda t}) .$$

With a 5 percent utilization factor and 10:1 failure rate reduction for standby status, the online transmitter has an effective failure rate found from

$$\lambda (0.05t) + (0.1\lambda) (0.95t) = 0.145\lambda t .$$

The transmitter unit reliability model is given by Figure G-7, from which the transmitter unit reliability formula is derived as

$$R_{XMTR} (t) = e^{-0.145\lambda t} (2.45 - 1.45e^{-0.1\lambda t}) .$$



The RF unit with the fixed antenna then has the reliability

$$R_1 = R_{ANT} \cdot R_{RCVR} \cdot R_{XMTR} ,$$

Figure G-7. Transmitter reliability model.

while the second RF unit has the reliability

$$R_2 = P_D R_1 .$$

The RF assembly reliability is then determined from the formula

$$R_{RF} = R_1 + R_2 - R_1 R_2 .$$

The reliability formula for the PSK demodulator units is of the same form as that used for the receivers, and the frequency multiplexer unit formula is:

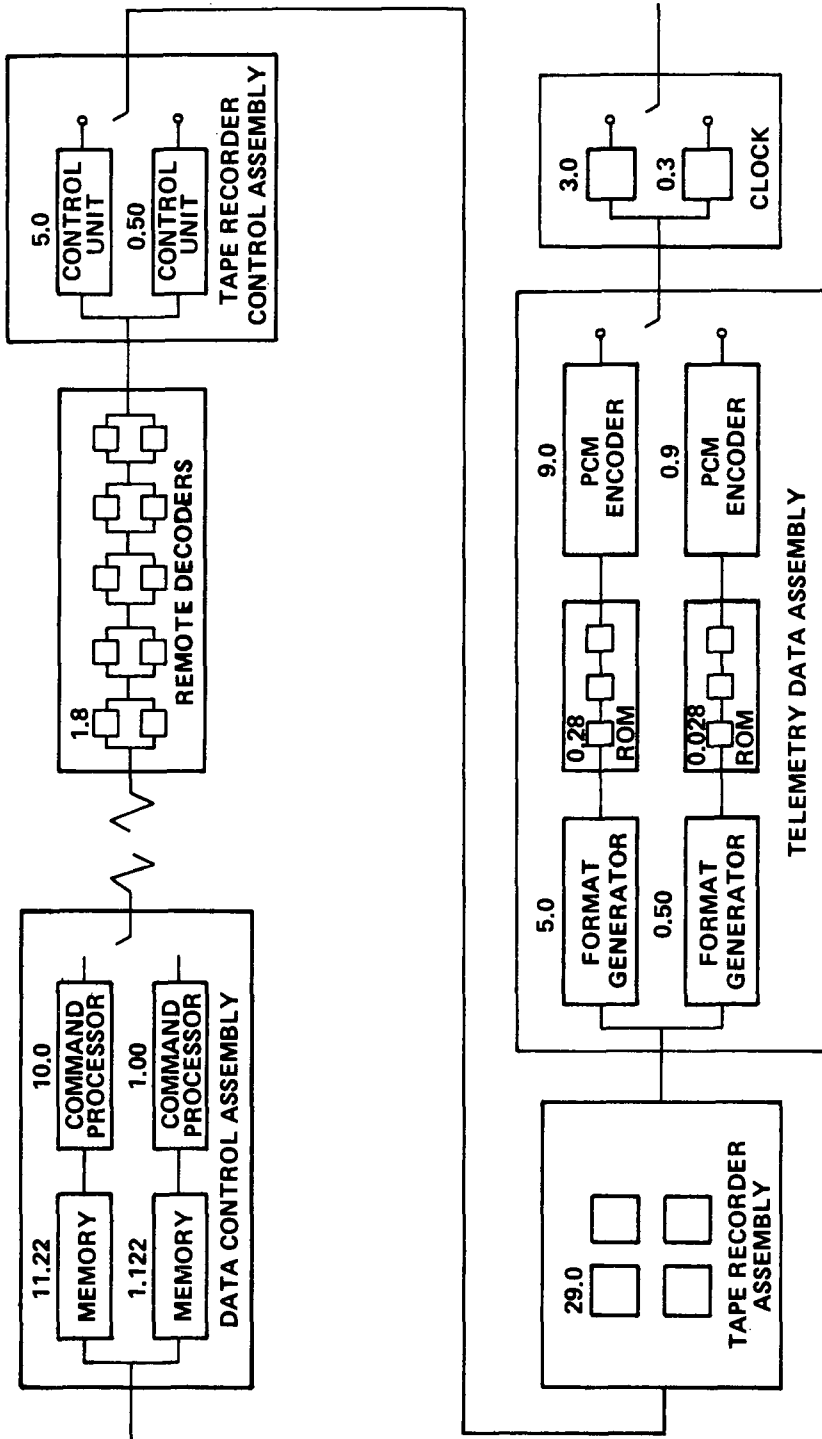
$$R(t) = e^{-\lambda t} (11 - 10e^{-\lambda t/10})$$

5. Data Handling System. The DHS reliability block diagram is given in Figure G-8. Table G-9 summarizes the DHS reliability analysis

TABLE G-9. DHS RELIABILITY NUMERIC SUMMARY

Assembly	Reliability	
	1 yr	2 yr
Data Control	0.98264	0.93899
Tape Recorder Control	0.99897	0.99602
Tape Recorder	1.00000	0.99996
Telemetry Data	0.99150	0.96890
Remote Decoder	0.99877	0.99518
Clock	0.99963	0.99853
Baseline DHS	0.98890	0.95895
Three-Recorder Assembly	0.99989	0.99919
Alternate DHS	0.98879	0.95823

The data control assembly is regarded as a convenience item: its loss entails a loss of stored-command capability, and a consequent loss of operational efficiency. The resulting loss of experimental data would be sensitive to the experiment program, which could, possibly, be arranged to greatly alleviate the effects of this loss.



NOTES:

1. REMOTE DECODERS FOR ASCS, GEP, EXPERIMENTER'S COMPUTER OMITTED.
2. ROM FOR LAUNCH FORMAT OMITTED.
3. TAPE RECORDER ASSEMBLY ANALYZED BY LOAD-SHARING MODEL WITH VARYING FAILURE RATES.
4. RELIABILITY OF DATA CONTROL ASSEMBLY DOES NOT AFFECT SYSTEM RELIABILITY.
5. APPROXIMATE CLOCK MODEL USED.

Figure G-8. DHS reliability model.

The clock assembly analyzed is that proposed by GAC in their Phase B HEAO-A and -B final reports; the clock proposed for the baseline is a new design for which insufficient data exist for a realistic reliability estimate.

Table G-9 also displays the reliability of a tape recorder assembly with three recorders in place of the four of the baseline, and, as an alternate, the effect of deleting one recorder on the baseline reliability. Clearly, the reliability numerics do not support a need for four recorders. The baseline was not altered because the tape recorder reliability data were received late in the study.

In normal operation, one memory/processor unit of the data control assembly is online at all times and the backup unit is subject to 5 percent utilization. Letting λ denote the memory/processor unit failure rate, the backup unit has an effective failure rate determined from

$$\lambda (0.05t) + (0.1 \lambda) (0.95t) = 0.145\lambda t .$$

The data control assembly reliability formula is then derived as

$$R(t) = \frac{1}{145} e^{-\lambda t} (1145 - 1000e^{-0.145t}) .$$

The failure rate of 1.8 PPMH for the remote decoder is an estimate for a proposed design. It was determined that the use of parallel decoders is necessary to prevent an unacceptable degradation of the DHS reliability. The remote decoder assembly reliability formula is, then,

$$R(t) = e^{-5\lambda t} (2 - e^{-\lambda t})^5 .$$

The baseline telemetry data assembly includes a ROM used during the launch phase. Since failure of this unit after completion of the launch phase has no effect, and since launch phase reliability has not been assessed, this ROM was omitted here. Letting λ denote the sum of the failure rates for the format generator, ROMs, and PCM encoder, the telemetry data assembly reliability formula is

$$R(t) = e^{-\lambda t} (11 - 10e^{-\lambda t/10})$$

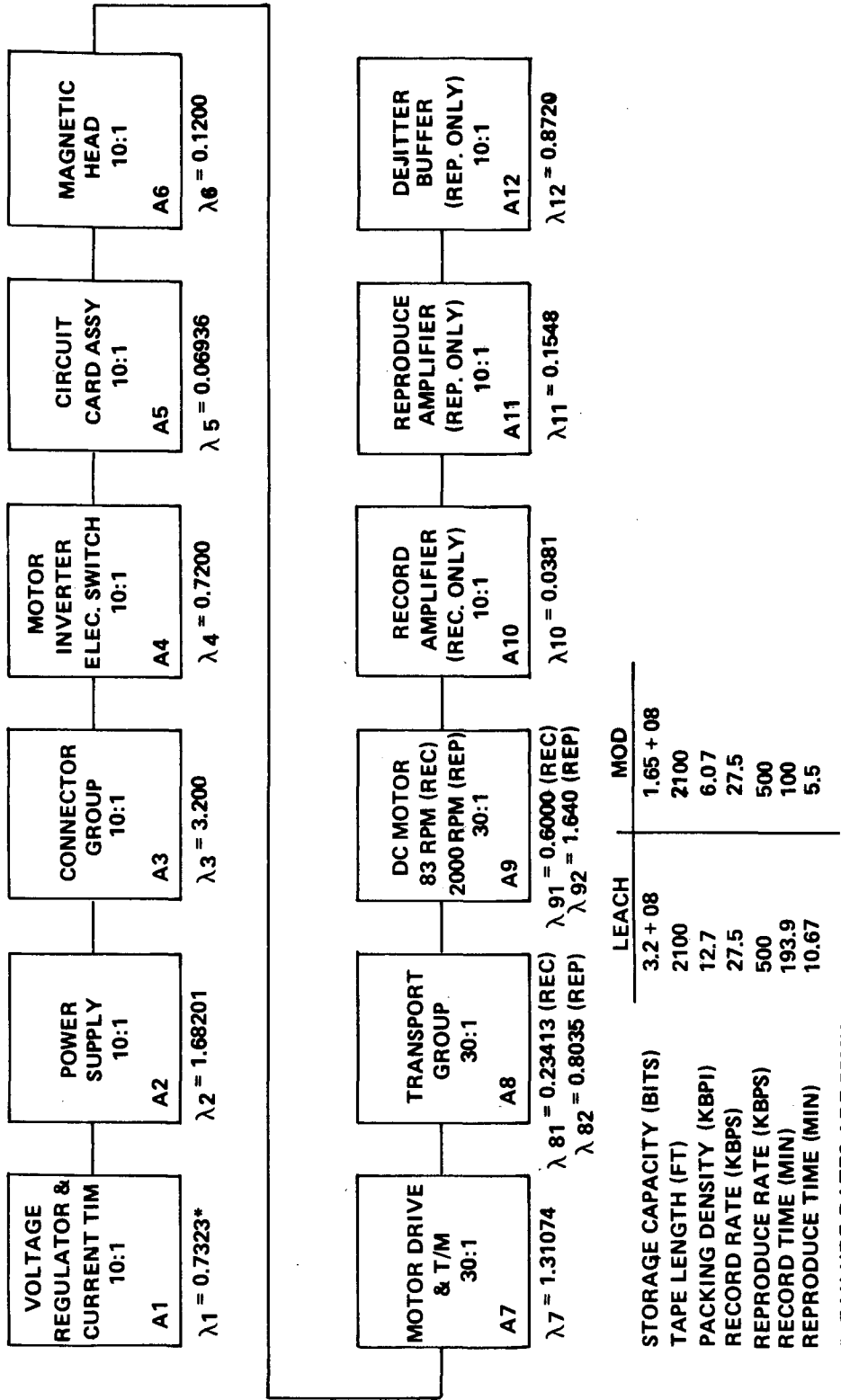
The reliability formula for the clock and tape recorder assemblies is of the same form. As noted above, lack of detailed piece-part information for the proposed clock design necessitates use of an approximate model.

Remote multiplexers are considered a part of the DHS although distributed throughout the other subsystems. An exercise was conducted to assess the reliability impact of multiplexing on the ASCS. The effect was found to be negligible when parallel units were employed. In view of this result, and the consideration that data multiplexing requirements will become firm only during the latter stages of the design process, it was decided to exclude these elements from the reliability analysis.

The tape recorders have been subjects of primary concern, with two potential life-limiting components being of particular interest: Magnetic heads and recorder springs. The head life problem appears to have been solved by the use of an alfesil alloy coating deposited directly on a standard ferrite core. While further testing should be required, the data of Reference G-5 indicate a head life potential approaching 40 000 hours continuous use.

Test data received from RCA [G-6] indicate a mean cycle life of approximately 10 000 cycles for a 301 stainless steel alloy negator spring, and additional test data from the Odetics Corporation [G-7] indicate a life in excess of 21 000 cycles for a second spring of the same material. The Leach Corporation has provided verbal assurance that the spring proposed for its recorder (of the same material) is guaranteed to 13 000 cycles by its manufacturer, and that a 22 000 cycle guarantee is available for a heavier spring. The variability in observed spring life may be explained by the test conditions. Thus, while life tests under the operating conditions of the HEAO applications is recommended for negator springs, a cycle life assumption of 10 000 cycles seems credible.

Figure G-9 gives a reliability block diagram applicable to the Leach 2000 series tape recorder as configured for the HEAO-C application. Changes from the original Leach configuration are given as a "mod." No failure rate adjustments for assemblies A7, A8, and A9 were made to compensate for the higher tape speed required by the lower packing density. Some change in the failure rate for assembly A5 will probably be warranted by the data encoding scheme used. The term "inverter switch" is a holdover from a



	LEACH	MOD
STORAGE CAPACITY (BITS)	3.2 + 08	1.65 + 08
TAPE LENGTH (FT)	2100	2100
PACKING DENSITY (KBPI)	12.7	6.07
RECORD RATE (KBPS)	27.5	27.5
REPRODUCE RATE (KBPS)	500	500
RECORD TIME (MIN)	193.9	100
REPRODUCE TIME (MIN)	10.67	5.5

* FAILURE RATES ARE PPMH

Figure G-9. Tape recorder block diagram.

configuration using an ac motor: A dc brushless motor is used. Figure G-10 condenses the reliability diagram and illustrates the procedures used to adjust the failure rates for duty-cycling. The effective failure rate shown for the case when one recorder is operational is predicated on the assumption that the recorder fills to capacity before dumping; this is slightly inaccurate, but should not affect the results significantly. Figures G-11 and G-12 describe the reliability models used. The use of these models is justified by the longer negator spring cycle life.

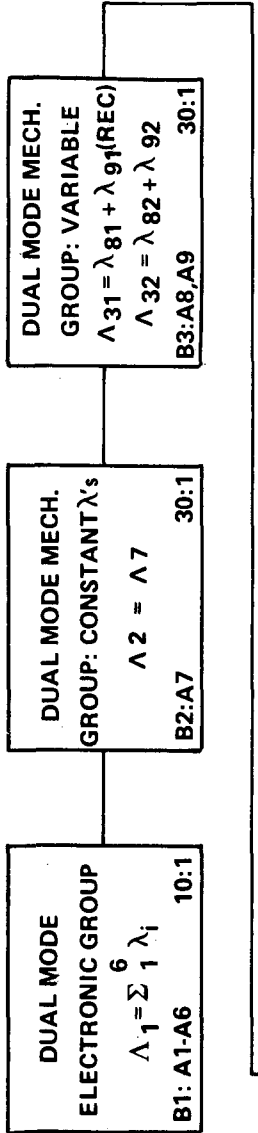
6. Reaction Control System. An RCS schematic is given by Figure G-13. The results of this analysis are summarized in Table G-10

TABLE G-10. RCS RELIABILITY NUMERICS SUMMARY

Assembly	Reliability	
	1 yr	2 yr
Propellant	1.00000	0.93920
Thruster	0.99739	0.98966
RCS Electronics	1.00000	0.99999
Baseline RCS	0.99739	0.92948

For reliability purposes, the RCS consists of three major serial blocks: thruster, propellant, and RCS electronics. The thruster block consists of four identical subblocks, each of which represents a reaction engine module (REM), as shown in Figure G-13. Each thruster, or reaction engine assembly (REA) consists of a valve, catalyst bed, combustion chamber, and temperature and pressure transducers. The Rocket Research Corporation MR-50A 5 lb thrust engine was selected for the baseline design as representative of this class of thruster. The REM failure modes are the following:

1. Any REA failed open and the accompanying latching valve failed open.



- $\Lambda_1 = 6.52367$
- $\Lambda_2 = 1.31074$
- $\Lambda_{31} = 0.83413$
- $\Lambda_{32} = 2.4435$
- $\Lambda_4 = 0.0381$
- $\Lambda_5 = 0.8720$

- $\lambda_{\text{eff}}^{(4)} = 3.0116 \ 32772$
- $\lambda_{\text{eff}}^{(3)} = 3.7260 \ 04252$
- $\lambda_{\text{eff}}^{(2)} = 5.1547 \ 47212$
- $\lambda_{\text{eff}}^{(1)} = 8.1968 \ 66919$

FAILURE RATE DUTY CYCLE ADJUSTMENT EXAMPLE: 4 RECORDERS

RECORD TIME = 100 MIN REPRO. TIME = 5.5 FILL/DUMP TIME = 400 MIN

B1: $\Lambda_1 (105.5/400t) + 0.1\Lambda_1 (400-105.5/400t) = 0.337375 \Lambda_1 t$

B2: $\Lambda_2 (105.5/400t) + 1/30 \Lambda_2 (400-105.5/400t) = (0.28829 \ 16666) \Lambda_2 t$

B3: $\Lambda_{31} (100/400t) + \Lambda_{32} (5.5/400t) + 1/30 \Lambda_{32} (400-5.5/400t) = 0.25 \Lambda_{31} t + 0.046625 \Lambda_{32} t$

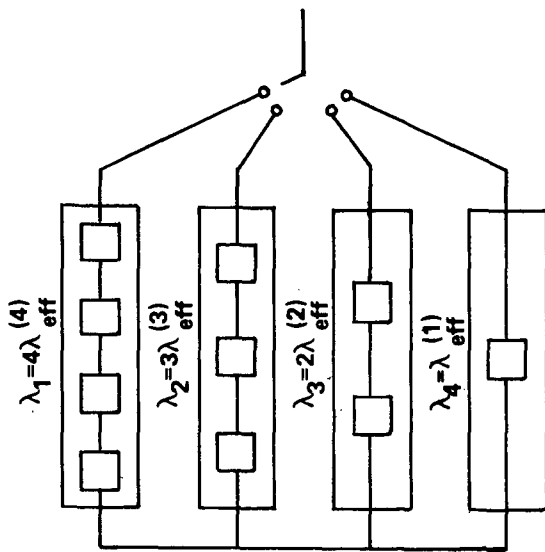
B4: $\Lambda_4 (100/400t) + 0.1\Lambda_4 (400-100/400t) = 0.325 \Lambda_4 t$

B5: $\Lambda_5 (5.5/400t) + 0.1\Lambda_5 (400-5.5/400t) = 0.112375 \Lambda_5 t$

EFFECTIVE FAILURE RATE

$\lambda_{\text{eff}}^{(4)} = (0.337375) \Lambda_1 + (0.28829 \ 1666) \Lambda_2 + (0.25) \Lambda_{31} + (0.046625) \Lambda_{32} + (0.325) \Lambda_4 + (0.112375) \Lambda_5$

Figure G-10. Tape recorder block diagram (condensed).



$$P_0(t) = e^{-\lambda_1 t}$$

$$P_1(t) = \frac{\lambda_1}{\lambda_2 \lambda_1} \left[e^{-\lambda_1 t} - e^{-\lambda_2 t} \right]$$

$$P_2(t) = \frac{\lambda_1 \lambda_2}{\lambda_2 \lambda_1} \left\{ \frac{1}{\lambda_3 \lambda_1} (e^{-\lambda_1 t} - e^{-\lambda_3 t}) - \frac{1}{\lambda_3 \lambda_2} (e^{-\lambda_2 t} - e^{-\lambda_3 t}) \right\}$$

$$P_3(t) = \frac{\lambda_1 \lambda_2 \lambda_3}{\lambda_2 \lambda_1} \left\{ \frac{1}{\lambda_4 \lambda_1} \left[\frac{1}{\lambda_3 \lambda_1} (e^{-\lambda_1 t} - e^{-\lambda_4 t}) - \frac{1}{\lambda_4 \lambda_3} (e^{-\lambda_3 t} - e^{-\lambda_4 t}) \right] - \frac{1}{\lambda_3 \lambda_2} \left[\frac{1}{\lambda_4 \lambda_2} (e^{-\lambda_2 t} - e^{-\lambda_4 t}) - \frac{1}{\lambda_4 \lambda_3} (e^{-\lambda_3 t} - e^{-\lambda_4 t}) \right] \right\}$$

PROBABILITY OF 2 OR MORE RECORDERS:

$$R(2;t) = \sum_{k=0}^2 P_k(t)$$

PROBABILITY OF 1 OR MORE RECORDERS

$$R(t) = \sum_{k=0}^3 P_k(t)$$

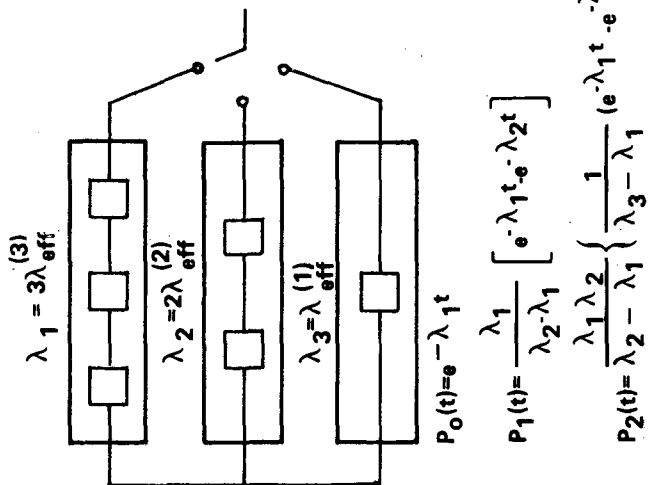
$$\lambda_1 = 12.046 \ 53108$$

$$\lambda_2 = 11.178 \ 01275$$

$$\lambda_3 = 10.309 \ 49442$$

$$\lambda_4 = 8.9168 \ 66919$$

Figure G-11. Reliability model: Four tape recorders.



$\lambda_1 = 11.178 \ 01275$
 $\lambda_2 = 10.309 \ 49442$
 $\lambda_3 = 8.9168 \ 66919$

PROBABILITY OF 2 OR MORE RECORDERS:

$$R(2;t) = \sum_{k=0}^1 P_k(t)$$

PROBABILITY OF 1 OR MORE RECORDERS:

$$R(t) = \sum_{k=0}^2 P_k(t)$$

Figure G-12. Reliability model: Three tape recorders.

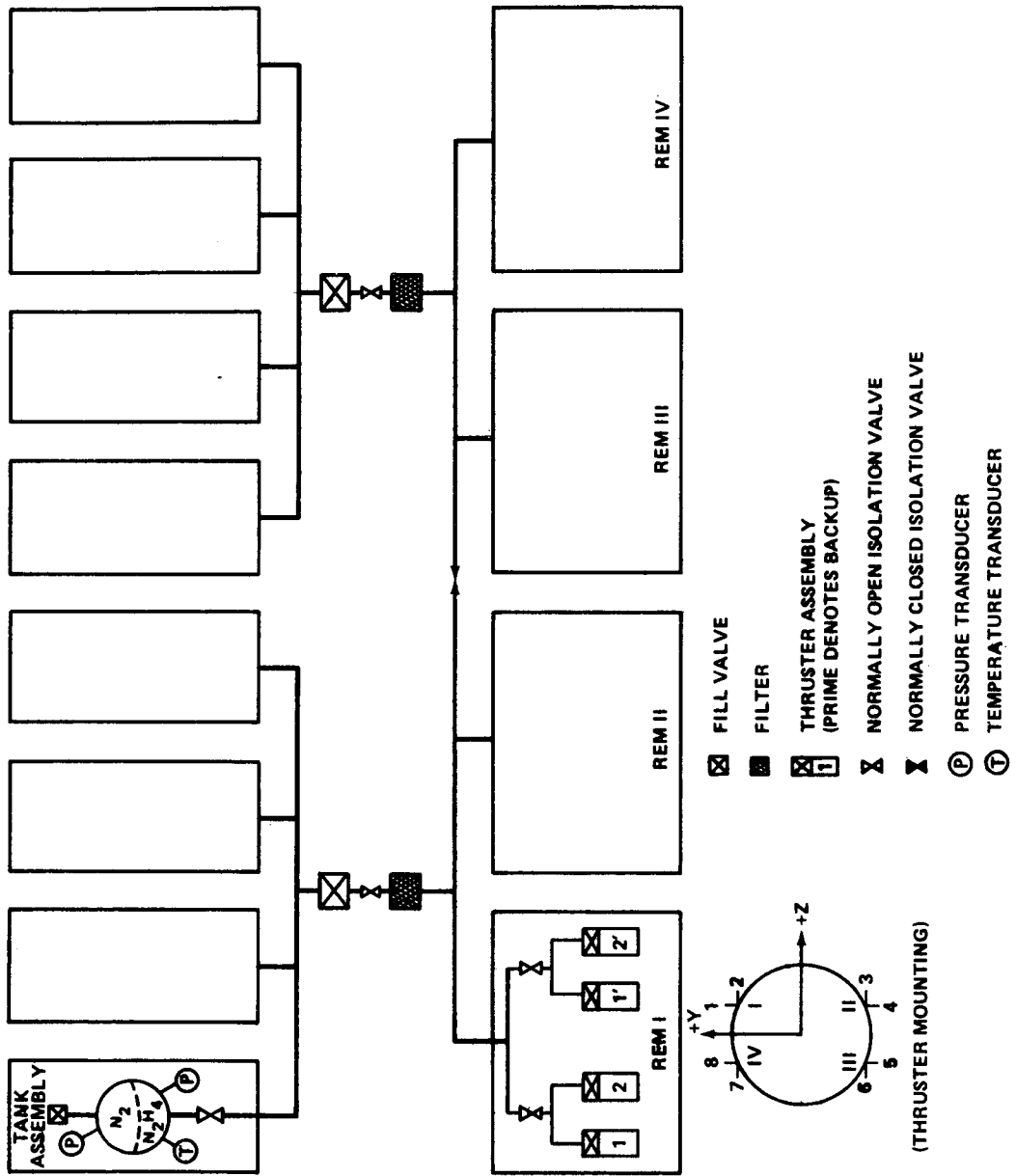


Figure G-13. RCS schematic.

2. Any REA failed open and either the latching valve of the redundant pair failed shut or either REA of the redundant pair failed.
3. Any two like-numbered REAs failed.
4. Any REA failed shut and the latching valve of the redundant pair failed shut.
5. Both latching valves failed shut.

The REA valves require current to remain open, so that any engine-open condition can be attributed to an RCS electronics failure. The Carleton Controls Corporation latching solenoid valve, Part No. 2217001, as qualified for Intelsat IV, was chosen for the baseline isolation valving to provide a source of numerical failure data. The REA isolation valves are normally open, are closed only in the event of an REA failure, and remain closed only in the case of an REA open or severe leakage condition. Thus, the reliability effect of operation of these valves is infinitesimal, and the problem of ambient leakage is minor when compared to the REA unreliability. The MR-50A is presently qualified for 175 000 cycles, which does not quite meet the current HEAO-C worst case single-thread estimate of 211 090 cycles. Taking 72 500 cycles as a more reasonable estimate converts the 0.7 PPMC failure rate quoted by GAC to 2.895 PPMH. Allowing a 30:1 failure rate reduction for standby status yields the reliability formula

$$R_{\text{REA}}(t) = e^{-8\lambda t} (31 - 30e^{-\lambda t/30})^8 .$$

Acceptance of these numbers should be contingent upon acceptance of the assumption that the impulse requirement for each REA is the same. With this assumption, each REA pair (primary and backup) has a total impulse requirement approaching the 18 000 lb-sec qualification limit of the MR-50A.

The propellant block consists of the propellant and pressurant fill valves, the tanks and their bladders, heaters, pressure and temperature sensors, various isolation valves, and the two filters as shown in Figure G-13. The normally closed central latching valve will be cycled as necessary to prevent buildup of a pressure differential between the two halves of the propellant block.

The two year propellant block reliability, because of the lack of a

propellant margin, is just the probability that all essential elements survive. Table G-11 is used to deduce the failure rate for this case.

TABLE G-11. TWO YEAR PROPELLANT BLOCK FAILURE RATES

Component	Failure Rate		
	Quantity, n	λ (PPMH)	λn
Fill Valve (leakage)	10	0.01	0.1
Tank	8	0.07	0.56
Bladder	8	0.33	2.64
Isolation Valve (leakage)	11	0.01	0.11
Temperature Transducer (leakage)	8	0.005	0.04
Pressure Transducer (leakage)	16	0.005	0.08
Filter (leakage)	2	0.024	0.048
TOTAL			<u>3.578</u>

The two year reliability is, then,

$$R(2 \text{ yr}) = \text{Exp} - (3.578 \times 10^{-6} \times 17532)$$

At any time t less than two years, the propellant block reliability is just the probability of having a positive amount of propellant in at least one tank and operational plumbing/valving by which this propellant may be delivered to the thruster block. For this case, the concept of a tank assembly (Fig. G-13) is introduced. The failure rate of each of these assemblies is then 0.435 PPMH. The contribution of the propellant fill valves, filters, and the remaining three isolation valves is negligible by comparison. The propellant block reliability is not less than the probability of success of four or more tank assemblies, and this number cannot be distinguished from unity by a careful calculation.

The RCS electronics block consists of two sets of RCS electronics. With the 1.63 PPMH failure rate quoted by GAC, a 5 percent utilization factor, and a 10:1 failure rate reduction for standby status (unpowered), the applicable formula is

$$R(t) = e^{-0.145\lambda t} (2.45 - 1.45e^{-0.1\lambda t})$$

Conclusions And Recommendations

Despite the limitations of the foregoing analyses, two conclusions are indicated:

1. Four CMGs with RCS momentum desaturation does not quite provide the desired reliability.
2. Three tape recorders are adequate to meet both reliability and operational requirements.

Certain further studies are clearly desirable in consequence of the reliability analyses above. These include the following:

1. CMG versus Magnetics. Although not a reliability study per se, two means of increasing the ASCS reliability are (a) use of additional CMGs, and (b) use of a magnetic coil momentum desaturation system. While operational capability will be the primary determinant for system selection, a reliability goal must be met.

2. Negator Spring Life Tests. The data referenced in this report indicate that the tape recorder negator spring cycle life estimates used in the phase B HEAO-A and -B studies have been unduly pessimistic: a mean cycle life in excess of 10 000 cycles may not be unreasonable, and this figure may be doubled by use of a heavier spring. It is recommended that negator spring life tests be conducted to determine empirical failure distribution laws with sufficient parametric data to apply these laws to the environments which this component will experience in the HEAO applications.

3. Alfesil Magnetic Head. While the lifetime of the alfesil-coated, ferrite core, magnetic recording head appears to be approximately an order of magnitude better than that obtainable with other head designs, a life test under the HEAO application environments should be conducted.

4. Battery Failure Rate Data. The problems encountered with battery reliability estimation have been described above. Accordingly, a careful survey of previous experience with this type of battery should be made to determine if the parameters noted can be adequately quantified. Particular attention should be paid to the environmental and operational conditions of the HEAO applications. If indicated, experimental demonstration of the battery reliability parameters should be undertaken.

5. Hardware Qualification Limits. A number of qualification limits are implied in the discussion above. Life-qualification of gyros and RCS thrusters under the impulse and cycle requirements of the HEAO applications are two additional qualification limits to be established. Additional qualification limits will become apparent as the design definition progresses.

A final recommendation is that Reference G-8 be taken as a basic source of failure rate data. Future HEAO studies should document k-factors used to adjust the failure rates of this source to specific applications, with deviations supported by test data or reliability analyses conducted in accordance with the applicable NASA standards.

While definitions of an overall numerical reliability requirement should be contingent upon the mission worth/cost studies described elsewhere in this report, an overall spacecraft one year numerical reliability goal of approximately 0.95 can be anticipated. As noted above, launch phase and experiment reliabilities and the reliability effects of the system integration hardware required for redundancy switching and for checkout and fault isolation have not been assessed. When these exclusions are taken into account, it is likely that the resulting reliability numerics will necessitate some additional redundancy and/or redesign.

Degraded Mode Assessment

The results of the classical numerical reliability analysis were used as a guide rather than a rigid requirement in designing the HEAO-C systems. Since such an analysis depends on the definition of "success," and success is a relative rather than an absolute quantity, engineering judgement must be utilized with the reliability numerical analysis to obtain a reliable but practical design. Using this philosophy, a concept of "Mission Worth" and degraded mode operation was defined giving a measure of the probability of having a fairly high degree of success in high failure conditions

of operation. The single parameter which gives the best indication of mission success (from the spacecraft systems standpoint) is "percent of valid data returned." Here it must be assumed that the data are "valid" if all systems are performing per specifications. The data collected early in the mission will be more valuable than data collected later in the mission, for several reasons, including the following ones:

1. The most interesting targets will be selected for viewing early in the missions.
2. Experiments and/or systems may degrade later in the mission.
3. More sophisticated experiments on other spacecraft may be launched during the mission.
4. HEAO-C priority on the tracking network decreases with time in orbit.

A quantity denoted as "Mission/Data Worth" was defined to be a measure of the instantaneous value of the data being generated at any time. A model showing the Mission/Data Worth for the entire mission is shown in Figure G-14 and a table showing cumulative Mission/Data Worth for each month of the mission is provided as Table G-12. Such a model seems to be practical and realistic to most Principal Investigators (PIs) and engineers with whom it was discussed during the study. The Mission/Data Worth does not decrease as rapidly as models generated earlier [G-1 and G-2] for Missions A and B (cube root and square root models); this seems to be logical, since HEAO-A and -B repeat their scans of the celestial sphere each 6 months (although they point at progressively more and more sources), whereas HEAO-C will point at different sources (albeit increasingly less interesting sources).

Consequently, using the foregoing philosophy, the quantity which should be utilized to measure mission success is the total returned data worth (the total data returned multiplied by the value of data). The common denominator for determining the contribution of each system to the mission success is the number of months of successful operation of that system.

The guidelines used for the degraded mode analysis are listed in Table G-13. An indication of the capability of the spacecraft to operate in high-failure conditions is provided in Table G-14. The level of success shown in the table is based on the capability of the spacecraft after the cited failure mode has occurred. The data in Table G-14 assume that the cited failures occurred early in the mission, which gives more pessimistic results than assuming failures are distributed over the entire mission lifetime. The true mission success level is dependent

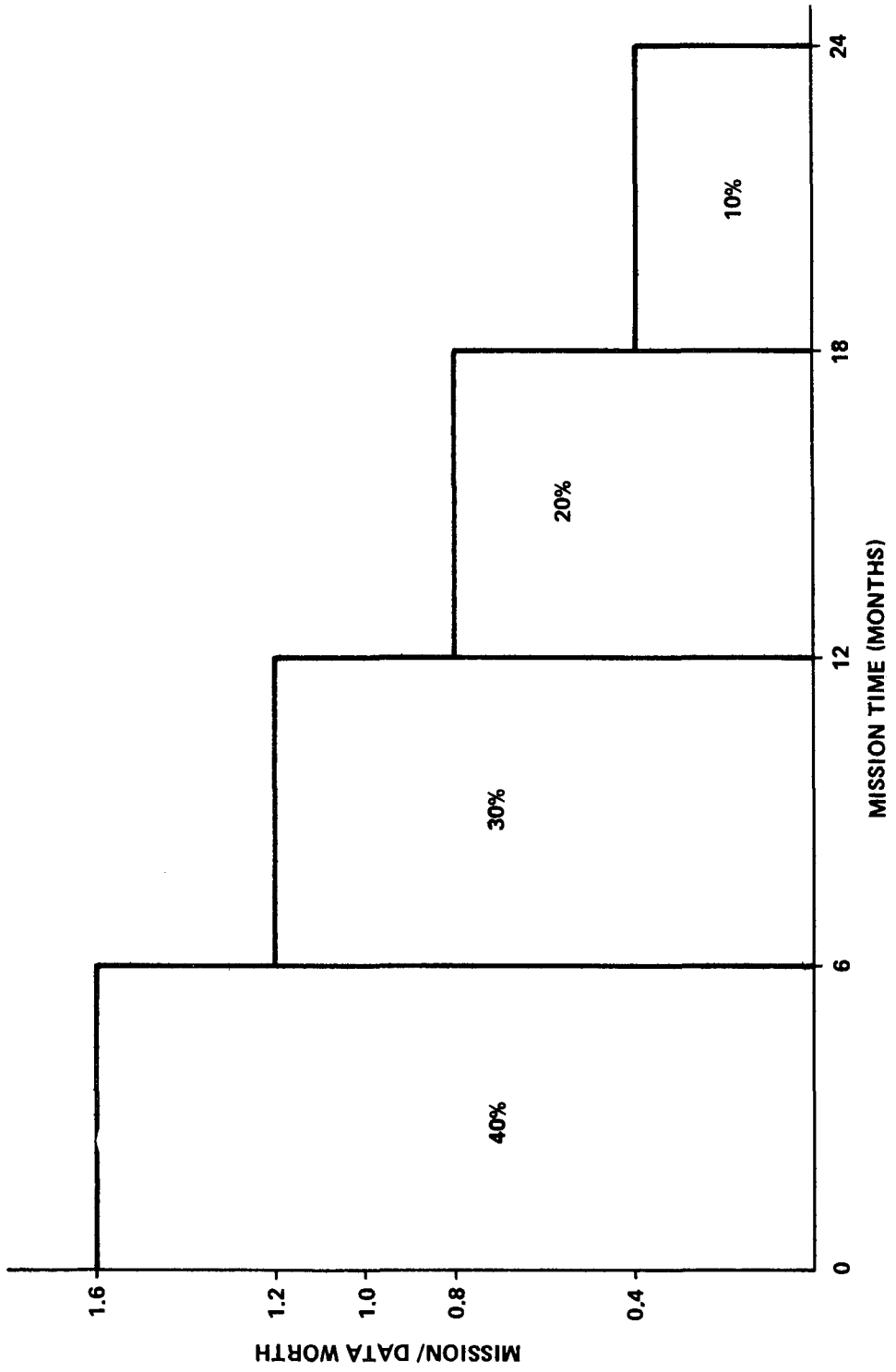


Figure G-14. Mission/Data Worth.

TABLE G-12. CUMULATIVE MISSION/DATA WORTH

(Months)	Cumulative Worth (%)	Time (Months)	Cumulative Worth (%)
1	6.67	13	73.35
2	13.34	14	76.68
3	20.01	15	80.01
4	26.68	16	83.34
5	33.35	17	86.67
6	40.02	18	90.00
7	45.02	19	91.67
8	50.02	20	93.34
9	55.02	21	95.01
10	60.02	22	96.68
11	65.02	23	98.35
12	70.02	24	100.02

TABLE G-13. DEGRADED MODE ANALYSIS GUIDELINES

- Degraded modes of operation should be analyzed to determine the overall spacecraft performance margin and should influence the reliability assessments to ensure a very practical approach to reliability.
- The basic trade performed in degraded mode analysis is level of data return versus lifetime; the basic criterion used for selection is total returned data worth.
- If there is a high probability of achieving at least 75 percent of the total mission/data worth in high failure conditions, then no additional redundancy should be added unless strongly justified.
- Component failures should be assumed to be distributed evenly over the two year mission period, for degraded mode analysis.

TABLE G-14. DEGRADED MODE ASSESSMENT

System	System 2 Yr Probability of X % or Better Success (Degraded)	Post-Failure Level of Success (X%)	Conditions Existing
Data Handling			
Degraded Mode 1	0.873	90	Loss of three tape recorders. Assume level of success due to required change in data dump scheme.
Degraded Mode 2	0.946	60 ^a	Loss of onboard command storage capability. Quantity of targets investigated limited to realtime commands.
Electrical Power			
Degraded Mode 1	0.971	40	Loss of four of the six batteries. Limits life of remaining batteries to 3000 total cycles (slightly over 6 months).
Degraded Mode 2	0.979	85	Loss of three of the four regulators. Limits the power available to 400 watts due to regulator rating. This is 55 percent of the power required for full operation.

a. Assumes all available MSFN stations usable.

TABLE G-14. DEGRADED MODE ASSESSMENT (Concluded)

System	System 2 Yr Probability of X % or Better Success (Degraded)	Post-Failure Level of Success (X%)	Conditions Existing
Attitude Sensing and Control			
Degraded Mode 1	0.803	>95	Loss of coarse sun sensing ability
Degraded Mode 2	0.935	~20	Loss of two CMGs. RCS used to control one axis. Experiment limited to flare detector, monitor proportional counter and solid-state detector due to pointing accuracy limitation.
Reaction Control Degraded Mode 1	0.998	85	Loss of two propellant tanks. Limits life of mission.

on the time of failure. For example, degraded mode two of the ASCS leaves enough capability to still perform some experiments. If this failure mode occurs at mission beginning, the most data available is approximately 20 percent of spacecraft capability. If this failure mode occurs at the one year point, the mission worth would be 70 percent (first year contribution) plus the worth after the failure.

It is recommended that a more extensive analysis of degraded modes of operation be undertaken in the next phase of the study. In particular, it would be desirable to have high(er) reliability and extra confidence in the functions and hardware which make the greatest contribution to the value of the scientific objectives. An attempt should be made to identify those spacecraft operating parameters and hardware components which would have the greatest adverse effect on the experiments in the event of their degradation or failure. Having identified these functions, a maximum amount of backup for them should be provided in the spacecraft design. Each Principal Investigator should be requested to help provide judgment of the relative value of his experiments by providing information such as that listed below, based on the present concept of his experiment:

1. Rank each of the experiments (combination of end items of hardware and the applicable modes) according to relative importance with respect to each other.
2. With each of the above experiments, which of the following spacecraft parameters are the most critical in terms of adverse effect on experiment if they degrade?
 - a. Long-term drift (stability).
 - b. Short-term drift (jitter rate).
 - c. Pointing accuracy.
 - d. Clock accuracy and resolution.
 - e. Clock stability.
 - f. Aspect quality (includes experiment aspect system).
 - g. Misalignment.

Even if coalignment degrades considerably, it is assumed that all experiments could still be pointed to a source sequentially. Therefore, the greatest effect that should be considered here is the loss of simultaneous data from a source on all experiments.

3. Provide a graph showing how the most critical experiment parameters vary as a function of the most critical spacecraft parameter(s) defined in item 2 above. On the same graph, show the data rate and data handling impact as a function of the variation in spacecraft parameter(s).

Reliability Versus Cost Assessment

Figure G-15 shows the cost penalty for increasing reliability above the level of the present baseline spacecraft. The redundancy has been added in a manner which optimizes reliability increase per cost increase. Table G-15 provides the data used for the two year lifetime curve. The sequence of addition of the components is shown, as well as the total quantity, the component cost (hardware only), and resulting spacecraft reliability. (The baseline spacecraft component quantities are listed in Table IV-1.) Costs of implementing the redundancy (design, integration, testing, failure detection, switching logic, etc.) were not included in this analysis; hence, the data is somewhat optimistic.

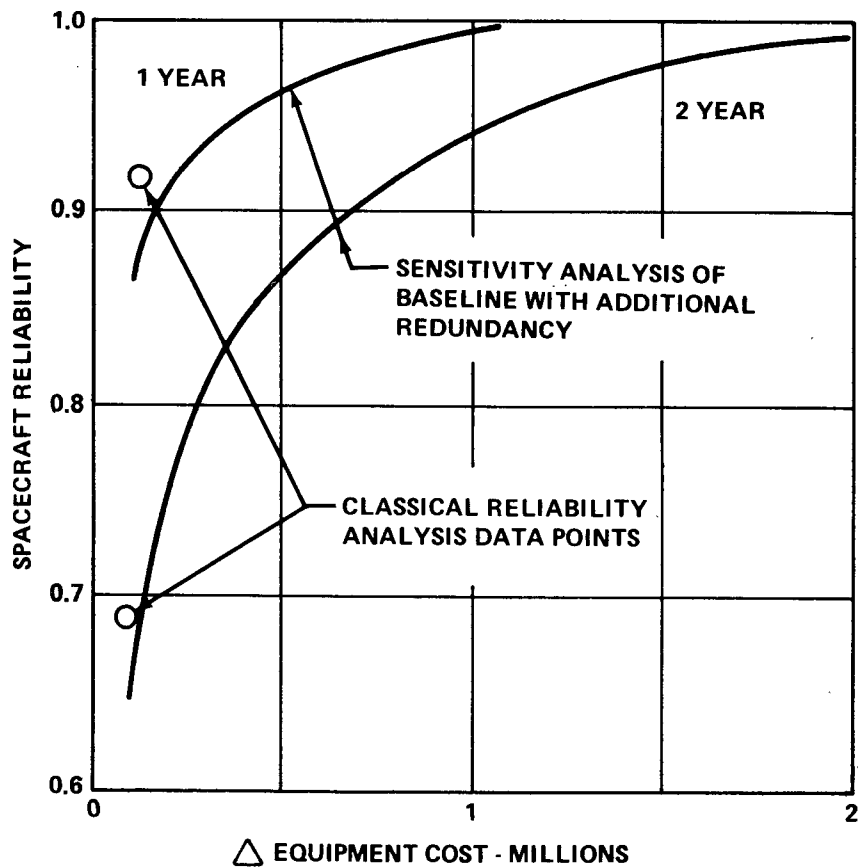


Figure G-15. Reliability versus Δ cost.

TABLE G-15. RELIABILITY VERSUS Δ COST DATA (2 YEAR LIFETIME)

Added Component	Spacecraft Total Quantity	Component Cost (\$)	Spacecraft Reliability
1. Baseline Spacecraft Total (2 yr)			0.6433
2. Read Only Memory	2	1 000	0.6541
3. Data Storage Control	2	30 000	0.6953
4. Electrical Integration Assembly	9	2 000	0.6972
5. Memory	3	20 000	0.7085
6. Receiver	5	37 500	0.7284
7. Command Processor	3	20 000	0.7380
8. Regulator	5	30 000	0.7506
9. CMG Electronics	5	172 000	0.8318
10. Solar Panel Deployment Mechanism	7	10 000	0.8362
11. Remote Decoder	13	8 000	0.8396
12. Processor/Computer	4	99 000	0.8658
13. Battery Charger	7	100 800	0.8872
14. Electrical Integration Assembly	10	2 000	0.8877
15. Transfer Assembly	2	99 000	0.9061
16. DSS Electronics	3	52 000	0.9153
17. Rate Gyros Set (3 Gyros)	3	60 000	0.9260
18. PCM Encoder	3	60 000	0.9359
19. Thruster Modules	5	57 000	0.9453
20. Read Only Memory	3	1 000	0.9454
21. CMG Electronics	6	172 000	0.9634
22. Remote Decoder	14	8 000	0.9642
23. Format Generator	3	40 000	0.9676
24. Power Control Assembly	3	25 000	0.9697
25. Regulator	6	30 000	0.9719
26. Data Storage Control	3	30 000	0.9738
27. Cabling Conversion Set	3	2 000	0.9739
28. Processor/Computer	5	99 000	0.9792
29. Clock	2	26 000	0.9806
30. Memory	4	20 000	0.9816
31. Tube Insulation	2	4 000	0.9818
32. Coatings	2	4 500	0.9819
33. Outer Shell Insulation	2	4 500	0.9821
34. Battery Charger	8	100 800	0.9860
35. Command Processor	4	20 000	0.9867
36. Electrical Integration Assembly	11	2 000	0.9868
37. CMG Electronics	7	172 000	0.9895
38. Remote Decoder	15	8 000	0.9896
39. Star Tracker Electronics	5	150 000	0.9913

These data were generated using a more simplified reliability model than that utilized in the numerical reliability analysis, but the correlation shown in Figure G-15 is fairly good and the curves can be used to represent trends.

There is no power increase for the added components, since they are in standby condition. Weight increases may become a critical factor as more and more redundancy is added (the total weight increase for the items in Table G-15 would approach 1500 pounds just for the components), but it is estimated that either a cost or complexity limit, or both, will be reached first. Volume limitations could also present a problem, particularly if mounting on the antisolar side of the spacecraft is required for thermal control reasons. A more detailed assessment of the cost and complexity factors associated with addition of redundant components should be made in the next phase of the study.

It is believed that the optimum program cost effectiveness across all missions will be achieved by specifying mission lifetimes and reliabilities as nearly the same as possible for all missions. This is, of course, more critical for the more life-limited hardware items but is true, in general, of all hardware.

REFERENCES

- G-1. TRW Systems Group: High Energy Astronomy Observatory Phase B Final Study Report. NASA Contract NAS8-26273, April 1971.
- G-2. Grumman Aerospace Corporation: High Energy Astronomy Observatory Phase B Final Study Report. NASA Contract NAS8-26272, April 1971.
- G-3. Gilmore, Jerold P.: A Non-Orthogonal Gyro Configuration. M.S. Thesis, M.I.T., 1967.
- G-4. Crisp, Robert, et al.: SIRU - A New Inertial System Concept for Inflight Reliability and Maintainability. MIT Instrumentation Lab. Report E-2407, 1969.
- G-5. NASA Tech. Brief 70-10521, 1970.
- G-6. RCA Defense Communication Systems Division: Design Study Report, Vol. I. Transport Unit, NAS5-11643, Goddard Space Flight Center.
- G-7. Bartholet, Stephen J.: Life Test of Constant Torque Spring Motors. Odetics Corp. Report, 1970.
- G-8. RADC Reliability Notebook, Vol. II.

HIGH ENERGY ASTRONOMY OBSERVATORY
MISSION C
PHASE A FINAL REPORT

Volume III – Appendices


By Program Development

The information in this report has been reviewed for security classification. Review of any information concerning Department of Defense or Atomic Energy Commission programs has been made by the MSFC Security Classification Officer. This report, in its entirety, has been determined to be unclassified.

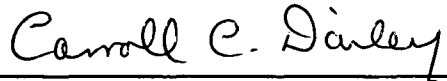
This document has also been reviewed and approved for technical accuracy.

APPROVAL:

CONCURRENCE:



JAMES W. HEYER, Assistant Director
Preliminary Design Office
Program Development



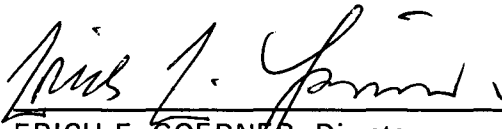
CARROLL C. DAILEY, Manager
HEAO Experiments Office
Program Management



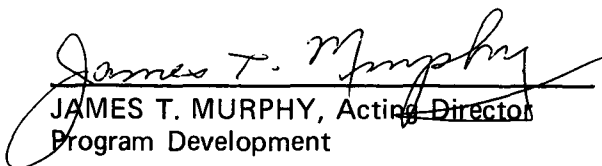
HERMAN P. GIEROW, Acting Director
Mission and Payload Planning Office
Program Development



F. A. SPEER, Manager
HEAO Office
Program Management



ERICH E. GOERNER, Director
Preliminary Design Office
Program Development



JAMES T. MURPHY, Acting Director
Program Development